Journal of Experimental and Theoretical Physics, Vol. 96, No. 6, 2003, pp. 1006–1018.
Translated from Zhurnal Éksperimental'noĭ i Teoreticheskoĭ Fiziki, Vol. 123, No. 6, 2003, pp. 1145–1159.

ATOMS, SPECTRA, RADIATION

Higher Orders of Perturbation Theory for the Stark Effect on an Atomic Multiplet

I. L. Bolgova[a], V. D. Ovsyannikov[a], V. G. Pal'chikov[b,*], A. I. Magunov[c], and G. von Oppen[d]

[a]*Physics Department, Voronezh State University, Voronezh, 394006 Russia*
[b]*National Research Institute for Physical–Technical and Radiotechnical Measurements, Mendeleevo, Moscow oblast, 141570 Russia*
**e-mail: palchikov@yahoo.com*
[c]*Institute of General Physics, Russian Academy of Sciences, Moscow, 119991 Russia*
[d]*Technical University, Berlin, D-10623, Germany*

Received November 28, 2002

Abstract—The contribution of higher order corrections to the Stark energy is calculated in the anticrossing region of atomic multiplet sublevels. Perturbation theory for close-lying levels is presented that is based on the Schrödinger integral equation with a completely reduced Green's function. Analytic formulas are obtained for the splitting of two interacting fine-structure sublevels as a function of the field strength. These formulas take into account fourth-order resonance and nonresonance corrections to both the diagonal and the off-diagonal matrix elements of the dipole moment operator. By the method of the Fues model potential, a numerical analysis of radial matrix elements of the second, third, and fourth orders is carried out that determine a variation in the transition energy between $n\,^3P_0$ and $n\,^3P_2$ sublevels of a helium atom for $n = 2, 3, 4, 5$ in a uniform electric field. It is shown that the contribution of the fourth-order corrections in the vicinity of anticrossing of levels for $n = 2, 3, 4, 5$ amounts to 0.1, 5, 10, and 15% of the total variation of energy, respectively. A comparative analysis is carried out with the results of calculations obtained by the method of diagonalization of the energy matrix, which, together with resonance terms, takes into account other states of the discrete spectrum with $n \le 6$.

1. INTRODUCTION

The Stark effect in a constant electric field was calculated for a hydrogen atom and described in detail in textbooks and monographs almost immediately after the origination of quantum mechanics (see, for example, [1, 2]). Nevertheless, this phenomenon has not yet been completely studied and still attracts attention in our time. The experimental studies of the Stark effect have been stimulated by the development of precision methods of laser spectroscopy [3–6]. Theoretical calculations of the shift and broadening of the Stark states in hydrogen atoms carried out by the beginning of the 1980s were based on the iterative solution of the Schrödinger equation involving the separation of variables in a parabolic system of coordinates [2]. The development of computer programs for analytic computations that allowed one to derive general expressions for the coefficients of power series in the field strength for both the shift and the broadening of atomic levels [7, 8] has served as a powerful incentive for the calculation of higher order corrections to energy. Analytic programming has also enabled one to obtain general expressions for perturbation theory series for the wave functions, matrix elements, and radiative transition probabilities between the Stark states of hydrogen [9, 10]. A comparison of the numerical data obtained by these expressions with the results of measuring the field dependence of the probability of radiative transitions between highly excited Rydberg states [11] has shown that the first three terms in powers of the field strength are quite sufficient for calculating the transition probabilities in virtually all situations of interest up to the field value when the above-barrier ionization of the upper level becomes possible.

By the end of 1970s, methods of laser spectroscopy of Rydberg levels had been developed that allowed one to accumulate a large volume of experimental data on the Stark effect in highly excited multielectron atoms [12–15]. These data stimulated the development of simple semiempirical calculation methods for the polarizabilities of atomic levels [16, 17] (including Rydberg levels [18]), as well as the development of exact *ab initio* methods that enable one to consistently take into consideration relativistic and quantum-electrodynamic effects, which play a significant role in the spectra of ions of high degree of ionization [19–22]. In [13–15, 23], it was observed that the Stark effect on multiplet sublevels deviates from the quadratic law even in weak fields. This phenomenon is accounted for by the Stark interaction between sublevels that leads to their repulsion in a field and is determined by the hyperpolariz-

ability of an atom. It was demonstrated that the main (resonance) contribution to the hyperpolarizability of a multiplet sublevel can be expressed in terms of the tensor polarizability of this multiplet [24]. Therefore, precision calculation [25] and measurement [3, 5, 26] of irreducible components of the polarizability tensor of multiplet states of atoms becomes topical.

Precision information about the Stark effect in higher order terms of perturbation theory plays a key role in modern optical frequency standards based on the application of magnetooptical traps in combination with the methods of laser cooling of atoms up to several nanokelvins [27], as well as in the problems of frequency stabilization in atomic standards of a new generation—atomic fountains [28].

The interaction between sublevels of a multiplet in a field may lead to an important phenomenon, the so-called anticrossing [29]. This phenomenon manifests itself when the polarizability of a higher energy sublevel is greater than the polarizability of a lower energy state. Then, in a weak field, the sublevels move closer to each other; i.e., the fine-structure splitting decreases. In a stronger field, the sublevels are repulsed from each other; this repulsion is determined by the resonance part of the hyperpolarizability. The field strength at which attraction turns into repulsion and the minimal value of splitting are uniquely determined by the atomic susceptibilities—the components of the polarizability and hyperpolarizability—and can be calculated theoretically. Usually, the field value corresponding to the anticrossing of levels is sufficiently high; therefore, an appreciable contribution to the energies of states may be made not only by the polarizability and the resonance part of the hyperpolarizability but also by nonresonance additions to the hyperpolarizability.

In [30], fourth-order nonresonance corrections have been calculated to the energy of separate sublevels of a helium atom multiplet. In this case, the resonance hyperpolarizability $\gamma^{(res)}$, which is determined by the off-diagonal matrix elements of the interaction operator between atom and field through the fine-structure states and is expressed in terms of the tensor polarizability α^t, is calculated only in the second order of perturbation theory. This is associated with the fact that, formally, the fourth-order corrections to an off-diagonal element make a correction of order F^6/δ, where δ is a fine-structure splitting value at $F = 0$, to the expression for the fine-structure splitting $\delta(F)$ depending on the field strength F. However, in the anticrossing region, the field amplitude may reach such values that $\alpha^t F^2 \sim \delta$; therefore, the fourth-order corrections to diagonal and off-diagonal matrix elements may make identical contributions to the energy of the multiplet sublevels. Since the fine-structure splitting is a rapidly decreasing function of the effective principal quantum number of an atomic level $\nu = 1/\sqrt{-2E_n}$ (E_n is the binding energy of the level), $\delta \sim \nu^{-3}$ [31], and the polarizabilities and hyperpolarizabilities are rapidly increasing functions, $\alpha \sim \nu^7$ and $\gamma \sim \nu^{17}$ [32], the anticrossing for higher levels occurs in weaker fields, and the contribution of higher order corrections becomes more significant. The first calculations of the nonresonance hyperpolarizability for the triplet state $3\,^3P$ in helium atoms [30] has shown that the contribution of the fourth-order field corrections to the diagonal elements may be several times greater than experimental errors. Therefore, the determination of corrections to the off-diagonal elements also becomes topical.

The main goal of the present paper is to determine the contribution of the fourth-order corrections in the field strength to the energy of multiplet states of an atom near the anticrossing of the fine-structure sublevels. In Section 2, we give a generalization of higher order perturbation theory for degenerate states [33] to the case of close-lying levels that have nonzero splitting in zero field. We obtain expansions of the matrix elements of the interaction Hamiltonian of an atom and a field in powers of the field strength F up to the fourth order. In Section 3, the coefficients of these expansions are expressed in terms of irreducible parts—scalar and tensor polarizabilities and hyperpolarizabilities—which, in turn, are represented by linear combinations of radial matrix elements of the second, third, and fourth orders. In Section 4, we derive general expressions for the field-dependent splitting of two interacting fine-structure sublevels. The fine-structure splitting of $n\,^3P$ states of helium ($n = 2, 3, 4, 5$) is calculated numerically as a function of F; in zero field, these states have total momenta of $J = 0, 2$ and a projection of $M = 0$. The contribution of the fourth-order corrections in the field region of level anticrossing is determined.

2. HIGHER ORDER PERTURBATION THEORY FOR CLOSE-LYING LEVELS

The calculation of higher order corrections to the Stark effect for atomic multiplet sublevels requires a consistent development of perturbation theory for close-lying levels. Suppose that $\hat{H}_0(\mathbf{r})$ is a one-electron Hamiltonian of a valence electron with eigenfunctions $\phi_{nLSJ}(\mathbf{r})$ and eigenvalues E_{nLSJ} that correspond to the sublevels of an atomic multiplet with the principal quantum number n and the quantum numbers of orbital L, spin S, and total J momenta (the Hamiltonian $\hat{H}_0(\mathbf{r})$ takes into account the spin–orbit interaction). Then,

$$\hat{H}_0(\mathbf{r})\phi_{nLSJ}(\mathbf{r}) = E_{nLSJ}\phi_{nLSJ}(\mathbf{r}). \quad (1)$$

Let us project the Schrödinger equation

$$(\hat{H}_0(\mathbf{r}) + \hat{V}_0(\mathbf{r}))\Psi_{nLSJM}(\mathbf{r}) = E\Psi_{nLSJM}(\mathbf{r}) \quad (2)$$

for an atom in a constant electric field, whose interaction is described by the operator $\hat{V}(\mathbf{r}) = Fz$, onto a wave function of a certain state of degenerate basis, assuming

that all projections of the vector of state Ψ_{nLSJM} onto the basis vectors are of the same (zero) order in the field,

$$\langle \Psi_{nLSJM}(\mathbf{r}) | \phi_{nLSJ}(\mathbf{r}) \rangle = a_J^{(\lambda)}.$$

Here, $J = J_1, \ldots, J_k$; $\lambda = 1, 2, \ldots, k$; and k is the number of interacting sublevels (which may not coincide with the multiplicity of the multiplet). Taking into account (1), we obtain the following expression as a result of the projection:

$$(E_{nLSJ} - E)a_J + \langle \phi_{nLSJ} | \hat{V} | \Psi \rangle = 0. \tag{3}$$

Next, we project Eq. (2) onto the Green's function $G_{\bar{E}}(\mathbf{r}, \mathbf{r}')$ of the unperturbed atom that satisfies the inhomogeneous equation

$$(\hat{H}_0 - \bar{E})G_{\bar{E}}(\mathbf{r}, \mathbf{r}') = \delta(\mathbf{r} - \mathbf{r}'), \tag{4}$$

whose right-hand side contains the Dirac δ function, and

$$\bar{E} = \frac{1}{k}\sum_{J=J_1}^{J_k} E_{nLSJ} \tag{5}$$

represents the mean value of the energy of interacting sublevels. For convenience, we introduce the following notation:

$$\varepsilon_J = E_{nLSJ} - \bar{E} \tag{6}$$

is the energy of a sublevel with a given J with respect to the mean value (5), and

$$\Delta E = E - \bar{E} \tag{7}$$

is the relative energy of the atom in the field. As a result of projection, we obtain

$$\Psi(\mathbf{r}) + G_{\bar{E}}(\mathbf{r}, \mathbf{r}')(\hat{V}(\mathbf{r}') - \Delta E)|\Psi(\mathbf{r}')\rangle = 0. \tag{8}$$

Let us select the states of the multiplet under consideration from the Green's function expressed as a spectral expansion [16, 17],

$$G_{\bar{E}}(\mathbf{r}, \mathbf{r}') = \sum_{n'L'S'J'} \frac{\phi_{n'L'S'J'}(\mathbf{r})\phi^*_{n'L'S'J'}(\mathbf{r}')}{E_{n'L'S'J'} - \bar{E}}, \tag{9}$$

by representing the latter function as

$$G_{\bar{E}}(\mathbf{r}, \mathbf{r}') = G'_{\bar{E}}(\mathbf{r}, \mathbf{r}') + \sum_{J'=J_1}^{J_k} \frac{\phi_{nLSJ'}(\mathbf{r})\phi^*_{nLSJ'}(\mathbf{r}')}{E_{J'}}. \tag{10}$$

Substitute (10) into (8). Taking into account (3) and (6), we obtain

$$\Psi(\mathbf{r}) = \sum_{J'} a_{J'}\phi_{nLSJ'}(\mathbf{r}) - G'_{\bar{E}}(\mathbf{r}, \mathbf{r}')(\hat{V}(\mathbf{r}') - \Delta E)|\Psi(\mathbf{r}')\rangle. \tag{11}$$

Using an iterative procedure, we represent the formal expression for a wave function as the Brillouin–Wigner series

$$\Psi(\mathbf{r}) = \sum_{J'} a_{J'} \times \sum_{q=0}^{\infty} [G'_{\bar{E}}(\mathbf{r}, \mathbf{r}')(\Delta E - \hat{V}(\mathbf{r}'))]^q |\phi_{nLSJ'}(\mathbf{r}')\rangle. \tag{12}$$

Applying the formula for the sum of a geometrical progression, we rewrite this expression as

$$\Psi(\mathbf{r}) = \sum_{J'} a_{J'}[1 + G'_{\bar{E}}(\mathbf{r}, \mathbf{r}')(\hat{V}(\mathbf{r}') - \Delta E)]^{-1} \times |\phi_{nLSJ'}(\mathbf{r}')\rangle. \tag{13}$$

Substituting (13) into (3), we obtain the following system of equations for coefficients a_J:

$$\sum_{J'} a_{J'}[W_{JJ'} + (\varepsilon_{J'} - \Delta E)\delta_{JJ'}] = 0, \tag{14}$$

where

$$W_{JJ'} = \langle \phi_{nLSJ} | \hat{V}[1 + G'_{\bar{E}}(\hat{V} - \Delta E)]^{-1} | \phi_{nLSJ'} \rangle \tag{15}$$

is a matrix element of the operator of interaction $\hat{V}$ between the atom and the field, which formally includes all orders of perturbation theory.

In the absence of an external field ($\hat{V} = 0$), system (14) is solvable if $\Delta E = \varepsilon_J$. Then, $a_J = 1$ and $a_{J' \neq J} = 0$. When $\hat{V} \neq 0$, the system has a nonzero solution if ΔE satisfies the secular equation

$$\det \| W_{JJ'} + (\varepsilon_{J'} - \Delta E)\delta_{JJ'} \| = 0. \tag{16}$$

To solve this equation, one has to know the matrix element $W_{JJ'}$, which depends on the strength of the external field F. Numerical calculations show that, when $F < F_0$ (F_0 is the field value at which the upper sublevel of the multiplet $|nLSJ\rangle$ occurs above the top of the potential barrier), one can use the expansion of $W_{JJ'}$ in powers of F^2. In spite of the fact that such a series is asymptotic, its first several terms form a decreasing sequence such that their sum determines $W_{JJ'}$ to a high degree of accuracy up to $F = F_0$. Practically, it suffices to take into consideration the first two terms of the series, in which the coefficients of F^2 and F^4 are determined by the polarizability and the hyperpolarizability of the atomic state. Since $\Delta E \sim \varepsilon_{J'} \sim F^2 \gg \Delta E F^2 \sim F^4 \gg F^6 \ldots$, such an expansion of the matrix element $W_{JJ'}$ is given by

$$W_{JJ'} = F^2 w^{(2)}_{JJ'} + F^2 \Delta E u_{JJ'} + F^4 w^{(4)}_{JJ'}, \tag{17}$$

where

$$w^{(2)}_{JJ'} = -\langle nLSJ|zG'_{\bar{E}}z|nLSJ'\rangle,$$

$$u_{JJ'} = -\langle nLSJ|z(G'_{\bar{E}})^2z|nLSJ'\rangle, \quad (18)$$

$$w^{(4)}_{JJ'} = -\langle nLSJ|zG'_{\bar{E}}zG'_{\bar{E}}zG'_{\bar{E}}z|nLSJ'\rangle$$

are matrix elements that contain one, two, and three Green's functions. The second and third terms on the right-hand side of (17) are on the order of F^4; moreover, it suffices to use a quadratic approximation for the factor of ΔE in the second term. Applying the apparatus of angular momentum theory [34], we can reduce these matrix elements to a sum of irreducible parts that contain scalar and tensor polarizabilities and hyperpolarizabilities.

The general formulas (16)–(18) of degenerate perturbation theory, which contain the second-, third-, and fourth-order field corrections, can be used for calculating the Stark effect in a multielectron atom. In this case, the state vector $|nLSJ\rangle$ is constructed within a given scheme of coupling between angular momenta (for example, in the *LS* or *JJ* representations); by the operator z in (18), we mean the z component of the dipole moment

$$D = \sum_i^N r_i\cos\theta_i$$

of the atom, and G'_E corresponds to the definition of a reduced Green's function of the N-electron atom.

3. DECOMPOSITION OF MATRIX ELEMENTS INTO IRREDUCIBLE PARTS

Using the Wigner–Eckart theorem and the properties of 6*j* symbols and the Clebsch–Gordan coefficients [34], we obtain the following expression for the first term in the matrix element (17):

$$w^{(2)}_{JJ'} = -\frac{1}{2}\sum_{j=0,2} C^{JM}_{J'Mj0}\left[\frac{(2J+2)_j(2J'+1)}{(2J+1-j)_{j+1}}\right]^{1/2} a^{(j)}_{JJ'}, \quad (19)$$

where $(b)_n = b(b+1)\ldots(b+n-1)$ is the Pochhammer symbol and

$$a^{(j)}_{JJ'} = 2(2L+1)C^{j0}_{1010}\left[\frac{(2J+1-j)_{j+1}(2j+1)}{(2J+2)_j}\right]^{1/2} \times\sum_{J''}(-1)^{J+J''}(2J''+1)\left\{\begin{array}{ccc} 1 & 1 & j \\ J & J' & J'' \end{array}\right\} \quad (20)$$

$$\times\sum_{L'=L\pm1}(C^{L'0}_{L010})\left\{\begin{array}{ccc} S & L & J \\ 1 & J'' & L' \end{array}\right\}\left\{\begin{array}{ccc} S & L & J' \\ 1 & J'' & L' \end{array}\right\}R^{11}_{L'J''}(S)$$

is the irreducible part of the matrix element. We will use the standard notation for the Clebsch–Gordan coefficients and the 6*j* symbols [34]. The radical factor in (19) is introduced in order that the coefficients of this expansion, as well as the coefficients of the expansion of the irreducible part (20) in terms of radial matrix elements R, should be rational numbers that do not contain radicals. For a matrix element of the $(N+1)$th order with N Green's functions, we use the notation

$$R^{n_1n_2\ldots n_{N+1}}_{L_1J_1,\,L_2J_2,\,\ldots,\,L_NJ_N}(S) \equiv \langle nLSJ|r_1^{n_1}g_{L_1J_1}(r_1,r_2)r_2^{n_2} \ldots r_N^{n_N}g_{L_NJ_N}(r_N,r_{N+1})r_{N+1}^{n_{N+1}}|nLSJ'\rangle, \quad (21)$$

where $g_{L'J'}(r, r')$ is the radial part of the Green's function (9) that determines its series expansion in spherical harmonics. The notation for the components of the polarizability tensor that is conventionally used in the literature is determined by the irreducible parts of the diagonal matrix element (19): $\alpha^s_{nLSJ} = a^{(0)}_{JJ}$ and $\alpha^t_{nLSJ} = a^{(2)}_{JJ}$ for scalar and tensor polarizabilities, respectively. Thus, for the diagonal matrix element (19), we have

$$w^{(2)}_{JJ} = -\frac{1}{2}\left[\alpha^s_{nLSJ} + \frac{3M^2 - J(J+1)}{J(2J-1)}\alpha^t_{nLSJ}\right], \quad (22)$$

where

$$\alpha^s_{nLSJ} = \frac{2}{3}(2L+1)\sum_{L'J''}(2J''+1)(C^{L'0}_{L010})^2 \times\left\{\begin{array}{ccc} S & L & J \\ 1 & J'' & L' \end{array}\right\}^2 R^{11}_{L'J''}(S), \quad (23)$$

$$\alpha^t_{nLSJ} = \left[\frac{10(2J-1)_3}{3(2J+2)_2}\right]^{1/2}(2L+1) \times\sum_{J''}(-1)^{J+J''}(2J''+1)\left\{\begin{array}{ccc} 1 & 1 & 2 \\ J & J & J'' \end{array}\right\} \times\sum_{L'=L\pm1}(C^{L'0}_{L010})^2\left\{\begin{array}{ccc} S & L & J \\ 1 & J'' & L' \end{array}\right\}^2 R^{11}_{L'J''}(S). \quad (24)$$

The decomposition of the matrix element $u_{JJ'}$ into irreducible parts is described by expressions that formally coincide with (19), (20), and (22)–(24) when the radial matrix elements with a single Green's function

are replaced by a matrix element with two Green's functions,

$$R^{11}_{L'J''}(S) = \langle nLSJ|rg_{L'J''}(r, r')r'|nLSJ'\rangle \longrightarrow R^{101}_{L'J'', L'J''}(S) = \langle nLSJ|rg_{L'J''}(r, r')g_{L'J''}(r', r'')r''|nLSJ'\rangle.$$

Similarly, a fourth-order diagonal matrix element can be expressed in terms of the hyperpolarizability components of an atomic level that generally has three independent irreducible parts $\gamma^{(j)}_{nLSJ}$, $j = 0, 2, 4$ [17, 30, 32]. The irreducible parts of the hyperpolarizability represent a linear combination of fourth-order radial matrix elements $R^{1111}_{L_1J_1, L_2J_2, L_3J_3}(S)$. The explicit form of these expressions is rather awkward, but they can be substantially simplified by neglecting the effect of the fine structure on the radial matrix element. In this approximation, the matrix elements (21) do not depend on the indices of the total momenta $J_1, J_2, \ldots, J_N$. As a result, the dependence of the matrix elements on the total angular momentum of the initial, intermediate, and final states is expressed only in terms of the coefficients of vector summation, which can be performed analytically, similar to the summation over J'' in (20) [34]. Then, a fourth-order matrix element can be represented as

$$w^{(4)}_{JJ'} = -\frac{1}{24}\sum_{j=0,2,4} C^{JM}_{J'Mj0}(-1)^{J'+L+S} \times\left[\frac{(2L+1)_{J+1}(2J'+1)}{(2L+1-j)_j}\right]^{1/2}\begin{Bmatrix} L & L & j \\ J' & J & S\end{Bmatrix}\gamma^{(j)}_{nLS}, \quad (25)$$

where

$$\gamma^{(j)}_{NLS} = 24\left[\frac{(2L+1-j)_{J+1}(2j+1)}{(2L+2)_j}\right]^{1/2} \times\sum_{j_1j_2}\sqrt{(2j_1+1)(2j_2+1)}C^{j_10}_{1010}C^{j_20}_{1010}C^{j0}_{j_10j_20} \times\sum_{L_2}(2L_2+1)\begin{Bmatrix} L & L & j \\ j_1 & j_2 & L_2\end{Bmatrix} \times\sum_{L_1L_3}C^{L_10}_{L010}C^{L_10}_{L_20\,10}C^{L_30}_{L_20\,10}C^{L_30}_{L010}\begin{Bmatrix} L & L_2 & j_1 \\ 1 & 1 & L_1\end{Bmatrix} \times\begin{Bmatrix} L & L_2 & j_2 \\ 1 & 1 & L_3\end{Bmatrix}R^{1111}_{L_1, L_2, L_3}(S) \quad (26)$$

is the irreducible part of the hyperpolarizability of the $|nLS\rangle$ level that is independent of the total momentum J and is identical for all components of the atomic multiplet. Substituting the numerical values for the coefficients of the vector summation into (26), we obtain the following expressions for three independent components of the hyperpolarizability:

$$\gamma^{(0)}_{nLS} = \frac{8}{5(2L+1)}\left[\frac{2L(L-1)}{2L-1}R^{1111}_{L-1, L-2, L-1}(S) + \frac{L(4L^2+1)}{4L^2-1}R^{1111}_{L-1, L, L-1}(S) + \frac{4L(L+1)}{2L+1}R^{1111}_{L-1, L, L+1}(S) + \frac{(L+1)(4L^2+8L+5)}{(2L+1)(2L+3)}R^{1111}_{L+1, L, L+1}(S) + \frac{2(L+1)(L+2)}{2L+3}R^{1111}_{L+1, L+2, L+1}(S)\right], \quad (27)$$

$$\gamma^{(2)}_{nLS} = -\frac{8L}{7(2L+1)}\left[\frac{4(L-1)}{2L-1}R^{1111}_{L-1, L-2, L-1}(S) + \frac{8L^2-6L+5}{4L^2-1}R^{1111}_{L-1, L, L-1}(S) + \frac{8(2L^2+2L+3)}{(2L+1)(2L+3)}R^{1111}_{L-1, L, L+1}(S) + \frac{(2L-1)(8L^2+22L+19)}{(2L+1)(2L+3)^2}R^{1111}_{L+1, L, L+1}(S) + \frac{4(L+2)(2L-1)}{(2L+3)^2}R^{1111}_{L+1, L+2, L+1}(S)\right], \quad (28)$$

$$\gamma^{(4)}_{nLS} = -\frac{48L(L-1)}{35(4L^2-1)}\left[R^{1111}_{L-1, L-2, L-1}(S) + \frac{2L-3}{2L+1}R^{1111}_{L-1, L, L-1}(S) + \frac{2(2L-3)(2L-1)}{(2L+1)(2L+3)}R^{1111}_{L-1, L, L+1}(S) + \frac{(2L-1)^2(2L-3)}{(2L+1)(2L+3)^2}R^{1111}_{L+1, L, L+1}(S) + \frac{(2L-1)^2(2L-3)}{(2L+3)^2(2L+5)}R^{1111}_{L+1, L+2, L+1}(S)\right]. \quad (29)$$

Thus, in the approximation used, all fourth-order matrix elements in the basis of the multiplet states are expressed in terms of three different components of the hyperpolarizability tensor (27)–(29) that depend only on the principal, spin, and orbital quantum numbers. The dependence of $w^{(4)}_{JJ'}$ on J and J' is described by the coefficients of vector summation in (25). As a rule, this approximation is fairly sufficient because the fourth-

order matrix element determines only the quadratic (in field) correction to the main quantity.

If we also neglect the effect of the fine structure on the second- and third-order matrix elements, we can also obtain expressions analogous to (25) for these quantities:

$$w^{(2)}_{JJ'} = -\frac{1}{2}\sum_{j=0,2} C^{JM}_{J'Mj0}(-1)^{J'+L+S} \times\left[\frac{(2L+1)_{J+1}(2J'+1)}{(2L+1-j)_j}\right]^{1/2}\begin{Bmatrix} L & L & j \\ J' & J & S\end{Bmatrix}\alpha^{(j)}_{nLS}, \quad (30)$$

where $\alpha^{(0)}_{nLS} \equiv \alpha^{s}_{nLS}$ and $\alpha^{(2)}_{nLS} \equiv \alpha^{t}_{nLS}$ are the scalar and tensor polarizabilities of the level, respectively. Both of these quantities can be represented as a linear combination of second-order radial matrix elements:

$$\alpha^{s}_{nLS} = \frac{2}{3(2L+1)}[LR^{11}_{L-1}(S) + (L+1)R^{11}_{L+1}(S)], \quad (31)$$

$$\alpha^{t}_{nLS} = -\frac{2L}{3(2L+1)}\left[R^{11}_{L-1}(S) + \frac{2L-1}{2L+3}R^{11}_{L+1}(S)\right]. \quad (32)$$

In this case, the scalar polarizability appears only in the expressions for the diagonal matrix elements and determines the energy shift that is identical for all sublevels of the multiplet, while the tensor polarizability determines the splitting into magnetic components, different for different sublevels, and appears in both the diagonal and the off-diagonal matrix elements. An expression for the third-order matrix element $u_{JJ'}$ is obtained from (30) by replacing $\alpha^{(j)} \longrightarrow \beta^{(j)}$, where $\beta^{(j)}$ is a superposition of third-order radial matrix elements, which is given by relations (31) and (32) in which one should make the following substitution: $R^{11}_{L'}(S) \longrightarrow R^{101}_{L'L'}(S)$.

Using the definition of the Green's function (9), one can easily verify that the maximal contribution to the radial matrix elements is made by the levels $n' = n$. For example, in [35], it was shown that, for $1s3p\ ^3P_J$ levels of helium, the contribution of resonance terms amounts to about 97%. For circular states with $n = L + 1$, the dominant correction with $n' = n$ is absent in R^{11}_{L+1}, and, hence, the inequality $R^{11}_{L+1} \ll R^{11}_{L-1}$ holds for the radial matrix elements in (31) and (32). Under this condition, we obtain the approximate equality $\alpha^{s} \approx -\alpha^{t}$ for the circular states.

Note also that relation (30) for an off-diagonal matrix element actually determines a transition from the *LS* scheme of coupling of angular momenta to the *J* representation for the second-order scalar and tensor components of electric susceptibilities of a multielectron atom. This transition was first analyzed in [36]. The comparison of (22)–(24) with (30)–(32) shows that the scalar and tensor components of the polarizability of a helium-like atom in these two representations are related by the following simple formulas:

Table 1. Coefficients of singlet–triplet mixing for a helium-like atom

Term	A_L	B_L
^1L_L	$\cos\varphi_{nL}$	$\sin\varphi_{nL}$
^3L_L	$-\sin\varphi_{nL}$	$\cos\varphi_{nL}$
$^3L_{L-1}$	0	1
$^3L_{L+1}$	0	1

$$\alpha^{s}(n^{1,3}L_J) \longrightarrow \alpha^{s}(n^{1,3}L), \quad \alpha^{t}(n^{1}L_L) \longrightarrow \alpha^{t}(n^{1}L), \quad (33)$$

$$\alpha^{t}(n^{3}L_{L+1}) \longrightarrow \alpha^{t}(n^{3}L), \quad (34)$$

$$\alpha^{t}(n^{3}L_L) \longrightarrow \frac{L^2+L-3}{L(L+1)}\alpha^{t}(n^{3}L), \quad (35)$$

$$\alpha^{t}(n^{3}L_{L-1}) \longrightarrow \frac{(L-1)(L+1)(2L-3)(2L+3)}{L^2(2L-1)(2L+1)}\alpha^{t}(n^{3}L). \quad (36)$$

Similar formulas for the scalar and tensor components of hyperpolarizabilities are more cumbersome and are not presented here to save space.

The above formulas do not take into account the singlet–triplet mixing of excited states of a helium atom. The contribution of these phenomena is quite significant for the states with $L \geq 3$; its correct consideration is required first for the comparative analysis of theoretical data with the results of precision measurements. For the quantitative and qualitative analysis of these phenomena, one should use an intermediate scheme for the coupling of angular momenta; in this case, the wave functions for the atomic multiplet components with $J = L$ are determined by the superposition of states in a "pure" *LS* coupling scheme of angular momenta

$$|nLSJ\rangle = A_L|n^1L\rangle + B_L|n^3L\rangle. \quad (37)$$

The coefficients A_L and B_L in (37) are calculated by the method of diagonalization of the energy matrix with regard to relativistic interactions (first of all, a spin–orbit interaction) in the total Hamiltonian of an atom (Table 1).

For a helium atom, the numerical values of the mixing angles φ_{nL} for $L = 1, 2, 3, 4$ are equal to 0.02°, 0.5°, 30°, and 44°, respectively, and virtually do not depend on the principal quantum number of a valence electron [37]. Taking into account the singlet–triplet mixing alters formulas (23) and (24); then, according to the

definition (37), the components of the polarizability tensor are expressed as

$$\alpha^s = \frac{2}{3}\sum_{L'J'}\Phi(J, J', L, L'), \tag{38}$$

$$\alpha^t = 4\left[\frac{5J(2J-1)}{6(2J+3)(J+1)}\right]^{1/2} \times \sum_{L'J'}(-1)^{J+J'}\left\{\begin{array}{ccc} 1 & 1 & 2 \\ J & J & J' \end{array}\right\}\Phi(J, J', L, L'). \tag{39}$$

Here,

$$\Phi(J, J', L, L') = (2J'+1)L_>\left[\frac{A_L A_{L'}}{\sqrt{(2L+1)(2L'+1)}}R^{11}_{L'J'}(0) - B_L B_{L'}\left\{\begin{array}{ccc} L & J & 1 \\ J' & L' & 1 \end{array}\right\}R^{11}_{L'J'}(1)\right]^2, \tag{40}$$

and $L_>$ is the maximum of L and L'.

As a result, the use of the intermediate coupling scheme of angular momenta requires that one should take into account the singlet–triplet mixing not only in the wave functions of the considered states with $L \geq 3$ but also in the spectrum of intermediate states. Note that the weak dependence of the coefficients A_L and B_L on the principal quantum number n allows one to apply the method of Green's functions for summing over the whole set of intermediate states.

For example, for a tensor component of a singlet ^1D level of helium, one can easily obtain an approximate formula that takes into account the mixing phenomena for the F component of the intermediate spectrum

$$\alpha^t(nd^1D_2) \approx \alpha^t(nd^1D) - \frac{4}{35}R^{11}_3(0)\sin^2\varphi_{nF}\left[1 - \frac{E_{n^1F} - E_{n^1D}}{E_{n^3F} - E_{n^1D}}\right]. \tag{41}$$

A numerical calculation has shown that the contribution of the mixing phenomena is no greater than 0.1% for arbitrary n. The case of a tensor component of the $^1F_3$ level is more interesting since, on the one hand, there are experimental data [38] for this case and, on the other hand, this case exhibits strong dependence of the mixing amplitude on the principal quantum number n:

$$\alpha^t(nf^1F_3) \approx \alpha^t(nf^1F) + \sin^2\varphi_{nF}\left[\frac{3}{4}\alpha^t(nf^3F) - \alpha^t(nf^1F)\right]. \tag{42}$$

In other words, the singlet–triplet mixing is determined by

$$\sin^2\varphi_{nF}\left[\frac{3}{4}\alpha^t(^3F) - \alpha^t(^1F)\right]. \tag{43}$$

For instance, for $n = 4$, this phenomenon is abnormally high (20%); for $n = 5$, its contribution is no higher than 1%; and, again, it amounts to several percent for $n > 5$.

Thus, up to the fourth order in the field strength, the matrix element (17) is determined by relations (25)–(32), which are sufficiently universal for all multiplet levels and can be used for calculating the variation of energies of specific atoms in a field with regard to the fine-structure effects in an atomic multiplet.

4. THE STARK EFFECT ON TRIPLET STATES OF HELIUM

In this section, we calculate the energy of $n\,^3P_{0,2}$ states of helium up to the fourth-order corrections with respect to field F neglecting the singlet–triplet mixing in the spectrum of intermediate states. The fourth-order corrections should be taken into consideration for the field corresponding to the anticrossing region of the triplet sublevels where the energy difference $\delta_{02} = E_0 - E_2$ is minimal. The attraction of sublevels to each other in a weak field and their subsequent repulsion are observed when the polarizability of the upper sublevel is greater than that of the lower one. This situation is characteristic of $n\,^3P_J$ states of helium ($n = 2, 3, ...$) with $J = 0, 2$ and the projection of the total momentum $M = 0$. The state with $J = 1$ and $M = 0$ remains isolated since there is no nonzero matrix element for the dipole electric transition to a state with a different value of the total momentum J. The sublevels $n\,^3P_J$ with $|M| = J = 2$ also remain isolated. The "repulsion" of interacting levels is attributed to the off-diagonal matrix element of the operator $\hat{V}(\mathbf{r})$ that makes a positive contribution to the energy of the upper level and a negative contribution to the energy of the lower level. Note that the states with $|M| = 1$ and $J = 1, 2$ of the multiplets considered have identical polarizabilities and hyperpolarizabilities; therefore, they immediately start to diverge, as the field strength increases, due to the interaction between sublevels, which is determined by the off-diagonal matrix element.

4.1. Field Dependence for Energies of Two Interacting Sublevels

To calculate the Stark splitting of two close-lying sublevels with relative energy shifts $\varepsilon_{J_1} = E_1 - \bar{E} = -\delta/2$ and $\varepsilon_{J_2} = E_2 - \bar{E} = \delta/2$, where $\bar{E} = (E_1 + E_2)/2$, one has to solve the secular equation (16) for ΔE. To determine the corrections to the energy up to the fourth

order in F, we substitute expression (17) for the matrix element $W_{JJ'}$ into Eq. (16), which can be rewritten as

$$\det\left\| \begin{array}{cc} c_{11} & c_{12} \\ c_{21} & c_{22} \end{array} \right\| = 0, \tag{44}$$

where

$$\begin{aligned} c_{11} &= -\frac{\delta}{2} - \Delta E + F^2 w^{(2)}_{J_1J_1} + F^2 \Delta E u_{J_1J_1} + F^4 w^{(4)}_{J_1J_1}, \\ c_{12} &= c_{21} = F^2 w^{(2)}_{J_1J_2} + F^2 \Delta E u_{J_1J_2} + F^4 w^{(4)}_{J_1J_2}, \\ c_{22} &= \frac{\delta}{2} - \Delta E + F^2 w^{(2)}_{J_2J_2} + F^2 \Delta E u_{J_2J_2} + F^4 w^{(4)}_{J_2J_2}. \end{aligned} \tag{45}$$

To determine ΔE from (44) up to the fourth-order terms in the field, one should retain the terms up to the sixth order in the equation:

$$\sim(\Delta E)^2F^2 \sim \Delta E F^2\delta \sim (\Delta E)^2\delta \sim \Delta E\delta^2 \sim F^2\delta^2 \sim F^4\delta \sim F^6.$$

Solving quadratic equation (44) for the field-dependent splitting of two interacting sublevels of the multiplet up to the fourth-order terms, we can obtain an expression of the form

$$\begin{aligned} \delta(F) = \Delta E^+ - \Delta E^- = \delta\Bigg\{\Bigg[1 + \frac{F^2}{2}(u_{J_1J_1} + u_{J_2J_2}) \\ + \frac{F^2}{\delta}(w^{(2)}_{J_2J_2} - w^{(2)}_{J_1J_1} + F^2(g_{J_2} - g_{J_1}))\Bigg]^2 \\ + \frac{4F^2}{\delta^2}\Bigg[w^{(2)}_{J_1J_2} + F^2\Bigg(w^{(4)}_{J_1J_2} + w^{(2)}_{J_1J_2}\frac{u_{J_1J_1} + u_{J_2J_2}}{2} \\ + u_{J_1J_2}\frac{w^{(2)}_{J_1J_1} + w^{(2)}_{J_2J_2}}{2}\Bigg)\Bigg]^2\Bigg\}^{1/2}, \end{aligned} \tag{46}$$

where

$$g_{J_i} \equiv w^{(4)}_{J_iJ_i} + w^{(2)}_{J_iJ_i}u_{J_iJ_i} \tag{47}$$

is the hyperpolarizability of a sublevel with the total momentum J_i. Note that the states with the total momenta J_1 and J_2 are mixed due to the field, so that the total momentum is no longer an integral of motion.

In the expression analogous to (46) that was obtained in [30] and in which the fourth-order phenomena were taken into account only in the diagonal matrix elements, all corrections to the off-diagonal matrix element (the term proportional to F^2 in the second set of square brackets under the sign of the radical) were absent. The interaction of levels was not taken into account when calculating the hyperpolarizabilities of individual sublevels in diagonal elements; this resulted in other combinations of products of matrix elements $w^{(2)}$ and u entering into $g_{J'}$ and led to the absence of the second term in the first set of square brackets in (46). Calculations show that the above terms have the same order of magnitude in the neighborhood of the anticrossing of levels as those taken into account in the diagonal elements.

4.2. Polarizabilities and Hyperpolarizabilities of Triplet Levels of Helium

Using (46), we determine the field dependence of the fine-structure splitting for the sublevels of triplet nP states with the total momenta $J_1 = 2$ (the lower sublevel) and $J_2 = 0$ (the upper sublevel) and the projections $M = 0$ onto the field direction. According to (25) and (30), the matrix elements are expressed in terms of irreducible parts as

$$\begin{aligned} w^{(2)}_{00} &= -\frac{1}{2}\alpha^s_{n\,^3P}, \quad u_{00} = -\frac{1}{2}\beta^s_{n\,^3P}, \\ w^{(4)}_{00} &= -\frac{1}{24}\gamma^{(0)}_{n\,^3P}, \\ w^{(2)}_{22} &= -\frac{1}{2}(\alpha^s_{n\,^3P} - \alpha^t_{n\,^3P}), \\ u_{22} &= -\frac{1}{2}(\beta^s_{n\,^3P} - \beta^t_{n\,^3P}), \\ w^{(4)}_{22} &= -\frac{1}{24}(\gamma^{(0)}_{n\,^3P} - \gamma^{(2)}_{n\,^3P}), \\ w^{(2)}_{20} &= w^{(2)}_{02} = -\frac{1}{\sqrt{2}}\alpha^t_{n\,^3P}, \\ u_{20} &= u_{02} = -\frac{1}{\sqrt{2}}\beta^t_{n\,^3P}, \\ w^{(4)}_{20} &= w^{(4)}_{02} = -\frac{1}{12\sqrt{2}}\gamma^{(2)}_{n\,^3P}. \end{aligned} \tag{48}$$

The same irreducible parts of polarizabilities and hyperpolarizabilities enter into similar expressions for the matrix elements that determine the field-dependence of the splitting of states $n\,^3P_1 - n\,^3P_2$ with the projection $|M| = 1$ of the total momentum:

$$\begin{aligned} w^{(2)}_{11} &= w^{(2)}_{22} = -\frac{1}{2}\left(\alpha^s_{n\,^3P} - \frac{1}{2}\alpha^t_{n\,^3P}\right), \\ u_{11} &= u_{22} = -\frac{1}{2}\left(\beta^s_{n\,^3P} - \frac{1}{2}\beta^t_{n\,^3P}\right), \\ w^{(4)}_{11} &= w^{(4)}_{22} = -\frac{1}{24}\left(\gamma^{(0)}_{n\,^3P} - \frac{1}{2}\gamma^{(2)}_{n\,^3P}\right), \\ w^{(2)}_{21} &= w^{(2)}_{12} = -\frac{3}{4}\alpha^t_{n\,^3P}, \\ u_{21} &= u_{12} = -\frac{3}{4}\beta^t_{n\,^3P}, \\ w^{(4)}_{21} &= w^{(4)}_{12} = -\frac{1}{16}\gamma_2(n\,^3P). \end{aligned} \tag{49}$$

Table 2. Scalar and tensor polarizabilities α^s, α^t, β^s, and β^t and hyperpolarizabilities $\gamma^{(0)}$ and $\gamma^{(2)}$ for the $n\,^3P$ state of a helium atom (in au)

State	α^s	α^t	β^s	β^t	$\gamma^{(0)}$	$\gamma^{(2)}$
$2\,^3P$	47.95	74.86	4.556(3)	–3.086(3)	7.797(6)	–3.427(6)
$3\,^3P$	17 255.6	374.0	7.935(6)	–1.031(6)	1.142(11)	–1.911(10)
$4\,^3P$	1.697(5)	1.664(3)	1.863(8)	–2.409(7)	1.314(14)	–1.921(13)
$5\,^3P$	8.976(5)	7.264(3)	1.936(9)	–2.477(8)	8.895(15)	–1.292(15)

Note: The number in parentheses indicates a power of ten: $a(k) \equiv a \times 10^k$.

Using (27)–(29), (31), and (32), we represent the irreducible parts of polarizabilities and hyperpolarizabilities entering into these expressions in terms of radial matrix elements as

$$\alpha^s_{n\,^3P} = \frac{2}{9}[R_0^{11}(1) + 2R_2^{11}(1)],$$
$$\alpha^t_{n\,^3P} = -\frac{2}{9}\left[R_0^{11}(1) + \frac{1}{5}R_2^{11}(1)\right], \quad (50)$$

$$\gamma^{(0)}_{n\,^3P} = \frac{8}{225}(25R_{010}^{1111}(1) + 40R_{012}^{1111}(1) + 34R_{212}^{1111}(1) + 36R_{232}^{1111}(1)), \quad (51)$$

$$\gamma^{(2)}_{n\,^3P} = -\frac{8}{1575}(175R_{010}^{1111}(1) + 280R_{012}^{1111}(1) + 49R_{212}^{1111}(1) + 36R_{232}^{1111}(1)). \quad (52)$$

Formulas (51) and (52) show that, when calculating the scalar and tensor components of hyperpolarizabilities, one has to take into account the F levels in the spectrum of intermediate states (in the radial matrix element $R_{232}^{1111}(1)$) that are characterized by significant singlet–triplet mixing, $\varphi_{nF} \approx 30°$. However, just as in the estimates of the polarizabilities of the D levels given above, the numerical contribution of these phenomena to $\gamma^{(0)}$ and $\gamma^{(2)}$ is small (≤0.1%).

Formulas (46) and (48) show that the sublevels of the state $n\,^3P$ with $J = 0, 2$ and $M = 0$ become closer to each other in a weak electric field if the tensor polarizability $\alpha^t_{n\,^3P}$ is positive. Then, the leading (first) term in the expression under the radical sign in (46) decreases as F increases. It continues decreasing until it becomes equal to the increasing second term, which is proportional to F^4 for $F = F_a$. When $F > F_a$, the levels start to diverge, which corresponds to the anticrossing of levels. As one can see from relations (49), the sublevels with $J = 1, 2$ and $|M| = 1$ are repulsed starting from $F = 0$ because the upper and lower levels have identical polarizabilities (the hyperpolarizabilities of these levels are also identical). Thus, the anticrossing field F_a, as well as the fine-structure splitting $\delta(F_a)$ in this field, may serve as quantitative characteristics for determining the components of the polarizability and hyperpolarizability tensors of the states considered.

To calculate the radial matrix elements in a one-electron approximation, we applied the Green's function method to the Fues model potential [16, 17]. The numerical values of susceptibilities α, β, and γ for the triplet nP states of helium atoms (n = 2, 3, 4, 5), obtained for the parameters of the model potential chosen in [25], are shown in Table 2.

These parameters were used for calculating the field dependence of the splitting $\delta_{02}(F)$ between the $n,^3P_2$ and $n,^3P_0$ sublevels of the fine structure with $M = 0$. The results are shown in Fig. 1 for the states with (a) $n = 3$ and (b) $n = 5$. This figure also represents the following field dependences calculated by (46): $\delta_{02}^{(2)}(F)$, which takes into account only the quadratic (in the field) corrections to the matrix elements, and $\delta_{02}^{(4)}(F)$, which takes into account the fourth-order corrections together with the quadratic ones. For all values of the field strength that are presented in the figures, the inequality $\delta_{02}^{(4)}(F) < \delta_{02}^{(2)}(F)$ holds.

For $2\,^3P$ states, the contribution of the fourth-order corrections is very small; it amounts to less than 0.1% of the second-order corrections even near the anticrossing. For $3\,^3P$ states, the fourth-order corrections near the anticrossing amount to 5% of the second-order corrections; for $4\,^3P$ states, 10%; and for $5\,^3P$, more than 15%. Here, the fourth-order corrections to the off-diagonal elements constitute more than half of the total fourth-order corrections.

In these calculations, we used the data available in the literature (see, for example, [39–42]) for the fine-structure splitting δ of triplet states $n\,^3P_0$–$n\,^3P_2$ of a free atom. The numerical values of these quantities are shown in Table 3. This table also presents the numerical values of the splitting $\delta_{02}(F_a)$ at the anticrossing point of levels, as well as the corresponding values of the field strength F_a.

Exact estimates for the contribution of continuum were obtained in [35] when calculating the polarizabilities of helium. For instance, for $1snp\ ^3P_{0,2}$ ($n = 2$) levels, this contribution to the scalar and tensor polarizabilities amounted to 23% and 3%, respectively, while, for $1snp\ ^3P_{0,2}$ ($n > 2$) levels, it was no greater than 1%.

To verify the results presented above, we also applied the method of diagonalization of the energy matrix that contains dipole matrix elements of the first order with regard to all possible fine-structure sublevels for states with $n \le 6$, $n \le 5$, and $n \le 4$. For the matrix elements between states with $n \le 4$ and $L = 0$–3, we used the data of precision relativistic calculations based on the method of configuration interaction, which involves the Coulomb and the Breit interaction operators in the total atomic Hamiltonian [25, 30]. In this case, one-particle basis orbitals used in the method of configuration interaction included *s*, *p*, *d*, *f*, and *g* partial waves with the use of a spline approximation for each wave. The relative accuracy of calculating the matrix elements was 10^{-4}–10^{-5} [25, 30]. For other states, the data of nonrelativistic variational calculations given in [43] were used.

Figure 2 represents the F dependence of the splitting δ_{02} between $n\ ^3P_0$ and $n\ ^3P_2$ sublevels of the fine structure with $M = 0$ as a function of the dimension of the basis set in the original energy matrix. The total number of matrix elements for $n \le 6$ with regard to all fine-structure components is greater than 10^3. Figures 2a and 2b show that, for the energy differences $E(2\ ^3P_0) - E(2\ ^3P_2)$ and $E(3\ ^3P_0) - E(3\ ^3P_2)$, the result is virtually independent of the dimension of the basis and agrees with the numerical data presented in Table 3 to within a few percent. This fact may provide a basis for the applicability of the resonance approximation discussed in Section 3. However, for highly excited states of helium-like atoms with $n \ge 4$, the resonance approximation is not sufficient (Fig. 2c). This fact requires the diagonalization of the energy matrix with a substantially greater number of basis elements.

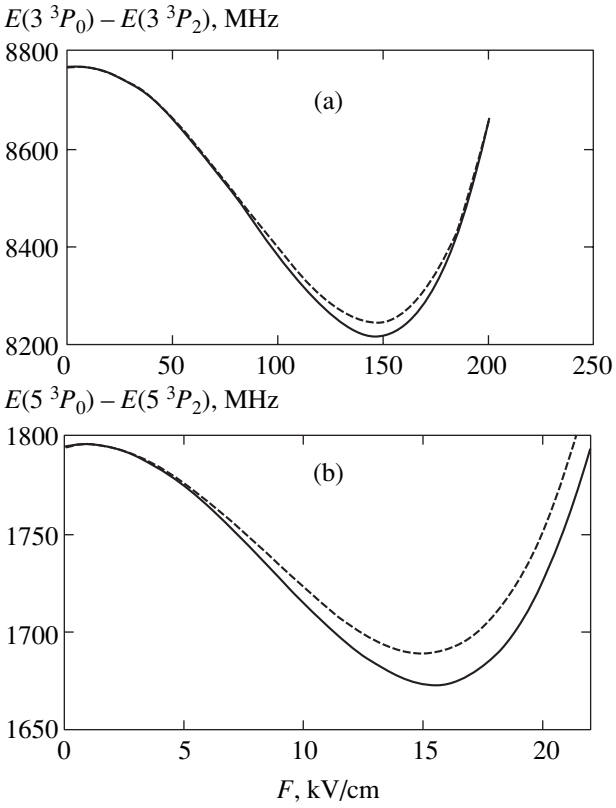

Fig. 1. Fine-structure splitting δ_{02} of sublevels with the momenta $J = 0$ and $J = 2$ of the triplet state $1snp\ ^3P_J$ of a helium atom as a function of the electric-field strength; (a) $n = 3$ and (b) $n = 5$. The dashed curve corresponds to calculations with regard to the quadratic (in field) corrections to the matrix elements, and the solid curve corresponds to calculations with regard to the second- and fourth-order terms.

Thus, the application of the Green's function formalism to calculating the Stark effect allows one to

Table 3. Numerical values of the splitting between the fine-structure sublevels of the $n\ ^3P_J$ state with the total momenta $J = 0$, 2 for a free atom (δ) and at the anticrossing point of levels with the projection $M = 0$, as well as the corresponding values of the field strength F_a at the anticrossing point

State	δ, MHz	$\delta_{20}^{(2)}(F_a^{(2)})$, MHz	$F_a^{(2)}$, kV/cm	$\delta_{20}^{(4)}(F_a^{(4)})$, MHz	$F_a^{(4)}$, kV/cm
$2\ ^3P$	31908	30081.6	617.05	30080.3	617.2
$3\ ^3P$	8772.5	8243.8	146.31	8216.2	146.91
$4\ ^3P$	3576.8	3348.7	44.82	3323.8	47.47
$5\ ^3P$	1797.4	1687.6	15.07	1672.2	15.53

Note: The quantity $\delta_{20}^{(2)}(F_a^{(2)})$ is calculated with regard to the quadratic corrections alone to the matrix elements and the relativistic corrections to the difference between the scalar components of polarizabilities [25], while $\delta_{20}^{(4)}(F_a^{(2)})$ is calculated with regard to the fourth-order corrections.

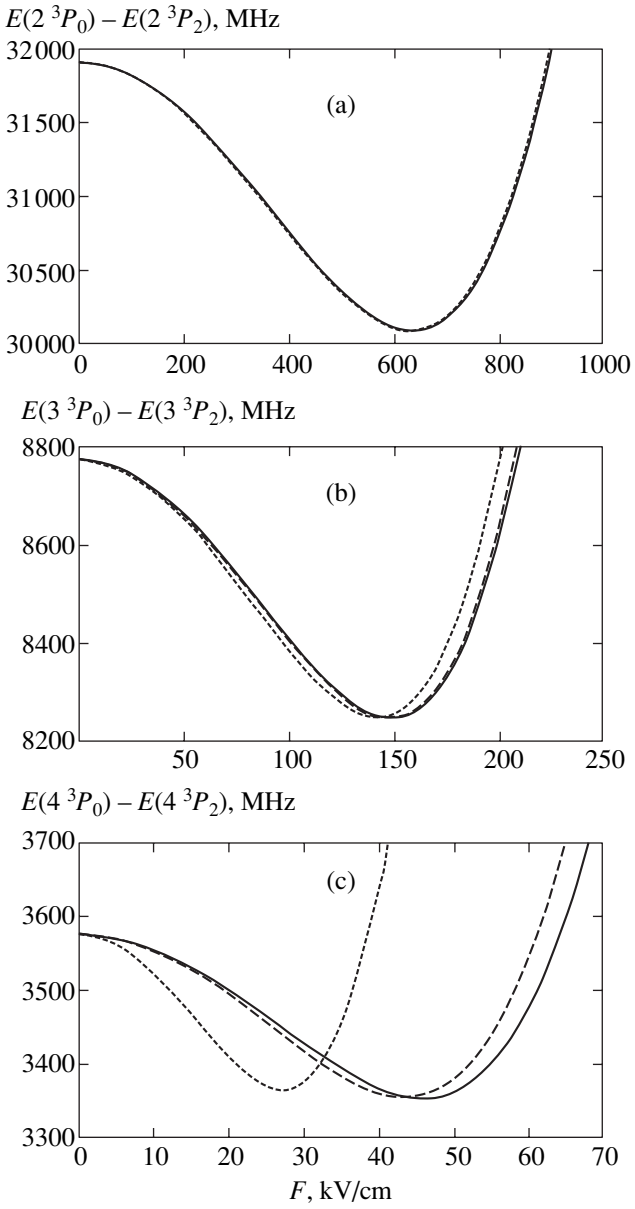

Fig. 2. Fine-structure splitting δ_{02} of sublevels with the momenta $J = 0$ and $J = 2$ of the triplet state $1snp\ ^3P_J$ of a helium atom as a function of the electric-field strength and the dimension of the energy matrix. The dashed curve corresponds to calculations with regard to the basis set of discrete states with $n \le 4$, the dotted curve, with $n \le 5$, and the solid curve, with $n \le 6$.

obtain exact values of electric susceptibilities for both the ground and the highly excited states by a simple and rational method and to analyze the F dependence in the spectra of helium-like atomic systems on the basis of the results obtained.

For triplet states of helium with $n = 3$, experimental measurements of δ_{02} at the anticrossing point of levels yield $\delta_{02}^{\text{exp}} = 8257 \pm 5$ MHz [26]. According to [26], the discrepancy between the experimental and theoretical data (obtained without taking into account field corrections $\sim F^4$) is attributed to the contribution of relativistic corrections to the difference between scalar components of the polarizabilities of the atomic multiplet. However, the results of exact relativistic calculations of the polarizabilities of helium levels $1s3p\ ^3P_{0,2}$ ($M = 0$) [25, 30] did not confirm this assumption; moreover, the contribution of relativistic corrections proved to be of opposite sign to the expected one; i.e., the consideration of these corrections led to a greater discrepancy between theory and experiment: $\delta_{02}^{\text{th}} = 8244$ MHz [25, 30]. This fact stimulated calculations for the Stark effect with regard to higher orders of perturbation theory (hyperpolarizabilities) whose contributions to δ_{02} are rather substantial for strong fields (on the order of 100–200 kV/cm) at the points of anticrossing of levels (Fig. 1). In [25, 30], together with relativistic corrections to the polarizability and the resonance hyperpolarizability, the authors also calculated nonresonance corrections to the hyperpolarizability of states; in this case, the field corrections $\sim F^4$ only to the diagonal matrix elements of the secular equation (16) were taken into account. To control the accuracy and reliability of calculations, two different methods were used in these works, a method of summation of relativistic forces of oscillators for a finite set of discrete states of the intermediate spectrum and a method using a Green's function for the model potential of Fues. These calculations yielded 8231 MHz and 8234 MHz, respectively [30]. The results of calculations carried out with regard to the full set of corrections $\sim F^4$ both to the diagonal and off-diagonal matrix elements of Eq. (16) (see Table 3) also do not agree with the results of measurements presented above.

Thus, we should admit that there is no satisfactory agreement between theoretical calculations of δ_{02} and the corresponding experimental data for the levels with $n = 3$ [26]. This fact makes topical new measurements of the anticrossing parameters for the triplet levels of helium in a static field. The details of the future experimental investigations of anticrossing for singlet and triplet levels of helium are described in [44, 45].

5. CONCLUSIONS

This paper has been initiated first of all by the necessity to give a theoretical interpretation to the results of precision measurements of the fine-structure intervals in helium atoms (the method of anticrossing of levels in an external field with the use of high-resolution laser spectroscopy [26]). The measurement error is ±5 MHz; however, the application of microwave techniques combined with the methods of laser cooling of atomic beams will allow one to reduce this error significantly in the nearest future [44]. An adequate interpretation of such measurements requires that one should take into consideration not only the quadratic Stark effect but also the contributions of higher orders of perturbation

theory associated with nonlinear corrections to the dipole moment of an atom induced by an external field.

In this paper, we have formulated an approach to the calculation of the Stark effect of higher orders in the spectra of helium-like atomic systems. For the first time, we have investigated analytically and numerically a full set of fourth-order corrections with respect to an external field and with regard to the fine-structure phenomena. We used the Fues model potential method [16, 17] as a basis for the numerical calculations; the parameters of this method for metastable ^3S states were chosen according to [25]. The summation of intermediate states over the whole spectrum was based on the Green's function method for a model potential. This fact has allowed us to take into account the contribution of discrete states and continuum and to simplify and unify the calculations, guaranteeing a reliable control of accuracy in all stages of theoretical analysis. We have presented theoretical results for the scalar and tensor components of the second- and fourth-order susceptibilities for helium levels $1snp\ ^3P_{0,2}$ (n = 2–5), determined the values of the electric-field strengths and the differences between energy levels at the anticrossing point, and analyzed the relative contributions of the field corrections.

The theoretical approach presented in this work is sufficiently universal and allows one not only to obtain a full set of fourth-order field corrections in the spectrum of a helium-like atom but also to outline a method for systematic calculations of the Stark effect in higher orders of perturbation theory that are of interest from the viewpoint of modern experiment.

ACKNOWLEDGMENTS

This work was supported by the Russian Foundation for Basic Research (project no. 01-02-97-013P), by the German Research Society (grant no. 96-02-00257, 436 RUS 113/164/O(*R*,*S*)), by the US Civil Research and Development Foundation (US CRDF), and by the Ministry of Education of the Russian Federation (grant no. VZ-010-0).

REFERENCES

1. E. U. Condon and G. H. Shortley, *The Theory of Atomic Spectra* (Cambridge Univ. Press, Cambridge, 1935).
2. H. A. Bethe and E. E. Salpeter, *Quantum Mechanics of One- and Two-Electron Atoms* (Springer, Berlin, 1957; Fizmatgiz, Moscow, 1960).
3. C. E. Tanner and C. Wieman, Phys. Rev. A **38**, 162 (1988).
4. A. Kips, W. Vassen, W. Hogervorst, and P. A. Dando, Phys. Rev. A **58**, 3043 (1998).
5. J. Xia, J. Clarke, J. Li, and W. A. van Wijngaarden, Phys. Rev. A **56**, 5176 (1997).
6. I. I. Ryabtsev and I. M. Beterov, Phys. Rev. A **61**, 063414 (2000).
7. N. Hoe, B. d'Elat, and G. Couland, Phys. Lett. A **85**, 327 (1981).
8. R. D. Damburg and V. V. Kolosov, in *Rydberg States of Atoms and Molecules*, Ed. by R. F. Stebbings and F. B. Dunning (Cambridge Univ. Press, Cambridge, 1983; Mir, Moscow, 1985).
9. A. A. Kamenski and V. D. Ovsiannikov, J. Phys. B **33**, 491 (2000); J. Phys. B **33**, 5543 (2000).
10. A. A. Kamenskiĭ and V. D. Ovsyannikov, Zh. Éksp. Teor. Fiz. **120**, 52 (2001) [JETP **93**, 43 (2001)].
11. M. Bellermann, T. Bergeman, A. Haffmans, *et al.*, Phys. Rev. A **46**, 5836 (1992).
12. R. T. Hawkins, W. T. Hill, F. V. Kovalski, *et al.*, Phys. Rev. A **15**, 967 (1977).
13. M. G. Littman, M. L. Zimmerman, T. W. Ducas, *et al.*, Phys. Rev. Lett. **36**, 788 (1976).
14. T. F. Gallagher, L. M. Humphrey, R. M. Hill, *et al.*, Phys. Rev. A **15**, 1937 (1977).
15. C. Fabre, S. Haroche, and P. Goy, Phys. Rev. A **18**, 229 (1978).
16. L. P. Rapoport, B. A. Zon, and N. L. Manakov, *Theory of Multiphoton Processes in Atoms* (Atomizdat, Moscow, 1978).
17. N. L. Manakov, V. D. Ovsiannikov, and L. P. Rapoport, Phys. Rep. **141**, 319 (1986).
18. V. A. Davydkin and B. A. Zon, Opt. Spektrosk. **52**, 600 (1982) [Opt. Spectrosc. **52**, 359 (1982)].
19. W. R. Johnson and K. T. Cheng, Phys. Rev. A **53**, 1375 (1996).
20. V. G. Pal'chikov and V. P. Shevelko, *Reference Data on Multicharged Ions* (Springer, Berlin, 1995).
21. K. Pachucki and J. Sapirstein, Phys. Rev. A **63**, 012504 (2001).
22. A. K. Bhatia and R. J. Drachman, Phys. Rev. A **58**, 4470 (1998).
23. D. Normand, G. Petite, and J. Morellec, Phys. Lett. A **65**, 290 (1978).
24. V. A. Davydkin and V. D. Ovsiannikov, J. Phys. B **17**, L207 (1984).
25. A. Derevyanko, W. R. Johnson, V. D. Ovsyannikov, *et al.*, Zh. Éksp. Teor. Fiz. **115**, 494 (1999) [JETP **88**, 272 (1999)].
26. R. Schumann, M. Dammasch, U. Eichmann, *et al.*, J. Phys. B **30**, 2581 (1997).
27. H. Katori, in *Proceedings of 6th Symposium on Frequency Standards and Metrology, St. Andrews, Scotland, 2001* (World Sci., New Jersey, 2002), p. 323.
28. Yu. S. Domnin and V. G. Pal'chikov, in *Proceedings of 14th European Frequency and Time Forum*, Torino, Italy (2000), p. 475.
29. V. G. Pokazan'ev and G. V. Skrotskiĭ, Usp. Fiz. Nauk **107**, 623 (1972) [Sov. Phys.–Usp. **15**, 452 (1972)].
30. A. Derevianko, W. R. Johnson, V. D. Ovsiannikov, *et al.*, Phys. Rev. A **60**, 986 (1999).
31. I. I. Sobel'man, *Atomic Spectra and Radiative Transitions* (Nauka, Moscow, 1977; Springer, Berlin, 1979).
32. V. A. Davydkin, V. D. Ovsiannikov, and B. A. Zon, Laser Phys. **3**, 449 (1993).
33. V. D. Ovsiannikov and S. V. Goossev, Phys. Scr. **57**, 506 (1998).

34. D. A. Varshalovich, A. N. Moskalev, and V. K. Khersonskiĭ, *Quantum Theory of Angular Momentum* (Nauka, Leningrad, 1975; World Sci., Singapore, 1988).
35. A. I. Magunov, V. D. Ovsiannikov, V. G. Pal'chikov, *et al.*, in *The Hydrogen Atom*, Ed. by S. G. Karshenboim, F. S. Pavone, G. F. Bassani, *et al.* (Springer, Berlin, 2001), p. 753.
36. J. P. P. Angel and P. G. H. Sandars, Proc. R. Soc. London, Ser. A **305**, 125 (1968).
37. E. S. Chang, Phys. Rev. A **35**, 2777 (1987).
38. A. S. Aynacioglu, G. von Oppen, W. D. Perschmann, and D. Szostak, Z. Phys. A **303**, 97 (1981).
39. T. A. Miller and R. S. Freund, Phys. Rev. A **4**, 81 (1971).
40. T. A. Miller and R. S. Freund, Phys. Rev. A **5**, 588 (1972).
41. P. B. Kramer and F. M. Pipkin, Phys. Rev. A **18**, 212 (1978).
42. D. H. Yang, P. McNicholl, and H. Metcalf, Phys. Rev. A **33**, 1725 (1986).
43. G. W. F. Drake, in *Handbook of Atomic, Molecular, and Optical Physics*, Ed. by G. W. F. Drake (AIP Press, New York, 1996), Chap. 11.
44. R. Schumann, C. Schubert, U. Eichmann, *et al.*, Phys. Rev. A **59**, 2120 (1999).
45. O. Reusch, C. Dieste, S. Garnica, and G. von Oppen, J. Phys. B **34**, 2145 (2001).

Translated by I. Nikitin

Journal of Experimental and Theoretical Physics, Vol. 96, No. 6, 2003, pp. 1019–1036.
Translated from Zhurnal Éksperimental'noĭ i Teoreticheskoĭ Fiziki, Vol. 123, No. 6, 2003, pp. 1160–1178.

ATOMS, SPECTRA, RADIATION

On Nonlinear Propagation of Extremely Short Pulses in Optically Uniaxial Media

S. V. Sazonov* and A. F. Sobolevskiĭ
Kaliningrad State University, Kaliningrad, 236041 Russia
**e-mail: nst@alg.kaliningrad.ru*
Received February 13, 2002; in final form, February 4, 2003

Abstract—Nonlinear wave equations describing the propagation of optical pulses of duration up to a period of electromagnetic oscillations in transparent media with uniaxial optical anisotropy are derived on the basis of a quantum-mechanical model of material response. The electron and electron-vibrational nonlinearities, electron and ion dispersion, and diffraction are taken into account. It is shown that the inclusion of the electron response alone leads to a system of two constitutive equations for the ordinary and extraordinary polarization components. When a pulse propagates across the optical axis, this system is reduced to an inhomogeneous model of the Henon–Heiles type and, hence, generalizes the Lorentz classical electron model. In order to take into account stimulated Raman scattering (SRS) processes, an anisotropic analog of the Bloembergen–Shen quantum-mechanical model taking into account the population dynamics of SRS sublevels is obtained. The generation of an extraordinary wave video pulse with the help of the high-frequency ordinary component in the Zakharov–Benney resonance mode is investigated. Some analytic soliton-like solutions in the form of propagating bound states of ordinary and extraordinary video pulses corresponding to different birefringence modes are considered and their stability to self-focusing is analyzed. *© 2003 MAIK "Nauka/Interperiodica".*

1. INTRODUCTION

In recent years, studies devoted to the interaction of light pulses of duration up to a period of electromagnetic oscillations (video pulses or extremely short pulses (ESP)) with matter have become very popular. This interest stems mainly from the generation of ESP in laboratory conditions [1–6]. The absolute duration τ_p of such pulses varies from hundreds of [6] to several [7] femtoseconds. The term "extremely short pulses" (or "ultimately short pulses") is being used more and more widely (see reviews [4, 5, 8] and article [9]), although the terminology has not settled as yet; some authors also use the terms "ultrashort" or "supershort" pulses in their communications and papers. The latter terms appear to be slightly confusing since they are sometimes applied to quasimonochromatic pulses to emphasize their short duration in absolute meaning. The term "few-cycle pulses" is also used quite often. The latter term is employed especially frequently in foreign literature [3]. The term "video pulses" is also encountered sometimes.

Since an ESP contains approximately one period of oscillations, its spectrum is so broad that the concept of carrier frequency loses its meaning. For obvious reasons, the standard approximation of slowly varying amplitudes and phases (SVAP) from the optics of quasimonochromatic pulses is inapplicable for theoretical investigations of the interaction between ESP and matter. The quasimonochromaticity condition implies that the spectral width $\delta\omega \sim 1/\tau_p$ of a pulse is considerably smaller than its carrier frequency ω; i.e., $\omega\tau_p \gg 1$. The effects of nonlinear propagation of ESP in isotropic media have been investigated quite thoroughly [8–26]. In view of the existence of a symmetry center in such media, the expansion of polarization **P** into a power series in the electric field **E** contains only odd powers of the field. Such an expansion can be carried out if the spectrum of a pulse belongs to the region of optical transparency of the medium, i.e., under the conditions [10, 13, 22–26]

$$(\omega_0/\bar{\omega})^{-1} \ll 1, \quad (\omega_0/\delta\omega)^{-1} \ll 1, \tag{1}$$

where ω_0 is the characteristic resonance frequency of the medium and $\bar{\omega}$ is the frequency corresponding to the center of the pulse spectrum.

The meaning of conditions (1) is that the frequencies of the Fourier components of the pulse lie much lower than the frequencies of resonance electron-optical absorption. In the case of quasimonochromatic pulses, we have $\bar{\omega} \approx \omega$, $\delta\omega \ll \omega$. In this case, the first condition in (1) has the form $(\omega_0/\omega)^{-1} \ll 1$, while the second is satisfied automatically. In the other limiting case $\bar{\omega}\tau_p \ll 1$ corresponding to video pulses ($\bar{\omega} \ll \delta\omega \sim 1/\tau_p$), it is sufficient to require that the second condition, which can be written in the form $(\omega_0\tau_p)^{-1} \ll 1$, is satisfied. In the general case, the fulfillment of both conditions in (1) is required.

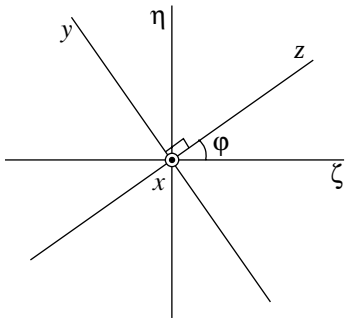

Fig. 1. Geometry of propagation of an ESP in a uniaxial birefringent medium; ζ is the optical axis; the pulse propagates along the *z* axis at an angle φ to the ζ axis. The ordinary component is polarized in the *xz* plane normal to the plane of the figure, while the extraordinary wave is polarized in the plane of the figure along the *y* axis.

By virtue of this condition, the ESP spectrum contains no resonance Fourier components; for this reason, the interaction with the medium is relatively weak [12].

Anisotropy of the medium is a necessary condition for the presence of even powers of electric field in the above-mentioned expansion. In the general case, the electromagnetic wave in such a medium is not completely transverse. In a uniaxial medium, there exist two preferred directions (along and across the optical axis) along which the wave field is strictly transverse [27]. In the former case, nonlinearities of only odd orders are left [28, 29], while, in the latter case, even powers appear, and quadratic nonlinearity plays the major role [30]. When a pulse propagates at right angles to the optical axis, we must generally take into account two components of its electric field, ordinary E_o and extraordinary E_e, and assume that nonlinear susceptibilities are tensor quantities. Some authors employ a scalar model, taking into account only one electric field component of the electric field of the ESP [31–33]. It should be noted that quadratic nonlinearity does not appear in media with induced anisotropy [34, 35] in view of the weakness of applied fields (electric, magnetic, and deformational) as compared to intra-atomic fields.

The theoretical models proposed in [28, 30, 31, 33, 35] are phenomenological by nature. These models are based on the expansion of **P**(**E**) in the presence of nonlinear susceptibility tensor of rank two and/or three [30, 35], or an anisotropic oscillator with a cubic or quadratic nonlinearity is proposed for the material model [28]. Under conditions (1), both approaches lead to identical systems of nonlinear wave equations for ordinary E_o and extraordinary E_e pulse components.

Here, we propose a simple quantum-mechanical model of an optically uniaxial medium, including the electron, electron-vibrational, and ion responses. We assume that anisotropy is natural, i.e., formed by a strong intrinsic electric field in which both electrons and ions are located. Such properties are typical of uniaxial single crystals, organic molecular structures, and so on [36]. In the case of single crystals, we must generally specify a symmetry class [36, 37]. In such cases, it is difficult to carry out appropriate quantum-mechanical calculations to take into account the above-mentioned types of material response. Uniaxial crystals include crystals of the tetragonal, trigonal, and hexagonal systems with the same structure of linear susceptibility tensor reduced to the principal axes: $\chi_{xx} = \chi_{yy} \neq \chi_{zz}$ [38]. In the optical transparency spectral range, the main contribution to the polarization response of the medium is determined by linear effects; in this case, nonlinearity plays the role of a perturbing factor. Since the structure of the linear susceptibility tensor is insensitive to a change in the symmetry class of uniaxial crystals and nonlinearity is weak under conditions (1), we can disregard the dependence of nonlinear susceptibility on the symmetry class. In this connection, the quantum-mechanical model proposed by us combines the optical properties of all media with natural uniaxial anisotropy in their spectral transparency region. On the basis of this material model and Maxwell equations, we can arrive at nonlinear wave equations describing the ESP dynamics in the spectral transparency range of uniaxial media and carry out their analysis; this forms the subject of the present paper.

2. ELECTRON AND ION RESPONSES

Let an electromagnetic pulse propagate in a uniaxial medium along the *z* axis at an angle φ to the optical axis (Fig. 1). The ordinary component E_o of the electric field of the ESP is perpendicular to the plane of the figure and is parallel to the *x* axis, while the extraordinary component E_e lies in this plane and is normal to the *z* axis (parallel to the *y* axis).

The evolution of the state of the medium is described by the equations for the elements of the density matrix $\hat{\rho}$:

$$\frac{\partial \rho_{\mu\nu}}{\partial t} = -i\omega_{\mu\nu}\rho_{\mu\nu} + \frac{i}{\hbar}V_{\mu\nu}(\rho_{\mu\mu} - \rho_{\nu\nu}) - \frac{i}{\hbar}\sum_{j\neq\mu,\nu}(V_{\mu j}\rho_{j\nu} - \rho_{\mu j}V_{j\nu}), \quad (2)$$

where $\hbar$ is Planck's constant, $V_{\mu\nu}$ is the matrix element of the Hamiltonian of the electric-dipole interaction between the pulse and the field, and $\omega_{\mu\nu}$ is the frequency of the quantum transition $\mu \longleftrightarrow \nu$. The subscripts in Eq. (2) run through the values $\mu, \nu = 1, 2, 3, \ldots, K$, where K is the total number of electron quantum levels formed by the strong intrinsic field and participating in the interaction with the ESP field (the value of $K \geq 3$ is regarded as arbitrary). Equations for diagonal elements can be obtained from Eq. (2) for $\mu = \nu$.

In a strong internal electric field of the medium, electron levels are not degenerate in the modulus of the total angular momentum component M [39]. As a result, π ($\Delta M = 0$) and σ ($\Delta M = \pm 1$) transitions, which are allowed in accordance with the electric-dipole selection rules, are formed in the electron subsystem.

In view of the uniaxial anisotropy, $[\hat{H}_0, \hat{M}^2]$ differs from zero ($\hat{H}_0$ is the intrinsic Hamiltonian of electrons in the internal electric field of the medium and $\hat{M}$ is the angular momentum operator). At the same time, $[\hat{H}_0, \hat{M}_\zeta] = 0$, where $\hat{M}_\zeta$ is the operator of the angular momentum component along the ζ axis, which has eigenvalues equal to M. For this reason, the wave function of an optical electron in an axisymmetric field can be written in the form

$$\psi_{\mu M} = R_\mu(\zeta, r)\exp(iM\varphi), \tag{3}$$

where r, φ, and ζ are the components of the cylindrical system of coordinates (the ζ axis of axial symmetry coincides with the optical axis) and μ is the set of quantum numbers corresponding to the cylindrical symmetry.

In addition, we choose the Cartesian system of coordinates x, η, ζ turned through angle φ relative to the x, y, z system in the (yz) plane (see Fig. 1). Using the above expression for $\psi_{\mu M}$, we obtain the Cartesian components of vector $\mathbf{d}_{\mu\nu}$ of the dipole moment of the $\mu \longleftrightarrow \nu$ transition in the coordinate system x, η, ζ:

$$d^x_{\mu\nu} = \frac{d_{\mu\nu}}{\sqrt{2}}|\Delta M_{\mu\nu}|, \quad d^\eta_{\mu\nu} = i\frac{d_{\mu\nu}}{\sqrt{2}}\Delta M_{\mu\nu},$$

$$d^\zeta_{\mu\nu} = D_{\mu\nu}(1 - |\Delta M_{\mu\nu}|),$$

where $\Delta M_{\mu\nu} \equiv M_\mu - M_\nu = 0, \pm 1$. The maximal values for dipole moments for σ ($\varphi = 0$) and π ($\varphi = \pi/2$) transitions can be written in the form

$$d_{\mu\nu} = -\sqrt{2}\pi e\int_0^\infty r^2 dr \int_{-\infty}^\infty R_\mu(z, r)R_\nu(z, r)dz,$$

$$D_{\mu\nu} = -2\pi e\int_0^\infty r dr \int_{-\infty}^\infty zR_\mu(z, r)R_\nu(z, r)dz,$$

where e is the elementary charge.

Carrying out the above-mentioned transformation of rotation through angle φ around the x axis, $\mathbf{d}' = \hat{L}\,\mathbf{d}$, where $\mathbf{d}' = (d^x_{\mu\nu}, d^y_{\mu\nu}, d^z_{\mu\nu})^T$ and $\mathbf{d} = (d^x_{\mu\nu}, d^\eta_{\mu\nu}, d^\zeta_{\mu\nu})^T$, we obtain

$$\begin{aligned} d^x_{\mu\nu} &= \frac{d_{\mu\nu}}{\sqrt{2}}|\Delta M_{\mu\nu}|, \\ d^y_{\mu\nu} &= i\frac{d_{\mu\nu}}{\sqrt{2}}\Delta M_{\mu\nu}\cos\varphi - D_{\mu\nu}(1 - |\Delta M_{\mu\nu}|)\sin\varphi, \\ d^z_{\mu\nu} &= i\frac{d_{\mu\nu}}{\sqrt{2}}\Delta M_{\mu\nu}\sin\varphi + D_{\mu\nu}(1 - |\Delta M_{\mu\nu}|)\cos\varphi. \end{aligned} \tag{4}$$

Accordingly, for the matrix elements of the interaction Hamiltonian $\hat{V}$, we have

$$\begin{aligned} V_{\mu\nu} &= -\mathbf{d}_{\mu\nu}\cdot\mathbf{E}(\mathbf{r}, t) \\ &= \left[D_{\mu\nu}(1 - |\Delta M_{\mu\nu}|)\sin\varphi - i\frac{d_{\mu\nu}}{\sqrt{2}}\Delta M_{\mu\nu}\cos\varphi\right]E_e \\ &\quad - \frac{d_{\mu\nu}}{\sqrt{2}}|\Delta M_{\mu\nu}|E_o \\ &\quad - \left[D_{\mu\nu}(1 - \Delta M_{\mu\nu})\cos\varphi + i\frac{d_{\mu\nu}}{\sqrt{2}}\Delta M_{\mu\nu}\sin\varphi\right]E_z. \end{aligned} \tag{5}$$

In the axisymmetric field, quantum levels do not possess any definite parity. This circumstance determines the selection rules for electric-dipole transitions in the strong field of the medium. In contrast to an isotropic medium, a much larger number of transitions are allowed in such a medium due to mixing of states with various parities with certain quantum levels. This is the reason for the emergence of quadratic and all other even nonlinearities. The internal field of the medium is strong and is able to form initially the electron quantum levels. For this reason, we assume that conditions (1) are satisfied for all (including forbidden) electron-optical transitions, except those between vibrational sublevels of the ground state (see below). The electric field $\mathbf{E}$ of the pulse depends on coordinates $\mathbf{r}$ and time t. This dependence presumes the fulfillment of conditions (1). In this case, system (2) can be solved by the method of successive approximations in small parameters (in the sense of relations (1)), which are proportional to the time derivatives in relation (2), as well as the summands of the sum appearing on the right-hand side of this equation. In this case, in the zero-order approximation, we obtain from Eq. (2)

$$\rho_{\mu\nu} = \frac{V_{\mu\nu}(\rho_{\mu\nu} - \rho_{\nu\nu})}{\hbar\omega_{\mu\nu}}.$$

Substituting this expression into the terms omitted earlier, we obtain $\rho_{\mu\nu}$ in the first approximation, and so on.

As a result, in the second approximation, we have

$$\rho_{\mu\nu} = -\frac{\rho_{\nu\nu}-\rho_{\mu\mu}}{\hbar\omega_{\mu\nu}}V_{\mu\nu} + \frac{1}{\hbar\omega_{\mu\nu}}\sum_{\lambda\neq\mu,\nu}\Bigg[(\alpha_{\nu\lambda}-\alpha_{\lambda\mu})V_{\mu\lambda}V_{\lambda\nu} + \frac{V_{\lambda\nu}}{\hbar\omega_{\mu\lambda}}\sum_{\eta\neq\mu,\nu}(\alpha_{\eta\mu}V_{\mu\lambda}V_{\eta\lambda}-\alpha_{\lambda\eta}V_{\mu\eta}V_{\eta\lambda}) + \frac{V_{\mu\lambda}}{\hbar\omega_{\nu\lambda}}\sum_{\eta\neq\lambda,\nu}(\alpha_{\eta\lambda}V_{\lambda\eta}V_{\eta\nu}-\alpha_{\nu\eta}V_{\lambda\eta}V_{\eta\nu})\Bigg] - i\frac{\alpha_{\nu\mu}}{\omega_{\mu\nu}}\frac{\partial V_{\mu\nu}}{\partial t} + \frac{\alpha_{\nu\mu}}{\omega_{\mu\nu}^2}\frac{\partial^2 V_{\mu\nu}}{\partial t^2}, \quad (6)$$

where $\alpha_{\mu\nu}\equiv(W_\nu - W_\mu)/\hbar\omega_{\mu\nu}$, W_μ being the initial occupancy of the μth level. In expression (6), we included the nonlinearity of not higher than third order and took into account the fact that, under conditions (1), the nonlinearity and dispersion (the last two terms in relation (6)) behave as additive quantities [12].

Substituting relation (6) into the right-hand side of Eq. (2), taking into account the Hermitian nature of operator $\hat{V}$, and integrating, we obtain the following expressions for the diagonal elements of $\hat{\rho}$:

$$\rho_{\mu\mu} = W_\mu - \sum_{\lambda\neq\mu}\frac{W_\mu - W_\lambda}{\hbar^2\omega_{\lambda\mu}^2}|V_{\mu\lambda}|^2. \quad (7)$$

We obtain the values of the polarization components corresponding to the electric field components E_o, E_e, and E_z of the pulse with the help of relations

$$P_{o,e,z} = N\sum_{\mu,\nu} d_{\mu\nu}^{(x,y,z)}\rho_{\mu\nu}^* + \text{c.c.},$$

where N is the concentration of valence electrons, and using relations (4)–(7). After cumbersome but simple transformations, we obtain

$$P_o = \chi_\perp E_o + 2\chi_{eo}^{(2)}E_eE_o + \chi_o^{(3)}E_o^3 + \chi_{eo}^{(3)}E_e^2E_o - \kappa_\perp\frac{\partial^2 E_o}{\partial t^2}, \quad (8)$$

$$P_e = \chi_eE_e + \chi_zE_z + \chi_e^{(2)}E_e^2 + \chi_{eo}^{(2)}E_o^2 + \chi_e^{(3)}E_e^3 + \chi_{eo}^{(3)}E_o^2E_e - \kappa_e\frac{\partial^2 E_e}{\partial t^2}, \quad (9)$$

$$P_z = \chi_zE_x + \chi_{ez}E_e, \quad (10)$$

where χ_e, χ_z, and χ_{ez} can be expressed in terms of the principal diagonal components $\chi_\perp$ and $\chi_\parallel$ of the linear instantaneous susceptibility tensor,

$$\chi_e = \chi_\perp\cos^2\varphi + \chi_\parallel\sin^2\varphi,$$
$$\chi_z = \chi_\perp\sin^2\varphi + \chi_\parallel\cos^2\varphi, \quad (11)$$
$$\chi_{ez} = (\chi_\perp - \chi_\parallel)\sin\varphi\cos\varphi,$$

$$\chi_\perp = N\sum_{\mu\neq\nu}\frac{d_{\mu\nu}^2|\Delta M_{\mu\nu}|}{\hbar\omega_{\mu\nu}}(W_\nu - W_\mu),$$
$$\chi_\parallel = 2N\sum_{\mu\neq\nu}D_{\mu\nu}^2\frac{1-|\Delta M_{\mu\nu}|}{\hbar\omega_{\mu\nu}}(W_\nu - W_\mu), \quad (12)$$

and nonzero components of the nonlinear susceptibility tensor of rank two are given by

$$\chi_{eo}^{(2)} = \chi_{xxy}^{(2)} = \chi_{xyx}^{(2)} = \chi_{yxx}^{(2)} = \frac{4N}{\hbar}\sin\varphi\sum_{\mu\neq\nu}\frac{D_{\mu\nu}}{\omega_{\mu\nu}}\sum_{\lambda\neq\mu,\nu}d_{\mu\lambda}d_{\nu\lambda}(\alpha_{\mu\lambda}-\alpha_{\nu\lambda}), \quad (13)$$

$$\chi_e^{(2)} = \chi_{yyy}^{(2)} = \frac{2N}{\hbar}\sin^3\varphi \times\sum_{\mu\neq\nu}\frac{D_{\mu\nu}}{\omega_{\mu\nu}}\sum_{\lambda\neq\mu,\nu}D_{\mu\lambda}D_{\nu\lambda}(\alpha_{\mu\lambda}-\alpha_{\nu\lambda}). \quad (14)$$

Cumbersome expressions for the third-order nonlinear susceptibilities $\chi_o^{(3)}$, $\chi_e^{(3)}$, and $\chi_{eo}^{(3)}$ are given in the Appendix.

It was noted above that, owing to condition (1), the frequencies of the Fourier components of the spectrum are far from the resonance frequencies of the medium. Consequently, for $\chi^{(2)}$ and $\chi^{(3)}$, the zero-dispersion approximation is realized, for which the Kleiman rule [36] holds. According to this rule, the components of nonlinear susceptibility tensors are invariant to any transposition of their indices.

While deriving Eqs. (8) and (9), we took into account the above-mentioned degeneracy of electron states in the modulus of M. The real parts of the terms in Eq. (6), containing the first derivatives with respect to time, correspond to σ transitions (see also Eq. (5)). In the course of summation in the expressions for polarization components, terms with $\Delta M = \pm 1$ and with identical values of $\omega_{\mu\nu}$ mutually cancel out on account of degeneracy. The imaginary parts of the terms in question, containing $|\Delta M_{\mu\nu}|$ in π and σ transitions (see Eqs. (5) and (6)), also cancel out during the summation with complex conjugate quantities in the expressions for components of **P**.

It should be noted in connection with the latter remarks that the application of a constant external magnetic field removes the degeneracy in modulus of M.

In this case, doublets are formed from each degenerate level, for which $\Delta M = \pm 1$ and the frequencies $\omega_{\mu\nu}$ of the corresponding transitions are not identical any longer. As a result, the right-hand sides of expansions of type (8) and (9) acquire the first time derivatives of **E** [29], which leads to Faraday's rotation of the polarization plane of the pulse. However, in our case, there is no external magnetic field, and the internal crystal electric field removes degeneracy only in the modulus of M.

The origin of the second time derivatives in Eqs. (8) and (9) can be explained most easily by using the dependence of linear electron susceptibilities on frequency ω:

$$\chi_{e,\perp}(\omega) = \chi_{e,\perp}\frac{\omega_{e,o}^2}{\omega_{e,o}^2 - \omega^2}.$$

For $\omega/\omega_{e,o} \ll 1$ (see relations (1)), we have the expansion

$$\chi_{e,\perp}(\omega) \approx \chi_{e,\perp}\left(1 + \frac{\omega^2}{\omega_{e,o}^2}\right).$$

Using the substitution $\omega \longrightarrow i\partial/\partial t$, we arrive at the second time derivatives in relations (8) and (9). Dispersion was disregarded in expression (10) since $P_z \ll P_e, P_o$, while dispersion in approximation (1) is an effect with a higher order of smallness than the linear instantaneous response.

The dispersion parameters $\kappa_\perp$ and κ_e in Eqs. (8) and (9), which take into account the weak (in the sense of conditions (1)) inertia of the electron response, can be written in terms of $\chi_\perp$ and χ_e, respectively, in the form

$$\kappa_\perp = \frac{1}{2}\left(\frac{\partial^2\chi_\perp}{\partial\omega^2}\right)_{\omega=0}, \quad \kappa_e = \frac{1}{2}\left(\frac{\partial^2\chi_e}{\partial\omega^2}\right)_{\omega=0}$$

and express the extent of dependence of linear susceptibilities on frequency ω. In explicit form, we have

$$\begin{aligned}\kappa_e &= \kappa_\perp\cos^2\varphi + \kappa_\parallel\sin^2\varphi,\\ \kappa_\perp &= N\sum_{\mu\neq\nu}\frac{d_{\mu\nu}^2|\Delta M_{\mu\nu}|}{\omega_{\mu\nu}^2}\alpha_{\mu\nu},\\ \kappa_\parallel &= 2N\sum_{\mu\neq\nu}D_{\mu\nu}^2\frac{1-|\Delta M_{\mu\nu}|}{\omega_{\mu\nu}^2}\alpha_{\mu\nu}.\end{aligned} \tag{15}$$

Usually, $|\chi_\perp - \chi_\parallel| \ll \chi_\perp, \chi_\parallel$ [40]. In this case, it can be seen from relations (11) that $\chi_{ez} \ll \chi_\perp, \chi_e$. This circumstance is responsible for the relative smallness of the longitudinal electric field component of the ESP: $E_z \ll E_o, E_e$ (see Section 4). For this reason, only the linear local response to component E_z is taken into account in expansions (8)–(10).

Expansions (8) and (9) can be reversed and written in the form of a system of differential equations for P_o and P_e with the right-hand sides depending on the electric field of the pulse. In the zero-order approximation, it follows from relations (8) and (9) that $E_o = P_o/\chi_\perp$ and $E_e = P_e/\chi_e$. Substituting these relations into the next terms of expansions (8) and (9), we obtain

$$\begin{aligned}&\frac{\partial^2 P_o}{\partial t^2} + \omega_o^2 P_o - 2\beta_{oe}^{(2)}P_eP_o - \beta_o^{(3)}P_o^3\\ &\quad - \beta_{oe}^{(3)}P_e^2P_o = \omega_o^2\chi_\perp E_o,\end{aligned} \tag{16}$$

$$\begin{aligned}&\frac{\partial^2 P_e}{\partial t^2} + \omega_e^2 P_e - \beta_e^{(2)}P_e^2 - \beta_{eo}^{(2)}P_o^2\\ &- \beta_e^{(3)}P_e^3 - \beta_{eo}^{(3)}P_o^2P_e = \omega_e^2\chi_e E_e.\end{aligned} \tag{17}$$

Here,

$$\omega_o^2 = \frac{\chi_\perp}{\kappa_\perp}, \quad \omega_e^2 = \frac{\chi_e}{\kappa_e}, \quad \beta_{oe}^{(2)} = \frac{\chi_{eo}^{(2)}}{\chi_e k_\perp},$$

$$\beta_{eo}^{(2)} = \frac{\chi_{eo}^{(2)}\chi_e}{\chi_\perp^2\kappa_e}, \quad \beta_e^{(2)} = \frac{\chi_e^{(2)}}{\chi_e\kappa_e}, \quad \beta_o^{(3)} = \frac{\chi_o^{(3)}}{\chi_\perp^2\kappa_\perp},$$

$$\beta_e^{(3)} = \frac{\chi_e^{(3)}}{\chi_e^2\kappa_e}, \quad \beta_{oe}^{(3)} = \frac{\chi_{eo}^{(3)}}{\chi_e^2\kappa_\perp}, \quad \beta_{eo}^{(3)} = \frac{\chi_{eo}^{(3)}}{\chi_\perp^2\kappa_e}.$$

This system generalizes the Lorentz classical anisotropic model [41] to the case when the nonlinearity of the electron response is taken into account. It should be noted that this system has been derived here on the basis of quantum-mechanical concepts concerning the medium by using the low-frequency resonance approximation (1). In this case, eigenfrequencies ω_o and ω_e are determined by the entire set of electron quantum levels (see relations (11), (12), (15) and expressions for ω_o and ω_e). In addition, it should be noted that frequency ω_e generally depends (although weakly) on angle φ. Obviously, in the nonresonant case, when $\omega \ll \omega_o, \omega_e$ (conditions (1) are satisfied), it is practically impossible to single out a quantum transition which interacts with the field most strongly. This also explains the collective nature of frequencies ω_o and ω_e. Usually, $\omega_o, \omega_e \sim 10^{16}$ s^{-1} [24]. Consequently, frequencies ω of the visible range can easily satisfy the condition $\omega \ll \omega_o, \omega_e$ (see also conditions (1)).

The system of equations (16), (17), as well as expansions (8)–(10), is invariant to substitutions $P_o \longrightarrow -P_o$ and $E_o \longrightarrow -E_o$, but is not invariant to transformations $P_e \longrightarrow -P_e$ and $E_e \longrightarrow -E_e$. The validity of this statement can easily be explained by the axial symmetry of the medium: reflections in planes normal to the optical axis are symmetry transformations, while reflections in planes parallel to this axis are not (see Fig. 1). The only exception are reflections perpendicular to the optical

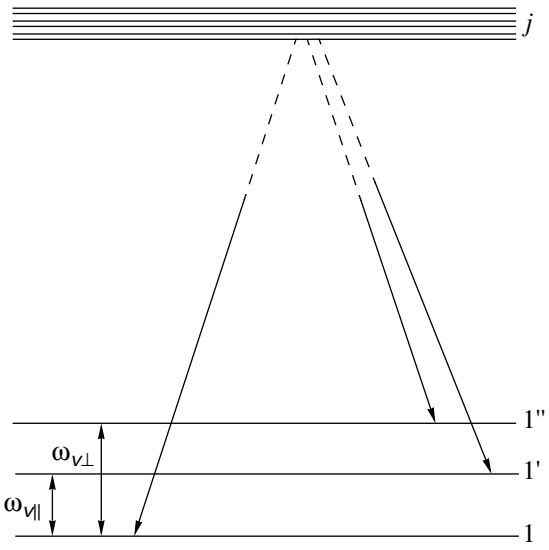

Fig. 2. Diagrams of transitions taking into account the SRS processes; 1' and 1" are the SRS sublevels in the vicinity of the ground electron state in an optically uniaxial medium; $\omega_{v\perp}$ and $\omega_{v\parallel}$ are the frequencies of normal optical modes of ion vibrations across and along the optical axis, respectively; j are upper-lying electron levels.

axis and corresponding to $\varphi = 0$. This circumstance explains the absence of nonlinearities of type P_o^2, P_e^2 and $P_o^2 P_e$ in Eq. (16) and nonlinearities of type $P_o P_e$ and $P_e^2 P_o$ in Eq. (17).

Let us consider two particular cases.

1. Let us assume that $\varphi = 0$. It follows from relations (11)–(15), formulas of the Appendix, and expressions for ω_o, ω_e, and nonlinear constants that $\chi_e = \chi_\perp$, $\omega_o = \omega_e$, $\beta_e^{(2)} = \beta_{oe}^{(2)} = \beta_{eo}^{(2)} = 0$, and $\beta_o^{(3)} = \beta_e^{(3)} = \beta_{oe}^{(3)} = \beta_{eo}^{(3)} = \beta^{(3)}$. In this case, Eqs. (16) and (17) can be written in the form of the Duffing equation for complex polarization $P \equiv P_o + iP_e$:

$$\frac{\partial^2 P}{\partial t^2} + \omega_o^2 P - \beta^{(3)}|P|^2 P = \omega_o^2 \chi_\perp E,$$

where $E = E_o + E_e$.

Here, the division of polarization into ordinary and extraordinary components P_o and P_e is completely arbitrary since both components behave as ordinary components. Using the operation of rotation around the optical axis, we can equate to zero one of the components. In this case, we obtain for polarization the conventional Duffing model, which is often used as the constitutive equation for isotropic dielectrics [15].

2. Let us now suppose that $\varphi = \pi/2$. In this case, the quadratic nonlinearity plays a dominating role. Disregarding the cubic nonlinearity, we obtain from Eqs. (16), (17) a system of constitutive equations of the type of the generalized Henon–Heiles model,

$$\frac{\partial^2 P_o}{\partial t^2} + \omega_o^2 P_o - 2\beta_{oe}^{(2)} P_e P_o = \omega_o^2 \chi_\perp E_o, \qquad (18)$$

$$\frac{\partial^2 P_e}{\partial t^2} + \omega_\parallel^2 P_e - \beta_e^2 P_e^{(2)} - \beta_{eo}^{(2)} P_o^2 = \omega_\parallel^2 \chi_\parallel E_e, \qquad (19)$$

where $\omega_\parallel = \chi_\parallel/\kappa_\parallel$.

It should be noted that the Henon–Heiles system permits both random and regular dynamics depending on the relation between the coefficients [42].

Ionic (vibrational) degrees of freedom, corresponding to the optical branch of vibrations of atomic nuclei at crystal lattice sites, may considerably affect the type of dispersion [24]. The characteristic frequencies of these vibrations are $w_i \sim 10^{13}$ s^{-1}. In this case, for the time scale $\tau_p \sim 10^{-14}$–10^{-15} s of the ESP for ordinary and extraordinary ionic polarizations $P_o^{(i)}$ and $P_e^{(i)}$, we have $\omega_i \tau_p \ll 1$.

In this approximation, we can neglect ionic anharmonism as well as elastic retrieving forces in the oscillator equations of motion [24]. This gives

$$\frac{\partial^2 P_{o,e}^{(i)}}{\partial t^2} = \frac{\omega_p^2 E_{o,e}}{4\pi}, \qquad (20)$$

where ω_p is the ionic plasma frequency [43].

3. DESCRIPTION OF SRS PROCESSES WITH THE HELP OF THE GENERALIZED BLOEMBERGEN–SHEN MODEL

Let us now consider the stimulated Raman scattering (SRS) processes corresponding to electron-vibrational nonlinearity. In view of the axial symmetry, SRS-active centers have at least two normal vibrational modes with frequencies $\omega_{v\parallel}$ and $\omega_{v\perp}$ along and across the optical axis, respectively. We will first derive a closed system of equations for the matrix elements of $\hat{\rho}$, corresponding to the vibrational sublevels of the ground electron state (Fig. 2), eliminating the remaining elements in the framework of the adiabatic approximation (1). The subscripts of the corresponding matrix elements will be labeled by Latin letters. In this case, in accordance with Eq. (2) ($j, k = 1, 1', 1''$), we write

$$\frac{\partial \rho_{jk}}{\partial t} = -i\omega_{jk}\rho_{jk} - \frac{i}{\hbar}\sum_{\lambda > 1''}(V_{j\lambda}\rho_{\lambda\kappa} - \rho_{j\lambda}V_{\lambda k}). \qquad (21)$$

Here, we have taken into account the fact that electron transitions between the sublevels in question are forbidden. Assuming in Eq. (21) that $j = k$, we obtain equations for diagonal elements of $\hat{\rho}$.

We can derive expressions for $\rho_{\lambda j}$ ($\lambda > 1''$, $j = 1, 1', 1''$) from Eq. (2) for $\partial\rho_{\lambda j}/\partial t = 0$ (see relations (1)):

$$\rho_{\lambda j} = -\frac{1}{\hbar\omega_{\lambda j}}\sum_{k=1}^{1''} V_{\lambda k}\rho_{kj} - \frac{1}{\hbar\omega_{\lambda j}}\sum_{\mu > 1''}(V_{\lambda\mu}\rho_{\mu j} - \rho_{\lambda\mu}V_{\mu j}). \quad (22)$$

The terms appearing in parentheses in this equation have been taken into account in the above analysis. These terms contribute to the electron polarization and, hence, can be omitted here. Substituting Eq. (22) into Eq. (21) and taking into account the above remark, we obtain

$$\frac{\partial R_{jk}}{\partial t} = -i\omega_{jk}R_{jk} + i[\hat{G}, \hat{R}]_{jk}, \quad (23)$$

where elements of matrix $\hat{G}$ have the form

$$G_{jl} = \hbar^{-2}\frac{\sum_{\lambda > 1''} V_{j\lambda}V_{\lambda l}}{\omega_{\lambda 1}},$$

and matrix $\hat{R}$ contains only those elements of $\hat{\rho}$ which correspond to the three lower quantum levels 1, 1', and 1'' (see Fig. 2):

$$\hat{R} = \begin{pmatrix} \rho_{1''1''} & \rho_{1''1'} & \rho_{1''1} \\ \rho_{1'1''} & \rho_{1'1'} & \rho_{1'1} \\ \rho_{11''} & \rho_{11'} & \rho_{11} \end{pmatrix}.$$

Here, we have disregarded the difference in frequencies $\omega_{\lambda j}$ of electron-optical transitions ($\lambda > 1''$, $j = 1, 1', 1''$) for different values of j, setting $\omega_{\lambda j} \approx \omega_{\lambda 1}$. It can be seen from the figure that $\omega_{1''1} = \omega_{\nu\perp}$ and $\omega_{1'1} = \omega_{\nu\parallel}$.

In our case, sublevels 1' and 1'' have exclusively vibrational origin; for this reason, they have identical angular momentum components M_j ($j = 1, 1', 1''$) along with the first level. For the sake of simplicity, we assume that $M_j = 0$. Following the approach developed by Bloembergen and Shen [44], we assume that $D_{\lambda j} \approx D_{\lambda 1}$ and $d_{\lambda j} \approx d_{\lambda 1}$ in view of the small spacing between the vibrational sublevels. Taking into account the above arguments, using relation (5), and neglecting component E_z, we obtain for matrix $\hat{G}$

$$\hat{G} = \frac{1}{4\hbar N}(\chi_e E_e^2 + \chi_\perp E_o^2)(\hat{\Sigma} - \hat{I}), \quad (24)$$

where $\hat{I}$ is a unit operator and $\hat{\Sigma}$ is matrix all of whose elements are equal to unity.

We can assume that the system of equations (23) derived by us together with relation (24) generalizes the quantum-mechanical Bloembergen–Shen model [45] to the description of SRS processes in an optically uniaxial medium. It should be noted in this connection that system (23) is completely equivalent to the equations for the density matrix for a three-level atom in which all three transitions excited by the square of the field are allowed. It is well known that the Bloembergen–Shen model [44, 45] has the corresponding analogy with a two-level atom.

Since $\omega_{\nu\perp}, \omega_{\nu\parallel} \sim 10^{13}\ \mathrm{s}^{-1}$, we have $\omega_{\nu\perp(\parallel)}\tau_p \ll 1$. Consequently, we can disregard the first term on the right-hand side of Eq. (23) in the zeroth approximation and write this equation in the following symbolic form:

$$\frac{\partial\hat{R}}{\partial t} = i[\hat{G}, \hat{R}].$$

Matrix $\hat{\Sigma}$ commutes with itself at various instants. In this case, the solution to this operator equation can be written in the form

$$\hat{R}(t) = \hat{U}\hat{R}(-\infty)\hat{U}^+, \quad \hat{U} = \exp(i\hat{\theta}/3). \quad (25)$$

Here,

$$\hat{\theta} = \theta(\hat{\Sigma} - \hat{I}), \quad \theta = \frac{3}{4\hbar N}\int_{-\infty}^{t}(\chi_e E_e^2 + \chi_\perp E_o^2)dt'. \quad (26)$$

Obviously operators $\hat{\Sigma}$ and $\hat{I}$ commute with each other; consequently, we have

$$\hat{U} = \exp\left(-\frac{i\theta}{3}\right)\exp\left(\frac{i\hat{\Sigma}\theta}{3}\right).$$

Since $\hat{\Sigma}^2 = (K+1)\hat{\Sigma}$, $\hat{\Sigma}^3 = (K+1)^2\hat{\Sigma}$, …, $\hat{\Sigma}^k = (K+1)^{k-1}\hat{\Sigma}$, …, the series corresponding to the exponential in the last expression can be easily summed. As a result, neglecting an insignificant C-number factor $\exp(-i\theta/3)$, we obtain

$$\hat{U} = \hat{I} - \frac{\hat{\Sigma}}{3}\left(2\sin^2\frac{\theta}{2} - i\sin\theta\right). \quad (27)$$

Matrix $\hat{R}(-\infty)$ is diagonal. The corresponding occupancies of the electron state and of the SRS sublevels are W_1, $W_{1'}$, and $W_{1''}$. Using expressions (25)–(27), we obtain the following expression for $j \neq k$:

$$R_{kj} = \frac{1}{9}\left[2(3W_l - 1)\sin^2\frac{\theta}{2} - 3i(W_k - W_j)\sin\theta\right], \quad l \neq j, k. \quad (28)$$

The expression for the electron contribution $P^{(ev)}$ to

polarization has the form

$$P^{(ev)} = N_v \sum_{\lambda > 1''} \sum_{j=1}^{1''} d^*_{\lambda j} \rho_{\lambda j} + \text{c.c.}$$
$$\approx N_v \sum_{\lambda > 1''} d^*_{\lambda 1} \sum_{j=1}^{1''} \rho_{\lambda j} + \text{c.c.},$$

where N_v is the concentration of molecules contributing to SRS.

Substituting Eq. (22) into this relation and subtracting the second sum taking into account the electron polarization considered above, we obtain

$$P^{(ev)} = -N_v \sum_{\lambda > 1''} \frac{d^*_{\lambda 1} V_{\lambda 1}}{\hbar \omega_{\lambda 1}} \sum_{k>j} R_{kj} + \text{c.c.} \qquad (29)$$

It can easily be seen from relation (5) that the factors in front of the second sum in Eq. (29) are real valued for both the ordinary and the extraordinary components. Using relation (28), we obtain

$$\sum_{k>j} R_{kj} + \text{c.c.} = 0.$$

In the first approximation in parameter $\omega_{v\perp(\|)}\tau_p$, we obtain from Eq. (21)

$$\frac{\partial}{\partial t} \sum_{k>j} R_{kj} + \text{c.c.} = i \sum_{k>j} \omega_{kj} (R^*_{kj} - R_{kj}).$$

This relation together with Eq. (29) gives

$$\frac{\partial}{\partial t} \sum_{k>j} R_{kj} + \text{c.c.} = \frac{2}{3} \sum_{k>j} \omega_{kj} (W_j - W_k) \sin\theta.$$

Integrating this expression with respect to t, substituting the result into Eq. (29), and using relation (5), we obtain

$$P^{(ev)}_{e,o} = \frac{N_v}{3N} \omega_v \chi_{e,o} E_{e,o} \int_{-\infty}^{t} \sin\theta \, dt', \qquad (30)$$

where

$$\omega_v = \omega_{v\|}(W_1 - W_{1'}) + \omega_{v\perp}(W_1 - W_{1''}) + (\omega_{v\perp} - \omega_{v\|})(W_{1'} - W_{1''}).$$

Let us estimate the value of the quantity θ appearing in the argument of the sine in expression (30). Considering that $E^2 \approx (4\pi/c)I$, where I is the ESP intensity, we obtain

$$\theta \sim 3\pi \frac{\chi}{N} \frac{I\tau_p}{\hbar c}.$$

Taking polarizability $\chi/N \sim 10^{-26}$ cm^3, $I \sim 10^{13}$ W/cm^2, and $\tau_p \sim 10^{-14}$ s, we have $\theta \sim 10^{-2}$–$10^{-3} \ll 1$. In these cases, we can set $\sin\theta \approx \theta$ in Eq. (30). Then, the expression for P for $\varphi = 0$ assumes the form derived in [24] for an isotropic dielectric disregarding the variation of occupancies in SRS sublevels. This estimate shows that the dynamics of populations of SRS sublevels can indeed be neglected for intensities of 10^{13} W/cm^2 and for ESP durations of 10 fs. However, for $I \sim 10^{15}$ W/cm^2 and $\tau_p \sim 100$ fs, we must take into account the change in occupancies since $\theta \sim 1$ in this case.

Let us estimate the relative contribution to the polarization from the electron cubic nonlinearity and the SRS nonlinearity. The above estimate, relations (8), (9), (12), (30), and the expressions for $\chi^{(3)}$ (see the Appendix) imply that

$$\chi \sim \frac{Nd^2}{\hbar\omega_0}, \quad \chi^{(3)} \sim \frac{Nd^4}{(\hbar\omega_0)^3}, \quad P^{(ev)} \sim \frac{Nd^4 \omega_v \tau_p^2 E^3}{\hbar^3 \omega_0^2}$$

(here, $N_v \approx N$ and d is the characteristic value of the dipole moments of the electron-optical transitions). Then, the sought ratio is

$$\frac{P^{(ev)}}{P^{(3)}} \sim \frac{\omega_v}{\omega_0} (\omega_0 \tau_p)^2,$$

where $P^{(3)}$ is the third-order nonlinear electron polarization. Setting $\omega_v \sim 10^{13}$ s^{-1}, $\omega_0 \sim 10^{16}$ s^{-1}, and $\tau_p \sim 10^{-15}$ s, we obtain $P^{(ev)}/P^{(3)} \sim 0.1$; i.e., the contribution of SRS can be disregarded as compared to the cubic electron nonlinearity for an ESP duration of several femtoseconds. This estimate is in accordance with the data given in [24].

A similar estimate shows that

$$\frac{P^{(ev)}}{P^{(2)}} \sim d \frac{(w_v \tau_p)^2}{\hbar \omega_v} \sqrt{\frac{I}{c}}.$$

For $d \sim 10^{-19}$ CGSE units, $(\omega_v\tau_p)^2 \sim 0.1$, $\omega_v \sim 10^{13}$ s^{-1}, and $I \sim 10^{13}$ W/cm^2, we obtain $P^{(ev)}/P^{(2)} \sim 0.1$. Considering that the quadratic nonlinearity plays the major role in the electron response for propagation across the optical axis, we arrive at the conclusion that this nonlinearity in such geometry also dominates over the SRS

mechanism for pulse durations on the order of a few tens of femtoseconds.

Let us now estimate the relative dispersion contribution of the ionic $P^{(i)}$ and electronic P degrees of freedom. From relations (8), (9), (15), and (20), we have

$$\frac{P^{(i)}}{P} \sim \frac{\omega_p^2}{\omega_0 \omega_c}(\omega_0 \tau_p)^4,$$

where $\omega_c = 4\pi d^2 N/\hbar$ is the cooperation frequency.

Setting $\omega_p \sim \omega_c \sim 10^{12}$–$10^{13}$ s^{-1}, $\omega_0 \sim 10^{16}$ s^{-1}, and $\tau_p \sim 10^{-15}$ s, we obtain the following estimate: $P^{(i)}/P \sim$ 1–10. It can be seen that this ratio strongly depends on parameter $\omega_0 \tau_p$.

4. NONLINEAR WAVE EQUATIONS

In order to analyze the self-consistent dynamics of pulses and the medium, the relations derived above for material responses should be supplemented with the Maxwell equations

$$\Delta \mathbf{E} - \nabla(\nabla \cdot \mathbf{E}) - \frac{1}{c^2}\frac{\partial^2 \mathbf{E}}{\partial t^2} = \frac{4\pi}{c^2}\frac{\partial^2 \mathbf{P}^{\Sigma}}{\partial t^2}, \qquad (31)$$

where the total polarization $\mathbf{P}^{\Sigma} = \mathbf{P} + \mathbf{P}^{(i)} + \mathbf{P}^{(ev)}$.

Henceforth, we will assume that diffraction effects are weak, considering that the pulse field components depend mainly on z and t. It was mentioned above that the longitudinal field component is much smaller than the transverse component. For this reason, we can disregard the derivatives with respect to transverse components in the equation for E_z, taking them into account for components E_0 and E_e only. Integrating twice the z component of Eq. (31) and considering that $P_z^{(i)} = P_z^{(ev)} = 0$, we obtain $E_z = -4\pi P_z$. This expression together with Eq. (10) gives

$$E_z = -\frac{4\pi \chi_{ez} E_e}{1 + 4\pi \chi_z}.$$

In order to write equations for E_o and E_e, we first represent components P_o and P_e of the electronic part of polarization in the form

$$P_{o,e} = \chi_{\perp,e} E_{o,e} - \kappa_{\perp,e}\frac{\partial^2 E_{o,e}}{\partial t^2} + P_{o,e}^{(nl)},$$

where $P_{o,e}^{(nl)}$ are the parts of the electron polarization containing quadratic and cubic nonlinearities.

In this case, we obtain the following equation in the x and y components from Eq. (31):

$$\frac{\partial^2 E_{o,e}}{\partial z^2} - \frac{n_{o,e}^2}{c^2}\frac{\partial^2 E_{o,e}}{\partial t^2} = \frac{4\pi}{c^2}\frac{\partial^2}{\partial t^2}$$

$$\times \left[P_{o,e}^{(nl)} - \kappa_{\perp,e}\frac{\partial^2 E_{o,e}}{\partial t^2} + P_{o,e}^{(i)} + P_{o,e}^{(ev)} \right] + \Delta_\perp E_{o,e},$$

where $n_{o,e} = \sqrt{1 + 4\pi\chi_{\perp,e}}$ are the refractive indices of the ordinary and extraordinary waves and $\Delta_\perp$ is the transverse Laplacian.

The right-hand sides of these equations describe nonlinearity, dispersion, and diffraction (which are effects with a higher order of smallness as compared to the instantaneous linear response appearing on the left-hand sides) through renormalization of the rates of field components with the help of refractive indices n_o and n_e.

This circumstance allows us to use the slowly varying profile approximation in the comoving frame of reference [46]. In accordance with this method, we can assume that the right-hand sides are equal to zero in the zeroth approximation in nonlinearity and dispersion and assume that the two components propagate in only one direction (along the z axis). Then, $E_{o,e} = E_{o,e}(\tau_{o,e})$, where $\tau_{o,e} = t - n_{o,e} z/c$. In the first approximation, the effect of the right-hand sides will be taken into account by introducing the "slow" coordinate $z' = \varepsilon z$ in addition to $\tau_{o,e}$ in the arguments of E_o and E_e [46]: $E_{o,e} = E_{o,e}(\tau_{o,e}; z')$, where $\varepsilon \ll 1$ is a small dimensionless parameter taking into account the effect of the right-hand sides of the latter equations. Passing from variables t and z to variables $\tau_{o,e}$ and z' in the equations for E_o and E_e, we can write

$$\frac{\partial}{\partial t} = \frac{\partial}{\partial \tau_{o,e}}, \quad \frac{\partial}{\partial z} = -\frac{n_{o,e}}{c}\frac{\partial}{\partial \tau_{o,e}} + \varepsilon\frac{\partial}{\partial z'},$$

$$\frac{\partial^2}{\partial z^2} \approx \frac{n_{o,e}^2}{c^2}\frac{\partial^2}{\partial \tau_{o,e}^2} - \frac{2\varepsilon n_{o,e}}{c}\frac{\partial^2}{\partial \tau_{o,e}\partial z'},$$

where we have neglected the term of the order of ε^2 in the last relation. This allows us to integrate the wave equations for E_o and E_e with respect to τ_o and τ_e, respectively, in view of the fact that the field of the pulse and all its derivatives tend to zero at infinity:

$$-\frac{2n_{o,e}\varepsilon}{c}\frac{\partial E_{o,e}}{\partial z'} = \frac{4\pi}{c^2}\frac{\partial}{\partial \tau_{o,e}}$$

$$\times \left[P_{o,e}^{(nl)} - \kappa_{\perp,e}\frac{\partial^2 E_{o,e}}{\partial \tau_{o,e}^2} + P_{o,e}^{(i)} + P_{o,e}^{(ev)} \right] + \Delta_\perp \int_{-\infty}^{\tau_{o,e}} E_{o,e} d\tau'_{o,e}.$$

Returning to the initial variables t and z and using formulas (8), (9), (20), and (29), we arrive at the follow-

ing system of nonlinear wave equations for the ordinary and extraordinary components of the pulse:

$$\frac{\partial E_o}{\partial z} + \frac{n_o}{c}\frac{\partial E_o}{\partial t} + a_2\frac{\partial (E_e E_o)}{\partial t} + a_3\frac{\partial (E_e^2 E_o)}{\partial t} + b_{3o}E_o^2\frac{\partial E_o}{\partial t} + \Lambda_o\frac{\partial}{\partial t}\left(E_o\int_{-\infty}^{t}\sin\theta\, dt'\right) - \delta_o\frac{\partial^3 E_o}{\partial t^3} + \sigma\int_{-\infty}^{t}E_o dt' = \frac{c}{2n_o}\Delta_\perp\int_{-\infty}^{t}E_o dt', \quad (32)$$

$$\frac{\partial E_e}{\partial z} + \frac{n_e}{c}\frac{\partial E_e}{\partial t} + a_2 E_o\frac{\partial E_o}{\partial t} + b_{2e}E_e\frac{\partial E_e}{\partial t} + a_3\frac{\partial (E_o^2 E_e)}{\partial t} + b_{3e}E_e^2\frac{\partial E_e}{\partial t} + \Lambda_e\frac{\partial}{\partial t}\left(E_e\int_{-\infty}^{t}\sin\theta\, dt'\right) - \delta_e\frac{\partial^3 E_e}{\partial t^3} + \sigma\int_{-\infty}^{t}E_e dt' = \frac{c}{2n_o}\Delta_\perp\int_{-\infty}^{t}E_e dt'. \quad (33)$$

Here,

$$a_2 = \frac{4\pi\chi_{eo}^{(2)}}{n_o c}, \quad b_{2e} = \frac{4\pi\chi_e^{(2)}}{n_o c}, \quad a_3 = \frac{2\pi\chi_{eo}^{(3)}}{n_o c},$$

$$b_{3e} = \frac{6\pi\chi_e^{(3)}}{n_o c}, \quad b_{3o} = \frac{6\pi\chi_o^{(3)}}{n_o c}, \quad \Lambda_o = \frac{2\pi N_v\omega_v\chi_o}{3Nn_o c},$$

$$\Lambda_e = \frac{2\pi N_v\omega_v\chi_e}{3Nn_o c}, \quad \delta_o = \frac{2\pi\kappa_\perp}{n_o c},$$

$$\delta_e = \frac{2\pi\kappa_e}{n_o c}, \quad \sigma = \frac{\omega_p^2}{2n_o c},$$

and the dynamic parameter θ is defined by formula (26).

The system of nonlinear wave equations (32), (33) describes the propagation of an ESP in a uniaxial medium at an arbitrary angle to the optical axis. These equations take into account the electron and electron-vibrational nonlinearities as well as the electron and ion dispersions. The terms on the right-hand sides describe the pulse diffraction.

It should be noted that the SVP approximation is not connected in any way with the approximation of slowly varying envelopes [47], which is traditional for quasi-monochromatic pulse optics, where the reduction in derivatives is attained due to the fact that the field envelope covers a large number of electromagnetic oscillations. System (32), (33) is written not for envelopes (which cannot be introduced for ESP), but directly for the electric field components E_o and E_e.

If the signal propagates along the optical axis ($\varphi = 0$), coefficients a_2, b_{2e}, and χ_{ez} vanish; in this case, $n_e = n_o$, $\chi_e = \chi_o$, $\delta_o = \delta_e$, $a_3 = 3b_{3o} = 3b_{3e}$, and $\Lambda_o = \Lambda_e$, and system (32), (33) is transformed into the following equation in $E = E_o + iE_e$:

$$\frac{\partial E}{\partial z} + a_3\frac{\partial}{\partial\tau}(|E|^2 E) - \delta_o\frac{\partial^3 E}{\partial\tau^3} + \sigma\int_{-\infty}^{\tau}E d\tau' + \Lambda_o\frac{\partial}{\partial\tau}\left(E\int_{-\infty}^{\tau}\sin\theta\, d\tau'\right) = \frac{c}{2n_o}\Delta_\perp\int_{-\infty}^{\tau}E d\tau';$$

here, $\tau = t - n_o z/c$.

Disregarding the dynamics of population of SRS sublevels, we obtain

$$\sin\theta \approx \theta = \frac{3\chi_o}{4\hbar N}\int_{-\infty}^{\tau'}|E|^2 d\tau''.$$

In this case, the last equation exactly coincides with the one derived in [24] for the ESP propagation in isotropic dielectrics.

Let us now suppose that $\varphi = \pi/2$. It was mentioned in the previous section that we can neglect the electronic cubic and electron-vibrational nonlinearities for pulses of intensity $I \sim 10^{13}$ W/cm^2 and of duration $\tau_p \sim$ 1–100 fs. In addition, $\chi_{ez} = 0$ (see formula (11)). In this case, Eqs. (32), (33) assume the form

$$\frac{\partial E_o}{\partial z} + \frac{n_o}{c}\frac{\partial E_o}{\partial t} + a_2\frac{\partial (E_e E_o)}{\partial t} - \delta_o\frac{\partial^3 E_o}{\partial t^3} + \sigma\int_{-\infty}^{t}E_o dt' = \frac{c}{2n_o}\Delta_\perp\int_{-\infty}^{t}E_o dt', \quad (34)$$

$$\frac{\partial E_e}{\partial z} + \frac{n_e}{c}\frac{\partial E_e}{\partial t} + a_2 E_o\frac{\partial E_o}{\partial t} + b_{2e}E_e\frac{\partial E_e}{\partial t} - \delta_e\frac{\partial^3 E_e}{\partial t^3} + \sigma\int_{-\infty}^{t}E_e dt' = \frac{c}{2n_o}\Delta_\perp\int_{-\infty}^{t}E_e dt'. \quad (35)$$

It should be noted that, if a pulse polarized in the plane of the principle cross section (i.e., in the plane formed by the optical axis and the direction of pulse propagation) enters the medium, it can be seen from Eqs. (34) and (35) that $E_o = 0$. In an anisotropic medium, only the extraordinary component of the ESP can propagate. If, in addition, we disregard ionic dispersion, the one-dimensional dynamics of this component will be described by the Korteweg–de Vries equation, which has soliton video-pulse solutions among other solutions. However, the input signals required for obtaining such solutions must also be in the form of video pulses, which can subsequently split into several solitons. A more interesting case when ESP (or video pulses) can be generated by the envelope pulses will be considered in the next section.

5. GENERATION OF EXTRAORDINARY COMPONENT VIDEO PULSE IN THE ZAKHAROV–BENNEY RESONANCE MODE WITH ORDINARY WAVE

Let us write the ordinary component of a pulse in the form of the envelope pulse with a carrier frequency ω and wave number k:

$$E_o = \xi(t, z, \mathbf{r}_\perp)\exp[i(\omega t - kz)] + \text{c.c.}, \qquad (36)$$

where ξ is the slowly varying complex envelope: $|\partial\xi/\partial\tau| \ll \omega|\xi|$, $|\partial\xi/\partial z| \ll k|\xi|$. In this case, E_e has no carrier frequency.

Substituting Eq. (36) into Eqs. (34) and (35), neglecting rapidly oscillating terms, and using the asymptotic expansion [24, 47]

$$\int_{-\infty}^{t} E_o dt' = \int_{-\infty}^{t} \xi\exp[i(\omega t - kz)]dt' + \text{c.c.}$$

$$= \left(-i\frac{\xi}{\omega} + \frac{1}{\omega^2}\frac{\partial\xi}{\partial t} + \frac{i}{\omega^3}\frac{\partial^2\xi}{\partial t^2} + \ldots\right)\exp[i(\omega t - kz)] + \text{c.c.},$$

we obtain, after simple transformations, a system of equations for ξ and E_e interacting in the Zakharov–Benney resonance mode:

$$i\frac{\partial\xi}{\partial z} + g\frac{\partial^2\xi}{\partial\tau^2} = a_2\omega\xi E_e + \frac{c}{2n_o\omega}\Delta_\perp\xi, \qquad (37)$$

$$\frac{\partial E_e}{\partial z} + b_{2e}E_e\frac{\partial E_e}{\partial\tau} - \delta_e\frac{\partial^3 E_e}{\partial\tau^3} + \sigma\int_{-\infty}^{\tau} E_e d\tau'$$

$$= -a_2\frac{\partial}{\partial\tau}(|\xi|^2) + \frac{c}{2n_o}\Delta_\perp\int_{-\infty}^{\tau} E_e d\tau'. \qquad (38)$$

Here, $g = 3\delta_o\omega - \sigma/\omega^3$, $\tau = t - z/v_g$, the group velocity v_g of the ordinary component is defined as

$$\frac{1}{v_g} = \frac{dk}{d\omega} = \frac{n_o}{c} + 3\delta_o\omega^2 + \frac{\sigma}{\omega^2},$$

and the dispersion equation has the form

$$k = \frac{n_o\omega}{c} + \delta_o\omega^3 - \frac{\sigma}{\omega}.$$

In Eq. (38), the Zakharov–Benney resonance condition [48] is taken into account, according to which the group velocity of the short-wave (ordinary) component is equal to the phase velocity of the long-wave (extraordinary) component: $v_g = c/n_e$.

If we disregard diffraction ($\Delta_\perp = 0$) and ionic dispersion ($\sigma = 0$), we arrive at the system analyzed in [49]. If, in addition, $b_{2e} = \delta_e = 0$, system (37), (38) is transformed into the Yadjima–Oikawa equations [50], which is a unidirectional version of the Zakharov equations [51]. The Yadjima–Oikawa system is integrable by the method of the inverse scattering problem [50]. The corresponding single-soliton two-parametric solution in the laboratory system of coordinates has the form

$$\xi = \xi_m\exp[-i(\Omega t - qz)]\operatorname{sech}\left(\frac{t - z/v}{\tau_p}\right),$$

$$E_e = -E_m\operatorname{sech}^2\left(\frac{t - z/v}{\tau_p}\right). \qquad (39)$$

Here,

$$\xi_m = \frac{6\delta_o}{a_2\tau_p}\sqrt{\omega\Omega}, \quad E_m = \frac{6\delta_o}{a_2\tau_p^2},$$

$$q = \frac{\Omega}{v} + g\left(\Omega^2 + \frac{1}{\tau_p^2}\right),$$

the velocity of the pulse satisfies the relation

$$\frac{1}{v} = \frac{1}{v_g} - 2g\Omega, \qquad (40)$$

parameter Ω determines the nonlinear frequency shift of the short-wave component to the red region since $\Omega > 0$ (see expression for ξ_m and Eq. (36)), while the other free parameter τ_p, which has the meaning of soliton duration, determines the spectral width: $\Delta\omega \sim 1/\tau_p$.

The ordinary component of the pulse is an envelope soliton, while the extraordinary component is a video soliton. It follows from Eqs. (37) and 38) that, if $E_e = 0$ at the input, a pulse of the envelope of the ordinary wave in the medium can generate an ESP of the extraordinary wave. In this case, each photon of the ordinary component increases the wavelength by transferring its energy to the extraordinary wave, which explains the nonlinear shift of the spectral peak of the pulse: $\omega \longrightarrow \omega - \Omega$. In view of the positive value of electron dispersion, the group velocity of the ordinary component (and, accordingly, of the extraordinary component) acquires a positive shift:

$$\frac{1}{v_g} = \frac{n_o}{c} + 3\delta_o\omega^2 \longrightarrow \frac{n_o}{c} + 3\delta_o(\omega - \Omega)^2$$

$$\approx \frac{n_o}{c} + 3\delta_o\omega^2 - 6\omega\delta_o\Omega = \frac{1}{v_g} - 2g\Omega,$$

which coincides with formula (40)

It should be noted that the mechanism of ESP generation associated with the Zakharov–Benney resonance is very close to the corresponding Cherenkov mechanism analyzed for the first time in [52]. The only difference is that the generation mode in the latter case is noncollinear: angle γ between the directions of propagation of ESP and the pulse generating it in a quadratically nonlinear medium, whose spectrum contains two close extreme frequencies ω_1 and ω_2 correspond-

ing to wave numbers k_1 and k_2, is determined by the formula [52, 47]

$$\cos\gamma = \frac{k_2(\omega_2) - k_1(\omega_1)}{k(\omega_2 - \omega_1)}.$$

The velocity of the nonlinear polarization wave at frequency $\omega_2 - \omega_1$ must be larger than the phase velocity of the wave in this medium at the same frequency:

$$\frac{\omega_2 - \omega_1}{k_2(\omega_2) - k_1(\omega_1)} > \frac{\omega_2 - \omega_1}{k(\omega_2 - \omega_1)}.$$

Proceeding to the limit $\omega_2 \longrightarrow \omega_1$ in this inequality and assuming that $\gamma = 0$ in the preceding equality, we arrive at the condition $d\omega/dk = v_{ph}(0)$, where $v_{ph}(0)$ is the phase velocity in the low-frequency dispersion-free limit. This case corresponds to the Zakharov–Benney resonance condition. This synchronism condition is usually difficult to satisfy in the collinear propagation mode [47]. In our case, the Zakharov–Benney resonance condition can be written in the form

$$\frac{n_e - n_o}{c} = 3\delta_o\omega^2. \tag{41}$$

Since the electron dispersion is positive in the transparency region ($\delta_o > 0$), the Zakharov–Benney resonance condition can be satisfied for $n_e > n_o$; i.e., the medium must possess positive birefringence. This conclusion remains unchanged if we take into account ionic dispersion (it can easily be seen from the expression for v_g that the substitution $3\delta_o\omega^2 \longrightarrow 3\delta_o\omega^2 + \sigma/\omega^2$ has been carried out on the right-hand side of the last relation). Taking into account the closeness of the values of n_e and n_o, we can write

$$n_e - n_o \approx \frac{n_e^2 - n_o^2}{2n_o} = \frac{2\pi(\chi_e - \chi_o)}{n_o}.$$

In addition, we have

$$\delta_o = \frac{2\pi\kappa_\perp}{n_o c} \approx \frac{2\pi\chi_o}{n_o c\omega_o^2}.$$

In this case, condition (41) can be written in the form

$$\frac{\chi_e - \chi_o}{3\chi_o} \approx \left(\frac{\omega}{\omega_0}\right)^2.$$

For crystalline quartz, $n_e = 1.55$ and $n_o = 1.54$ [40]. Then, $(\chi_e - \chi_o)/3\chi_0 \approx 0.01$. Consequently, $\omega/\omega_0 \approx 0.1$. Setting $\omega_0 \sim 10^{16}$ s^{-1}, we obtain $\omega \sim 10^{15}$ s^{-1}. For the input pulse, we have $\omega\tau_p \gg 1$; hence, its duration $\tau_p \sim$ 10–100 fs. In accordance with Eq. (39), the generated ESP (or video soliton) will have a duration of approximately the same order of magnitude. Selecting appropriately the carrier frequency of the input signal, we can satisfy the Zakharov–Benney resonance condition and, hence, realize the effective generation of ESP.

Nonlinearity and dispersion of the extraordinary component in Eq. (38) are effects of the same order of smallness. Consequently, the condition under which these effects can be neglected and for which solutions (39) were written can be represented in the form $b_{2e}E_m^2 \ll a_2\xi_m^2$. Substituting the above expressions for E_m^2 and ξ_m^2 into this condition, we obtain $\omega\tau_p\Omega\tau_p \gg b_{2e}/a_2$.

Considering that b_{2e} and a_2 are quantities of the same order of magnitude and taking into account the quasimonochromaticity condition $\omega\tau_p \gg 1$ of the ordinary component, we conclude that the condition in question can easily be satisfied in a wide range of free parameters Ω and τ_p.

The generation of the extraordinary component with the help of the ordinary component in the second harmonic generation mode was considered in [30]. The situation of long-wave–short-wave resonance considered here corresponds to energy pumping from the high-frequency ordinary wave to the zeroth harmonic; as a result, ESPs of the extraordinary wave are generated. It can easily be proved that, using a representation of form (36) for E_e and taking into account the substitutions $\omega \longrightarrow 2\omega$ and $\xi \longrightarrow \xi_e$, Eqs. (34) and (35) in the SVAP approximation lead to the well-known system [47] describing the nonstationary process of second harmonic generation. It can easily be found, using the dispersion relations that takes into account the electron dispersion alone, that the phase synchronism condition $2k_o(\omega) = k_e(2\omega)$ for the second harmonic generation in our case has the form

$$\frac{n_o - n_e}{2} = (4\delta_e - \delta_o)\omega^2 \approx 3\delta_o\omega^2,$$

which has the sign opposite to that in condition (41). This means that the collinear mode of the second harmonic generation can be realized in media with negative birefringence. This must enable us to distinguish between the two effects under the experimental conditions.

The stability of solutions (39) is an equally important factor. Let us analyze the stability using the Ritz–Whitham method of averaged Lagrangian [53]. Since solution (39) corresponds to $b_{2e} = \delta_e = \sigma = 0$, we will consider the stability under the same conditions. It should be noted that this problem can also be solved for b_{2e}, δ_e, $\sigma \neq 0$, but the expressions will be cumbersome. In view of the above remarks, system (37), (38) can be obtained from the Lagrangian density

$$L = \frac{i}{2\omega}\left(\xi\frac{\partial\xi^*}{\partial z} - \xi^*\frac{\partial\xi}{\partial z}\right) + 3\delta_o\left|\frac{\partial\xi}{\partial\tau}\right|^2 - \frac{c}{2n_o\omega^2}|\nabla_\perp\xi|^2 + \frac{1}{2}\frac{\partial U}{\partial z}\frac{\partial U}{\partial\tau} - \frac{c}{2n_o}(\nabla_\perp U)^2 + a_2|\xi|^2\frac{\partial U}{\partial\tau}. \tag{42}$$

Here, the electric field of the extraordinary wave is $E_e = \partial U/\partial\tau$.

In accordance with Eq. (39), we choose the trial solution in the form

$$\xi = A\exp\left[-i\left(\Omega t + \omega n_o\frac{\Phi}{c}\right)\right]\operatorname{sech}\left[R\left(t-\frac{z}{v}\right)\right],$$
$$U = B\tanh\left[R\left(t-\frac{z}{v}\right)\right], \quad (43)$$

where A, B, and R are slowly varying functions of z and $\mathbf{r}_\perp$; Φ is a rapidly varying function of the same variables; and Ω and v are constant parameters connected through relation (40).

Substituting relations (43) into Eq. (42), taking into account the derivatives of "fast" variables only [53], and integrating with respect to t, we obtain the "average" Lagrangian

$$\langle L\rangle \equiv \frac{1}{2}\int_{-\infty}^{\infty} L\,dt = \frac{n_o}{cR}A^2\frac{\partial\Phi}{\partial z} - \delta_o A^2 R - \frac{3\delta_o\Omega^2A^2}{R}$$
$$+\frac{n_o}{2cR}A^2(\nabla_\perp\Phi)^2 - 2\delta_o\omega\Omega B^2R - \frac{2}{3}a_2A^2B,$$

whose variation over dynamic parameters A, B, R, and Φ leads to the following system of equations in planar fluid dynamics of an ideal liquid (continuity equations and Cauchy integral):

$$\frac{\partial\rho}{\partial z} + \nabla_\perp(\rho\mathbf{v}_\perp) = 0,$$
$$\frac{\partial\Phi}{\partial z} + \frac{\mathbf{v}_\perp^2}{2} + \int\frac{dP}{\rho} = 3\frac{c}{n_o}\delta_o\Omega^2. \quad (44)$$

Here, the z coordinate plays the role of time, $\mathbf{v}_\perp = \nabla_\perp\Phi$, and "pressure" P is connected with "density" $\rho = A^2/R$ through the equation

$$\frac{dP}{d\rho} = 6\frac{c}{n_o}\delta_o\left(\frac{a_2}{6\delta_o\sqrt{\omega\Omega}}\right)^4\rho^2. \quad (45)$$

Parameters A and B are given by

$$A = \frac{6\delta_o R\sqrt{\omega\Omega}}{a_2}, \quad B = -\frac{6\delta_o R}{a_2}.$$

In the one-dimensional case, $R = 1/\tau_p$, the solutions obtained here are transformed into solution (39) on account of the fact that $E_e = \partial U/\partial\tau$. Obviously, the stability of the solutions in question is equivalent to the stability of the ideal liquid flow of type (44), (45). In this case, soliton (39) is stable for $dP/d\rho > 0$, which follows from Eq. (45). Thus, the above analysis leads to the conclusion that soliton solutions (39) exhibit transverse stability. Consequently, a video pulse of the extraordinary wave can be generated with the help of the ordinary component through the Zakharov–Benney mechanism under the experimental conditions.

Let us estimate the intensity of the input pulse for which a video soliton can be formed in the medium. Equation (38) for $b_{2e} = \delta_e = \sigma = \Delta_\perp = 0$ leads to

$$E_e \sim \left(\frac{1}{v}-\frac{1}{v_g}\right)^{-1}a_2|\xi|^2 \sim -\frac{a_2|\xi|^2}{2g\Omega}.$$

Substituting this estimate into Eq. (37), we arrive at the nonlinear Schrödinger equation (NSE)

$$i\frac{\partial\xi}{\partial z} + g\frac{\partial^2\xi}{\partial\tau^2} + q|\xi|^2\xi = 0,$$

where $q = \omega a^2/2g\Omega$ (naturally, we can speak about an equation only conditionally since the expression for coefficient q contains parameter Ω of the soliton solution of system (37), (38)). It is well known [48] that the formation of a soliton of the NSE requires the fulfillment of the threshold condition

$$\xi_0 > \frac{\chi_o}{\chi_{eo}}\frac{\sqrt{\omega\Omega}}{\omega_0^2}.$$

Since

$$\frac{\chi_o}{\chi_{eo}} \sim \frac{\chi^{(1)}}{\chi^{(2)}} \sim \frac{\hbar\omega_0}{d}$$

(see [3]), where d is the characteristic value of the dipole moment of quantum transitions participating in the interaction with the pulse, we have

$$\xi_0 > \xi_{\text{th}} \sim \frac{\hbar\sqrt{\omega\Omega}}{d\omega_0\tau_p}.$$

Setting $\Omega \sim 1/\tau_p \sim 10^{14}$ s^{-1}, $\omega \sim 10^{15}$ s^{-1}, $\omega_0 \sim 10^{16}$ s^{-1}, and $d \sim 10^{-20}$ CGSE units, we obtain the following estimate for the threshold intensity: $I_{\text{th}} \sim c\xi_{\text{th}}^2/4\pi \sim 10^{13}$–$10^{14}$ W/cm^2. Then, the intensity of the video soliton being generated is

$$I_e \sim cE_m^2/4\pi \sim c\xi_m^2/4\pi\omega\tau_p$$
$$\sim 0.1I_{\text{th}} \sim 10^{12}\text{–}10^{13}\ \text{W/cm}^2.$$

Such an estimation procedure cannot be regarded as rigorous, but nevertheless provides reasonable values of threshold intensities attainable in modern lasers.

6. SOLITON-LIKE SOLUTIONS OF THE TYPE OF VIDEO PULSES

In this section, we consider two solutions of system (34), (35) in the form of bound states of the ordinary and extraordinary components of an ESP, propagating across the optical axis. As before, we will disregard ionic dispersion.

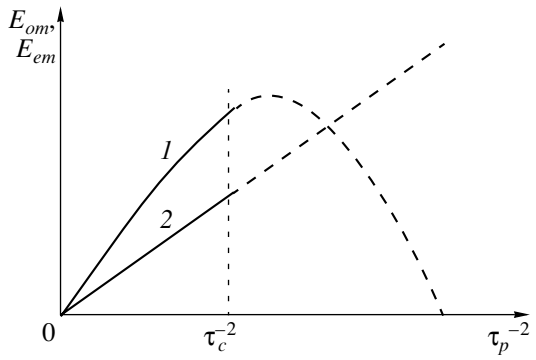

Fig. 3. Amplitudes of the ordinary (*1*) and extraordinary (*2*) components of a soliton-like ESP of type (46) as functions of the square of reciprocal duration. Dashed segments of the curves correspond to the instability region.

Direct substitution readily shows that, for $b_{2e}/a_2 = 6\delta_e/\delta_o$, system (34), (35) has one-dimensional solutions

$$E_o = \pm E_{om}\operatorname{sech}\left(\frac{t - z/v}{\tau_p}\right),$$
$$E_e = -E_{em}\operatorname{sech}\left(\frac{t - z/v}{\tau_p}\right), \tag{46}$$

where

$$E_{om} = \frac{2}{a_2\tau_p}\sqrt{\delta_o\left(\frac{n_e - n_o}{c} - \frac{4\delta_e - \delta_o}{\tau_p^2}\right)},$$

$$E_{em} = \frac{12\delta_e}{b_{2e}\tau_p^2},$$

and velocity v is connected with pulse duration τ_p through the relation

$$\frac{1}{v} = \frac{n_o}{c} - \frac{\delta_o}{\tau_p^2}. \tag{47}$$

The spectral widths of the ordinary and extraordinary components (46) can be estimated as $\Delta\omega_o \sim 1/\tau_p$ and $\Delta\omega_e \sim 2/\tau_p \sim 2\Delta\omega_o$. Thus, the spectrum of the extraordinary component is twice as wide as that of the ordinary component. Consequently, solutions (46) can be regarded as an analog of the second harmonic generation for quasimonochromatic pulses.

It follows from the expressions for E_{om} and E_{em} that solution (46) can be realized, for example, in a medium with positive birefringence ($n_e > n_o$); in the transparency region of this medium, we can disregard the difference in the dispersion of the ordinary and extraordinary refractive indices (i.e., we assume that $\delta_e \approx \delta_o$). In the case of strict equality $\delta_e = \delta_o$, the condition for the existence of the exact solution (46) has the form $b_{2e} = 6a_2$, which corresponds to one of the cases of integrability of the Henon–Heiles model [42].

Analysis shows that, in the case under investigation the duration of an ESP (and, hence, the velocity of its propagation) is bounded from below. This question is closely related to the stability of solution (46) and will therefore be considered in greater detail. As in the previous section, we will use the method of averaged Lagrangian. The density of the Lagrangian corresponding to system (34), (35) in the absence of ionic dispersion has the form

$$L = \frac{1}{2}\sum_{i=o,e}\left[\frac{\partial U_i}{\partial z}\frac{\partial U_i}{\partial t} + \frac{n_i}{c}\left(\frac{\partial U_i}{\partial t}\right)^2 + \delta_i\left(\frac{\partial^2 U_i}{\partial t^2}\right)^2 - \frac{c}{2n_o}(\nabla_\perp U_i)^2\right] + \frac{b_{2e}}{6}\left(\frac{\partial U_e}{\partial t}\right)^3 + \frac{a_2}{2}\left(\frac{\partial U_o}{\partial t}\right)^2\frac{\partial U_e}{\partial t}. \tag{48}$$

Here, the ESP field components can be expressed in terms of "potentials" U_o and U_e as $E_o = \partial U_o/\partial t$ and $E_e = \partial U_e/\partial t$.

In accordance with Eqs. (46), we choose trial solutions in the form

$$U_o = \frac{A_o}{R}\arctan\{\sinh[R(t - \Phi)]\},$$

$$U_e = -\frac{A_e}{R}\tanh[R(t - \Phi)],$$

where A_o, A_e, and R are slowly varying functions of variables z and $\mathbf{r}_\perp$, while Φ is a rapidly varying function of the same variables.

Substituting these expressions into Eq. (48) and integrating with respect to t, we arrive at the "averaged" Lagrangian which leads to equations of motion of type (44) except for the substitution $3c\delta_o/n_o \longrightarrow n_o/c$ in the Cauchy integral. In this case, $\mathbf{v}_\perp = \nabla_\perp\Phi$ and "density" ρ is connected with parameter R through the relation

$$\rho = \frac{4\delta_o(n_e - n_o)R}{a_2^2 c} - \frac{28\delta_o^2 R^3}{3a_2^2}.$$

Quantities A_o and A_e coincide with E_{om} and E_{em} upon the substitution $1/\tau_p \longrightarrow R$ and for $\delta_e = \delta_o$, $b_{2e} = 6a_2$. The relation between the "pressure" and "density" is given by the equation $\int dP/\rho = \delta_o R^2$, whence

$$\frac{dP}{d\rho} = \frac{dP}{dR}\left(\frac{d\rho}{dR}\right)^{-1} = 2\delta_o R^2\frac{(n_e - n_o)/c - (7\delta_o/3)R^2}{(n_e - n_o)/c - 7\delta_o R^2}.$$

In this case, the stability criterion $dP/d\rho > 0$ taking into account the fact that $R = 1/\tau_p$ can be written in the form

$$\tau_p > \tau_c \equiv \sqrt{\frac{7\delta_o c}{n_e - n_o}}.$$

It follows hence that, in accordance with Eq. (47), the value of velocity v lies in the interval

$$\frac{c}{n_o} < v < \frac{c}{n_o}\left(1 + \frac{n_e - n_o}{7n_o}\right).$$

Here, we have used the fact that $(n_e - n_o)/7n_o \ll 1$.

On segment $\tau_p > \tau_c$, the amplitudes of both components increase with decreasing τ_p (Fig. 3). Consequently, the intense central part of the ESP in the cross section leads the peripheral parts, and the pulse is stable on the whole.

Using the estimates obtained in the previous section,

$$n_e - n_o \approx \frac{2\pi(\chi_e - \chi_o)}{n_o}, \quad \delta_o \sim \frac{2\pi\chi_o}{n_o c\omega_o^2},$$

we can write the expression for τ_c in the form

$$\tau_c = \omega_0^{-1}\sqrt{\frac{7\chi_o}{\chi_e - \chi_o}},$$

which at least does not contradict condition (1).

As in the case of solutions (46), we can verify by direct substitution that, for $n_e = n_o$ and $3b_{2e}/a_2 = 1 + 2\delta_e/\delta_o$, system (34), (35) has the solutions

$$E_o = \pm E_{om}\tanh\left(\frac{t - z/v}{\tau_p}\right)\mathrm{sech}\left(\frac{t - z/v}{\tau_p}\right),$$
$$E_e = -E_{em}\mathrm{sech}^2\left(\frac{t - z/v}{\tau_p}\right), \tag{49}$$

where

$$E_{om} = \frac{2}{a_2\tau_p}\sqrt{3\delta_o(\delta_0 - 4\delta_e)}, \quad E_{em} = \frac{6\delta_o}{a_2\tau_p^2},$$

and the velocity and duration are connected through relation (47) as before.

The profile of the ordinary component in (49) has a bipolar form; consequently, its spectrum is centered at frequency $\omega_c \sim 1/\tau_p$. In view of the unipolarity of E_e, the spectrum of the extraordinary component of the ESP is centered at zero frequency.

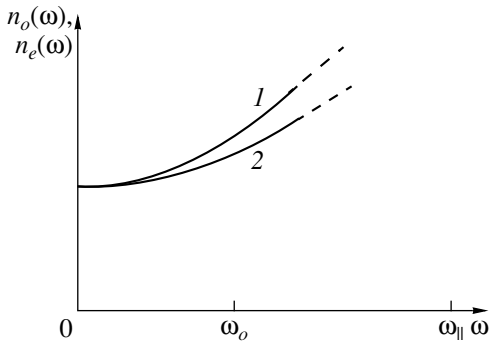

Fig. 4. Dispersion dependences of the ordinary (*1*) and extraordinary (*2*) refractive indices in the low-frequency transparency regions, corresponding to solution (49).

For testing relations (49) for stability, we choose the corresponding test solutions in the form

$$U_o = \mp\frac{A_o}{R}\mathrm{sech}[R(t - \Phi)],$$

$$U_e = -\frac{A_e}{R}\tanh[R(t - \Phi)].$$

The application of averaged variational principle using these expressions and Lagrangian (48) also leads in this case to a system of equations of type (44) taking into account the substitution $3c\delta_o/n_o \longrightarrow n_o/c$ in the Cauchy integral. As in the previous case, $\int dP/\rho = \delta_o R^2$, and the relation between R and "density" ρ is given by the relation

$$\rho = \frac{12\delta_o^2(3a_2 - 2b_{2e})R^3}{a_2^3}.$$

Consequently, $dP/d\rho = 2\rho^2/3 > 0$ and an ESP of type (49) is stable to self-focusing. This conclusion is also confirmed by qualitative considerations formulated above for solution (46) taking into account the fact that the amplitudes of both components and the velocity increase with decreasing duration. It can be seen from the expression for E_{om} that solution (49) can be realized for $\delta_o > 4\delta_e$. At the same time, $n_e = n_o$. Thus, solution (49) corresponds to the situation when birefringence emerges exclusively due to dispersion and is absent in the dispersion-free (low-frequency) region. From expressions (18) and (19) for the ordinary ($\chi_\perp(\omega)$) and extraordinary ($\chi_\parallel(\omega)$) electron susceptibilities, we obtain the following dispersion relations:

$$\chi_\perp(\omega) = \frac{\omega_o^2\chi_\perp}{\omega_o^2 - \omega^2}, \quad \chi_\parallel(\omega) = \frac{\omega_\parallel^2\chi_\parallel}{\omega_\parallel^2 - \omega^2}.$$

At the same time, we have

$$\delta_{o,e} = \frac{4}{cn_o}\left(\frac{\partial^2\chi_{\perp,\parallel}}{\partial\omega^2}\right)_{\omega=0} = \frac{\pi}{cn_o}\frac{\chi_{\perp,\parallel}}{\omega_{o,\parallel}^2}.$$

Since $n_e = n_o$, $\chi_\perp = \chi_\perp(0) = \chi_\parallel = \chi_\parallel(0)$. From these relations and from the condition $\delta_o > 4\delta_e$, we obtain $\omega_\parallel > 2\omega_o$. It can be seen from relation (12) that the susceptibilities of the ordinary and extraordinary waves are formed by σ and π transitions, respectively. Consequently, the characteristic frequency of π transitions must be more than twice the frequency of σ transitions for the realization of solution (49).

Thus, solution (49) can be realized in media with dispersion origin of birefringence (Fig. 4). In this case, $n_o(\omega) > n_e(\omega)$; i.e., the medium must possess negative birefringence in the dispersion frequency range.

7. CONCLUSIONS

The analysis carried out by us here reveals differences in the ESP dynamics in isotropic and optically uniaxial media. In the latter media, the quadratic nonlinearity of the electron response, which is absent in an isotropic dielectric, plays a significant role. The system of constitutive equations (16), (17) as an analog of the Lorentz classical model, which receives its quantum-mechanical substantiation here, can be used in subsequent investigations for describing the electron response in the low-frequency transparency range. In the Voigt geometry (when ESP propagates at right angles to the optical axis), these equations are transformed into the Henon–Heiles system (18), (19). It is remarkable that the Henon–Heiles system (its homogeneous version) permits both regular and chaotic motion depending on the relation between the coefficients [42]. Consequently, it cannot be ruled out that chaotic modes of ESP propagation can be observed in some anisotropic media.

The Henon–Heiles system is an analog of the Duffing equation describing a nonresonant nonlinear response of an isotropic medium in the low-frequency region. It was shown in [21] that the Duffing equation fails to provide an adequate response of an isotropic dielectric to an intense external action in the high-frequency region. In the same publication, a nonlinear model is proposed in the form of two parametrically coupled oscillators; it was found that this model holds in the low- and high-frequency regions. Proceeding from this remark, we can say that an analogous modification of the Henon–Heiles model is forthcoming.

The generalization of the Bloembergen–Shen quantum-mechanical system proposed by us here for describing SRS processes in media with uniaxial anisotropy enabled us to derive expressions (30) for the electron-vibrational response taking into account the dynamics of population of the SRS sublevels.

The obtained system of wave equations (32), (33) is written directly for the ordinary and extraordinary components of the electric field of the pulse, and not for their envelopes as in earlier publications. This circumstance makes it possible to use this system for analyzing the propagation of quasimonochromatic pulses as well as optical pulses of duration of only a few periods (including video pulses). The mechanism of generation of a video pulse of the extraordinary wave in the Zakharov–Benney resonance mode with a quasimonochromatic ordinary component (see Section 5), which can be realized in media with positive birefringence, may serve as an illustration of the previous statement. The role of SRS processes in the generation of video pulses due to continuous energy pumping from high-frequency Fourier components to the Stokes components of the spectrum is well known [45]. In this connection, the investigation of the combined effect of the electron quadratic nonlinearity and SRS on the process of ESP generation with the help of pulses initially possessing a clearly manifested carrier frequency is of considerable interest.

The soliton-like solutions (46) and (49) in the form of coupled states of the ordinary and extraordinary ESP components presented here are, in addition to relations (39), only a minor illustration of possible solutions contained in Eqs. (32), (33). In all probability, other solutions will mainly be obtained with the help of numerical experiments, which does not preclude further analytic investigations.

ACKNOWLEDGMENTS

This study was supported by the Russian Foundation for Basic Research (project no. 02-02-17710a)

APPENDIX

The expressions for third-order nonlinear susceptibilities in terms of the microscopic parameters of the medium have the form

$$\chi_{eo}^{(3)} = \chi_{xyyx}^{(3)} = \chi_{yxxy}^{(3)} = \frac{2N}{\hbar^2}\left\{2\sum_{\mu\neq\nu}\Delta_{\mu\nu}(\varphi)\right.$$

$$\left.\times\sum_{j\neq\mu,\nu} d_{\mu j}^2\left(\frac{\alpha_{\mu j}}{\omega_{j\mu}\omega_{\mu\nu}} + \frac{\alpha_{\mu\nu}}{\omega_{j\nu}\omega_{\mu\nu}} + \frac{\alpha_{\mu\nu}}{\omega_{\mu j}\omega_{j\nu}}\right)\right.$$

$$\left.- \cos^2\varphi\sum_{\mu\neq\nu} d_{\mu\nu}^4\frac{\alpha_{\mu\nu}}{\omega_{\mu\nu}^2} + \sin^2\varphi\sum_{\mu\neq\nu}\frac{D_{\mu\nu}}{\omega_{\mu\nu}}\right.$$

$$\times \sum_{j \neq \mu,\nu} \sum_{k \neq \mu,\nu,j} (d_{\mu j} d_{k\nu} D_{jk} + d_{jk} d_{k\nu} D_{\mu j} + d_{\mu j} d_{kj} D_{k\nu})$$

$$\times \left(\frac{\alpha_{\mu j} + \alpha_{kj}}{\omega_{\mu k}} + \frac{\alpha_{k\nu} + \alpha_{kj}}{\omega_{j\nu}} \right) \Bigg\},$$

$$\chi_e^{(3)} = \chi_{yyyy}^{(3)} = \frac{2N}{\hbar^2} \Bigg\{ \sum_{\mu \neq \nu} \Delta_{\mu\nu}(\varphi) \sum_{j \neq \mu,\nu} \Delta_{\mu j}(\varphi)$$

$$\times \left(\frac{\alpha_{\mu j}}{\omega_{j\mu}\omega_{\mu\nu}} + \frac{\alpha_{\mu\nu}}{\omega_{j\nu}\omega_{\mu\nu}} + \frac{\alpha_{\mu\nu}}{\omega_{\mu j}\omega_{j\nu}} \right)$$

$$- \sum_{\mu \neq \nu} (d_{\mu\nu}^4 \cos^4\varphi + D_{\mu\nu}^4 \sin^4\varphi) \frac{\alpha_{\mu\nu}}{\omega_{\mu\nu}^2}$$

$$+ \frac{1}{2} \sin^2\varphi \sum_{\mu \neq \nu} \frac{D_{\mu\nu}}{\omega_{\mu\nu}} \sum_{j \neq \mu,\nu} \sum_{k \neq \mu,\nu,j} D_{\mu j} D_{k\nu} D_{jk}$$

$$\times \left(\frac{\alpha_{\mu j} + \alpha_{kj}}{\omega_{\mu k}} + \frac{\alpha_{k\nu} + \alpha_{kj}}{\omega_{j\nu}} \right) \Bigg\},$$

where

$$\Delta_{\mu\nu}(\varphi) = \frac{d_{\mu\nu}^2}{2} \cos^2\varphi + D_{\mu\nu}^2 \sin^2\varphi.$$

The expression for $\chi_o^{(3)} = \chi_{xxxx}^{(3)}$ can be obtained from the formula for $\chi_e^{(3)}$ for $\varphi = 0$.

REFERENCES

1. P. C. Becker, H. L. Fragnito, J. Y. Bigot, *et al.*, Phys. Rev. Lett. **63**, 505 (1989).
2. K. Tamura and M. Nakazawa, Opt. Lett. **21**, 68 (1996).
3. T. Brabec and F. Krausz, Rev. Mod. Phys. **72**, 545 (2000).
4. A. M. Zheltikov, Vestn. Mosk. Univ., Ser. 3: Fiz., Astron., No. 4, 3 (2001).
5. A. M. Zheltikov, Usp. Fiz. Nauk **172**, 743 (2002) [Phys. Usp. **45**, 687 (2002)].
6. D. H. Auston, K. P. Cheung, J. A. Valdmanis, and D. A. Kleinman, Phys. Rev. Lett. **53**, 1555 (1984).
7. A. V. Kim and M. Yu. Ryabikin, Usp. Fiz. Nauk **169**, 58 (1999) [Phys. Usp. **42**, 54 (1999)].
8. A. I. Maĭmistov, Kvantovaya Élektron. (Moscow) **30**, 287 (2000).
9. A. A. Zabolotskiĭ, Zh. Éksp. Teor. Fiz. **121**, 1012 (2002) [JETP **94**, 869 (2002)].
10. É. M. Belenov and A. V. Nazarkin, Pis'ma Zh. Éksp. Teor. Fiz. **51**, 252 (1990) [JETP Lett. **51**, 288 (1990)].
11. É. M. Belenov, P. G. Kryukov, A. V. Nazarkin, *et al.*, Pis'ma Zh. Éksp. Teor. Fiz. **47**, 442 (1988) [JETP Lett. **47**, 523 (1988)].
12. É. M. Belenov, A. V. Nazarkin, and V. A. Ushchapovskiĭ, Zh. Éksp. Teor. Fiz. **100**, 762 (1991) [Sov. Phys. JETP **73**, 422 (1991)].
13. A. I. Maĭmistov and S. O. Elyutin, Opt. Spektrosk. **70**, 101 (1991) [Opt. Spectrosc. **70**, 57 (1991)].
14. A. I. Maimistov and S. O. Elyutin, J. Mod. Opt. **39**, 2201 (1992).
15. A. V. Vederko, O. B. Dubrovskaya, F. M. Marchenko, and A. P. Sukhorukov, Vestn. Mosk. Univ., Ser. 3: Fiz., Astron. **33**, 4 (1992).
16. A. I. Maĭmistov, Opt. Spektrosk. **76**, 636 (1994) [Opt. Spectrosc. **76**, 569 (1994)].
17. S. V. Sazonov and E. V. Trifonov, J. Phys. B **27**, 369 (1994).
18. A. I. Maĭmistov, Opt. Spektrosk. **78**, 483 (1995) [Opt. Spectrosc. **78**, 435 (1995)].
19. A. V. Andreev, Zh. Éksp. Teor. Fiz. **108**, 796 (1995) [JETP **81**, 434 (1995)].
20. A. E. Kaplan and P. L. Shkolnikov, Phys. Rev. Lett. **75**, 2316 (1995).
21. S. A. Kozlov, Opt. Spektrosk. **79**, 290 (1995) [Opt. Spectrosc. **79**, 267 (1995)].
22. S. V. Sazonov, Fiz. Tverd. Tela (St. Petersburg) **37**, 1612 (1995) [Phys. Solid State **37**, 875 (1995)].
23. S. V. Sazonov, Opt. Spektrosk. **79**, 282 (1995) [Opt. Spectrosc. **79**, 260 (1995)].
24. S. A. Kozlov and S. V. Sazonov, Zh. Éksp. Teor. Fiz. **111**, 404 (1997) [JETP **84**, 221 (1997)].
25. I. V. Mel'nikov and D. Mihalache, Phys. Rev. A **56**, 1569 (1997).
26. S. V. Sazonov, Zh. Éksp. Teor. Fiz. **119**, 419 (2001) [JETP **92**, 361 (2001)].
27. M. Born and E. Wolf, *Principles of Optics*, 4th ed. (Pergamon Press, Oxford, 1969; Nauka, Moscow, 1973).
28. A. I. Maĭmistov, Opt. Spektrosk. **87**, 104 (1999) [Opt. Spectrosc. **87**, 96 (1999)].
29. S. V. Sazonov, Zh. Éksp. Teor. Fiz. **107**, 20 (1995) [JETP **80**, 10 (1995)].
30. O. B. Dubrovskaya and A. P. Sukhorukov, Izv. Akad. Nauk, Ser. Fiz. **56**, 184 (1992).
31. E. V. Kazantseva and A. I. Maĭmistov, Opt. Spektrosk. **89**, 838 (2000) [Opt. Spectrosc. **89**, 772 (2000)].
32. S. V. Sazonov and A. F. Sobolevskiĭ, Opt. Spektrosk. **90**, 449 (2001) [Opt. Spectrosc. **90**, 390 (2001)].
33. E. V. Kazantseva, A. I. Maimistov, and B. A. Malomed, Opt. Commun. **188**, 195 (2001).
34. G. Agrawal, *Nonlinear Fiber Optics* (Academic, San Diego, 1995; Mir, Moscow, 1996).
35. S. V. Sazonov and A. F. Sobolevskiĭ, Kvantovaya Élektron. (Moscow) **30**, 917 (2000).
36. *Nonlinear Properties of Organic Molecules and Crystals*, Ed. by D. S. Chemla and I. Zyss (Academic, Orlando, 1987; Mir, Moscow, 1989).
37. L. N. Ovander, Usp. Fiz. Nauk **86**, 3 (1965) [Sov. Phys. Usp. **8**, 337 (1965)].

38. R. H. Pantell and H. E. Puthoff, *Fundamentals of Quantum Electronics* (Wiley, New York, 1969; Mir, Moscow, 1972).

39. I. I. Sobel'man, *Atomic Spectra and Radiative Transitions* (Nauka, Moscow, 1977; Springer, Berlin, 1979).

40. R. E. Stoiber and S. A. Morse, *Microscopic Identification of Crystals* (Ronald, New York, 1972; Mir, Moscow, 1974).

41. E. I. Butikov, *Optics* (Vysshaya Shkola, Moscow, 1986).

42. A. J. Lichtenberg and M. A. Lieberman, *Regular and Stochastic Motion* (Springer, New York, 1982; Mir, Moscow, 1984).

43. D. N. Klyshko, *Physical Fundamentals of Quantum Electronics* (Mir, Moscow, 1986).

44. Y. R. Shen and N. Bloembergen, Phys. Rev. A **137**, 1738 (1965).

45. É. M. Belenov, P. G. Kryukov, A. V. Nazarkin, and I. P. Prokopovich, Zh. Éksp. Teor. Fiz. **105**, 28 (1994) [JETP **78**, 15 (1994)].

46. M. B. Vinogradova, O. V. Rudenko, and A. P. Sukhorukov, *The Theory of Waves*, 2nd ed. (Nauka, Moscow, 1990).

47. S. A. Akhmanov, V. A. Vysloukh, and A. S. Chirkin, *The Optics of Femtosecond Pulses* (Nauka, Moscow, 1988).

48. R. K. Dodd, J. C. Eilbeck, J. Gibbon, and H. C. Morris, *Solitons and Nonlinear Wave Equations* (Academic, New York, 1982; Mir, Moscow, 1988).

49. E. S. Benilov and S. P. Burtzev, Phys. Lett. A **98**, 256 (1983).

50. N. Yadjima and M. Oikawa, Prog. Theor. Phys. **56**, 1719 (1976).

51. V. E. Zakharov, Zh. Éksp. Teor. Fiz. **62**, 1745 (1972) [Sov. Phys. JETP **35**, 908 (1972)].

52. U. A. Abdullin, G. A. Lyakhov, O. V. Rudenko, and A. S. Chirkin, Zh. Éksp. Teor. Fiz. **66**, 1295 (1974) [Sov. Phys. JETP **39**, 633 (1974)].

53. S. K. Zhdanov and B. A. Trubnikov, *Quasi-Gaseous Unstable Media* (Nauka, Moscow, 1991).

Translated by N. Wadhwa

Journal of Experimental and Theoretical Physics, Vol. 96, No. 6, 2003, pp. 1037–1044.
Translated from Zhurnal Éksperimental'noĭ i Teoreticheskoĭ Fiziki, Vol. 123, No. 6, 2003, pp. 1179–1187.

PLASMA, GASES

Analysis of Macroparticle Charging in the Near-Electrode Layer of a High-Frequency Capacitive Discharge

O. S. Vaulina[a,*], A. A. Samarian[b], B. James[b], O. F. Petrov[a,*], and V. E. Fortov[a]

[a] *Institute of High Energy Densities, IVTAN, Russian Academy of Sciences, Izhorskaya ul. 13/19, Moscow, 127412 Russia*

[b] *School of Physics, University of Sydney, NSW 2006, Sydney, Australia*

**e-mail: industpl@redline.ru*

Received November 6, 2002

Abstract—Spatial variation of dust particle charges are estimated numerically for typical laboratory experiment conditions in a radio-frequency (rf) capacitive discharge. The surface potentials of macroparticles levitating in the upper part of the near-electrode layer of the rf discharge are measured. A model is proposed for the formation of irregular dust oscillations due to stochastic motion of dust in the bulk of a spatially inhomogeneous plasma (in the presence of a dust charge gradient). This mechanism is used for analyzing the results of measurements of the amplitude of vertical vibrations of dust particles in the near-electrode layer of the rf discharge. It is found that the dust charge gradient may be responsible for the development of such vibrations. © *2003 MAIK "Nauka/Interperiodica".*

1. INTRODUCTION

The charge of a dust particle is an important parameter for investigating various transport processes in dusty plasmas, such as phase transitions, diffusion processes, propagation of waves, and formation of self-excited dust vibrations. Considerable attention in the study of plasmas is paid to the methods and results of measurements of dust particle charges. A large number of methods for determining macroparticle charges are based on the measurement of the dynamic response of dust particles to various external perturbations [1–9]. The charges of macroparticles can also be determined without perturbing the system in question by external agencies, but from an analysis of their diffusion or from the equilibrium conditions for a stationary particle in the gravitational field of the Earth and in the electric field of the trap [9–11].

Since the charge of dust particles is a function of the parameters of the surrounding plasma (concentrations $n_{e(i)}$ and velocities $v_{e(i)}$ of electrons and ions), the variation of these parameters may lead to a change in the macroparticle charge and to evolution of various instabilities in plasma-dust systems [12, 13]. Available experimental observations demonstrate that, under certain conditions (upon a variation of pressure or an increase in the number of particles), dust particles in the strata of a dc glow discharge or in the near-electrode layer of a capacitive rf discharge may acquire energies on the order of 1–100 eV and perform regular or stochastic vertical vibrations (in the direction of the gravitational field) [13–17].

The reason for the evolution of such vibrations may be related to the inhomogeneity of the surrounding plasma. The formation of various self-induced dust vibrations in the field the gravitational force orthogonal to the macroparticle charge gradient was considered in [12]. However, this mechanism can hardly be responsible for the evolution of the observed vibrations of dust particles in capacitive rf discharges in view of considerable uniformity of the parameters of the capacitive rf discharge plasma in the radial direction (orthogonal to the gravitational force). Stochastic fluctuations of dust charges due to discreteness of plasma currents charging a macroparticle may lead to "anomalous heating" of dust particles in gas-discharge plasmas [18], but cannot be responsible for high kinetic energies (>0.1 eV) acquired by light particles of radius 1–2 μm (density $\rho \approx 1.5$–2 g/cm^3) under gas pressures $P > 0.02$ Torr.

One of the possible mechanisms of evolution of irregular vibrations of dust particles is associated with stochastic changes in their charge, which are determined by the random position of a particle in a spatially inhomogeneous plasma (in the presence of a dust charge gradient in the direction of gravity) due to thermal or other fluctuations, e.g., due to the above-mentioned discreteness of the charging current. This mechanism was considered for the first time in [14]. However, in the proposed model, it was proposed that particles move in the free diffusion mode, which is unsuitable for describing spatially bounded trajectories of macroparticles, which are observed both in the dust layer formed in the rf discharge and under the conditions of a bulk dust cloud in a dc glow discharge [13, 16, 17, 19]. It should also be noted that the very possibility of formation of irregular dust vibrations in the framework of this model was determined by the initial energy

of the system, which is not always observed in real experiments, including the one described below.

Here, we propose a model of formation of irregular dust vibrations due to stochastic motion of dust in a spatially inhomogeneous plasma, which takes into account the limitations imposed by an electric field on the displacements of macroparticles in a preferred direction. This mechanism is used for analyzing vertical vibrations of macroparticles in the near-electrode layer of a capacitive rf discharge. The material is arranged in the following order. In Section 2, the estimates of spatial variation of the charge of a dust particle in the near electrode layer of the discharge are obtained. In Section 3, basic relations are derived for estimating the kinetic energy acquired by a dust particle in an inhomogeneous plasma. The last two sections are devoted to experiments on dust particle charging and on the dynamics of formation of stochastic dust vibrations in the rf discharge plasma.

2. SPATIAL VARIATIONS OF THE MACROPARTICLE CHARGE IN GAS-DISCHARGE PLASMAS

In gas-discharge plasmas, where emission processes are insignificant as a rule, the charge of a dust particle is negative. The estimate of the macroparticle surface potential obtained in the orbital-motion-limited (OML) approximation gives the following expression for its value:

$$\varphi_e = -\frac{e\langle Z_p\rangle}{a_p} \equiv -\frac{zT_e}{e};$$

here, $\langle Z_p\rangle$ is the equilibrium (time-averaged) charge of a dust particle, T_e is the electron temperature in electronvolts, and $z \approx 2$–4 for most experiments on dusty plasmas under the discharge conditions in inert gases [20, 21].

Using the formulas of the OML approximation, we can estimate the small variation $\Delta_n Z_p$ of the equilibrium charge $\langle Z_p\rangle$ of a macroparticle due to violation of electroneutrality of the surrounding plasma, $\delta n = n_i - n_e$ [19]:

$$\frac{\Delta_n Z_p}{\langle Z_p\rangle} \approx -\frac{\mathrm{div}\mathbf{E}}{4\pi e n_0(1+z)}. \quad (1)$$

Here, E is the electric field strength and n_0 is the concentration of the neutral plasma, where $n_e = n_i = n_0$. Obviously, as long as condition $\delta n \ll n_0$ holds, the requirement of the smallness of charge variation,

$$\Delta_n Z_p \ll \langle Z_p\rangle,$$

is satisfied automatically.

A similar relation

$$|\Delta_i Z_p = Z_p - \langle Z_p\rangle| \ll \langle Z_p\rangle$$

for estimating the charge variation in a plasma layer can be obtained under the assumption $|e\varphi/T_e| \ll 1$ (where φ is the electric potential) provided that the directional velocity of ions u_i is much higher than their thermal velocity v_i^T:

$$\frac{\Delta_i Z_p}{\langle Z_p\rangle} \approx -\frac{2z\delta n/n_0 - e\varphi(z-s)/T_e}{z(1+s+z)}. \quad (2)$$

Here, $\langle Z_p\rangle$ is the equilibrium charge in a plasma layer with $\delta n \approx 0$ and concentration n_0 and $s = m_i u_i^2/2T_e$. Relation (2) can be used for estimating the charge variation in the vicinity of the upper boundary of the electrode layer, where levitation of macroparticles is normally observed. In this case, $s = 0.5$, considering that ions enter the layer at the Bohm velocity $v_B = \sqrt{T_e/m_i}$ and $n_0 = n_B \approx n_0^*/2.7$, where n_0^* is the concentration of the unperturbed plasma. It should be noted that such an approach is suitable only for very low pressures, when the mean free path l_i for ions colliding with gas neutrals is much longer than the electron Debye radius λ_{De}. For average pressures (0.05–1 Torr), which are working pressures in most experiments on dusty plasmas, $l_i \sim \lambda_{De}$. In this case, the velocity of ions $u_i(0)$ at the layer boundary is smaller than the Bohm velocity v_B by approximately a factor of $\sqrt{\pi\lambda_{De}/2l_i}$ [22].

It should be noted that we assumed, while deriving relation (2), that ionization processes in the plasma layer can be neglected ($n_i u_i = \mathrm{const}$). The analytic theory of the near-electrode layer in an rf discharge developed for this case is described in [22]. In this case, it is assumed that the layer is in contact not with the unperturbed plasma, but with a preliminary layer in which the electroneutrality of the plasma is quite high: $\delta n/n_0 \ll 1$. An analysis of the proposed system of equations for low pressures ($\lambda_{De} \ll l_i$) gives for the averaged electric field $E(y)$ of the near-electrode layer in the vicinity of its upper boundary a distribution close to a linear function:

$$E(y) = C_1 y. \quad (3)$$

For average pressures ($\lambda_{De} \sim l_i$), the solution of the equations of the analytic theory [22] leads to the following linear approximation for the gradient $E(y)$ of this field:

$$E(y) = C_2 y^2. \quad (4)$$

Let us analyze the conditions realized in some experiments in a dusty plasma of a capacitive rf discharge [16, 17]. These experiments show that levitation of macroparticles is observed in the vicinity of the upper boundary of the near-electrode layer whose thickness $d_{\max}$ lies approximately between 0.5 and 1.5 cm under experimental conditions ($P = 0.015$–0.2 Torr).

We can estimate the macroparticle charge gradients

$$\beta_y = \frac{dZ_p}{dy} \equiv \frac{d(\Delta_i Z_p)}{dy}$$

arising as a result of a change in the charging conditions for light particles of radius a_p = 1–2 μm and density ρ = 1.5–2 g/cm^3, assuming that the electric fields E confining particles in the gravitational field of the Earth are equal to 1–4 V/cm, the plasma density at the layer boundary is $n_e = 10^8$–10^9 cm^{-3}, the electron temperature is T_e = 2 eV, and the gas used in experiments is argon ($z \approx 3$–4 [20, 21]). Then, in the case of linear field (3) for C_1 = 12 V/cm^2, the particle in question will be suspended at distance $y = y_0 \approx 0.1$–0.33 cm from the upper boundary of the layer, where the condition of balance between the gravitational force and the electric field is observed:

$$m_p g + \langle Z_p \rangle eE(y_0) = 0. \quad (5)$$

The relative change in the macroparticle charge gradient $\beta_y/\langle Z_p \rangle$ in this region, which is obtained from joint solution of Eqs. (2) and (3) for the conditions of the problem, varies from –0.1 to –0.3 cm^{-1}. Thus, in the model described here, the charge of a dust particle decreases as it approaches the electrode, the rate of this approach being the higher, the lower this particle is located. The same qualitative pattern is observed for nonlinear field (4) also. In this case, the charge gradients $\beta_y/\langle Z_p \rangle$ of macroparticles levitating at distance $y_0 \approx$ 0.25–0.5 cm from the upper boundary of the layer (C_2 = 12 V/cm^3) changes with increasing y_0 from –0.15 to –0.39 cm^{-1}.

Concluding the section, we note that, in spite of considerable charge gradients $\beta_y/\langle Z_p \rangle = -(0.1$–$0.4)$ cm^{-1}, the relative change in its value $\langle Z_p \rangle$ did not exceed 7% ($|\Delta_i Z_p/\langle Z_p \rangle| < 0.07$) in all analyzed cases. The perturbation of plasma electroneutrality was $|\delta n/n_0| < 0.09$, and $|e\varphi/T_e| < 0.35$, which is a good approximation for linearizing equations of the analytical theory of the layer [22] as well as equations of the OLM approximation [20, 21] and, accordingly, for estimating the charge variation in the layer from relations (2)–(4).

3. EFFECT OF CHARGE FLUCTUATIONS OF MACROPARTICLES ON THEIR KINETIC TEMPERATURE IN A SPATIALLY INHOMOGENEOUS PLASMA

Let us consider the 2D problem in the cylindrical ry geometry, simulating a layer of macroparticles levitating above an electrode of the rf oscillator (see Fig. 1 below) in the presence of a dust charge gradient $\beta_y = dZ_p/dy$ in the direction of gravity (y axis), taking into account the fluctuations of particle interaction forces determined by particle charge variations

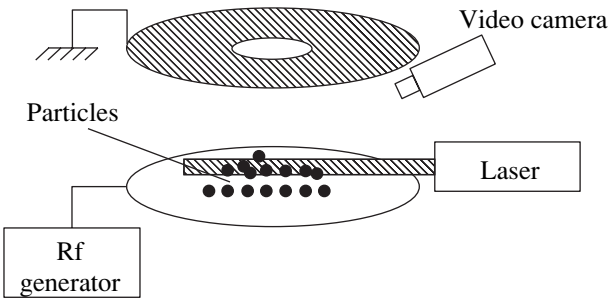

Fig. 1. Simplified diagram of experimental setup.

$$\tilde{Z}_s = \beta_y y_\Sigma$$

due to a random variation in their positions in the layer in question. Deviations (r, y) of an individual particle in such a layer from its equilibrium (r_0, y_0) position can be described by the linearized system of equations

$$m_p y'' = -m_p \nu_{fr} y' - \alpha_y e\langle Z_p \rangle y + e\beta_y E_y y + F_y, \quad (6a)$$

$$m_p r'' = -m_p \nu_{fr} r' - \alpha_r e\langle Z_p \rangle r + e\tilde{Z}_s E_r + F_r, \quad (6b)$$

where ν_{fr} is the friction coefficient, which is defined in the free-molecule approximation as

$$\nu_{fr}\ [\mathrm{s}^{-1}] \approx \frac{C_\nu P\ [\mathrm{Torr}]}{a_p\ [\mu\mathrm{m}]\ \rho\ [\mathrm{g/cm}^3]}$$

(where $C_\nu \approx 820$ μm g/s Torr cm^3 for argon); primes denote the time derivatives of coordinates; $\mathbf{F} = (F_y, F_r)$ is a random force leading to stochastic motion of particles; and $\alpha_{y,r} = dE_{y,r}/dy$ are the gradients of the external electric field $\mathbf{E} = (E_y, E_r)$. Here,

$$E_y = \frac{m_p g}{e\langle Z_p \rangle}$$

is determined by the balance between the vertical electric force and the gravitational force of the Earth; the value of E_r can be estimated by taking into account the balance of the radial electric force and the forces of interaction between particles. For a homogeneous extended layer of particles, we can assume that radial fields are linear, i.e.,

$$E_r \approx \alpha_r r \approx \alpha_r N_r l_p,$$

where l_p is the average particle spacing and N_r is the number of particles located in the region between the axis of the cylindrical system and the particle in ques-

tion, the gradient of this field for a planar dust cloud being

$$\alpha_r \propto \frac{e\langle Z_p\rangle}{l_p^3}.$$

It should be recalled that the origin of force $eE_r\tilde{Z}_s$ in (6b) is determined by the collective action of the remaining particles of the layer on an individual particle. In the formulation considered here, the change in $\tilde{Z}_s$ is determined by the random quantity y_Σ defined by Eq. (6a) with a different value of random force $\tilde{F}_{s,y} \neq F_y$, whose parameters can be determined using the procedure described in [18]. It should be noted that, in order to solve the problem, it is sufficient to assume that the action of the random forces considered here is not correlated ($\langle\tilde{\mathbf{F}}_s\mathbf{F}\rangle = 0$); the correlation of these forces with "slow" displacements $\mathbf{l} = (r, y)$ of particles is also absent ($\langle\mathbf{Fl}\rangle = 0$ and $\langle\tilde{\mathbf{F}}_s\mathbf{l}\rangle = 0$) [23, 24]. In this case, an additional kinetic energy $\Delta^s T_r$, proportional to the amplitude of charge fluctuations

$$\langle\tilde{Z}_s^2\rangle = \beta_y^2\langle y^2\rangle,$$

is supplied to the system in the radial direction r (see [18]), where $\langle y^2\rangle$ is the mean square deviation in the y direction:

$$\langle y^2\rangle = \frac{T_n + \Delta^f T + \Delta^s T_y}{m_p\omega_y^2}. \tag{7}$$

In this equation,

$$\omega_y^2 = \frac{e\langle Z_p\rangle\alpha_y - \beta_y E_y}{m_p};$$

T_n is the temperature of the surrounding gas; $\Delta^f T$ is the stochastic energy acquired by a particle in the plasma due to other mechanisms, e.g., due to discreteness of charging currents; and $\Delta^s T_y$ is a part of the kinetic energy $\Delta^s T_r$ transferred in the y direction through the particle interaction. The coefficient

$$\gamma = \frac{\Delta^s T_y}{\Delta^s T_r}$$

of energy transfer due to particle interaction in the dust cloud differs from zero and is determined by the reaction of the dust system to transverse perturbations of the system and by the amplitude of particle displacement [12, 18]. The derivatives corresponding to these perturbations are excluded from system (6a), (6b) since we will henceforth assume that the kinetic energy acquired by a macroparticle is redistributed uniformly over degrees of freedom:

$$\Delta^s T_r \approx \Delta^s T_y \approx \Delta^s T.$$

Simulation shows that, for parameters close to experimental conditions, such an assumption is justified for a large number of particles (n_p), low buffer gas pressures (small ν_{fr}), and the formation of additional dust layers [12, 18]. In this case, the value of the kinetic energy $\Delta^s T$ acquired by a dust particle due to random variation of its charge in an inhomogeneous plasma can be defined as

$$\Delta^s T \approx \frac{T_0 + \Delta^f T}{1 - \theta_1}, \tag{8}$$

where

$$\theta_1 = \left(\frac{\beta_y}{\langle Z_p\rangle}\right)^2 \frac{e^2\langle Z_p\rangle^2 E_r^2\omega_r^2}{m_p^2\nu_{fr}^2(\omega_r^2 + \omega_y^2)\omega_y^2}. \tag{9}$$

Here,

$$\omega_r^2 = \frac{e\langle Z_p\rangle\alpha_r}{m_p}.$$

If necessary, relation (8) can take into account the fraction γ of redistributed energy:

$$\Delta^s T = \frac{(T_0 + \Delta^f T)(1 + (1-\gamma)\theta_1)}{1 - \gamma\theta_1}. \tag{10}$$

Thus, for $\gamma \approx 1$, the value of kinetic energy $\Delta^s T$ is determined by the value of coefficient θ_1, which strongly depends on the parameters of the dust system. If we take into account the fact that

$$\frac{|\beta_y|}{\langle Z_p\rangle} \ll \frac{a_y}{E_y}$$

in the vicinity of the upper boundary of the near-electrode layer (see Section 2) and also assume that

$$E_r \approx N_r e\langle Z_p\rangle/l_p^2, \quad \omega_r^2 \approx \omega_y^2,$$

we can obtain a simpler relation for estimating θ_1:

$$\theta_1 \approx \left(\frac{\beta_y}{\langle Z_p\rangle}\right)^2 \frac{N_r^2 e^2\langle Z_p\rangle^2}{2m_p\nu_{fr}^2 l_p},$$

which gives $\theta_1 \approx 0.25$ for $N_r = 10$, $l_p = 300$ μm, $\langle Z_p\rangle = 5 \times 10^3 e$, $|\beta_y|/\langle Z_p\rangle = 0.2$ cm^{-1}, $\nu_{fr} \approx 13$ s^{-1} (argon, $P \approx 0.03$ Torr), $a_p = 1$ μm, and $\rho = 2$ g/cm^3. It can easily be seen that coefficient θ_1 tends to unity under the same conditions if $N_r \longrightarrow 20$ or $|\beta_y|/\langle Z_p\rangle \longrightarrow 0.4$. In this case, we find that kinetic energy $\Delta^s T$ increases indefinitely with an increase in deviation (y, r) of particles from their equilibrium positions. However, the linearized system of equations (6a), (6b) in this case does not provide a correct analysis of the dynamics of particles since the amplitude of their motion can be limited due

Table

R, μm	r, g cm^{-3}	h, mm	$(\varphi_s E)_{\exp}$, V^2/cm	E, V/cm	$\langle Z_p \rangle$	$\langle Z_p^c \rangle$	δ, %
1	2	10.06	7.38	1.12	4579	4632	1
1.39	1.5	9.65	10.71	1.67	6200	6438	4
2.12	1.5	7.70	24.89	3.93	9332	9820	5
3.07	1.5	4.80	52.21	7.38	15079	14220	6

to various nonlinear effects. In addition, relation (8) was obtained under the assumption of smallness of mean square deviations of particles,

$$\langle y^2 \rangle \ll l_0^2 \approx l_p^2 + \langle y^2 \rangle,$$

where l_0 and l_p are particle spacings in the perturbed and unperturbed layers of macroparticles.

An estimate of the maximum value $\Delta^s T^{\max}$ of kinetic energy (disregarding nonlinear effects and possible variation of system parameters within the trajectory of particles) can be obtained by additionally taking into account deviations $\langle y^2 \rangle$ (7) in Eq. (6b) through variation of field $E_r \propto l_0^2$. In this case, for $\theta_1 \longrightarrow 1$, we obtain

$$\Delta^s T^{\max} = \frac{4}{3} l_p^2 \omega_y^2 m_p, \tag{11}$$

while the maximum amplitude $A_y^{\max} = \sqrt{2\langle y^2 \rangle}$ of particle displacement in the y direction is given by

$$A_y^{\max} \approx 1.6 l_p. \tag{12}$$

For the example considered above (a_p = 1 μm, ρ = 2 g/cm^3, l_p = 300 μm, and $\theta_1 \longrightarrow 1$), for $\alpha_y \approx$ 6–12 V/cm^2 (see Section 2), the value of $\Delta^s T^{\max} \approx$ 25–50 eV and $A_y^{\max} \approx$ 480 μm. It should be noted that the growth of amplitude and kinetic energy is limited both in real experiments and in simulation of systems with a macroparticle charge gradient [15, 16].

It should be noted in conclusion that the mechanism considered here can explain parametric buildup of vibrations of particles with charge gradients, which is observed in a numerical experiment [12] upon a decrease in the frictional force (ν_{fr}) below a certain critical value. The reason behind such a buildup remains unclear in the framework of [12] since the effects associated with collective thermal fluctuations of particles in a dust cloud were eliminated from the theoretical analysis. In the case of "anomalous heating" of macroparticles due to discreteness of charging currents, external electric forces also serve as the main source of additional energy of a dust particle [18]. On the other hand, the proposed mechanism is ensured by collective effects, which are possible only when the number of particles in a dust cloud is large enough and, accordingly, can develop upon an increase in the concentration of the dust component.

4. DETERMINING PARTICLE CHARGE IN THE NEAR-ELECTRODE LAYER OF RF DISCHARGE

The experiment was carried out in a capacitive rf discharge in argon under pressure P = 0.1 Torr for a discharge power W = 60 W. The schematic diagram of the experimental setup is shown is Fig. 1. Melamine formaldehyde particles with different sizes a_p were suspended above the lower electrode at different distances h from its surface (see table). The surface potential φ_s of macroparticles could be derived from balance equation (5) for the gravitational force $m_p g$ and the electric force $e\langle Z_p \rangle E(y)$; proceeding from this equation, the relation between the value of φ_s and electric field $E(y)$ can be defined by the relation

$$\varphi_s(y) E(y) = \frac{m_p g}{a_p}, \tag{13}$$

which can be used for determining the dependence of function $\varphi_s(y)E(y)$ on height h from the results of measurements (see table and Figs. 2a and 2b).

The spatial potential φ in the near-electrode plasma layer was measured by a compensated Langmuir probe at various heights relative to the electrode. The measured potential difference Δφ between points h = 1.1 cm and h = 0.6 cm amounted to 1.5 V. Then, the experimental data were approximated under the assumption of small variation of charge $\langle Z_p \rangle$ ($\varphi_s \approx$ const, see Section 2) by linear (3) and quadratic (4) functions for E, where $y = d_{\max} - h$. The near-electrode layer thickness $d_{\max}$ and coefficients C_1 and C_2 in these approximations were obtained through the best fitting of experimental data and were $C_1 \approx 12$ V/cm^2 and $d_{\max} \approx$ 1.1 cm for the linear field (3), and $C_2 \approx 16.2$ V/cm^3 and $d_{\max} \approx 1.26$ cm for the quadratic dependence (4). The results of approximation are shown in Figs. 2a and 2b. The mean-square errors of the linear and quadratic approximations are approximately equal to 4% and 10%, respectively. The higher value of error in the latter case is explained by the strong mismatching between

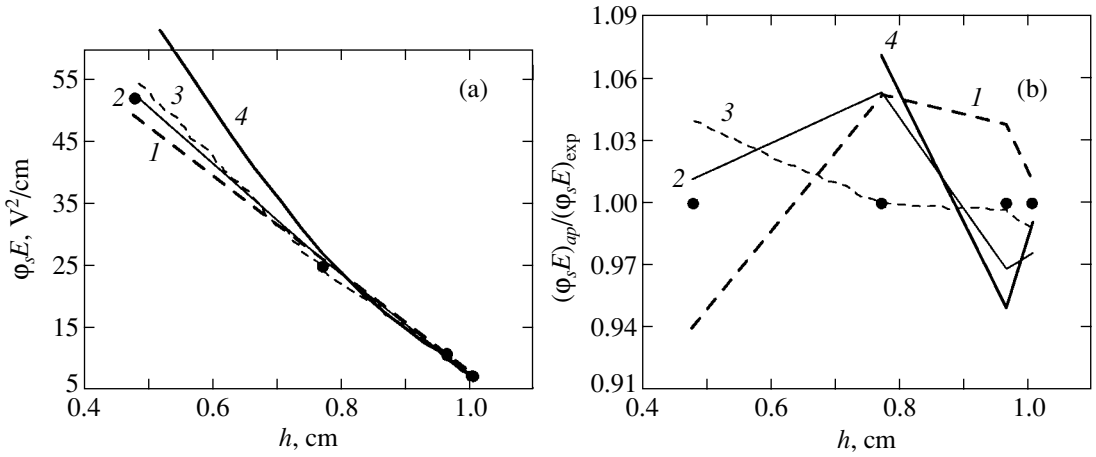

Fig. 2. Dependence of (a) $\varphi_s E$ and (b) the ratio of various approximations $(\varphi_s E)_{ap}$ to experimental values $(\varphi_s E)_{exp}$ on the height h over the electrode cut for a linear field E (3) (*1*), formula (15a) (*2*), formula (15b) (*3*), and quadratic approximation of E (4) (*4*). The dots show the results of measurements.

the nonlinear approximation (4) and the results of measurements that is observed as we approach the electrode (upon a decrease in h).

The electric fields and charges $\langle Z_p \rangle$ of macroparticles reconstructed in the linear electric field approximation are given in the table. It can easily be seen that the error

$$\delta = \frac{\left|\langle Z_p \rangle - \langle Z_p^c \rangle\right|}{\langle Z_p^c \rangle}$$

in the measured charge $\langle Z_p \rangle$ relative to the value given by the relation

$$\langle Z_p^c \rangle = -\frac{\varphi_s a_p}{e} \equiv C a_p, \qquad (14)$$

where $C = 4632\ \mu m^{-1}$, is completely determined by the error in the linear approximation of E. Since the field E was determined by gravity both in the linear (3) and in quadratic (4) approximation, a close coefficient $C = 4598\ \mu m^{-1}$ for relation (14) was determined with an error δ from 7% (for $h = 0.77$ cm) to 30% ($h = 0.48$ cm) in this case also (see Figs. 2a and 2b). Thus, we could not detect in our experiments any appreciable changes in the charge of macroparticles due to a change in their charging conditions in the layer, which is in complete accordance with the theoretical predictions described in Section 2.

Considering that $\varphi_s = -zT_e/e$ in the OLM approximation ($z \approx 3$–4 for argon [19, 20]), we can estimate the electron temperature from the reconstructed value of $C = 4600\ \mu m^{-1}$: $T_e \approx 1.7$–2.2 eV. This value matches the values of $T_e \approx 1.9 \pm 0.3$ eV obtained from independent probe measurements of electron temperature in the near-electrode layer of the experimental setup in the absence of dust.

In spite of a low probability of determining the macroparticle charge gradient $\beta_y = dZ_p/dy$ correctly, we approximated the experimental data by the following functions:

$$\varphi_s E = C_1(y + \beta_y y^2), \qquad (15a)$$

$$\varphi_s E = C_2(y^2 + \beta_y y^3). \qquad (15b)$$

Thus, we have taken into account possible gradients of macroparticle charges in the linear (3) and in quadratic (4) approximations of the field for the measured function $(\varphi_s E)$ (13). As a result, we obtained close values of fields $E(y)$, charges Z_p, and the layer thickness d_{max} in both cases. The charge gradient for the linear field (15a) turned out to be positive ($\beta_y/\langle Z_p \rangle \approx 0.2\ cm^{-1}$), which readily follows from the behavior of the linear approximation (curve *1* in Fig. 2a) of the results of measurements, but contradicts the theoretical predictions (see Section 2). For (15b), the reconstructed charge gradient was $\beta_y/\langle Z_p \rangle \approx -0.37\ cm^{-1}$, which may be true in fact since the relative changes in the charge, $\Delta_i Z_p/\langle Z_p \rangle$, did not exceed 20% in this case even for the closest point to the electrode with $h = 0.48$ cm.

5. ANALYSIS OF THE RESULTS OF EXPERIMENTAL OBSERVATIONS OF VERTICAL VIBRATIONS OF PARTICLES IN THE NEAR-ELECTRODE LAYER OF AN RF DISCHARGE

The results of experiments described in the previous section indicate that variations of the charging conditions in the upper part of the near-electrode layer of an rf discharge do not affect significantly the charge of light macroparticles levitating in this region. However, even an insignificant change in the dust charge (see

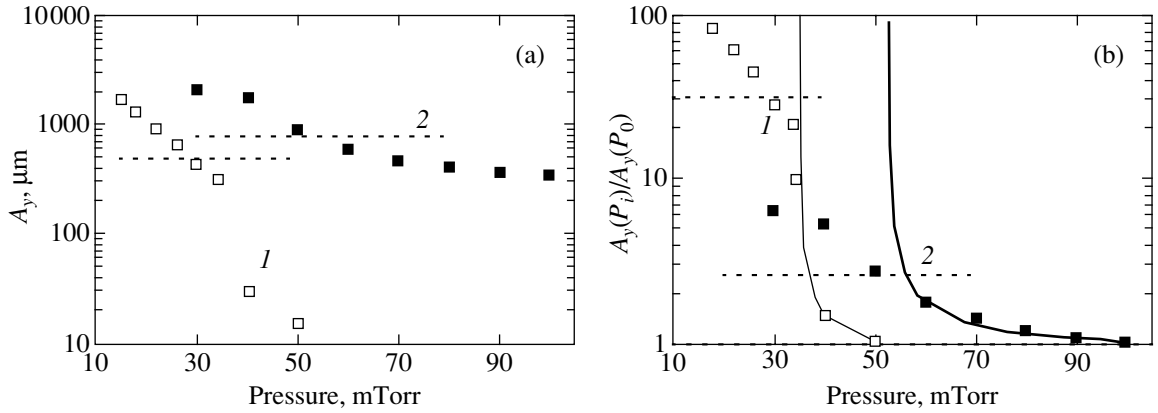

Fig. 3. Dependence of (a) amplitude A_y of vertical vibrations and (b) the ratio $A_y(P_i)/A_y(P_0)$ on pressure P of the rf discharge in argon for particles of radius a_p = 1 (*1*) and 2.1 μm (*2*). Dashed lines correspond to the values of $A_y^{\max}$ (a) and $A_y^{\max}/A_y(P_0)$ (b), while solid lines in (b) correspond to approximation (16).

Section 3) may cause gradients β_y sufficient for the evolution of stochastic dust vibrations.

Experiments were conducted for particles with different sizes (a_p = 1 and 2.1 μm) in the near-electrode layer of a capacitive rf discharge in argon under pressures from 0.1 to 0.015 Torr. Under certain conditions (upon a decrease in pressure or upon an increase in the number of particles), dust particles acquired energies on the order of 1–10 eV and performed irregular vertical vibrations (in the direction of the gravitational field). Here, we consider only one of the possible mechanisms of evolution of such vibrations due to stochastic variation of their charges in a spatially inhomogeneous plasma on the basis of the numerical estimates described in Section 3. Since the value of kinetic energy $\Delta^s T$ acquired by a dust particle due to macroparticle charge gradients strongly depends on the accuracy of determining the parameters of particles and the surrounding plasma, we will analyze the relative changes in the amplitude A_y of vibrations of dust particles upon a decrease in pressure P in the discharge. We will assume that such a decrease in P changes the friction coefficient ν_{fr} for macroparticles, but does not lead to a noticeable perturbation of the surrounding plasma parameters. In this case, we obtain from relations (7) and (8)

$$\frac{A_y(P_i)}{A_y(P_0)} = \sqrt{\frac{1-\theta_1(P_0)}{1-\theta_1(P_i)}}, \qquad (16)$$

where $A_y(P_i)$ is the amplitude of vibrations of particles for various pressures P_i (i = 1, 2, ..., N).

Dependences $A_y(P)$ measured for particles of two sizes are shown in Fig. 3a. The dashed line in the same figure shows the boundaries at which the amplitude of particle vibrations attains a value close to $A_y^{\max} \approx 1.6 l_p$ (12), where l_p corresponds to the radial particle spacing in an unperturbed dust layer. The average kinetic energy of lighter particles of radius a_p = 1 μm, which was obtained from an analysis of their velocity spectrum for the minimal pressure, exceeded 3 eV, while the energy of particles with a_p = 2.1 μm attained ~10 eV.

Considering that $P_i^2\theta_1(P_i) = P_0^2\theta_1(P_0)$ (see relation (10)), the value of $\theta_1(P_0)$ can be obtained from relation (16) with the help of best matching of calculated and experimental data in the range where $A_y(P_i) < l_0$. This procedure gives $\theta_1 \approx 0.5$ for P_0 = 0.05 Torr for particles of radius a_p = 1 μm and $\theta_1 \approx 0.28$ (P_0 = 0.1 Torr) for particles with a_p = 2.1 μm. The results of calculation of $A_y(P_i)/A_y(P_0)$ (solid line) are shown in Fig. 3b. The dashed line shows the ratio of the maximal amplitude $A_y^{\max}$ (12) of particle displacement to its initial value $A_y(P_0)$ measured in experiments.

Thus, the evolution of the amplitudes of vibrations being analyzed upon a change in the discharge pressure is in qualitative agreement with the proposed mechanism of formation of such vibrations. The quantitative difference between the proposed approximations and the results of measurements can be due to the fact that the possible change in the plasma parameters upon a decrease in pressure or within the trajectory of dust particles was disregarded in the calculation of amplitude $A_y^{\max}$ and function $\theta_1(P_i)$.

6. CONCLUSIONS

The effect of nonuniform conditions on dust particle charging in the upper part of the near-electrode layer of an rf discharge is analyzed numerically. Simple analytic expressions are given for determining the macroparticle charge gradients. The surface potentials of macroparticles of different sizes are measured in the near-electrode plasma of the rf discharge. The measure-

ments show that the inhomogeneity of the surrounding plasma does not noticeably affect the charges of light dust particles levitating in the upper part of the near-electrode layer of the discharge in question ($|\beta_y|/\langle Z_p \rangle < 0.4$ cm^{-1}). The results of measurements are in good agreement with the analytic estimates of the macroparticle charge gradients obtained in the OLM approximation.

A possible mechanism of evolution of random vibrations of macroparticles due to their stochastic motion in the bulk of a spatially inhomogeneous plasma is proposed (in the presence of slight variation of dust charges). Analytic expressions are derived for estimating the amount of kinetic energy acquired by macroparticles due to the given mechanism. These estimates show that the kinetic energy of light dust particles may attain values on the order of 1–10 eV, which is close to the experimentally observed energies. The proposed mechanism forms the basis of analysis of the values of amplitude of macroparticle vibrations with different sizes measured in the near-electrode layer of the rf discharge under various pressures. It is shown that the given mechanism may be responsible for the evolution of stochastic vertical vibrations.

ACKNOWLEDGMENTS

This work was partly financed by the Russian Foundation for Basic Research (project nos. 01-02-16658 and 00-02-17520), INTAS (grant no. 01-0391), and Australian Council of Scientific Research. The research work of A.A. Samarian was supported by the University of Sydney research scholarship U2000.

REFERENCES

1. T. Trottenberg, A. Melzer, and A. Piel, Plasma Sources Sci. Technol. **4**, 450 (1995).
2. J. B. Pieper and J. Goree, Phys. Rev. Lett. **77**, 3137 (1996).
3. A. A. Homann, A. Melzer, S. Petrs, and A. Piel, Phys. Rev. E **56**, 7138 (1997).
4. A. A. Homann, A. Melzer, and A. Piel, Phys. Rev. E **59**, R3835 (1999).
5. U. Konopka, G. E. Morfill, and L. Ratke, Phys. Rev. Lett. **84**, 891 (2000).
6. A. A. Samaryan, A. V. Chernyshev, O. F. Petrov, *et al.*, Zh. Éksp. Teor. Fiz. **119**, 524 (2001) [JETP **92**, 454 (2001)].
7. V. Fortov, A. Nefedov, V. Molotkov, *et al.*, Phys. Rev. Lett. **87**, 205002 (2001).
8. C. Zafiu, A. Melzer, and A. Piel, Phys. Rev. E **63**, 066403 (2001).
9. E. B. Tomme, D. A. Low, B. M. Anaratone, and J. E. Allen, Phys. Rev. Lett. **85**, 2518 (2000).
10. E. Thomas, B. Annaratone, G. Morfill, and H. Rothermel, Phys. Rev. E **66**, 016405 (2002).
11. A. P. Nefedov, O. S. Vaulina, O. F. Petrov, *et al.*, Zh. Éksp. Teor. Fiz. **122**, 778 (2002) [JETP **95**, 673 (2002)].
12. O. S. Vaulina, A. P. Nefedov, O. F. Petrov, and V. E. Fortov, Zh. Éksp. Teor. Fiz. **118**, 1319 (2000) [JETP **91**, 1147 (2000)].
13. S. Nunomura, T. Misawa, N. Ohno, and S. Takamura, Phys. Rev. Lett. **83**, 1970 (1999).
14. V. E. Fortov, A. G. Khrapak, S. A. Khrapak, *et al.*, Phys. Plasmas **7**, 1374 (2000).
15. V. V. Zhakhovskiĭ, V. I. Molotkov, A. P. Nefedov, *et al.*, Pis'ma Zh. Éksp. Teor. Fiz. **66**, 392 (1997) [JETP Lett. **66**, 419 (1997)].
16. A. Samarian, B. James, O. Vaulina, *et al.*, in *Proceedings of 25th International Conference on Phenomena in Ionized Gases*, Nagoya Univ., Nagoya, Japan (2001), Vol. 1, p. 17.
17. A. Samarian, B. James, S. Vladimirov, and N. Cramer, Phys. Rev. E **64**, 025402 (2001).
18. O. S. Vaulina, S. A. Khrapak, A. P. Nefedov, and O. F. Petrov, Phys. Rev. E **60**, 5959 (1999).
19. O. S. Vaulina, A. P. Nefedov, O. F. Petrov, *et al.*, Zh. Éksp. Teor. Fiz. **120**, 1369 (2001) [JETP **93**, 1184 (2001)].
20. S. A. Khrapak, A. P. Nefedov, O. F. Petrov, *et al.*, Phys. Rev. E **59**, 6017 (1999).
21. J. Goree, Plasma Sources Sci. Technol. **3**, 400 (1994).
22. Yu. P. Raĭzer, M. N. Shneĭder, and N. A. Yatsenko, *High-Frequency Capacitive Discharge: Physics; Experiment Technology; Applications* (MFTI–Nauka "Fizmatlit," Moscow, 1995).
23. A. A. Ovchinnikov, S. F. Timashev, and A. A. Belyĭ, *Kinetics of Diffusely-Controlled Chemical Processes* (Khimiya, Moscow, 1986).
24. *Photon Correlation and Light Beating Spectroscopy*, Ed. by H. Z. Cummins and E. R. Pike (Plenum, New York, 1974; Mir, Moscow, 1978).
25. A. A. Samarian and B. W. James, Phys. Lett. A **287**, 125 (2001).

Translated by N. Wadhwa

Journal of Experimental and Theoretical Physics, Vol. 96, No. 6, 2003, pp. 1045–1054.
Translated from Zhurnal Éksperimental'noĭ i Teoreticheskoĭ Fiziki, Vol. 123, No. 6, 2003, pp. 1188–1199.

SOLIDS
Structure

The Effect of Superstructural Ordering on the Properties of High-Temperature Oxide Superconductor Systems

N. V. Anshukova[a], A. I. Golovashkin[a,*], L. I. Ivanova[b], and A. P. Rusakov[b]

[a]*Lebedev Institute of Physics, Russian Academy of Sciences, Moscow, 119991 Russia*
[b]*Moscow Institute of Steel and Alloys, Moscow, 117936 Russia*
**e-mail: golov@sci.lebedev.ru*

Received November 12, 2002

Abstract—The effect of superstructural ordering in the oxygen sublattice (in addition to the influence of the antiferromagnetic interaction of copper ions) on the electron and phonon characteristics of oxide high-temperature superconductor (HTSC) systems has been studied. Taking into account this ordering effect, it is possible to explain a wide range of experimental data, including doping-induced changes in shape of the Fermi surface, features of the phonon spectra, the existence of stripes, the presence of a pseudogap and its coexistence with the superconducting gap, and some peculiarities in the phase diagrams of HTSCs. © *2003 MAIK "Nauka/Interperiodica".*

1. INTRODUCTION

In recent years, there was considerable progress in the development of methods for the synthesis of high-quality single crystals of various high-temperature superconductor (HTSC) systems—compounds characterized by high T_c values in a certain range of compositions. By changing the level of doping, it is possible to vary the state of such compounds from insulating to metallic. The availability of high-quality samples allowed the electron, phonon, and other characteristics of oxide superconductors, as a function of the level of doping, to be thoroughly studied. Such investigations have been performed for HTSC compounds belonging to various systems, including $La_{2-x}Sr_xCuO_{4-\delta}$, $YBa_2Cu_3O_{6+x}$, $Bi_2Sr_2Ca_{1-x}Y_xCu_2O_{8-\delta}$, etc. Some new features in the electron and phonon properties were found for HTSCs at low doping levels and in the vicinity of the dielectric–metal transition. For example, the data of angle-resolved photoelectron spectroscopy (ARPES) showed [1, 2] that compounds of the $La_{2-x}Sr_xCuO_{4-\delta}$ system with $x \geq 0.05$ are characterized, in the vicinity of the dielectric–metal transition, by a Fermi surface with wide flat regions in the plane of (k_x, k_y) wavevectors, these regions being parallel to the [100] and equivalent directions. The cross section of this Fermi surface initially possesses a finite area close to that characteristic of the optimum doping level, rather than changing in proportion to the parameter x. As the x value increases up to $x \approx 0.15$, the shape of the Fermi surface remains virtually unchanged, since only intensity of the ARPES lines increases. Only upon doping to a level exceeding the optimum ($x \geq 0.17$) does the Fermi surface exhibit significant changes, and, on reaching $x \approx 0.25$, it becomes parallel to directions of the [110] type.

In a low-doped $La_{2-x}Sr_xCuO_{4-\delta}$ compound ($x \approx 0.07$) occurring in the metallic state, ARPES measurements revealed coexisting dielectric and metallic phases on a microscopic level [1, 2]. In these experiments, a sample exhibited two branches in the plot of energy E versus wavevector $\mathbf{k}$, one of these branches being characteristic of a purely dielectric phase and the other, of an optimum doped metallic phase. Only one of these branches $E(\mathbf{k})$—namely, that with a higher binding energy—is retained in the dielectric state at $x < 0.05$, while only the second branch remains in the metallic state at a high level of doping ($x \geq 015$).

Analogous coexistence of two phases (dielectric and metallic) on the microscopic level was revealed by neutron diffraction in the study of the dispersion of high-frequency longitudinal optical (LO) phonons in $La_{2-x}Sr_xCuO_{4-\delta}$ [3, 4], $YBa_2Cu_3O_{6+x}$ [5, 6], and other HTSC systems. At an intermediate level of doping, two LO phonon frequencies ω_{LO} were observed, one of these being characteristic of a metallic phase (observed in strongly doped compounds) and the other, of a purely dielectric low-doped phase. When the level of doping was varied, both ω_{LO} values remained virtually unchanged and only the intensities of the corresponding neutron diffraction lines exhibited redistribution. As the x value increased, the volume of the metallic phase exhibited growth at the expense of decreasing content of the dielectric phase.

The whole body of these and other experimental observations (including data on the static and dynamic magnetic superstructure modulation [7], negative thermal expansion at low temperatures [8], etc.) poses a question about coexistence and mutual ordering of the metallic and dielectric phases on the microscopic level in HTSCs. All these experimental data can hardly be

explained within the framework of the existing theoretical models assuming uniform electron density distribution in the course of doping.

As will be demonstrated below, the new data have a natural explanation if we take into account the presence of a superstructural charge order in the oxygen sublattice, in addition to the well-known antiferromagnetic order in the sublattice of copper ions in cuprate HTSCs. We will consider some features of the superstructural order in the oxygen sublattice, which influence the electron and phonon spectra of these HTSC systems. Allowance for this superstructural charge order in the oxygen sublattice explains the nature of coexisting dielectric and metallic phases on the microscopic level observed in doped samples of high-T_c cuprate superconductors.

2. DIELECTRIC STATE OF HTSC SYSTEMS

Let us consider the dielectric state of HTSC systems using an example of the $La_{2-x}Sr_xCuO_{4-\delta}$ system, beginning with a compound with $x = 0$ and $\delta = 0$. Theoretical calculations show that this undoped compound in the initial state must occur in the metallic state [9]. According to these calculations, the lower and upper Hubbard bands (composed mostly of the 3*d* states of copper) are separated by a wide band composed predominantly of the 2*p* states of oxygen. It is the presence of the latter band that imparts metallic properties to the compound; such a metal is referred to as the praphase. Previously [10], we have demonstrated that oxygen ions in the CuO_2 planes of the praphase can exist in two charged states, O^{-2} and $O^{-1.5}$, which correspond to the Cu–O^{-2} ionic bonds and the Cu–$O^{-1.5}$ ionic-covalent bonds, respectively. Ordering of the latter covalent bonds, with allowance of the antiferromagnetic ordering of copper ions, leads to doubling of the lattice period of the metallic praphase of the CuO_2 plane in the [100] and equivalent directions. This situation is equivalent to the appearance of a charge density wave (CDW) in the sublattice of oxygen ions. For this reason, a narrow oxygen band (instead of the aforementioned wide band) and a dielectric gap with a width of $E_g \sim 2$ eV appear at the top of the lower Hubbard band. As a result, a dielectric state rather than a metallic state is observed in real undoped HTSC systems of the type under consideration.

In the neighboring CuO_2 plane, the Cu–$O^{-1.5}$ covalent bonds are ordered in the perpendicular direction, whereby a dielectric gap appears in the *c*-axis direction as well. As a result, a new unit cell is formed that contains four $O^{-1.5}$ ions in addition to the O^{-2} ions. An exact chemical formula describing the dielectric compound La_2CuO_4 with allowance for the period doubling in all three directions can be written as

$$8(La_2CuO_4) = La_{16}^{+3}Cu_8^{+1.75}O_4^{-1.5}O_{28}^{-2}. \quad (1)$$

This formula unit precisely corresponds to the unit cell of the dielectric compound La_2CuO_4.

The above mechanism of period doubling is essentially a manifestation of the Jahn–Teller effect typical of oxygen-containing copper compounds. This effect removes degeneracy between the $2p_x$ and $2p_y$ states of oxygen ions in the CuO_2 planes, which is accompanied both by elastic straining and by charge redistribution between ions in the lattice. As a result, the system achieves an energy gain, typically of about 1 eV per unit cell [11]. In the case under consideration, this is manifested by the appearance of a bandgap $E_g \sim 2$ eV. According to the neutron diffraction data [12, 13], a characteristic displacement of oxygen ions in the CuO_2 plane for a period modulation comparable with the lattice period is on the order of 0.004 Å. Such changes can hardly be detected at the existing level of accuracy in phonon dispersion measurements or X-ray diffraction analysis.

Four oxygen ions in the charged state $O^{-1.5}$ (per unit cell with a period doubled in three directions) is the minimum number of ions for which the degeneracy is removed for all oxygen octahedra. The lattice period doubling leads to the appearance of a new reciprocal lattice vector $\mathbf{G}_2 = \mathbf{G}/2 = (\pi/a)[100]$, where $\mathbf{G} = (2\pi/a)[100]$ is the vector of a reciprocal lattice without period doubling and *a* is the Cu–Cu distance in the CuO_2 plane. Recently, Sachdev [14] has independently demonstrated that the period doubling follows from a general theoretical analysis of HTSC systems.

Since $O^{-1.5}$ ions are less strongly bound to the lattice than the O^{-2} ions, the electron states of the former ions are situated most closely to the chemical potential μ of the dielectric. Therefore, these states are at the top of a complex valence band including a narrow oxygen band and the lower Hubbard band. The aforementioned ordering of these weakly bound $O^{-1.5}$ ions leads, as noted above, to the appearance of a narrow about (0.3 eV), almost purely oxygen valence band formed by 2*p* states of $O^{-1.5}$ ions, lying above the wide (~3 eV) mixed copper–oxygen Hubbard band formed by Cu(3*d*)–O^{-2}(2*p*) states. This energy band diagram is schematically depicted in Fig. 1a, indicating typical experimental energy values [15]. A small width of the upper valence band formed by the 2*p* states of $O^{-1.5}$ ions is determined by a relatively small overlap of these states, since the unit cell contains only four such ions (against 28 of O^{-2} ions).

The upper valence oxygen band formed by 2*p* states of $O^{-1.5}$ ions contains $4 \times 1.5 = 6$ electrons per cell. These electrons fill the Brillouin zones for a square quasi-two-dimensional lattice including two CuO_2 planes. In the case of a dielectric, the structure of three first Brillouin zones filled with electrons is schematically depicted in Fig. 2a. The third Brillouin zone con-

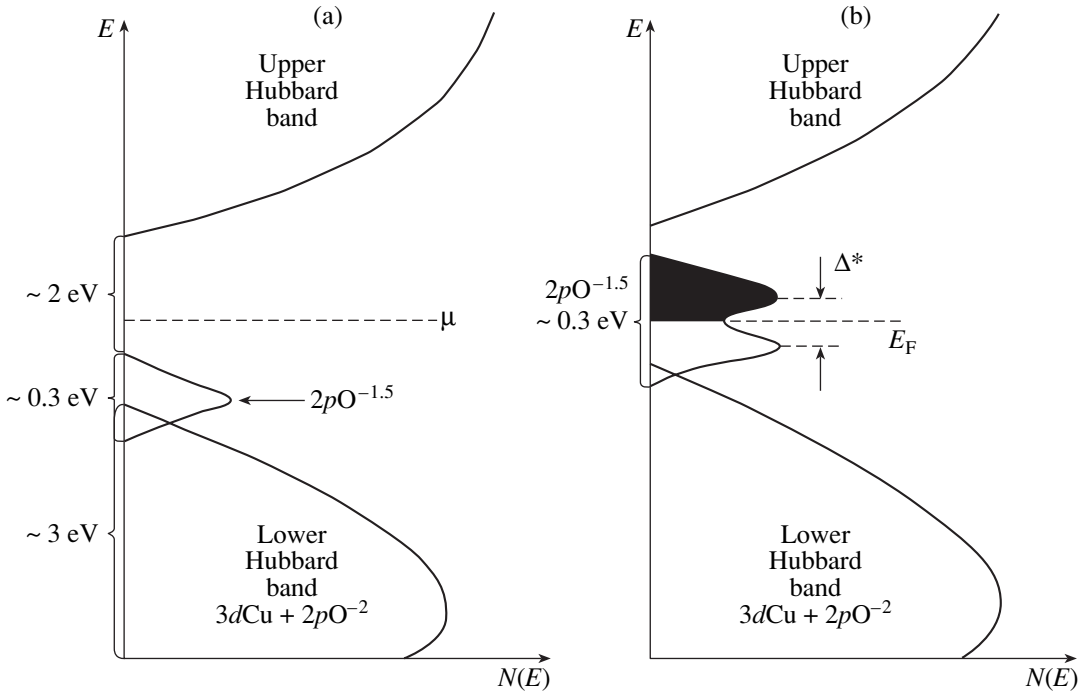

Fig. 1. Energy band diagram of cuprate HTSCs in the (a) dielectric and (b) metallic state at an optimum level of doping. The arrow in (a) indicates a narrow band formed by the 2*p* states of $O^{-1.5}$ ions; blackened region in (b) is filled by holes upon doping (*E* is the energy; μ is the chemical potential; E_F is the Fermi energy; *N*(*E*) is the density of electron states; Δ* is the Peierls energy gap).

tains two electrons, which corresponds to $x = x_c = 1/8 = 0.25$ electron per copper ion in formula unit (1).

3. DOPING AND ELECTRON STRUCTURE

In $La_{2-x}Sr_xCuO_4$ slightly doped with strontium, charge carriers (holes) might be expected at the top of the narrow oxygen valence band. In the case of degeneracy, the Fermi surface would pass near the boundaries of the third Brillouin zone. The distance between the boundaries of the third Brillouin zone and the Fermi surface must be proportional to the dopant concentration (i.e., to the *x* value). However, as mentioned above, ARPES reveals the Fermi surface far from the boundaries of the third Brillouin zone (Fig. 2b). For example, the Fermi surface passes approximately in the middle between points (0, 1) and (1/2, 1), that is, close to the point (1/4, 1). This boundary remains almost unshifted when the level of doping increases up to the optimum level of $x = 0.15$ [1]. In the case on weak doping ($0.05 < x < 0.13$), the system exhibits, as was also noted above, coexistence of the metallic and dielectric phases [2].

These and other new experimental data can be explained within the framework of the model considered below. The results presented in Fig. 2 are obtained by direct calculations of the electron structure. The values of the dispersion $E(\mathbf{k})$ obtained by these calculations for the upper valence bands can be approximated, within the framework of the tight binding method, by the formula [16–18]

$$E(\mathbf{k}) = -2t(\cos k_x + \cos k_y) - 4t'\cos k_x \cos k_y - 2t''(\cos 2k_x + \cos 3k_y) - t_\perp(\cos k_x - \cos k_y)^2/4, \quad (2)$$

where $\mathbf{k} = (k_x, k_y)$ is the dimensionless wavevector of the quasi-two-dimensional reciprocal lattice; *t*, *t*', and *t*'' are the overlap integrals with the nearest neighbor, next-to-nearest, and third-shell ions; and $t_\perp$ is the overlap integral for the interaction between adjacent CuO_2 planes. The maxima calculated for the valence bands coincide with the boundaries of the Brillouin zones for the dielectric state (Fig. 2a) corresponding to $t = 386$ meV, $t'/t = -0.272$, $t''/t = 0.223$, and $t_\perp = 150$ meV.

Figure 2b presents the shape of the Fermi surface calculated [16] for doped $La_{2-x}Sr_xCuO_4$ with $x = 3x_c/4 = 0.1875$, which corresponds to $t = 0.5$ eV, $t'/t = -0.3$, $t''/t = 0.2$, and $t_\perp = 0.15$ eV in formula (2). Using the overlap integrals, it is possible to estimate the dispersion $E(\mathbf{k})$ for the line between points (0, 1) and (1/2, 1). The corresponding dispersion curves are constructed in Fig. 3 for both pure dielectric and a doped compound. In Fig. 3a, point (1/2, 1) corresponds to the boundary of the third Brillouin zone. The width of the band filled with electrons is about 0.3 eV. In the case of slight doping, holes might appear at the top of this valence band as depicted in Fig. 3b. In the case of degeneracy, the Fermi surface would pass near the

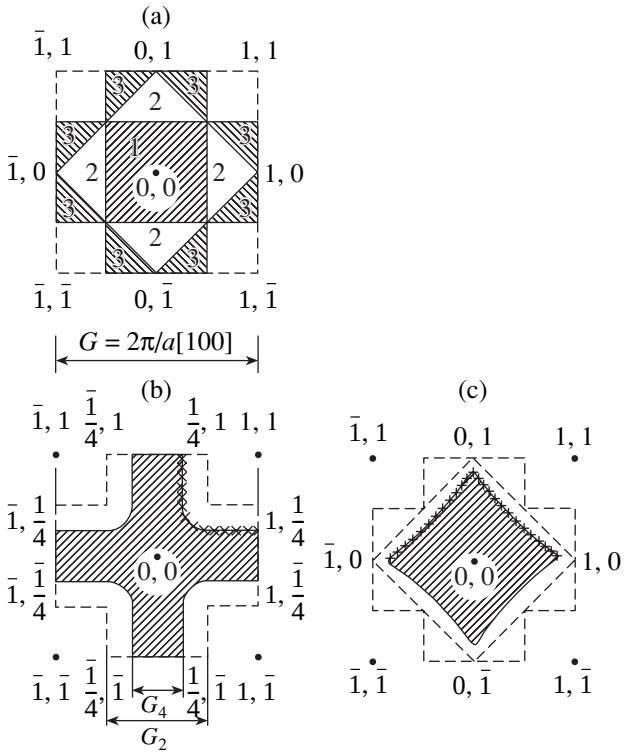

Fig. 2. The Brillouin zones and the Fermi surface shapes in cuprate HTSCs at various levels of doping. Positions of the symmetry points are indicated in π/a units (a is the minimum Cu–Cu distance). Crosses indicate the experimental ARPES data [1, 2]: (a) the first three Brillouin zones (indicated by numbers) for a flat CuO_2 lattice with doubled period (for the dielectric phase); dashed line shows the first Brillouin zone for the flat CuO_2 lattice without period doubling; (b) the Fermi surface (solid curve) for $La_{2-x}Sr_xCuO_4$ with $0.05 \le x \le 0.15$; dashed line shows the boundary of the third Brillouin zone; cross-hatched region corresponds to filled electron states; $\mathbf{G}_4 = \mathbf{G}_2/2 = \mathbf{G}/4$ are reciprocal lattice vectors, where $\mathbf{G} = (2\pi/a)[100]$; (c) the Fermi surface (solid curve) in the case of strong doping ($x > 0.25$); dashed line shows the boundary of the second and third Brillouin zones (for $x = 0.25$, the Fermi surface coincides with the boundaries of the second Brillouin zone); cross-hatched region corresponds to filled electron states (for $x = 0.3$).

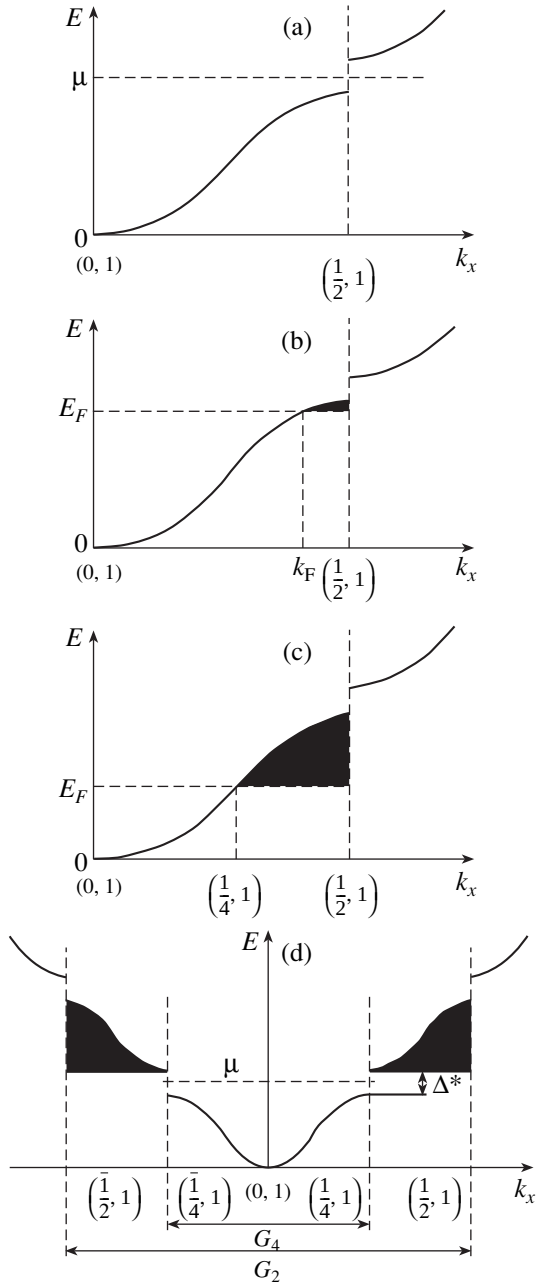

Fig. 3. Schematic dispersion curves $E(\mathbf{k})$ for cuprate HTSCs in the direction between points (0, 1) and (1/2, 1): (a) dielectric state; (b) the case of weak doping in the model of uniform hole distribution (shaded region corresponds to the states occupied by holes); (c) the case of a Brillouin zone half-filled with holes with respect to the momentum, i.e., up to the point (1/4, 1); (d) the formation of the Peierls gap Δ^* and the new reciprocal lattice vector as a result of nesting by the vector $\mathbf{G}_4 = \mathbf{G}/4$.

boundaries of the third Brillouin zone. However, in the case of a narrow band and weak screening, as in the system under consideration, it is energetically favorable to fill this band in separate regions of the crystal to half of the reciprocal lattice vector (Fig. 3c) at the expense of holes liberated from some intermediate regions. For such regions half-filled with holes, the lattice period can exhibit another doubling in the [100] direction. These regions are characterized by the reciprocal lattice vector $\mathbf{G}_4 = \mathbf{G}/4$ (Fig. 3d) representing the nesting vector (here, $\mathbf{G}$ is the reciprocal lattice vector for the initial undoubled direct lattice).

As is well known, nesting gives rise to the Peierls instability with the formation of a dielectric gap Δ^* (Fig. 3d). As a result, instead of the uniform band filling over the whole sample as depicted in Fig. 3b, the crystal exhibits separation into dielectric regions free of holes (with the dispersion such as in Fig. 3a) and half-filled regions with the Peierls gap and fourfold lattice period (with the dispersion such as in Fig. 3d). The densities of states corresponding to the dielectric regions and the

regions with Peierls gaps Δ* are presented in Figs. 1a and 1b, respectively. This scheme provides for a certain energy gain: the dielectric regions are characterized by a decrease in the Coulomb energy of repulsion between holes, while the regions with Peierls gaps exhibit a decrease in the kinetic energy as a result of the formation of gap Δ*. It should be emphasized that this phase separation takes place in the crystal with ordered $Cu–O^{-1.5}$ covalent bonds.

In the above scheme, the system separates into the metallic stripes with half-filled zone and the intermediate dielectric regions. Degeneracy of the charge carriers (holes) appears upon the formation of the first metallic stripes. For example, in $La_{2-x}Sr_xCuO_4$ the degeneracy is experimentally observed for $x \approx 0.02$–0.05, depending on the crystal quality [20].

Figure 4a shows schematic dispersion curves $E(\mathbf{k})$ for the upper valence band along some symmetric directions in the Brillouin zone of cuprate HTSCs. The curves, obtained from an analysis of relation (2), refer to a dielectric state (Fig. 4a) and a metallic state at optimum doping ($x = x_0 = 0.1875$).

Since doping in $La_{2-x}Sr_xCuO_4$ is realized in the form of homogeneously distributed strontium ions, the inhomogeneous distribution of holes must lead (according to the above scheme) to an additional Coulomb interaction between the metallic regions, resulting in a certain ordering of these regions (Fig. 5). Owing to the charge density fluctuations, this order can possess a dynamic character. Indeed, a dynamic order of this kind was observed in $La_{2-x}Sr_xCuO_4$ [19]. On the other hand, in the presence of defects (appearing upon doping with atoms possessing strongly different atomic dimensions, such as La and Nd), a static order in the metallic regions can appear as well. Such a static ordering was also experimentally observed in $(La,Nd)_{2-x}Sr_xCuO_4$ [12, 20] and $La_2CuO_{4+\delta}$ [21].

Experimental data [22] showed that ordering leads to the formation of a stripe structure. The stripes are spatially separated and oriented either along vector [100] or along [010] [22]. In the case under consideration, with the unit cell containing two CuO_2 planes, it would be natural to assume that direction [100] is characteristic of one of these planes and direction [010], of the adjacent plane. This ordering of stripes in two mutually perpendicular directions in the adjacent CuO_2 planes in a particular case of $(La,Nd)_{2-x}Sr_xCuO_4$ was experimentally revealed [12] by analysis of the experimental neutron diffraction data.

Figure 5 schematically illustrates the distribution of charge density in one of the symmetric directions in the CuO_2 plane. An analogous pattern is observed in the perpendicular direction in the adjacent CuO_2 plane. As can be seen in Fig. 2b, the conditions of nesting with the vector $\mathbf{G}_4 = \mathbf{G}/4$ are satisfied on a considerable part of the Fermi surface, so that this pattern holds for almost all these states (except regions of the vicinity of points of the (1/4, 1/4) type. Note also that the Peierls gap is not formed along the stripes.

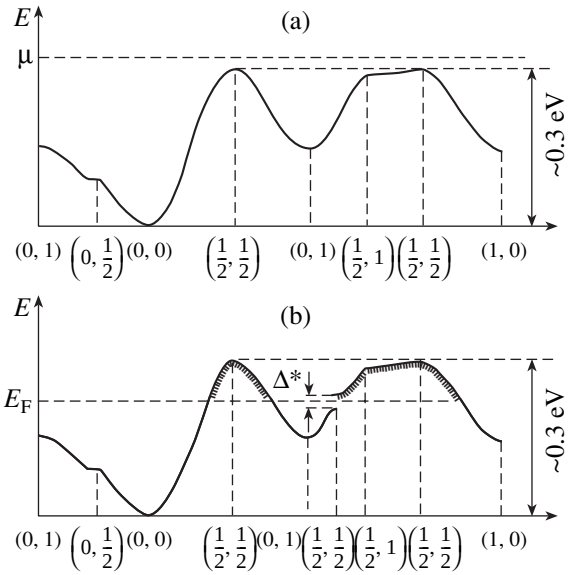

Fig. 4. Schematic dispersion curves $E(\mathbf{k})$ for the upper valence band of cuprate HTSCs along some symmetric directions in the Brillouin zone: (a) dielectric state; (b) metallic state at the optimum doping ($x = x_0$); cross-hatched regions correspond to the states filled by holes.

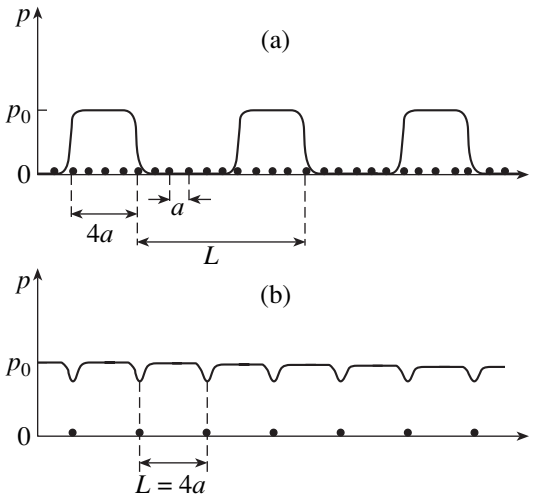

Fig. 5. Schematic diagrams of charge distribution in one of the symmetric directions in the CuO_2 plane (a) in the case of intermediate doping ($0 < x < x_0$) and (b) in the absence of dielectric spacers between metallic stripes ($x \approx x_0 = 0.1875$) (p is the hole density; $p_0 = 0.1875$ is the hole density per copper ion in a metal stripe; L is the period of charge modulation).

According to the scheme under consideration, the metallic conductivity of doped samples is related to the fact that the Peierls gap is not formed in the vicinity of points of the (1/4, 1/4) type. According to this, the Peierls gap Δ* in Fig. 1b is depicted as partly filled and

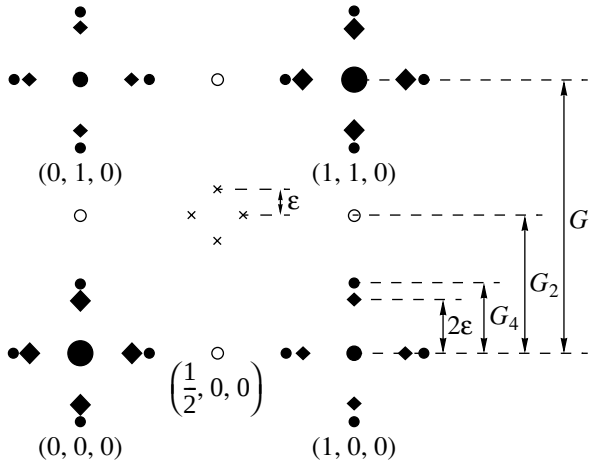

Fig. 6. Schematic diagrams showing the pattern of Bragg reflections and their splitting for the reciprocal lattice of oxide HTSCs in the region of coexistence of the dielectric and metal phases according to the proposed model of superstructural ordering: large black circles indicate reflections from the lattice without superstructural modulation; open circles indicate reflections due to the lattice period doubling; dots indicate reflections due to fourfold lattice periods; squares indicate reflections due to the distribution of metallic stripes with the period L ($2\varepsilon = 2\pi/L$); crosses indicate reflections due to the antiferromagnetic ordering of copper ions. Positions of the symmetry points are indicated in $2\pi/a$ units; $G_4 = G_2/2 = G/4 = (2\pi/a)/4$; $0 \le 2\varepsilon \le G_4$. The intensity of superstructural reflections is lower by many orders of magnitude than that of the main Bragg reflections.

the Fermi level (E_F) is indicated rather than the chemical potential.

The charge ordering depicted in Fig. 5 must be accompanied by elastic straining with the same spatial period. According to the neutron diffraction data for $(La,Nd)_{2-x}Sr_xCuO_4$ [12, 13], the deformation (e.g., the shift of oxygen ions in the CuO_2 plane) amounts to approximately 0.004 Å for $x = 0.12$. The period L of charge ordering in Fig. 5 is related to the doping level x as

$$L = 3a/4x, \tag{3}$$

where x can vary within the interval $0 \le x \le x_0 = 0.1875$. Theoretical calculations (reviewed in [12]) indicate that charged metallic stripes in the strained CuO_2 planes with antiferromagnetically ordered spins of copper ions play the role of the boundaries of domains with different phases of antiferromagnetic order. From this, it follows that the charge modulation period L corresponds to the superstructural antiferromagnetic modulation with a period of $2L$. In the reciprocal space, the charge ordering corresponds to the vector 2ε with the modulus $2\varepsilon = 2\pi/L$, and the antiferromagnetic ordering corresponds to the vector ε with the modulus $\varepsilon = 2\pi/2L = \pi/L$.

The relationship between the charge and magnetic ordering in the reciprocal space according to the proposed scheme is illustrated in Fig. 6, which shows the main Bragg diffraction reflections and their splitting upon superstructural modulation. The superstructural reflections differ in intensity by many orders of magnitude from the main reflections (observed for the lattice without superstructural modulation). All the superstructural reflections were separately observed in experiment [12, 14, 20]. In particular, reflections corresponding to the period doubling were reported in [14]. Reflections related to the antiferromagnetic ordering of copper ions, as well as the 2ε reflections due to a periodic distribution of metallic regions with the spatial period L, we reported in [12, 20] and in some other papers. The intensity of, for example, 2ε reflections was smaller by six orders of magnitude (about one million times) as compared to that of the main Bragg reflections [12]. The intensity of superstructural reflections related to the period doubling can be even smaller. Apparently, this smallness accounts for the absence of experimental data simultaneously revealing all types of reflections depicted in Fig. 6.

The value of 2ε varies, depending on the level of doping, from $2\varepsilon = 0$ for $x = 0$ (i.e., for $L \longrightarrow \infty$) to $2\varepsilon = G/4$ for $L = 4a$ (G is the absolute value of vector **G**). The latter case (depicted in Fig. 5b) corresponds to the absence of dielectric spacers between metallic stripes, whereby the entire crystal consists of regions with fourfold lattice period. In this case, holes fill three-quarters of states in the third Brillouin zone (see the cross-hatched region in Fig. 7a). Complete filling of the third Brillouin zone is attained at a hole density corresponding to $x = 0.25$ per copper ion, while filling of the three-quarters of states in this zone corresponds to a doping level of $x = x_0 = 0.25 \times 3/4 = 0.1875$.

Figure 7b shows dependence of the superstructural charge modulation 2ε on the doping level x. Here, the dashed curve shows our estimate constructed as

$$2\varepsilon(x) = (4x/3)(2\pi/a), \quad 0 \le x \le x_0, \tag{4}$$

$$2\varepsilon(x) = (1/4)(2\pi/a), \quad x_0 \le x \le 0.25. \tag{5}$$

Symbols in Fig. 7b represent the experimental data for $La_{2-x}Sr_xCuO_4$ and $(La,Nd)_{2-x}Sr_xCuO_4$ [12]. As can be seen, the experimental points fit the calculated curve well. At $x > 0.1875$, the value of 2ε ceases to change and remains equal to $2\varepsilon = G_4 = G/4 = 0.25$. The corresponding magnetic modulation is $\varepsilon = 0.125$. The value of $x_0 = 0.1875$ corresponds to a certain critical point on the $T(x)$ phase diagram.

For $x \ge 0.1875$, holes appear at the top of the valence band (below the Peierls gap Δ^*) near the point (1/4, 1) as depicted in Fig. 3d. A further increase in the level of doping ($x > 0.1875$) leads to a decrease in the Peierls gap width Δ^* (related to an increase in the hole screening) and is accompanied by a decrease in intensity of the neutron diffraction lines corresponding to superstructural charge and spin ordering. In addition, it is possible to calculate a change in the Fermi surface for

$x > 0.1875$ by formula (2) taking into account the dependence of t' and t'' on x,

$$t' = t'_0(0.25 - x)/0.25, \quad (6)$$

$$t'' = t''_0(0.25 - x)/0.25, \quad (7)$$

where $t'_0 = -0.15$ eV and $t''_0 = 0.1$ eV are the parameters for the state with $x = 0.1875$ (Figs. 2b and 3c) in which the metallic stripes are not separated by dielectric spacers.

A maximum value of x, corresponding to the third Brillouin zone completely filled with holes, is 0.25 per copper ion. For $x \geq 0.25$, the Fermi surface acquires the shape represented by the solid curve in Fig. 2c, where crosses represent the experimental data [1] for $x = 0.3$. As can be seen, the calculated shape of the Fermi surface qualitatively agrees with experiment. At $x = 0.25$, the Fermi surface coincides with the boundaries of the second Brillouin zone. In this case, according to the proposed model, the Fermi surface acquires an electron character. This fact has been established in numerous experiments.

Thus, the proposed scheme for $x < 01875$ features coexistence of two phases, dielectric and metallic, on a local level. This situation is reflected by the ARPES data [2]. At a higher level of doping, there exists a single (metallic) phase, as experimentally confirmed in [1].

4. EFFECT OF DOPING ON THE PHONON SPECTRUM

As noted above, doped HTSC systems exhibit an anomaly in the high-frequency LO phonon dispersion curve $\omega_{LO}(\mathbf{Q})$ in the metallic phase. The presence of such anomaly also follows from the proposed scheme of electron ordering in HTSCs. As is known [23], the longitudinal optical phonons obey an approximate relation

$$\omega^2_{LO}(\mathbf{Q}) \approx \omega^2_{TO} + \omega^2_p/\varepsilon(\mathbf{Q}), \quad (8)$$

where ω_{TO} is the frequency of transverse optical phonons (for simplicity, the dispersion of these phonons is ignored), ω_p is the plasma frequency of ions given by the formula

$$\omega^2_p = 4\pi N(e^*)^2/\Omega M, \quad (9)$$

e^* is the effective charge of oxygen ions, N/Ω is the number of oxygen ions per unit cell, $\varepsilon(\mathbf{Q})$ is the macroscopic permittivity of the electron subsystem, and M is the mass of an oxygen ion. For the dielectric phase ($x = 0$ for $La_{2-x}Sr_xCuO_4$) in the long-wave approximation ($Q \longrightarrow 0$), we have $\varepsilon(\mathbf{Q}) \longrightarrow \varepsilon_\infty$, where ε_∞ is the optical dielectric constant. As the Q value increases from 0 to $Q = G/2$, the permittivity $\varepsilon(\mathbf{Q})$ remains positive.

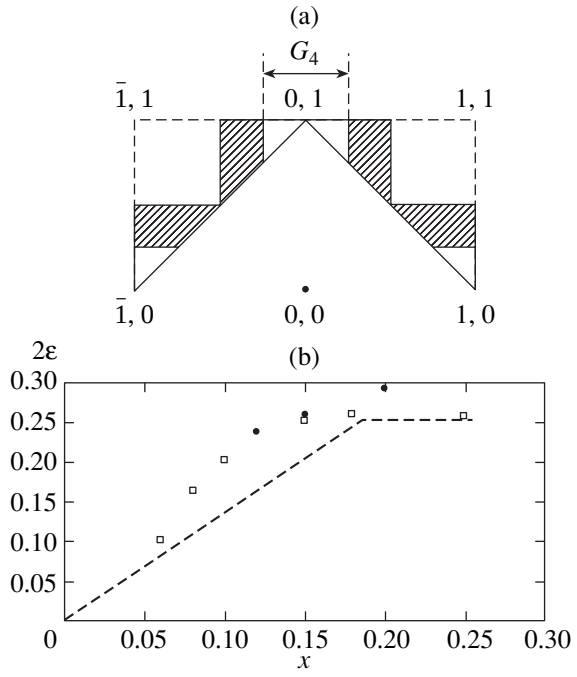

Fig. 7. Superstructural modulation 2ε and filling of the third Brillouin zone with holes: (a) three-quarters of the zone are filled with holes for $x = x_0 = 0.1875$; (b) the dependence of 2ε on x calculated by Eqs. (4) and (5) (dashed line) and plotted from the experimental data for $La_{1.6-x}Nd_{0.4}Sr_xCuO_4$ and $La_{2-x}Sr_xCuO_4$ (dots and squares, respectively) [12].

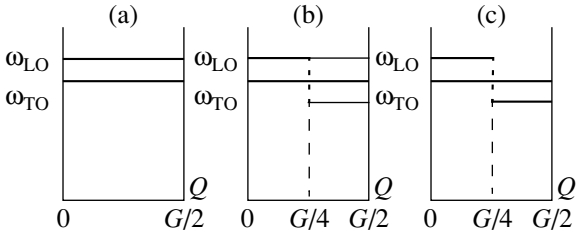

Fig. 8. The effect of doping on the dispersion of the phonon frequency ω_{LO} for HTSCs (a) in the dielectric state (the dispersion of ω_{TO} is ignored), (b) in the case of intermediate doping ($0.05 < x < 0.l875$; the thickness of lines approximately reflects the dielectric to metallic phase ratio in the crystal), and (c) for $x \geq 0.1875$.

Figure 8a shows a schematic diagram illustrating the dispersion of ω_{LO} and ω_{TO} in the dielectric state (with neglect of the dispersion of $\varepsilon(\mathbf{Q})$). Upon doping, the system exhibits separation into the dielectric and metallic phases on the microscopic level. For the dielectric phase, the dependence of ω_{LO} on Q remains qualitatively the same as in Fig. 8a for $x = 0$. In contrast, the metallic phase exhibits significant changes. The phonons with $G/4 \leq Q \leq G/2$ connect flat congruent regions of the Fermi surface as depicted in Fig. 9.

As is known [24–27], in the presence of congruent regions of the Fermi surface and nesting for the

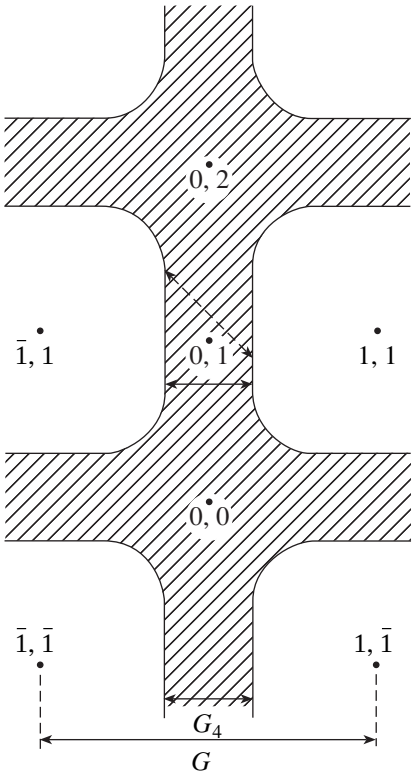

Fig. 9. Schematic diagram showing reciprocal lattice vector $\mathbf{G}_4 = \mathbf{G}/4$ connecting flat congruent regions of the Fermi surface (solid arrow) and $\mathbf{G}_4 + \mathbf{Q}$ vector connecting states on the Fermi surface that are symmetric relative to the point (0, 1) (dashed arrow).

wavevectors $\mathbf{Q}$, whereby $E(\mathbf{k}) = E(\mathbf{k} + \mathbf{Q})$, the static electron susceptibility

$$\chi(\mathbf{Q}) = \frac{1}{\Omega}\sum_{k}\frac{f(\mathbf{k}) - f(\mathbf{k} + \mathbf{Q})}{E(\mathbf{k} + \mathbf{Q}) - E(\mathbf{k})} \qquad (10)$$

exhibits divergence when $\mathbf{Q}$ is equal to the nesting vector (f is the distribution function). In the case under consideration, this must take place for $\mathbf{Q} = \mathbf{G}_4 = \mathbf{G}/4$. Under these conditions, the macroscopic permittivity $\varepsilon(\mathbf{Q})$ of the electron subsystem becomes negative. This follows from the relation [24, 26, 27]

$$\varepsilon(\mathbf{Q}) = 1 + \frac{(4\pi e^2/Q^2)\chi(\mathbf{Q})}{1 - (4\pi e^2/Q^2)L(\mathbf{Q})\chi(\mathbf{Q})} + \Delta\varepsilon, \qquad (11)$$

where e is the electron charge, $\Delta\varepsilon$ is the nonspecific contribution to the permittivity, and $L(\mathbf{Q})$ is a correction for the local crystal field ($0 < L(\mathbf{Q}) < 1$). In Eq. (11), $\chi(\mathbf{Q})$ denotes the modulus of the static electron susceptibility. In the case under consideration,

$$\omega_{\mathrm{LO}}^2(\mathbf{Q}) \approx \omega_{\mathrm{TO}}^2 - \omega_p^2/|\varepsilon(\mathbf{G}_4)| \qquad (12)$$

for $\mathbf{G}_4 \le \mathbf{Q} \le \mathbf{G}_2$.

Thus, the frequency ω_{LO} at $\mathbf{Q} = \mathbf{G}_4 = \mathbf{G}/4$ must decrease in a jumplike manner by the value $2\omega_p^2/|e(\mathbf{G}_4)|$ as schematically depicted in Fig. 8b. Taking into account that a crystal with $0.05 < x < 0.1875$ contains two phases, the real spectrum will display two lines with different frequencies ω_{LO}. The intensity of these phonon lines will be proportional to the volume of the corresponding phase in the crystal. As the content of the metallic phase increases with the level of doping, the intensity of the neutron diffraction lines corresponding to the ω_{LO} value of this phase grows, while the intensity of lines corresponding to the dielectric phase in the interval $\mathbf{Q}_4 \le \mathbf{Q} \le \mathbf{G}_2$ drops. This is reflected by different line thicknesses in Fig. 8b.

For $x \ge 0.1875$, whereby there is no dielectric spacers between metallic stripes, the dispersion of ω_{LO} acquires the shape schematically depicted in Fig. 8c. When $x \longrightarrow 0.25$, the shape of the Fermi surface changes, as can be seen from the comparison of Figs. 2b and 2c. This must be accompanied by qualitative changes in the dispersion of ω_{LO}, but these effects are beyond the scope of this paper. The model described above is qualitative corroborated by experiment [3–6, 15].

As was noted above, the appearance of double and fourfold lattice periods is accompanied by very small shifts of ions (on the order of 0.004 Å). Direct observation of such shifts through the measurement of phonon dispersion is difficult, but the effect can be detected through broadening of the neutron diffraction lines [3, 4]. It was established [4] that the line half-width significantly increases and exhibits a maximum for the wavevectors corresponding to a doubled lattice period. It was also demonstrated [3] that the appearance of the fourfold lattice period also leads to considerable broadening of the lines.

With decreasing temperature, the low-frequency transverse acoustic phonon branches ω_{TA} exhibit softening at the boundaries of the Brillouin zone. It can be shown that, without allowance for the interaction between ions and the charge density wave, the HTSC structure would be unstable [10]. The structure stabilizes (i.e., ω_{TA} becomes positive at the boundaries of the Brillouin zone) only in the presence of this interaction. On heating from $T = 0$, the amplitude of the charge density wave and, hence, the intensity of this interaction decrease, which must lead to contraction of the crystal (in the temperature range where the charge density wave contribution is decisive). Thus, HTSC systems (especially their dielectric phases) must exhibit negative thermal expansion at low temperatures. This anomalous thermal expansion was actually observed in experiment [34–37].

5. SUPERCONDUCTIVITY IN HTSC SYSTEMS

Let us study the possibility of superconducting pairing within the framework of the model proposed above.

In Fig. 9, the vector $\mathbf{G}_2 = \mathbf{G}/2 = (\pi/a)[100]$ is a translation vector and the point (0, 1) can be considered as the center of symmetry. The pairing of carriers occurring on the Fermi surface and connected by vectors $\mathbf{G}_4 + \mathbf{Q}$ passing through the point (0, 1) yields zero total momentum and can be superconducting (such a vector is shown by the dashed arrow in Fig. 9). These vectors can be the wavevectors of phonons. Thus, at a sufficiently low temperature, the states on the Fermi surface that satisfy the condition of nesting and are symmetric with respect to point (0, 1) are involved in interactions of two types. One interaction leads to the formation of the dielectric Peierls gap Δ*, while the other leads to the appearance of a superconducting gap Δ_s.

The spectrum of single-particle excitations $E(\mathbf{k})$ in such cases can be described by the formula [24, 28]

$$E(\mathbf{k}) = [(k^2/2m + \Delta^*)^2 + \Delta_s^2]^{1/2}, \quad (13)$$

where $\mathbf{k}$ is the electron wavevector for the states near E_F and m is the electron mass. This leads to the appearance of a common temperature-dependent gap

$$\Delta(T) = \sqrt{(\Delta^*)^2 + \Delta_s^2}. \quad (14)$$

At low temperatures ($T < T_c$), the total gap width Δ exceeds Δ_s and the material is superconducting. At $T > T_c$, $\Delta_s(T) = 0$ and $\Delta(T) = \Delta^*$. As can be seen from formula (14), the value of Δ (and T_c) with an allowance for the Peierls pairing can be significantly greater than in the absence of such pairing, even for a usual phonon mechanism of superconductivity. The dependence of the Δ* value on the position of the state on the Fermi surface is illustrated by Fig. 2b, showing that no Peierls gap appears (i.e., Δ* = 0) in the vicinity of points (±1/4, ±1/4) where the conditions of nesting are violated.

Thus, Δ* depends on the direction in the (k_x, k_y) plane as described by the solid curve in Fig. 10. This figure shows an approximate position of the point where Δ* = 0 (exact calculation of the dispersion curve is difficult, since the regions of all three Brillouin zones occur in the vicinity of this point). The dashed curve in Fig. 10 shows variation of the gap Δ(*T*) depending on the direction at $T < T_c$ according to formula (14). As can be seen, Δ* and Δ vary in a similar manner. Analogous curves are obtained even for *s* pairing (imitating the behavior for *d* pairing). Such dependences for HTSCs are observed experimentally, for example, by ARPES, for the superconducting gap Δ [29, 30] and pseudogap Δ* [31].

The existence of a pseudogap Δ* at $T > T_c$ and of a superconducting gap Δ(*T*) described by formula (14) at $T < T_c$ was confirmed by the tunneling study of the temperature dependence of the gap (see, e.g., [32, 33]). Qualitative agreement of the experimental data with the behavior predicted by the proposed model allows us to conclude that the experimentally observed pseudogap is essentially the Peierls gap Δ*.

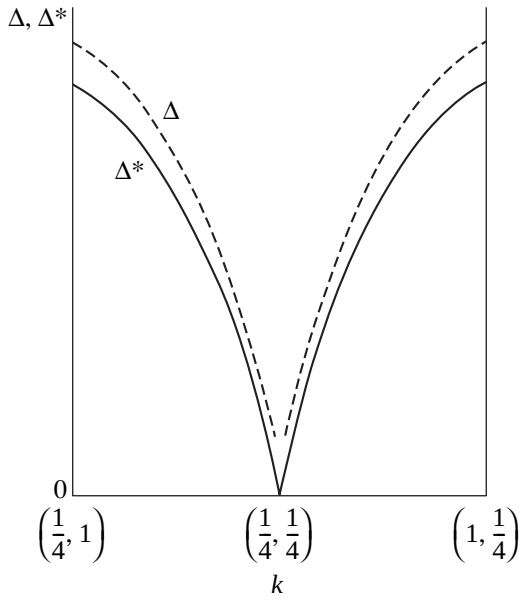

Fig. 10. Dependence of the superconducting gap Δ (dashed curve) and the Peierls gap Δ* (solid curve) on the direction in the (k_x, k_y) plane of an HTSC crystal.

6. CONCLUSION

New experimental data obtained using high-quality single crystals can be explained within the framework of the model of superstructural ordering in the oxygen sublattice, with allowance for the antiferromagnetic ordering of copper ions. In particular, the metallic stripes with a width of 4*a* and dielectric spacers predicted by the model agree well with the stripe models discussed in the literature.

According to formula (3), the distance between the metallic stripes in the $La_{2-x}Sr_xCuO_4$ system with $x \approx 0.06$ is about 30 Å. This value is close to the coherence (correlation) length ξ(*T*) in the *ab* plane of CuO_2. In these compositions, the stripes exhibit Josephson's coupling and the entire crystal occurs in a coherent state. This behavior is qualitatively consistent with the experimental phase diagram $T_c(x)$ of $La_{2-x}Sr_xCuO_4$. The same conclusion follows from an analysis of the effect of doping on T_c in some other HTSC systems. At $x \geq 0.25$, the third Brillouin zone is fully depleted of electrons and the Fermi surface acquires the shape depicted in Fig. 2c. The conditions of nesting for vector $\mathbf{G}_4 = \mathbf{G}/4$ are violated and the Peierls gap disappears, which leads to breakage of the superconducting state. The proposed model provides for a natural explanation of the shape of the Fermi surface for $La_{2-x}Sr_xCuO_4$ and other HTSC systems.

The dielectric Peierls gap Δ* formed according to the proposed model is identified with the experimen-

tally observed pseudogap. The dependences of the superconducting gap (Δ) and the dielectric gap (Δ^*) on the direction in the (k_x, k_y) plane predicted by the model agree well with experiment even in the case of *s* pairing.

The proposed model qualitatively explains the nature of the anomalous phonon dispersion, the onset and breakage of superconductivity in doped HTSC systems, and the origin of superstructural reflections in the neutron diffraction patterns. High critical temperatures observed for cuprate HTSCs are related to their quasi-two-dimensional character and the coexistence of dielectric and metallic pairing in such systems.

ACKNOWLEDGMENTS

This study was supported by the Russian Foundation for Basic Research (project no. 01-02-16395) and by the Federal Targeted Scientific-Technological Program "Superconductivity."

REFERENCES

1. A. Ino, C. Kim, T. Mizokawa, *et al.*, J. Phys. Soc. Jpn. **68**, 1496 (1999).
2. A. Ino, C. Kim, M. Nakamura, *et al.*, Phys. Rev. B **62**, 4137 (2000).
3. L. Pintschovius and M. Braden, Phys. Rev. B **60**, R15039 (1999).
4. R. J. McQueeney, Y. Petrov, T. Egami, *et al.*, Phys. Rev. Lett. **82**, 628 (1999).
5. Y. Petrov, T. Egami, R. J. McQueeney, *et al.*, cond-mat/0003414.
6. R. J. McQueeney, T. Egami, J.-H. Chung, *et al.*, cond-mat/0105593.
7. N. Ichikawa, S. Uchida, J. M. Tranquada, *et al.*, Phys. Rev. Lett. **85**, 1738 (2000).
8. A. I. Golovashkin, N. V. Anshukova, L. I. Ivanova, *et al.*, Physica C (Amsterdam) **341**–**348**, 1945 (2000).
9. W. E. Pickett, Rev. Mod. Phys. **61**, 433 (1989).
10. A. I. Golovashkin and A. P. Rusakov, Usp. Fiz. Nauk **170**, 192 (2000) [Phys. Usp. **43**, 184 (2000)].
11. B. Normand and A. P. Kampf, Phys. Rev. B **64**, 024521 (2001).
12. J. M. Tranquada, J. D. Axe, N. Ichikawa, *et al.*, Phys. Rev. B **54**, 7489 (1996).
13. M. Braden, M. Meven, W. Reichardt, *et al.*, Phys. Rev. B **63**, 140510 (2001).
14. S. Sachdev, Science **288**, 475 (2000).
15. *Electronic Properties and Mechanisms of High-T_c Superconductors*, Ed. by T. Oguchi, K. Kadowaki, and T. Sasaki (Elsevier, Amsterdam, 1992).
16. A. I. Liechtenstein, O. Gunnarsson, O. K. Andersen, and R. M. Martin, Phys. Rev. B **54**, 12505 (1996).
17. O. P. Sushkov, G. A. Sawatzky, R. Eder, and H. Eskes, Phys. Rev. B **56**, 11769 (1997).
18. T. Mishonov and E. J. Penev, J. Phys.: Condens. Matter **12**, 143 (2000).
19. K. Yamada, C. H. Lee, K. Kurahashi, *et al.*, Phys. Rev. B **57**, 6165 (1998).
20. N. Ichikawa, S. Uchida, J. M. Tranquada, *et al.*, Phys. Rev. Lett. **85**, 1738 (2000).
21. Y. S. Lee, R. J. Birgeneau, M. A. Kastner, *et al.*, Phys. Rev. B **60**, 3643 (1999).
22. J. M. Tranquada, Physica B (Amsterdam) **241**–**243**, 745 (1997).
23. M. J. Rice and Y. R. Wang, Physica C (Amsterdam) **157**, 192 (1989).
24. L. N. Bulaevskiĭ, V. L. Ginzburg, G. F. Zharkov, *et al.*, in *Problems in High-Temperature Superconductivity*, Ed. by V. L. Ginzburg and D. A. Kirzhnits (Nauka, Moscow, 1977).
25. Yu. V. Kopaev, Tr. Fiz. Inst. im. P.N. Lebedeva, Akad. Nauk SSSR **86**, 3 (1975).
26. E. G. Maksimov, Tr. Fiz. Inst. im. P.N. Lebedeva, Akad. Nauk SSSR **86**, 101 (1975).
27. V. L. Ginzburg and E. G. Maksimov, Sverkhprovodimost: Fiz. Khim. Tekh. **5**, 1543 (1992).
28. R. S. Markiewicz, C. Kusko, and V. Kidambi, Phys. Rev. B **60**, 627 (1999).
29. H. Ding, M. R. Norman, J. C. Campuzano, *et al.*, Phys. Rev. B **54**, R9678 (1996).
30. J. Mesot, M. R. Norman, H. Ding, *et al.*, Phys. Rev. Lett. **83**, 840 (1999).
31. H. Ding, T. Yokoya, J. C. Campuzano, *et al.*, Nature **382**, 51 (1996).
32. V. M. Krasnov, A. Yurgens, D. Winkler, *et al.*, Phys. Rev. Lett. **84**, 5860 (2000).
33. V. M. Krasnov, Phys. Rev. B **65**, 140504 (2002).
34. N. V. Anshukova, A. I. Golovashkin, L. I. Ivanova, *et al.*, Int. J. Mod. Phys. B **12**, 3251 (1998).
35. N. V. Anshukova, A. I. Golovashkin, L. I. Ivanova, and A. P. Rusakov, Pis'ma Zh. Éksp. Teor. Fiz. **71**, 550 (2000) [JETP Lett. **71**, 377 (2000)].
36. H. You, U. Welp, and Y. Fang, Phys. Rev. B **43**, 3660 (1991).
37. Z. J. Yang, M. Yewondwossen, D. W. Lawther, *et al.*, J. Supercond. **8**, 223 (1995).

Translated by P. Pozdeev

Journal of Experimental and Theoretical Physics, Vol. 96, No. 6, 2003, pp. 1055–1064.
Translated from Zhurnal Éksperimental'noĭ i Teoreticheskoĭ Fiziki, Vol. 123, No. 6, 2003, pp. 1200–1211.

SOLIDS
Structure

The Influence of Oxygen Vacancies on the Magnetic State of $La_{0.50}D_{0.50}MnO_{3-\gamma}$ (D = Ca, Sr) Manganites

I. O. Troyanchuk[a], S. V. Trukhanov[a,*], E. F. Shapovalova[a], V. A. Khomchenko[a], M. Tovar[b], and H. Szymczak[c]

[a]*Institute of Solid-State and Semiconductor Physics, Belarussian Academy of Sciences, ul. Brovki 17, Minsk, 220072 Belarus*
[b]*Hahn-Meitner-Institute (BENSC), D-14109, Berlin, Germany*
[c]*Institute of Physics, Polish Academy of Sciences 02-668, Warsaw, Poland*
**e-mail: truhanov@ifttp.bas-net.by*
Received December 25, 2002

Abstract—The crystal structure and magnetic and electric transport properties of polycrystalline $La_{0.50}D_{0.50}MnO_{3-\gamma}$ manganites (D = Ca, Sr) were studied experimentally depending on the concentration of oxygen vacancies. The $La_{0.50}Sr_{0.50}MnO_{3-\gamma}$ system of anion-deficient compositions was found to be stable and possess a perovskite structure only up to the $\gamma = 0.25$ concentration of oxygen vacancies, whereas, for the $La_{0.50}Ca_{0.50}MnO_{3-\gamma}$ system, we were able to obtain samples with the concentrations of oxygen vacancies up to $\gamma = 0.50$. The stoichiometric $La_{0.50}D_{0.50}MnO_3$ (D = Ca, Sr) compositions had *O*-orthorhombic (Ca) and tetragonal (Sr) unit cells. The unit cell of the anion-deficient $La_{0.50}Sr_{0.50}MnO_{3-\gamma}$ manganites also became *O*-orthorhombic when the concentration of oxygen vacancies increased ($\gamma > 0.16$). Oxygen deficiency in $La_{0.50}Sr_{0.50}MnO_{3-\gamma}$ first caused the transition from the antiferromagnetic to the ferromagnetic state ($\gamma \sim 0.06$) and then to the spin glass state ($\gamma \sim 0.16$). Supposedly, the oxygen vacancies in the reduced $La_{0.50}Sr_{0.50}MnO_{3-\gamma}$ samples with $\gamma \geq 0.16$ were disordered. The special feature of the $La_{0.50}Ca_{0.50}MnO_{3-\gamma}$ manganites was a nonuniform distribution of oxygen vacancies in the $La_{0.50}Ca_{0.50}MnO_{2.75}$ phase. In the $La_{0.50}Ca_{0.50}MnO_{2.50}$ phase, the type of oxygen vacancy ordering corresponded to that in $Sr_2Fe_2O_5$, which led to antiferromagnetic ordering. The specific electric resistance of the $La_{0.50}D_{0.50}MnO_{3-\gamma}$ anion-deficient samples increased with increasing oxygen deficiency. The magnetoresistance of all samples gradually increased as a result of the transition to the magnetically ordered state. Supposedly, the $La_{0.50}Ca_{0.50}MnO_{3-\gamma}$ manganites in the range of oxygen vacancy concentrations $0.09 \leq \gamma \leq 0.50$ had a mixed state and contained microdomains with different types of magnetic ordering. The experimentally observed properties can be interpreted based on the model of phase layering and the model of superexchange magnetic ordering. © *2003 MAIK "Nauka/Interperiodica"*.

1. INTRODUCTION

The discovery of such collective electron phenomena as giant magnetoresistance and metal–dielectric or charge order–disorder phase transitions induced by an external magnetic field aroused interest in $Ln_{1-x}D_xMnO_3$-type compounds, where Ln is a trivalent rare-earth metal (La^{3+} or Y^{3+}) and D is a divalent metal such as Ca^{2+}, Sr^{2+}, Ba^{2+}, Cd^{2+}, and Pb^{2+} or Bi^{3+} [1–3]. The magnetic and electric properties of these hole-substituted manganites have been the object of many experimental and theoretical studies [4–7]. The reason for this interest is the abundance and diversity of properties of metals and dielectrics combined in compounds of one type, which include systems with crystal structure, spin, orbital, and charge ordering and, lastly, systems that experience phase layering. These properties are a consequence of close interactions between the lattice, charge, and spin degrees of freedom, which result in complex phase diagrams of compounds of this class [8–10].

Currently, the systems studied most thoroughly are $La^{3+}_{1-x}D^{2+}_xMn^{3+}_{1-x}Mn^{4+}_xO_3$ (D = Ca^{2+}, Sr^{2+}). The base compound for the type of compositions under consideration is $LaMnO_3$. It exhibits antiferromagnetic dielectric properties [5], and its magnetic structure is of the *A* type and represents a collection of antiferromagnetically arranged (001) ferromagnetic planes. The small ferromagnetic component, which is a consequence of the noncollinearity of the magnetic moments of manganese ions, arises because of antisymmetric Dzyaloshinski–Moriya exchange [11]; $LaMnO_3$ is therefore a weak ferromagnet.

The replacement of La^{3+} by Ca^{2+} (Sr^{2+}) ions increases the mean manganese valence, which preserves compound electroneutrality, and formally results in the formation of Mn^{4+} ions with the t^3_{2g} electronic configuration (total spin $S = 3/2$) [12]. It is assumed that, in these systems, the e_g electrons of Mn^{3+} are delo-

calized and play the role of charge carriers. Such substituted manganite systems exhibit metal–dielectric concentration phase transitions at $0.12 < x < 0.50$ [12]. The properties of ferromagnets and metals appear in the $La_{1-x}Ca_xMnO_3$ and $La_{1-x}Sr_xMnO_3$ systems almost simultaneously. It is, however, not completely clear whether or not the arising of properties of one type favors the appearance of properties of another [13].

Two special concentrations x of substituent ions are of interest for the $La_{1-x}Ca_xMnO_3$ system. Most of the recent works on these materials were concentrated on the compositions with $x = 0.30$, which exhibit giant magnetoresistance (on the order of 10^8% [14]) related to the first-order phase transition from the paramagnetic dielectric to the ferromagnetic metallic state at $T_C = 270$ K [15]. Another critical level of doping is $x = 0.50$. In contrast to $x = 0.30$, the magnetoresistance of this composition is related to the first-order antiferromagnet–ferromagnet transition and the dielectric–metal transition induced by an external magnetic field [16, 17].

The $La_{0.50}Ca_{0.50}MnO_3$ compound is a paramagnetic semiconductor above $T_C \approx 260$ K and a charge-ordered antiferromagnet (of the *CE* type) below $T_N \approx 180$ K (during heating). The *CE* magnetic structure type is a chessboard ordering of *C*- and *E*-type magnetic unit cells. The *C* magnetic structure type is in turn a collection of antiferromagnetically coupled (110) ferromagnetic planes, and the *E* structure type is a collection of antiferromagnetically coupled $(1\bar{1}0)$ ferromagnetic planes. Between T_C and T_N, $La_{0.50}Ca_{0.50}MnO_3$ consists of ferromagnetic and paramagnetic phases [18, 19]. In zero field, $La_{0.50}Ca_{0.50}MnO_3$ is a dielectric in the whole temperature range. Note that long-range charge and antiferromagnetic orders in $La_{0.50}Ca_{0.50}MnO_3$ are established simultaneously ($T_N = T_{C_0}$). Short-range charge ordering, however, begins to arise at about 210 K, that is, at a temperature much higher than that of the ferromagnet–antiferromagnet phase transition [20]. The e_g electrons in the charge-ordered state are localized in the crystal lattice, which results in a time-independent periodic distribution of the Mn^{3+} and Mn^{4+} ions.

The properties of $La_{0.50}Sr_{0.50}MnO_3$ resemble those of $La_{0.50}Ca_{0.50}MnO_3$ in many respects. Ferromagnetic ordering occurs in the $La_{0.50}Sr_{0.50}MnO_3$ manganite at $T_C = 320$ K [12, 21]. Long-range antiferromagnetic order arises at $T_N = 180$ K, and the ferromagnetic and antiferromagnetic phases coexist even to helium temperatures [22]. No ordering of manganese ions of different valences (no charge ordering) occurs in the $La_{0.50}Sr_{0.50}MnO_3$ manganite; accordingly, an *A*-type antiferromagnetic structure is formed.

In is generally believed that double exchange between Mn^{3+}–Mn^{4+} pairs determines the magnetic and electric properties of manganites with perovskite structures [23, 24]. This model is based on real electron exchange between two partially filled *d* shells of Mn^{3+} and Mn^{4+}. However, the ferromagnetic properties of manganites cannot be explained solely by double exchange. According to Goodenough [25], the ferromagnetic properties are determined not only by double exchange but also by the special nature of superexchange interactions in the Mn^{3+}–O–Mn^{3+} and Mn^{3+}–O–Mn^{4+} Jahn–Teller ionic systems. The orbital configuration of 3*d* electrons depends on the positions of manganese nuclei if static Jahn–Teller distortions are removed (the Goodenough quasi-static hypothesis). In the superexchange model, the ferromagnetic contribution is determined by the virtual electron transitions from the Mn^{3+} half-filled e_g orbitals to the unoccupied e_g orbitals.

The contributions of double exchange and superexchange interactions can be controlled by varying the Mn^{3+}/Mn^{4+} ratio. It is, therefore, of interest to study the properties of the $La_{1-x}D_xMnO_{3-\gamma}$ compounds depending on the mean valence of manganese ions. The Mn^{3+}/Mn^{4+} ratio can be varied by at least three methods: (1) by the replacement of lanthanum with divalent alkaline-earth metal ions, (2) by the replacement of manganese by magnetic and nonmagnetic ions of various valences, and (3) by controlling oxygen nonstoichiometry [26].

The dependence of magnetic and magnetoresistive properties on oxygen nonstoichiometry in hole-substituted manganites with perovskite structures has scarcely been studied. The removal of oxygen anions from the crystal lattice of $La^{3+}_{1-x}D^{2+}_xMn^{3+}_{1-x+2\gamma}Mn^{4+}_{x-2\gamma}O^{2-}_{3-\gamma}$ transforms Mn^{4+} ions into Mn^{3+} and decreases the coordination number of manganese ($6 \longrightarrow 5$).

Very interesting magnetic and magnetoresistive properties have recently been reported for the $La_{1-x}Ca_xMnO_{3-\gamma}$ [27–29] and $La_{1-x}Ba_xMnO_{3-\gamma}$ [30, 31] oxygen-deficient compositions. The results of these studies were evidence of such unusual properties of these strongly reduced manganites as a large ferromagnetic component, a high magnetic ordering temperature, and a large magnetoresistance in spite of the absence of Mn^{3+}–Mn^{4+} pairs.

In this work, we studied the magnetic and electric properties of the anion-deficient $La_{0.50}D_{0.50}MnO_{3-\gamma}$ manganites (D = Sr, Ca). In spite of equal substitution levels, the reduced samples exhibited quite different properties determined by the special features of the arrangement of oxygen vacancies.

2. EXPERIMENTAL

Polycrystalline stoichiometric $La_{0.50}D_{0.50}MnO_3$ (D = Sr, Ca) samples were prepared by the standard ceramic technique; namely, La_2O_3 (99.99%), $CaCO_3$ (99.99%), and MnO_2 (99.99%) were mixed in the required ratio between the cations and thoroughly ground. Prior to weighing, La_2O_3 was annealed at 1000°C for 5 h to remove H_2O and CO_2. The mixtures

were pressed into pellets 2 cm in diameter and 1.5 cm high with a hydraulic press in a steel press mold under an approximately 10^8 Pa pressure and calcined at 1100°C for 2 h in air. The pellets were then reground, pressed, and sintered at 1550°C for 2 h in air, which was followed by slow cooling in a furnace to room temperature. The rate of cooling was 100 K h^{-1}. During the synthesis, the samples were on the surface of platinum. The temperature in the furnace with chromide–lanthanum heaters was measured by a platinum–platinum–rhodium (10%) thermocouple. The cold thermocouple junction was in ice. The rate of heating and cooling the samples was controlled by an RIF-101 device.

The chemical reaction of the synthesis of $La_{0.50}D_{0.50}MnO_3$ manganites (D = Sr, Ca) can be written as

$$0.25La_2O_3 + 0.50Ca(Sr)CO_3 + 0.50Mn_2O_3 \longrightarrow La_{0.50}Ca(Sr)_{0.50}MnO_z + 0.50CO_2\uparrow. \quad (1)$$

The content of oxygen in all synthesized samples was determined thermogravimetrically. It was found that oxygen concentrations were slightly lower than stoichiometric and corresponded to the formula $La_{0.50}D_{0.50}MnO_{2.99\pm0.01}$ (D = Ca, Sr). The X-ray powder patterns were obtained at room temperature on a DRON-3 diffractometer (CrK_α radiation) in the angle range $30° \le 2\theta \le 100°$. The neutron diffraction patterns of $La_{0.50}Ca_{0.50}MnO_{2.50}$ were recorded at the Neutron Scattering Center (BENSC, Hahn–Meitner Institute, Berlin) on an E9 (FIREPOD) neutron powder diffractometer with a λ = 1.79686 Å wavelength and a $\Delta\theta \sim 0.002$ scan step.

Oxygen vacancies in the samples synthesized as described above were formed by annealing the samples in evacuated quartz ampules at 900°C for 24 h with the use of tantalum metal as an oxygen absorber. The following anion-deficient compositions were prepared: $La_{0.50}Ca_{0.50}MnO_{3-\gamma}$ (γ = 0.01, 0.04, 0.10, 0.12, 0.17, 0.20, 0.22, 0.25, 0.27, 0.30, 0.31, 0.32, 0.35, 0.37, 0.45, 0.48, and 0.50) and $La_{0.50}Sr_{0.50}MnO_{3-\gamma}$ (γ = 0.01, 0.06, 0.09, 0.12, 0.16, 0.17, 0.20, and 0.25). The reduction followed the reaction

$$La_{0.50}Ca(Sr)_{0.50}MnO_3 + \frac{2\gamma}{5}Ta \longrightarrow La_{0.50}Ca(Sr)_{0.50}MnO_{3-\gamma} + \frac{\gamma}{5}Ta_2O_5. \quad (2)$$

The final oxygen contents were calculated from sample mass changes after the reduction. Usually, a 2–3 g sample was loaded into the ampule to decrease the error of measurements. The relative error of measurements did not exceed 0.3%. The content of oxygen in the reduced samples was controlled by subjecting them to oxidation in air at 900°C for 24 h. The corresponding chemical reaction can be written as

$$La_{0.50}Ca(Sr)_{0.50}MnO_{3-\gamma} + \frac{\gamma}{2}O_2 \longrightarrow La_{0.50}Ca(Sr)_{0.50}MnO_3. \quad (3)$$

An increase in the weight of the samples after their oxidation corresponded to the weight loss in the reduction. This is evidence of a topotactic reduction character. Note that an important feature of the anion-deficient perovskite compounds is the possibility of their oxidation with restoration of the initial composition, structure, and physical properties.

The magnetization measurements were performed on an MPMS-7 quantum SQUID magnetometer and an OI-3001 commercial vibrating-coil magnetometer in the temperature range 4–380 K. The magnetic transition temperature was assumed to correspond to the onset of a sharp increase in the dynamic magnetic susceptibility or static magnetization measured in a 100-Oe field. Dynamic magnetic susceptibilities were measured with a mutual induction bridge in the temperature range 77–350 K. The field amplitude was 200 A/m, and the field frequency was 1200 Hz. The specific resistance of the samples was measured by the standard four-point technique in the temperature range 77–350 K. Indium contacts were formed by ultrasonic deposition. Magnetoresistance calculations were performed by the equation

$$MR[\%] = \{[\rho(H) - \rho(0)]/\rho(0)\} \times 100\%, \quad (4)$$

where MR[%] is the negative isotropic magnetoresistance, $\rho(H)$ is the specific electric resistance in a 9-kOe magnetic field, and $\rho(0)$ is the specific electric resistance in zero magnetic field. The electric current was directed along the longer side of the samples. The magnetic field was applied parallel to the electric current in the sample.

3. RESULTS AND DISCUSSION

The anion-deficient samples of the $La_{0.50}Sr_{0.50}MnO_{3-\gamma}$ series (La–Sr) were obtained in the single-phase state up to the γ = 0.25 concentration of oxygen vacancies. The sample with the nominal content of oxygen vacancies γ = 0.30 contained small amounts of two impurity phases with K_2NiF^{4-} and NaCl-type structures in addition to the major perovskite phase. Supposedly, these impurities were the $La_{2-x}Sr_xMnO_4$ and MnO oxides. According to the X-ray data, the La–Sr samples with $0 \le \gamma < 0.16$ had tetragonal unit cells (Fig. 1). An increase in the concentration of oxygen vacancies above γ = 0.16 resulted in the formation of *O*-orthorhombic unit cells, although the degree of symmetry distortion decreased. The unit cell parameters for the anion-deficient $La_{0.50}Sr_{0.50}MnO_{3-\gamma}$ compositions are listed in the table.

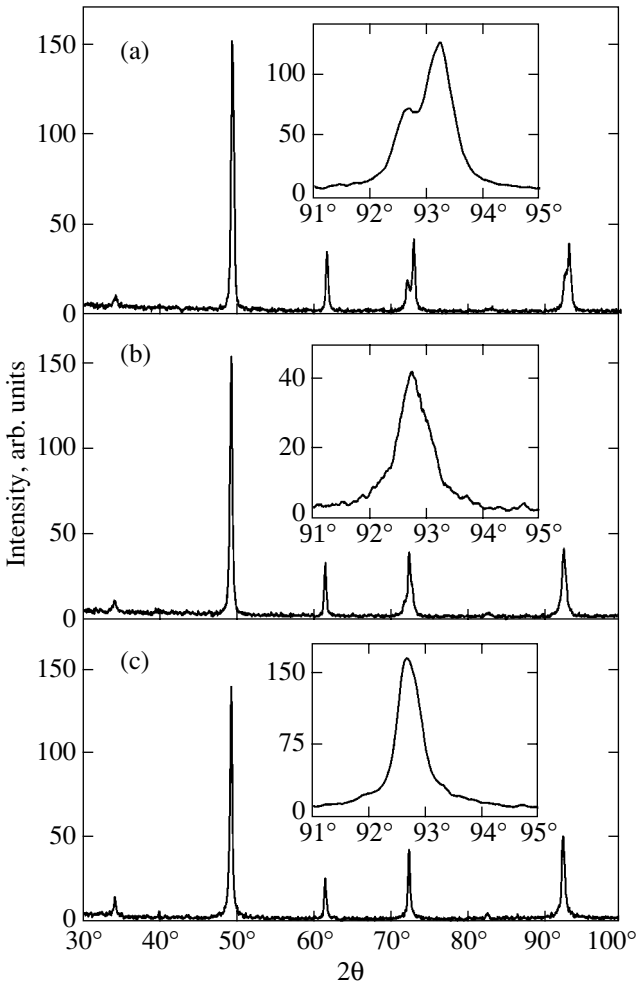

Fig. 1. X-ray powder patterns of $La_{0.50}Sr_{0.50}MnO_{3-\gamma}$ anion-deficient samples with (a) $\gamma = 0.01$, (b) $\gamma = 0.12$, and (c) $\gamma = 0.17$ recorded at room temperature. Shown in the insets are the (211) X-ray reflections for the corresponding samples.

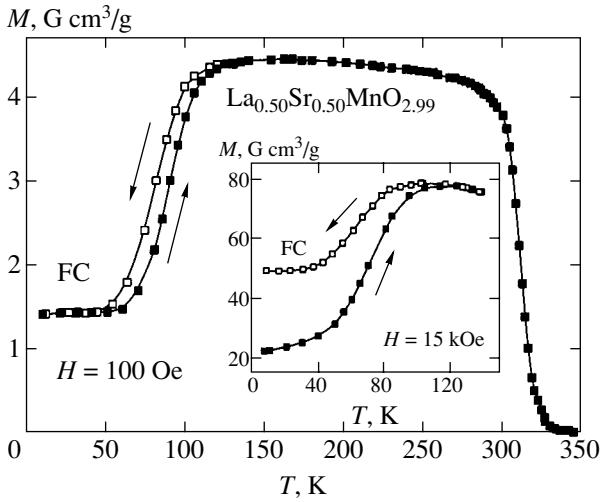

Fig. 2. Temperature dependence of magnetization for the $La_{0.50}Sr_{0.50}MnO_{2.99}$ anion-deficient sample in a 100-Oe external magnetic field. Shown in the inset is the low-temperature dependence of magnetization of the same sample in a 15-kOe field. Measurements were performed after cooling the sample in the corresponding magnetic field (FC). Arrows indicate the direction of measurements.

The anion-deficient samples of the $La_{0.50}Ca_{0.50}MnO_{3-\gamma}$ series (La–Ca) had *O*-orthorhombic unit cells. Starting with $\gamma = 0.27$, X-ray crystal structure reflections corresponded to those characteristic of an $Sr_2Fe_2O_5$-type structure with MnO_4 tetrahedra and MnO_6 octahedra as basic structure units [32, 33]. The unit cell parameters of several anion-deficient $La_{0.50}Ca_{0.50}MnO_{3-\gamma}$ samples were reported in [28, 29].

According to the dynamic magnetic susceptibility data, the $La_{0.50}Sr_{0.50}MnO_{2.99}$ anion-deficient sample has a magnetic ordering temperature of 320 K, which is almost equal to the temperature T_C of stoichiometric $La_{0.50}Sr_{0.50}MnO_3$ [22]. The temperature of the magnetic transition from the antiferromagnetic to the ferromagnetic state, however, sharply decreases compared with the stoichiometric sample, for which it equals 180 K [22]. According to magnetization measurements, the transition in $La_{0.50}Sr_{0.50}MnO_{2.99}$ in a 100-Oe field during heating begins at 55 K and ends at 100 K (Fig. 2). A 5 K

Symmetry type and parameters *a*, *b*, *c*, and *V* of unit cells for $La_{0.50}Sr_{0.50}MnO_{3-\gamma}$ ($0 < \gamma \le 0.25$) anion-deficient compositions

Chemical composition	Unit cell symmetry	*a*, Å	*b*, Å	*c*, Å	*V*, Å^3
$La_{0.50}Sr_{0.50}MnO_{2.99}$	Tetragonal	5.457		7.760	231.08
$La_{0.50}Sr_{0.50}MnO_{2.94}$	Tetragonal	5.454		7.792	231.76
$La_{0.50}Sr_{0.50}MnO_{2.91}$	Tetragonal	5.454		7.793	231.78
$La_{0.50}Sr_{0.50}MnO_{2.88}$	Tetragonal	5.484		7.753	233.19
$La_{0.50}Sr_{0.50}MnO_{2.84}$	*O*-Orthorhombic	5.462	5.484	7.757	232.37
$La_{0.50}Sr_{0.50}MnO_{2.83}$	*O*-Orthorhombic	5.462	5.484	7.757	233.88
$La_{0.50}Sr_{0.50}MnO_{2.80}$	*O*-Orthorhombic	5.480	5.487	7.759	233.52
$La_{0.50}Sr_{0.50}MnO_{2.75}$	*O*-Orthorhombic	5.506	5.511	7.783	236.16

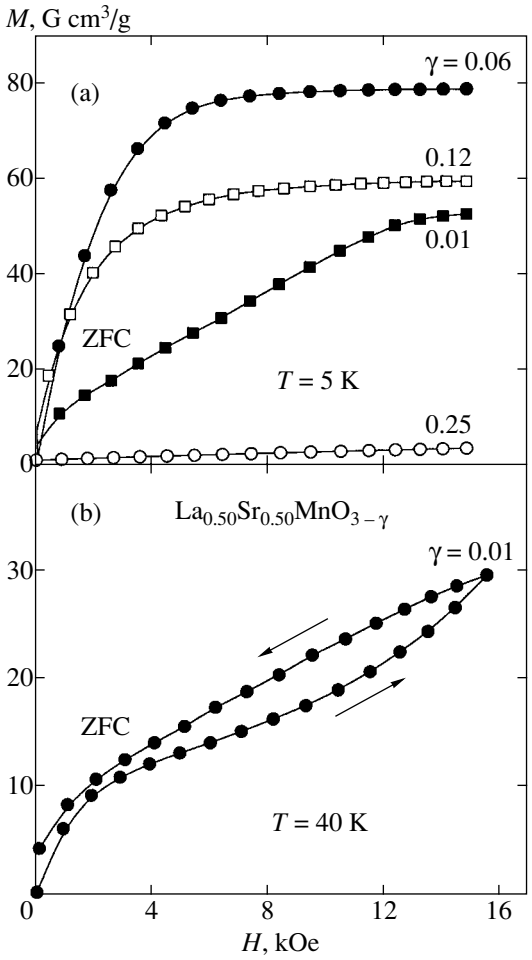

Fig. 3. Field dependences of magnetization for the $La_{0.50}Sr_{0.50}MnO_{3-\gamma}$ anion-deficient samples with $\gamma = 0.01$, 0.06, 0.12, and 0.25 at (a) 5 and (b) 40 K. The samples were zero-field-cooled (ZFC). The arrows denote the directions of field variations. The measurements shown in the upper figure were performed in the field decreasing mode.

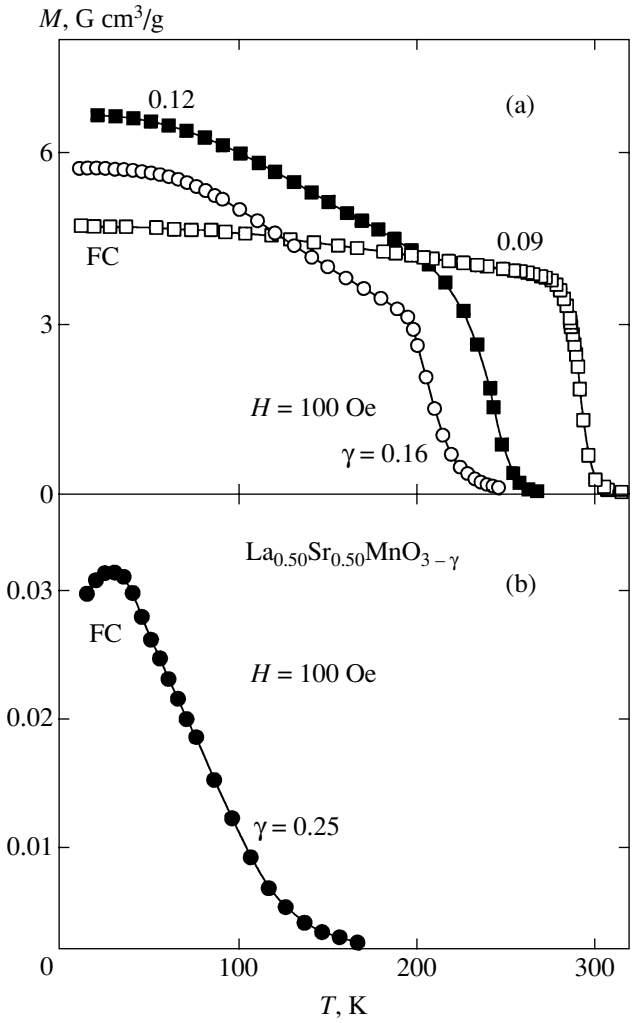

Fig. 4. Temperature dependences of FC magnetization in a 100-Oe field for the $La_{0.50}Sr_{0.50}MnO_{3-\gamma}$ anion-deficient samples with $\gamma = 0.09$, 0.12, and 0.16 (a) and 0.25 (b).

temperature hysteresis is evidence of a first-order phase transition.

An increase in the field to 15 kOe weakly influences the temperature interval of the phase transition in the $La_{0.50}Sr_{0.50}MnO_{2.99}$ anion-deficient sample during heating. During cooling, a large magnetization hysteresis is observed, which is evidence that the magnetic field effectively stabilizes the ferromagnetic phase in $La_{0.50}Sr_{0.50}MnO_{2.99}$. The magnetic moment in the ferromagnetic phase of this $La_{0.50}Sr_{0.50}MnO_{2.99}$ sample is close to the expected value for the parallel orientation of all manganese ion spins, the magnetic moments of Mn^{3+} and Mn^{4+} being equal to $4\mu_B$ and $3\mu_B$, respectively (Fig. 2).

The field dependences of magnetization at various temperatures for the anion-deficient $La_{0.50}Sr_{0.50}MnO_{3-\gamma}$ samples are shown in Fig. 3. An increase in the concentration of oxygen vacancies initially causes an increase in the spontaneous magnetic moment, which then gradually decreases. A maximum spontaneous magnetic moment is observed for the $La_{0.50}Sr_{0.50}MnO_{2.94}$ anion-deficient sample; it equals $2.97\mu_B$/formula unit. This value is below that calculated for completely ferromagnetic ordering of manganese ion spins ($3.62\mu_B$/formula unit). Below 100 K, the $La_{0.50}Sr_{0.50}MnO_{3-\gamma}$ anion-deficient compositions exhibit metamagnetic behavior in fields higher than 6 kOe. The highest attainable field on the unit that we used, 16 kOe, however, proved to be too low for effecting the complete transition to the ferromagnetic state. A field magnetization hysteresis was observed for the $La_{0.50}Sr_{0.50}MnO_{2.99}$ sample at 40 K (Fig. 3).

An increase in the concentration of oxygen vacancies to $\gamma = 0.06$ lowers the Curie temperature to T_C = 300 K, and the low-temperature phase transition from the antiferromagnetic to the ferromagnetic state disappears. In $La_{0.50}Sr_{0.50}MnO_{2.94}$, the Curie temperature

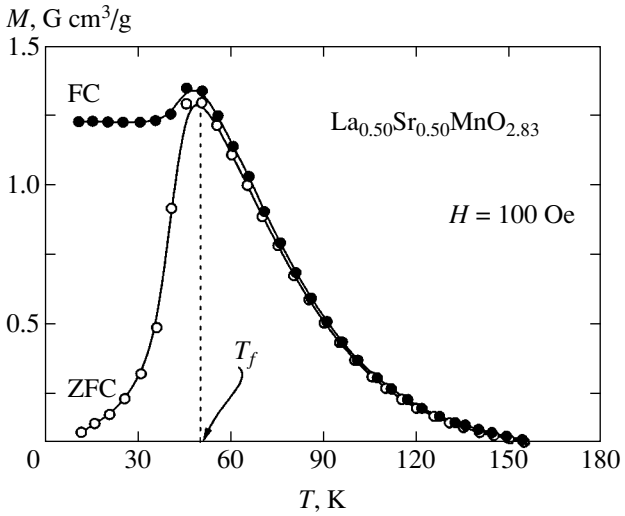

Fig. 5. Temperature dependences of ZFC and FC magnetizations in a 100-Oe field for the $La_{0.50}Sr_{0.50}MnO_{2.83}$ anion-deficient sample.

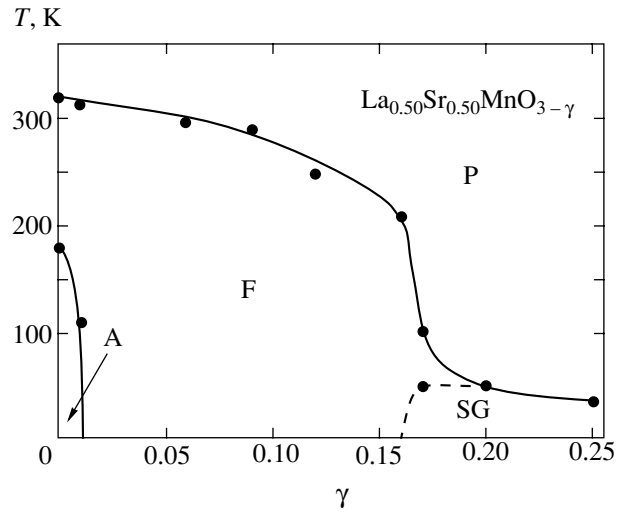

Fig. 6. Magnetic phase diagram of the system of $La_{0.50}Sr_{0.50}MnO_{3-\gamma}$ anion-deficient compositions; A stands for antiferromagnet; F, for ferromagnet; P, for paramagnet; and SG, for spin glass.

decreases to 212 K (Fig. 4). No magnetization saturation is observed in fields up to 16 kOe, as is characteristic of magnets with weakened cooperative magnetic interactions. The Curie temperatures for the $La_{0.50}Sr_{0.50}MnO_{2.88}$ and $La_{0.50}Sr_{0.50}MnO_{2.84}$ samples are 248 and 209 K, respectively (Fig. 4). For the samples with $0.17 \le \gamma \le 0.25$, the temperature of the transition to the paramagnetic state is difficult to determine because of substantial transition smearing. The temperature dependences of zero-field-cooled (ZFC) and field-cooled (FC) magnetizations differ insignificantly for the compositions with $0 \le \gamma \le 0.16$. Such a magnetization behavior is evidence that these compounds retain long-range ferromagnetic order in the temperature interval under consideration.

The smeared phase transition and the characteristic temperature behavior of the ZFC magnetization show that the magnetic state of the $0.17 \le \gamma \le 0.25$ anion-deficient compositions is drastically different. The $La_{0.50}Sr_{0.50}MnO_{2.83}$ composition exhibits different ZFC and FC magnetization behaviors. The temperature dependences of magnetization obtained by heating this composition in a 100-Oe field after field cooling (FC) and zero field cooling (ZFC) are shown in Fig. 5. Both curves have maxima at about $T_f = 50$ K. The ZFC and FC magnetizations are approximately equal above this temperature but substantially different below it. The ZFC magnetization first increases to its maximum value at 50 K as temperature grows and then smoothly decreases to zero, whereas the FC magnetization is almost constant at low temperatures. A sharp increase in the ZFC magnetization in the temperature interval 40–45 K is evidence of a strong decrease in magnetic anisotropy, which is characteristic of cooperative phenomena. Above T_f, no anomalous magnetization behavior is observed. The low spontaneous magnetic moment value corresponding to the $La_{0.50}Sr_{0.50}MnO_{2.83}$ anion-deficient composition is likely caused by a nonuniform magnetic state, which is a collection of antiferromagnetically and ferromagnetically ordered clusters. The competition between antiferromagnetic and ferromagnetic cluster interactions can lead to the spin glass state [34]. Also note that a temperature of 50 K is typical of cluster spin glass states in manganites [35]. Spontaneous magnetization measurements for $La_{0.50}Sr_{0.50}MnO_{2.83}$ encounter certain difficulties because of the Langevin shape of the field dependence of its magnetization, which is characteristic of spin glasses or superparamagnets.

A further decrease in the content of oxygen to $\gamma = 0.25$ sharply decreases the magnetic susceptibility of the La–Sr samples, but the field and temperature dependences of magnetization remain qualitatively unchanged (Figs. 3, 4). The temperature corresponding to the ZFC and FC curve maxima for the $La_{0.50}Sr_{0.50}MnO_{2.75}$ sample ($T_f = 40$ K) is slightly lower than that for the La–Sr sample with $\gamma = 0.17$.

Magnetic property measurements allowed us to construct the magnetic phase diagram shown in Fig. 6. The loss of oxygen causes a sharp decrease in the temperature and then the disappearance of the transition to the antiferromagnetic state for the La–Sr samples with $0.01 < \gamma < 0.06$, whereas the Curie temperature and spontaneous magnetization decrease comparatively insignificantly. The transition from the long-range to short-range ferromagnetic order occurs close to the threshold value of the concentration of oxygen vacancies, at $\gamma \sim 0.16$. Simultaneously, the critical temperature decreases severalfold in a very narrow interval of vacancy concentrations. We observe a well-defined trend of magnetic susceptibility and spontaneous magnetization lowering as the concentration of oxygen vacancies increases.

A fundamentally different trend is observed for the La–Ca series. According to [28, 29], the behavior of $La_{0.50}Ca_{0.50}MnO_{3-\gamma}$ at $\gamma \le 0.15$ is in many respects similar to that of the La–Sr samples. In both systems, the low-temperature antiferromagnetic state is suppressed because of the development of the ferromagnetic component, which is subsequently replaced by the spin glass component. However, at concentrations of vacancies above $\gamma = 0.15$, the behaviors of the two systems become qualitatively different. In the La–Sr series, an increase in the concentration of oxygen vacancies causes a sharp decrease in magnetic susceptibility, whereas, in the La–Ca series, the ferromagnetic component sharply increases and reaches a maximum at a $\gamma \sim 0.30$ concentration of vacancies [29]. A further increase in the number of oxygen vacancies ($\gamma > 0.30$) in the La–Ca samples fairly smoothly decreases the ferromagnetic component and the temperature of the transition to the paramagnetic state. The decrease in the ferromagnetic component coincides with the development of a perovskite-like structure of the $Sr_2Fe_2O_5$ type based on the initial perovskite cell.

In order to understand what happens with the magnetic structure at high oxygen vacancy concentrations, we performed a neutron diffraction study of $La_{0.50}Sr_{0.50}MnO_{2.50}$ at various temperatures. The neutron diffraction patterns show that additional reflections begin to appear below 100 K (Fig. 7). As the transition from the magnetically ordered to the paramagnetic state occurs at 120 K (this follows from the results of magnetic measurements), the conclusion can be made that the additional reflections have a magnetic nature. Note that the intensity of different magnetic reflections increases differently as temperature lowers, which can be caused by a rearrangement of the magnetic structure or the presence of a weak magnetic sublattice. The spontaneous magnetization value is very small, and the magnetic contribution to nuclear reflections is insignificant. This leads us to conclude that the magnetic structure is antiferromagnetic.

The electric resistance of the $La_{0.50}Ca_{0.50}MnO_{3-\gamma}$ anion-deficient samples with $0.09 \le \gamma \le 0.50$ is characteristic of semiconductors and continuously increases as temperature lowers (Fig. 8). At low temperatures, the specific resistance of the La–Ca samples satisfies the equation $\ln(\rho) \propto T^{-1}$ (see inset in Fig. 8). The behavior of the magnetoresistance of the samples with $0.09 \le \gamma \le 0.50$ correlates with the absence of any electric resistance anomalies close to the temperature of the transition to the magnetically ordered state. Below this temperature, magnetoresistance begins to increase continuously toward liquid nitrogen temperatures without a peak on its temperature dependence. Note that the electric transport properties of the La–Sr samples with $0.06 \le \gamma \le 0.25$ are similar to those of the La–Ca samples shown in Fig. 8.

We modernized the magnetic phase diagram of the $La_{0.50}Ca_{0.50}MnO_{3-\gamma}$ system, which was initially suggested in [28], taking into account the new experimental data. The evolution of the magnetic state of the La–Ca system is depicted in the phase diagram (Fig. 9). Long-range ferromagnetic order in the stoichiometric $La_{0.50}Ca_{0.50}MnO_3$ sample is established at $T = 250$ K, and long-range antiferromagnetic order, at $T = 180$ K [18, 19]. Deviations from stoichiometry weakly influence the ferromagnetic critical point, whereas the antiferromagnetic state becomes sharply suppressed by the ferromagnetic state. In the concentration range $0.02 < \gamma < 0.09$, the samples behave as ferromagnets with inclusions of clusters with substantially weakened exchange interactions. Below 40 K, the ZFC magnetization of the anion-deficient compositions increases as temperature grows. This is evidence of changes in anisotropy likely caused by sample inhomogeneity. At $\gamma > 0.09$, we observe a sharp decrease in spontaneous magnetization, whereas the anomalous behavior of magnetization below 40 K becomes more pronounced. Nevertheless, the divergence of the ZFC and FC mag-

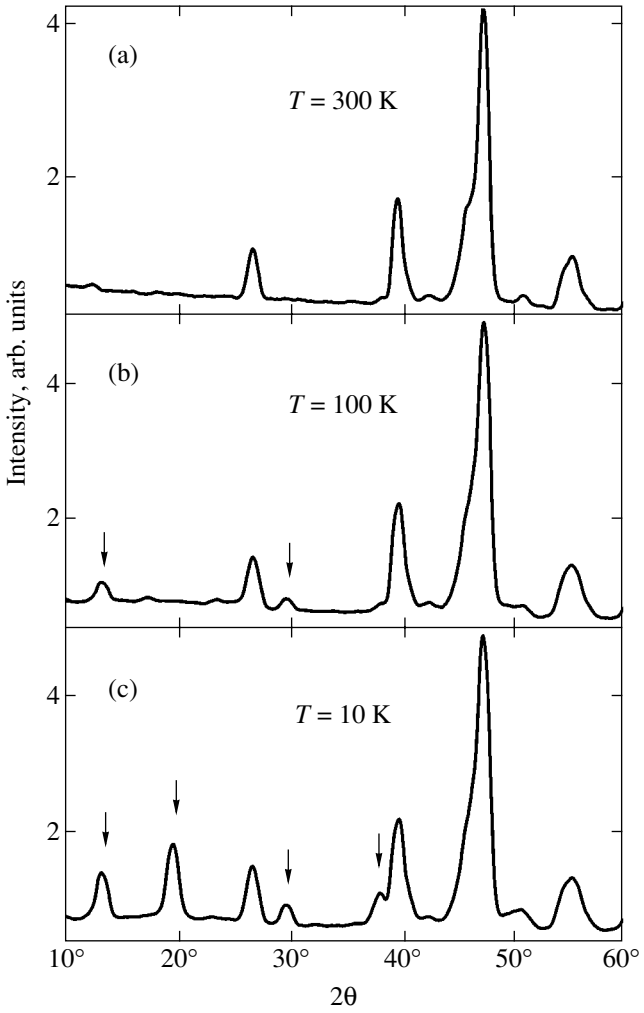

Fig. 7. Neutron diffraction powder patterns of the $La_{0.50}Ca_{0.50}MnO_{2.50}$ anion-deficient sample at (a) 300, (b) 100, and (c) 10 K.

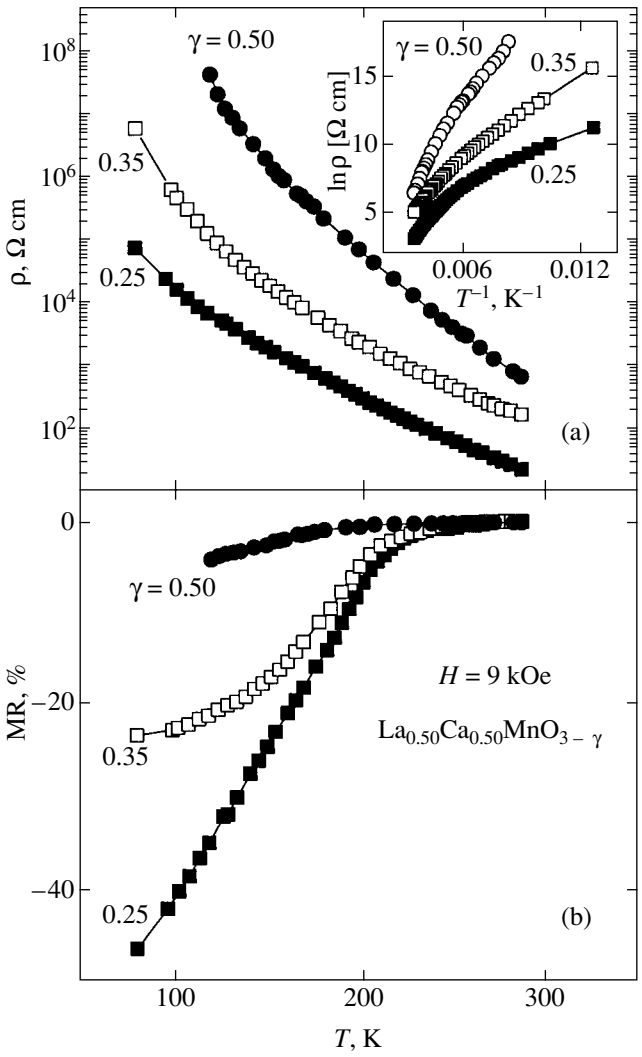

Fig. 8. Temperature dependences of (a) specific electric resistance and (b) magnetoresistance measured in a 9-kOe external magnetic field for the $La_{0.50}Ca_{0.50}MnO_{3-\gamma}$ anion-deficient samples with $\gamma = 0.25$, 0.35, and 0.50. Shown in the inset are the dependences of the logarithm of the specific electric resistances of the same samples on reciprocal temperature.

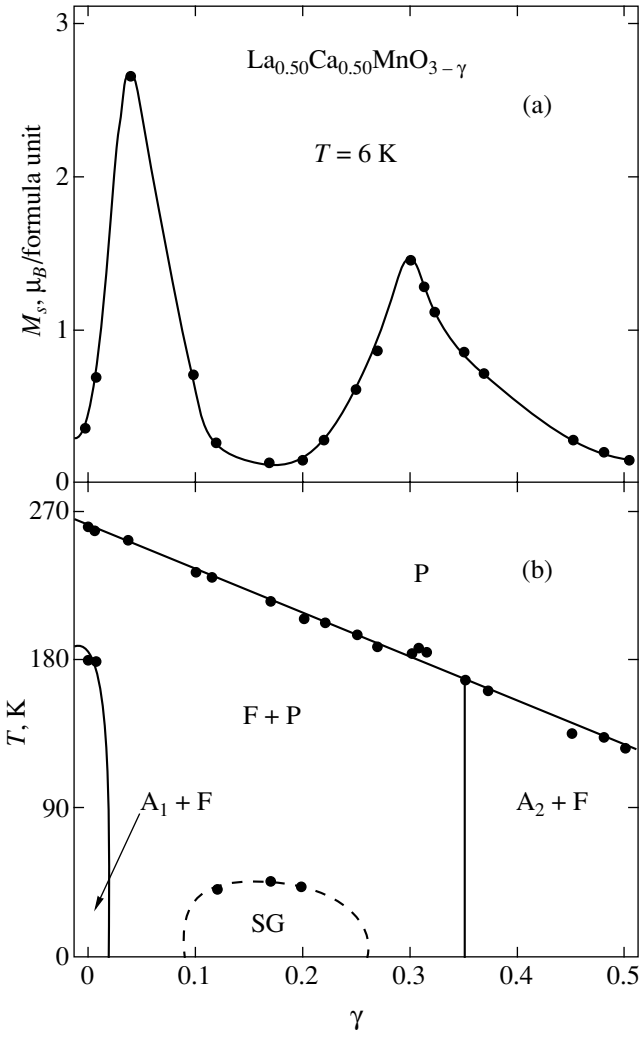

Fig. 9. (a) Dependence of spontaneous magnetic moment on the concentration of oxygen vacancies and (b) magnetic phase diagram of the $La_{0.50}Ca_{0.50}MnO_{3-\gamma}$ system of anion-deficient compositions; A_1 stands for charge-ordered antiferromagnet; A_2, for charge-disordered antiferromagnet; F + P, for inhomogeneous ferromagnet; P, for paramagnet; and SG, for spin glass.

netizations begins at fairly high temperatures and linearly decreases as the concentration of vacancies increases. Close to the $\gamma = 0.30$ concentration of oxygen vacancies, spontaneous magnetization sharply increases (Fig. 9) and reaches a maximum of about 40% of the value calculated for purely ferromagnetic ordering of the manganese ion spins. According to Gonzáles-Calbet *et al.* [36–38], the $La_{0.50}Ca_{0.50}MnO_{2.75}$ sample is a pure phase with a unique temperature dependence of the distribution of oxygen vacancies. Judging from high-resolution electron microscopy data, oxygen vacancies predominantly concentrate in the domain walls of microdomains, which have a small thickness compared with the other two dimensions.

The behavior of magnetic properties shows that vacancy distributions of the same type as in the $La_{0.50}Ca_{0.50}MnO_{2.75}$ phase are observed in a fairly wide range of oxygen vacancy concentrations, namely, $0.09 \le \gamma \le 0.50$. It is most likely that spin-glass-type systems with a fairly uniform distribution of oxygen vacancies and phases of the $La_{0.50}Ca_{0.50}MnO_{2.75}$ type coexist in the $0.09 < \gamma < 0.30$ concentration interval. In the $0.30 \le \gamma \le 0.50$ interval, the $La_{0.50}Ca_{0.50}MnO_{2.50}$ antiferromagnetic phase gradually replaces the $La_{0.50}Ca_{0.50}MnO_{2.75}$ phase. As the Curie (Néel) temperature depends on the concentration of vacancies almost linearly, it can be suggested that either the composition of the $La_{0.50}Ca_{0.50}MnO_{2.75}$ phase is not strictly constant, or microdomains of this phase are exceedingly small,

and the Curie point is determined by the interaction of magnetic domains of different types. $La_{0.50}Ca_{0.50}MnO_{2.75}$-type phases are not formed in the La–Sr samples, because the perovskite phase becomes thermodynamically unstable in these systems.

The Mn^{3+}–O–Mn^{3+} superexchange interactions are anisotropic in orbitally ordered phases (positive in the (001) plane and negative in the [001] direction) and isotropic in orbitally disordered phases (positive in all directions). The $La_{0.50}Ca(Sr)_{0.50}MnO_3$ stoichiometric compositions are orbitally ordered in the ground state. For this reason, Mn^{3+}–O–Mn^{3+} superexchange is negative and does not contribute to magnetization. The appearance of oxygen vacancies removes orbital ordering and increases double exchange (Mn^{3+}–O–Mn^{4+}) and superexchange (Mn^{3+}–O–Mn^{3+}) contributions to the resultant magnetization. The mean valence and the coordination number of manganese ions and, accordingly, the ferromagnetic double exchange contribution decrease as the concentration of oxygen vacancies increases. A decrease in the coordination number of manganese changes the sign of Mn^{3+}–O–Mn^{3+} superexchange from positive to negative. It follows that the antiferromagnetic component of exchange interactions increases as the concentration of oxygen vacancies grows. In the La–Sr compositions with $0.06 \le \gamma \le 0.16$, this results in a gradual Curie temperature and spontaneous magnetic moment lowering without radical changes in the magnetic state. The $\gamma = 0.17$ concentration of oxygen vacancies is likely to be critical; at this concentration, the volumes of two phases (ferromagnetic and antiferromagnetic) become comparable. The system is divided into clusters with different types of magnetic ordering. The competition between ferromagnetically and antiferromagnetically ordered cluster interactions results in the arising of a spin-glass-type state with an approximately 50 K temperature of freezing the magnetic moments of clusters.

4. CONCLUSIONS

We performed an experimental study of the crystal structure, magnetic, and electric transport properties of the $La_{0.50}D_{0.50}MnO_{3-\gamma}$ (D = Ca, Sr) anion-deficient manganites with perovskite structures. The $La_{0.50}Sr_{0.50}MnO_{3-\gamma}$ anion-deficient compositions were found to be stable and form perovskite structures only up to the $\gamma = 0.25$ concentration of oxygen vacancies, whereas we were able to obtain samples with oxygen vacancy concentrations up to $\gamma = 0.50$ for $La_{0.50}Ca_{0.50}MnO_{3-\gamma}$. The critical concentrations of oxygen vacancies at which unit cell symmetry type changed were observed. An increase in the concentration of oxygen vacancies first suppressed the orbitally ordered antiferromagnetic state and established long-range ferromagnetic order and then caused long-range ferromagnetic order destruction. The competition between ferromagnetically and antiferromagnetically ordered clusters resulted in the formation of the spin glass state. The specific electric resistance of $La_{0.50}D_{0.50}MnO_{3-\gamma}$ anion-deficient samples grew and the metal–semiconductor transition disappeared as oxygen deficiency increased. The magnetoresistance of all anion-deficient samples gradually increased depending on temperature in the transition to the magnetically ordered state. Supposedly, oxygen vacancies were disordered in the $La_{0.50}Sr_{0.50}MnO_{3-\gamma}$ reduced compositions with $\gamma \ge 0.16$. The special feature of the $La_{0.50}Ca_{0.50}MnO_{3-\gamma}$ manganites was a nonuniform distribution of oxygen vacancies in the $La_{0.50}Ca_{0.50}MnO_{2.75}$ phase. This increased the ferromagnetic component. In the $La_{0.50}Ca_{0.50}MnO_{2.50}$ phase, oxygen vacancies were ordered as in $Sr_2Fe_2O_5$, which resulted in antiferromagnetic ordering. The observed experimental properties can be interpreted based on the model of phase layering and the superexchange magnetic ordering model.

ACKNOWLEDGMENTS

This work was financially supported by the Belarussian Foundation for Basic Research (grant no. F02R-122), the Committee on Science of the Republic of Poland (KBN grant 5 PO3B 016 20), and the Scientific Program of the European Community (The Improving Human Potential Program, contract HPRI-CT-1999-00020).

REFERENCES

1. R. M. Kusters, D. A. Singleton, D. A. Keen, *et al.*, Physica B (Amsterdam) **155**, 362 (1989).
2. Y. Tokura and Y. Tomioka, J. Magn. Magn. Mater. **200**, 1 (1999).
3. E. Dagotto, T. Hotta, A. Moreo, *et al.*, Phys. Rep. **344**, 1 (2001).
4. E. E. Havinga, Philips Res. Rep. **21**, 432 (1966).
5. G. Matsumoto, J. Phys. Soc. Jpn. **29**, 606 (1970).
6. K. Kubo, J. Phys. Soc. Jpn. **33**, 21 (1972).
7. E. L. Nagaev, Phys. Rep. **346**, 387 (2001).
8. P. Schiffer, A. P. Ramírez, W. Bao, *et al.*, Phys. Rev. Lett. **75**, 3336 (1995).
9. A. Urushibara, Y. Moritomo, T. Arima, *et al.*, Phys. Rev. B **51**, 14103 (1995).
10. V. M. Loktev and Yu. G. Pogorelov, Fiz. Nizk. Temp. **26**, 231 (2000) [Low Temp. Phys. **26**, 171 (2000)].
11. I. Dzialoshinsky, J. Phys. Chem. Solids **4**, 241 (1958).
12. G. H. Jonker and J. H. Van Santen, Physica (Utrecht) **16**, 337 (1950).
13. J. M. D. Coey, M. Viret, and S. von Molnar, Adv. Phys. **48**, 167 (1999).
14. S. Jin, T. H. Tiefel, M. McCormack, *et al.*, Science **264**, 413 (1994).
15. J. W. Lynn, R. W. Erwin, J. A. Borchers, *et al.*, Phys. Rev. Lett. **76**, 4046 (1996).
16. Y. Tomioka, A. Asamitsu, Y. Moritomo, and Y. Tokura, Phys. Rev. Lett. **74**, 5108 (1995).

17. Y. Moritomo, A. Machida, S. Mori, *et al.*, Phys. Rev. B **60**, 9220 (1999).
18. F. Rivadulla, M. Freita-Alvite, M. A. López-Quintela, *et al.*, J. Appl. Phys. **91**, 785 (2002).
19. P. Levy, F. Parisi, G. Polla, *et al.*, Phys. Rev. B **62**, 6437 (2000).
20. C. H. Chen and S.-W. Cheong, Phys. Rev. Lett. **76**, 4042 (1996).
21. H. Watanabe, J. Phys. Soc. Jpn. **16**, 433 (1961).
22. S. I. Patil, S. M. Bhagat, Q. Q. Shu, *et al.*, Phys. Rev. B **62**, 9548 (2000).
23. C. Zener, Phys. Rev. **82**, 403 (1951).
24. P.-G. De Gennes, Phys. Rev. **118**, 141 (1960).
25. J. B. Goodenough, A. Wold, R. J. Arnott, and N. Menyuk, Phys. Rev. **124**, 373 (1961).
26. I. O. Troyanchuk, S. V. Trukhanov, D. D. Khalyavin, *et al.*, Fiz. Tverd. Tela (St. Petersburg) **42**, 297 (2000) [Phys. Solid State **42**, 305 (2000)].
27. I. O. Troyanchuk, S. V. Trukhanov, H. Szymczak, *et al.*, Zh. Éksp. Teor. Fiz. **120**, 183 (2001) [JETP **93**, 161 (2001)].
28. S. V. Trukhanov, I. O. Troyanchuk, H. Szymczak, and K. Barner, Phys. Status Solidi B **229**, 1417 (2002).
29. S. V. Trukhanov, N. V. Kasper, I. O. Troyanchuk, *et al.*, J. Solid State Chem. **169**, 85 (2002).
30. S. V. Trukhanov, I. O. Troyanchuk, I. M. Fita, *et al.*, J. Magn. Magn. Mat. **237**, 276 (2001).
31. S. V. Trukhanov, I. O. Troyanchuk, M. Hervieu, *et al.*, Phys. Rev. B **66**, 184424 (2002).
32. J. M. González-Calbet, M. Vallet-Regi, M. A. Alario-Franko, *et al.*, Mater. Res. Bull. **18**, 285 (1983).
33. J. B. Wiley, M. Sabat, S. J. Hwu, *et al.*, J. Solid State Chem. **87**, 250 (1990).
34. S. V. Trukhanov, I. O. Troyanchuk, N. V. Pushkarev, and G. Szymczak, Zh. Éksp. Teor. Fiz. **122**, 356 (2002) [JETP **95**, 308 (2002)].
35. S. V. Trukhanov, N. V. Kasper, I. O. Troyanchuk, *et al.*, Phys. Status Solidi B **233**, 321 (2002).
36. J. M. González-Calbet, E. Herrero, N. Rangavittal, *et al.*, J. Solid State Chem. **148**, 158 (1999).
37. J. Alonso, E. Herrero, J. M. González-Calbet, *et al.*, Phys. Rev. B **62**, 11328 (2000).
38. J. Alonso, A. Arroyo, J. M. González-Calbet, *et al.*, Phys. Rev. B **64**, 172410 (2001).

Translated by V. Sipachev

Journal of Experimental and Theoretical Physics, Vol. 96, No. 6, 2003, pp. 1065–1077.
Translated from Zhurnal Éksperimental'noĭ i Teoreticheskoĭ Fiziki, Vol. 123, No. 6, 2003, pp. 1212–1226.

SOLIDS
Structure

Ordered States and Structural Transitions in a System of Abrikosov Vortices with Periodic Pinning

M. V. Zyubin, I. A. Rudnev, and V. A. Kashurnikov*
Moscow Institute of Engineering Physics, Kashirskoe sh. 31, Moscow, 115409 Russia
**e-mail: kash@cityline.ru*
Received November 27, 2002

Abstract—A system of Abrikosov vortices in a quasi-two-dimensional HTSC plate is considered for various periodic lattices of pinning centers. The magnetization and equilibrium configurations of the vortex density for various values of external magnetic field and temperature are calculated using the Monte Carlo method. It is found that the interaction of the vortex system with the periodic lattice of pinning centers leads to the formation of various ordered vortex states through which the vortex system passes upon an increase or a decrease in the magnetic field. It is shown that ordered vortex states, as well as magnetic field screening processes, are responsible for the emergence of clearly manifested peaks on the magnetization curves. Extended pinning centers and the effect of multiple trapping of vortices on the behavior of magnetization are considered. Melting and crystallization of the vortex system under the periodic pinning conditions are investigated. It is found that the vortex system can crystallize upon heating in the case of periodic pinning. © *2003 MAIK "Nauka/Interperiodica".*

1. INTRODUCTION

A large number of recent publications are devoted to experimental investigations on the interaction of an Abrikosov vortex lattice with a periodic artificially created structure of pinning centers in the form of microholes as well as submicrometer particles of a magnetic or nonmagnetic material (see, for example, [1–3] and the literature cited therein). Experiments reveal singularities on the magnetization curves as well as on the curves describing the magnetic field dependence of the critical current and resistivity, which are interpreted as regimes of matching between the vortex lattice and the lattice of pinning centers. Direct observation of the regimes of matching the vortex system to the periodic lattice of pinning centers was carried out using Lorentz force microscopy [4] and scanning Hall magnetometry [5].

The complexity of such experiments and the interpretation of the observed effect necessitate the use of numerical simulation, including that based on the Monte Carlo method. The Monte Carlo technique was used earlier for obtaining new results for phase transitions and the dynamics of a two-dimensional Abrikosov vortex lattice in a model system imitating layered high-temperature superconductors (HTSC). For example, it was shown in [6–11] that a phase transition (melting of a triangular lattice resulting in the formation of vortex liquid) is observed in the absence of defects. In the presence of defects, a phase of "rotating lattice" is formed between the phases of the vortex crystal and the vortex liquid. The vortex system in this phase has the form of lattice islands rotating around pinning centers. The results of numerical calculation of magnetization and magnetic flux distribution in a quasi-two-dimensional HTSC plate with a random distribution of pinning centers were reported in our earlier publications [12–14], where a new method based on the Monte Carlo algorithm was developed for a large canonical ensemble with a number of singularities reflecting the behavior of vortex systems in layered HTSC materials. This method enabled us to obtain the equilibrium distribution of vortex density upon a change in the external magnetic field H and to calculate the $M(H)$ dependences for an arbitrary arrangement of pinning centers at various temperatures.

Here, we report on new results of simulation of the Abrikosov vortex system using the Monte Carlo method in the case of periodic pinning. The magnetization curves and the patterns of vortex density distribution are calculated for various defect lattices in a wide range of temperatures and fields. It is shown that, in the case of periodic pinning, the curves describing the magnetic field dependence of magnetization display a number of peaks associated with the interaction between the vortex lattice and the lattice of pinning centers. Different reasons for the emergence of these singularities on the magnetization curve are indicated for the first time.

In addition, we discovered an ordering of the vortex system with periodic pinning upon heating, viz., the inverse crystallization effect. Such a peculiar behavior of correlated systems is extremely uncommon in nature. Inverse crystallization was observed in some magnetic materials [15] as well as in polymer systems [16]. In a recent publication [17], inverse crystallization was discovered in a system of vortices with random pinning. Inverse crystallization in a system of Abrikosov vortices with periodic pinning is predicted by us for

the first time and has a fundamentally different physical origin as compared to random pinning.

2. MODEL AND COMPUTATIONAL PROCEDURE

Let us consider a three-dimensional bulk sample of a layered (in the *xy* plane) HTSC. The sample has a finite size l in the x direction and is infinitely large in the y and z directions. It is placed in a magnetic field parallel to the z axis, which rules out demagnetization effects. Assuming that the interaction between layers in HTSC is weak, we will carry out calculations for a quasi-two-dimensional (in the *xy* plane) plate of thickness d, which simulates a superconducting layer. In other words, we "cut" a layer of thickness d, which will be treated below, along the z axis.

We consider a 2D system of Abrikosov vortices in the form of model classical particles with a long-range potential in the plate placed in an external magnetic field H. The thermodynamic Gibbs potential of the vortex system in such a plate has the form

$$G = N\varepsilon d - Nd\frac{\Phi_0 H}{4\pi} + d\frac{\Phi_0 H}{4\pi}\sum_i\left[\exp\left(-\frac{x_i}{\lambda}\right) + \exp\left(-\frac{l-x_i}{\lambda}\right)\right] + \frac{1}{2}\sum_{i\neq j}U(r_{ij}) + \sum_i U_p(r_i) + U_{\text{surf}},$$

where N is the number of vortices in the system;

$$\varepsilon = \left(\frac{\Phi_0}{4\pi\lambda}\right)^2\left(\ln\frac{\lambda_0}{\xi_0} + 0.52\right)$$

is the self-energy of a vortex [18]; $\Phi_0 = hc/2e$; λ is the magnetic field penetration depth in the superconductor; $\lambda_0 = \lambda(T = 0)$; d is the superconducting layer thickness; $Nd\Phi_0 H/4\pi$ is the energy of interaction of a vortex with the external field H; $U(r_{ij}) = U_0 K_0(r_{ij}/\lambda)$ is the energy of paired interaction of vortices; $U_0 = \Phi_0^2 d/8\pi^2\lambda^2$; K_0 is the Bessel function of the imaginary argument; r_{ij} is the distance between vortices;

$$d\frac{\Phi_0 H}{4\pi}\left[\exp\left(-\frac{x_i}{\lambda}\right) + \exp\left(-\frac{l-x_i}{\lambda}\right)\right]$$

is the energy of interaction between the ith vortex and Meissner currents passing in the y direction over the plate surface; $U_p(r_i)$ is the energy of interaction between the ith vortex and pinning centers; U_{surf} is the energy of interaction of the vortex system with the superconductor surface [14]; and ξ_0 is the vortex core size for $T = 0$.

We introduce pinning centers to study the behavior of a system with defects. In this case, the energy of interaction with a pinning center was chosen in the model form,

$$U_p(T, r) = -\alpha\frac{U_0(T)}{U_0(0)}\frac{1}{r/\xi + 1}\exp\left(-\frac{r}{2\xi}\right),$$

where α is the parameter characterizing the depth of the potential well of a defect and ξ is the coherence length. Such a choice of the sizes and depth of pinning corresponds to the case when only one vortex can be pinned at the center.

The magnetic field induction in the given geometry was calculated using the following formula taking into account the contribution of Meissner currents:

$$B = \frac{N\Phi_0}{S} + \frac{2\lambda H}{l}(1 - e^{-l/\lambda}).$$

We have also taken into account the fact that the flux carried by each vortex depends on the distance from the plate edge [14].

In our computations, we used the approach developed earlier and based on the Monte Carlo algorithm for a grand canonical ensemble [13, 14]. The method enables us to obtain the equilibrium vortex density distribution for given extrinsic parameters (magnetic field H, temperature T, and the distribution and type of pinning centers). Using this distribution, we can calculate magnetization M and induction B. Thus, the method makes it possible to determine both integrated characteristics of a superconductor and visual patterns of magnetic flux distribution. Such an approach differs fundamentally in some respects from familiar computational methods; namely, it ensures the most correct inclusion of the effect of the plate boundary, operation in a wide range of temperatures $0 < T < T_c$, and inclusion of any distribution of any type of defects.

For simulating, we use parameters of a layered superconductor $Bi_2Sr_2CaCu_2O_8$: $d = 0.27$ nm, $\lambda_0 = 180$ nm, $\xi_0 = 2$ nm, and $T_c = 84$ K [19]. The temperature dependence of the magnetic field penetration depth is given in the form [11]

$$\lambda(T) = \frac{\lambda(0)}{\sqrt{1 - (T/T_c)^{3.3}}}.$$

Computations were made for plates having a size of 5×3 and 5×2.25 μm^2. The x size in the region in question was chosen so that our analysis could be confined to only the first terms in the expression for the interaction of vortices with the surface and, on the other hand, considerable errors due to the application of periodic

boundary conditions in the computation of vortex interaction could be avoided. The *y* size varied depending on the pinning lattice period so that the periodic boundary conditions were not violated. The maximal range of variation of the external field H is limited only by the computer power and, accordingly, computer time. In the computations described here, the range of the external field variation was $-0.1\ \text{T} \le H \le 0.1\ \text{T}$.

3. RESULTS AND DISCUSSION

The presence of the lattice of pinning centers leads to the emergence of commensurability effects between the number of vortices and the number of defects responsible for the formation of ordered configurations of the system of vortices, which often differ considerably from the conventional triangular lattice. In turn, the ordered structure of the vortex system leads to singularities in the magnetization and in the magnetic field dependences of the critical current and resistivity.

Reichhardt *et al.* [20] used the molecular dynamics method to analyze the behavior of a vortex system in the presence of square and triangular lattices of point defects and discovered a variety of ordered configurations. They discovered that the vortex system is ordered only for definite matching fields, when the number of vortices is multiple to the number of defects. However, the calculations in [20] were made under periodic boundary conditions in the canonical ensemble, i.e., for a given fixed number of vortices. In addition, the authors of [20] considered the behavior of the vortex system only at $T = 0$.

The formation of ordered configurations in the case of matching between the number of vortices and the number of defects can also be demonstrated in the framework of a canonical ensemble for periodic boundary conditions. However, while studying the effect of the defect structure geometry on the magnetic flux penetration and distribution, we must allow for the vortex production/destruction, i.e., consider a grand canonical ensemble and take into account surface effects.

We carried out computations for the following lattices of point pinning centers: square, triangular, and kagome lattices.[1] We also considered square lattices of extended pinning centers, at which more than one vortex could be pinned. We will analyze in detail all the above-mentioned configurations of pinning centers.

3.1. Triangular Lattice of Point Defects

Figure 1 shows the magnetization curves obtained for various concentrations of defects forming a triangular lattice. We considered the concentrations $n_d = 11.18$, 5.7, and 3.63 μm^{-2} corresponding to the triangular lattice periods $a = 0.32$, 0.45, and 0.56 μm. The dependence exhibits a number of singularities. It is expedient

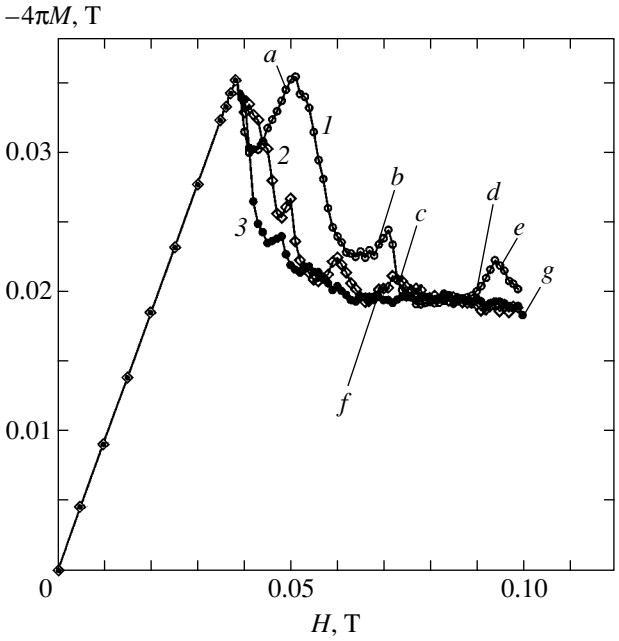

Fig. 1. Magnetization curves for a triangular lattice of point pinning centers for different concentrations of defects n_d, μm^{-2}: 11.18 (*1*), 5.7 (*2*), and 3.63 (*3*). Temperature $T = 1$ K. Points *a*–*g* correspond to vortex density distributions in Fig. 2.

to consider the difference between the value of magnetization in the case of ordered arrangement of defects and its value in the case of random pinning for the same concentration of defects as a quantitative characteristic of singularities emerging on the magnetization curve. The results of calculations show that, in the case of random pinning with concentration $n_d = 11.18\ \mu\text{m}^{-2}$, the initial segment of the magnetization curve coincides with the magnetization of a defect-free superconductor. The effect of random pinning on the behavior of magnetization is manifested for concentrations $n_d > 16.7\ \mu\text{m}^{-2}$ [14]. For this reason, the emergence of singularities on the magnetization curves for concentrations $n_d \le 11.18\ \mu\text{m}^{-2}$ should be attributed just to the ordered arrangement of pinning centers.

Table 1 shows the number and characteristics of singularities emerging on the magnetization curves for the investigated defect concentrations $n_d = 11.8$, 5.7, and 5.63 μm^{-2}, corresponding to the defect spacing $a = 0.32$, 0.45, and 0.56 μm. Line *H* gives the positions of peaks corresponding to the point of maximal ascent of magnetization (it will be shown below that ordered configurations are formed at the peak base), while line ΔM gives the heights of the peaks measured from the magnetization M_0 of a defect-free superconductor, and $\delta = \Delta M/M_0$. Letters S and M in the line Reason indicate, respectively, that a singularity appears due to screening or due to matching of the vortex system with the lattice of pinning centers (formation of an ordered configura-

[1] This term indicates a superlattice with an increased period superimposed on the initial lattice and is often used for spin systems.

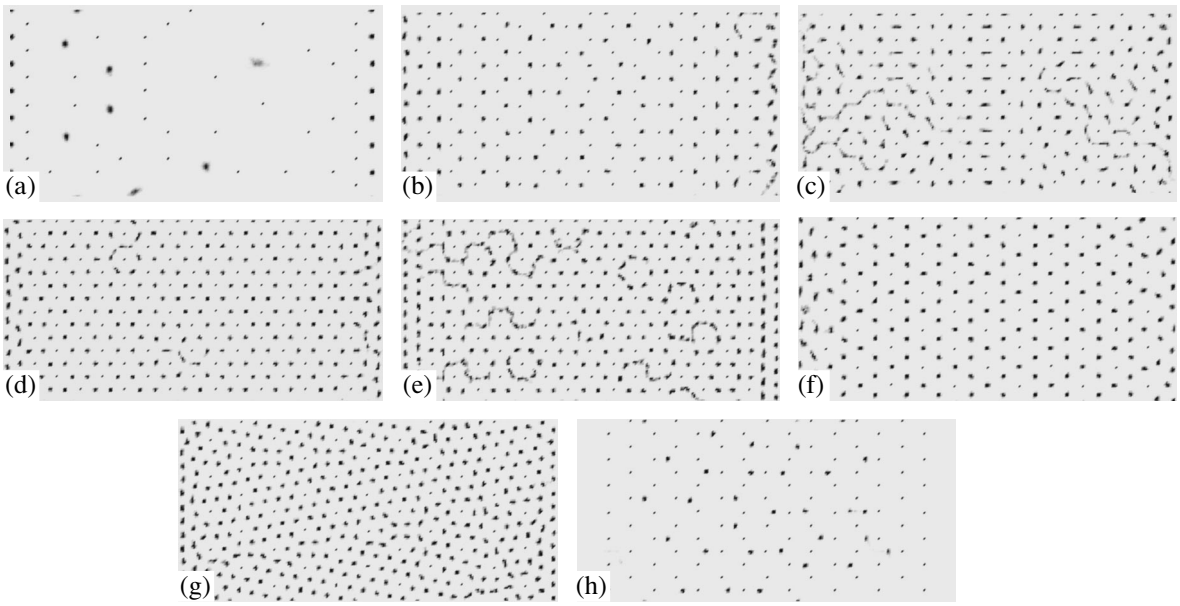

Fig. 2. Vortex density distribution for $n_d = 11.18\ \mu m^{-2}$, $H = 0.049$ (a), 0.07 (b), 0.074 (c), 0.09 (d), 0.096 T (e); for $n_d = 5.7\ \mu m^{-2}$, $H = 0.068$ (f), 0.1 T (g); and for $n_d = 11.18\ \mu m^{-2}$, $H = 0$ (h). The size of the system is $5 \times 2.25\ \mu m^2$. Temperature $T = 1$ K.

tion). We will call the singularities associated with screening first-type singularities, while the singularities associated with matching the vortex system to the defect structure will be called second-type singularities.

The reasons for the emergence of singularities can be explained by comparing the vortex density distribution with corresponding points on the magnetization curves.

Table 1. Characteristics of singularities on the magnetization curves for a triangular lattice of point defects (see text)

	a, μm	0.32	0.45	0.56
	n_d, μm^{-2}	11.18	5.7	3.63
	Number of peaks	3	3	2
Peak 1	H, T	0.051	0.05	0.048
	ΔM, 10^{-3} T	13.67	4.34	1.01
	δ, %	62.7	19.9	4.5
	N_v/N_d	–	2	3
	Reason	S	M	M
Peak 2	H, T	0.071	0.06	0.054
	ΔM, 10^{-3} T	5.05	2.06	0.77
	δ, %	25.9	10.6	1.9
	N_v/N_d	2	3	4
	Reason	M	M	M
Peak 3	H, T	0.094	0.072	–
	ΔM, 10^{-3} T	3.26	1.73	–
	δ, %	17.1	8.9	–
	N_v/N_d	3	4	–
	Reason	M	M	–

For $H = 0.049$ T, $n_d = 11.18\ \mu m^{-2}$ (Fig. 2a), lines from pinned vortices formed in the surface regions prevent further penetration of the magnetic flux. Free vortices, which cannot enter the plate as yet, also form lines. A delay in the magnetic flux penetration leads to a considerable increase in magnetization. It can be seen from the vortex density distribution that this singularity on the magnetization curve is due not to the formation of an ordered configuration of the vortex system, but to the screening of the surface regions by pinned vortices.

It should be noted that a certain number of vortices managed to penetrate to the bulk of the sample even prior to the formation of lines of pinned vortices. This indicates the low efficiency of point pinning centers as far as the probability of vortex pinning is concerned.

For $H = 0.07$ T, $n_d = 11.18\ \mu m^{-2}$ (Fig. 2b), a lattice corresponding to $N_v/N_d = 2$ is formed, where N_v and N_d are the numbers of vortices and defects, respectively. A local ordering is observed: the number of vortices at the center is insufficient, while an excess concentration emerges in the surface regions. However, the formation of the given configuration leads to a singularity on the magnetization curve. The point lies at the base of the peak.

For $H = 0.074$ T, $n_d = 11.18\ \mu m^{-2}$ (Fig. 2c), an insignificant change in the external field leads to the destruction of the vortex lattice. The lines of entrance of "new" vortices can be clearly seen. The destruction of the ordered structure is accompanied by a decrease in magnetization.

For $H = 0.09$ T, $n_d = 11.18\ \mu m^{-2}$ (Fig. 2d), the vortex system forms a nearly perfect triangular lattice. The given matching is characterized by the ratio $N_v/N_d = 3$. The point lies at the base of a peak on the magnetization curve.

For $H = 0.096$ T, $n_d = 11.18\ \mu m^{-2}$ (Fig. 2e), destruction of the ordered configuration is observed, which leads to a decrease in magnetization. The limited power of computer equipment does not permit the tracing of higher order matching in the case of a large number of pinning centers. However, by reducing the number of defects, we can obtain other configurations of the vortex system in the same range of fields. For example, for $n_d = 5.7\ \mu m^{-2}$, the effect associated with the screening of the surface by pinned vortices is also observed. However, in contrast to the previous case, a delay in the magnetic flux propagation does not lead to the emergence of a peak, but is accompanied just by a change in the slope of the curve. The magnetization curve displays three singularities associated with the formation of ordered configurations. As expected (Figs. 2f and 2g), a decrease in the defect concentration leads to a displacement of singularities towards lower fields and to a decrease in the magnitude of the singularities. For $H = 0.048$ and 0.057 T (these cases are not shown in the figure), the second and third matching are realized, respectively (the fields correspond to the beginning of the peaks and are not shown in the figures). Field $H = 0.068$ T is characterized by the formation of a lattice with $N_v/N_d = 4$ (Fig. 2f). In the strongest field $H = 0.1$ T (Fig. 2g), even the seventh matching is realized ($N_v/N_d = 7$). In this case, several regions with different orientations of the vortex lattice are observed. All the ordered configurations of the vortex structure described above are in accordance with the results obtained in [20], in which the behavior of the vortex system was also investigated for stronger fields and the existence of a triangular lattice was detected for $N_v/N_d = 9$, 12, 13, 16, 19, 21, 25, and 28.

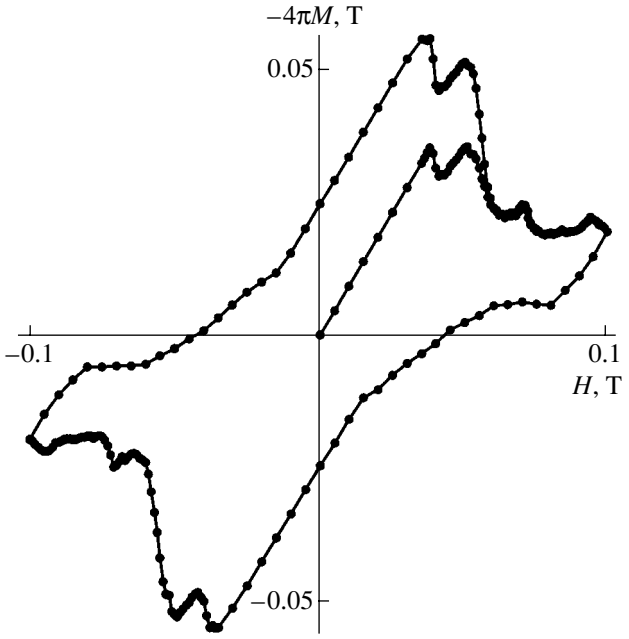

Fig. 3. Magnetization loop for a triangular lattice of pinning centers with defect concentration $n_d = 11.18\ \mu m^{-2}$. Temperature $T = 1$ K.

In the case of a still lower defect concentration $n_d = 3.63\ \mu m^{-2}$, the effects associated with screening are not observed. Insignificant singularities corresponding to the third and fourth matching are observed. An analysis of the vortex density distribution shows that ordered configurations are extremely sensitive to a change in the external magnetic field. Lattices are destroyed even for small variations of the external field, which does not result in noticeable singularities on the magnetization curves.

It should be noted that a decrease in the number of defects leads to coordinated disappearance of singularities associated with screening as well as singularities associated with the formation of vortex lattices. This is not surprising since both types of defects appear due to the interaction of free vortices with vortices pinned at pinning centers. Figure 3 shows a complete magnetization loop in the case of a high concentration of defects,

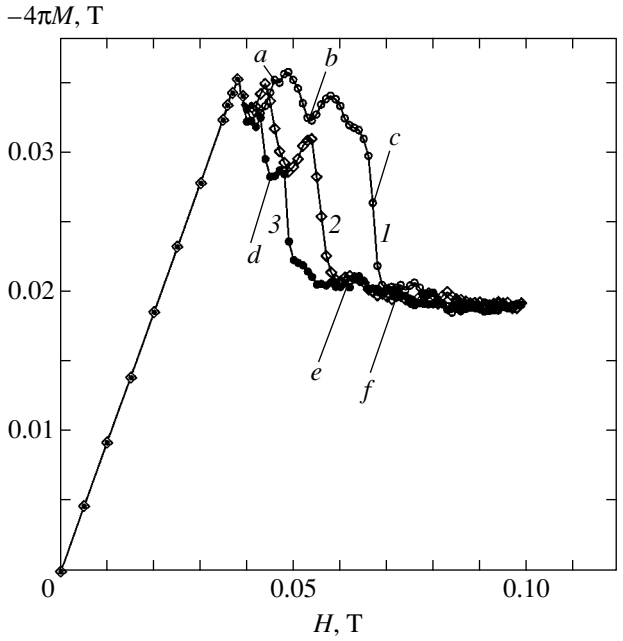

Fig. 4. Magnetization curves for a square lattice of point pinning centers for different concentrations of defects n_d, μm^{-2}: 9.68 (*1*), 7.11 (*2*), and 4.94 (*3*). Temperature T = 1 K. Points *a*–*g* correspond to vortex density distributions in Fig. 5.

n_d = 11.18 μm^{-2}. In the reverse direction, no singularities are observed on the magnetization curve. This is apparently due to the fact that singularities appear on the magnetization curve due to repulsion between vortices. As the applied magnetic field increases, the "rigid" vortex lattice prevents the magnetic flux penetration. When the field is removed, the vortex system tends to expand upon a decrease in the surface barrier; as a result, some of the vortices are expelled from the plate. The vortex density distribution after the removal of the magnetic field (H = 0) is shown in Fig. 2h for defect concentration n_d = 11.18 μm^{-2}. Vortex trapping is observed both due to pinning at the pinning centers and due to collective interaction with pinned vortices.

When the overheating field of the Meissner state is attained, vortices of the opposite sign (antivortices) start entering the plate. However, antivortices are pinned at the surface pinning centers and prevent subsequent penetration of the magnetic flux, leading to the emergence of a singularity on the magnetization curve. It can be seen from Fig. 3 that this singularity is observed in the same fields as for the singularity appearing during initial magnetization and associated with screening.

3.2. Square Lattice of Point Defects

Figure 4 shows the magnetization curves for various concentrations of pinning centers forming a square lattice.

For a high concentration of defects (n_d = 9.68 μm^{-2}), strong effects associated with the screening of the surface by pinned vortices are observed (Fig. 5a for H = 0.043 T and Fig. 5b for H = 0.054 T). The vortex density distribution shown in Fig. 5c (H = 0.068 T) corresponds to the penetration of vortices into the sample. The square lattice of defects forms peculiar channels

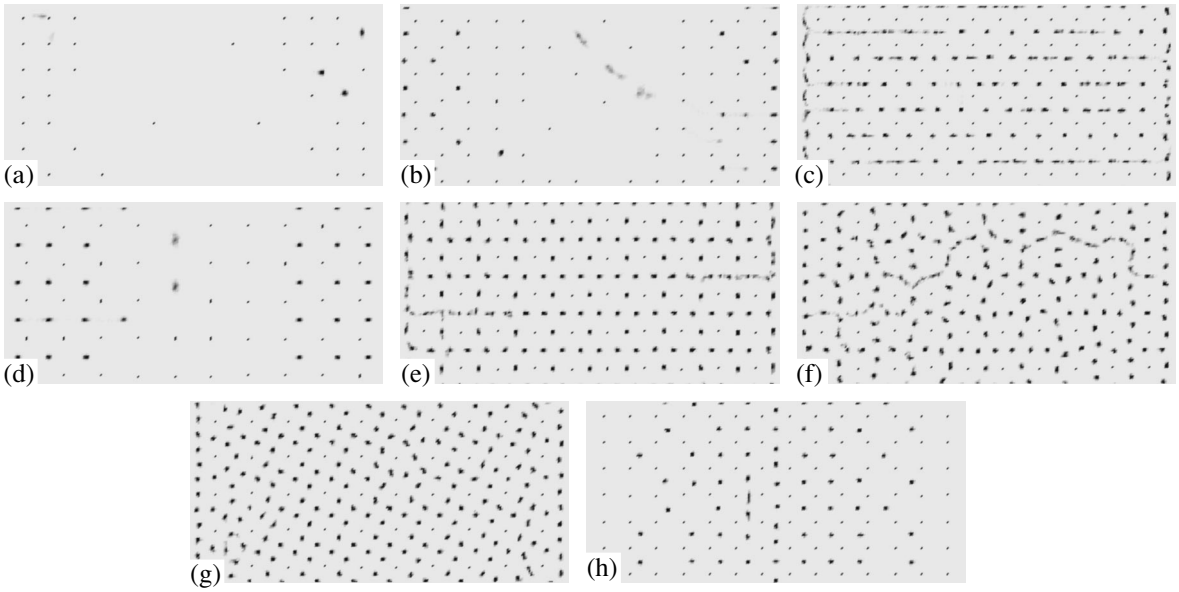

Fig. 5. Vortex density distribution for n_d = 9.68 μm^{-2}, H = 0.043 (a), 0.054 (b), 0.068 T (c); for n_d = 4.94 μm^{-2}, H = 0.046 (d), 0.062 (e), 0.066 (f), 0.072 T (g); and for n_d = 9.68 μm^{-2}, H = 0 (h) (magnetic field trapping). The size of the system is 5×2.25 μm^2. Temperature T = 1 K.

Table 2. Characteristics of singularities on the magnetization curves for a square lattice of point defects (see text)

	a, μm	0.32	0.375	0.45
	n_d, μm^{-2}	9.68	7.11	4.94
	Number of peaks	2	3	3
Peak 1	H, T	0.048	0.044	0.043
	ΔM, 10^{-3} T	12.7	10.29	7.37
	δ, %	55.3	41.7	29.3
	N_v/N_d	–	–	–
	Reason	S	S	S
Peak 2	H, T	0.057	0.054	0.047
	ΔM, 10^{-3} T	13.02	9.93	5.39
	δ, %	62.4	47.1	23.1
	N_v/N_d	–	–	2
	Reason	S	S	M
Peak 3	H, T	–	0.079	0.064
	ΔM, 10^{-3} T	–	0.31	1.59
	δ, %	–	0.95	4.68
	N_v/N_d	–	4	4
	Reason	–	M	M

along which the magnetic flux propagates. Naturally, the active entrance of vortices into the sample is accompanied by a decrease in magnetization.

Even the defect concentration $n_d = 4.94$ μm^{-2} is sufficient for the emergence of new singularities associated both with screening and with matching. In a field $H = 0.043$ T, a singularity associated with screening is observed. In a field of 0.047 T (Fig. 5d), a square centered lattices is formed but only in the surface regions; this is reflected in the emergence of a peak on the magnetization curve (see Fig. 4).

The vortex density distributions shown in Figs. 5e and 5g show that the vortex system forms ordered configurations in stronger fields also. However, the formation of lattices is not accompanied by the emergence of noticeable singularities on the magnetization curve. The point with $H = 0.062$ T can be put in correspondence with the beginning of a magnetization peak, while the point with $H = 0.072$ T corresponding to the emergence of a configuration with $N_v/N_d = 5$ (Fig. 5g) is not singled out on the magnetization curve.

The competition between the tendency of the vortex system to form a triangular lattice and the symmetry of the square lattice of defects leads to the emergence of various ordered configurations. For example, the vortex system exhibits a structural transition from the triangular lattice of pinning centers to the square lattice via a disordered state; this is illustrated by the sequence of Figs. 5e–5g.

As in the case of a triangular lattice of pinning centers, an ordered system of trapped vortices (Fig. 5h) is left in a superconductor with a square lattice of pinning centers after the removal of the applied field.

On the whole, noticeable singularities associated with the screening of the surface (often even more significant than in the case of a triangular lattice with the same period) are observed in the case of a square lattice. However, the formation of vortex lattices either does not affect the magnetization at all or is accompanied by extremely weak effects, which are observed predominantly when the vortex system forms triangular lattices.

Basic characteristics of singularities on the magnetization curve are given in Table 2.

3.3. Kagome Lattice of Point Defects

A kagome lattice can be obtained from a triangular lattice by eliminating alternate defects in alternate rows (Fig. 6a). For the same period, the density of the kagome lattice is 3/4 of the density of the triangular lattice. By virtue of symmetry, we can expect the formation of triangular lattices in the vortex system, which is confirmed by simulation (Figs. 6b and 6d). However, the ratios N_v/N_d are different in the configuration formed: $N_v/N_d = 4$ (Fig. 6b) and $N_v/N_d = 16/3$ (Fig. 6d) as against $N_v/N_d = 3$ and $N_v/N_d = 4$ for the triangular

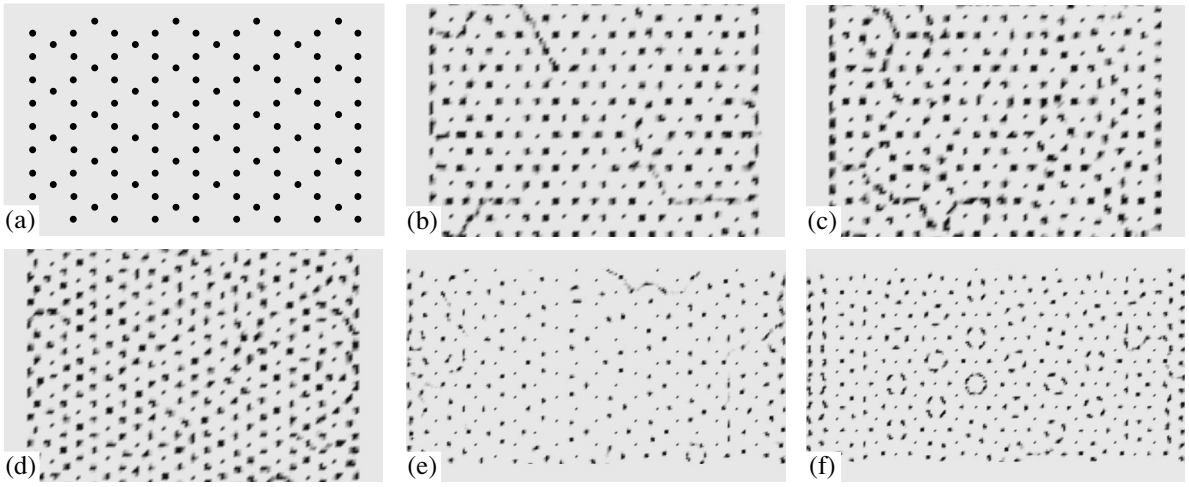

Fig. 6. Configuration of pinning centers (a) and vortex density distribution for $n_d = 4.27\ \mu m^{-2}$, $H = 0.057$ (b), 0.06 (c), 0.068 T (d), and for $n_d = 10.95\ \mu m^{-2}$, $H = 0.077$ (e), 0.091 T (f). Temperature $T = 1$ K.

defect lattice. In intermediate fields, no configurations with a long-range order are formed.

Since the kagome lattice was obtained from the triangular lattice, it would be interesting to compare the singularities on the magnetization curve in the cases of kagome and triangular lattices. It was noted above that, for the same lattice period, the vortex system forms identical ordered configurations in the same fields (see Figs. 6b and 6d), which is reflected in the behavior of magnetization. Figure 7 shows the magnetization curves for triangular (curve *1*) and kagome (curve *3*) lattices of pinning centers with a period $a = 0.45$ μm. However, the height of the peaks on the magnetization curve for the kagome lattice is smaller since the density of the kagome lattice is 3/4 of the density of the triangular lattice with the same period.

In the case of identical density, the period of the kagome lattice is smaller than the period of the triangular lattice (curve *2* in Fig. 7 depicts the magnetization curve with a density close to that of the triangular lattice and with period $a = 0.375$ μm); for this reason, a noticeable peak associated with the screening effect is observed. Since ordered configurations are formed for the kagome lattice for larger values of N_v/N_d , the singularities associated with the matching of the vortex system to the lattice of pinning centers are observed in stronger fields. For example, a peak observed for $H = 0.091$ T due to the emergence of a configuration with $N_v/N_d = 16/3$ has a height approximately equal to that of the peak for the triangular lattice in the field $H = 0.072$ T.

The configurations realized in the structure considered here were called by Laguna *et al.* [21] an interstitial phase (Fig. 6f). Interstitial configurations are characterized by filling of the second coordination sphere (we are speaking of the second coordination sphere for the triangular lattice); as a result, cells in which vortex rotation takes place are formed.

Figures 6e and 6f show the configurations of the vortex system, illustrating a transition to the interstitial phase. For $H = 0.077$ T, interstitial positions are still vacant, and the cells between defects contain three lattices each and no rotation is observed. As the applied magnetic field increases, the second coordination

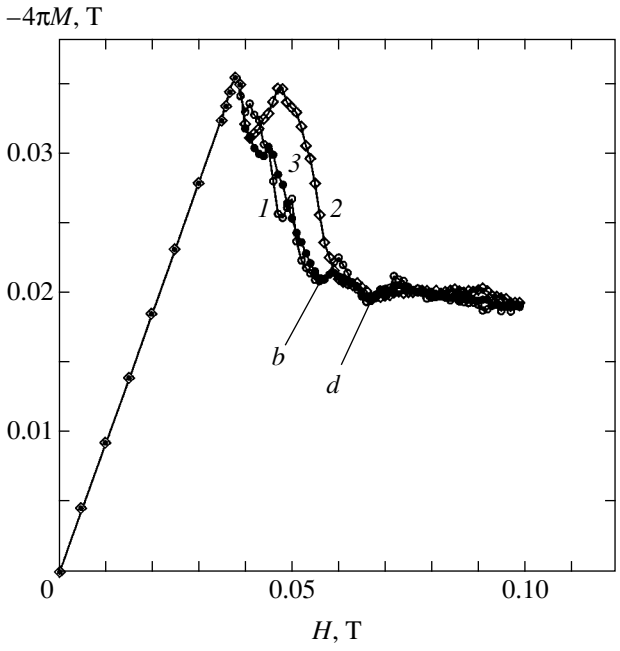

Fig. 7. Magnetization curves for different concentrations of point defects: triangular lattice, $n_d = 5.7\ \mu m^{-2}$ (*1*); kagome lattice, $n_d = 6.15\ \mu m^{-2}$ (*2*); and kagome lattice, $n_d = 4.27\ \mu m^{-2}$ (*3*). Temperature $T = 1$ K. Marked points correspond to the vortex density distributions shown in Fig. 6.

sphere is filled, which is accompanied by active rotation of vortices in the "cells." This transition is not accompanied by the formation of a singularity on the magnetization curve.

3.4. Square Lattice of Extended Defects

We have considered so far the lattices of point pinning centers at which only one vortex can be pinned. However, artificially created defects are not point defects as a rule. Recent experiments proved that several vortices could be trapped at an "extended" pinning center [22].

Reichhardt *et al.* [23] analyzed the effect of multiple trapping of vortices on the current–voltage characteristics in the case of a square defect lattice by the molecular dynamics method. It was shown that the matching effects between the number of vortices and the number of defects must also be observed in the case of multiple trapping, the critical depinning force being larger in the case of multiple trapping of vortices at a pinning center.

Here, we consider the effect of multiple trapping of vortices on the behavior of magnetization. Following Reichhardt *et al.* [23], we choose the potential of interaction of a vortex with an extended pinning center in the following model form:

$$U_p = \begin{cases} \alpha \dfrac{U_0(T)}{U_0(0)}\left(\dfrac{|\mathbf{r}_v - \mathbf{r}_p|^2}{r_{\text{pin}}^2} - 1\right), & |\mathbf{r}_v - \mathbf{r}_p| < r_{\text{pin}}, \\ 0, & |\mathbf{r}_v - \mathbf{r}_p| > r_{\text{pin}}, \end{cases}$$

where α is a coefficient with the dimensions of energy characterizing the depth of the pinning center; r_{pin} is the radius of the pinning center; and $\mathbf{r}_v$ and $\mathbf{r}_p$ are the radius vectors of the vortex and the pinning center, respectively.

Calculations were made for a square lattice of pinning centers with a period $a = 0.6$ μm, which corresponds to density $n_d = 4$ μm^{-2}. We analyzed pinning centers of radius $r_{\text{pin}} = 0.15$ μm and depth $\alpha = 0.1$ eV as well as of radius $r_{\text{pin}} = 0.2$ μm and depth $\alpha = 0.2$ eV. A stronger pinning will be considered below. Figure 8 shows the magnetization curves for extended pinning centers arranged chaotically and forming a square lattice. In the case of a random distribution of defects, the magnetization curve displays no effects, while, in the case of the square lattice of pinning centers, the curve has a number of singularities. Let us consider the vortex density distributions in greater detail and compare these distributions with the behavior of magnetization.

For $H = 0.043$ T (Fig. 9a), extended defects effectively trap vortices. In the rows of surface defects, two vortices are pinned simultaneously at each defect. The rotation of pinned vortex pairs takes place.

For $H = 0.048$ T (Fig. 9b), the propagation of the magnetic flux to the bulk of the semiconductor is terminated since two vortices are pinned at each defect near the surface. The magnetization curve displays a clearly manifested peak.

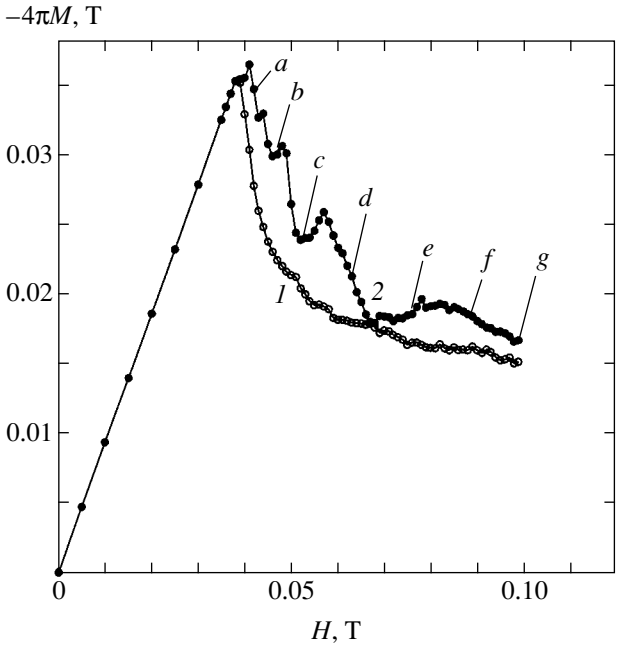

Fig. 8. Magnetization curves for extended pinning centers with concentration $n_d = 4$ μm^{-2}, distributed chaotically (curve *1*) and forming a square lattice (curve *2*). Temperature $T = 1$ K. Marked points correspond to the vortex density distributions shown in Fig. 9.

For $H = 0.054$ T (Fig. 9c), three vortices are pinned at each pinning center in the surface rows of defects, preventing the penetration of new vortices. This leads to an increase in the magnetization.

For $H = 0.064$ T (Fig. 9d), an interstitial center between defects exhibits a tendency to the formation of a triangular lattice; two vortices are pinned at each defect. In the surface region, three vortices are trapped at a defect.

For $H = 0.076$ T (Fig. 9e), an ordered configuration is observed. Three vortices are pinned at each defect. The trapped vortices rotate. Free vortices form a lattice arranged between defects and having fourfold symmetry. The formation of this configuration leads to an increase in the magnetization.

For $H = 0.079$ T (Fig. 9f), the previous configuration is destroyed. Vortices flow along the channels formed in the square lattice of defects. Point *f* in Fig. 8 corresponding to this case lies in the region of decreasing magnetization.

For $H = 0.09$ T (Fig. 9g), four vortices are trapped at each defect. Free vortices form a square lattice with interstitial vortices.

For $H = 0.1$ T (Fig. 9h), five vortices are trapped at a defect in the surface region and four vortices are pinned at each defect at the center. Free vortices form a

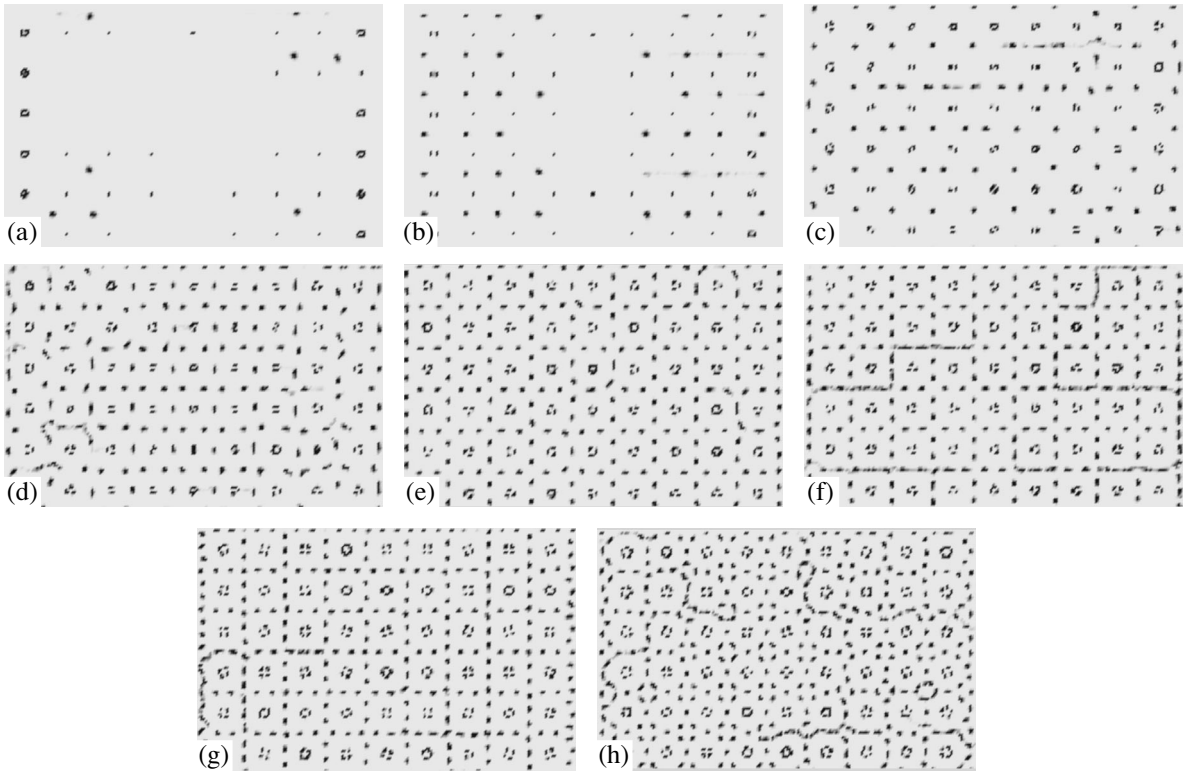

Fig. 9. Vortex density distribution for a square lattice of extended defects with concentration $n_d = 4\ \mu m^{-2}$, $H = 0.043$ (a), 0.048 (b), 0.054 (c), 0.064 (d), 0.076 (e), 0.079 (f), 0.09 (g), and 0.1 T (h). The size of the system is $5 \times 3\ \mu m^2$. Temperature $T = 1$ K.

fourfold symmetry lattice with interstitial vortices. Vortices flow along the channels, in which free vortices rotate in the regions between defects.

Thus, the analysis of the vortex density distribution leads to the conclusion that singularities on the magnetization curve in the case of extended pinning centers appear as a result of structural transitions as well as the screening of the plate surface by pinned vortices. On the whole, it can be stated that multiple trapping of vortices leads to a considerable enhancement of both types of singularities (associated both with matching and with screening) on the magnetization curve. It should be recalled that, according to our calculations, a square lattice of point defects with density $n_d = 4.94\ \mu m^{-2}$ (see Fig. 4) does not lead to any appreciable effects in the behavior of magnetization. However, in view of the large size of extended defects, their density cannot be increased further. At the same time, the results of computations proved that an increase in the density of point defects leads to considerable effects associated with the surface screening.

In the case of multiple trapping of vortices at defects, the process of magnetization reversal of the superconductor can be demonstrated more visually on the magnetic induction distribution. This structure is distinguished by the fact that several vortices can be pinned at a defect, and the front of the magnetic flux annihilation [14] cannot propagate any further to the bulk of the superconductor until all vortices at a defect are suppressed (Fig. 10). This leads to a partial arrest of the annihilation front at the rows of pinned vortices.

3.5. Behavior of the Vortex System upon a Change in Temperature in the Case of a Triangular Lattice of Point Defects

Ordered configurations of the vortex system are obviously observed at quite low temperatures. For this reason, we analyzed in the previous sections the effect of ordered configurations of the vortex system on the behavior of magnetization using curves calculated for $T = 1$ K. In this section, we consider the effect of temperature of a triangular lattice of point defects on the behavior of the vortex system in the case of periodic pinning.

Figure 11 shows the magnetization curves obtained at different temperatures for concentration $n_d = 5.7\ \mu m^{-2}$. It was established in Section 3.1 that, for such a concentration, all three singularities appear as a result of matching of the vortex lattice to the lattice of defects.

As the temperature increases, the Meissner state overheating field decreases for all magnetization curves, and the curves become lower. The peaks associated with the formation of ordered configurations are

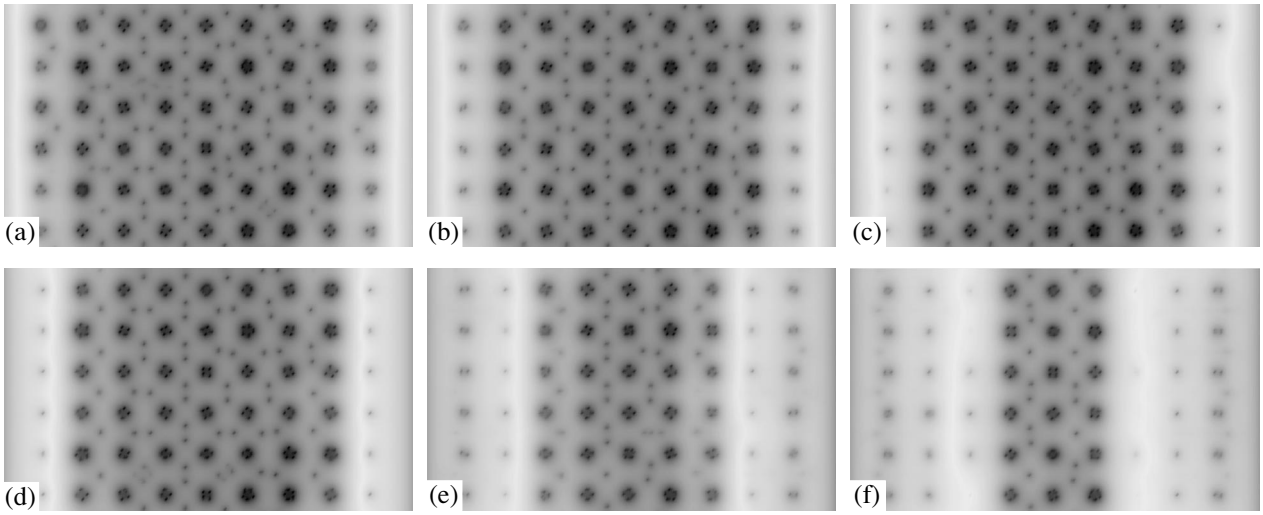

Fig. 10. Magnetic field distribution (dark regions correspond to the field) for a square lattice of extended defects with concentration $n_d = 4\ \mu m^{-2}$, $H = -0.025$ (a), -0.03 (b), -0.035 (c), -0.04 (d), -0.045 (e), and -0.046 T (f). The size of the system is $5 \times 3\ \mu m^2$. Temperature $T = 1$ K.

displaced towards lower fields, and the peak heights decrease upon heating. A further increase in temperature suppresses the singularities associated with matching. Analysis of the vortex density distributions indicates that the peaks vanish due to melting of the vortex lattice.

It was noted in Section 3.1 that ordered configurations are observed at the base of the peaks on the magnetization curve, and the segments on which the magnetization decreases correspond to the disordered state of the vortex system. Since the positions of the peaks change with temperature, a situation is possible where

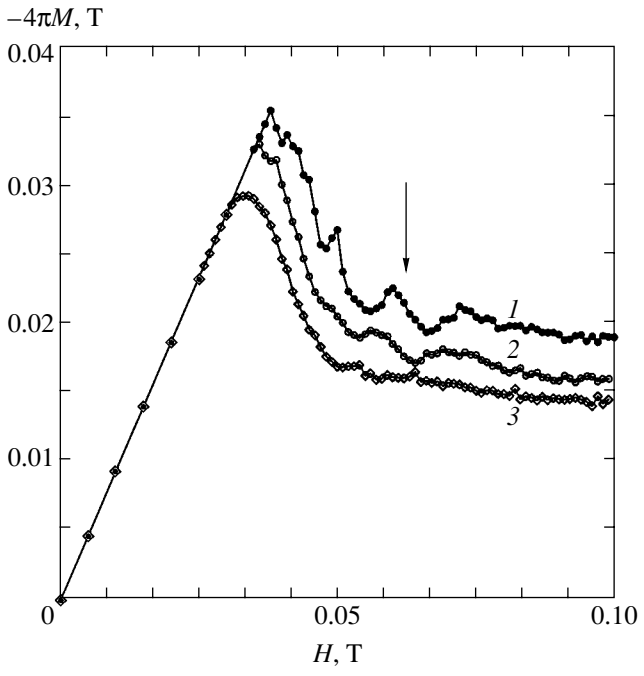

Fig. 11. Magnetization curves for a triangular lattice of point pinning centers with concentration $n_d = 5.7\ \mu m^{-2}$ for different temperatures T, K: 1 (*1*), 5 (*2*), and 10 (*3*). The arrow corresponds to the magnetic field in which inverse crystallization of the vortex system is observed.

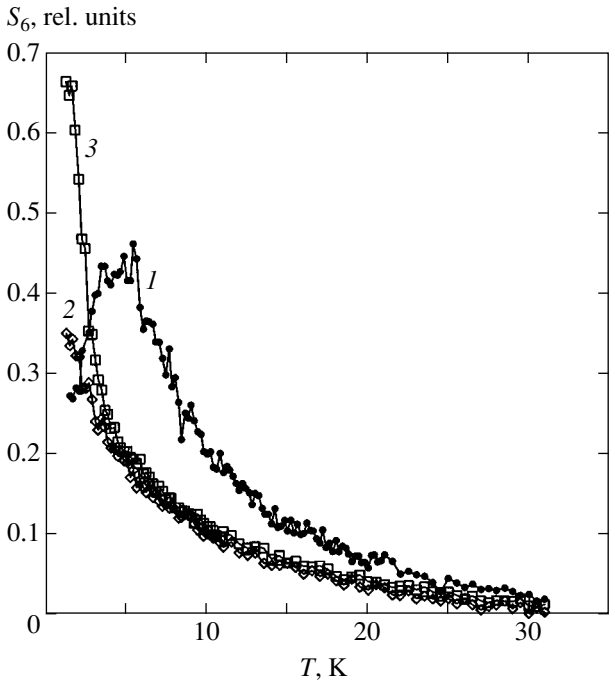

Fig. 12. Temperature dependence of structural factor S_6 for a triangular lattice of defects, $n_d = 5.7\ \mu m^{-2}$ (*1*); random distribution of defects, $n_d = 5.7\ \mu m^{-2}$ (*2*); and pure superconductor (*3*).

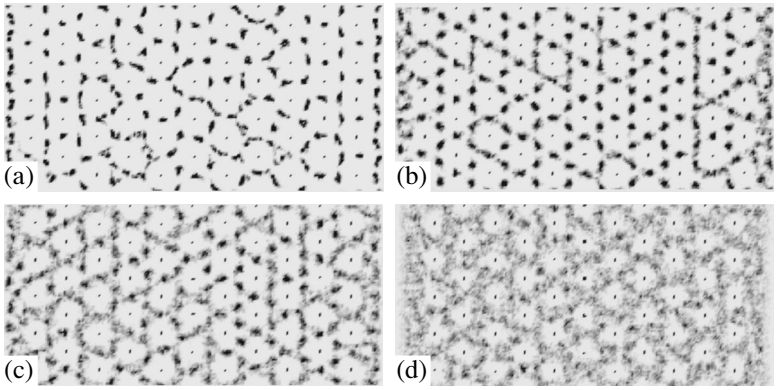

Fig. 13. Vortex density distribution for different temperatures in field $H = 0.062$ T for a triangular lattice of defects, $n_d = 5.7\ \mu m^{-2}$: $T = 1$ (a), 5.2 (b), 10 (c), and 25 K (d). The size of the system is $5 \times 2.25\ \mu m^2$.

the region of decrease at a low temperature corresponds to the base of the peak at a higher temperature (e.g., the region of decrease behind the peak marked by the arrow at $T = 1$ K and the base of the peak at $T = 5$ K in Fig. 11). Thus, as the temperature increases, it is possible to pass from a disordered configuration to the ordered one.

In order to verify this assumption, we calculated the configurations of the vortex system for a fixed field $H = 0.062$ T at various temperatures. We analyzed the following situations: a triangular lattice of point defects ($n_d = 5.7\ \mu m^{-2}$), a random distribution of point defects ($n_d = 5.7\ \mu m^{-2}$), and a pure sample.

In order to characterize the extent of ordering of the system, we calculated the standard structural factor S_6 reflecting the tendency of the system to be aligned into a triangular lattice:

$$S_6 = \sum_{i=1}^{N} \frac{1}{Z_i} \sum_{j=1}^{Z_j} e^{6i\theta_{ij}},$$

where Z_i is the number of nearest neighbors of the ith vortex and θ_{ij} is the angle between the nearest neighbors.

Figure 12 shows the temperature dependences of factor S_6. In the case of a periodic arrangement of pinning centers in the range $T = 1$–5.8 K, an increase in the value of S_6 is observed; i.e., the system of vortices becomes ordered upon heating. At $T = 1$ K (Fig. 13a), the vortex system is disordered despite the low temperature because the number of vortices is not a multiple of the number of defects. As the temperature increases, new vortices enter the sample, and a stable ordered configuration is formed (Fig. 13b); upon a further increase in temperature, it melts (Figs. 13c and 13d). Thus, in the case of a periodic arrangement of defects, the "crystallization" of the vortex system is possible upon heating. It should be noted that a gradual decrease in the structural parameters is observed upon an increase in temperature both in the case of a random distribution of defects and for a pure defect-free sample.

It should be observed that inverse crystallization of the system of vortices was experimentally observed in the case of chaotic pinning by Avraham *et al.* [17]. For a random distribution of defects, the vortex system ordering is due to the fact that the effect of pinning becomes weaker upon heating and the interaction of vortices leads to the formation of a triangular vortex lattice. It was noted above that pinning centers were assumed to be rather deep to exclude temperature-induced depinning. For this reason, inverse crystallization in the case considered here is of fundamentally different physical origin. The ordering of the system upon heating occurs due to matching between the number of vortices and the number of defects [24].

4. CONCLUSIONS

We have considered the effect of periodic pinning on the behavior of magnetization and on the magnetic flux penetration, distribution, and trapping. It is shown that, for a periodic pinning, there exist two types of effects leading to the emergence of singularities on magnetization curves, namely, the screening of the superconductor surface by the vortices pinned in the surface region and the formation of ordered configurations by the vortex system. Effects of the first type are observed in weak fields, while effects of the second type occur in fields in which the number of vortices is multiple to the number of defects.

It is found that ordered configurations are not located at the point of a local magnetization peak, but lie at the base of the segment of increasing magnetization. On segments where magnetization decreases, the destruction of vortex lattices takes place. The position of singularities on the magnetization curve is determined by the density of defects. As the density of defects decreases, the singularities are displaced towards weaker fields and their absolute magnitude

decreases. A decrease in the density of defects leads to a correlated disappearance of singularities associated both with screening and with the formation of ordered configurations.

We have analyzed the behavior of magnetization upon a change in temperature in the case of a triangular lattice of point defects. It is found that an increase in temperature suppresses the singularities, which are displaced to the region of weak fields. After the attainment of the melting point for the vortex lattice, the singularities associated with the formation of ordered configurations disappear.

It is shown that inverse crystallization of the vortex system, which is caused by the entrance of new vortices and the formation of a stable configuration, is possible in the case of periodic pinning. Inverse crystallization of the vortex system can be observed visually on superconductors with a periodic arrangement of artificial pinning centers with the help of magnetooptical methods or using high-resolution scanning magnetometry.

Various lattices of pinning centers are considered. It is found that the most striking effects associated with the matching of the vortex system to the defect lattice are observed for a triangular lattice of defects.

The effect of multiple trapping of vortices on the behavior of magnetization is analyzed. In the case of extended pinning centers at which more than one vortex can be pinned, the magnetization curve displays considerable effects associated both with screening and with matching.

ACKNOWLEDGMENTS

This study was supported financially by the Russian Foundation for Basic Research (project no. 00-02-17803), the Federal Special Program “Integration” (project no. B0048), and the State Science and Engineering Program “Important Trends in the Physics of Condensed State” (Subprogram “Superconductivity”).

REFERENCES

1. V. V. Moshchalkov, M. Baert, V. V. Metlushko, *et al.*, Phys. Rev. B **57**, 3615 (1998).
2. V. Metlushko, U. Welp, G. W. Grabtree, *et al.*, Phys. Rev. B **59**, 603 (1999).
3. D. J. Morgan and J. B. Ketterson, J. Low Temp. Phys. **122**, 37 (2001).
4. E. Rossel, M. Van Bael, M. Baert, *et al.*, Phys. Rev. B **53**, R2983 (1996).
5. A. N. Grigorenko, G. D. Howells, S. J. Bending, *et al.*, Phys. Rev. B **63**, 052504 (2001).
6. M. E. Gracheva, V. A. Kashurnikov, and I. A. Rudnev, Pis’ma Zh. Éksp. Teor. Fiz. **66**, 269 (1997) [JETP Lett. **66**, 291 (1997)].
7. M. E. Gracheva, M. V. Katargin, V. A. Kashurnikov, and I. A. Rudnev, Fiz. Nizk. Temp. **23**, 1151 (1997) [Low Temp. Phys. **23**, 863 (1997)].
8. M. E. Gracheva, V. A. Kashurnikov, and I. A. Rudnev, Fiz. Nizk. Temp. **25**, 148 (1999) [Low Temp. Phys. **25**, 105 (1999)].
9. M. E. Gracheva, V. A. Kashurnikov, O. V. Nikitenko, and I. A. Rudnev, Fiz. Nizk. Temp. **25**, 1027 (1999) [Low Temp. Phys. **25**, 765 (1999)].
10. V. A. Kashurnikov, I. A. Rudnev, M. E. Gracheva, and O. V. Nikitenko, Zh. Éksp. Teor. Fiz. **117**, 196 (2000) [JETP **90**, 173 (2000)].
11. I. A. Rudnev, V. A. Kashurnikov, M. E. Gracheva, and O. A. Nikitenko, Physica C (Amsterdam) **332**, 383 (2000).
12. A. V. Eremin, O. S. Esikov, V. A. Kashurnikov, *et al.*, Supercond. Sci. Technol. **14**, 690 (2001).
13. V. A. Kashurnikov, I. A. Rudnev, and M. V. Zubin, Supercond. Sci. Technol. **14**, 695 (2001).
14. V. A. Kashurnikov, I. A. Rudnev, and M. V. Zyubin, Zh. Éksp. Teor. Fiz. **121**, 442 (2002) [JETP **94**, 377 (2002)].
15. Y. Yeshurun, M. B. Salamon, K. V. Rao, *et al.*, Phys. Rev. Lett. **45**, 1366 (1980).
16. A. L. Greer, Nature **404**, 34 (2000).
17. N. Avraham, B. Khaykovich, Y. Myasoedov, *et al.*, Nature **411**, 451 (2001).
18. V. V. Pogosov, A. L. Rakhmanov, and K. I. Kugel’, Zh. Éksp. Teor. Fiz. **118**, 676 (2000) [JETP **91**, 588 (2000)].
19. S. L. Lee, P. Zimmermann, H. Keller, *et al.*, Phys. Rev. Lett. **71**, 3862 (1993).
20. C. Reichhardt, C. J. Olson, and F. Nori, Phys. Rev. B **57**, 7937 (1998).
21. M. F. Laguna, C. A. Balseiro, D. Domínguez, and F. Nori, Phys. Rev. B **64**, 104505 (2001).
22. S. Field, S. S. James, J. Barentine, *et al.*, cond-mat/0003415.
23. C. Reichhardt, G. T. Zimanyi, R. T. Scalettar, and I. K. Schuller, cond-mat/0102266.
24. M. V. Zyubin, I. A. Rudnev, and V. A. Kashurnikov, Pis’ma Zh. Éksp. Teor. Fiz. **76**, 263 (2002) [JETP Lett. **76**, 227 (2002)].

Translated by N. Wadhwa

Journal of Experimental and Theoretical Physics, Vol. 96, No. 6, 2003, pp. 1078–1088.
Translated from Zhurnal Éksperimental'noĭ i Teoreticheskoĭ Fiziki, Vol. 123, No. 6, 2003, pp. 1227–1238.

SOLIDS
Structure

Normal Processes of Phonon–Phonon Scattering and the Drag Thermopower in Germanium Crystals with Isotopic Disorder

I. G. Kuleev[a,*], I. I. Kuleev[a], A. N. Taldenkov[b], A. V. Inyushkin[b], V. I. Ozhogin[b], K. M. Itoh[c], and E. E. Haller[d]

[a]*Institute of Physics of Metals, Ural Division, Russian Academy of Sciences, Yekaterinburg, 620219 Russia*

**e-mail: kuleev@imp.uran.ru*

[b]*Institute of Molecular Physics, Russian Research Center Kurchatov Institute, Moscow, 123182 Russia*

[c]*Department of Applied Physics and Physico-Informatics, Keio University, Yokohama 223-8522, Japan*

[d]*University of California and Lawrence Berkeley National Laboratory, Berkeley, CA, 94720, USA*

Received December 10, 2002

Abstract—A strong dependence of the thermopower of germanium crystals on the isotopic composition is experimentally found. The theory of phonon drag of electrons in semiconductors with nondegenerate statistics of current carriers is developed, which takes into account the special features of the relaxation of phonon momentum in the normal processes of phonon–phonon scattering. The effect of the drift motion of phonons on the drag thermopower in germanium crystals of different isotopic compositions is analyzed for two options of relaxation of phonon momentum in the normal processes of phonon scattering. The phonon relaxation times determined from the data on the thermal conductivity of germanium are used in calculating the thermopower. The importance of the inelasticity of electron–phonon scattering in the drag thermopower in semiconductors is analyzed. A qualitative explanation of the isotope effect in the drag thermopower is provided. It is demonstrated that this effect is associated with the drift motion of phonons, which turns out to be very sensitive to isotopic disorder in germanium crystals. © *2003 MAIK "Nauka/Interperiodica".*

1. INTRODUCTION

Recently, high-quality single crystals of germanium of different chemical compositions have been successfully grown, including a uniquely pure (both chemically and isotopically) crystal with 99.99% ^{70}Ge isotopic enrichment [1], hereinafter referred to as ^{70}Ge (99.99%). Experimental investigations of the thermal conductivity [2, 3] of these crystals have revealed that, for monoisotopic samples of ^{70}Ge (99.99%), the maximal values of thermal conductivity are an order of magnitude higher than those for crystals with natural isotopic composition. It is evident that this effect is associated with the increase in the free path of thermal phonons because of the decrease in the scattering by "impurity" isotopes; the normal processes of phonon–phonon scattering play an important part in the case of isotopically pure crystals at temperatures in the vicinity of the maximum of thermal conductivity [3–5]. A variation in the isotopic composition must also affect the thermoelectric phenomenon of the phonon drag thermopower $\alpha_{ph}(T)$, which explicitly depends on phonon lifetime. Therefore, a decrease in the degree of isotopic disorder must further result in an increase in the absolute values of the phonon drag thermopower. However, the Herring theory [6] predicts a very weak dependence of $\alpha_{ph}(T)$ on the impurity concentration in the case of a fairly pure semiconductor (see also [7–9]). Within a standard one-parameter approximation, the phonon relaxation rate in the normal processes (N processes) of phonon–phonon scattering was included in the total phonon relaxation rate, which was the only parameter defining the nonequilibrium phonon distribution function. This approach is justified in the case of "impure" semiconductors, when the phonon relaxation rate in the N processes, $\nu_{phN}(q)$, is much lower than the phonon relaxation rate in the resistive processes of scattering, $\nu_{phR}(q)$, caused by the phonon–phonon scattering in the umklapp processes, and from the defects and boundaries of the sample. In the opposite extreme case of fairly pure semiconductors, one must take into account the phonon system drift caused by the N processes of phonon–phonon scattering [10, 11].

In nondegenerate conductors, the electrons interact only with long-wavelength phonons whose wave vector is much less than the wave vector of thermal phonons making the main contribution to thermal conductivity. Because the probability of isotopic scattering of a phonon is proportional to the fourth power of its wave vector q, the thermopower calculated within a one-parameter approximation turns out to be insensitive to the degree of isotopic disorder. Kozlov and Nagaev [12] called attention to the anomalies of thermopower arising in such a situation as long as 30 years ago. They have demonstrated that, in the case of very perfect crystals, the thermal phonon drag of long-wavelength phonons may cause anomalously high values of thermopower. In contrast to the Herring thermopower, this thermopower (two-stage drag thermopower) is inversely proportional to the impurity concentration [13] and is closely associated with the mechanism of relaxation of long-wavelength phonons from thermal phonons in the normal processes of phonon–phonon scattering.

The first attempt at detecting the effect of isotopic phonon scattering on the thermopower was made by Oskotskii *et al.* [14], who investigated the thermal conductivity and thermopower of Te crystals with two different isotopic compositions, of which one was subjected to 92% ^{128}Te isotopic enrichment. The isotopic enrichment resulted in a threefold increase in the maximal values of thermal conductivity; however, Oskotskii *et al.* [14] observed no effect of isotopic disorder on the phonon drag thermopower at low temperatures. This negative result is possibly due either to the different concentrations of charged impurities in the investigated samples or to the relatively weak contribution of the N processes to the overall phonon relaxation rate.

In recent measurements of the thermopower in germanium crystals of different isotopic compositions, we found an almost twofold increase in the thermopower at low temperatures in a monoisotopic sample of ^{70}Ge (99.99%) compared to Ge of natural isotopic composition [15]. This result is indicative of the important part played by the N processes in the relaxation of the phonon system for isotopically enriched germanium crystals. The importance of these processes in the lattice thermal conductivity without the separation of the contributions made by longitudinal and transverse phonons is studied quite well [16–18]. In the N processes of scattering, the phonon momentum is conserved. These processes make no direct contribution to the thermal resistance; they provide for the relaxation of the phonon subsystem to the drift locally equilibrium distribution. Therefore, the N processes redistribute the energy and momentum between different phonon modes to form the nonequilibrium phonon distribution function and prevent a strong deviation of each phonon mode from the equilibrium distribution. This is accompanied by a variation of the relative contribution by various resistive processes of scattering (scattering from defects and boundaries of the sample and in the phonon–phonon umklapp processes) to thermal resistance. The drift motion of phonons must be taken into account under conditions in which the phonon relaxation rate in the N processes, $\nu_{phN}(q)$, is higher than or comparable to the rate of relaxation in resistive processes of scattering, $\nu_{phR}(q)$. It is evident that, in isotopically pure Ge samples at low temperatures, when the phonon–phonon umklapp processes are largely frozen, the rate of relaxation of longitudinal phonons in the N processes significantly exceeds the resistive rate of relaxation $\nu_{phR}(q)$ which is mainly due to isotopic disorder. In this paper, we will demonstrate that the inclusion of the phonon drift caused by the N processes enables one to qualitatively explain the significant effect of isotopic disorder on the drag thermopower in Ge crystals.

In describing the drag thermopower, in contrast to the previous investigations, we will separate the contributions by longitudinal and transverse phonons and take into account the redistribution of the phonon momentum in the N processes of scattering both within each vibrational branch (Simons mechanism [19]) and between different vibrational branches of phonons (Herring mechanism [20]). In this approximation, the nonequilibrium of the phonon system is described by six parameters, namely, by the rates of phonon relaxation in the resistive and normal processes of scattering and by the average drift velocities for each branch of the phonon spectrum. This description of phonon nonequilibrium enables one to reveal new features of relaxation of the momentum of quasi-particles and their effect on the thermopower and thermal conductivity of semiconductors. We will demonstrate below that the drift velocity of phonons (as well as the thermal conductivity) is largely defined by thermal phonons for which the scattering from defects plays a significant part. Therefore, when the drift of the phonon system is taken into account, the thermopower becomes sensitive to the degree of isotopic disorder. We further give the results of measurements and quantitative analysis of the isotope effect in the drag thermopower.

2. EXPERIMENTAL RESULTS

In this paper, we analyze the experimental data on the thermopower $\alpha(T)$ of single crystals of germanium with three different isotopic compositions, namely, the natural composition and compositions subjected to ^{70}Ge isotopic enrichment of 96.3% and up to 99.99%. Ge crystals of the n and p types with the concentration of charged impurities of $|N_d - N_a| < 2 \times 10^{13}$ cm^{-3} were used. Note that Geballe and Hull [21] found that, in the case of highly pure samples of Ge of the n and p types, the phonon drag thermopower very weakly depends on the concentration of electrically active impurities at a doping level below 10^{15} cm^{-3} and decreases in magnitude at higher concentrations. Our samples were shaped as parallelepipeds of square cross section. The samples

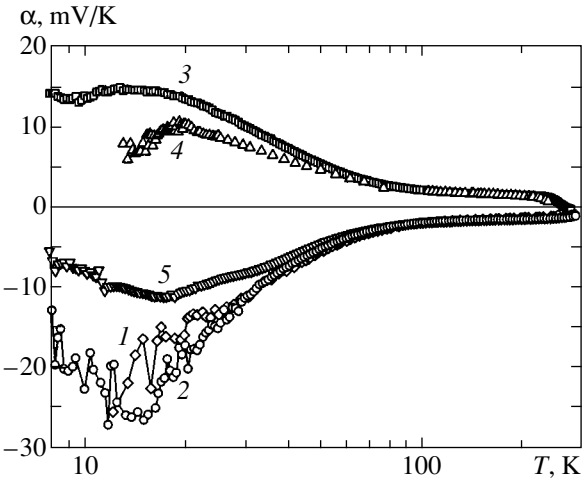

Fig. 1. The magnitude of differential thermopower as a function of temperature for samples of germanium crystals with different isotopic compositions: (*1*) sample no. G2, (*2*) G7, (*3*) G70, (*4*) Gn21, (*5*) S1.

had a total length of approximately 40 mm, with the square side in cross section of approximately 2.5 mm. The thermopower was measured using the method of steady longitudinal heat flux in vacuum in the temperature range from 8 to 300 K. The heat flux was directed along the longer axis of the sample; the temperature difference along the sample did not exceed 1% of its average temperature. The parameters of five investigated samples are given in the table.

The experimental data on the temperature dependence of the thermopower are given in Fig. 1. One can see in the figure that, at temperatures above 70 K, the thermopower is almost independent of temperature. The diffusion component of thermopower $\alpha_e(T)$ predominates in this temperature range; this component is defined by the degree of doping and by the band parameters of the semiconductor and is independent of the phonon lifetime. At low temperatures, where the phonon drag thermopower $\alpha_{ph}(T)$ predominates, $\alpha(T)$ increases with decreasing isotopic disorder; in so doing, the thermopower at the maximum for isotopically pure ^{70}Ge (99.99%) is approximately twice as high as that for germanium with the natural isotopic composition (^{nat}Ge). Compared to the thermal conductivity, the thermopower of germanium turned out to be approximately five times less sensitive to the variation of the degree of isotopic disorder. Note that, in the case of samples with the same isotopic composition, the thermopower is independent of the degree of doping within the experimental error. This is in good agreement with the well-known fact of the weak sensitivity of the magnitude of the drag thermopower to the dopant concentration in fairly pure germanium crystals [6, 21]. These special features of thermopower call for detailed theoretical treatment.

Given below are the results of quantitative analysis of the isotope effect in the thermopower of germanium. Attention is focused on the investigation of the effect of the drift motion of the phonon system, due to the normal processes of phonon scattering, and of the inelasticity of electron–phonon scattering on the drag thermopower. The effect of the normal processes of phonon scattering on the mutual drag of electrons and phonons in metals and in degenerate semiconductors is treated in [10, 11]. In our paper, this theory is generalized to the case of semiconductors with nondegenerate statistics of current carriers. We have treated the redistribution of the momentum of longitudinal and transverse phonons in the *N* processes of scattering both within each vibrational branch and between different vibrational branches. Previously, this approach made it possible to successfully explain the effect of the isotopic composition on the thermal conductivity of germanium and silicon crystals [22, 23]. Here, this method is used to investigate the effect of isotopic disorder on the drag thermopower. In calculating the emf, we used the times of phonon relaxation determined from the data on the thermal conductivity for the same samples of germanium [3, 22]. It is demonstrated that, in fairly pure semiconductors, both the thermopower and the lattice thermal conductivity [22] (with the separation of the contributions by longitudinal and transverse phonons)

Parameters of investigated samples of Ge crystals

Sample no.	Isotopic composition, % ^{70}Ge	g, 10^{-5}	Axis	$\lvert N_d - N_a\rvert$, 10^{12} cm^{-3}
G2	99.99	0.008	[100]	2.7
G7	99.99	0.008	[111]	20
G70	96.6	7.75	[100]	2
Gn21	natural	58.9	[100]	0.5
S1	natural	58.9	[111]	4

Note: $g = \sum_i f_i \left(\frac{M_i - \overline{M}}{\overline{M}}\right)^2$ is the factor characterizing the isotopic disorder of the crystal [3].

largely depend on the mechanism of relaxation of the phonon momentum in the *N* processes of scattering.

3. THE EFFECT OF THE *N* PROCESSES OF PHONON–PHONON SCATTERING ON THE RELAXATION OF MOMENTUM OF ELECTRONS AND PHONONS IN A NONEQUILIBRIUM ELECTRON–PHONON SYSTEM

For simplicity, we will treat a semiconductor with the isotropic law of dispersion of current carriers. We will calculate a charge flow caused by the effect of electric field $\mathbf{E} = \{E_x, 0, 0\}$ and the temperature gradient $\nabla T = (\nabla_x T, 0, 0)$. The set of kinetic equations for the nonequilibrium electron $f(\mathbf{k}, \mathbf{r})$ and phonon $N^{\lambda}(\mathbf{q}, \mathbf{r})$ distribution functions in view of the *N* processes of scattering has the form [11]

$$\begin{aligned}\frac{e}{\hbar}\mathbf{E}_0 \cdot \frac{\partial f_{\mathbf{k}}}{\partial \mathbf{k}} + (\mathbf{v}_k \cdot \nabla_r) f_{\mathbf{k}} &= I_{ei}(f_{\mathbf{k}}) + I_{e\,\mathrm{ph}}(f_{\mathbf{k}}, N_q^{\lambda}),\\ \mathbf{v}_q^{\lambda} \cdot \nabla_r N_q^{\lambda} &= -(N_q^{\lambda} - N_{q\lambda}^{(0)})\nu_{\mathrm{ph}}^{(1)\lambda}\\ -(N_q^{\lambda} - N(\mathbf{q}\cdot\mathbf{u}_{\lambda}))\nu_{\mathrm{ph}N}^{\lambda} &+ I_{\mathrm{ph}\,e}(N_q^{\lambda}, f_{\mathbf{k}}).\end{aligned} \tag{1}$$

Here, $\mathbf{v}_q^{\lambda} = s_{\lambda}\mathbf{q}/q$ is the group velocity of acoustic phonons with polarization λ; $N_{q\lambda}^0$ is the Planck function; $\nu_{\mathrm{ph}N}^{\lambda}(q)$ is the phonon relaxation rate in the *N* processes of scattering; and the rate

$$\nu_{\mathrm{ph}}^{(1)\lambda}(q) = \nu_{\mathrm{ph}i}^{\lambda}(q) + \nu_{\mathrm{ph}B}^{\lambda}(q) + \nu_{\mathrm{ph}U}^{\lambda}(q)$$

includes all of the nonelectron resistive rates of phonon relaxation, due to the phonon scattering from phonons in the umklapp processes, $\nu_{\mathrm{ph}U}^{\lambda}(q)$, from defects and isotopic disorder, $\nu_{\mathrm{ph}i}^{\lambda}(q)$, and from the boundaries of the sample, $\nu_{\mathrm{ph}B}^{\lambda}(q)$. The collision integrals of electrons with impurities, I_{ei}, and with phonons, $I_{e\,\mathrm{ph}}$, and of phonons with electrons, $I_{\mathrm{ph}\,e}$, were determined in [7–9, 24–27]. In Eq. (1), it is taken into account that the *N* processes of scattering bring the phonon subsystem to the locally equilibrium Planck distribution with the drift velocity $\mathbf{u}_{\lambda}$ which may be different for phonons of different polarizations [16–18],

$$\begin{aligned}N(\mathbf{q}, \mathbf{u}_{\lambda}) &= \left[\exp\left(\frac{\hbar\omega_{q\lambda} - \hbar\mathbf{q}\cdot\mathbf{u}_{\lambda}}{k_B T}\right) - 1\right]^{-1}\\ &\approx N_{q\lambda}^0 + \frac{\hbar\mathbf{q}\cdot\mathbf{u}_{\lambda}}{k_B T} N_{q\lambda}^0(N_{q\lambda}^0 + 1).\end{aligned} \tag{2}$$

We will represent the electron and phonon distribution functions in the form [3–5]

$$\begin{aligned}f_{\mathbf{k}} &= f_0(\varepsilon_k) + \delta f_{\mathbf{k}}, \quad \delta f_{\mathbf{k}} = -\frac{\partial f_0}{\partial \varepsilon_k}\mathbf{v}_k \cdot \boldsymbol{\chi}(\varepsilon),\\ N_{\mathbf{q}}^{\lambda} &= N_{q\lambda}^0 + g_{\lambda}(\mathbf{q}),\end{aligned} \tag{3}$$

where $f_0(\varepsilon_k)$ is the equilibrium electron distribution function, and $\delta f_{\mathbf{k}}$ and $g_{\lambda}(\mathbf{q})$ are nonequilibrium additions to the distribution functions, which are linear as regards the external effects. We will linearize the collision integrals with respect to these additions. We will represent the collision integrals $I_{ie}(\delta f_{\mathbf{k}})$ and $I_{\mathrm{ph}\,e}(f_0, g_{\lambda}(\mathbf{q}))$, as well as $I_{e\,\mathrm{ph}}(\delta f_{\mathbf{k}}, N_{q\lambda}^0)$ in the approximation of elastic scattering, in terms of relaxation rates [27]. In calculating the collision integral $I_{\mathrm{ph}\,e}(f_0, g_{\lambda}(\mathbf{q}))$, we will not restrict ourselves to the linear approximation with respect to the inelasticity parameter [7–9, 24–28] and will take into account the inelasticity of collisions between nonequilibrium phonons and equilibrium electrons.

We will substitute expressions (2) and (3) into (1) to derive, similar to [11], the expression for the phonon distribution function $g_{\lambda}(\mathbf{q})$,

$$\begin{aligned}g_{\lambda}(\mathbf{q}) &= -\frac{N_{q\lambda}^0(N_{q\lambda}^0 + 1)}{\nu_{\mathrm{ph}}^{\lambda}(q)}\frac{\hbar\omega_{q\lambda}}{k_B T^2}\mathbf{v}_q^{\lambda}\cdot\nabla T\\ &+ \frac{\hbar\mathbf{q}\cdot\mathbf{u}_{\lambda}}{k_B T} N_{q\lambda}^0(N_{q\lambda}^0 + 1)\frac{\nu_{\mathrm{ph}N}^{\lambda}(q)}{\nu_{\mathrm{ph}}^{\lambda}(q)}.\end{aligned} \tag{4}$$

Here,

$$\begin{aligned}\nu_{\mathrm{ph}}^{\lambda}(q) &= \nu_{\mathrm{ph}}^{(1)\lambda}(q) + \nu_{\mathrm{ph}\,e}^{\lambda}(q) + \nu_{\mathrm{ph}N}^{\lambda}(q)\\ &= \nu_{\mathrm{ph}N}^{\lambda}(q) + \nu_{\mathrm{ph}R}^{\lambda}(q)\end{aligned}$$

is the total rate of relaxation of phonons with the wave vector *q* and polarization λ, and $\nu_{\mathrm{ph}\,e}^{\lambda}(q)$ is the rate of relaxation of momentum of phonons from electrons [24–27]. The first term in expression (4) is defined by the diffusion motion of phonons, and the second term takes into account the drift phonon motion and is associated with the normal processes of phonon–phonon scattering. The phonon drift velocity $\mathbf{u}_{\lambda}$ is found from the balance equation for phonon momentum, which follows from the law of conservation of momentum in the normal processes of phonon–phonon scattering,

$$\begin{aligned}\frac{1}{V}\sum_{q,\lambda}\hbar\mathbf{q}\nu_{\mathrm{ph}N}^{\lambda}(q)(N_q^{\lambda} - N(\mathbf{q}, \mathbf{u}_{\lambda})) &= \frac{1}{V}\sum_{q,\lambda}\hbar\mathbf{q}\nu_{\mathrm{ph}N}^{\lambda}(q)\\ \times\left[g_{\lambda}(\mathbf{q}) - \frac{\hbar\mathbf{q}\cdot\mathbf{u}_{\lambda}}{k_B T} N_{q\lambda}^0(N_{q\lambda}^0 + 1)\right] &= 0.\end{aligned} \tag{5}$$

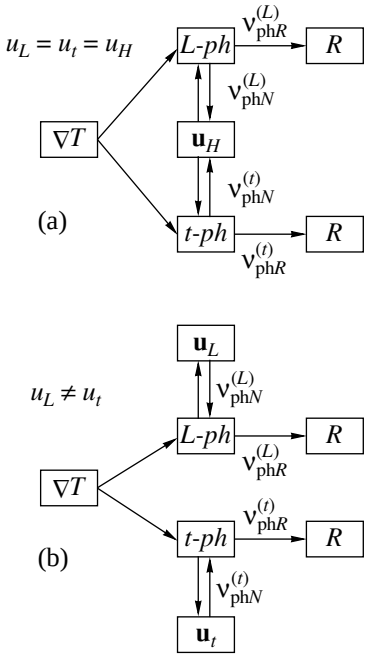

Fig. 2. A scheme illustrating the relaxation of momentum in a phonon system for two mechanisms of phonon scattering in the normal processes: (a) for the Herring mechanism, (b) for the Simons mechanism.

A scheme illustrating the redistribution and relaxation of the momentum received by a phonon system from the temperature gradient is given in Fig. 2. The phonon scattering in the resistive processes of scattering (*R*) (from isotopic disorder, electrons, and sample boundaries, and the phonon–phonon scattering in the umklapp processes) brings about the relaxation of the momentum of the phonon system. The *N* processes redistribute the momentum between different phonon modes (*L-ph* and *t-ph*) and bring about the phonon drift with an average velocity $\mathbf{u}_\lambda$. As in [10, 11, 16–18], we assume that the drift velocity is independent of the wave vector of phonons. Two mechanisms of normal three-phonon processes of scattering are usually examined, namely, the Herring [20] and Simons [19] mechanisms. In the Herring mechanism of *N* processes, phonons of different polarizations are involved: the rate of relaxation of transverse phonons in the Herring mechanism is defined by the scattering processes ($t + L \longleftrightarrow L$) in which one transverse and two longitudinal phonons are involved; in this case, the main contribution to the rate of relaxation of longitudinal phonons is made either by the processes of decay of a longitudinal phonon into two transverse phonons belonging to different branches or by the fusion of two transverse phonons to form a longitudinal phonon ($L \longleftrightarrow t_1 + t_2$). This relaxation mechanism provides for redistribution of the drift momentum between longitudinal and transverse phonons (see Fig. 2) and tends to establish a locally equilibrium distribution with a drift velocity that is the same for phonons of both polarizations, $u_L = u_t = u_H$. The Simons mechanism of relaxation [19] involves phonons of one polarization. In the case of this mechanism of scattering, the law of conservation of momentum in the *N* processes is valid for each branch of the phonon spectrum, and the drift velocity of longitudinal phonons differs from that of transverse phonons. Therefore, we will treat below two options for the relaxation of the phonon momentum in the *N* processes.

We use expressions (4) and the balance equation for phonon momentum (5) to find the phonon drift velocity $\mathbf{u}_\lambda$ for the Herring (*H*) and Simons (*S*) mechanisms of relaxation, as was done in [11]. After this, we derive, for the phonon distribution function $g_\lambda(q)$,

$$g_\lambda(\mathbf{q}) = -\frac{N_{q\lambda}^0(N_{q\lambda}^0+1)}{\tilde{\nu}_{\rm ph}^\lambda(q)}\frac{\hbar\omega_{q\lambda}}{k_BT^2}\mathbf{v}_q^\lambda\cdot\nabla T, \qquad (6)$$
$$\tilde{\nu}_{\rm ph}^{\lambda(S,H)}(q) = \tilde{\nu}_{\rm ph}^\lambda(q)\left(1+\tilde{\nu}_{{\rm ph}N}^\lambda(q)\beta_{(S,H)}\right)^{-1},$$

$$\beta_S = \frac{\Psi_N^\lambda}{\Psi_{NR}^\lambda}, \quad \beta_H = \left(\frac{s_L}{s_\lambda}\right)^2\frac{\Psi_N^L+2S_*^2\Psi_N^t}{\Psi_{NR}^L+2S_*^5\Psi_{NR}^t}. \qquad (7)$$

Here, $S_* = s_L/s_t$, and the remaining functions are defined by the expressions

$$\Psi_N^\lambda = \left\langle\frac{\nu_{{\rm ph}N}^\lambda(q)}{\nu_{\rm ph}^\lambda(q)}\right\rangle_{z_{d\lambda}}$$
$$\equiv\int_0^{z_{d\lambda}}dz_q^\lambda(z_q^\lambda)^4\frac{\nu_{{\rm ph}N}^\lambda(q)}{\nu_{\rm ph}^\lambda(q)}N_{q\lambda}^0(N_{q\lambda}^0+1), \qquad (8)$$
$$\Psi_{NR}^\lambda = \left\langle\frac{\nu_{{\rm ph}R}^\lambda(q)\nu_{{\rm ph}N}^\lambda(q)}{\nu_{\rm ph}^\lambda(q)}\right\rangle_{z_{d\lambda}},$$

where

$$z_q^\lambda = \frac{\hbar\omega_{q\lambda}}{k_BT} = \frac{q}{q_{T\lambda}}, \quad q_{T\lambda} = \frac{k_BT}{\hbar s_\lambda},$$

$$z_{2k}^\lambda = \frac{2k}{q_{T\lambda}}, \quad z_{d\lambda} = \frac{\hbar\omega_{d\lambda}}{k_BT}$$

($\omega_{d\lambda}$ is the Debye frequency of phonons with polarization λ). One can see in expression (6) that the inclusion of the normal processes of phonon–phonon scattering reduces to the renormalization of the rate of relaxation of phonon momentum. The phonon drift motion caused by the *N* processes leads to a decrease in the effective phonon relaxation rate; this decrease is different for the Herring [20] and Simons [19] relaxation mechanisms.

We will now consider the electron subsystem. The electron scattering from impurities, ν_{ei}, results in the relaxation of electron momentum, and the mechanisms of electron–phonon relaxation characterized by the rates $\nu_{e\,\mathrm{ph}}$ and $\nu_{\mathrm{ph}\,e}$ bring about the redistribution of momentum within an electron–phonon system; in so doing, the electrons interact only with long-wavelength phonons. We do not treat the renormalization of the thermopower due to the mutual drag of electrons and phonons. Note that the quantities such as the thermopower and thermal conductivity are found from the condition that the total current through the sample is zero. In this case, the average velocity of ordered electron motion in any physically small sample volume is zero. Therefore, the transfer of momentum of ordered electron motion to the phonon subsystem is low, and the effect of electron nonequilibrium on the electrons via the phonon subsystem may be ignored [11]. On the other hand, a steady phonon flow from the hot end of the sample to the cold end exists in the presence of a temperature gradient, and the magnitude of thermopower is largely defined by the transfer of momentum of ordered phonon motion to electrons. Note that, for longitudinal phonons in Ge crystals at low temperatures, when the electron–phonon drag makes a marked contribution to the thermopower, the relaxation rate $\nu_{\mathrm{ph}N}(q) \gg \nu_{\mathrm{ph}R}(q)$ [22]. It follows from the foregoing that the relaxation of phonon momentum in a nonequilibrium electron–phonon system must be taken into account more rigorously than was done in the case of one-parameter approximation [7–9, 24–28].

The purpose of this theoretical analysis is to investigate the effect of the phonon drift caused by the *N* processes on the drag thermopower. In this case, one can ignore the mutual drag of electrons and phonons and obtain, as was done in [27], the following solution for the function $\boldsymbol{\chi}(\varepsilon)$:

$$\boldsymbol{\chi}(\varepsilon) = -e\tau(\varepsilon)\left[\mathbf{E} + \frac{k_B}{e}\left(\tilde{A}_{\mathrm{ph}}(\varepsilon) + \frac{\varepsilon-\zeta}{k_BT}\right)\nabla T\right], \quad (9)$$

$$\tilde{A}_{\mathrm{ph}}(\varepsilon) = \sum_\lambda \frac{ms_\lambda^2}{k_BT}\int_0^{z_{2k}^\lambda} dz_q^\lambda \frac{\nu_{e\,\mathrm{ph}}^\lambda(k,q)}{\tilde{\nu}_{\mathrm{ph}}^\lambda(q)}. \quad (10)$$

Here, $\tau(\varepsilon)$ is the total relaxation time of electrons;

$$\tau^{-1}(\varepsilon_k) = \nu_e(k) = \nu_{ei}(k) + \nu_{e0}(k) + \nu_{e\,\mathrm{ph}}(k);$$

the rates of electron relaxation from neutral, $\nu_{e0}(k)$, and charged, $\nu_{ei}(k)$, impurities have the known form (see, for example, [7], formulas (10.29) and (10.50)); and the electron–phonon collision rate is defined by the expression

$$\nu_{e\,\mathrm{ph}}^\lambda(k) = \sum_\lambda \langle \nu_{e\,\mathrm{ph}}^\lambda(k,q)\rangle_{z_{2k}^\lambda},$$

$$\nu_{e\,\mathrm{ph}}^\lambda(k,q) = \frac{m_e|C_{0\lambda}|^2}{2\pi\hbar^2k^3}q^5N_{q\lambda}^0(N_{q\lambda}^0+1) \times\left\{\left(1-\frac{2ms_\lambda}{\hbar q}\right)F^+(\varepsilon_k) + \left(1+\frac{2ms_\lambda}{\hbar q}\right)F^-(\varepsilon_k)\right\}, \quad (11)$$

where

$$F^\pm(\varepsilon_k) = \pm\frac{f_0(\varepsilon_k) - f_0(\varepsilon_k \pm \hbar\omega_q)}{f_0(\varepsilon_k)(1-f_0(\varepsilon_k))}, \quad |C_{0\lambda}|^2 = \frac{E_{0\lambda}^2\hbar}{s_\lambda\rho},$$

$E_{0\lambda}$ is the deformation potential constant, and ρ is the density. For semiconductors with nondegenerate statistics of current carriers,

$$f_0(\varepsilon) \approx \exp\left(-\frac{\varepsilon-\zeta}{k_BT}\right),$$

the $F^\pm$ functions may be represented in the form

$$F^+ \approx 1 - e^{-z}, \quad F^- \approx e^z - 1;$$

then, in view of the inelasticity of electron–phonon scattering, we find

$$(\tau_{e\,\mathrm{ph}}(\varepsilon))^{-1} = \sum_\lambda (\tau_{0e\,\mathrm{ph}}^\lambda)^{-1}x^{-3/2}J_{1\lambda}(x),$$

$$J_{1\lambda}(x) = \frac{1}{2}(J_{1\lambda}^+(x) + J_{1\lambda}^-(x)),$$

$$J_{1\lambda}^\pm(x) = \int_0^{z_{\max,\lambda}^\pm} J_{1\lambda}^\pm(z)dz,$$

$$J_{1\lambda}^+(z) = \frac{z^3(z-\delta_\lambda)}{e^z-1}, \quad (12)$$

$$J_{1\lambda}^-(z) = \frac{z^3(z+\delta_\lambda)}{e^z-1}e^{-z},$$

$$(\tau_{0e\,\mathrm{ph}}^\lambda)^{-1} = \frac{m_e|C_{0\lambda}|^2}{2\pi\hbar^3}q_{T\lambda}^3\delta_\lambda^{-3/2}.$$

The upper limits of integration in Eqs. (12) are defined by the expressions

$$z^{\pm}_{\max,\lambda} = \frac{2\hbar s_\lambda k}{k_B T} = 2\delta_\lambda^{1/2} x^{1/2} \pm \delta_\lambda,$$
$$\delta_\lambda = \frac{2m_e s_\lambda^2}{k_B T} = \frac{T_{s\lambda}}{T}, \qquad (13)$$
$$T_{s\lambda} = \frac{2m_e s_\lambda^2}{k_B}, \quad x = \frac{\varepsilon}{k_0 T},$$

where δ_λ is the inelasticity parameter. In the case of semiconductors, the effective temperature $T_{s\lambda}$ defining the inelasticity of electron–phonon scattering is, as a rule, less than 1 K; for example, in the case of Ge, $T_{sL} \approx 0.8$ K at $s_L \approx 5.21 \times 10^5$ cm/s, $m_e \approx 0.22 m_0$. Therefore, even at $T > 10$ K, $\delta_\lambda \ll 1$ and $z_{\max} \ll 1$; therefore, expressions (12) may be expanded in powers of z. In a zero approximation with respect to the inelasticity parameter δ_λ, we will derive from Eqs. (12) the known expression for the electron–phonon relaxation time,

$$\tau^\lambda_{e\,\mathrm{ph}}(\varepsilon) = \tau^\lambda_{0e\,\mathrm{ph}}(2\delta_\lambda)^{-2} x^{-1/2}. \qquad (14)$$

In the same approximation, the expression for the inverse time of phonon–electron relaxation has the form

$$\nu^\lambda_{\mathrm{ph}\,e}(k, q) = \frac{m_e^2 |C_{0\lambda}|^2 k_B T}{\pi\hbar^5} e^{\eta}(1 - e^{-z}) e^{-x_m},$$
$$x_m = \frac{(z - \delta_\lambda)^2}{4\delta_\lambda}. \qquad (15)$$

The concentrations of electrons, n_e, and of charged donors, N_{d+}, and the reduced Fermi level $\eta = \zeta/k_B T$ are found from the condition of electroneutrality for germanium (see [7], formula (6.9)): $N_d \approx 10^{12}$–10^{13} cm^{-3}, $\varepsilon_d \approx 0.01$ eV, and $m_e \approx 0.22 m_0$. For these values of the parameters, the criterion of nondegenerate statistics is well valid.

In the approximation we adopted, the $\chi(\varepsilon)$ function allows for the direct effect of the electric field and temperature gradient on the electron subsystem, as well as for the effect of the phonon drag of electrons.

4. THE DRAG THERMOPOWER IN SEMICONDUCTORS WITH NONDEGENERATE STATISTICS OF CURRENT CARRIERS

We will examine the effect of the normal processes of phonon–phonon scattering on the thermal electromotive force of semiconductors with nondegenerate statistics of current carriers. We will calculate the conduction current $\mathbf{j}$ by dividing it into three parts proportional to nonequilibrium additions to the electron distribution function $\chi(\varepsilon)$,

$$\mathbf{j} = -\frac{e}{3\pi^2}\int_0^\infty d\varepsilon\left(-\frac{\partial f_0}{\partial\varepsilon}\right)\frac{k^3}{m(\varepsilon)}\chi(\varepsilon) \qquad (16)$$
$$\approx \mathbf{j}_{dr} + \mathbf{j}_{\mathrm{drag}} + \mathbf{j}_{\mathrm{dif}} = 0.$$

From the condition $\mathbf{j} = 0$, we find

$$\alpha = \alpha_{\mathrm{ph}} + \alpha_{\mathrm{dif}}. \qquad (17)$$

We will not consider below the diffusion component of thermopower: for germanium crystals at $T < 100$ K, this contribution is small. In the case of nondegenerate statistics, the expression for the phonon drag thermopower may be represented in the form

$$\alpha_{\mathrm{ph}} = -\frac{k_B}{e}\frac{\langle\langle \tau(\varepsilon)\tilde{A}_{\mathrm{ph}}(\varepsilon)\rangle\rangle}{\langle\langle \tau(\varepsilon)\rangle\rangle},$$
$$\langle\langle f(\varepsilon)\rangle\rangle = \frac{\int_0^\infty dx e^{-x} x^{3/2} f(\varepsilon)}{\int_0^\infty dx e^{-x} x^{3/2}}, \quad x = \frac{\varepsilon}{k_0 T}, \qquad (18)$$

$$\tilde{A}_{\mathrm{ph}}(\varepsilon) = \sum_\lambda \frac{m_e |C_{0\lambda}|^2}{4\pi\hbar^3} q_{T\lambda}^2 \delta_\lambda^{-1/2} x^{-3/2}(J^+_{2\lambda}(x) + J^-_{2\lambda}(x)), \qquad (19)$$

$$J^\pm_{2\lambda}(x) = \int_0^{z^\pm_{\max,\lambda}} \frac{J^\pm_{1\lambda}(z)dz}{\tilde{\nu}^\lambda_{\mathrm{ph}}(q)},$$
$$J^+_{1\lambda}(z) = \frac{z^3(z - \delta_\lambda)}{e^z - 1}, \qquad (20)$$
$$J^-_{1\lambda}(z) = \frac{z^3(z + \delta_\lambda)}{e^z - 1} e^{-z}.$$

The upper integration limits in Eqs. (20) are defined by expressions (13). First of all, note that the drag thermopower includes, as does the lattice thermal conductivity [11, 22], the phonon momentum relaxation rate renormalized by the N processes. Unlike standard one-parameter approximations for the drag thermopower [7–9, 24–28], expressions (18)–(20) include the inelasticity of electron–phonon scattering, as well as the contribution made by the phonon drift motion. This contribution has different forms for the Herring and Simons mechanisms of relaxation. Because the phonon drift velocity is defined by all thermally excited phonons, the thermopower becomes sensitive to the

degree of isotopic disorder. It follows from formulas (6), (19), and (20) that the inclusion of the drift of the phonon subsystem, which is associated with the normal processes of phonon scattering, brings about a decrease in the effective relaxation rate of phonons and, accordingly, an increase in the fraction of momentum transferred to electrons by phonons. This result is of practical importance as regards the interpretation of experimental data on the thermopower of germanium crystals with isotopic disorder.

In the extreme case of $\nu_{phN}(q) \ll \nu_{phR}(q)$, one can ignore the contribution of the phonon drift motion and use the expression for the drag thermopower that was previously derived with a one-parameter approximation [7–9, 24–28]. With $\nu_{phN}(q) \gg \nu_{phR}(q)$, the normal processes of phonon–phonon scattering and the drift of the phonon system associated with this scattering lead to a significant increase in the absolute values of thermopower. Note that, in interpreting the experimental data on the drag thermopower in previous studies involving the use of a one-parameter approximation (see [7–9, 24–28]), the relaxation rate in the normal processes $\nu_{phN}(q)$ was included in the total phonon relaxation rate $\nu^{\lambda}_{ph}(q)$ as the resistive mechanism of phonon scattering, and, at $\nu_{phN}(q) \gg \nu_{phR}(q)$, it was treated as the only mechanism of relaxation of momentum of long-wavelength phonons [7, 8]. However, it follows from expressions (18)–(20) that, in this extreme case, the relaxation rate $\nu_{phN}(q)$ is eliminated from the drag thermopower, and α_{ph} is fully defined by the averaged relaxation rate of phonons in the resistive processes of scattering,

$$\alpha_{ph}^{(S,H)} \approx -\frac{k_B}{e}\sum_{\lambda}\frac{m_F s_\lambda^2}{k_B T}\frac{\langle\langle\tau(\varepsilon)\nu^{\lambda}_{e\,ph}(\varepsilon)\rangle\rangle}{\langle\nu^{\lambda}_{ph\,R}(q)\rangle^{(S,H)}_{z_{d\lambda}}\langle\langle\tau(\varepsilon)\rangle\rangle},$$
$$\langle\nu^{\lambda}_{phR}(q)\rangle^{(S)} = \frac{\langle\nu^{\lambda}_{phR}\rangle}{J^{(4)}_{\lambda}},$$
$$\langle\nu^{\lambda}_{phR}(q)\rangle^{(H)} = \frac{\langle\nu^{L}_{phR}\rangle + 2S_*^5\langle\nu^{t}_{phR}\rangle}{J^{(4)}_{L} + 2S_*^3 J^{(4)}_{t}}, \quad (21)$$
$$J^{(4)}_{\lambda} = \int_0^{z_{d\lambda}}\frac{dz z^4 e^z}{(e^z-1)^2}.$$

A one-parameter approximation yields in this case an entirely different result,

$$\alpha_{ph}^{(S,H)} \approx -\frac{k_B}{e}$$
$$\times\sum_{\lambda}\frac{m_F s_\lambda^2}{k_B T}\frac{1}{\langle\langle\tau(\varepsilon)\rangle\rangle}\left\langle\left\langle\tau(\varepsilon)\int_0^{z^{\lambda}_{2k}}dz^{\lambda}_{q}\frac{\nu^{\lambda}_{e\,ph}(k,q)}{\nu^{\lambda}_{ph\,N}(q)}\right\rangle\right\rangle. \quad (22)$$

Therefore, the inferences previously made with respect to the temperature and field dependences of the drag thermopower [7–9, 24–28] need to be refined. It is evident that, in the case of one-parameter approximation (22), the drag thermopower α_{ph} is insensitive to the degree of isotopic disorder. Note that a different approach to the calculation of the drag thermopower was suggested in [12, 13]. This approach is based on dividing the entire system into two subsystems, namely, the subsystem of long-wavelength phonons ($q < 2k$) with which electrons interact and the subsystem of thermal phonons ($q > q_{T\lambda}$). The authors of [12, 13] suggested a mechanism of two-stage drag: the phonon drift motion is defined by the thermal phonons, which, in turn, drag the long-wavelength phonons. By their physical content, our method and the approach developed in [12, 13] coincide, because, in our theory, it is the thermal phonons that define the phonon drift motion, as well as the thermal conductivity. However, our method is more general: we treat correctly the *N* processes of scattering of thermal phonons with regard for their drift and diffusion motion, identify the contributions by phonons of different polarizations, and treat both the intrabranch and interbranch redistribution of the phonon momentum in the *N* processes of scattering.

5. THE RESULTS OF CALCULATION OF THE DRAG THERMOPOWER OF GERMANIUM CRYSTALS OF DIFFERENT ISOTOPIC COMPOSITIONS

Given below are the results of numerical analysis of the drag thermopower in germanium crystals of different isotopic compositions, which, in view of the assumptions made, may only pretend to be a qualitative explanation of the effect. The main results include the isotropic band approximation and the assumption that the phonon drift velocity is independent of the wave vector, i.e., the drift velocities of thermal and long-wavelength phonons are the same. The calculation of the drag thermopower with a real band structure of germanium within the suggested method of inclusion of the normal processes of phonon scattering, with the long-wavelength and thermal phonons treated separately, is of interest *per se*. In this analysis, we restrict ourselves to examining the effect of the phonon drift motion and of the inelasticity of electron–phonon scattering on the drag thermopower in germanium crystals. The values of the parameters defining the phonon relaxation rate were borrowed from the results of analysis of the data on the thermal conductivity of Ge crystals of different isotopic compositions, obtained in [3, 22]. The use of these parameters made it possible to fit the results of calculations of thermal conductivity for the Herring mechanism of relaxation [22] to the experimental data of [3] in a wide temperature range in the entire investigated range of isotopic enrichment. In our calculation of the drag thermopower, these parameters are not varied. The fitting parameter of the theory is the

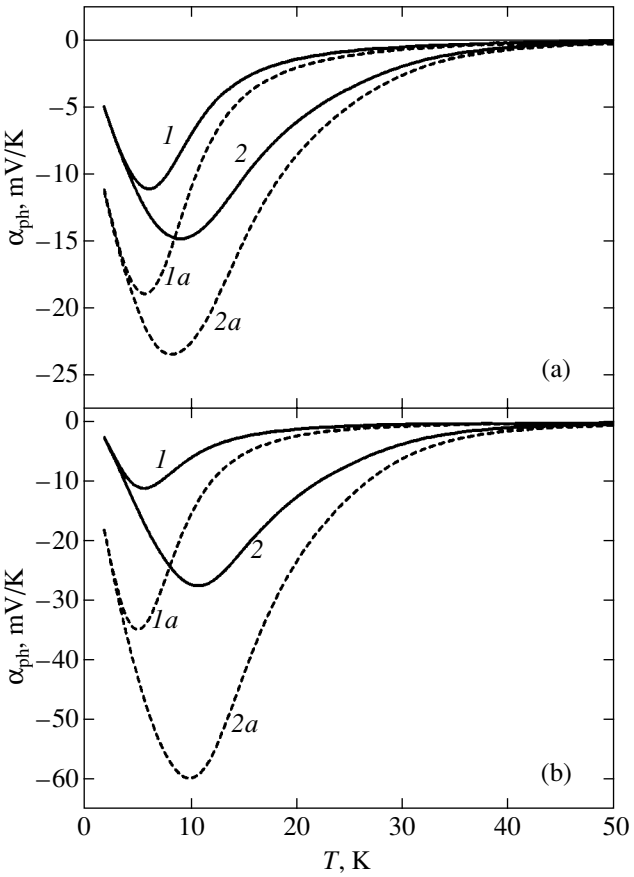

Fig. 3. The temperature dependence of the drag thermopower for the following values of parameters: (a) $m_e \approx 0.22m_0$, $E_{0L} = 16$ eV; (b) $m_e = m_0$, $E_{0L} = 4$ eV. Curves *1* and *1a* are for germanium of natural isotopic composition ($N_d = 4 \times 10^{12}$ cm^{-3}), and curves *2* and *2a* are for germanium with 99.99% ^{70}Ge ($N_d = 2 \times 10^{13}$ cm^{-3}). Curves *1* and *2* allow for the inelasticity of electron–phonon scattering, and curves *1a* and *2a* are plotted in a linear approximation with respect to the parameter of inelasticity of electron–phonon scattering.

deformation potential constant. Given a fixed effective mass of electrons, this constant is selected on the basis of the condition of agreement between the calculated value of absolute thermopower at the point of maximum and the experimentally obtained values for germanium of natural isotopic composition and is then used to calculate the thermopower of ^{70}Ge (99.99%). Because the effective mass of one of four ellipsoids in the crystallographic direction [111] is $m_e \approx 1.68m_0$, its average magnitude was varied from the value of the effective mass of the density of states $m_e \approx 0.22m_0$ to the value of $m_e \approx m_0$.

We will first examine the part played by the inelasticity during the transfer of momentum from nonequilibrium phonons to equilibrium electrons. Figures 3a and 3b give the results of calculations of the drag thermopower for ^{nat}Ge and ^{70}Ge (99.99%) at $m_e \approx 0.22m_0$ and $m_e \approx m_0$. One can see in the figures that the exact inclusion of the inelasticity of electron–phonon scattering brings about a marked suppression of the contribution of phonon drag in the thermopower. The maximal values of thermopower $|\alpha_{max}|$ decrease by a factor of 1.6–1.7 for the value of $m_e \approx 0.22m_0$. However, the importance of inelasticity increases with the effective mass of electrons: at $m_e \approx m_0$, the value of $|\alpha_{max}|$ decreases by a factor of 3 for ^{nat}Ge and by a factor of 2.2 for ^{70}Ge (99.99%). This result came as a surprise to us. The thing is that analysis of the time of relaxation of electrons from phonons [7–9] revealed that, for temperatures $T \gg T_{s\lambda}$ ($T_{sL} \approx 0.8$ K for Ge at $m_e \approx 0.22m_0$), the importance of inelasticity is minor and, at temperatures above 5 K, it may be ignored. Therefore, in the previously published papers dealing with the drag thermopower in semiconductors [6–9, 24–30], the inelasticity of electron–phonon scattering was taken into account in a linear approximation with respect to the inelasticity parameter $\hbar\omega_{q\lambda}/k_BT$.

Note that the inclusion of scattering from charged and neutral donor impurities at concentrations of the order of 10^{12}–10^{13} cm^{-3} has little effect on the magnitude of the thermopower (this scattering introduces a contribution of less than 3%), while the magnitude of the electron mobility varies more significantly in the low-temperature region.

Figure 4 gives the contributions of the phonon drift and diffusion motions into the drag thermopower for ^{nat}Ge and ^{70}Ge (99.99%). One can see in the figure that, in the case of ^{nat}Ge, the predominant contribution to the thermopower is made by the phonon diffusion motion. The contribution by the drift motion is small and amounts to 21% of the diffusion contribution at the maximum of $|\alpha|$. In contrast, in the case of ^{70}Ge (99.99%), the drift contribution to the drag thermopower predominates. It is six times the diffusion contribution. In view of the foregoing, indeed, the isotope effect in the thermopower for Ge is associated with the drift motion of thermal phonons. As was already observed in analyzing the thermal conductivity of Ge and Si crystals of different isotopic compositions [22, 23], a decrease in the degree of isotopic disorder brings about an abrupt increase in the contribution made by the drift motion of longitudinal phonons to the thermal conductivity. The same effect shows up in the drag thermopower.

Figure 5 gives the theoretically and experimentally obtained temperature dependence of the drag thermopower for ^{nat}Ge and ^{70}Ge (99.99%). One can see in the figure that the theory provides a qualitative explanation of the isotope effect in the thermopower: the maximal values of $|\alpha_{max}|$ in the case of transition from ^{nat}Ge to ^{70}Ge (99.99%) increase by a factor of 1.3 for the value of $m_e \approx 0.22m_0$ and by a factor of 2.25 for $m_e \approx m_0$, which actually agrees with the experimentally observed increase in the direction [111]. This may point to the

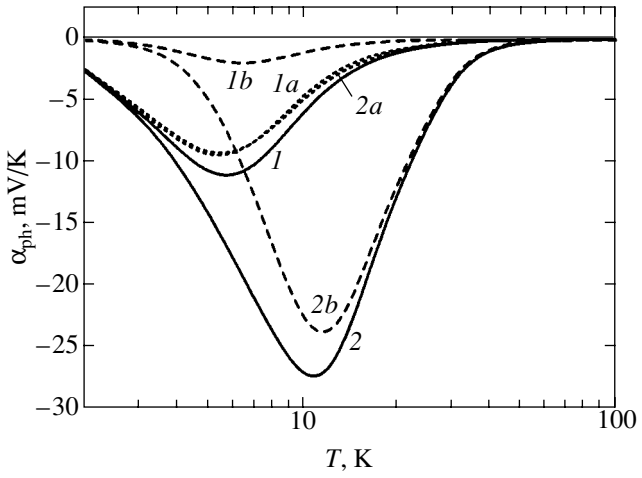

Fig. 4. The temperature dependence of (*1*, *2*) the drag thermopower, as well as of the contributions by (*1a*, *2a*) the diffusion and (*1b*, *2b*) drift of phonons for germanium of different isotopic compositions ($m_e = m_0$, $E_{0L} = 4$ eV) allowing for the inelasticity of electron–phonon scattering. Curves *1*, *1a*, and *1b* are for germanium of natural isotopic composition ($N_d = 4 \times 10^{12}$ cm^{-3}), and curves *2*, *2a*, and *2b* are for germanium with 99.99% ^{70}Ge ($N_d = 2 \times 10^{13}$ cm^{-3}).

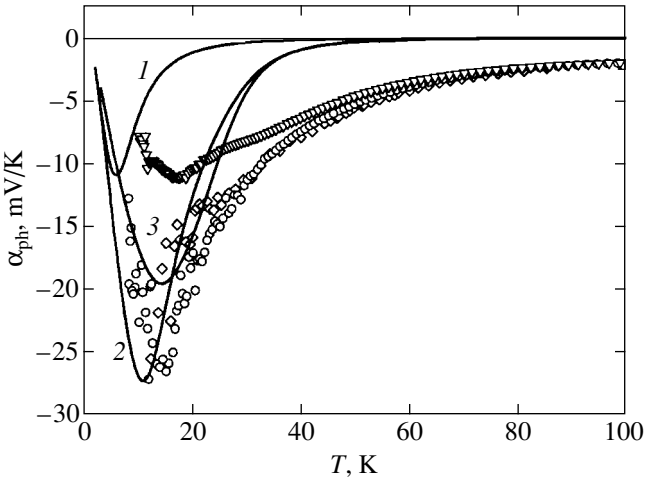

Fig. 5. The temperature dependence of the drag thermopower ($E_{0L} = 4$ eV). Curve *1* is for germanium of natural isotopic composition ($m_e = m_0$, $N_d = 4 \times 10^{12}$ cm^{-3}), curve *2* is for germanium with 99.99% ^{70}Ge ($m_e = m_0$, $N_d = 2 \times 10^{13}$ cm^{-3}) in the direction [111], and curve *3* is for germanium with 99.99% ^{70}Ge ($m_e \approx 0.9m_0$, $N_d = 2 \times 10^{12}$ cm^{-3}) in the direction [100]; the symbols indicate the experimental data.

predominant part played by one of four ellipsoids with the maximal effective mass along the direction [111]. However, the position of maxima for ^{nat}Ge (see Figs. 3, 4, and 5) turns out to be shifted to the low-temperature region, $T_{max} \approx 6$ K, while experiment gives $T_{max} \approx 17$ K. For ^{70}Ge (99.99%), calculation gives $T_{max} \approx 10$ K, while experiment produces $T_{max} \approx 15$ K. In calculating the thermopower in the direction [100] (see Fig. 5, curve *3*), the deformation potential constant was not varied, and the velocities of sound were taken to be $s_L = 4.92 \times 10^5$ cm/s and $s_t = 3.55 \times 10^5$ cm/s, in accordance with [31]. In this case, the isotope effect in the thermopower with the same constant of deformation potential turned out to be 35% lower, which may be indicative of some anisotropy of the drag thermopower.

Note that the contribution by longitudinal phonons alone was taken into account in the calculation of the drag thermopower. Analysis revealed that, within the assumptions made, the isotope effect for transverse phonons was low and, upon transition from ^{nat}Ge to highly enriched germanium, this contribution increased by approximately 10%. This is associated with the predominant part played by the diffusion motion of transverse phonons (for more detail, see [22]). Therefore, in this analysis, we ignored the contribution of transverse phonons, although the position of the maximum of $|\alpha_{ph}^t|$ is found at approximately 20–22 K. The inclusion of this contribution could have markedly improved the agreement between the calculated curves and the experimental data at temperatures above the maximum. However, the introduction of an additional fitting parameter into the theory hardly added anything to the physical content of this paper.

6. CONCLUSIONS

In this paper, we have interpreted the experimentally found strong dependence of the thermopower of germanium crystals on the isotopic composition. We have developed a theory of phonon drag of electrons in semiconductors with nondegenerate statistics of current carriers, which takes into account the effect of the phonon drift motion associated with the normal processes of phonon scattering. A qualitative explanation has been given of the isotope effect in the drag thermopower. It has been demonstrated that the rigorous inclusion of inelastic electron scattering brings about a significant (by factor of more than two) reduction of the absolute values of the drag thermopower. In our opinion, the isotropic band approximation for conduction electrons, as well as the assumption of the equality of the drift velocities of long-wavelength and thermal phonons, failed to provide for quantitative agreement with the experimental data on the drag thermopower, in contrast to calculations of thermal conductivity [22].

The inclusion of both of the above-identified factors requires significant mathematical effort, namely, a separate study of the relaxation of thermal and long-wavelength phonons and analysis of the Simons mechanism of normal processes of scattering, which leads to the redistribution of momentum between the thermal and long-wavelength phonons of different vibrational branches.

ACKNOWLEDGMENTS

We are grateful to A.P. Tankeev for the discussion of our results and critical comments.

This study was supported by the Russian Foundation for Basic Research (project nos. 00-02-16299 and 01-02-17469), by the CRDF (grant no. RP2-2274), and by the Dinastiya and MTsFFM Foundations.

REFERENCES

1. K. Itoh, W. L. Hansen, E. E. Haller, *et al.*, J. Mater. Res. **8**, 1341 (1993).
2. V. I. Ozhogin, A. V. Inyushkin, A. N. Taldenkov, *et al.*, Pis'ma Zh. Éksp. Teor. Fiz. **63**, 463 (1996) [JETP Lett. **63**, 490 (1996)].
3. M. Asen-Palmer, K. Bartkowski, E. Gmelin, *et al.*, Phys. Rev. B **56**, 9431 (1997).
4. A. P. Zhernov and D. A. Zhernov, Zh. Éksp. Teor. Fiz. **114**, 1757 (1998) [JETP **87**, 952 (1998)].
5. A. P. Zhernov, Fiz. Tverd. Tela (St. Petersburg) **41**, 1185 (1999) [Phys. Solid State **41**, 1079 (1999)].
6. C. Herring, Phys. Rev. **96**, 1163 (1954).
7. V. M. Askerov, *Electronic Transport Phenomena in Semiconductors* (Nauka, Moscow, 1985), p. 318.
8. I. M. Tsidil'kovskiĭ, *Thermomagnetic Effects in Semiconductors* (Nauka, Moscow, 1960; Academic, New York, 1962).
9. P. S. Zyryanov and M. I. Klinger, *Quantum Theory of Electron Transport Phenomena in Crystalline Semiconductors* (Nauka, Moscow, 1976), p. 480.
10. I. G. Kuleev, Fiz. Met. Metalloved. **90** (1), 14 (2000).
11. I. G. Kuleev, Fiz. Tverd. Tela (St. Petersburg) **42**, 649 (2000) [Phys. Solid State **42**, 423 (2000)]; Fiz. Tverd. Tela (St. Petersburg) **44**, 215 (2002) [Phys. Solid State **44**, 223 (2002)].
12. V. A. Kozlov and É. L. Nagaev, Pis'ma Zh. Éksp. Teor. Fiz. **13**, 639 (1971) [JETP Lett. **13**, 455 (1971)].
13. A. A. Bel'chik and V. A. Kozlov, Fiz. Tekh. Poluprovodn. (Leningrad) **20**, 53 (1986) [Sov. Phys. Semicond. **20**, 31 (1986)].
14. V. S. Oskotskiĭ, A. M. Pogarskiĭ, I. N. Timchenko, and S. S. Shalyt, Fiz. Tverd. Tela (Leningrad) **10**, 3247 (1968) [Sov. Phys. Solid State **10**, 2569 (1968)].
15. A. N. Taldenkov, A. V. Inyushkin, V. I. Ozhogin, *et al.*, in *Proceedings of IV Conference on Physicochemical Processes under Atom and Molecule Selection, Zvenigorod, 1999* (TRINITI, Troitsk, 1999), p. 243.
16. J. Callaway, Phys. Rev. **113**, 1046 (1959).
17. R. Berman, *Thermal Conduction in Solids* (Clarendon Press, Oxford, 1976; Mir, Moscow, 1979).
18. B. M. Mogilevskiĭ and A. F. Chudnovskiĭ, *Thermal Conductivity of Semiconductors* (Nauka, Moscow, 1972), p. 536.
19. S. Simons, Proc. Phys. Soc. London **82**, 401 (1963); Proc. Phys. Soc. London **83**, 799 (1963).
20. C. Herring, Phys. Rev. **95**, 954 (1954).
21. T. H. Geballe and G. W. Hull, Phys. Rev. **94**, 1134 (1954).
22. I. G. Kuleev and I. I. Kuleev, Zh. Éksp. Teor. Fiz. **120**, 1952 (2001) [JETP **93**, 568 (2001)].
23. I. G. Kuleev and I. I. Kuleev, Zh. Éksp. Teor. Fiz. **122**, 558 (2002) [JETP **95**, 480 (2002)].
24. L. É. Gurevich and I. Ya. Korenblit, Fiz. Tverd. Tela (Leningrad) **6**, 856 (1964) [Sov. Phys. Solid State **6**, 661 (1964)].
25. I. G. Lang and S. T. Pavlov, Zh. Éksp. Teor. Fiz. **63**, 1495 (1972) [Sov. Phys. JETP **36**, 793 (1973)].
26. I. G. Kuleev, Fiz. Met. Metalloved. **87**, 5 (1999).
27. I. G. Kuleev, Fiz. Tverd. Tela (St. Petersburg) **42**, 979 (2000) [Phys. Solid State **42**, 1009 (2000)].
28. E. Kaden and H.-L. Günter, Phys. Status Solidi B **126**, 733 (1984).
29. A. G. Samoilovich, I. S. Buda, and I. V. Dakhovski, Phys. Status Solidi **23**, 229 (1967).
30. A. G. Samoĭlovich and I. S. Buda, Fiz. Tekh. Poluprovodn. (Leningrad) **3**, 400 (1969) [Sov. Phys. Semicond. **3**, 340 (1969)].
31. R. Truel, C. Elbaum, and B. B. Chick, *Ultrasonic Methods in Solid State Physics* (Academic, New York, 1969; Mir, Moscow, 1972).

Translated by H. Bronstein

Journal of Experimental and Theoretical Physics, Vol. 96, No. 6, 2003, pp. 1089–1103.
Translated from Zhurnal Éksperimental'noĭ i Teoreticheskoĭ Fiziki, Vol. 123, No. 6, 2003, pp. 1239–1255.

SOLIDS
Structure

The Evolution of Longitudinal and Transverse Acoustic Waves in a Medium with Paramagnetic Impurities

A. A. Zabolotskii*

Institute of Automatics and Electrometry, Siberian Division, Russian Academy of Sciences, Universitetskii pr. 1, Novosibirsk, 630090 Russia

**e-mail: zabolotskii@okibox.iae.nsk.su*

Received December 10, 2002

Abstract—We study the bipartial interaction of longitudinal and transverse acoustic pulses with a system of paramagnetic impurities with an effective spin $S = 1/2$ in a crystalline layer or on a surface in the presence of an arbitrarily directed external constant magnetic field. We derive a new system of evolution equations that describes this interaction and show that, in the absence of losses, for equal phase velocities of these acoustic components, and under the condition of their unidirectional propagation, the original system reduces to a new integrable system of equations. The derived integrable system describes the pulse dynamics outside the scope of the slow-envelope approximation. For one of the reductions of the general model that corresponds to the new integrable model, we give the corresponding equations of the inverse scattering transform method and find soliton solutions. We investigate the dynamics and formation conditions of the phonon avalanche that arises when the initial completely or incompletely inverted state of the spin system decays. We discuss the application of our results to describing the interaction dynamics of spins and acoustic pulses in various systems with an external magnetic field. © *2003 MAIK "Nauka/Interperiodica".*

1. INTRODUCTION

At present, the nonlinear coherent optical phenomena associated with soliton and other self-similar solutions [1, 2] have been analytically studied in detail in terms of integrable models [3]. When elastic waves propagate in paramagnetic crystals, similar soliton-like pulses can be produced by effects related to anharmonic oscillations and dispersion [4] as well as under conditions of nonlinear coherent interaction between acoustic waves and paramagnetic impurities in the medium and in the case of acoustic self-induced transparency (ASIT) [5–8]. The nonlinear coherent phenomena associated with the acoustic paramagnetic resonance and the propagation of acoustic pulses have also been studied for a long time. In several studies (see, e.g., [5–10]), the authors constructed models for the evolution of acoustic pulses in bulk crystals with impurity paramagnetic particles and found the simplest soliton solutions. The coherent effects that arise during the evolution of Rayleigh-type surface acoustic waves were investigated in [6, 10] and other works. Such waves can propagate along the interface. Similar phenomena can be observed during the evolution of plane waves in bulk media [11–14].

As a rule, the authors of the above papers used an analogy between optical and acoustic effects. At the same time, the evolution of an acoustic pulse in a crystal with paramagnetic impurities has a number of qualitative distinctions from the dynamics of light waves in a medium, which stem, for example, from the fact that an acoustic wave in a crystal can be longitudinal–transverse, i.e., generally, a three-component one [7, 8]. The approximation of a quasi-monochromatic wave was used to find soliton solutions of the equations that described the surface acoustic waves in the papers known to us, except [7] and our paper [15]. In general, the characteristic length of an acoustic pulse is no less than 10^{-4} cm, i.e., much larger than the lattice constant. At the same time, for a picosecond acoustic pulse of duration $\tau_a \sim 10$ pc, its length is 10^{-7}–10^{-6} cm, and prospects for the physics and engineering of such ultrashort acoustic pulses look appealing. The spatial extent of such a pulse in a solid is only an order of magnitude larger than the characteristic size of the lattice cell, which is of fundamental interest in acoustic spectroscopy and diagnostics. Therefore, ideally, media with lengths of only hundreds or tens of characteristic lattice sizes can be used to produce such pulses. In spectral language, the passage to picosecond acoustic pulses implies mastering the hitherto inaccessible frequency range above 100 GHz. The concentration of acoustic energy for such short intervals also allows strong acoustic pressures exceeding 10^9 bars to be produced.

Recently [4], the generation of picosecond acoustic solitons has been observed experimentally. The solitons were formed at a distance much smaller than 1 mm due to the balance between the dispersion attributable to the positions of atoms in the crystal lattice and the nonlinearity that arose from the anharmonicity of interatomic forces. An acoustic resonance effect, an analogue of optical self-induced transparency, was observed in low-temperature crystalline samples with paramagnetic

impurities. This effect was observed on Fe^{2+} impurities in MgO [11] and $LiNbO_3$ [12] crystal matrices when the longitudinal acoustic pulse propagated at an angle to the external field.

In general, the group velocities of the longitudinal ($v_\parallel$) and transverse ($v_\perp$) components of an acoustic pulse in a solid are different. As a result, the local interaction between the pulses of these components with a characteristic length l_a is limited by the time

$$t_{\text{int}} \sim \frac{l_a}{v_\parallel - v_\perp}.$$

The interaction of the pulses is most effective at close group velocities, $v_\parallel \approx v_\perp$. This situation takes place in elastic-isotropic crystals, in which the velocities of the longitudinal and transverse elastic field components do not depend on the direction. These conditions are best satisfied for ion crystals of alkali metal galogenides with central forces of interatomic interaction, for example, in NaBr [16].

The theory of ASIT in a medium of paramagnetic impurities with spin 1/2 for longitudinal–transverse acoustic waves was developed by Voronkov and Sazonov [7, 8], who derived the equations describing the dynamics of acoustic pulses. These authors used several constraints on the interaction geometry and dynamics to solve the general evolution equations. As a result, they obtained complex (for analysis), exactly nonintegrable systems of equations and then reduced the problem either to the standard (sine-Gordon-type) equations or to the dispersion equations that corresponded to the evolution of low-amplitude pulses. The latter equations cannot be used to describe the dynamics of intense picosecond acoustic pulses.

At the same time, the rich structure of the evolution equations that describe the dynamics of acoustic waves in paramagnetic media makes it possible to reduce them, for quite realistic approximations, to integrable models without imposing similar stringent constraints. These equations not only can correspond to a more general physical model but also allow new physical phenomena in a similar or different interaction geometry to be described analytically. This paper is a continuation of our paper [15], in which we derived such integrable equations and used them to describe ASIT. Here, however, we consider a completely different interaction geometry of acoustic waves described by a different (than the system found in [15]) new original physical system of equations and, accordingly, by qualitatively new integrable reductions of this system.

In contrast to [15], in which we studied the interaction dynamics of three acoustic pulse components, here, we consider the "bipartial" dynamics of acoustic waves; i.e., we take into account the interaction of one transverse and one longitudinal acoustic wave component in the *xz* plane. The contribution of the *y* acoustic field component was disregarded. The simplest types of surface waves—bipartial Rayleigh surface waves and shear surface waves (see, e.g., [17])—can correspond to this case. Other physical prerequisites for the realization of this model in a bulk crystal can be associated with its strong anisotropy, for example, when the spin–phonon coupling coefficients that correspond to the *y* acoustic wave component are relatively small. Other conditions can be a similarity of the group velocities for the longitudinal and transverse waves and their large deviation from the group velocity of another transverse component (see below and [17]).

In this interaction geometry, we show that, to pass from the original evolution equations that describe the coherent dynamics of acoustic pulses to an integrable system of equations, it will suffice to use the approximation of unidirectional wave propagation and the condition of equal phase velocities for the longitudinal and transverse acoustic waves.

Since our new integrable system of evolution equations is complex for analysis, we developed the apparatus of the inverse scattering transform method (ISTM) [3] for its special case. The ISTM application to this model allows the various evolution regimes of picosecond acoustic pulses to be studied outside the scope of the slow-envelope approximation. Based on the ISTM, we found a soliton solution of the model that explicitly described, in particular, the dependence of the soliton shape on the relative contribution of the longitudinal and transverse components.

Apart from the soliton solutions associated with ASIT, other pulse evolution regimes can also be analyzed in terms of the ISTM. For example, an unstable state of the system arises in the case of initially complete or incomplete spin inversion, with a weak seed acoustic wave being sufficient to remove it from this state (in the case of complete inversion). We discuss the use of the ISTM to describe the emerging phonon avalanche that was observed experimentally [13, 14] and for other physical situations related to the dynamics of spin–phonon systems in a magnetic field.

This paper has the following structure. The basic system of evolution equations that describes the dynamics of a longitudinal–transverse wave is derived in the next section. The most general integrable reduction of the original system of equations for this system is found in Section 3. The ISTM apparatus for the reduction of the general model is developed in the next section, and a one-soliton solution of this model is found. In Section 5, we discuss our results and their applications. In the Appendix, we give the Lax representation for the general integrable model and integrable reductions of the general model.

2. THE DERIVATION OF BASIC EQUATIONS

Below, we derive the equations that describe the dynamics of a longitudinal–transverse wave in a crystal

with paramagnetic impurities following [7, 15]. The external constant and uniform magnetic field **B** is assumed to be directed along the *z* axis. The Zeeman interaction of the magnetic moment $\hat{\mu}^{(a)}$ at point *a* gives the following contribution to the total Hamiltonian:

$$\hat{H}_a = -\hat{\mu}^{(a)}\mathbf{B}.$$

The $\hat{\mu}^{(a)}$ components can be expressed in terms of the $\mathbf{S}^{(a)}(\mathbf{r}_a)$ spin components, where $\mathbf{r}_a$ is the radius vector of spin *a*, as

$$\hat{\mu}_j^{(a)} = -\sum_k \mu_B g_{jk} \hat{S}_k^{(a)}.$$

Here, μ_B is the Bohr magneton and g_{jk} are the Lande tensor components. Thus,

$$\hat{H}^z = \sum_{a=1}^{N} \hat{H}_a^z = \mu_B \sum_a \sum_{j,k} B_j g_{jk} \hat{S}_k^{(a)}, \quad (1)$$

where *N* is the total number of spins. The diagonal values of the Lande tensor can differ.

Since the effective spin is 1/2, it can be decomposed into Pauli matrices:

$$\hat{S}_x^a = \frac{1}{2}\begin{pmatrix} 0 & 1 \\ 1 & 0 \end{pmatrix}, \quad \hat{S}_y^a = \frac{1}{2}\begin{pmatrix} 0 & -i \\ i & 0 \end{pmatrix}, \quad \hat{S}_z^a = \frac{1}{2}\begin{pmatrix} 1 & 0 \\ 0 & -1 \end{pmatrix}. \quad (2)$$

We assume that the *x*, *y*, and *z* coordinates along the principal Lande tensor axes coincide with the crystal symmetry axes. The Lande tensor is then diagonal in a nondeformed unperturbed medium:

$$g_{jk} = g_{jk}^{(0)} = g_{jj}\delta_{jk},$$

where δ_{jk} is the delta function. The deformation of the crystal by an acoustic wave is described by linear corrections to the Lande tensor:

$$g_{jk} = g_{jk}^{(0)} + \sum_{p,q} \left(\frac{\partial g_{jk}}{\partial \mathscr{E}_{pq}}\right)_0 \mathscr{E}_{pq} + \ldots, \quad (3)$$

where $\mathscr{E}$ is the elastic strain tensor of the crystal at the spin location. The derivatives are taken at the point of zero deformation. The strain tensor components can be expressed in terms of the components of displacement vector $\mathbf{U} = (U_x, U_y, U_z)$ as

$$\mathscr{E}_{pq} = \frac{1}{2}\left(\frac{\partial U_p}{\partial x_q} + \frac{\partial U_p}{\partial x_p}\right). \quad (4)$$

Hamiltonian (1) takes the form

$$\hat{H}_s = \sum_\alpha \sum_j \mu_B g_{jj} B_j \hat{S}_j^{(a)}. \quad (5)$$

The spin–phonon interaction in the linear (in $\mathscr{E}_{pq}$) approximation is described by the Hamiltonian

$$\hat{H}_{\text{int}} = \sum_\alpha \sum_{j,k,p,q} \mu_B B_j F_{jk,pq} \mathscr{E}_{pq} \hat{S}_k^{(a)}. \quad (6)$$

Here, $F_{jk,pq} = (\partial g_{jk}/\partial \mathscr{E}_{pq})$ are the spin–phonon coupling constants [12, 18].

The dynamics of the acoustic field in a crystal without anharmonicity is described by the Hamiltonian

$$H_a = \int \left(\frac{1}{2n_0}\sum_j p_j^2 + \frac{1}{2}\sum_{j,k,l,m} \lambda_{jklm} \frac{\partial U_j}{\partial x_k}\frac{\partial U_l}{\partial x_m}\right) d\mathbf{r}, \quad (7)$$

where n_0 is the mean crystal density, p_j ($j = x, y, z$) are the momentum density components that arise during dynamic displacements, and λ_{jklm} is the elastic modulus tensor of the crystal [19]. The integral in (7) is taken over the crystal volume. We assume that the number of phonons is large and that the classical description of the acoustic-field dynamics is valid. At the same time, a two-level spin system requires a quantum-mechanical description. For $S = 1/2$ and in the presence of a sufficiently strong magnetic field, the terms quadratic in spin operators can be disregarded (for more detail, see [20]). Here, an analogy with the interaction of a classical electromagnetic field with an optical quantum two-level medium holds [21].

As in the case of an optical medium, we can pass from the description of the spin dynamics to the evolution equations for the density matrix elements $\hat{\rho}$ of the two-level medium:

$$i\hbar \frac{\partial \hat{\rho}}{\partial t} = [\hat{H}, \hat{\rho}], \quad (8)$$

$$\frac{\partial \mathbf{U}}{\partial t} = \frac{\partial H}{\partial \mathbf{p}}, \quad \frac{\partial \mathbf{p}}{\partial t} = -\frac{\partial H}{\partial \mathbf{U}}. \quad (9)$$

Here,

$$H = H_a + \langle \hat{H}_{\text{int}} \rangle,$$

where the interaction between the spin and the field of an elastic pulse is described by the classical Hamiltonian equations for a continuous medium:

$$\langle \hat{H}_{\text{int}} \rangle = \sum_\alpha \sum_{j,k,p,q} \mu_B B_j F_{jk,pq} \int \mathscr{E}_{pq}(\mathbf{r}) \langle \hat{S}_k^{(a)}(\mathbf{r}) \rangle d\mathbf{r}. \quad (10)$$

Here, *n* is the paramagnetic impurity density. The summation over the spin-1/2 ions uniformly distributed in the crystal is substituted with integration over the entire

space. The angular brackets denote an averaging over the quantum states:

$$\langle \hat{S}_k^{(a)}(\mathbf{r}) \rangle = \mathrm{Tr}\hat{S}_k^{(a)}\hat{\rho}.$$

We consider the bipartial dynamics of the acoustic fields; i.e., we assume that only the longitudinal and transverse field components ($\mathscr{E}_{xz}$ and $\mathscr{E}_{zz}$) contribute to the interaction. Such a situation is possible if the coefficients $F_{yx,\,zz}$ and $F_{yz,\,yz}$ are much smaller than the coefficients $F_{xz,\,zz}$, $F_{xz,\,xz}$, and $F_{zz,\,zz}$. A different mechanism that leads to quasi-two-dimensional dynamics can be associated with the difference between the elasticity coefficient λ_{yz} and the coefficients $\lambda_{xz} \approx \lambda_{zz}$. The phase velocities of the acoustic wave components are proportional to $\sqrt{\lambda_{yz}}$. Since the interaction efficiency in a nonlinear pulse regime is determined by the interaction length, for waves with almost equal phase velocities ($v_1 \approx v_2 \approx v$), this interaction is much more effective than the interaction with a wave whose phase velocity significantly differs from v. The "escape" of the acoustic wave component from the interaction region is also used to motivate the passage to the "bipartial" description of the dynamics of acoustic waves (see, e.g., [17]), i.e., with the contribution of the y acoustic wave component disregarded. Since, as we show below, the group velocities of the generated acoustic pulses in the models under study are close to the phase velocities, the restriction to the bipartial interaction is justified. Taking into account these conditions (see also the Introduction), we may formally set the transverse field component equal to zero ($\mathscr{E}_{yz} \equiv 0$).

We assume that the acoustic waves propagate along the z axis. The direction of the magnetic field **B** in space can be arbitrary. Since only the **B** projection onto the xz plane contributes to the interaction, we assume, without loss of generality, that

$$B = \sqrt{B_x^2 + B_z^2},$$

where B_j are the components of vector **B**. Under these conditions, the following arbitrary real effective spin–phonon coupling coefficients remain:

$$\begin{aligned} f_1 &= \frac{1}{B}\sum_{j=x,z} B_j F_{jz,\,xz}, \\ f_2 &= \frac{1}{B}\sum_{j=x,z} B_j F_{jz,\,zz}, \\ f_3 &= \frac{1}{B}\sum_{j=x,z} B_j F_{jx,\,xz}, \\ f_4 &= \frac{1}{B}\sum_{j=x,z} B_j F_{jx,\,zz}. \end{aligned} \tag{11}$$

Below, when deriving the general integrable system of equations, we impose no additional constraints on the coefficients f_k, $k = 1$–4. Given the above conditions, the expressions for $\hat{H}_s$ and $\hat{H}_{\mathrm{int}}$ take the form

$$\hat{H}_s = \int \sum_{\alpha} n\hbar\omega_B \hat{S}_z^{(\alpha)} d\mathbf{r}, \tag{12}$$

$$\begin{aligned} \hat{H}_{\mathrm{int}} = \int \sum_{\alpha} \frac{n\hbar\omega_B}{g} \\ \times \{(f_1\mathscr{E}_{zz} + f_2\mathscr{E}_{xz})\hat{S}_z^{(\alpha)} + (f_3\mathscr{E}_{xz} + f_4\mathscr{E}_{zz})\hat{S}_x^{(\alpha)}\} d\mathbf{r}. \end{aligned} \tag{13}$$

Here, $\omega_B = g\mu_B B/\hbar$ is the Zeeman splitting frequency of the Kramers doublet, $g = \|\hat{g}\|$, and n is the ion density in the medium. The coefficients f_k, $k = 1$–4, describe the coupling of the longitudinal and transverse acoustic fields with the spin system; the first two of these coefficients correspond to the frequency shift that depends on the acoustic-field amplitude. The physical nature of this shift can be different. By analogy with the case of an optical medium with a constant dipole moment described above (see [22]), the nonzero f_1 may result from the presence of a constant magnetic moment in the two-level medium. The mechanism described in [10] gives a similar contribution to the frequency shift.

Under the above symmetry conditions, the Hamiltonian H_a takes the form

$$\hat{H}_a = \frac{1}{2}\int \left\{ \frac{p_x^2 + p_z^2}{n_0} + \lambda_{11}\left(\frac{\partial U_z}{\partial z}\right)^2 + \lambda_{44}\left(\frac{\partial U_x}{\partial z}\right)^2 \right\} d\mathbf{r}. \tag{14}$$

Here, the Vogt notation [18] is used for the subscripts:

$$xx \longrightarrow 1, \quad zz \longrightarrow 3, \quad xz \longrightarrow 5.$$

Since the anharmonic effects are disregarded, there is no direct interaction between the longitudinal and transverse fields (it arises indirectly, only through their interaction with the spin system). This and the condition of equal phase velocities (see below) allow us to pass to a new effective transverse (or quasi-transverse [17]) field—a linear combination of the stress tensor components, which interacts with the x spin component (see Hamiltonian (13)):

$$\mathscr{W} = \mathscr{E}_{xz} + \frac{f_4}{f_3}\mathscr{E}_{zz}. \tag{15}$$

With this substitution, the interaction of the acoustic field $\mathscr{W}$ with a two-level spin medium (see formula (8)) is described by the Hamiltonian

$$\hat{H}_s + \hat{H}_{\mathrm{int}} = \int \frac{n\hbar\omega_B}{g}[\sigma_3(g + f\mathscr{E}_{zz}) + f_3\hat{v}\mathscr{W}]d\mathbf{r}, \tag{16}$$

where

$$f = f_2 - \frac{f_1 f_4}{f_3}.$$

The effective magnetic operator moment $\mu_B \hat{\nu}$, where

$$\hat{\nu} = \begin{pmatrix} a & 1 \\ 1 & -a \end{pmatrix} \tag{17}$$

and $a = f_1/f_3$ is the constant magnetic moment, corresponds to the last term in (16).

Using (8)–(10) and (16), we derive the equations of motion for the components of spin S describing the transitions in an effective two-level medium arising during Zeeman splitting:

$$\frac{\partial}{\partial t} S_z = \frac{f_3}{\hbar} \mathcal{W} S_y,$$

$$\frac{\partial}{\partial t} S_y = \left(\omega_B + \frac{f}{\hbar} \mathcal{E}_{zz} + \frac{f_1}{\hbar} \mathcal{W} \right) S_x - \frac{f_3}{\hbar} \mathcal{W} S_y, \tag{18}$$

$$\frac{\partial}{\partial t} S_x = -\left(\omega_B + \frac{f}{\hbar} \mathcal{E}_{zz} + \frac{f_1}{\hbar} \mathcal{W} \right) S_y,$$

where

$$S_\gamma = \mathrm{Tr} \hat{S}_\gamma^{(a)} \hat{\rho}, \quad \gamma = x, y, z,$$

i.e.,

$$S_z = \frac{1}{2}(\rho_{11} - \rho_{22}), \quad S_x = \frac{1}{2}(\rho_{12} + \rho_{21}),$$

$$S_y = \frac{i}{2}(\rho_{12} - \rho_{21}).$$

It is easy to show that

$$S_z^2 + S_x^2 + S_y^2 = (\rho_{11} + \rho_{22})^2 \equiv 1 \tag{19}$$

(here, the spin length was normalized to unity). In deriving system (18), we assume that the classical description of the acoustic field (the number of phonons is large) is valid.

To derive the evolution equations that describe the dynamics of the classical fields (linear combinations of the stress tensor components) $\mathcal{W}$ and $\mathcal{E}_{zz}$, we first obtain the wave equations for the displacements U and then differentiate them with respect to z and use the expressions for these fields in terms of the differentials of the displacements with respect to z that follow from definition (4). We also assume that the phase velocities that correspond to the displacement components U_z and U_x are equal. As a result, we obtain the system of evolution equations for the acoustic fields with averaging over the quantum states

$$\frac{\partial^2 \mathcal{W}}{\partial t^2} - v_1^2 \frac{\partial^2 \mathcal{W}}{\partial z^2} = \frac{n\hbar\omega_B f_3}{g n_0} \frac{\partial^2 \mathrm{Tr} \hat{\nu} \hat{\rho}}{\partial z^2}, \tag{20}$$

$$\frac{\partial^2 \mathcal{E}_{zz}}{\partial t^2} - v_2^2 \frac{\partial^2 \mathcal{E}_{zz}}{\partial z^2} = \frac{2n\hbar\omega_B f}{g n_0} \frac{\partial^2 S_3}{\partial z^2}, \tag{21}$$

where

$$v_1 = \sqrt{\frac{\lambda_{11}}{n_0}} = v_2 = \sqrt{\frac{\lambda_{44}}{n_0}}.$$

On the right-hand side of (20),

$$\mathrm{Tr} \hat{\nu} \hat{\rho} = 2aS_z + 2S_x.$$

The derived new system of evolution equations (18)–(21) describes the propagation of acoustic pulses in a two-level medium. In the Bloch equations (18), the longitudinal acoustic field component $\mathcal{E}_{zz}$ leads only to nonlinear phase modulation. However, as we show below, the longitudinal component is related to the transverse component and its allowance leads to qualitatively new acoustic-pulse dynamics.

3. THE DERIVATION OF A GENERAL INTEGRABLE MODEL

In this section, we derive the most general integrable reduction of the basic system of equations (18)–(21), which arises for a minimum number of physical constraints. To be more precise, we find the reduction of the physical system of nonlinear equations (18)–(21) derived above in the Lax representation and show that the ISTM apparatus is applicable.

Above, we have already assumed that the phase velocities of the effective longitudinal and transverse acoustic waves are equal:

$$v_1 = v_2 = v.$$

We seek additional integrability conditions by assuming that the reduction of the original system (18)–(21) must describe the dynamics of acoustic pulses with a duration of the order of or shorter than $\pi\omega_B^{-1}$. Under this condition, the slow-envelope approximation is inapplicable. As was noted above, in real media, picosecond acoustic pulses can correspond to this case. We also disregard the relaxation effects, which is valid for the chosen range of pulse durations.

The equations that describe the dynamics of such pulses are complex for analysis, but system (20) and (21) can be simplified at a sufficiently low density of

paramagnetic impurities. Such a physical situation takes place in all of the known cases. This approximation is similar to the approximation used in [23] to derive the reduced Maxwell–Bloch equations for a two-level optical medium and is called the condition of unidirectional wave propagation. The latter condition corresponds to the following approximate formal equality:

$$\partial_z \approx -v^{-1}\partial_t + O(\epsilon),$$

where ϵ is a small parameter. Physically, this means that the acoustic pulses propagate in the medium at a velocity close to the phase velocity v. The fulfillment condition for the approximation is that the normalized impurity density is of the same order of smallness as the derivative of the acoustic-field amplitudes

$$\partial_{\tilde{\chi}} = \partial_z + v^{-1}\partial_t.$$

In this approximation, the derivative with respect to z on the right-hand sides of Eqs. (20) and (21) can be substituted with $v^{-1}\partial_t$ with an accuracy $O(\epsilon^2)$. Thus, when the condition of unidirectional acoustic pulse propagation is satisfied, system (20) and (21) reduces to

$$\frac{\partial \mathcal{W}}{\partial \tilde{\chi}} = \frac{n\hbar\omega_B f_3}{2v^2 n_0 g}\frac{\partial \mathrm{Tr}(\hat{v}\hat{\rho})}{\partial t}, \tag{22}$$

$$\frac{\partial \mathcal{E}_{zz}}{\partial \tilde{\chi}} = \frac{n\hbar\omega_B f}{v^2 n_0 g}\frac{\partial S_3}{\partial t}. \tag{23}$$

Here, we chose $f \neq 0$. The case $f \longrightarrow 0$ is discussed in the Appendix. When calculating the derivatives with respect to t, we take into account the Bloch equations (18) and reduce Eqs. (22) and (23) to

$$\frac{\partial \mathcal{W}}{\partial \tilde{\chi}} = -\frac{n\hbar\omega_B f f_3}{v^2 n_0 g}\left(\frac{\hbar\omega_B}{f} + \mathcal{E}_{zz}\right)S_y, \tag{24}$$

$$\frac{\partial \mathcal{E}_{zz}}{\partial \tilde{\chi}} = \frac{n\hbar\omega_B f f_3}{v^2 n_0 g}\mathcal{W} S_y. \tag{25}$$

It is now easy to find from Eqs. (24) and (25) that the amplitudes of the longitudinal and effective transverse fields are related by

$$\mathcal{W}^2 + \left(\mathcal{E}_{zz} + \frac{\omega_B\hbar}{f}\right)^2 = U_0^2(t). \tag{26}$$

Here, the arbitrary real function $U_0(t) \neq 0$ is determined by the boundary conditions. The dependence of U_0 on t leads only to a renormalization of the variable t and the functions $\mathcal{E}_{zz}$ and $\mathcal{W}$. It follows from (26) that $\forall t$ $U_0(t) \neq 0$ and the ISTM apparatus developed for an infinite interval can be used. On the other hand, acoustic solitons and other coherent structures can be formed in crystals less than one millimeter in thickness [4]. Therefore, we can easily create conditions under which the interval where

$$U_0(t) \neq \frac{\omega_B\hbar}{f}$$

is much larger than the formation time scales of solitons and other nonlinear structures.

Using (26), we obtain a new integrable system of evolution equations from (18), (24), and (25):

$$\begin{aligned} \partial_\chi E &= -bUS_y, \\ \partial_\tau S_y &= (aE + bU)S_x - ES_z, \\ \partial_\tau S_x &= -(aE + bU)S_y, \\ \partial_\tau S_z &= ES_y. \end{aligned} \tag{27}$$

Here, all functions are real and

$$E(\chi, \tau) = \frac{\mathcal{W}(\chi, \tau)}{U_0(t)}, \quad U^2(\chi, \tau) + E^2(\chi, \tau) = 1,$$

$$\chi = \tilde{\chi}\frac{n\omega_B f_3^2}{gn_0 v^2}, \quad \tau = \frac{f_3}{\hbar}\int_0^t U_0(t')dt', \quad b = \frac{f}{f_3}.$$

The representations of this system as a condition for the simultaneity of two linear systems with an arbitrary (spectral) parameter are given in the Appendix. It is also pointed out in the Appendix that system (27) is complex enough for the ISTM to be applied. Therefore, here, we restrict our analysis to its physically interesting reduction that arises if we set $a = 0$. This reduction, probably, also corresponds to the new integrable system of equations.

4. THE ISTM APPARATUS FOR $a = 0$

The condition $a = 0$ implies that the contribution of the effective transverse acoustic field to the frequency modulation of the density matrix component ρ_{12} is disregarded. Such a physical situation arises if the x and z coordinates along the principal Lande tensor axes coincide with the crystal symmetry axes. In this case, the Lande tensor is diagonal in a nondeformed unperturbed medium. The magnetic field **B** is assumed to be directed along the z axis, i.e., along the axis of propagation of the acoustic waves.

We solve the problem on the entire axis for a rapidly decaying field at infinity:

$$E(\tau) \longrightarrow 0, \quad \tau \longrightarrow \pm\infty.$$

We assume that the spin system at the initial and final times is in a stable ground state corresponding to mini-

mum energy, i.e.,

$$S_z(\tau, \chi) = -1, \quad \tau \longrightarrow \pm\infty.$$

A pulse of acoustic field $E(\tau, 0)$ with an area large enough for the formation of solitons is assumed to be injected into the crystal. To describe the corresponding soliton dynamics, it is convenient to choose the following Lax representation for the system of equations (27) at $a = 0$:

$$\partial_\tau \Phi = \begin{pmatrix} -i\lambda U & (\lambda+\beta)E \\ -(\lambda-\beta)E & i\lambda U \end{pmatrix}\Phi = \hat{L}_0\Phi, \quad (28)$$

$$\partial_\chi \Phi = \frac{b}{b^2 - 4\lambda^2} \times \begin{pmatrix} -i\lambda S_z & (\lambda+\beta)(bS_x - 2i\lambda S_y) \\ (\beta-\lambda)(2i\lambda S_y + bS_x) & i\lambda S_z \end{pmatrix}\Phi = \hat{A}_0\Phi. \quad (29)$$

Here,

$$U^2 + E^2 = 1, \quad \beta = \frac{1}{2}\sqrt{b^2 - 1},$$

where λ is the spectral parameter.

The spectral problem (28) for real fields may be considered to be related to the problems for complex fields that arise when solving the integrable Landau–Lifshitz equations [24] and the equations of Raman scattering or four-wave mixing [25] in terms of the ISTM. The ISTM apparatus for these problems has been developed in sufficient detail. Soliton and periodic solutions were found for these related models. Previously [26], we found an expression that defined the quasi-self-similar asymptotics describing the decay of an initial unstable state. Given the specifics attributable to the fact that the field E is real and that the problem is symmetric, these results can be used for model (28) after appropriate modification.

The solutions of the spectral problem (28) have the involution

$$\Phi = \hat{M}\Phi(\lambda^*)^*\hat{M}^{-1}, \quad (30)$$

where

$$\hat{M} = \begin{pmatrix} 0 & \kappa \\ -1 & 0 \end{pmatrix}, \quad \kappa = \begin{cases} \dfrac{\lambda+\beta}{\lambda-\beta}, & |b| > 1, \\ 1, & |b| \le 1. \end{cases} \quad (31)$$

In finding soliton solutions, we should determine the stable ground state of the system against the background of which the solitons propagate. Consider the regime in which the asymptotic limits $\tau \longrightarrow \pm\infty$ correspond to the stable ground states that, in turn, correspond to a zero field, $E(\chi, \tau) = 0$. These states are different for different $|b|$. It is easy to show that the following ground states of the system are stable in the linear approximation:

$$E = 0, \quad S_3 = \pm 1, \quad S_+ = 0, \quad S_- = 0, \quad |b| > 1, \quad (32)$$

$$E = 0, \quad S_3 = -1, \quad S_+ = 1, \quad S_- = 0, \quad |b| < 1, \quad (33)$$

$$ES_3 = -S_+U, \quad S_- = 0, \quad |b| = 1. \quad (34)$$

For $|b| = 1$, the ground state (34) is indifferently stable.

For a potential that vanishes at infinity ($\tau = \pm\infty$), we introduce the Jost function $\Psi^\pm$ in a standard way (the solutions of (28) with asymptotics):

$$\Psi^\pm = \exp(-i\lambda\sigma_3\tau), \quad \tau \longrightarrow \pm\infty, \quad |b| < 1, \quad (35)$$

$$\Phi^\pm = \begin{pmatrix} 1 & \dfrac{\xi}{\beta-\lambda} \\ \dfrac{\xi}{\beta+\lambda} & 1 \end{pmatrix}\exp(-i\lambda\sigma_3\tau), \quad \tau \longrightarrow \pm\infty, \quad |b| > 1. \quad (36)$$

The symmetry properties (30) and (31) correspond to the following matrix form of the Jost functions:

$$\Psi^\pm = \begin{pmatrix} \psi_1^\pm & -\psi_2^{\pm *}\kappa \\ \psi_2^\pm & \psi_1^{\pm *} \end{pmatrix}.$$

These solutions are related by the scattering matrix $\hat{T}$:

$$\Psi^- = \Psi^+\hat{T}. \quad (37)$$

It follows from the symmetry properties (30) and (31) that the scattering matrix can be chosen in the form

$$\hat{T} = \begin{pmatrix} \mathcal{A}^* & \mathcal{B}\kappa \\ -\mathcal{B}^* & \mathcal{A} \end{pmatrix}. \quad (38)$$

The Jost functions have standard analytical properties (cf., e.g., [27]). The function $a(\lambda)$ is holomorphic in the upper half-plane λ, where its zeros correspond to the soliton solutions.

Let us represent the Jost functions as

$$\Psi^+(\tau) = \exp(-i\lambda\sigma_3\tau) + \int_\tau^\infty \begin{pmatrix} \lambda K_1(\tau, s) & (\lambda+\beta)K_2(\tau, s) \\ -(\lambda-\beta)K_2^*(\tau, s) & \lambda K_1^*(\tau, s) \end{pmatrix} \times \exp(-i\lambda\sigma_3 s)\,ds. \quad (39)$$

It follows from system (37) that

$$\psi_1^{+*} = \frac{\psi_1^{-*}}{\mathcal{A}} - \frac{\mathcal{B}}{\mathcal{A}}\kappa\psi_2^{+}, \tag{40}$$

$$\psi_2^{+*} = -\frac{\psi_2^{-*}}{\mathcal{A}} + \frac{\mathcal{B}}{\mathcal{A}}\psi_1^{+}. \tag{41}$$

We substitute the components of these functions from (39) into (40) and (41) and integrate the resulting equations (40) and (41) over λ from $-\infty$ to ∞ with the weights $\exp(-i\lambda y)[2\pi(\lambda - \beta)]^{-1}$ and $\exp(-i\lambda y)(2\pi\lambda)^{-1}$, respectively. As a result, we obtain the Marchenko equations for the right end of the axis ($y \geq \tau$):

$$K_2^*(\tau, y) = F_\beta(\tau + y) + i\int_\tau^\infty K_1(\tau, s) i\partial_y F_\beta(s + y) ds, \tag{42}$$

$$K_1^*(\tau, y) = -\int_\tau^\infty K_2(\tau, s)(\pm\beta + i\partial_y) F_0(s + y) ds. \tag{43}$$

On the right-hand side of Eq. (43), the plus (+) and minus (–) signs in front of β correspond to $b^2 > 1$ and $b^2 < 1$, respectively. The kernel F_β is defined as

$$F_\beta(y) = \int_{\mathcal{C}} \frac{\mathcal{B}(\chi)}{\mathcal{A}(\chi)} \frac{e^{-i\lambda y}}{2\pi(\lambda - \beta)} d\lambda, \tag{44}$$

where $\mathcal{C}$ is the contour that includes the real axis and that passes above all poles in the upper half of the complex plane, $F_0 = F_\beta$ ($\beta = 0$).

Given the residues at poles λ_k in the upper half-plane, the kernel F_0 can be represented as

$$F_\beta(y) = \int_{-\infty}^{\infty} \frac{\mathcal{B}}{\mathcal{A}} \frac{e^{-i\lambda y}}{2\pi(\lambda - \beta)} d\lambda - i\sum_k \frac{\mathcal{B}}{\partial_\lambda \mathcal{A}(\lambda = \lambda_k)} \frac{e^{-i\lambda_k y}}{\lambda_k - \beta}. \tag{45}$$

The Marchenko equations for the left end of the axis (for y $y \leq \tau$) can be found in a similar way. Using the results obtained below, we can then easily show that the corresponding solutions are joined at $y = \tau$ (for more detail, see [27]).

Substituting expression (39) for Ψ^+ into the spectral problem (28) and equating the expressions for different powers of λ yields, in particular,

$$K_2(\tau, \tau)[1 + U(\tau)] = E(\tau)[1 - iK_1(\tau, \tau)]. \tag{46}$$

Using this relation, we can easily find a relationship between the potential F_3 and the kernels $K_{1,2}$ in the form

$$E(\tau) = \frac{2[1 - iK_1(\tau, \tau)]K_2^*(\tau, \tau)}{[1 + iK_1^*(\tau, \tau)][1 - iK_1(\tau, \tau)] + |K_2(\tau, \tau)|^2}. \tag{47}$$

4.1. A One-Soliton Solution of the Model for $|b| < 1$

The soliton solutions associated with ASIT describe the propagation of acoustic pulses without any change of their shape against the background of a stable ground state. This state for system (28) at $|b| < 1$ is (33). The condition for the field E being real imposes constraints on the soliton parameters. In particular, the discrete eigenvalues must either be imaginary or enter into the form of anticonjugate pairs $\{\lambda, -\lambda^*\}$.

Let us find the one-soliton solution of the problem associated with the only eigenvalue λ. We represent the kernel F that corresponds to this value of $\lambda = i\eta$ as

$$F_\beta(y) = \frac{iC_1(\chi)\exp(-i\lambda y)}{\eta - \beta_0}. \tag{48}$$

Here,

$$\beta = i\beta_0, \quad \mathrm{Im}\beta_0 = 0.$$

The dependence of the real quantity

$$C_1 = \left.\frac{\mathcal{B}(\chi; \lambda)}{\partial_\eta \mathcal{A}(\chi; \eta)}\right|_{\eta = \lambda}$$

on χ is derived below.

To solve the Marchenko equations, we introduce new functions:

$$Q_n(\tau) = \int_\tau^\infty K_n(\tau, s) e^{-i\lambda s} ds, \quad n = 1, 2.$$

Substituting these functions into the Marchenko equations (43) and (44) and integrating them over y yields

$$K_1(z, z) = \frac{-i|\gamma_1|^2 \exp(4\eta z)}{2\eta^2[1 + |\gamma_1(\chi)|^2 \exp(4\eta z)]}, \tag{49}$$

$$K_2(z, z) = \frac{C_1 \exp(2\eta z)}{(\eta - \beta_0)[1 + |\gamma_1(\chi)|^2 \exp(4\eta z)]}, \tag{50}$$

where we denoted

$$\gamma_1(\chi) = \frac{C_1(\chi)}{2\eta}.$$

Next, it is necessary to find the function $C_0(\chi)$, which can be determined from system (29) for

$$S_z(\pm\infty, \chi) \equiv -1, \quad E(\pm\infty, \chi) = 0.$$

In a more general case, for the time interval $[\tau_0, \infty]$, this function can be found by using the formula (see [26] and the derivation in [27])

$$\partial_\chi \hat{T} = -\hat{T}\hat{V}_0\hat{A}_s(\tau_0, \chi)\hat{V}_0^{-1} + \hat{V}_\infty\hat{A}_s(\infty, \chi)\hat{V}_\infty^{-1}\hat{T}. \quad (51)$$

Here, $\hat{V}_0$ and $\hat{V}_\infty$ are the matrices composed of the eigenvectors, the solutions of problem (27) that were found at the initial time τ_0 and for $\tau = \infty$, respectively. Let

$$E(\tau, 0) = 0, \quad \tau = \tau_0, \infty,$$

then

$$\hat{V}_0 = \hat{V}_+ = \exp(-i\sigma_3\lambda\tau), \quad \tau = \tau_0, \infty.$$

Hence, for the chosen initial and boundary conditions that correspond to soliton dynamics, we obtain

$$\gamma_1(\chi) = \gamma_0\exp\left(\frac{-2b\chi\eta}{4\eta^2 + b^2}\right), \quad (52)$$

where γ_0 is a constant. Using (47), (49), (50), and (52), we find a one-soliton solution of model (28) for $a = 0$ in the form

$$E(\tau, \chi) = \frac{4\gamma_0\eta(\eta - \beta_0)(1 + |\gamma_0|^2 e^{2\phi})e^{\phi}}{(\eta - \beta_0)^2[1 + |\gamma_0|^2 e^{2\phi}]^2 + (2|\gamma_0|\eta)^2 e^{2\phi}}, \quad (53)$$

where

$$\phi = 2\eta\left(\tau - \frac{b\chi}{b^2 + 4\eta^2}\right).$$

We see from solution (53) that the soliton shape and velocity depend on the coefficient b. The soliton velocity decreases with increasing b, starting from the phase velocity v in the medium. At $b \sim 2\eta$, the velocity reaches a minimum and then again tends to the phase velocity. In Fig. 1, the soliton amplitude $E(\tau)$ is plotted against τ for different values of b. We see from the figure that $E(\tau)$ has a dip to zero at the center. As b decreases, a breakup into a soliton and an antisoliton whose separation tends to infinity when $b \longrightarrow 0$ takes place.

It also follows from formula (50) that the normalized soliton amplitude does not exceed unity. Therein lies an important difference between the acoustic-field

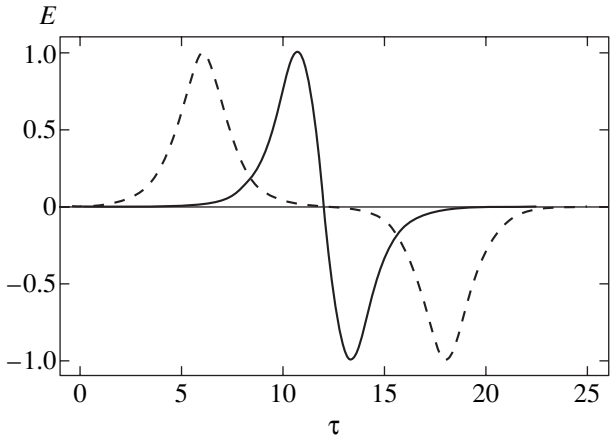

Fig. 1. The amplitude of the effective transverse acoustic pulse component E versus τ. The solid line corresponds to $b = 0.9$, and the dashed line corresponds to $b = 0.1$ and $\eta = 0.5$. The soliton position on the τ axis is arbitrary.

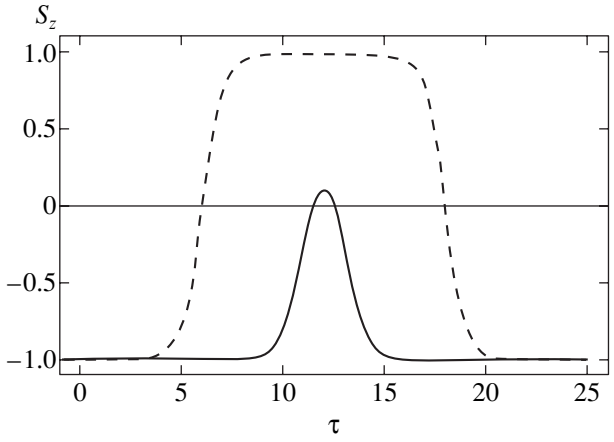

Fig. 2. The amplitude of the level population difference versus τ for a soliton regime. The solid and dashed lines correspond to $b = 0.9$ and 0.1, respectively.

dynamics in our model and the dynamics studied, e.g., in [5]. The soliton solution (53) describes the energy transfer between the longitudinal and transverse field components caused by the interaction with the spin system. In Fig. 2, the level population difference is plotted against τ.

4.2. The Decay of an Inverted Initial State of the Spin System

A completely inverted spin system is unstable and tends to a stable ground state after the action of a weak perturbation. This dynamics in nonlinear two-level optical media is described by the self-similar asymptotic solution. In [26], we showed that the asymptotic behavior of the fields in the case of Raman scattering for general initial and boundary conditions is described by a complex first-order differential equation with the right-hand side proportional to a known function. This

function can be expressed in terms of the solution to the transcendental Painleve equation of the third type (P_{III}) [28]. The solution corresponds to the nonsoliton, radiation dynamics associated with the continuum of the corresponding spectral problem. Following the results of [26], we can show that this dynamics is characteristic of arbitrary $S_\gamma(\chi, 0)$ slowly changing with χ and a sufficiently small seed acoustic field pulse $|E(\tau, 0)| \ll 1$. For such small field amplitudes and its derivatives, it is easy to determine the scattering coefficient

$$\rho(\chi; \lambda) = \frac{\mathcal{B}(\chi; \lambda)}{\mathcal{A}(\chi; \lambda)}$$

at $\chi = 0$ by using the spectral problem (28):

$$\begin{aligned}\rho(0; \lambda) = \rho_0 &= \frac{\mathcal{B}(0; \lambda)}{\mathcal{A}(0; \lambda)} \\ &\approx \frac{-\lambda}{2}\int_{-\infty}^{\infty} E^*(\tau, 0)e^{2i\lambda\tau}d\tau.\end{aligned} \tag{54}$$

If $E(\tau, 0) = \text{const}$, then the scattering coefficient ρ_0 does not depend on λ.

We solve the initial-value (for $\chi = 0$) problem with the trivial boundary conditions that correspond to an unstable (at $\tau = 0$) state (complete inversion) and a small (seed) acoustic deformation of the crystal:

$$|E(\tau, 0)| = \text{const} \ll 1, \quad S_z(0, \chi) = 1. \tag{55}$$

The seed field $E(\tau, 0)$ causes this state to decay and the system tends to a stable state,

$$E = 0, \quad S_z(0, \chi) = -1,$$

which is reached for $\chi \longrightarrow \infty$.

The scattering coefficient $\rho_0(\chi)$ depends on λ. Let us calculate the kernel F (45) by taking into account the dependence of the scattering data on χ and conditions (55), i.e., with the discrete spectrum disregarded. For the initial and boundary conditions (55), it will suffice to take into account the contribution of only the continuous spectrum of the problem. The dependence $\rho(\chi)$ can be determined by using expression (51):

$$\rho(\chi) = \rho_0 \exp\left(\frac{2ib\chi\lambda}{b^2 - 4\lambda^2}\right). \tag{56}$$

Let us now find the linear solution of the problem that corresponds to the initial stage of the decay of an inverted state and the formation of a phonon avalanche. Since, as we show below, the range of large $|\lambda|$ mainly contributes to the solution, we assume that $4|\lambda|^2 \gg b^2$. To calculate the kernels, we introduce a new integration variable on the right-hand side of (45),

$$\lambda = \frac{i\nu}{2\sqrt{b\chi/\tau}},$$

and reduce it to the form

$$\begin{aligned}F_\beta(\chi, \tau) &= \frac{\rho_0}{2\pi}\int_{-\infty}^{\infty}\frac{\exp[(\vartheta/2)(\nu - 1/\nu)]}{\nu - 2\beta_0\sqrt{\tau/b\chi}}d\nu \\ &\approx i\rho_0\left[I_0(\vartheta) + 2\beta_0\sqrt{\frac{\tau}{b\chi}}I_1(\vartheta) + \ldots\right],\end{aligned} \tag{57}$$

where $I_{0,1}$ are modified Bessel functions and $\vartheta = \sqrt{4b\chi\tau}$. We assumed that

$$4\beta_0\sqrt{\tau/b\chi} \ll 1.$$

It follows from (42), (47), and (57) that the field amplitude increases at the linear stage:

$$E(\chi, \tau) \approx 2K_2(\chi, \tau, \tau) \approx 2F_\beta(\chi, 2\tau) \sim \rho_0 e^\vartheta. \tag{58}$$

Another conclusion that follows from the derived expressions for kernel (57) is that the solution for the acoustic field is concentrated in the range $\vartheta \gg 1$ for small ρ_0 such that $-\ln|\rho_0| \gg 1$. In this range, the integrals in the Marchenko equations (41) and (43) can be approximately calculated by the saddle-point method. It follows from the Marchenko equations that the kernels $K_{1,2}$ exponentially increase with τ at the initial stage; i.e., the solution for $|E|$ can reach values of the order of unity for arbitrarily small seed field amplitudes $E(0, \tau)$.

Complete spin inversion can be achieved by using sufficiently strong laser radiation [13]. Incomplete initial inversion of the medium, i.e.,

$$-1 < S_z(0, \chi) < 1,$$

corresponds to a more general situation. In this case, a mixed initial-value–boundary-value problem arises on the semiaxis ($\tau \in [0, \infty)$), whose solution is much more complex than the cases where $S_z(0, \chi) = \pm 1$. For some of the nonlinear systems of equations, this problem was solved in the case where $E(\tau, 0) = 0$ (the Dirichlet problem [26, 29]; see also the method for solving a more general problem in [30, 31]).

Below, we use the results of [26] to find the asymptotic solution of the Dirichlet problem that is applicable to describing the dynamics of the phonon and spin avalanches that arise under the following initial and boundary conditions:

$$\begin{aligned}S_z(0, \chi) \equiv S_z(0, 0) &= S_x^{(0)}, \\ S_x(0, \chi) \equiv S_x(0, 0) &= S_x^{(0)}, \\ S_y(0, \chi) \equiv 0, \quad E(\tau, 0) &\equiv 0.\end{aligned} \tag{59}$$

To this end, following [26], we will reduce the spectral problem (28) to the Zakharov–Shabat problem [3] by a

simple gauge transformation of the form

$$\Psi \longrightarrow \hat{D}^{-1}\Phi, \quad \hat{L}_0 \longrightarrow \hat{D}\hat{L}_0\hat{D}^{-1} - \hat{D}\partial_\tau\hat{D}^{-1}, \qquad \hat{D} = \hat{I}\cos(\nu/2) + i\hat{\sigma}_1\sin(\nu/2). \tag{60}$$

Here, $\hat{I}$ and $\hat{\sigma}_1$ are the unit and Pauli matrices, respectively. We use the following notation:

$$E = \sin\nu, \quad U = \cos\nu.$$

Transformation (60) reduces the spectral problem (28) to

$$\partial_z\Psi = \begin{pmatrix} -i\lambda & V \\ -V^* & i\lambda \end{pmatrix}\Psi \equiv L_1\Psi, \tag{61}$$

$$V(\chi, \tau) = \frac{i}{2}(\sqrt{1-b^2}\sin\nu + \partial_\tau\nu), \tag{62}$$

where we assume that $b^2 < 1$. The solution of the problem reduced to analyzing a simpler spectral problem and restoring E from the known solution $V(\tau, \chi)$ using (62).

The Marchenko equations for the Zakharov–Shabat problem are well known (for more detail, see [3]). They are given in the Appendix for reference. For an arbitrarily inverted medium at the initial time ($S_x^{(0)} \neq 0$), the scattering coefficient $\rho(\chi)$ and the kernels in the Marchenko equations can be calculated by the asymptotic method suggested in [26]. To determine the dependence of the scattering data on χ using formula (51), we should find the values of the matrix

$$\hat{A}_0'(\tau) = \hat{V}_\tau(\hat{D}\hat{A}_0\hat{D}^{-1} - \hat{D}\partial_\tau\hat{D}^{-1})\hat{V}_\tau^{-1} \tag{63}$$

at the ends of the interval ($\tau = 0, \infty$). In [26], we showed that the large $|\lambda| \gtrsim |\lambda_a|$, i.e., in the case under consideration, $|\lambda_a| \gg b, \sqrt{1-b^2}/2$, mainly contributed to the radiation asymptotic solution. For this asymptotics and conditions (59), the components of matrix $\hat{A}_0'$ are

$$[A_0'(0)]_{11} = -[A_0'(0)]_{22} \approx \frac{ibS_z^{(0)}}{4\lambda},$$
$$[A_0'(0)]_{21} = -[A_0'(0)]_{12} \approx \frac{bS_x^{(0)}}{4\lambda},$$
$$[A_0'(\infty)]_{11} = -[A_0'(\infty)]_{22} \approx \frac{-ib}{4\lambda},$$
$$[A_0'(0)]_{12} = (-[A_0'(\infty)]_{21}) = 0. \tag{64}$$

These boundary conditions give rise to an infinite series of $\rho(\chi)$ poles whose positions depend on χ. To find the solution for nonsmall χ, we should determine the total contribution of all these poles. For sufficiently large χ, the kernels F_r in the Marchenko equations (76) and (77) can be calculated asymptotically in the same way as was done in [26] for a different problem. Using the results of [26], after modification associated with the values of matrix $\hat{A}_0'$ at zero, it is easy to show that the kernel F_r for conditions (59) and large χ is

$$F_r(\tau + \tau', \chi) = \frac{2\chi b|S_x^{(0)}|}{\theta'[\Omega_0 + |S_z^{(0)}|]^2}I_1(\theta'), \tag{65}$$

where

$$\theta' = \sqrt{2(\tau + \tau')b\chi}, \quad \Omega_0 = [1 - S_x^{(0)2}(1-b^2)]^{1/2},$$

I_1 is a Bessel function. This kernel corresponds to the condition

$$\pi/2 > \alpha_0 > \pi/4, \quad S_x^{(0)} = \sin\alpha_0.$$

For $\pi/4 \geq \alpha_0 > 0$, we should substitute $I_1 \longrightarrow J_1$.

For this kernel, in [26], we found a solution to the Marchenko equations (76) and (77) and an explicit solution for $V(\tau, \chi)$ composed of a set of oscillations that were damped with increasing χ. This solution, to within the factor χ, is a self-similar solution that depends on the variable $\theta = 2\sqrt{b\tau\chi}$.

In the limit $b \longrightarrow 1$, the asymptotic solution for the acoustic-wave amplitude is described by the equation

$$\partial_\tau\nu = \frac{8b\chi}{\theta}\mathcal{B}(\theta), \tag{66}$$

where $\mathcal{B}(\theta)$ is the self-similar solution of the sine-Gor-

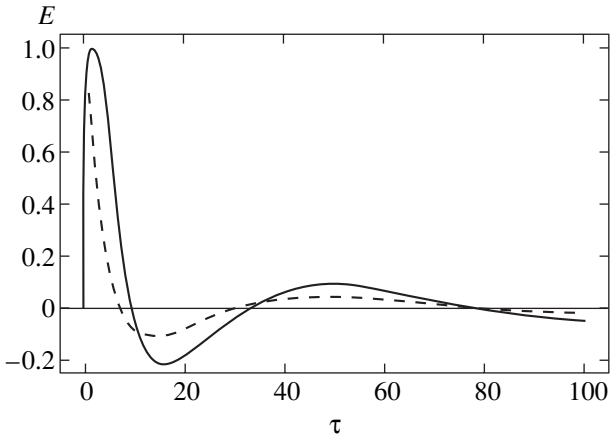

Fig. 3. The acoustic-pulse amplitude E versus τ for incomplete initial inversion of the medium $S_x^{(0)} = \sin(\pi/2.7)$. The solid line corresponds to $b = 0.9$, and the dashed line corresponds to $b = 0.1$ and $\eta = 0.5$.

don equation

$$\left(\frac{d}{d\theta}\right)^2 \mathcal{B} + \frac{1}{\theta}\frac{d}{d\theta}\mathcal{B} = \sin\mathcal{B}(\theta), \quad (67)$$

with the boundary conditions

$$\mathcal{B}(0) = S_x^{(0)}, \quad \left.\frac{d\mathcal{B}(\theta)}{d\theta}\right|_{\theta=0} = 0.$$

This self-similar solution can be expressed in terms of the solution to P_{III} in a standard way [28].

The results of our numerical calculations of the original system for conditions (59) are shown in Fig. 3. These results and analysis of the asymptotics for the original system of equations and solutions (66) indicate that the general solution consists of a packet of damped nonlinear pulsations with an increasing duration. In real media, the relaxation and diffraction processes lead to a significant relative suppression of the oscillation amplitudes compared to the leading edge. Therefore, in practice, it is often sufficient to find an expression for the first nonlinear oscillation. Our solution shows that the asymptotics (at large χ) is a nonsoliton one and characterized by the self-similar variable $\sqrt{b\chi\tau}$. This solution for the acoustic-wave amplitude describes the phonon avalanche and the avalanche transition of the spin system to a stable state.

5. DISCUSSION OF THE RESULTS AND THEIR PHYSICAL APPLICATIONS

We studied the dynamics of acoustic pulses with a duration close to ω_B^{-1} in terms of integrable reductions of the evolution equations. These systems of equations describe the evolution of longitudinal–transverse waves that propagate along the magnetic field in a medium of impurity ions with an effective spin of 1/2. In studying the coherent dynamics of acoustic pulses, we used only the condition of equal phase velocities for the longitudinal and transverse waves and the approximation of unidirectional acoustic-wave propagation. As a result, we were able to find an integrable model that corresponded to the most general physical situation for the interaction geometry under consideration. On the other hand, milder physical conditions than those in the models constructed and studied by other authors, for example, by Voronkov and Sazonov [7], are required to observe the behavior of the field described here, because our models can be applied at higher temperatures and lower magnetic-field strengths.

In pure form, the soliton dynamics associated with ASIT requires producing a sufficiently intense pulse with a nearly soliton shape at the boundary of the medium for its observation. On the other hand, as we showed above, if the spin system is initially partially or completely inverted and is in an unstable state, then the solution that describes the transition to a stable state is a nonsoliton one. Similar phonon dynamics was observed in a series of experiments by the authors of [13, 14]. These authors investigated the stimulated emission of resonant acoustic phonons produced by the decay of the initial population inversion in a system of Kramers doublets $\tilde{E}(^2E)$ of impurity Cr^{3+} ions in a ruby (Al_2O_3). An external magnetic field of approximately 3.48 T in strength led to Zeeman doublet splitting. The crystal was at a temperature of 1.8 K. The initial level population inversion, i.e., the spin inversion, was caused by laser pumping at a wavelength of 693 nm. These authors found that a nonmonotonic time dependence of the lower level population arose for a sufficiently large effective length of the inverted medium. This kind of field dynamics can be described in terms of model (27) under the initial condition (59). In [13, 14], this effect, called a phonon avalanche, is explained by using an analogy between the dynamics of transverse acoustic waves and the dynamics of photons during superfluorescence for quasi-monochromatic waves. Our results indicate that a similar phonon avalanche can be observed for acoustic pulses with a duration close to ω_B^{-1} and in the more general case of a longitudinal–transverse wave and for incomplete inversion.

The new integrable models obtained here can also be used in other fields of physics, for example, in systems with spatially localized electrons. Let us consider a phonon-induced transition with the change in electron orientation between the Zeeman sublevels in a system of quantum dots in GaAs. In [32], the rate of this transition was estimated for various spin–orbit interaction mechanisms. The spin–lattice relaxation for the electrons localized at quantum dots was shown to be much smaller than that for free electrons. For a sufficiently large strength of the applied magnetic field, the contribution of the spin–phonon interaction can be significant. It was shown in [32] that, for a phonon wavelength much larger than the size of one quantum dot ($g_0\mu_B B \ll \sqrt{mv^2\hbar\omega_0}$, where v is the speed of sound, m is the electron mass, and $\hbar\omega_0$ is the typical separation between the orbital levels at a quantum point), the spin–phonon interaction is described by a Hamiltonian similar to (13). Taking into account the evolution of the longitudinal–transverse acoustic wave in a system of such quantum dots and following the above assumptions, we obtain a system similar to (27). Since the picosecond duration of an acoustic pulse corresponds to its limiting length $l_s \sim 10^{-7}$ cm and since an acoustic soliton can be formed at several lengths l_s, an allowance for the coherent phonon dynamics for such evolution scales can be of importance in controlling the electron behavior in an ensemble of quantum dots.

Analysis of the soliton solutions (53) indicates that the time dependence of the spin direction for a longitu-

dinal–transverse wave depends on the relative contribution of the longitudinal wave. The relation between E and S_z for a one-phase soliton solution can be easily derived from system (27). For solution (53) and the conditions when $\tau \longrightarrow -\infty$, we find that

$$S_z = S_z(-\infty, \chi) - \frac{U}{b^2 + 4\eta^2}, \qquad S_z(-\infty, \chi) = \frac{1}{b^2 + 4\eta^2} - 1. \tag{68}$$

The dependence $S_z(\tau)$ for different b is shown in Fig. 2.

Below, we give another example of the physical situation that can be described by using the qualitative results obtained above. The relaxation of magnetic spins from an inverted initial state to a final (stable) state in the presence of a magnetic field at low temperatures (1–5 K) can be accompanied by elastic crystal deformations [33]. A Hamiltonian similar to $\hat{H}_{\text{int}}$ (13) can be used to describe this spin–phonon interaction. This interaction gives rise to a spin–phonon avalanche [33], which was observed in experiments aimed at studying the decays of Mn_{12} magnetization in the presence of a magnetic field and at temperatures of 1.9–5 K. In contrast to the model considered above, which leads to a two-level medium, the situation studied in [33] corresponds to a multilevel (more precisely, 21-sublevel) medium. In this case, the cascade transitions (or, following the terminology of [33], the phonon-induced tunneling) between sublevels can be described in the quasi-classical approximation in terms of the model of an adiabatically changing spin. Since we consider the time range of acoustic pulses that corresponds to the spectral range including all sublevel transitions, the effective Hamiltonian of the spin–phonon interaction in this approximation is similar to (10). Some of the qualitative results obtained above can be used to explain the dynamics of spins in such a multilevel medium with cascade tunneling, for example, the behavior of the system during the decay of an inverted state.

At the same time, when the cascade transition in the adiabatic approximation is replaced with a two-level medium, the smoothing of the oscillating tail structure of the phonon avalanche is disregarded. Indeed, the formation time of the leading edge of the avalanche is determined by the initial fluctuation (noise), to which the system is insensitive. To be more precise, the delay of the leading edge is determined by the logarithm of the seed area (proportional to $\ln\rho_0$; cf. (57)). On the other hand, a phase difference of the order of π between the pulses generated at different transitions is accumulated in a time of the order of the duration of the first pulse, because the coupling constants between phonons and different tunneling transitions differ significantly (by several times). As a result, the shapes of the generated phonon and spin avalanches must consist of one intense pulse. The subsequent pulses that must have been observed in a two-level medium suppress each other. This picture was observed experimentally [33].

Here, we disregarded the nonlinear effects related to the anharmonicity of the crystal lattice. They can be included in the integrable models found above in the form of additional perturbing terms.

ACKNOWLEDGMENTS

I am grateful to E.V. Podivilov for fruitful discussions of the physical problems touched on in this paper. This study was partly supported by the Russian Foundation for Basic Research, project no. 03-02-16297.

APPENDIX

The Lax representation for the system of equations (27) is

$$\partial_\tau \Phi = \begin{pmatrix} -i\lambda U & G\left(\frac{a}{b}ZU + E\right) \\ \tilde{G}\left(\frac{a}{b}ZU + E\right) & i\lambda U \end{pmatrix}\Phi, \tag{69}$$

$$\partial_\chi \Phi = \begin{pmatrix} iY\lambda b(-S_z + aS_x) & A_{12} \\ A_{21} & iY\lambda b(S_z - aS_x) \end{pmatrix}\Phi, \tag{70}$$

where $U^2 + E^2 = 1$, λ is the spectral parameter,

$$A_{12} = G[aYZS_z + (1 + 4\lambda^2 Y)S_x - i2Yb\lambda S_y],$$

$$A_{21} = \tilde{G}[aYZS_z + (1 + 4\lambda^2 Y)S_x + i2Yb\lambda S_y],$$

$$Y = \frac{-2}{4\lambda^2 - 1 - a^2 - b^2 + \sqrt{(4\lambda^2 + 1 + a^2 - b^2)^2 + 4a^2b^2}},$$

$$Z = \frac{1}{2a^2}[-4\lambda^2 - 1 - a^2 + b^2 + \sqrt{(4\lambda^2 + 1 + a^2 - b^2)^2 + 4a^2b^2}].$$

Here, $\tilde{G}(\lambda)$ and $G(\lambda)$ are arbitrary piecewise smooth functions that are not identically equal to zero and that are related by

$$G\tilde{G} = -\frac{1}{8}[4\lambda^2 + 1 + a^2 - b^2 + \sqrt{(4\lambda^2 + 1 + a^2 - b^2)^2 + 4a^2b^2}]. \tag{71}$$

This parametrization contains ambiguities related to the square roots of the powers of λ in the matrix ele-

ments on the right-hand sides of (69) and (70). Below, we give a different special form of the Lax representation for system (27) with the parametrization of the coefficients via the Jacobi elliptic functions:

$$\partial_\tau \Phi = \begin{pmatrix} -i\dfrac{B_+ \mathrm{cn}(\xi, k)\mathrm{dn}(\xi, k)}{\sqrt{8}\,\mathrm{sn}(\xi, k)} U & \dfrac{ab}{\sqrt{2}B_- \mathrm{sn}(\xi, k)} U + \dfrac{B_- \mathrm{sn}(\xi, k)}{\sqrt{8}} E \\ -\dfrac{ab}{\sqrt{2}B_- \mathrm{sn}(\xi, k)} U - \dfrac{B_- \mathrm{sn}(\xi, k)}{\sqrt{8}} E & i\dfrac{B_+ \mathrm{cn}(\xi, k)\mathrm{dn}(\xi, k)}{\sqrt{8}\,\mathrm{sn}(\xi, k)} U \end{pmatrix} \Phi, \tag{72}$$

$$\partial_\chi \Phi = \frac{b}{\sqrt{2}B_- \mathrm{sn}(\xi, k)[2(1 + a^2) - B_-^2 \mathrm{sn}^2(\xi, k)]} \times \begin{pmatrix} iA_0(-S_z + aS_x) & A_{12} \\ A_{21} & iA_0(S_z - aS_x) \end{pmatrix} \Phi. \tag{73}$$

Here, $U^2 + E^2 = 1$; ξ is the spectral parameter; $\mathrm{sn}(\xi, k)$, $\mathrm{cn}(\xi, k)$, and $\mathrm{dn}(\xi, k)$ are the Jacobi elliptic functions with the modulus

$$k = \frac{B_+}{B_-};$$

$$B_\pm = \{1 + a^2 - b^2 \pm [(1 + a^2 - b^2)^2 + 4a^2 b^2]^{1/2}\}^{1/2},$$

$$A_0 = B_- B_+ \mathrm{cn}(\xi, k)\mathrm{dn}(\xi, k),$$

$$A_{12} = 2abS_z - b[2a^2 - B_-^2 \mathrm{sn}^2(\xi, k)]S_x + i2B_- B_+ \mathrm{cn}(\xi, k)\mathrm{dn}(\xi, k)S_y,$$

$$A_{21} = -2abS_z + b[2a^2 - B_-^2 \mathrm{sn}^2(\xi, k)]S_x + i2B_- B_+ \mathrm{cn}(\xi, k)\mathrm{dn}(\xi, k)S_y.$$

This system can be solved in terms of the ISTM on a torus in a way similar to the cases of a biaxial chiral field [34] and related Landau–Lifshitz equations [35]. However, the following additional difficulty arises here: the nondiagonal matrix elements on the right-hand sides of (69) and (70) do not become zero for the vacuum solution $E = 0$ against the background of which the solitons propagate. Therefore, in contrast to the main chiral field and the Landau–Lifshitz equations, another ambiguity arises here. This ambiguity makes the analytical properties of the problem much more complicated.

For the special case $a = 0$, the Lax representation (69) and (70) transforms into (28) and (29), respectively.

Formally passing to the limit in (27),

$$a \neq 0, \quad b \longrightarrow 0, \quad b\chi \longrightarrow \chi', \tag{74}$$

where χ' is a new variable, we obtain the well-known integrable system [28]—the reduction of the original system of equations (27):

$$\partial_{\chi'} E = -U \sin\theta, \tag{75}$$

where

$$\theta = \sqrt{1 + a^2}\int_0^\tau E(\tau')d\tau', \quad S_y = \sin\theta,$$

$$aS_x - S_z = \sqrt{1 + a^2}\cos\theta.$$

However, we made this passage to the limit in system (27) after applying the unidirectionality approximation and then used relation (26) between the longitudinal and quasi-transverse fields. If we take the original physical system (18), (20), and (21) with $f = b = 0$ as the basic one, then we will obtain (after applying the same approximations) a different integrable system of equations that is formally equivalent to the integrable system recently found by Agrotis *et al.* [22] and used by these authors to describe the dynamics of optical solitons in a two-level medium with a constant dipole moment. The same (to within the notation) system emerges as the reduction (27) in the low-amplitude limit, $E \ll 1$, for which the function U in this system can be formally substituted with unity.

Below, we give the Marchenko equations for the Zakharov–Shabat problem (61) [3] on the entire axis $\tau \in (-\infty, \infty)$ and for the field $V(\tau, 0)$ and its derivatives that rapidly become zero at infinity:

$$K_1(\tau, \tau') + F(\tau + \tau') + \int_0^\tau F(\tau' + s)K_2(\tau, s)ds = 0, \tag{76}$$

$$\bar{K}_2(\tau, \tau') - \int_0^\tau \bar{K}_1(\tau, s)F(\tau' + s)ds = 0. \tag{77}$$

Here, the kernel

$$F_r = F(\tau, \chi) = \int_{\mathbb{R}} \rho(\chi; \lambda) \frac{\exp(-i\lambda\tau)}{2\pi} d\lambda \qquad (78)$$

for conditions (59) is completely determined by the real spectrum of problem (61). The relation between the potential V and the kernel K_1 has the standard form

$$V(\tau, \chi) = 4K_1(\tau, \tau, \chi). \qquad (79)$$

REFERENCES

1. A. I. Maimistov and A. M. Basharov, *Nonlinear Optical Waves* (Kluwer Academic, Dordrecht, 1999).
2. A. I. Maĭmistov, Kvantovaya Élektron. (Moscow) **30**, 287 (2000).
3. V. E. Zakharov, S. V. Manakov, S. P. Novikov, and L. P. Pitaevskiĭ, *Theory of Solitons: the Inverse Scattering Method* (Nauka, Moscow, 1980; Consultants Bureau, New York, 1984).
4. H.-Y. Hao and H. J. Maris, Phys. Rev. B **64**, 064302 (2001).
5. G. A. Denisenko, Zh. Éksp. Teor. Fiz. **60**, 2269 (1971) [Sov. Phys. JETP **33**, 1220 (1971)].
6. G. T. Adamashvili, Zh. Éksp. Teor. Fiz. **97**, 235 (1990) [Sov. Phys. JETP **70**, 131 (1990)].
7. S. V. Voronkov and S. V. Sazonov, Fiz. Tverd. Tela (St. Petersburg) **43**, 1969 (2001) [Phys. Solid State **43**, 2051 (2001)].
8. S. V. Voronkov and S. V. Sazonov, Zh. Éksp. Teor. Fiz. **120**, 269 (2001) [JETP **93**, 236 (2001)].
9. P. A. Fedders, Phys. Rev. B **12**, 2046 (1975).
10. G. T. Adamashvili, Physica B (Amsterdam) **266**, 173 (1999).
11. N. S. Shiren, Phys. Rev. B **2**, 2471 (1970).
12. V. V. Samartsev, B. P. Smolyakov, and R. Z. Sharipov, Pis'ma Zh. Éksp. Teor. Fiz. **20**, 644 (1974) [JETP Lett. **20**, 296 (1974)].
13. H. W. de Wijn, P. A. van Walree, and A. F. M. Arts, Physica B (Amsterdam) **263**–**264**, 30 (1999).
14. L. G. Tilstra, A. F. M. Arts, and H. W. de Wijn, Physica B (Amsterdam) **316**–**317**, 311 (2002).
15. A. A. Zabolotskii, Pis'ma Zh. Éksp. Teor. Fiz. **76**, 709 (2002) [JETP Lett. **76**, 607 (2002)].
16. C. Kittel, *Introduction to Solid State Physics*, 4th ed. (Wiley, New York, 1971; Nauka, Moscow, 1974).
17. M. K. Balakirev and I. A. Gilinskiĭ, *Waves in Piezoelectric Crystals* (Nauka, Novosibirsk, 1982).
18. J. W. Tucker and V. W. Rampton, *Microwave Ultrasonics in Solid State Physics* (North-Holland, Amsterdam, 1972; Mir, Moscow, 1975).
19. L. D. Landau and E. M. Lifshitz, *Course of Theoretical Physics*, Vol. 7: *Theory of Elasticity*, 3rd ed. (Nauka, Moscow, 1987; Pergamon, New York, 1986).
20. S. A. Al'tshuller and B. M. Kozyrev, *Electron Paramagnetic Resonance in Compounds of Transition Elements*, 3rd ed. (Nauka, Moscow, 1981; Halsted, New York, 1975).
21. Y. R. Shen, *The Principles of Nonlinear Optics* (Wiley, New York, 1984; Nauka, Moscow, 1989).
22. M. Agrotis, N. M. Ercolani, S. A. Glasgow, and J. V. Moloney, Physica D (Amsterdam) **138**, 134 (2000).
23. J. D. Gibbon, P. J. Coudrey, J. K. Eilbeck, and R. K. Bullough, J. Phys. A: Math. Gen. **6**, 1237 (1973).
24. A. E. Borovik and S. I. Kulinich, Pis'ma Zh. Éksp. Teor. Fiz. **39**, 320 (1984) [JETP Lett. **39**, 384 (1984)].
25. A. A. Zabolotskii, Physica D (Amsterdam) **40**, 283 (1989).
26. A. A. Zabolotskii, Zh. Éksp. Teor. Fiz. **115**, 1158 (1999) [JETP **88**, 642 (1999)].
27. L. A. Faddeev and L. A. Takhtajan, *Hamiltonian Methods in the Theory of Solitons* (Nauka, Moscow, 1986; Springer, Berlin, 1987).
28. A. C. Newell, *Solitons in Mathematics and Physics* (SIAM, Philadelphia, PA, 1985; Mir, Moscow, 1989), CBMS-NSF Regional Conference Series, Vol. 48.
29. J. Leon and A. V. Mikhailov, Phys. Lett. A **53**, 33 (1999); M. Boiti, J.-G. Caputo, J. Leon, and F. Pempinelli, Inverse Probl. **16**, 303 (2000).
30. A. Fokas, J. Math. Phys. **41**, 4188 (2000).
31. A. Degasperis, S. V. Manakov, and P. M. Santini, nlin.SI/0210058.
32. A. V. Khaetskii, Physica E (Amsterdam) **10**, 27 (2001).
33. E. del Barco, J. M. Hernández, M. Sales, *et al.*, Phys. Rev. B **60**, 11898 (1999).
34. I. V. Cherednik, Teor. Mat. Fiz. **47**, 755 (1981).
35. A. M. Mikhailov, Phys. Lett. A **92**, 51 (1982).

Translated by V. Astakhov

Journal of Experimental and Theoretical Physics, Vol. 96, No. 6, 2003, pp. 1104–1112.
Translated from Zhurnal Éksperimental'noĭ i Teoreticheskoĭ Fiziki, Vol. 123, No. 6, 2003, pp. 1256–1265.

SOLIDS
Structure

Magnetorefractive Effect in Magnetic Nanocomposites

A. B. Granovsky[a,*], I. V. Bykov[a], E. A. Gan'shina[a], V. S. Gushchin[a], M. Inoue[b,c], Yu. E. Kalinin[d], A. A. Kozlov[a], and A. N. Yurasov[a]

[a]*Moscow State University, Vorob'evy gory, Moscow, 119992 Russia*
[b]*Toyohashi University of Technology, Toyohashi 441-8580, Japan*
[c]*CREST, Japan Science & Technology Corporation, Kawaguchi 332-0012, Japan*
[d]*Voronezh State Technical University, Moskovskiĭ pr. 14, Voronezh, 394026 Russia*
**e-mail: granov@magn.ru*

Received December 30, 2002

Abstract—The magnetorefractive effect in ferromagnetic metal–insulator granular nanostructures (CoFeZr)–SiO_n, Co–Al–O, $FeSiO_n$, and (CoFe)–(Mg–F) is investigated in the infrared spectral region in a wavelength range from 5 to 20 μm. The magnitude of the effect varies from 0.1 to 1.5% for different nanocomposites and strongly depends on the frequency of light and magnetoresistance. It is shown that the reflection coefficient changes in a magnetic field not only due to the magnetorefractive effect, but also due to the even magnetooptical effect. Simple relations describing this effect are given for the case when the reflection from the substrate is insignificant and in the case of a three-layer (insulator–film–substrate) system. The expression for the frequency dependence of the magnetorefractive effect in nanocomposites is derived and its features in the case of high-frequency spin-dependent tunneling are analyzed. © *2003 MAIK "Nauka/Interperiodica".*

1. INTRODUCTION

The magnetorefractive effect (MRE) is a frequency analog of giant magnetoresistance and is manifested in a change in light reflectance *R*, transmittance *T*, and absorptance *A* for samples with a considerable magnetoresistance upon their magnetization [1, 2].

Traditional magnetooptical effects (MOE), even and odd in magnetization, are associated with the influence of spin–orbit interaction on intraband (in the IR spectral region) or interband (in the visible spectral region) optical transitions. The MRE is not associated with the spin–orbit interaction and is due to spin-dependent scattering or tunneling. The conductivity $\sigma(\omega)$ of magnetic materials with a giant, tunnel, or colossal magnetoresistance changes significantly upon magnetization; for this reason, the permittivity

$$\varepsilon(\omega) = \varepsilon_r(\omega) - i\frac{4\pi\sigma(\omega)}{\omega},$$

which determines the refractive indices and is a linear function of conductivity $\sigma(\omega)$, is a function of the applied magnetic field also. Here, $\varepsilon_r(\omega)$ is the permittivity taking into account the contributions of displacement currents. The MRE must be manifested most clearly in the IR spectral region, in which intraband transitions dominate.

It should be noted that, in the case of reflection in ferromagnetic metals as well as in alloys and composites based on such metals in the IR spectral region, traditional magnetooptical effects odd and even in magnetization do not exceed 0.01%. For this reason, the search for materials with a strong MRE is of considerable practical importance. The MRE can also be used for a contactless analysis of giant magnetoresistance [3]. Finally, the study of the MRE in metal–insulator systems is a direct method for investigating high-frequency spin-dependent tunneling.

The MRE was investigated theoretically and confirmed experimentally for the first time for Fe/Cr multilayers [1]. The MRE theory for metallic multilayers was also developed in [4–6]. In spite of certain inconsistencies in the results of these publications (see, for example, discussion in [6]) concerning the relative magnitude and frequency dependence of the MRE, this effect is reliably observed in the near-IR spectral region and amounts to 0.1–0.5% for reflection [1, 6].

The MRE theory for granular metal–metal alloys was constructed in [2] and modified recently in [7]. The experimentally measured values of MRE for Co–Ag granular systems [3, 7] in strong magnetic fields did not exceed 1%. The simplest relation for the MRE in metallic systems was derived in [2] for the Hagen–Rubens spectral range ($\omega\tau \ll 1$, where τ is the electron relaxation time) for the normal incidence of light:

$$\frac{\Delta R}{R} = \frac{R(H=0) - R(H)}{R(H=0)} = -\frac{1}{2}(1-R)\frac{\rho(H=0) - \rho(H)}{\rho(H=0)} = -\frac{1}{2}(1-R)\frac{\Delta\rho}{\rho}. \quad (1)$$

1063-7761/03/9606-1104$24.00

Here, $R(H = 0)$ and $R(H)$ are the coefficients of light reflection from samples in zero magnetic field and in a magnetic field H, $\rho(H = 0)$ and $\rho(H)$ are the corresponding resistivities, and $\Delta\rho/\rho$ is the absolute value of magnetoresistance. Expression (1) implies that high values of the MRE must be observed in systems with a large magnetoresistance and with a low reflectance, i.e., in nonmetallic systems. Indeed, a considerable MRE was recently detected in granular metal–insulator films of Co–Al–O [8, 9] and CoFe–MgF [10].

In this study, an attempt is made at a detailed investigation of the MRE in magnetic composites. Section 2 is devoted to analysis of possible contributions to the measured reflectance from the MRE and from even magnetooptical effects. It was assumed earlier (see, for example, [1–10]) that the change in the reflectance in a magnetic field is precisely the magnetorefractive effect; however, this is justified only if the MRE exceeds 0.1%. In the same section, simple relations are given for calculating the MRE in the model of a semi-infinite space (insulator–magnetic medium) and possible features of the MRE are analyzed in the case of high-frequency spin-dependent tunneling. It should be noted in this connection that expression (1) is obviously inapplicable for describing the MRE in nanocomposites since it has been derived on the basis of the frequency dependence of a Drude–Lorentz-type metallic conductivity. The methods for preparing samples are described in Section 3. Section 4 deals with the experimental methods and details and, in particular, describes a setup modified as compared to that in [8]. The results of experiments for a number of nanocomposites and their analysis are given in Section 5. Main attention is paid to analysis of the frequency dependence of the MRE, the dependence of the signal on the polarization of radiation, the correlation between the MRE and magnetoresistance, and the influence of optical parameters on the MRE. The results are summarized in the Conclusions.

2. THEORY

The permittivity tensor for a medium magnetized along the z axis has the form

$$\hat{\varepsilon} = \begin{pmatrix} \varepsilon_{xx} & \varepsilon_{xy} & 0 \\ \varepsilon_{yx} & \varepsilon_{yy} & 0 \\ 0 & 0 & \varepsilon_{zz} \end{pmatrix}, \quad (2)$$

where it follows from symmetry considerations that $\varepsilon_{xx} = \varepsilon_{yy}$ and $\varepsilon_{yx} = -\varepsilon_{xy}$. The nondiagonal components are linear, while the diagonal components are quadratic in magnetization M; i.e.,

$$\varepsilon_{xx} = \varepsilon_d(1 + bM^2), \quad b = b_a + b_{MRE}, \quad \varepsilon_{xy} = aM. \quad (3)$$

Here, b_a characterizes the contribution due to induced anisotropy of the magnet [11–13], while b_{MRE} describes the MRE contribution. The nondiagonal elements of the permittivity tensor are responsible for the magnetooptical Kerr and Faraday effects, which are linear in magnetization, while the orientational magnetooptical effect, which is even in magnetization [12, 13], is associated both with the contribution $\varepsilon_d b_a M^2$ to the diagonal elements and with nondiagonal elements. Consequently, the results of MRE measurements always contain the contribution from the even magnetooptical effect along with the true MRE.

2.1. Model of Semi-infinite Space

Let us first consider a thick sample for which the reflection from the substrate can be disregarded. For p-polarized light incident in the xy plane from a transparent insulator (medium 1 with a real refractive index n_1) at an angle ϕ_0 on the sample (medium 2 with a complex refractive index $\eta_2 = n_2 - ik_2$), the reflectance R can be written in the form [14]

$$R = \left|r_{12}^p\right|^2,$$
$$r_{12}^p = \frac{g_1\eta_2^2 - g_2 n_1^2}{g_1\eta_2^2 + g_2 n_1^2} - \frac{g_1\eta_2^2\varepsilon_{xy}}{g_2 n_1^2(g_1\eta_2^2 + g_2 n_1^2)^2}, \quad (4)$$

$$g_1 = \sqrt{n_1^2 - n_1^2\sin^2\phi_0}, \quad g_2 = \sqrt{\eta_2^2 - n_1^2\sin^2\phi_0}. \quad (5)$$

Since $(\varepsilon_2)_{xx} = \eta_2^2 = (n_2 - ik_2)^2$ by definition, it can easily be seen, in view of relations (2) and (3), that the term quadratic in magnetization in relation (4) is determined by the MRE, induced anisotropy, and nondiagonal terms. The contributions of induced anisotropy and nondiagonal terms are on the order of the square of the magnetooptical factor Q, i.e., are quadratic in the spin–orbit interaction. The magnetooptical factor Q in the visible spectral region does not exceed 0.02, and there are no grounds to expect an increase in this factor in the IR spectral region.[1] Consequently, the even magnetooptical effect may lead to a change in R upon magnetization by not more than 0.1%. The numerical calculations made for specific alloys with experimentally determined optical and magnetooptical parameters [15] confirmed this estimate. Thus, the influence of the even magnetooptical effect on the MRE can be neglected in all cases when the MRE exceeds 0.1%. Then we can set $a = 0$ and $b_a = 0$ in relation (3),

$$n_2 = n_2^0(1 + cM^2), \quad k_2 = k_2^0(1 + dM^2), \quad (6)$$

[1] The nondiagonal components of the permittivity tensor depend on the ratio of the anomalous Hall coefficient to the square of resistance. The anomalous Hall effect in nanocomposites in the vicinity of the percolation threshold attains giant values which are four orders of magnitude larger than in metals; however, the resistivity increases even more strongly in this case.

where coefficients c and d are determined by spin-dependent scattering or tunneling.

If medium 1 is vacuum ($n_1 = 1$) and the incidence of light is close to normal ($\phi_0 = 0$), expression (4) is simplified considerably,

$$R = \frac{(1-n_2)^2 + k_2^2}{(1+n_2)^2 + k_2^2}, \tag{7}$$

and then

$$\frac{\Delta R}{R} = (1-R)M^2 \times \left[c\frac{1-(n_2^0)^2+(k_2^0)^2}{(1-n_2^0)^2+(k_2^0)^2} - 2d\frac{(k_2^0)^2}{(1-n_2^0)^2+(k_2^0)^2} \right]. \tag{8}$$

2.2. The Insulator–Magnetic Film–Substrate Three-Layer System

In the case of a three-layer system consisting of a magnetic film (medium 2) of thickness h on a substrate (medium 3) and an insulator (medium 1), the expression for the reflectance of p-polarized radiation incident from medium 1 has the form

$$R = \left|r_{jkl}^p\right|^2, \quad r_{jkl}^p = \frac{r_{jk}^p + F_k^2 r_{kl}^p}{1 + F_k^2 r_{jk}^p r_{kl}^p},$$
$$r_{jk}^p = \frac{g_j\eta_k^2 - g_k\eta_j^2}{g_j\eta_k^2 + g_k\eta_j^2}, \quad g_j = \sqrt{\eta_j^2 - \eta_1^2\sin^2\phi_0}, \tag{9}$$

$$F_k = \exp(-2\pi i\lambda^{-1}g_k h_k), \tag{10}$$

where the presence of factor F_k, which appears due to transmission of light through the film and reflection from the substrate and contains the complex refractive index of the magnetic medium, may lead to a considerable enhancement of the MRE. Some examples of the results of calculations based on formulas (4) and (9) will be given below together with microscopic expressions for parameters c and d.

2.3. Peculiarities of the Frequency Dependence of Magnetorefractive Effect for Nanocomposites

At low frequencies, tunneling probability is independent of frequency. However, at high frequencies, both a decrease in the tunnel transparency (when the period of an electromagnetic wave becomes smaller than the characteristic time of tunneling) and an increase in the tunneling probability due to absorption may be observed. In addition, a tunnel junction is essentially a capacitor; for this reason, the conductance of the tunnel junction at finite frequencies is determined by the resistive and capacitive components. We will prove that the former two factors are insignificant for the formation of the MRE, while the latter factor considerably modifies the frequency dependence as compared to a dependence for metallic systems.

The simplest estimate for the tunneling time τ is the ratio of the tunnel gap width, i.e., the spacing s between granules, to the Fermi velocity v_F. For a spacing s = 1–3 nm typical of tunneling, we find that the tunneling time is on the order of 10^{-16} s; i.e., in the IR range $\omega\tau \ll 1$, when λ = 1–10 μm, and the tunneling probability is the same as in the static case [16]. Since $\omega\tau \ll 1$ and the electron tunneling probability at frequency $E_F + \hbar\omega$ depends on the factor $[e^{\omega\tau} - 1]^2$ and on the incident radiation power [16], the tunnel resistivity ρ in the IR range is independent of frequency for a radiation power in the flare spot much lower than 1 W/cm^2 (which is obviously the case). However, the tunnel gap can be regarded a resistor and a capacitor with permittivity ε_{ins} connected in parallel. Then, the expression for the conductance of such a system and of the granular film as a hole at finite frequencies can be written in the form

$$\sigma(\omega, H) = \frac{1 + i\omega\varepsilon_{ins}\rho(H)/4\pi}{\rho(H)}, \tag{11}$$

which differs significantly from the Drude–Lorentz frequency dependence for metallic systems. It should be noted that expression (11) was successfully used in [17] for interpreting the experimental data on magnetoimpedance of tunnel systems. By definition, we have

$$\varepsilon_{xx} = \varepsilon_r - i\frac{4\pi\sigma(\omega)}{\omega} = \varepsilon' - i\varepsilon''. \tag{12}$$

Here, $\varepsilon' = n^2 - k^2$, $\varepsilon'' = 2nk$, and $\varepsilon_r = 1$ for the Drude model. It follows from relations (11) and (12) that only the imaginary part of the permittivity depends on the tunnel resistivity of nanocomposites. Assuming that the magnetoresistance

$$\frac{\Delta\rho(H)}{\rho} = \frac{\rho(0) - \rho(H)}{\rho(0)} \tag{13}$$

is small and using relations (8), (12), and (13), we obtain

$$(c+d)M^2 = \frac{\Delta\rho}{\rho}, \quad \frac{c}{d} = \left(\frac{k^0}{n^0}\right)^2, \tag{14}$$

which is equivalent to the relations

$$dM^2 = \frac{\Delta\rho}{\rho}\frac{1}{1+(k^0/n^0)^2},$$
$$cM^2 = \frac{\Delta\rho}{\rho}\frac{(k^0/n^0)^2}{1+(k^0/n^0)^2}, \tag{15}$$

in which index "2" indicating the magnetic medium has been omitted. Expression (15) combined with for-

mulas (4) or (10) for the reflectance completely defines the MRE in nanocomposites for *p*-polarized light in terms of magnetoresistance and optical parameters. In the particular case of normal incidence, it follows from Eqs. (8) and (15) that

$$\frac{\Delta R}{R} = -(1-R)\frac{\Delta\rho}{\rho}k^2\left[\frac{3n^2-k^2-1}{(n^2+k^2)[(1-n)^2+k^2]}\right]. \quad (16)$$

This expression represents the main result of this section. It shows that the MRE in nanocomposites with a tunnel magnetoresistance is a complex function of optical parameters. In particular, the MRE must be manifested most clearly in the spectral regions where weak reflection takes place and both negative and positive MRE are possible; this enables us to interpret the experimental data obtained in [9].

3. SAMPLES

The objects of investigations were nanocomposite films with a considerable tunnel magnetoresistance.

The films of amorphous ferromagnetic alloy $Co_{45}Fe_{45}Zr_{10}$ in the amorphous matrix of silicon dioxide α-SiO_2 were obtained by ion-beam sputtering of compound targets. A multicomponent target had the form of a molded base having a size of 270×80 mm^2 and made of the corresponding ferromagnetic alloy. Quartz plates having a width of 9 mm were placed on the surface of the base at right angles to its longitudinal axis. Sputtering was carried out in a vacuum of 1×10^{-5} Torr onto fixed glass-ceramic substrates. A granular structure with a wide and continuous set of metal-phase concentrations was formed in a single production cycle during simultaneous sputtering of the metallic alloy and the dielectric from the compound target with a varying spacing between the quartz plates. The values of the metal phase concentration x varied from 30 to 65 at. %. The middle of this interval (so-called percolation threshold) corresponds to samples with structures in which the highest values of magnetoresistance are observed. The film thickness in the region of the percolation threshold amounted to approximately 4 μm. According to the results of electron microscopic investigations carried out with the help of a high-resolution transmission electron microscope, the synthesized composites consisted of amorphous metallic grains with a size from 2 to 5 nm, distributed in the amorphous matrix. Smaller grain sizes correspond to lower concentrations of the metallic phase, while larger sizes are typical of samples with concentration x exceeding 60 at. %. The grains formed as a result of growth are not insulated absolutely in the dielectric matrix (even in the case of a high SiO_2 concentration), but form small conglomerates and chains, which in turn form a labyrinth structure.

The use of CoFeZr–SiO_n films for studying the MRE makes it possible to minimize the influence of the even magnetooptical effect on the MRE since the induced anisotropy effect is obviously insignificant for amorphous metals (see discussion following formula (5) in Section 1). In addition, the wide range of compositions obtained makes it possible to study the MRE in the range of metal and insulator phases as well as near the percolation threshold.

Granular ferromagnetic metal–insulator films of $Co_x(Al_2O_3)_{1-x}$ with a high magnetoresistance attaining 8% in a field of 12 kOe at room temperature were prepared by the method of tandem rf magnetron sputtering from various targets of Co_xAl_{1-x} alloys in argon and oxygen atmosphere onto uncooled glass substrates. The film thickness was 2 μm and the size of Co grains varied from 2 to 5 nm. A detailed description of the sample preparation procedure, as well as the methods and results of measurements of chemical, structural, electrical, and magnetic parameters of the samples, is given in [18, 19]. Nanogranular samples of the (FeCo)–(MgF) system, whose magnetoresistance attained 13.3% at room temperature in a magnetic field of 10 kOe, were synthesized according to basically the same technology [20].

Films of the Fe–SiO_n system were prepared by the double ion-beam sputtering of Fe and SiO_2 from a compound target onto silicon substrates, which permitted one to vary the proportion between the ferromagnet and the insulator. The characteristic grain size was approximately equal to 4 nm and the film thickness was 0.2–0.8 μm. The maximal value of magnetoresistance in a field of 10 kOe at room temperature attained values of 1–3% depending on the film composition. The structural, electrical, and magnetoresistive properties of films belonging to this system are described in [21].

4. METHODS OF INVESTIGATION AND EXPERIMENTAL DETAILS

Optical reflection and magnetooptical effects in magnetic nanocomposites were studied in a wide range of wavelengths from 1.43 to 20 μm (7000–500 cm^{-1}). In the frequency range 500–7000 cm^{-1}, we used a FTIR PU9800 commercial Fourier spectrometer with a spectral resolution of approximately 4 cm^{-1} and a photometric transmission accuracy ΔT = 0.1–0.01%. Optical reflection will be represented below by the frequency dependence of energy reflectance $R(\omega)$, while the magnetooptical effects will be characterized by the relative variation of the intensity of radiation reflected from the ferromagnet during its magnetization. In the experimental geometry used for observing the magnetooptical effect for a *p* wave of linearly polarized light (**E** ⊥ **M**), three intense effects can be detected simulta-

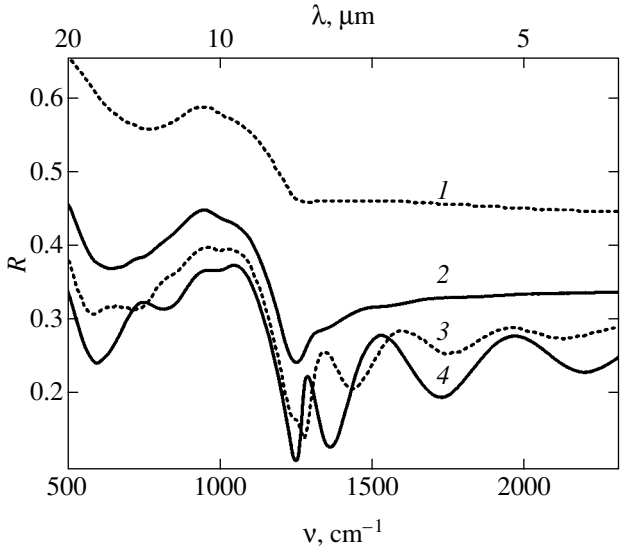

Fig. 1. Frequency dependence of the reflectance of granular $(Co_{45}Fe_{45}Zr_{10})_x(SiO_{1.7})_{100-x}$ films: x = 57 (*1*), 47 (*2*), 40 (*3*), and 34 (*4*); φ = 10°.

neously, viz., the transversal Kerr effect (which is linear in magnetization **M**) and two effects which are quadratic in **M** (the orientation effect and the MRE).

We measured the magnetorefractive effect on a setup described in [8] with a number of modifications concerning mainly the design of the magnetooptical attachment of the Fourier spectrometer.

First, the radiation from the IR spectrometer was turned through 90° with the help of plane and aspherical off-axis mirrors, which made it possible to direct radiation at an angle φ ≈ 10° to the normal of the sample placed in the gap of the magnet. The MRE measurements for an angle of light incidence close to the normal allowed us to avoid the influence of the transversal Kerr effect (which is equal to zero for the normal incidence); such a geometry is most convenient for interpreting the experimental results. Second, the rotating permanent magnet was replaced by an electromagnet, which created (in a gap of 7×10 mm^2) either a constant magnetic field H_{max} = 1700 Oe or a varying field whose amplitude value also attained 1700 Oe depending on whether a dc or an ac current was fed to the magnet winding. By reducing the varying field to zero, we could demagnetize the sample almost completely (i.e., obtain a state with $\mathbf{M}_r = 0$).

We also developed a new method for measuring the difference in the intensities $I(0)$ and $I(H)$ of radiation reflected from the sample in the demagnetized and magnetized states instead of the ratio of these intensities, as was done earlier [8]. This allowed us to reduce the "contribution" from noise, which is especially important for small values of the effects being measured. The division of difference ΔI by the intensity of light measured for $H = 0$ determines the value of the MRE, which is given by the formula

$$\xi(\omega) = \frac{I(0) - I(H)}{I(0)} = \frac{R(0) - R(H)}{R(0)}, \qquad (17)$$

where the light intensities are replaced by the energy reflectances, which are proportional to them.

Such modifications and improvements enabled us to measure the optical reflectance and the MRE not only in the case of oblique incidence of light, but also for angles close to normal incidence and not in the state of residual magnetization, as before, but on completely demagnetized samples. Despite the complication of the optical path of the setup, the noise level did not exceed that in [8]. The noise level was lowered to 1×10^{-4} in the frequency range 500–1000 cm^{-1} and to 3×10^{-4} for 2000 cm^{-1} due to the application of storage operations (over 1000 scans), mutually reversible cycles, and smoothing. Optical reflection and MRE measurements were made for angles of incidence φ = 10° and 50° in the frequency range 500–5000 cm^{-1} with a spectral resolution of 2 cm^{-1} at room temperature.

Magnetoresistance was measured using a two-point potentiometer at room temperature in a magnetic field of strength up to 12 kOe oriented parallel to the sample surface and was determined, as usual, in accordance with formula (13).

5. EXPERIMENTAL RESULTS AND DISCUSSION

An analysis of the frequency dependence of optical reflection in nanocomposites belonging to the $(CoFeZr)_x(SiO_2)_{100-x}$ system proved (Fig. 1) that the reflectance $R(\nu)$ is 2–3 times lower than for pure metals constituting grains for all concentrations in the frequency range 500–7000 cm^{-1} and is practically independent of frequency in the range 2500–7000 cm^{-1}. For frequencies below 2500 cm^{-1}, the value of $R(\nu)$ decreases insignificantly for samples with concentrations below 47 at. %. In the frequency range 1100–1400 cm^{-1}, a sharp decrease in $R(\nu)$ followed by its increase associated with absorption in the silicon dioxide matrix is observed. The minimal values of $R(\nu)$ correspond to samples with concentrations from the range 34–47 at. %, which corresponds to the region of percolation threshold. The oscillatory behavior of $R(\nu)$ for samples in this concentration range in the frequency interval 1100–1400 cm^{-1} is associated with the interference of light reflected at the film–air and film–substrate interfaces. The strongest changes in $R(\nu)$ correspond to a narrow interval of 1300 ± 100 cm^{-1} in which the reflectance changes by a factor larger than 2. The reflection spectra for IR radiation in Fig. 1 correspond to an angle of incidence φ = 10°. For φ = 50°, individual

absorption bands are shifted by 20–40 cm^{-1} towards higher frequencies.

Figures 2 and 3 show the results of measurements of magnetoresistance and MRE of the $(CoFeZr)_x(SiO_2)_{100-x}$ system. The data on magnetoresistance and MRE are given for the same value of field (1700 Oe).

The percolation threshold determined from the results of resistance measurements for this system of amorphous granular alloys amounts to $x \approx 43$ at. %; near this threshold, the magnetoresistance attains its maximal value of 3.5%. For samples with a high concentration of the metal phase ($x = 57$ at. %), the magnetoresistance is close to zero ($\Delta\rho/\rho \approx 0.2\%$), which correlated with an insignificant MRE in accordance with the theory developed in Section 1. It is interesting to compare the MRE for samples with the same magnetoresistance, but with concentrations x smaller and larger than 43 at. %, i.e., on the left and right of the percolation threshold. It can be seen from Fig. 3 that the MRE for samples in the dielectric phase is stronger than in the metallic phase ($x > 47$ at. %) for virtually equal values of magnetoresistance (see Fig. 2). In accordance with formula (16), this is due to smaller values of the reflectance for the "dielectric" sample (see Fig. 1). Finally, the frequency for which the maximal value of MRE is observed exactly coincides with the frequency (1200 cm^{-1}) for which the reflectance has the minimal value.

Since the MRE is weak (less than 0.1% on the average) in this system of alloys, we had to prove that the measured dependences are associated precisely with the MRE. Figure 4 shows the frequency dependences of MRE for one of the samples for natural light and for a *p* wave of linearly polarized light. It can be seen that the polarization dependence is practically absent in the spectral region where the signal exceeds 0.05%, which is direct proof of the fact that the signal being measured is just the MRE. However, the situation is different in the frequency ranges 2500–1300 and 1000–800 cm^{-1}, where the signal is weaker than 0.05% and the influence of the even orientation effect becomes noticeable.

A correlation between magnetoresistance and MRE is reliably observed for all nanocomposites. For example, the magnetoresistance of Fe–SiO_n composites in a field of 2.2 kOe does not exceed 1.2%; accordingly, the frequency dependence of the MRE shows that the magnitude of this effect attains a value of 0.2% (Fig. 5).

In the vicinity of the percolation threshold, nanocomposites become relatively transparent (see Fig. 1); consequently, the interference of light associated with the reflection from the substrate cannot be disregarded completely even for relatively thick films. In particular, interference beats of the reflectance can be clearly seen in Fig. 1 for films with $x = 40$, 34 at. %. A quantitative description of the effect must be based on the theory for the model of a three-layer system described in Section 1. Figure 6 shows the spectra describing the frequency dependence of the MRE for a $Co_{43}Al_{22}O_{35}$ sample,

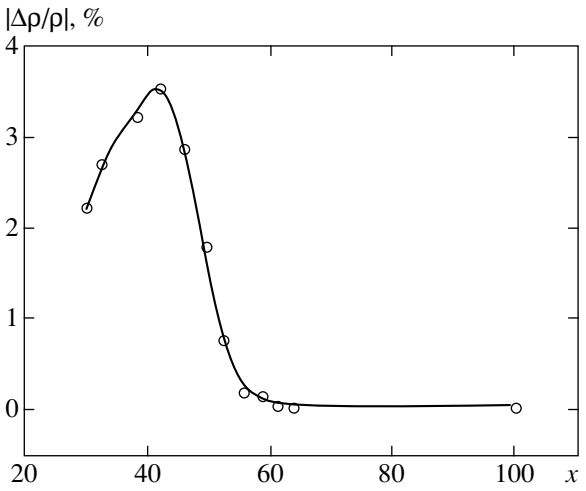

Fig. 2. Concentration dependence of the magnetoresistance of granular $(Co_{45}Fe_{45}Zr_{10})_x(SiO_{1.7})_{100-x}$ composite.

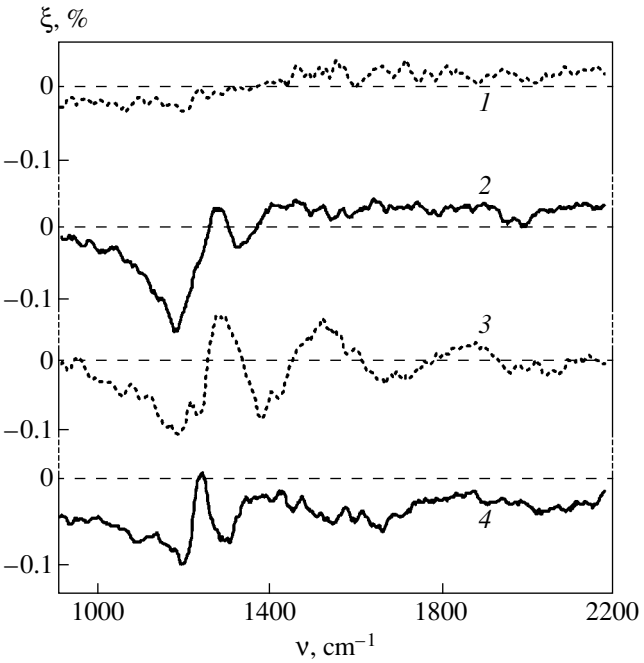

Fig. 3. Frequency dependence of the magnetorefractive effect of granular $(Co_{45}Fe_{45}Zr_{10})_x(SiO_{1.7})_{100-x}$ composites: $x = 57$ (*1*), 47 (*2*), 40 (*3*), and 34 (*4*); magnetic field is 1700 Oe; $\varphi = 10°$.

which were obtained for an angle of incidence of 10° and for which the effect of interference is pronounced most clearly. The theoretical $\xi(\nu)$ dependences corresponding to these spectra are shown in Fig. 7.

Figure 8 shows the experimental data on dispersion of the MRE (for two values of magnetic field of 1500 and 1700 Oe) and of the reflectance of a nanocomposite $(Co_{0.4}Fe_{0.6})_{48}(Mg_{52}F)$ film with a tunnel conductivity and a high magnetoresistance (7.5% in a field of 1700 Oe) for an angle of incidence $\varphi = 10°$. It can be

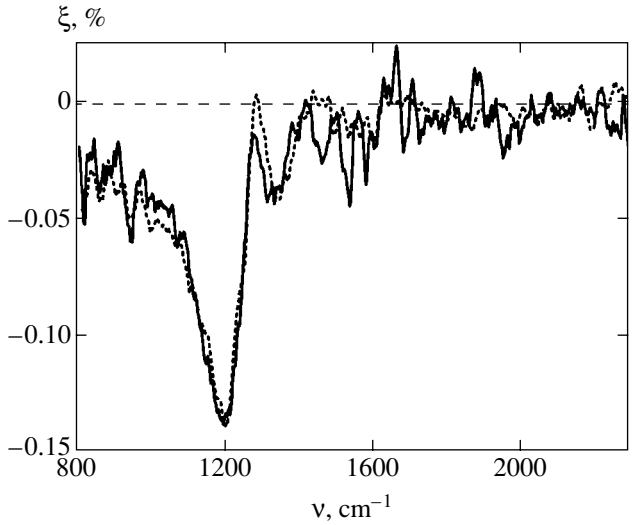

Fig. 4. Frequency dependences of the MRE for natural (dotted curve) and *p*-polarized (solid curve) light for granular $(Co_{45}Fe_{45}Zr_{10})_{47}(SiO_{1.7})_{53}$ film in a magnetic field of 1700 Oe; φ = 10°.

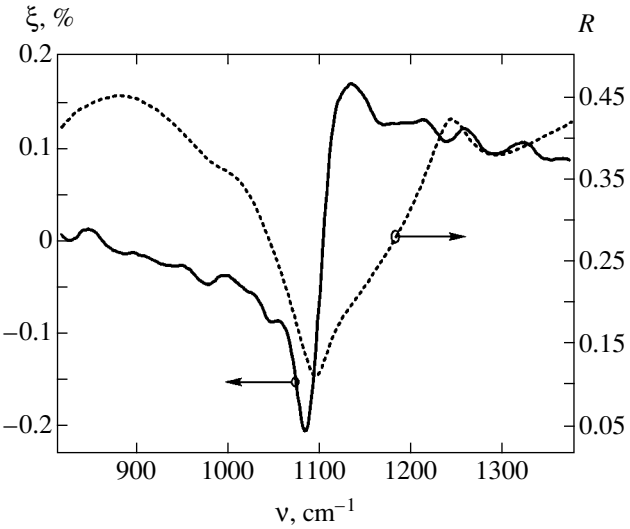

Fig. 5. Frequency dependences of the reflectance (dotted curve) of a Fe–SiO_2 film on a Si substrate and of the MRE (solid curve) for a magnetic field H = 2200 Oe.

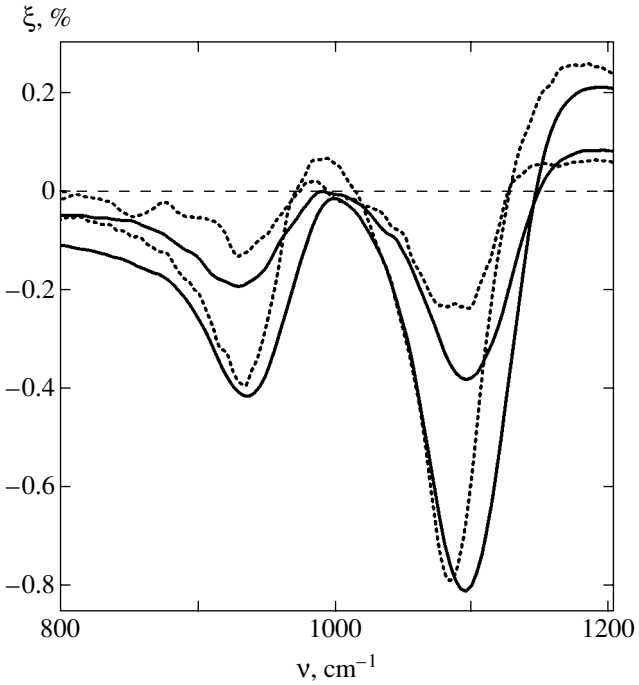

Fig. 6. Frequency dependences of the MRE of a $Co_{43}Al_{22}O_{35}$ film for two values of field ΔH = 2200 and 100 Oe: solid and dotted curves correspond to angles of incidence φ = 45° and 10°, respectively.

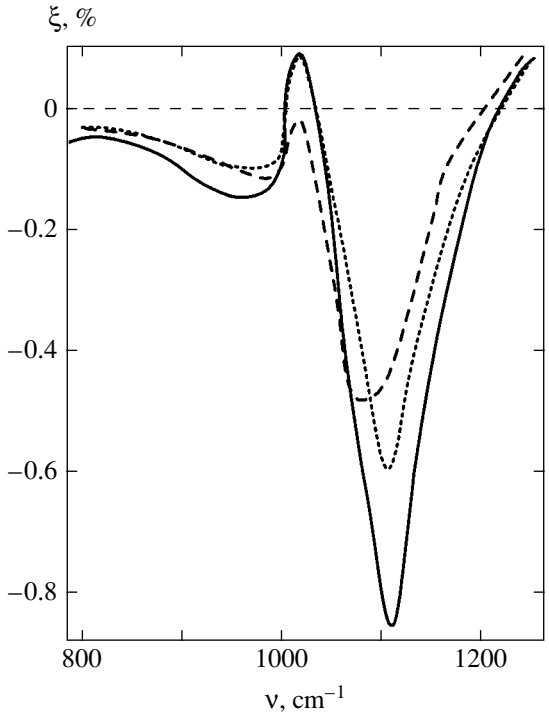

Fig. 7. Theoretical dependences of the MRE for a $Co_{43}Al_{22}O_{35}$ film: $\Delta\rho/\rho$ = 3% (solid curve); $\Delta\rho/\rho$ = 1%, φ = 45° (dotted curve); and $\Delta\rho/\rho$ = 1%, φ = 10° (dashed curve).

seen from the figure that the MRE attains a value of 1.5%, which is a record high for all metallic and nonmetallic systems studied and is two orders of magnitude stronger than the traditional magnetooptical effects. In accordance with relation (16), such a magnitude of the MRE is due to a low reflectance and a high magnetoresistance. It should be emphasized that expression (16) does not rule out higher values (on the order of 10%). Figure 9 shows the spectra of frequency dependences of the MRE for the same sample in a wider frequency range for φ = 45° and for three values of the magnetizing field H = 0, 1500, and 1700 Oe. The spectrum for H = 0 shows the noise level from which the response of the investigated signal to the action of

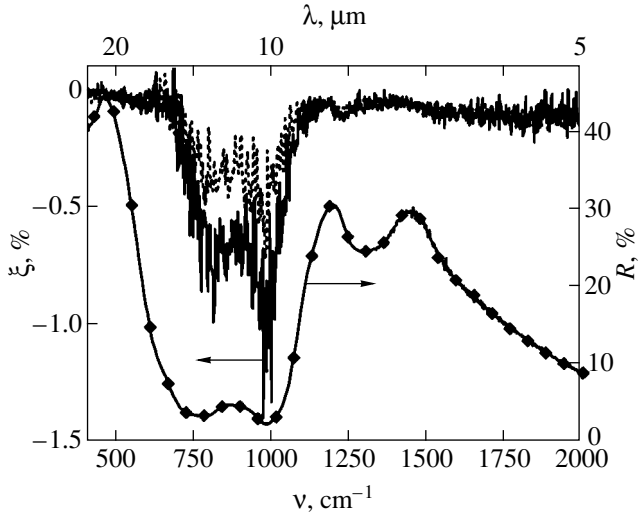

Fig. 8. Spectra of MRE ξ in fields $H = 1700$ Oe (solid curve) with a resolution of 2 cm^{-1} and $H = 1500$ Oe (dotted curve) with a resolution of 4 cm^{-1} and reflectance $R_{H=0}$ for a $(Co_{0.4}Fe_{0.6})_{48}(Mg_{52}F)$ film after averaging over 300 scans; $\varphi = 10°$.

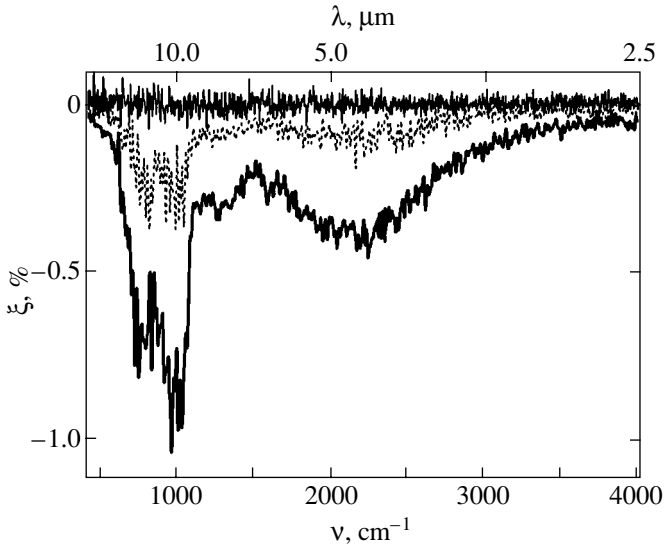

Fig. 9. Spectra of MRE ξ in fields $H = 1700$ Oe (solid curve) and $H = 1500$ Oe (dotted curve) and of noise with a resolution of 4 cm^{-1} for a $(Co_{0.4}Fe_{0.6})_{48}(Mg_{52}F)$ film after averaging over 300 scans; $\varphi = 45°$.

the magnetic field is separated. The magnitudes of the MRE for the above values of the field imply that the ξ(*H*) dependence is nonlinear.

The following two facts, which cannot be described in the framework of the theory developed in Section 1, are worth noting. First, it can be seen from Fig. 8 that the values of reflectance for λ = 20, 5 μm differ by a factor of 4, while the magnitude of the MRE is practically the same for these wavelengths. Second, the presence of two narrow and sharp MRE peaks in the vicinity of λ = 10 μm does not correlate with the behavior of the reflectance either. Finally, we cannot explain a considerable MRE "noise" in fields of 1.5 and 1.7 kOe in a wavelength range of 15–10 μm. These features are probably associated with an additional influence of the magnetic field on elementary excitations in the dielectric MgF matrix. It should also be borne in mind that the simple theory of high-frequency tunneling developed above disregards such factors as, for example, the effect of electron–electron interaction [20].

6. CONCLUSIONS

The experiments described here prove the existence of a new magnetooptical effect, viz., MRE, associated with spin-dependent tunneling in magnetic nanocomposites in the vicinity of the percolation threshold. The MRE obviously correlates with the tunnel magnetoresistance. Depending on the magnetoresistance and optical properties of the nanocomposite, the magnitude of the MRE varies over a wide range from 0.1 to 1.5%, which is one or two orders of magnitude higher than the even magnetooptical effect. The developed theory provides a qualitative and semiquantitative explanation for a number of experimental data and promises the attainment of even higher magnitudes of the MRE. It would undoubtedly be interesting to continue the investigation of the angular, polarization, and temperature dependences of the MRE; the search for mechanisms responsible for the MRE in metal–semiconductor systems; and the advancement to the far-IR spectral region as well as to the visible region for which new effects associated with the dependence of the tunnel transparency on the light frequency should be expected.

ACKNOWLEDGMENTS

The authors are grateful to S. Ohnuma, B. Aronzon, and M. Sedova, who supplied a number of Co–Al–O, Fe–SiO_2, and CoFe–MgF samples, and to A. Vedyaev and E. Shalygina for fruitful discussions.

This study was supported financially by the Russian Foundation for Basic Research (project no. 00-02-17797), the Ministry of Education, Science, Sports, and Culture of Japan (grant no. 14-205045), and the program Universities of Russia (project nos. 01.03.003 and 01.03.006).

REFERENCES

1. J. C. Jacquet and T. Valet, Mater. Res. Soc. Symp. Proc. **384**, 477 (1995).
2. A. B. Granovskiĭ, M. V. Kuzmichev, and J. P. Clerc, Zh. Éksp. Teor. Fiz. **116**, 1762 (1999) [JETP **89**, 955 (1999)].
3. M. Gester, A. Schlapka, R. A. Pickford, *et al.*, J. Appl. Phys. **85**, 5045 (1999).
4. H. F. Kubrakov, A. K. Zvezdin, K. A. Zvezdin, and V. A. Kotov, Zh. Éksp. Teor. Fiz. **114**, 1101 (1998) [JETP **87**, 600 (1998)].

5. G. M. Genkin, Phys. Lett. A **241**, 293 (1998).
6. S. Uran, M. Grimsditch, E. Fullerton, and S. D. Bader, Phys. Rev. B **57**, 2705 (1998).
7. V. G. Kravets, D. Bosec, J. A. D. Matthew, *et al.*, Phys. Rev. B **65**, 054415 (2002).
8. I. V. Bykov, E. A. Gan'shina, A. B. Granovskiĭ, and V. S. Gushchin, Fiz. Tverd. Tela (St. Petersburg) **42**, 487 (2000) [Phys. Solid State **42**, 498 (2000)].
9. D. Bozec, V. G. Kravets, J. A. D. Matthew, and S. M. Thompson, J. Appl. Phys. **91**, 8795 (2002).
10. A. B. Granovsky, E. A. Ganshina, V. S. Gushchin, *et al.*, in *Digests of INTERMAG-2003*, Boston, USA (2003).
11. G. S. Krinchik and M. V. Chetkin, Zh. Éksp. Teor. Fiz. **36**, 1924 (1959) [Sov. Phys. JETP **9**, 1368 (1959)].
12. G. S. Krinchik and V. S. Gushchin, Pis'ma Zh. Éksp. Teor. Fiz. **10** (1), 35 (1969) [JETP Lett. **10**, 24 (1969)].
13. G. A. Bolotin, Fiz. Met. Metalloved. **39**, 731 (1975).
14. V. M. Maevskiĭ, Fiz. Met. Metalloved. **59**, 213 (1985).
15. A. B. Granovskiĭ and A. N. Yurasov, Fiz. Met. Metalloved. (2003) (in press).
16. M. Buttiker and R. Landauer, Phys. Rev. Lett. **49**, 1739 (1982).
17. H. Kaiju, S. Fujita, T. Morozumi, and K. Shiiki, J. Appl. Phys. **91**, 7430 (2002).
18. S. Mitani, H. Fujimori, and S. Ohnuma, J. Magn. Magn. Mat. **165**, 141 (1997).
19. S. Ohnuma, K. Hono, E. Abe, *et al.*, J. Appl. Phys. **82**, 5646 (1997).
20. N. Kobayashi, S. Ohnuma, T. Masumoto, and H. Fujimori, J. Appl. Phys. **90**, 4159 (2001).
21. B. A. Aronzon, A. E. Varfolomeev, A. A. Likal'ter, *et al.*, Fiz. Tverd. Tela (St. Petersburg) **41**, 944 (1999) [Phys. Solid State **41**, 857 (1999)].
22. S. T. Chui and L. Hu, Appl. Phys. Lett. **80**, 273 (2002).

Translated by N. Wadhwa

Journal of Experimental and Theoretical Physics, Vol. 96, No. 6, 2003, pp. 1113–1121.
Translated from Zhurnal Éksperimental'noĭ i Teoreticheskoĭ Fiziki, Vol. 123, No. 6, 2003, pp. 1266–1275.

SOLIDS
Electronic Properties

The Thermodynamic Properties and Special Features of Spectra of Elementary Excitations of Unstable Valence Sm- and Ce-Based Compounds

E. V. Nefedova*, P. A. Alekseev, V. N. Lazukov, and I. P. Sadikov

Kurchatov Institute, Russian Research Center, Moscow, 123182 Russia

**e-mail: elene@isssph.kiae.ru*

Received December 5, 2002

Abstract—The experimental data on the spectra of elementary excitations measured by inelastic neutron scattering and on the heat capacity and the coefficient of thermal expansion are used to analyze the correlation between the spectral characteristics of the electron and phonon subsystems and the special features of the temperature dependence of the thermodynamic properties of a number of unstable valence Sm- and Ce-based compounds. The anomalous behavior of the thermodynamic properties of these compounds is defined by the special features of their phonon and electron (4*f* and conduction electrons) spectra. The rearrangement of the 4*f*-electron spectrum as a result of temperature variation plays a decisive part in the formation of temperature dependences of the heat capacity and the coefficient of thermal expansion of unstable valence systems. © *2003 MAIK "Nauka/Interperiodica".*

1. INTRODUCTION

Unstable valence compounds on the basis of rare-earth elements are characterized by the presence of a fairly large anomalous (or additional) contribution to the temperature dependences of the heat capacity and the coefficient of thermal expansion as compared to their isostructural analogs with an open or filled 4*f* shell [1, 2]. It is known that, in the case of rare-earth compounds with a stable magnetic moment, the anomalous contribution to the thermodynamic properties is due to the presence of 4*f* multiplets split in a crystal electric field [3]. This "traditional" interpretation of the anomalous contribution to thermodynamics cannot be employed in the case of unstable valence compounds, because no effects in a crystal electric field in the ordinary sense are present in these systems as a result of partial delocalization of 4*f* electrons.

As a rule, the anomalous contribution in unstable valence compounds, which is obtained as the difference between the heat capacities or the coefficients of thermal expansion of an unstable valence compound and its structural analog, is taken to be electronic by nature and directly associated only with the valence instability, i.e., with a nonintegral population of the 4*f* shell. In one of the early papers [4], the electron anomaly of the coefficient of thermal expansion of unstable valence compounds was interpreted as a result of variation of the population of the 4*f* shell of a rare-earth ion with temperature. As a matter of fact, in all of the subsequent papers, the population of the 4*f* shell was one of the main parameters treated in analyzing the thermodynamic properties [5–7]. The development of concepts of the effect of valence was marked by the need for taking into account various interactions observed in unstable valence systems (in particular, the electron–phonon interaction [8]) and leading to a variation of the internal energy and entropy of unstable valence systems. Note that the treatment of partial components associated with different interactions made it possible to interpret the thermal properties of heavy-fermion compounds in a wide temperature range, in particular, of $CeRu_2Si_2$ [9]. However, in the case of quantitative calculations of the anomalous thermodynamic and elastic properties of unstable valence compounds, an integral characteristic was introduced, as a rule. In particular, Takke *et al.* [10] used a phenomenological scaling function for the electron part of free energy, proportional to the universal energy scale T_0 characteristic of the systems being treated. The volume dependence of the electron part of free energy is defined by the volume dependence of T_0. This enables one to introduce the electron Grueneisen parameter $\Gamma_{el} = -d[\ln T_0]/d[\ln V]$ (where V is the volume) for the description of the electron and electron–phonon contributions: in terms of this parameter, the majority of thermodynamic quantities may be calculated. The above-described approach produces adequate agreement between theory and experiment at $T < T_0$; however, the problem of physical understanding of special features of the anomalies of the thermal expansion coefficient for different compounds (sign, amplitude, range of existence) cannot be fully solved. For example, in spite of the fact that the characteristic temperature ($T_0 \sim 150$ K) and the values of variation of valence

in the temperature range from 4 to 300 K ($|\Delta v_{RE}| \sim 0.05$) are comparable for SmB_6 [11] and CeNi [12], the anomalous contributions to the coefficient of thermal expansion of SmB_6 [13, 14] and CeNi [15, 16] have opposite signs, as well as essentially different scales and ranges of this anomaly.

In analyzing the thermodynamic properties of a number of specific unstable valence compounds (the so-called Kondo-insulators) in which, at a low temperature, a gap is formed in the electron density of states in the vicinity of the Fermi energy, it is the presence of the gap that is regarded as the main reason for the emergence of a significant additional contribution to the heat capacity and to the coefficient of thermal expansion. For example, the marked anomaly revealed in the electron component of heat capacity and coefficient of thermal expansion of SmB_6 was interpreted as the contribution arising as a result of excitation of electrons via a semiconductor gap of the order of 5 meV [17]. Adequate agreement was obtained between a model calculation and experiment; however, in this case, Mandrus *et al.* [17] examined a fairly narrow temperature range ($T < 80$ K) and restricted themselves to one binary compound. The significant negative component of the coefficient of thermal expansion in the higher temperature range ($T > 100$ K) [14]) remained unexplained.

Therefore, in analyzing the thermodynamic properties, the authors of the publications known to us either introduced (within the phenomenological approach) the universal integral parameter or treated a concrete special feature of the system being examined. However, they have, first of all, failed to take into account the real energy spectrum of excitations of 4*f* electrons and its rearrangement with temperature, which is known to be significant. The second important point to be noted is the need for taking into account the electron–phonon interaction. Indeed, a number of Sm- and Ce-based unstable valence compounds exhibit significant changes in the phonon dispersion curves compared to structural analogs [18, 19]. A renormalization of phonon frequencies in unstable valence compounds may bring about the emergence of an additional contribution to the heat capacity and coefficient of thermal expansion compared to the data for an isostructural analog. And, thirdly, in treating Kondo insulators, i.e., systems with a valence instability and a gap in the electron density of states in the vicinity of the Fermi energy, one must take into account the special features of the density of states of conduction electrons in the vicinity of the Fermi energy along with (rather than instead of) the 4*f*-electron contribution and the special features of the lattice vibration spectrum.

It was the objective of our study to estimate, using the example of $Sm_{1-x}La_xB_6$ and $Ce_{1-x}La_xNi$ compounds, the contribution made to the thermodynamics of unstable valence compounds due to the special features of the real spectral characteristics of the electron (4*f* and conduction electrons) and lattice subsystems and to use the resultant estimates to determine the part played by separate contributions in the formation of anomalous heat capacity and coefficient of thermal expansion in a wide temperature range. Samarium hexaboride (SmB_6) is known as a "classical" unstable valence compound with a "strong" intermediate valence. The valence of Sm ions at room temperature is $v_{Sm} \sim 2.55$ and decreases with cooling to $v_{Sm} \sim 2.50$ [11]. An important feature of SmB_6 is the presence of a narrow gap in the electron density of states in the vicinity of the Fermi energy, which was estimated in early papers at approximately 5–10 meV [2, 13]. Detailed investigations of the kinetic characteristics of SmB_6 were recently performed using high-quality samples [20–22]. It was experimentally shown in the latter papers and theoretically substantiated in [23] that the electron transport in SmB_6 is defined by at least two different energy scales, namely, the hybridization gap of approximately 10–20 meV and the "impurity" band in the vicinity of the bottom of the conduction band ($\Delta \sim$ 3 meV). The smaller energy scale is defined by the formation of a bound electron–polaron complex as a result of fast valence fluctuations on each Sm ion. The carrier concentration in the "impurity" band is estimated at approximately 10^{17} cm^{-3} [23]. CeNi is an intermetallic unstable valence compound with a "moderate" intermediate valence ($v_{Ce} \sim 3.11$ at room temperature and $v_{Ce} \sim 3.14$ at $T = 10$ K [12]). The spectra of lattice and 4*f*-electron excitations of SmB_6 and CeNi have been studied in sufficient detail [24]. In addition, the valent state of a rare-earth ion in both compounds may be purposefully varied when a Sm (or Ce) ion is replaced by a La ion. A variation of the valent state leads to a marked transformation of the 4*f*-electron and phonon spectra. Therefore, a study of dilute systems ($Sm_{1-x}La_xB_6$ and $Ce_{1-x}La_xNi$) offers a possibility of checking the generality of the inferences made for stoichiometric compounds and of more reliably determining the general regularities of the formation of anomalies in the thermodynamic properties.

2. CALCULATION OF THERMODYNAMIC PROPERTIES

Anomalous contributions to the thermodynamic properties of unstable valence $Sm_{1-x}La_xB_6$ and $Ce_{1-x}La_xNi$ compounds were treated within a unified approach as a result of summation of independent (in a first approximation) components associated with the actual special features of the phonon and electron (4*f* electrons and conduction electrons) spectra.

The following expression was used to calculate the anomalous contribution to the heat capacity:

$$\Delta C(T) = C_f(T) + \Delta C_{lat}(T) + C_g(T), \qquad (1)$$

where C_f is the heat capacity due to the special features of the 4*f*-electron excitation spectrum. The value of C_f was determined on the basis of the experimentally measured 4*f*-electron excitation spectrum for unstable valence compounds; the structure of this latter spectrum provides information about the density of states of 4*f* electrons. In calculating the heat capacity, the multiplicity of degeneracy of the ground state of a rare-earth ion was taken into account; ΔC_{lat} is the additional lattice contribution to the heat capacity of unstable valence compounds, which arises as a result of renormalization of phonon frequencies in unstable valence compounds compared to isostructural materials. This latter contribution was obtained as a difference between the lattice contribution to the heat capacity of an unstable valence compound and the corresponding contribution to the heat capacity of an isostructural analog containing no 4*f* electrons. In the case of SmB_6, the density of phonon states was obtained from the experimentally measured dispersion curves [18] on the basis of model calculations which take into account the contribution by the exciton–phonon interaction. For CeNi, we used the phonon density of states obtained from experiments in inelastic neutron scattering [25]; the value of C_g is the contribution to the heat capacity, which is due to the gap in the electron density of states in the vicinity of the Fermi level. This contribution was obtained for $Sm_{1-x}La_xB_6$ compounds as the difference between the total experimentally obtained anomalous contribution to the heat capacity and the calculated contributions C_f and ΔC_{lat}.

The corresponding partial contributions to the coefficient of thermal expansion of unstable valence compounds (α_i) were determined on the basis of the Grueneisen relation by fitting the Grueneisen coefficients (Γ_i). In the calculation, the possible temperature dependence of the Grueneisen coefficients was ignored. The total anomalous contribution to the coefficient of thermal expansion ($\Delta\alpha$) was obtained as the sum of separate partial contributions,

$$\begin{aligned}\Delta\alpha(T) &= \alpha_f(T) + \Delta\alpha_{\text{lat}}(T) + \alpha_g(T)\\ &= V^{-1}X_T[\Gamma_f C_f(T) + \Gamma^*_{\text{lat}}\Delta C_{\text{lat}}(T) + \Gamma_g C_g(T)],\end{aligned} \quad (2)$$

where α_f is the contribution defined by the 4*f*-electron excitation spectrum, $\Delta\alpha_{\text{lat}}$ is the additional lattice contribution associated with the transformation of phonon spectra, α_g is the contribution by the gap in the density of electron states in the vicinity of the Fermi energy, V is the molar volume, and X_T is the isothermal compressibility. For the compounds treated by us, the molar volume and isothermal compressibility depend little on temperature. In the calculation, their values were taken to be constant parameters. The values of isothermal compressibility for SmB_6 (0.125×10^{-4} cm^3 J^{-1}) and CeNi (1.02×10^{-4} cm^3 J^{-1}) were borrowed from [26] and [27], respectively.

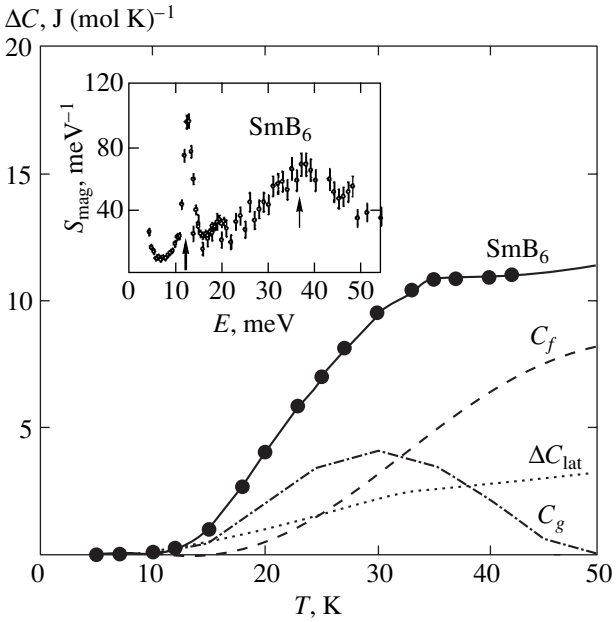

Fig. 1. The temperature dependence of the experimentally obtained anomalous contribution to the heat capacity of SmB_6 (●) [14] and the calculated partial contributions. The dashed line indicates the contribution associated with the 4*f*-electron states (C_f). The dotted line indicates the additional lattice contribution (ΔC_{lat}). The dot-and-dash line indicates the contribution describing the electron gap in the vicinity of the Fermi energy (C_g). The solid line indicates the total calculated contribution to the anomalous heat capacity of SmB_6. Shown in the inset is the low-energy part of the magnetic response for SmB_6 [24]. The bold arrow indicates the low-energy excitation at $E_{\text{ex}} \approx 14$ meV, and the thin arrow indicates the strongly broadened spin–orbit transition $J_0 \longrightarrow J_1$ for Sm^{2+} ($E \approx 36$ meV).

3. RESULTS AND DISCUSSION

All of the calculations and analysis were based on the experimental information obtained by us over a number of years for spectra of 4*f*-electron and lattice excitations [14, 18, 19, 24, 25] and detailed data on the temperature dependences of the coefficient of thermal expansion for $Sm_{1-x}La_xB_6$ and $Ce_{1-x}La_xNi$ [14, 16] and of the heat capacity for $Sm_{1-x}La_xB_6$ [14].

3.1. $Sm_{1-x}La_xB_6$ Compound

We will examine the possible components (or reasons for) the anomalous heat capacity of SmB_6. Figure 1 gives the temperature dependences of the experimentally observed anomalous contribution to the heat capacity of SmB_6 [14] in the low-temperature region, which was already analyzed in the literature [2, 17], as

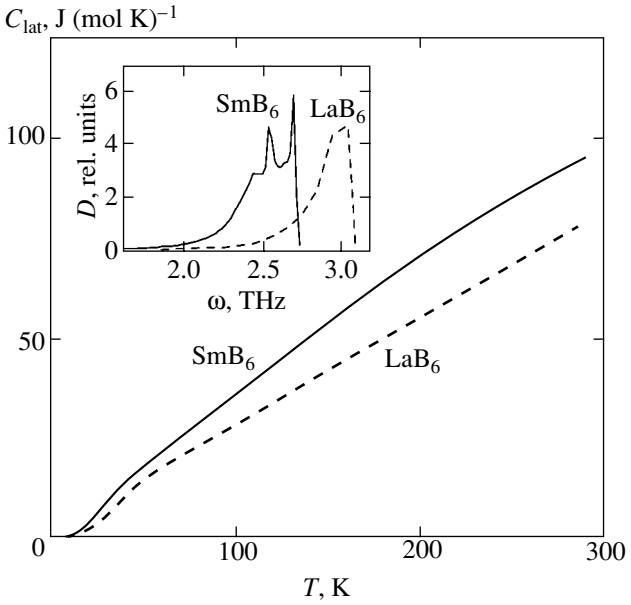

Fig. 2. The temperature dependence of the lattice contribution to the heat capacity for SmB_6 (solid line) and LaB_6 (dashed line), calculated from the phonon density of states (see the text). Shown in the inset is the phonon density of states of acoustic branches in SmB_6 (solid line) and LaB_6 (dashed line).

well as the calculated (total and partial) contributions to the heat capacity of SmB_6.

The phonon dispersion curves of SmB_6 significantly differ from those of its isostructural analog LaB_6 [18]. These differences are associated with the presence of resonant interaction of normal lattice vibrations with dipole (*f–d*) and monopole (*f–f*) excitations of the 4*f* shell of Sm; i.e., it would appear that the electron–phonon interaction is superimposed on the phonon spectrum of LaB_6 and distorts this spectrum by virtue of the nonadiabaticity of the electron subsystem that arises upon formation of the unstable valence state. As a result, the density of phonon states of SmB_6 shift to the region of lower frequencies with respect to LaB_6 (Fig. 2, inset). This cannot but reflect on the temperature behavior of the heat capacity. Figure 2 gives the calculated lattice components of heat capacity C_{lat} for SmB_6 and LaB_6. One can see that the value of heat capacity C_{lat} for SmB_6 markedly exceeds that for LaB_6 in a wide temperature range. Consequently, because of the strong electron–phonon interaction and corresponding renormalization of the phonon frequencies, the unstable valence state of Sm brings about the emergence of an additional contribution to the lattice heat capacity (ΔC_{lat}) at $T < 300$ K in SmB_6 (compared to LaB_6), which represents an appreciable fraction of the entire anomalous heat capacity of SmB_6 (Fig. 1).

Along with singularities in the atomic vibration spectrum, samarium hexaboride has a specific spectrum of 4*f*-electron excitations [24] (Fig. 1, inset). The main special features of the 4*f*-electron spectrum of SmB_6 include the great width of spin–orbit excitation ($J_0 \longrightarrow J_1$) and the presence of additional narrow low-energy excitation (marked by arrow in the inset in Fig. 1) associated with the formation, at low temperature, of a new ground, quantum-mechanically mixed state of samarium ion. As the temperature rises, the intensity of low-energy excitation decreases; however, a quasi-elastic component arises. Such a spectrum of 4*f*-electron states and its transformation with temperature produce additionally a significant contribution C_f to the anomalous heat capacity of SmB_6 (Fig. 1).

After the sum of two components ($C_{lat} + C_f$) is subtracted from the experimentally determined anomalous heat capacity of SmB_6, the part with a maximum at $T \approx 30$ K remains in $\Delta C(T)$; this latter part is apparently associated with the effect of excitation of electrons via the gap in the spectrum of electron states in the vicinity of the Fermi energy (C_g). As was mentioned in the Introduction, it has now been reliably found that two energy scales are characteristic of SmB_6, namely, the hybridization gap and "impurity" band [21]. If a two-level model is used to evaluate the gap from the temperature dependence $C_g(T)$, a value on the order of 60 K is obtained. This value is close to the scale of hybridization effects (in this case, one must take into account the possible temperature dependence of the gap size proper). The absence of a marked effect of the "impurity" band on the thermodynamic properties is apparently due, first, to the low density of states in this band and, second, to the thermal dissociation of the "impurity" states at $T \sim 15$ K [23].

Therefore, the formation of an anomalous contribution to the heat capacity of samarium hexaboride is associated with three special features of this system, namely, the strong electron–phonon interaction, the specific spectrum of 4*f*-electron states, and the existence of a gap in the density of electron states in the vicinity of the Fermi energy. In accordance with the Grueneisen relation given by Eq. (2), the anomalous contribution to the coefficient of thermal expansion of SmB_6 must also have three components. Figure 3a gives the anomalous contribution to the experimentally obtained coefficient of thermal expansion of SmB_6 [14] and the calculated components of the coefficient of thermal expansion. One can see that the overall calculated coefficient of thermal expansion reproduces the main special features of the temperature dependence of the experimentally determined anomalous contribution to the coefficient of thermal expansion. However, the temperature dependence curve of the calculated coefficient of thermal expansion is smoother than that of the experimentally obtained coefficient. This is possibly associated with the somewhat simplified approach employed by us. It was assumed in the calculation that the Grueneisen coefficient was temperature-indepen-

dent. Apparently, when treating systems with a strong interaction of the electron and lattice subsystems, one must take into account some temperature dependence of the Grueneisen coefficient.

The calculated negative values of partial Grueneisen coefficients (Table 1) are experimentally validated. The information about the sign of Γ may be provided, for example, by experiments performed under pressure, because $\Gamma \propto d(\ln E)/dP$ (where E is the characteristic energy of the subsystem and P is the pressure). Investigations of the electric resistance of samarium hexaboride as a function of pressure revealed a linear decrease in the gap size with increasing pressure [28]. Consequently, the Grueneisen coefficient Γ_g must be negative.

Neutron experiments performed under pressure have revealed that, at $E_{ex} = 14$ meV (the inset in Fig. 1), the exciton-like magnetic excitation observed under normal external pressure shifts to the region of lower energies ($E_{ex} = 7$ meV at $P = 7$ GPa) [29]. This indicates that the value of Γ_f is negative.

The situation is somewhat more complicated in the case of the Grueneisen coefficient for the additional lattice contribution. No measurements have been performed up to now of the phonon dispersion curves of SmB_6 under pressure. Therefore, we restrict ourselves to qualitative considerations with respect to the possibility of emergence of a negative value of Γ^*_{lat}. In normal cubic systems with integral valence, a decrease in the volume of a unit cell leads to an increase in the phonon frequencies. In SmB_6, which is characterized by partly delocalized 4*f* electrons, a softening of the photon spectrum has been experimentally observed as compared to LaB_6 [18], in spite of the significantly smaller volume of a unit cell of samarium hexaboride. Because, when a minor external pressure is applied, samarium ions become more "intermediately valent" [29] (the valence of samarium ions under pressure is $v_{Sm} \longrightarrow 3^+$ [30]), it is logical to assume that this results in a still further softening of the phonon frequencies in SmB_6. That is, the negative value of the Grueneisen coefficient Γ^*_{lat} does not contradict the physical patterns discussed above for this compound. In order to arrive at a final conclusion with respect to the sign of Γ^*_{lat}, one needs to perform direct measurements of phonon dispersion curves under pressure.

Analysis of the anomalous coefficient of thermal expansion of SmB_6 has revealed (Fig. 3a) that, at a low temperature ($T < 100$ K), coefficient $\Delta\alpha(T)$ is largely associated with special features of the 4*f*-electron spectrum and with the gap in the density of electron states in the vicinity of the Fermi energy. Previously, the anomalous contribution to the coefficient of thermal expansion at $T < 100$ K was interpreted either as a result of the presence of the gap [17] or as a result of the temperature variation of the valence of a Sm ion [2]. At $T > 100$ K, the significant negative contribution is largely defined by the strong electron–phonon interaction. Note that the reasons for the emergence of the additional component of the coefficient of thermal expansion at $T > 100$ K were not understood heretofore, because the valence of samarium ions at temperatures above 110 K remains a constant quantity [11], and the

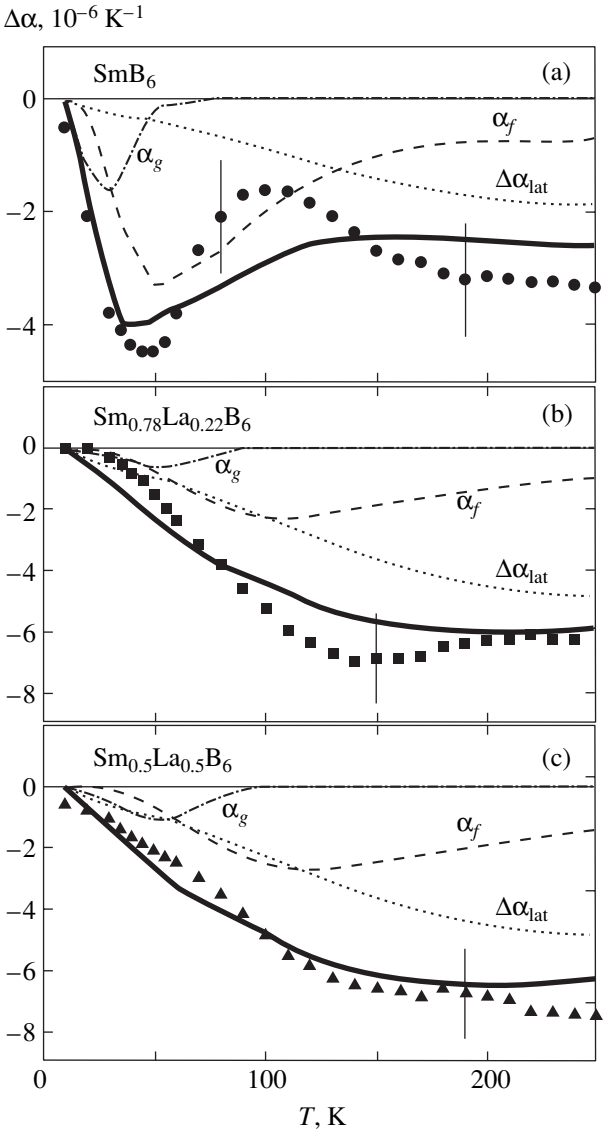

Fig. 3. The temperature dependence of the experimentally obtained anomalous contribution to the coefficient of thermal expansion for $Sm_{1-x}La_xB_6$ [14] and the calculated partial contributions: (a) $x = 0$, (b) $x = 0.22$, (c) $x = 0.5$. The dotted line indicates the additional lattice contribution ($\Delta\alpha_{lat}$). The dashed line indicates the contribution associated with the 4*f*-electron states (α_f). The dot-and-dash line indicates the contribution describing the electron gap in the vicinity of the Fermi energy (α_g). The solid line indicates the total calculated contribution to the coefficient of thermal expansion of $Sm_{1-x}La_xB_6$.

Table 1. The Grueneisen coefficients of partial components of the anomalous contribution to the coefficient of thermal expansion for $Sm_{1-x}La_xB_6$ compounds

Sample	Γ_f	Γ^*_{lat}	Γ_g
SmB_6	–1.5	–0.4	–1.5
$Sm_{0.78}La_{0.22}B_6$	–1.2	–0.9	–1.0
$Sm_{0.5}La_{0.5}B_6$	–1.0	–1.2	–1.0

effect of the electron components is significantly weakened.

We will treat SmB_6-based compounds for which the valent state of samarium ion varies upon substitution of Sm by La ($Sm_{1-x}La_xB_6$). All ternary compounds are likewise characterized by the presence of the additional negative contribution to the coefficient of thermal expansion (Figs. 3b and 3c); however, the main singularity (a minimum of $\Delta\alpha(T)$ at $T < 100$ K) shifts to the region of higher temperatures. We will discuss the dependence $\Delta\alpha(T)$ for dilute compounds from the standpoint of the importance of all components responsible for the anomalous coefficient of thermal expansion in SmB_6. An investigation of spectra of lattice excitations of $Sm_{1-x}La_xB_6$ has revealed that all dilute compounds exhibit a general softening of acoustical phonons compared with LaB_6; however, compared with SmB_6, the variation of the phonon frequencies in those dilute compounds is insignificant [14]. Therefore, the exciton model suggested for the description of spectra of lattice vibrations for SmB_6 is apparently valid for dilute systems as well. Consequently, the anomalous coefficient of thermal expansion of dilute samples must incorporate the component $\Delta\alpha_{lat}$ associated with the electron–phonon interaction. Because the lanthanum doping failed to bring about significant changes in the phonon spectrum of samarium hexaboride, the value of $\Delta\alpha_{lat}$ in dilute systems remained the same as in SmB_6 (Figs. 3b and 3c).

In $Sm_{1-x}La_xB_6$ compounds, the component $\alpha_f(T)$ due to the presence of 4*f* electrons significantly differs from the analogous component for SmB_6; this is associated with qualitative changes in the 4*f*-electron excitation spectra. According to the data on the inelastic magnetic scattering of neutrons, the low-energy excitation in La-substituted samples, which is associated with the new ground state of samarium ions, is characterized by different experimentally observed values of parameters such as the energy, intensity, and temperature dependence [29]. The substitution by La brings about an increase in the energy of "low-energy excitation" observed in SmB_6 to 25–30 meV; in so doing, the temperature dependence of the intensity also varies and becomes smoother. This leads to a marked shift of the $\alpha_f(T)$ maximum to the region of higher temperatures and to its weakening. Finally, the $\alpha_g(T)$ component remains in dilute samples, which is largely due to the gap in the vicinity of the Fermi energy, by analogy with SmB_6. This fact must be given special attention, because it is generally taken that, when SmB_6 is doped with lanthanum, the gap in the spectrum of electron states disappears even at a low concentration of La [2]. The results of our thermodynamic measurements [14] point to the existence of a gap in all dilute samples up to $x = 0.5$. The statement about the absence of a gap in dilute samples is based on the results of measurements of electric resistance alone and apparently fails to fully reflect the microscopic properties, because the additional states introduced by lanthanum ions "shunt" the gap in kinetic measurements. However, the form of the density of states suffers no cardinal changes. Additional states show up, for example, in the marked increase in the value of the Sommerfeld coefficient at low temperatures [14].

By and large, the values of $\Delta\alpha_{cal}(T)$ for $Sm_{1-x}La_xB_6$ are in adequate agreement with experiment. Consequently, the anomalous contribution to the coefficient of thermal expansion for $Sm_{1-x}La_xB_6$ has three components. For dilute systems, the high-temperature anomalous negative contribution to the coefficient of thermal expansion is largely defined by the electron–phonon interaction and, at $T < 150$ K, it is defined by the special features of the spectrum of states of 4*f* electrons. One can clearly see that the shift of position of the minimum of $\Delta\alpha(T)$ at $T < 100$ K in dilute compounds relative to SmB_6 is largely the result of qualitative variation of the 4*f*-electron spectrum.

Analysis of the temperature dependence of the coefficient of thermal expansion in a wide temperature range for $Sm_{1-x}La_xB_6$ compounds revealed the following. For all of the treated compounds, the anomalous contribution $\Delta\alpha(T)$ may be interpreted in view of the main special features of these compounds, namely, the presence of a narrow gap in the spectrum of electron states in the vicinity of the Fermi energy and the unstable valence state of samarium ion, which affects the parameters of spectra of magnetic and lattice excitations. It was found that, at low temperatures, the value of $\Delta\alpha(T)$ is largely defined by the contribution associated with the 4*f*-electron spectrum and by the presence of a gap in the spectrum of electron states. The significant contribution to the coefficient of thermal expansion and to the heat capacity at $T > 80$–100 K is associated with the manifestation of electron–phonon interaction, i.e., with the result of the effect of the unstable valence state of Sm ions on the lattice dynamics.

3.2. $Ce_{1-x}La_xNi$ Compound

Since CeNi is a metal, $\Delta C(T)$ and $\Delta\alpha(T)$ will be determined only by the effect of the unstable valence state on the spectrum of magnetic and lattice excitations.

We will treat the temperature dependence of the anomalous contribution to the heat capacity of CeNi. In CeNi, as in SmB_6, one can expect the emergence of a contribution associated with the renormalization of phonon frequencies, because a strong softening of phonon vibrations in CeNi compared to LaNi was experimentally observed recently [19]. In contrast to SmB_6, the difference between the spectra of lattice vibrations of CeNi and LaNi leads to the emergence of the heat capacity component ΔC_{lat} only at low temperatures (Fig. 4). The reason for the difference between the additional lattice contributions ΔC_{lat} in CeNi and SmB_6 is associated with the much "softer" vibrational spectrum of CeNi (Fig. 4, inset). The entire RNi spectrum fits the 0–5 THz range; the acoustic region in which the softening is observed corresponds to the 0–2 THz range [24]. The total SmB_6 spectrum extends up to 40 THz. The inset in Fig. 2 shows only the acoustic region for SmB_6.

The heat capacity component C_f due to the presence of 4*f* electrons was calculated using the experimental data on the 4*f*-electron spectrum in CeNi in view of the temperature dependence of the latter spectrum [24]. Figure 4 shows that the calculated heat capacity by and large enables one to describe the main special features of the experimentally obtained heat capacity. The main reason for the formation of an anomalous contribution to the heat capacity of CeNi was found to be due to the existence of an unusual spectrum of states of 4*f* electrons at a low temperature and to its rearrangement with increasing temperature. However, the experimentally observed anomalous contribution to the heat capacity differs in magnitude from that calculated at $T < 200$ K. The value of entropy for the 4*f*-electron contribution (about 9 J (mol K)$^{-1} \approx R\ln 3$, where R is the gas constant) obtained upon integration of the calculated anomalous contribution to the heat capacity is much lower than the value of entropy determined by integration of the experimentally obtained value in the same temperature range (about 13.5 J (mol K)$^{-1} \approx R\ln 5$). This fact indicates that, along with the treated contributions, this system is characterized by additional degrees of freedom which were disregarded in our calculations but could have resulted in changes of the internal energy of the system. In particular, the presence of coherence in the rare-earth ion sublattice, most likely associated with magnetic interaction, and its importance in the formation of low-temperature properties were observed during investigations of $Ce_{1-x}(Y,La)_xNi$ compounds [12, 16].

We will now turn to the anomalous contribution to the coefficient of thermal expansion, $\Delta\alpha(T)$, for CeNi (Fig. 5a). The anomalous contribution to the coefficient of thermal expansion of CeNi, $\Delta\alpha(T)$, is adequately described in a wide temperature range in the case of the values of the partial Grueneisen coefficient of $\Gamma \sim 2$ (Table 2). Unlike SmB_6-based compounds, the Grueneisen coefficients Γ_f and Γ^*_{lat} of CeNi have positive

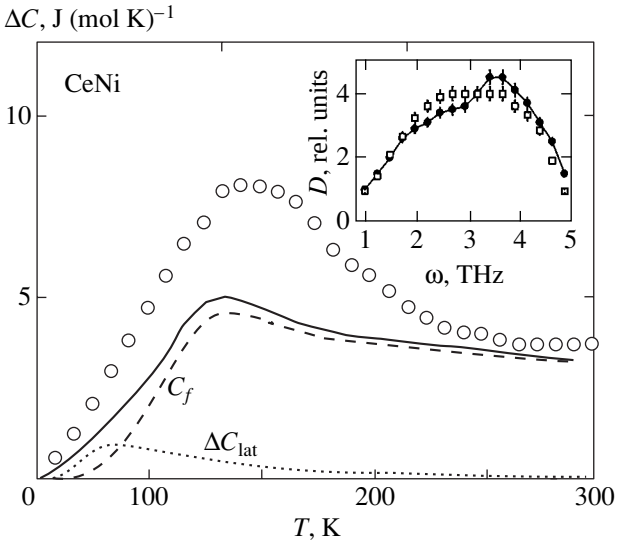

Fig. 4. The temperature dependence of the experimentally obtained anomalous contribution to the heat capacity of CeNi (○) [15] and the calculated partial contributions. The dashed line indicates the contribution associated with the 4*f*-electron states (C_f). The dotted line indicates the additional lattice contribution ($\Delta\alpha_{lat}$). The solid line indicates the total calculated contribution to the anomalous heat capacity of CeNi. Shown in the inset is the generalized function of phonon states for CeNi (•) and LaNi (□) obtained from experiments in inelastic neutron scattering [25].

values. The positive value of Γ_f may be validated by the results of investigation of the spectrum of magnetic excitations with applied "chemical" pressure. Indeed, the substitution of Ce by La (the introduction of lanthanum ions into the CeNi lattice causes the latter to expand, which is equivalent to the application of "negative" external pressure) brings about the shift of the 4*f*-electron spectrum to the region of lower energies [25]. In order to validate the positive sign of Γ^*_{lat}, additional experiments are required to investigate phonon curves under pressure or with chemical substitution.

One can see in Fig. 5a that, for CeNi, the great positive anomaly in $\Delta\alpha(T)$ is largely defined by the spectrum of states of 4*f* electrons. This inference was strongly supported by the results of calculation of $\Delta\alpha(T)$ for $Ce_{1-x}La_xNi$ compounds in which the valence of a cerium ion approaches 3^+ as Ce is substituted by La. In studying the spectra of excitations of 4*f* electrons

Table 2. The Grueneisen coefficients of partial components of the anomalous contribution to the coefficient of thermal expansion for $Ce_{1-x}La_xNi$ compounds

Sample	Γ_f	Γ^*_{lat}
CeNi	2.0	2.0
$Ce_{0.5}La_{0.5}Ni$	1.5	1.0

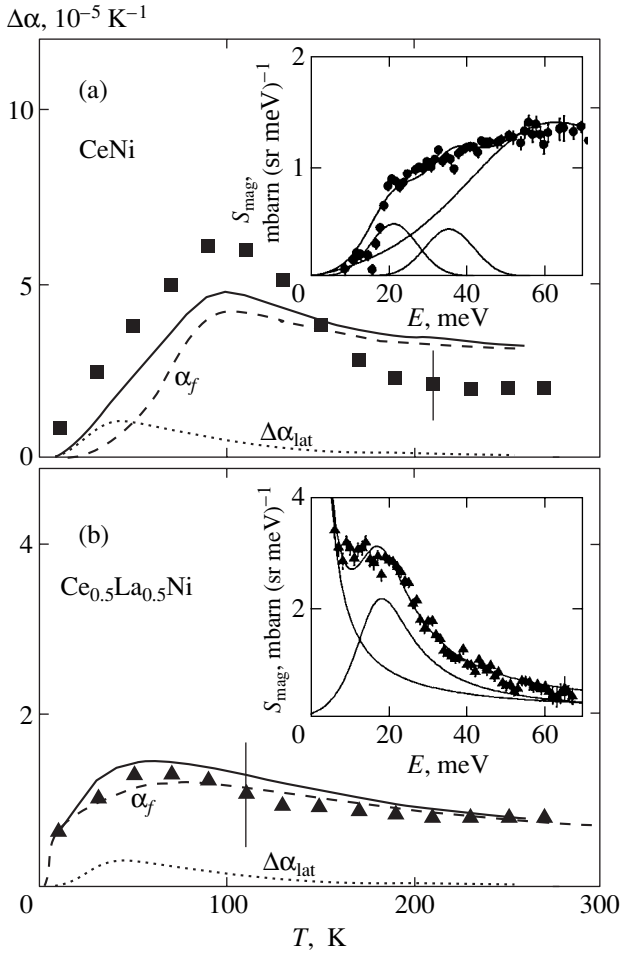

Fig. 5. The temperature dependence of the experimentally obtained anomalous contribution to the coefficient of thermal expansion for $Ce_{1-x}La_xNi$ [16] and the calculated partial contributions: (a) $x = 0$, (b) $x = 0.5$. The dotted line indicates the additional lattice contribution ($\Delta\alpha_{lat}$). The dashed line indicates the contribution associated with the 4*f*-electron states (α_f). The solid line indicates the total calculated contribution to the coefficient of thermal expansion. The insets show the magnetic response for CeNi and $Ce_{0.5}La_{0.5}Ni$. The lines in the insets indicate the result of fitting [25].

using the method of inelastic neutron scattering [25], it was observed that a qualitative transformation of the 4*f*-electron spectrum occurs when CeNi is doped with lanthanum (insets in Figs. 5a and 5b). The reason for this transformation is associated with the transition of Ce ions from a state with intermediate valence to a state with an almost localized magnetic moment (Kondo state). One can see that the calculated contribution $\Delta\alpha(T)$ for the $Ce_{0.5}La_{0.5}Ni$ compound agrees well with the experimentally observed anomalous contribution; this calculated contribution both allows for the shift of the maximum to the region of lower temperatures and reflects a gradual decrease in this maximum (Fig. 5b). The dilution results in the violation of coherence in the rare-earth ion sublattice; i.e., the possible additional contribution to the coefficient of thermal expansion, which was discussed when analyzing CeNi, disappears in dilute compounds. Indeed, the description of the temperature dependence of the coefficient of thermal expansion is significantly improved in the case of a dilute compound. Therefore, the main reason for the strong variation in $\Delta\alpha(T)$ in $Ce_{1-x}La_xNi$ is due to the modification of the spectrum of excitations of 4*f* electrons as a result of transition of a Ce ion from a state with intermediate valence to a state with an almost localized magnetic moment. It will be recalled that the substitution with lanthanum in SmB_6 did not cause the disappearance of either the calculated or the experimentally obtained extremum of the coefficient of thermal expansion. The unstable valence state of a Sm ion is characteristic of all of the samarium compounds treated by us [14].

In view of the foregoing, the temperature dependence of the coefficient of thermal expansion of $Ce_{1-x}La_xNi$ is largely defined by the spectrum of excitations of 4*f* electrons. At low temperatures, however, one cannot but take into account the component associated with the special features of the spectrum of lattice excitations.

4. CONCLUSIONS

The anomalous contribution to the temperature dependence of the thermodynamic quantities of Ce- and Sm-based unstable valence systems in a wide temperature range may be described in view of the actual special features of the excitation spectra of the electron and phonon subsystems. It has been found that the reason for the emergence of a low-temperature ($T < 80$ K) anomaly of the heat capacity and of the coefficient of thermal expansion of SmB_6 is due to the specific spectrum of 4*f*-electron states and to the presence of a gap in the electron density of states in the vicinity of the Fermi energy. At $T > 100$ K, a significant negative anomaly of the coefficient of thermal expansion arises because of the strong electron–phonon interaction and associated variation of the phonon frequencies. The renormalization of the phonon frequencies in CeNi relative to LaNi leads to the emergence of a marked component at a low temperature. The anomalous contribution to the heat capacity and the great positive anomalous contribution to the coefficient of thermal expansion of CeNi are largely defined by the unusual spectrum of 4*f* electrons. The general and main reason for the strong modification of the temperature dependence of the coefficient of thermal expansion for Sm- and Ce-based compounds consists in the transformation of the spectrum of 4*f*-electron states.

ACKNOWLEDGMENTS

We are grateful to A.S. Mishchenko, K.A. Kikoin, V.G. Vaks, A.A. Chernyshov, E.S. Klement'ev, and J.-M. Mignot for valuable discussions.

This study was supported by the Russian Foundation for Basic Research (project nos. 02-02-16521 and 03-02-17467), the Leading Scientific Schools Program, and the NIKS Russian State Program.

REFERENCES

1. J. M. Lawrence, P. S. Riseborough, and R. D. Parks, Rep. Progr. Phys. **44**, 24 (1981).
2. P. Wachter, in *Handbook on the Physics and Chemistry of Rare Earth*, Ed. by K. A. Gschneidner, Jr., L. Eyring, G. H. Lander, and G. R. Choppin (North-Holland, Amsterdam, 1994), Vol. 19, p. 177.
3. H.-G. Purwins, Ann. Phys. **7**, 329 (1972).
4. E. Müller-Hartmann, Solid State Commun. **31**, 113 (1979).
5. N. E. Bickers, D. L. Cox, and J. W. Wilkins, Phys. Rev. B **36**, 2036 (1987).
6. A. S. Edelstein and N. C. Koon, Solid State Commun. **48**, 269 (1983).
7. R. Pott, R. Schefzyk, D. Wohlleben, *et al.*, Z. Phys. B: Condens. Matter **44**, 17 (1981).
8. G. Creuzet and D. Gignoux, Phys. Rev. B **33**, 515 (1986).
9. A. Lacerda, A. de Visser, P. Haen, *et al.*, Phys. Rev. B **40**, 8759 (1989).
10. R. Takke, M. Niksch, W. Assmus, *et al.*, Z. Phys. B: Condens. Matter **44**, 33 (1981).
11. J. M. Tarascon, Y. Isikawa, B. Chevalier, *et al.*, J. Phys. (Paris) **41**, 1135 (1980).
12. V. N. Lazukov, E. V. Nefedova, V. V. Sikolenko, *et al.*, Fiz. Met. Metalloved. **93**, 61 (2002).
13. J. M. Tarascon, Y. Isikawa, B. Chevalier, *et al.*, J. Phys. (Paris) **41**, 1141 (1980).
14. E. V. Nefedova, P. A. Alekseev, E. S. Klement'ev, *et al.*, Zh. Éksp. Teor. Fiz. **115**, 1024 (1999) [JETP **88**, 565 (1999)].
15. D. Gignoux, F. Givord, R. Lemaire, *et al.*, J. Less-Common Met. **94**, 165 (1983).
16. V. N. Lazukov, P. A. Alekseev, E. S. Klement'ev, *et al.*, Zh. Éksp. Teor. Fiz. **113**, 1731 (1998) [JETP **86**, 943 (1998)].
17. D. Mandrus, J. L. Sarrao, A. Lacerda, *et al.*, Phys. Rev. B **49**, 16809 (1994).
18. P. A. Alekseev, A. S. Ivanov, B. Dorner, *et al.*, Europhys. Lett. **10**, 457 (1989).
19. E. S. Clementyev, M. Braden, V. N. Lazukov, *et al.*, Physica B (Amsterdam) **259**–**261**, 42 (1999).
20. B. Gorshunov, N. Sluchanko, A. Volkov, *et al.*, Phys. Rev. B **59**, 1808 (1999).
21. N. E. Sluchanko, V. V. Glushkov, B. P. Gorshunov, *et al.*, Phys. Rev. B **61**, 9906 (2000).
22. S. Gabáni, K. Flachbart, E. Konovalova, *et al.*, Solid State Commun. **117**, 641 (2001).
23. S. Curnoe and K. A. Kikoin, Phys. Rev. B **61**, 15714 (2000).
24. P. A. Alekseev, V. N. Lazukov, J.-M. Mignot, and I. P. Sadikov, Physica B (Amsterdam) **281**–**282**, 34 (2000).
25. V. N. Lazukov, P. A. Alekseev, E. S. Clementyev, *et al.*, Europhys. Lett. **33** (2), 141 (1996).
26. S. Nakamura, T. Goto, M. Kasaya, and S. Kunii, J. Phys. Jpn. **60**, 4311 (1991).
27. D. Gignoux, C. Vettier, and J. Voiron, J. Magn. Magn. Mat. **70**, 388 (1987).
28. I. V. Berman, N. B. Brant, V. V. Moshchalkov, *et al.*, Pis'ma Zh. Éksp. Teor. Fiz. **38**, 393 (1983) [JETP Lett. **38**, 477 (1983)].
29. P. A. Alekseev, J.-M. Mignot, V. N. Lazukov, *et al.*, J. Solid State Chem. **133**, 230 (1997).
30. J. Röhler, in *Handbook on the Physics and Chemistry of Rare Earth*, Ed. by K. A. Gschneidner, Jr., L. Eyring, and S. Hüfner (North-Holland, Amsterdam, 1987), Vol. 10, p. 453.

Translated by H. Bronstein

Journal of Experimental and Theoretical Physics, Vol. 96, No. 6, 2003, pp. 1122–1123.
Translated from Zhurnal Éksperimental'noĭ i Teoreticheskoĭ Fiziki, Vol. 123, No. 6, 2003, pp. 1276–1277.

SOLIDS
Electronic Properties

Peculiarities of Emission of Subminiature Injection Lasers

V. P. Strakhov

Lebedev Physics Institute, Russian Academy of Sciences, Leninskiĭ pr. 53, Moscow, 119991 Russia

Received December 10, 2002

Abstract—The emission spectrum of an injection GaAs laser with a four-sided resonator with a square cross section of size 13×13 μm^2 is presented. This laser is the world's smallest laser, having the threshold current $I_{th} = 0.7$ mA and a photon flight time in the resonator that is shorter than the thermal relaxation time T_2. It is shown that the emission spectrum of the laser drastically differs from the spectrum emitted by lasers of usual size. © *2003 MAIK "Nauka/Interperiodica".*

It has been shown in paper [1] that the spontaneous emission of injection lasers with a four-sided resonator of small size (30×30 μm^2) saturates above the lasing threshold, and single-frequency lasing lasts up to the tenfold excess over the lasing threshold.

The study was continued with lasers of even smaller size. Lasers of a square shape with a four-sided resonator of size 13×13 μm^2 were fabricated. It is important that the length of such a resonator is $L < 37$ μm, and the photon flight time in the resonator is $t < 5 \times 10^{-13}$ s, which is shorter than the thermal relaxation time T_2 in semiconductors at 77 K.

The lasing spectrum shown in the figure drastically differs from typical single-frequency emission spectra obtained in [1]. Here, *a* is the spontaneous emission spectrum observed when the current is slightly below the threshold; *b* and *c* are the lasing spectra at the threshold $I_{th} = 0.7$ mA recorded with wide and narrow slits of a spectrometer, respectively. Lasing appears at the threshold simultaneously on all equidistant axial modes in the long-wavelength part of the gain band and is observed up to two- to threefold excess over I_{th}; then, as a rule, the laser is destroyed. The width of the emission spectrum exceeds 100 Å, and the mode interval is $\Delta\lambda \approx 21$ Å, corresponding to the resonator length $L \approx 37$ μm. Note that an amplification deficit exists for the longest wavelength modes, and no lasing should be observed at these wavelengths under usual conditions. The width of the emission spectrum of usual lasers is 20–30 Å, while lasers with a four-sided resonator of a larger size (30×30 μm^2) exhibit single-mode lasing. Only in the presence of a dominating short-wavelength mode developing for the time $t < 10^{-12}$ s is an anomaly produced in the active region, resulting in the unusual development of lasing.

The possibility of the appearance of two modes in the spectra of semiconductor lasers was discussed in [2]; however, this cannot explain the result presented above. I would be grateful to V.F. Elesin and Yu.V. Kopaev if they would explain this result theoretically.

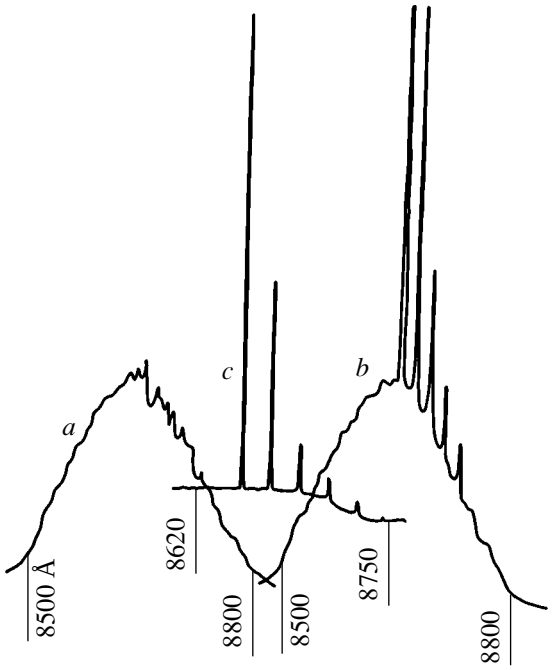

Emission spectrum of a subminiature laser.

1063-7761/03/9606-1122$24.00 © 2003 MAIK "Nauka/Interperiodica"

Unfortunately, lasers of such a small size are of one-time use. Stresses produced upon mounting such a miniature laser with a cross section as small as 10^{-6} cm^2 give rise to pressures up to thousands of atmospheres. For this reason, we failed to study the temporal parameters of the lasers, although the generation of controllable ultrashort light pulses is expected. It is necessary to perform experiments at room temperature, but because T_2 at 300 K is even shorter, the resonator size should be smaller than 10×10 μm^2, which can only be achieved using advanced nanotechnology.

REFERENCES

1. P. G. Eliseev and V. P. Strakhov, Pis'ma Zh. Éksp. Teor. Fiz. **16**, 606 (1972) [JETP Lett. **16**, 428 (1972)].
2. V. F. Elesin and Yu. V. Kopaev, Zh. Éksp. Teor. Fiz. **72**, 334 (1977) [Sov. Phys. JETP **45**, 177 (1977)].

Translated by M. Sapozhnikov

Journal of Experimental and Theoretical Physics, Vol. 96, No. 6, 2003, pp. 1124–1130.
Translated from Zhurnal Éksperimental'noĭ i Teoreticheskoĭ Fiziki, Vol. 123, No. 6, 2003, pp. 1278–1285.

SOLIDS
Electronic Properties

Frustrated Antiferromagnetism in the Sr_2YRuO_6 Double Perovskite

E. V. Kuz'min[a], S. G. Ovchinnikov[a,*], and D. J. Singh[b]

[a]*Kirenskiĭ Institute of Physics, Siberian Division, Russian Academy of Sciences, Akademgorodok, Krasnoyarsk, 660036 Russia*
[b]*Naval Research Laboratory, Washington, DC, USA*
**e-mail: sgo@iph.krasn.ru*

Received December 9, 2002

Abstract—The spins of Ru^{5+} ions in Sr_2YRuO_6 form a face-centered cubic lattice with antiferromagnetic nearest neighbor interaction $J \approx 25$ meV. The antiferromagnetic structure of the first type experimentally observed below the Néel temperature $T_N = 26$ K corresponds to four frustrated spins of 12 nearest neighbors. In the Heisenberg model in the spin-wave approximation, the frustrations already cause instability of the antiferromagnetic state at $T = 0$ K. This state is stabilized by weak anisotropy D or exchange interaction I with the next-nearest neighbors. Low $D/J \sim I/J \sim 10^{-3}$ values correspond to the experimental T_N and sublattice magnetic moment values. © *2003 MAIK "Nauka/Interperiodica".*

1. INTRODUCTION

Like cuprates and manganates, perovskite-like ruthenates have been attracting much interest of researchers in recent years. Initially, this interest was caused by the discovery of exotic superconductivity in Sr_2RuO_4 [1]. This is the only oxide superconductor isostructural to cuprates that does not contain copper. Later, it was found that other ruthenates have very interesting magnetic and electric properties. Increasing x in the $Sr_{2-x}Ca_xRuO_4$ system results in a complex sequence of structural phase transitions, competition between ferromagnetic and antiferromagnetic exchange interactions, and the Mott–Hubbard metal–dielectric transition in Ca_2RuO_4 [2, 3]. Another ruthenate, $SrRuO_3$, is the only metallic ferromagnet with $T_C \approx 165$ K and magnetization $m \approx 1.6\mu_B$ per Ru ion among 4*d* metal oxides [4, 5]. The Sr_2YRuO_6 double perovskite has an elpasolite structure, which can be obtained from $SrRuO_3$ by replacing each second Ru ion with nonmagnetic Y; below $T_N = 26$ K, the face-centered cubic (FCC) lattice of Ru^{5+} spins experiences ordering to produce an antiferromagnetic structure of the first type [6, 7]. In this structure, (001) ferromagnetic planes exhibit antiparallel ordering along the *c* axis.

One of the reasons for our interest in the magnetic properties of Sr_2YRuO_6 is its low T_N temperature and small value of the sublattice magnetic moment per ruthenium ion, $m = 1.85\mu_B$, compared with the exchange integral $J \approx 25$ meV and the nominal $m(S = 3/2) = 3\mu_B$ per Ru ion for the d^3 configuration of Ru^{5+}. The m value was measured by neutron diffraction [6, 7], and the J value was calculated theoretically [8]. Another reason for our interest in the double perovskite is the appearance of superconductivity with $T_c \approx 50$ K after doping it with copper [9, 10]. A study of a possible magnetic mechanism of superconductivity in this system requires understanding the magnetic properties of undoped Sr_2YRuO_6.

Earlier, an attempt was made to explain the smallness of T_N by frustration effects in the Ising model, but the suppression of T_N in the Ising model proved to be too weak [8]. In this paper, we show that the major contribution is made by fluctuations of transverse spin components in the Heisenberg model. If only the nearest neighbors are taken into account, the antiferromagnetic state is unstable in the spin-wave approximation. Its stabilization requires including exchange with the next-nearest neighbors I or anisotropy D. Our calculations show that very small $I/J \sim D/J \sim 10^{-3}$ values are sufficient for obtaining the observed T_N and magnetic moment values.

2. THE SPECIAL FEATURES OF THE STRUCTURE AND EXCHANGE INTERACTION IN Sr_2YRuO_6

As distinct from other ruthenates and cuprates, neighboring RuO_6 octahedra in Sr_2YRuO_6 do not share anions (Fig. 1). This justifies applying the cluster approach to the description of its magnetic structure. Similarly, the electronic structure of Sr_2YRuO_6 is well modeled in first-principles band calculations by a system of RuO_6 clusters, which form an FCC lattice [8]. From the magnetic point of view, the replacement of Ru^{5+} magnetic by Y^{3+} nonmagnetic ions is diamagnetic

substitution. The FCC lattice of spins in Sr_2YRuO_6 can therefore be treated as produced by diamagnetic dilution of spins in the $SrRuO_3$ perovskite to a 0.5 concentration of nonmagnetic vacancies, which are spatially ordered (Fig. 1b). The presence of vacancies considerably changes the exchange interaction between neighboring Ru spins. Whereas ferromagnetic exchange interaction is characteristic of $SrRuO_3$, strong competition between ferromagnetic and antiferromagnetic interactions is observed in Sr_2RuO_4 [11], $Sr_{2-x}Ca_xRuO_4$ exhibits a trend toward antiferromagnetism as x increases (see discussion in review [12]), and Sr_2YRuO_6 is characterized by strong antiferromagnetic interaction. It follows that exchange interactions in various ruthenates vary to a greater extent than in cuprates, where these interactions are always antiferromagnetic.

The reason for the diversity of exchange interactions in ruthenates is the special features of their electronic structure formed by the $(t_{2g} - p)$–π bonds. The orbital degeneracy of the t_{2g} states results in the presence of three intersecting bands at the Fermi level and the metallic state of undoped $SrRuO_3$ and Sr_2RuO_4. The estimation of correlation effects in $SrRuO_3$ and Sr_2RuO_4 shows that intermediate correlations $U \le W$, where U is the Hubbard Coulomb parameter and $W = z|t|$ is the band half-width, occur in these compounds [12]. Because of the diamagnetic dilution in Sr_2YRuO_6, the nearest neighbor Ru–Ru hopping integral t is strongly suppressed, and the substance is in the mode of strong electron correlations with the dielectric ground state. In the zeroth approximation with respect to hopping t, we have a system of independent RuO_6 clusters.

Consider the electronic structure of the RuO_6 cluster. The crystal field splits the Ru 4d level into the t_{2g} and e_g sublevels. The p orbitals of oxygen participate in the $pd\pi$ and $pd\sigma$ bonds with Ru. A detailed calculation of molecular orbitals and their comparison with first-principles calculations by the linearized augmented plane wave method were performed in [8]; in this work, we only give the results necessary for analyzing exchange interactions. After the inclusion of intracluster p–d Ru–O hoppings, we obtain the following cluster molecular orbitals: 13 nonbonding molecular orbitals $4 \times E_0(p_\sigma) + 9 \times E_0(p_\pi)$, 5 bonding orbitals $2 \times E_-(E_g) + 3 \times E_-(T_{2g})$, and 5 antibonding molecular orbitals $2 \times E_+(E_g) + 3 \times E_+(T_{2g})$. Here, E_0 are the ionic levels, and the energies of the bonding and antibonding terms are

$$\begin{aligned} E_\pm(E_g) &= 0.5\{E_0(p_\sigma) + E_0(e_g) \\ &\pm [(E_0(p_\sigma) - E_0(e_g))^2 + 16t_\sigma^2]^{1/2}\}, \\ E_\pm(T_{2g}) &= 0.5\{E_0(p_\pi) + E_0(t_{2g}) \\ &\pm [(E_0(p_\pi) - E_0(t_{2g}))^2 + 16t_\pi^2]^{1/2}\}. \end{aligned} \quad (1)$$

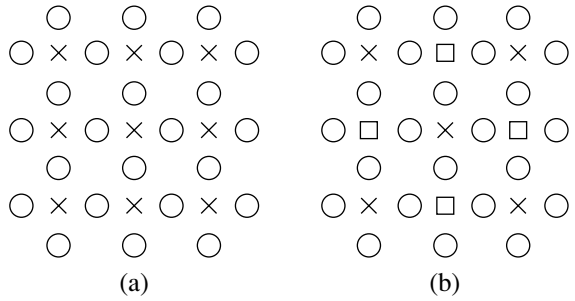

Fig. 1. Ordered diamagnetic replacement of every second Ru ion by Y ion in (a) $SrRuO_3$ leads to (b) the Sr_2YRuO_6 lattice: (×) Ru; (○) O; (□) Y.

The order of the levels is determined by the conditions

$$E_-(T_{2g}) \approx E_-(E_g) < E_0(p_\sigma) < E_0(p_\pi) < E_+(T_{2g}) < E_+(E_g),$$

and their filling with 39 valence electrons is such that 36 electrons completely fill the $E_-(T_{2g})$, $E_-(E_g)$, $E_0(p_\sigma)$, and $E_0(p_\pi)$ molecular orbitals. The remaining three electrons fill three $E_+(T_{2g})$ orbitals with parallel spins to form the $S = 3/2$ high-spin state. T_{2g} symmetry of molecular orbitals coincides with t_{2g} symmetry of Ru atomic orbitals.

The true crystal lattice of Sr_2YRuO_6 is somewhat more complex than that shown in Fig. 1; RuO_6 clusters are rotated through $\varphi \approx 12°$, which results in $P21/n$ monoclinic symmetry. We will, however, analyze exchange interactions in terms of the undistorted structure (Fig. 1). Including distortions gives corrections which prove to be small according to the estimates made in [8]. From the point of view of the indirect exchange mechanism, exchange between the nearest neighbors J is formed by the Ru–O–O–Ru coupling. However, in terms of molecular orbitals, the same coupling of neighboring RuO_6 clusters is effected by the xy–xy hopping with the amplitude $\tau_\sigma = 0.75t_{dd\sigma}$.

The arising exchange energy per cluster can be estimated as $2J_0 \sim \tau_\sigma^2/\Delta$, where Δ is the exchange splitting of the T_{2g} molecular orbitals. The estimation of the τ_σ and Δ parameters by linearized augmented plane wave calculations in [8] gives $2J_0 \approx 0.05$ eV; this J value also corresponds to the energy difference between the ferromagnetic and antiferromagnetic states per cluster in spin polarization calculations [8], which equals 0.095 eV with and 0.12 eV without allowance for octahedron turns.

The magnetic properties of a system of localized spins will be described in terms of the isotropic Heisenberg model with the Hamiltonian

$$\begin{aligned} H &= -\frac{1}{2}\sum_{f,R} J(R)\mathbf{S}_f \cdot \mathbf{S}_{f+R}, \\ J(\mathbf{R}) &= J(-\mathbf{R}), \quad J(0) = 0. \end{aligned} \quad (2)$$

The FCC lattice contains $z = 12$ nearest neighbors with the exchange $J(\mathbf{R}_1) = -J$. We also take into account exchange with the next-nearest spins $J(R_2) = I$ on the assumption of ferromagnetic exchange. Exchange for the next-nearest spins arises as the Ru–O–O–Ru–O–O–Ru coupling; it can be estimated as

$$I \sim \tau_\sigma^4/\Delta^3 \leq 10^{-2} J_0.$$

In order to describe the antiferromagnetic state, we introduce sublattices A (sites $\boldsymbol{\alpha}$) with spins upward and B (sites $\boldsymbol{\beta}$) with spins downward, $\langle S_A^z \rangle = -\langle S_B^z \rangle \equiv \mathbf{S}$, where the magnetization of the sublattices depends on temperature. For the antiferromagnetic state of the first type, we have ferromagnetically ordered xy planes with an antiferromagnetic alternation of the planes. Set lattice parameter $a = 1$; the length of the $\mathbf{R}_1 \equiv \boldsymbol{\Delta}$ vectors connecting the nearest neighbors is then $\Delta = 1/\sqrt{2}$, and that of the $\mathbf{R}_2 \equiv \mathbf{a}$ vectors, $a = 1$. Let us divide the $\boldsymbol{\Delta}$ vectors into two groups, those lying in the xy planes $\mathbf{d}$ and interplanar vectors $\boldsymbol{\delta}$,

$$\mathbf{d} = \left(\pm\frac{1}{2}, \pm\frac{1}{2}, 0\right)(xy),$$

$$\boldsymbol{\delta}_1 = \left(0, \pm\frac{1}{2}, \pm\frac{1}{2}\right)(yz), \quad \boldsymbol{\delta}_2 = \left(\pm\frac{1}{2}, 0, \pm\frac{1}{2}\right)(xz).$$

The distribution of the $\langle S_f^z \rangle$ means in this model is as follows:

$$\begin{gathered}\langle S_{\boldsymbol{\alpha}}^z \rangle = \mathbf{S}, \quad \langle S_{\boldsymbol{\alpha}+\mathbf{d}}^z \rangle = \mathbf{S}, \quad \langle S_{\boldsymbol{\alpha}+\boldsymbol{\delta}}^z \rangle = -\mathbf{S}, \\ \langle S_{\boldsymbol{\alpha}+\mathbf{a}}^z \rangle = \mathbf{S}, \quad \langle S_{\boldsymbol{\beta}}^z \rangle = -\mathbf{S}, \quad \langle S_{\boldsymbol{\beta}+\mathbf{d}}^z \rangle = -\mathbf{S}, \\ \langle S_{\boldsymbol{\beta}+\boldsymbol{\delta}}^z \rangle = \mathbf{S}, \quad \langle S_{\boldsymbol{\beta}+\mathbf{a}}^z \rangle = -\mathbf{S}.\end{gathered} \tag{3}$$

Because of the ferromagnetic order in the xy plane, all four antiferromagnetic bonds in this plane are frustrated (energetically unfavorable). Eight interplanar antiferromagnetic bonds, however, give energy gain for the antiferromagnetic state. For this reason, frustrations decrease the mean field acting on a spin even in the molecular field approximation. Without frustrations, the mean field is $\bar{h} = 2J\bar{S} = 12J\bar{S}$; taking frustrations into account makes it $\bar{h} = 4J\bar{S}$. Without frustrations in the mean-field approximation, $T_N^{MF} = zJS(S+1)/3$, which is much higher than the experimental T_N value. A decrease in T_N by a factor of 3 caused by frustrations in the mean-field approximation does not solve the problem. A similar result is obtained for the Ising model, where frustrations decrease T_N [13]. The T_N value (700–900 K [8]) is, however, as previously, high compared with the experimental one. In the next section, we consider the spin-wave theory of a frustrated antiferromagnet to take into account transverse spin component fluctuations.

3. THE SPIN-WAVE THEORY OF A FRUSTRATED ANTIFERROMAGNET ON AN FCC LATTICE

The exact equation of motion ($\hbar = 1$) for S_f^+ is linearized in the Tyablikov approximation:

$$i\dot{S}_{\mathbf{f}}^+ \approx \sum_R J(\mathbf{R})(\langle S_{\mathbf{f}+\mathbf{R}}^z \rangle S_{\mathbf{f}}^+ - \langle S_{\mathbf{f}}^z \rangle S_{\mathbf{f}+\mathbf{R}}^+). \tag{4}$$

The $h = H/zJ$ dimensionless Hamiltonian can conveniently be used. For the antiferromagnetic state of the first type, taking into account (3) then allows (4) to be written as ($\lambda = I/J$)

$$\begin{aligned} i\dot{S}_{\boldsymbol{\alpha}}^+ &= \frac{\bar{S}}{z}\left[\sum_{\mathbf{d}}(S_{\boldsymbol{\alpha}+\mathbf{d}}^+ - S_{\boldsymbol{\alpha}}^+) + \sum_{\boldsymbol{\delta}}(S_{\boldsymbol{\alpha}+\boldsymbol{\delta}}^+ + S_{\boldsymbol{\alpha}}^+)\right] \\ &\quad + \frac{\lambda\bar{S}}{2z_2}\sum_{\mathbf{a}}(S_{\boldsymbol{\alpha}}^+ - S_{\boldsymbol{\alpha}+\mathbf{a}}^+), \\ i\dot{S}_{\boldsymbol{\beta}}^+ &= -\frac{\bar{S}}{z}\left[\sum_{\mathbf{d}}(S_{\boldsymbol{\beta}+\mathbf{d}}^+ + S_{\boldsymbol{\beta}}^+) + \sum_{\boldsymbol{\delta}}(S_{\boldsymbol{\beta}+\boldsymbol{\delta}}^+ + S_{\boldsymbol{\beta}}^+)\right] \\ &\quad - \frac{\lambda\bar{S}}{2z_2}\sum_{\mathbf{a}}(S_{\boldsymbol{\beta}}^+ - S_{\boldsymbol{\beta}+\mathbf{a}}^+). \end{aligned} \tag{5}$$

Performing the Fourier transform over the sublattices

$$S_A^+(\mathbf{q}) = \sqrt{2/N}\sum_{\boldsymbol{\alpha}} S_{\boldsymbol{\alpha}}^+ \exp(i\mathbf{q}\cdot\boldsymbol{\alpha}),$$

$$S_B^+(\mathbf{q}) = \sqrt{2/N}\sum_{\boldsymbol{\beta}} S_{\boldsymbol{\beta}}^+ \exp(i\mathbf{q}\cdot\boldsymbol{\beta}),$$

we obtain

$$\begin{aligned} i\dot{S}_A^+(\mathbf{q}) &= \bar{S}(\alpha_q S_A^+(\mathbf{q}) + \beta_q S_B^+(\mathbf{q})), \\ i\dot{S}_B^+(\mathbf{q}) &= -\bar{S}(\alpha_q S_B^+(\mathbf{q}) + \beta_q S_A^+(\mathbf{q})), \end{aligned} \tag{6}$$

where

$$\begin{gathered}\alpha_q = 0.33(1 + c_x c_y) + 0.5\lambda(1 - \gamma_q), \\ \beta_q = 0.33(c_x + c_y)c_z, \\ c_i = \cos(q_i/2), \quad i = x, y, z, \\ \gamma_q = 0.33(\cos q_x + \cos q_y + \cos q_z).\end{gathered}$$

The thermodynamic properties will be calculated using two-time retarded commutator Green's functions at finite temperatures

$$\langle\langle S_F^+(\mathbf{q}) \big| S_G^-(-\mathbf{q})\rangle\rangle_\omega = G_{FG}(\mathbf{q}, \omega).$$

Here, sublattice indices F and G take on two values, A and B. For simplicity, we will only consider the spin

$S = 1/2$. Of course, spin-wave theory also can be constructed for an arbitrary spin S, including $S = 3/2$ for Sr_2YRuO_6. Such a theory will, however, be fairly cumbersome, whereas the main results for $\bar{S}$ and T_N will differ by unimportant multipliers of the $S(S + 1)$ type. Equations of motion (6) allow us to easily obtain the corresponding Green's functions

$$G_{AA} = \frac{2\bar{S}(\omega + \bar{S}\alpha_q)}{D(\mathbf{q}, \omega)}, \quad G_{BB} = \frac{2\bar{S}(\omega - \bar{S}\alpha_q)}{D(\mathbf{q}, \omega)}, \qquad G_{AB} = G_{BA} = -\frac{2\bar{S}^2\beta_q}{D(\mathbf{q}, \omega)}, \tag{7}$$

$$D(q, \omega) = \omega^2 - \Omega_q^2, \quad \Omega_q = \bar{S}\varepsilon_q, \qquad \varepsilon_\mathbf{q} = (\alpha_q^2(\lambda) - \beta_q^2)^{1/2}. \tag{8}$$

Applying the standard procedure yields the spectral density

$$n_{AA}(\mathbf{q}, \omega) = -\frac{1}{\pi}\mathrm{Im}G_{AA}(\mathbf{q}, \omega) = \bar{S}\left[\left(1 + \frac{\alpha_q}{\varepsilon_q}\right)\delta(\omega - \Omega_q)\right]$$

and the transverse spin correlator

$$C_{AA}(q) = \langle S_A^+(q)S_A^-(-q)\rangle = \int_{-\infty}^{\infty}\frac{\exp(\omega/\tau)}{\exp(\omega/\tau) - 1}n_{AA}(\mathbf{q}, \omega)d\omega = \bar{S}\left(1 + \frac{\alpha_q}{\varepsilon_q}\coth\frac{\Omega_q}{2\tau}\right). \tag{9}$$

Here, $\tau = T/zJ$ is the dimensionless temperature. For $S = 1/2$,

$$\frac{2}{N}\sum_q C_{AA}(q) = \frac{2}{N}\sum_\alpha \langle S_\alpha^+ S_\alpha^-\rangle = \frac{1}{2} + \bar{S}, \tag{10}$$

and the equation for the order parameter $\bar{S}$ therefore reads

$$\bar{S}(\tau) = \frac{1/2}{I(\tau)}, \quad I(\tau) = \frac{2}{N}\sum_q \frac{\alpha_q}{\varepsilon_q}\coth\frac{\bar{S}(\tau)\varepsilon_q}{2\tau}. \tag{11}$$

At $\tau = 0$, the hyperbolic cotangent equals one, and

$$\bar{S}(0) = \frac{0.5}{I_1(\lambda)}, \quad I_1(\lambda) = 2N^{-1}\sum_q \frac{\alpha_q(\lambda)}{\varepsilon_q(\lambda)}. \tag{12}$$

In the other limit $\tau \longrightarrow \tau_N$, $\bar{S} \longrightarrow 0$ ($\coth x \longrightarrow 1/x$ as $x \longrightarrow 0$), Eq. (11) yields the Néel temperature

$$\tau_N = \frac{1}{4}I_2(\lambda), \quad I_2(\lambda) = 2N^{-1}\sum_q \frac{\alpha_q(\lambda)}{\varepsilon_q^2(\lambda)}. \tag{13}$$

Consider the integrands in the expressions for I_1 and I_2 in the neighborhood of the Brillouin zone points $\Gamma = (0, 0, 0)$ and $X = (0, 0, 2\pi)$. In the neighborhood of Γ, we have

$$\alpha_q \approx \frac{1}{3}\left[2 - \frac{q_x^2 + q_y^2}{8} + \frac{\lambda q^2}{4}\right], \quad q^2 = q_x^2 + q_y^2 + q_z^2,$$

$$\beta_q \approx \frac{1}{3}\left[2 - \frac{q_x^2 + q_y^2}{8} - \frac{q_z^2}{4}\right], \quad \varepsilon_q^2 = \frac{q_z^2 + \lambda q^2}{9}$$

and the integrand in I_1 takes the form

$$\frac{\alpha_q(\lambda)}{\varepsilon_q(\lambda)} = \frac{2 - (q_x^2 + q_y^2)/8 + \lambda q^2/4}{(q_z^2 + \lambda q^2)^{1/2}}. \tag{14}$$

If only exchange J between the nearest neighbors is taken into account, the $\lambda = 0$ spectrum in the vicinity of Γ becomes one-dimensional with the special direction z, along which A and B layer spins alternate. At $\lambda = 0$, the integral I_1 logarithmically diverges, which means that $\bar{S}(0) \longrightarrow 0$; that is, the antiferromagnetic state is already unstable at $T = 0$. The integral I_2 in the vicinity of Γ behaves as $\int dq_z/q_z^2 \propto 1/q$, that is, diverges by a power law. As a result, $T_N \longrightarrow 0$. In the vicinity of X, the I_1 and I_2 integrals exhibit similar behaviors. It follows that, if only nearest neighbor exchange J is taken into account, the effect of frustrations is strong to the extent that the antiferromagnetic state is completely suppressed. Precisely this is, in our view, the main reason why T_N and $\bar{S}$ are small in Sr_2YRuO_6. The antiferromagnetic state can be stabilized both by exchange with the next-nearest spins I and by anisotropy.

4. THE STABILIZATION OF ANTIFERROMAGNETIC STATES BY NEXT-NEAREST-NEIGHBOR EXCHANGE

The instability of the antiferromagnetic state in FCC lattices has long been known and treated within the frameworks of both the spin-wave approach and the Bete–Peierls–Weiss cluster approximation [14–16]. The stabilization of the antiferromagnetic state by next-nearest-neighbor exchange has been considered in detail in [17, 18]. Ferromagnetic exchange I stabilizes the antiferromagnetic phase of the first type, which is observed in Sr_2YRuO_6, and antiferromagnetic exchange I stabilizes the phase of the third type. The Néel temperature as a function of the $\lambda = I/J$ ratio was calculated in [17, 18] only numerically, and the $T_N(\lambda)$ plots with a characteristic nonanalytic dependence for

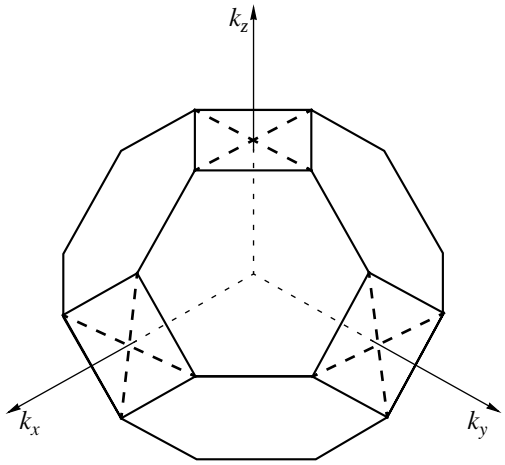

Fig. 2. Brillouin zone of a face-centered cubic lattice. Squares indicate dangerous directions leading to magnetic moment and Néel temperature divergences.

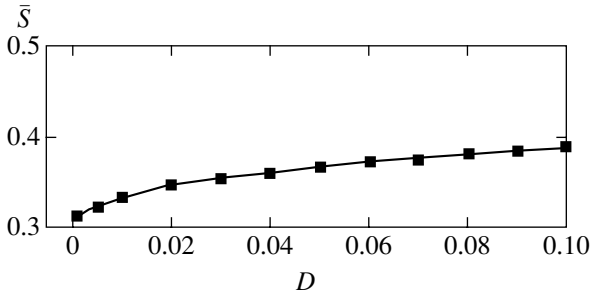

Fig. 3. Dependence of sublattice magnetic moment $\bar{S}$ on exchange anisotropy D.

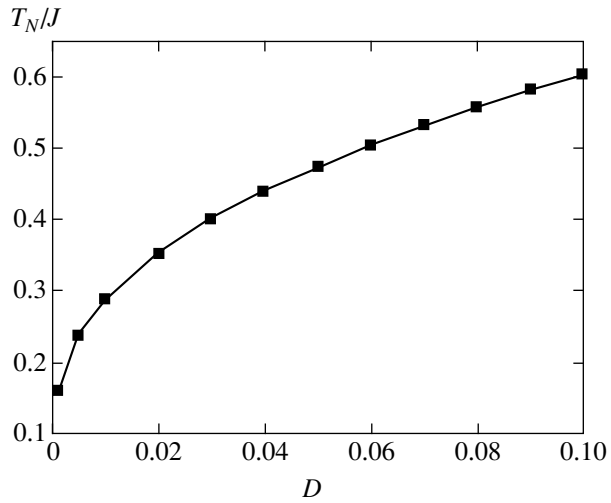

Fig. 4. Dependence of the Néel temperature on exchange anisotropy D.

$\lambda \longrightarrow 0$ were similar to the $T_N(D)$ plot (see Fig. 4 below). At the same time, it was claimed in [17, 18] that anisotropy of exchange interactions per se, without taking exchange I into account, could not stabilize the antiferromagnetic state of the first type. This conclusion is at variance with our results. Indeed, anisotropy creates a gap in the spectrum of magnons that cuts off the divergences as λ tends to 0. This problem is considered in more detail in the next section.

5. THE STABILIZATION OF THE ANTIFERROMAGNETIC STATE BY ANISOTROPY

The turns of the octahedra and the monoclinic distortion of the Sr_2YRuO_6 lattice can cause anisotropy of two types, namely, single-ion anisotropy of the DS_z^2 type or exchange coupling anisotropy. In our simplified model with $S = 1/2$, the single-ion anisotropy is absent; therefore, consider the exchange anisotropy. The Hamiltonian of the system can then be written as

$$H = -\frac{1}{2}\sum_{f,R} J(R)(S_f^+ S_{f+R}^- + \xi_R S_f^z S_{f+R}^z), \quad \xi_R \neq 1.$$

Equation (4) now transforms into

$$i\dot{S}_{\mathbf{f}}^+ \approx \sum_R J(\mathbf{R})(\xi_{\mathbf{R}}\langle S_{\mathbf{f}+\mathbf{R}}^z\rangle S_{\mathbf{f}}^z - \langle S_{\mathbf{f}}^z\rangle S_{\mathbf{f}+\mathbf{R}}^+).$$

In the simplest situation, it suffices to take into account exchange anisotropy for the nearest neighbors ignoring exchange anisotropy for the next-nearest spins. This implies that

$$\xi_\Delta = 1 + D, \quad \xi_a = 1,$$

where D is the dimensionless anisotropy parameter. As the lattice distortions are small, we can assume that $D \ll 1$. The spin-wave theory described in Section 3 can easily be generalized to systems with anisotropy. After the $\alpha_q \longrightarrow \alpha_q(D)$ renormalization,

$$\begin{aligned}\alpha_q(\lambda, D) &= 0.33(1 + D + c_x c_y) + 0.5\lambda(1 - \gamma_d),\\ \varepsilon_q(D) &= (\alpha_q^2(\lambda, D) - \beta_q^2)^{1/2},\end{aligned} \tag{15}$$

all the other equations obtained in Section 3 remain valid. The order parameter at $T = 0$ is

$$\begin{aligned}\bar{S}(\lambda, D) &= \frac{0.5}{I_1(\lambda, D)},\\ I_1(\lambda, D) &= \frac{2}{N}\sum_q \frac{\alpha_q(\lambda, D)}{\varepsilon_q(\lambda, D)}.\end{aligned} \tag{16}$$

For the Néel temperature, we obtain

$$\begin{aligned}\tau_N(\lambda, D) &= \frac{0.25}{I_2(\lambda, D)},\\ I_2(\lambda, D) &= \frac{2}{N}\sum_q \frac{\alpha_q(\lambda, D)}{\varepsilon_q^2(\lambda, D)}.\end{aligned} \tag{17}$$

If $\lambda = 0$ and $D \longrightarrow 0$, both integrals I_1 and I_2 diverge, which yields $\bar{S} = 0$ and $\tau_N = 0$. It follows that anisotropy per se, in the absence of next-nearest-neighbor spin exchange, stabilizes the antiferromagnetic state in an FCC lattice.

To single out the diverging asymptotic functions, we analytically calculated the contributions to the integrals in the neighborhood of the dangerous Brillouin zone points Γ and X (see Fig. 2). The high-symmetry points will be denoted as follows:

$$\Gamma(0, 0, 0), \quad L = (\pi, \pi, \pi), \quad K = (3\pi/2, 3\pi/2, 0)$$

$$Z(0, 0, 2\pi), \quad W_1(\pi, 0, 2\pi), \quad W_2 = (0, \pi, 2\pi),$$

$$X = (2\pi, 0, 0), \quad \tilde{W}_1 = (2\pi, \pi, 0), \quad \tilde{W}_2 = (2\pi, 0, \pi),$$

$$Y = (0, 2\pi, 0), \quad W_1^* = (\pi, 2\pi, 0), \quad W_2^* = (0, 2\pi, \pi).$$

Along several Brillouin zone directions shown by squares in Fig. 2, $\varepsilon_q = 0$ at $D = \lambda = 0$. Some points of this set are dangerous in the sense that the I_1 and I_2 integrals diverge at $D = \lambda = 0$. Further, we will study the role played by anisotropy D on the assumption $\lambda = 0$.

Consider the small volume $v = (\pi/4)^3$ in the neighborhood of Γ (recall that the total Brillouin zone volume is $32\pi^3$). All integrals normalized with respect to v will be denoted by $\tilde{I}$. Expanding all cosines into series and performing fairly simple calculations, we can analytically find the contributions that diverge as $D \longrightarrow 0$. For instance, for I_1, we obtain

$$\tilde{I}_1(D) \approx 0.5 \ln D - 1.9.$$

For the integral $\tilde{I}_2$, analytic calculations give

$$\tilde{I}_2(D) \approx 12/\sqrt{D}.$$

Similar asymptotic behaviors ($\ln D$ for I_1 and $\sqrt{D}$ for I_2) can also be obtained for the other dangerous Brillouin zone points. As a result, we find $\bar{S}(D)$ and $T_N(D)/J$.

The $\bar{S}(D)$ and $T_N(D)/J$ dependences at $\lambda = 0$ are shown in Figs. 3 and 4. The curves labeled by squares are described by the approximations

$$\bar{S}(D) \approx \frac{1/2}{0.043 \ln D + 1.256}, \tag{18}$$

$$T_N(D) = J\begin{cases} 4\sqrt{D}/(1 + 4\sqrt{D}), & 0 < D < 0.05, \\ 0.342 + 2.6D, & 0.05 < D < 0.1. \end{cases} \tag{19}$$

6. RESULTS AND DISCUSSION

Our results are based on a study of the Tyablikov approximation, which is, in essence, a mean-field approximation variant. However, as distinct from the trivial Weiss mean field with $J_{ij}\mathbf{S}_i\mathbf{S}_j \longrightarrow J_{ij}\langle S_i^z\rangle S_j^z$, which does not depend on the space dimension, the Tyablikov approximation takes into account transverse spin density fluctuations in the form of collective excitations, that is, spin waves. As a result, the Tyablikov approximation reveals the absence of long-range order at finite temperatures in agreement with the exact Mermin–Wagner theorem [17, 18]. As long as there is long-range magnetic order in the system and spin fluctuations at low temperatures can be described in terms of spin waves, we can hope that the results obtained using the Tyablikov approximation will be in at least qualitative agreement with experiment.

Note that the stabilization of the antiferromagnetic state of the first type takes place not at arbitrary signs of exchange and anisotropy, but only at ferromagnetic next-nearest-neighbor exchange I and anisotropy $D > 0$. Indeed, ferromagnetic exchange I prevents frustrations and is intrasublattice. Conversely, antiferromagnetic next-nearest-neighbor exchange would only strengthen the effect of frustrations. As far as anisotropy is concerned, $D > 0$ is evidence of Ising-type anisotropy, $J_\parallel > J_\perp$. In the limit $D \longrightarrow \infty$, we can ignore transverse spin components and obtain the Ising model, for which frustrations partially suppress the antiferromagnetic phase, but T_N and $\bar{S}$ remain finite [13]. At all $D > 0$ values, a gap appears in the spectrum of magnons, which is the factor that stabilizes the antiferromagnetic phase. At $D < 0$, the $\varepsilon_q(D)$ spectrum of magnons becomes imaginary at certain wave vectors, which is evidence of antiferromagnetic phase instability. At $D = 0$, the antiferromagnetic state with a long-range order is unstable and is replaced by a state with a spin-liquid-type short-range order [19, 20].

A comparison of our results with the experimental data on Sr_2YRuO_6 should be performed bearing in mind that the monoclinic distortion of the lattice and the spin $\bar{S} = 3/2$ can lead not only to exchange but also to single-ion anisotropy. The Dzyaloshinski–Moriya anisotropic exchange is also possible. Clearly, all anisotropic interactions are weak compared with J, which allows us to qualitatively compare our results with experiment taking into account exchange anisotropy with $D \ll J$ only. It follows from (18) and (19) that, to obtain $T_N = 30$ K and $J = 300$ K, we must set $D = 8 \times 10^{-4}$. This means that the exchange anisotropy $J_\parallel - J_\perp = D_J = 0.24$ K is exceedingly small. At such an anisotropy value,

$$\bar{S}(8 \times 10^{-4}) = 0.32,$$

which amounts to 64% of the nominal spin and very closely agrees with the neutron data on the magnetic moment of ruthenium.

Note in conclusion that frustrations in an FCC system with nearest neighbor exchange lead to soft mag-

non modes along several Brillouin zone directions. In particular, in the vicinity of the Γ point, the spectrum becomes one-dimensional. For this reason, divergences in spin-wave theory similar to divergences in low-dimensional systems are not surprising. Very weak perturbations in the form of ferromagnetic next-nearest-neighbor exchange or an Ising-type exchange anisotropy are sufficient for the antiferromagnetic state to be stabilized.

ACKNOWLEDGMENTS

One of the authors (S.G.O.) thanks the Naval Research Laboratory for financial support of his visit to the Department of the Theory of Complex Systems in August 2001, where this work was initiated, and I.I. Mazin and the other members of the department for hospitality.

This work was financially supported by the Russian Foundation for Basic Research (project no. 00-02-16110), RFFI-KKFN "Enisei" (project no. 02-02-97705), INTAS (grant 01-0654), and the Quantum Macrophysics Program of the Russian Academy of Sciences.

REFERENCES

1. Y. Maeno, H. Hasimoto, K. Yoshida, *et al.*, Nature **372**, 532 (1994).
2. S. Nakatsnuji and Y. Maeno, Phys. Rev. Lett. **84**, 2666 (2000).
3. S. Nakatsnuji and Y. Maeno, Phys. Rev. B **62**, 6458 (2000).
4. J. J. Randall and Ward, J. Am. Chem. Soc. **81**, 2629 (1959).
5. J. M. Longo, P. M. Raccah, and J. B. Goodenough, J. Appl. Phys. **39**, 1327 (1968).
6. P. D. Battle and W. J. Macklin, J. Solid State Chem. **54**, 245 (1984).
7. G. Cao, Y. Xin, C. S. Alexander, and J. E. Crow, Phys. Rev. B **63**, 184432 (2001).
8. I. I. Mazin and D. J. Singh, Phys. Rev. B **56**, 2556 (1997).
9. M. K. Wu, D. Y. Chen, F. Z. Chein, *et al.*, Z. Phys. B **102**, 37 (1997).
10. H. A. Blackstead, *Abstract of the International Conference on Modern Problems of Superconductivity*, Yalta, Ukraine (2002).
11. I. I. Mazin and D. J. Singh, Phys. Rev. Lett. **82**, 4324 (1999).
12. S. G. Ovchinnikov, Usp. Fiz. Nauk **173**, 27 (2003).
13. R. Liebmann, *Statistical Mechanics of Periodic Frustrated Ising Systems* (Springer, Berlin, 1986).
14. Y. Y. Li, Phys. Rev. **84**, 721 (1951).
15. J. M. Ziman, Proc. R. Soc. London, Ser. A **66**, 89 (1953).
16. D. ter Haar and M. E. Lines, Philos. Trans. R. Soc. London, Ser. A **255**, 1 (1962).
17. M. E. Lines, Proc. R. Soc. London **271**, 105 (1963).
18. M. E. Lines, Phys. Rev. A **135**, 1336 (1964).
19. H. Shimara and S. Takida, J. Phys. Soc. Jpn. **60**, 2394 (1991).
20. A. Barabanov and O. Starykh, J. Phys. Soc. Jpn. **61**, 704 (1992).

Translated by V. Sipachev

Journal of Experimental and Theoretical Physics, Vol. 96, No. 6, 2003, pp. 1131–1139.
Translated from Zhurnal Éksperimental'noĭ i Teoreticheskoĭ Fiziki, Vol. 123, No. 6, 2003, pp. 1286–1296.

SOLIDS
Electronic Properties

Coexistence of Superconducting and Spiral Spin Orders: Models of Ruthenate

M. Ya. Ovchinnikova

Joint Institute of Chemical Physics, Russian Academy of Sciences, ul. Kosygina 4, Moscow, 117334 Russia
e-mail: movchin@center.chph.ras.ru

Received November 19, 2002

Abstract—The effect of a spiral spin structure on superconducting (SC) pairing in a three-band Hubbard model related to Sr_2RuO_4 is analyzed in the mean-field approximation. Such a structure with incommensurate vector $Q = 2\pi(1/3, 1/3)$ is the simplest one that removes the nesting instability of α and β bands. It is assumed that there is an intralayer pairing interaction between two types of neighbor sites, those with attraction in a singlet channel and with attraction in both two-singlet and triplet channels. In both cases, a mixed singlet–triplet SC order is observed in the γ band: a *d*-wave singlet order is accompanied by the formation of *p*-wave triplet pairs $(k, -k - Q)_{\uparrow\uparrow}$ and $(k, -k + Q)_{\downarrow\downarrow}$ with large total momenta $\mp Q$ and the spin projections ±1 onto an axis perpendicular to the spin rotation plane of the spiral spin structure. Both the SC and normal states are states with broken time-reversal symmetry. In contradiction to the experiment, the models give different scales of T_c for the γ band and for α and β bands. This fact shows that the models with intralayer interactions or with the spin structure assumed are insufficient. © *2003 MAIK "Nauka/Interperiodica".*

1. INTRODUCTION

The problem of interplay between superconducting (SC) and spin orders still remains topical for systems with strong electron correlations. Among such systems, a single-layer quasi-two-dimensional ruthenate attracts considerable attention as a superconductor ($T_c \sim 1.5$ K) with a possible triplet type of pairing [1, 2]. One of arguments in favor of this type of pairing is the behavior of the Knight shift [3]. It was also assumed that the pairing is determined by ferromagnetic (FM) fluctuations that clearly manifest themselves in the parent FM compound $SrRuO_3$. The spin-triplet SC order parameter (OP) $\Delta_{ss'}(k) = (i\sigma_2\sigma_i)_{ss'}d_i(k)$ with $d_z(k) \propto k_x + ik_y$, suggested in [4, 5], agrees with the fact that the Knight shift is invariant under the SC transition [3] and with an increase in the rate of the muon spin relaxation observed for $T < T_c$ [6]. Such an order parameter corresponds to a nodeless gap function on the quasi-two-dimensional Fermi surface. These nodeless gaps are naturally derived from weak-coupling theory [5]. However, the experimentally observed power-law behavior, as $T \longrightarrow 0$, of the specific heat, $C(T) \propto T^2$ [7]; the NMR relaxation rate, $T_1^{-1} \propto T^3$ [8]; the thermal conductivity, $\kappa(T) \propto T^2$ [9, 10]; the penetration depth [11]; and the ultrasonic attenuation [12] points to the existence of node lines in the SC gap.

In view of these results, other possible types of symmetry of the SC gap were discussed in [13–17]. In particular, the *f*-wave symmetry of the gap with a horizontal node plane was assumed in [13]. This type of symmetry is likely to support the observed fourfold symmetry of anisotropic thermal conductivity in Sr_2RuO_4 in a magnetic field with the field vector lying in the RuO_4 plane [9, 10]. However, the observed anisotropy also agrees with the conventional *d*-wave SC order. However, this assumption requires a new interpretation for the behavior of the Knight shift.

Recently, models with pairing interaction of electrons in adjacent sites (including the interlayer interaction of orbitals with *xz* and *yz* symmetries) have been considered; the constants of these models were chosen to describe a simultaneous transition to the *p*-wave SC state in all three bands [18, 19]. In all SC state tests, it is usually assumed that the bands have already been renormalized by correlations due to a strong on-site repulsion. Such a renormalization is necessary for matching the band widths obtained from LDA calculations to those obtained from photoemission data. The renormalization mechanism is certainly determined by spin correlations or, in the static limit, by local spin structures in a system that should substantially affect the SC order. Therefore, the study of the effect of the spin order on SC pairing in the ruthenate models remains a topical problem.

The situation with the SC order and magnetic properties may be complicated if the normal state of the RuO_4 plane possesses a certain static or dynamic spin structure. In particular, spiral spin structures have recently been studied [20] as the simplest structures that describe an incommensurate peak in the spin susceptibility $\chi''(q, \omega)$ for $q \sim Q = 2\pi(1/3, 1/3)$ that was observed in inelastic neutron scattering (INS) [21, 22] and some features of the ARPES spectra [23] for

Sr_2RuO_4. The quasi-one-dimensional sheets of the Fermi surface for α and β valence bands with a full population of four electrons per site in the RuO_4 plane are characterized by the nesting with $q = Q$ [24, 25]. The spiral structure with $q = Q$ removes the instability due to nesting simultaneously in two quasi-one-dimensional bands and reduces the on-site interaction energy. The spiral structure is not the only structure that removes this type of instability of the system. Periodic spin structures with a 3×3 unit cell in the RuO_4 plane may also be responsible for the incommensurate peak at $q = Q$ observed in INS. However, the spiral state is the simplest state that allows one to study the effect of the spin structure and umklapp processes on SC pairing. In the mean-field approximation, the energy of the spiral state is indeed lower than the energies of para-, ferro-, and antiferromagnetic states [20]. The coexistence of SC pairing and the spiral spin order, as well as the coexistence of antiferromagnetic (AF) and SC orders in cuprates, remains an intriguing problem. These questions are of interest due to the facts that even a normal state with a spiral spin structure is a state with broken time-reversal symmetry and that a whole series of new mixed SC states with a simultaneous formation of singlet and triplet pairs arises in the system.

The aim of the present paper is to study the possibility of coexistence of a spiral spin order and superconductivity in models related to Sr_2RuO_4. We consider models with pairing interactions of neighbor sites within the RuO_4 plane. We will study the symmetry and the interplay of triplet and singlet SC OPs. We will demonstrate that both types of pairs survive simultaneously in the SC state in the presence of a spiral spin structure. In the models under test, one γ band is distinguished as an active band with respect to the SC transition. In this band, singlet *d*-wave pairs coexist with triplet bands. Earlier [16], the possibility of a mixed SC order in Sr_2RuO_4 was presumed because the energies of states with different SC-order symmetries are close to each other. The SC order was described by the spin susceptibility with a peak at the incommensurate momentum. In contrast to [16], a spiral spin structure gives rise to microscopic mixing of *d*-wave singlet and *p*-wave triplet orders. First, we analyze models with large constants κ of pairing interactions. Then, we calculate the phase curves $T_c(\kappa)$ for more realistic values of κ.

First, we have to stress several points.

1. Supposing that the attraction between electrons has an electronic (correlation) nature, we simulate it by the interaction

$$V = \sum_{\langle nm\rangle, \nu} V_\nu n_{\nu n} n_{\nu m} + J_\nu \mathbf{S}_{\nu n}\mathbf{S}_{\nu m} \qquad (1)$$

between two adjacent sites for each of the three bands $\nu = \alpha, \beta, \gamma$. This situation corresponds to taking into consideration the lowest *k* harmonics in the momentum representation of the pairing interaction $V_{kk'}$, as was done in [4]. Interaction (1) corresponds to the SC pairing constants $\kappa^s = 2V + J/2$ and $\kappa^t = 2V - 3J/2$ in the singlet and triplet channels for every bond $\langle nm\rangle$. The natural signs $V > 0$ and $J > 0$ are expected from the theory of strongly correlated systems. In single-band models, these signs correspond to $\kappa^t > 0$ and $\kappa^s < 0$ in the triplet and singlet channels. They correspond to attraction in the singlet rather than in the triplet channel. In the present paper, however, we consider models with either sign of the triplet constant κ^t.

2. The electron structure of Sr_2RuO_4 is determined by three almost independent bands α, β, and γ constructed from the *d* orbitals of Ru^{+2} of *xz*, *yz*, and *xy* symmetries and the corresponding combinations of the π orbitals of oxygen [24, 25]. A small hybridization of bands of *xz* and *yz* nature occurs only in their intersection domain for $k_x = \pm k_y$. According to [4, 5], the orbital symmetry also significantly suppresses the interband scattering of Cooper pairs. Therefore, we study the SC order arising in each separate band and choose the most active band from the viewpoint of SC instability. We do not touch upon the interband scattering and the proximity phenomena discussed in [4].

3. In contrast to [4], we begin with a normal mean-field state with broken time-reversal symmetry, namely, the state with a local spiral spin structure characterized by a diagonal vector $Q = 2\pi(1/3, 1/3)$. This is a normal state with nonzero spin currents $j_\uparrow = -j_\downarrow$ of opposite directions for two spin polarizations that are perpendicular to the spin rotation plane of the spiral structure. This means that electrons with polarizations ↑ or ↓ predominantly occupy *k* states with $\mathbf{k}\cdot\mathbf{Q} < 0$ or $\mathbf{k}\cdot\mathbf{Q} > 0$, respectively. According to [20], this leads to a polarization asymmetry of the Fermi surface and may lead to the formation of a mixed triplet–singlet SC order in the system.

2. MEAN-FIELD APPROXIMATION IN A SPIRAL SPIN CONFIGURATION

A three-band model of the RuO_4 plane is described by the Hamiltonian [25]

$$H = T + H_U + V, \quad T = \sum_{\nu,\sigma}\sum_{k} \epsilon_{\nu k} c^\dagger_{\nu k\sigma} c_{\nu k\sigma}, \qquad (2)$$

$$H_U = \sum_{n,\nu}\left\{ U n_{\nu n\uparrow} n_{\nu n\downarrow} + \sum_{\nu'\neq\nu}\left[U_2 \frac{1}{4} n_{\nu n} n_{\nu' n} - J\mathbf{S}_{\nu n}\mathbf{S}_{\nu' n}\right]\right\}.$$

Here, $\nu = 1, 2, 3$ (or α, β, γ) correspond to bands of *xz*, *yz*, and *xy* natures; $\epsilon_{\nu,k}$ and H_U are zero band energies and on-cite interactions with the parameters defined in [25]. The interband interaction

$$T_{\alpha\beta} = \sum_{k,\sigma} 4t_{\alpha\beta}\sin k_x \sin k_y (c^\dagger_{1k\sigma} c_{2k\sigma} + \text{H.c.})$$

is small. Thus, in the normal state with an arbitrary spin structure, there are three almost independent bands with weak mixing of α and β bands at the crossing point of their Fermi surfaces. We will neglect this mixing. For simplicity, we retain the notation α and β for unmixed bands of *xz* and *yz* natures. The interaction between bands occurs through the common value of the chemical potential and the mean fields produced by the electrons of all three bands. These fields depend on spins due to the on-site exchange interaction. The interaction $V_{\langle nm\rangle}$ of type (1) of nearest neighbors is included in the simulation of the possible SC pairing in the system.

In the mean-field approximation, the energy averaged over an arbitrary BCS-type state is calculated as an explicit function

$$\overline{H} = \overline{H}^{\mathrm{N}}(y_i) + \overline{H}^{\mathrm{SC}}(w_j, \theta_j) \tag{3}$$

that depends on normal (y_i) and anomalous (w_i, θ_j) one-electron means. The normal OPs $\{y_i\}$ include on-site ($l = 0$) and bond ($l = e_x, e_y$) densities

$$r^{\nu}(l) = \left\langle \frac{1}{2}\sum_{\sigma} c^{\dagger}_{n,\nu,\sigma} c_{n+l,\nu,\sigma} \right\rangle,$$

the mean kinetic energies

$$T^{\nu} = \left\langle 1/N \sum\nolimits_{k\sigma} \epsilon_{\nu k} c^{\dagger}_{\nu k\sigma} c_{\nu k\sigma} \right\rangle,$$

and local ($l = 0$) or nonlocal (($l = e_x, e_y$) spin densities $\mathbf{d}^{\nu}(l)$ in each band ν. The local spin densities

$$d^{\nu}(0) = [d^{\nu}(0)]^{*} = \langle e^{iQn} c^{\dagger}_{n\nu\uparrow} c_{n\nu\downarrow}\rangle \tag{4}$$

determine the spiral spin structure with the spirality vector $Q = 2\pi(1/3, 1/3)$:

$$\langle \mathbf{S}_{n\sigma}\rangle = d_{\nu}[\mathbf{e}_x \cos Qn + \mathbf{e}_y \sin Qn]. \tag{5}$$

Previous calculations [20] have shown that the energy of the normal state with a spin structure with such Q is lower than the energies of similar para-, ferro-, and antiferromagnetic mean-field solutions. Such a spin structure removes the instability due to the nesting of α and β bands. Simultaneously, exchange fields also induce a similar spin structure in the γ band. The solutions give collinear contributions to the total local spin of the site from each band.

Three-band models that describe Sr_2RuO_4 were derived in [24, 25]. In the case of the spiral spin structure, the normal state Fermi surfaces were studied in [20]. It was shown that, for a certain spin polarization, a spiral SDW order opens up a gap along half of the unperturbed Fermi boundary of a paramagnetic solution. Other regions of the Fermi surface remain metallic (gapless). In addition, a number of new shadow Fermi boundaries arise that are attributed to umklapp processes. As a result, the bands are split into the lower and upper Hubbard subbands; this increases the densities of states in the subbands and on the Fermi level. Therefore, one can expect that (any) spin structure increases T_c as compared with the T_c in paramagnetic solutions.

Since the Fermi surfaces are different for all three bands, it suffices to take into account only the intraband anomalous means. Only these means are determined by the contributions of a large phase volume along the entire Fermi surface. The formation of electron pairs $(c^{\dagger}_{k\nu\uparrow} c^{\dagger}_{-k\nu'\downarrow})$ that belong to different bands $\nu \neq \nu'$ can be effective only in a small domain of k near the intersection of their Fermi surfaces. Therefore, we retain only anomalous means within each subband and neglect the interband scattering of pairs. Then, the expression for the contribution $\overline{H}^{\mathrm{SC}}$ to the mean energy (3) has the form

$$\frac{1}{N}\overline{H}^{\mathrm{SC}} = U|w_{\nu}(0)|^2 + \sum_{\nu,\, l = e_x, e_y} \left\{ \kappa^{\mathrm{s}}_{\nu}(l)|w_{\nu}(l)|^2 + \kappa^{\mathrm{t}}_{\nu}(l) \sum_{\mu = 0, \pm 1} \frac{1}{1 + |\mu|} |\theta_{\mu,\nu}(l)|^2 \right\}. \tag{6}$$

Here, $w(l)$ and $\theta(l)$ are singlet and triplet SC OPs either at the same site ($l = 0$) or at neighboring sites ($l = e_x$ or $l = e_y$). These quantities are given by the expressions

$$w_{\nu}(l) = \frac{1}{2N}\sum_{n,\,\sigma} \frac{\sigma}{|\sigma|} \langle c^{\dagger}_{\nu,n,\sigma} c^{\dagger}_{\nu,n+l,-\sigma}\rangle \tag{7}$$

and

$$\theta_{\nu\mu}(l) \quad \frac{1}{2N}\sum_{n,\,\sigma} e^{i\mu Q(n + l/2)} (\sigma_{\mu}\sigma_y)_{ss'} \langle c^{\dagger}_{\nu,n,s} c^{\dagger}_{\nu,n+l,s'}\rangle. \tag{8}$$

Here, the matrices σ_{μ} are equal to σ_z or $\mp(\sigma_x \pm i\sigma_y)$ for $\mu = 0, \pm 1$, respectively, and $\sigma_{x,y,z}$ are Pauli matrices. The phases $\phi(n, l) = \mu Q(n + l/2)$ for $\mu = 0, \pm 1$ in the definition of the triplet OPs (8) guarantee that each term of the sum in (8) for each bond $\langle n, n + l\rangle$ is independent of the bond number n. This is analogous to the situation when cyclic spin components $\langle S_{n\mu} e^{-i\mu Qn}\rangle$ for $\mu = \pm 1$ are independent of n for a state with a spiral spin structure. These phases are associated with the existence of spin currents in the spiral state. Below, we will show that the triplet Cooper pairs ($\uparrow\uparrow$) or ($\downarrow\downarrow$) with spin $\mu = 1$ or $\mu = -1$ are moving pairs that carry large total momenta $\pm Q$. The constants $\kappa^{\mathrm{s,t}}$ of SC pairing in (6) are related to the constants $V(l)$ and $J(l)$ of interaction between neighboring sites in Eq. (1).

Let us take into account that the α and β bands are independent of the γ band. This is associated with the fact that the symmetry of the α and β bands with respect to the reflection about the *ab* plane of ruthenate bands is different from that of the γ band. For instance, a direct interband mixing of these bands due to hopping within

the RuO_4 plane is forbidden. This property of bands was discussed in [4, 17], where the authors also evaluated a small interband interaction due to interlayer hopping. We will neglect interlayer interactions and will analyze a possible SC order in each band separately, as well as its symmetry and compatibility with the spiral spin order. We will also neglect the interband scattering of pairs and take into account only the intraband constants κ^s and κ^t in (7). To reduce the number of SC OPs, we apply arguments typical for all strongly correlated systems. For any interaction $V_{\langle nm\rangle}$ in (1), a large on-site repulsion $U > 0$ suppresses the singlet *s*-wave OP $w(0)$ in the γ band according to (6), so that, of the singlet OPs, we retain only the $d_{x^2-y^2}$ wave OP; i.e., we set $w_\gamma(0) = 0$ and $w_\gamma(e_x) = -w_\gamma(e_y)$. This guarantees that the pair function is orthogonal to the forbidden *s*-wave pair function. For quasi-one-dimensional bands α and β (here, α and β refer to the bands of *xz* and *yx* natures rather than to their combinations), the same on-site interaction suppresses all singlet OPs, i.e., those of both *s* and *d* symmetries. As a result, we set $w_{\alpha(\beta)}(0) = w_\alpha(e_x) = w_\beta(e_y) = 0$ because both combinations $w_\alpha(e_x) \pm w_\alpha(e_y)$ are nonorthogonal to the on-site pair function $w(0)$ for quasi-one-dimensional bands with a broken tetragonal symmetry.

In the BCS approximation, an interaction of type (1) may induce an SC order only under the condition that some of the constants κ^s_ν or κ^t_ν in (6) are negative. One may assume that such an attraction is of correlational or kinematic origin or is attributed to the hybrid nature of the site orbitals composed of the *d* and p_π orbitals of ruthenium and oxygen. Therefore, we may assume that the corresponding parameters $\kappa^s_\nu(l)$ and $\kappa^t_\nu(l)$ or, equivalently, the parameters $V_\nu(l)$ and $J_\nu(l)$ in the model interaction (1) take nonzero values only for those bonds $\langle nm\rangle$, $m = n + l$, and orbitals for which the hopping integral t^ν_{nm} is different from zero. This assumption has been inspired by the expression $J_{nm} \propto 4t^2_{nm}/U$ for the exchange interaction in the *t*–*J* model. In light of the aforesaid, of all the constants, we assign nonzero values only to the following singlet (s) and triplet (t) pairing constants:

$$\kappa^{s(t)}_\alpha(e_x) = \kappa^{s(t)}_\beta(e_y) = \kappa^{s(t)}_\gamma(e_x) = \kappa^{s(t)}_\gamma(e_y) = \kappa^{s(t)}. \quad (9)$$

By the same analogy with the *t*–*J* model, one could expect that these constants have the following signs: $\kappa^s = -\kappa^t < 0$. However, in view of the expected triplet type of the SC order in Sr_2RuO_4 [1], we extend the calculations to the two limiting cases of triplet constants of different signs

$$\text{I: } \kappa^s = -\kappa^t < 0, \quad \text{II: } \kappa^s = \kappa^t < 0. \quad (10)$$

The first case corresponds to the attraction of particles only in the singlet channel and repulsion in the triplet channel. The second case corresponds to the attraction in both channels.

To solve the problem, we apply the standard procedure of mean-field approximation. From the explicit dependence of the mean energy $\bar{H}(z_i)$ on the one-particle OPs $z_j = \{y_i, w_i, \theta_i\}$, we obtain the linearized Hamiltonian

$$H_{\text{Lin}} - \mu N = \frac{\partial(\bar{H} - \mu\bar{N})}{\partial z_i}(\hat{z}_i - z_i) + \bar{H}(z_i) - \mu\bar{N}, \quad (11)$$

where $\hat{z}_i$ are operators corresponding the appropriate means z_i. The BCS-type state is an eigenstate of H_{Lin}; it allows one to calculate, in turn, the values of z_i. In this way, one obtains a self-consistent solution.

For the state with a spiral spin structure, the most convenient basis set of the Nambu representation is a basis of the following Fermi operators for each band ν:

$$b^\dagger_{i\nu k} = \{c^\dagger_{\nu k\uparrow}, c^\dagger_{\nu,\,k+Q,\downarrow}, c_{\nu,\,-(k+Q),\uparrow}, c_{\nu,\,-k,\downarrow}\}_i \quad . \quad (12)$$

Here, $i = 1, \ldots, 4$, and the quasimomentum k runs over the domain F that constitutes half of the total momentum space and is bounded by the conditions

$$k \in F\colon (k + Q/2)Q < 0. \quad (13)$$

For a vector $\mathbf{Q}$ with $Q_x = Q_y = 2\pi/3$, Eq. (13) implies that the components k_x and k_y range within the limits

$$-\pi - \frac{Q_x}{2} < k_{x,y} < \pi - \frac{Q_x}{2}, \quad k_x + k_y + Q_x < 0.$$

The linearized Hamiltonian H_{Lin} is determined by independent contributions each of which refers to the basis set (12):

$$H_{\text{Lin}} = \sum_{k\in F} \hat{h}^\nu_k, \quad \hat{h}^\nu_k = h^\nu_{ij} b^\dagger_{i\nu k} b_{j\nu k}. \quad (14)$$

The Hermitian matrix h^ν_{ij} of rank four is determined by the matrix elements (here, the omitted band index ν is implied)

$$\begin{aligned} h_{11} &= \epsilon_\nu(k_1) - \mu, \quad h_{22} = \epsilon_\nu(k_2) - \mu, \\ h_{12} &= -\frac{1}{2}\partial\bar{H}/\partial d_\nu, \\ h_{14} &= A(k_1) + B_0(k_1), \\ h_{23} &= -A(k_2) + B_0(k_2), \quad h_{13(24)} = B_{\pm1}(\bar{k}), \\ h_{33} &= -h_{22}, \quad h_{44} = -h_{11}, \quad h_{34} = -h_{12}, \end{aligned} \quad (15)$$

where

$$k_1 = k, \quad k_2 = k + Q, \quad \bar{k} = (k_1 + k_2)/2$$

and the functions A and B_μ are given by

$$A(k) = \sum_{l = e_x, e_y} \kappa_\nu^s(l) w_\nu(l) \cos kl,$$
$$B_\mu(k) = \sum_{l = e_x, e_y} \kappa_\nu^t(l) \theta_{\mu\nu}(l) \sin kl. \quad (16)$$

For the γ band, the d symmetry of the singlet OP requires the antisymmetry $A^\gamma(k_x, k_y) = -A^\gamma(k_y, k_x)$ of functions with respect to the replacement $k_x \longleftrightarrow k_y$. The solution also yields identical values for the triplet OPs θ_μ for $\mu = \pm 1$. Thus, we actually have only three real OPs for the γ band:

$$z_i = (w_d, \theta, \theta_0)_i, \quad i = 1, 2, 3,$$
$$w_d = \frac{1}{2}[w(e_x) - w(e_y)],$$
$$\theta_0 = \frac{1}{2}[\theta_0(e_x) - \theta_0(e_y)], \quad (17)$$
$$\theta = \frac{1}{4}\sum_{\mu = \pm 1} [\theta_\mu(e_\mu) - \theta_\mu(e_y)].$$

We apply the same symmetry with respect to the replacement $x \longleftrightarrow y$ to the solutions in the α and β bands subject to the simultaneous replacement $\alpha \longleftrightarrow \beta$ ($xz \longleftrightarrow yz$). The solution yields identical values θ_μ for two projections $\mu = \pm 1$ in the α and β bands as well. As a result, we retain the following triplet OPs for the α and β bands that correspond to a nonzero triplet constant in (9):

$$\theta_{\mu, \alpha}(e_x) = -\theta_{\mu, \beta}(e_y), \quad |\mu| = 0, 1. \quad (18)$$

If the initial values of the OP satisfy Eqs. (17) and (18), subsequent iterations of the self-consistency procedure preserve the same symmetry of the solution.

There was one more simplification. In fact, an interaction of type (1) yields contributions to both parts $\bar{H}_N(y_i)$ and $\bar{H}_{SC}$ of the mean energy (3). We may assume that the first contribution, which depends on the normal means—the charge and spin densities—has already been taken into account in the renormalized band energies $\epsilon_\nu(k)$ whose parameters were chosen earlier [25] for the correct description of the observed magnetic quantum oscillations. Thus, we retain only the part of $\langle V \rangle$ in $\bar{H}$ that depends on anomalous means. The definitions of triplet OPs (8) allow one to deal with real solutions. They have a certain symmetry with respect to the reflection in the diagonal plane (z, $x = y$) that contains the spirality vector Q under a simultaneous permutation of bands $xz \longleftrightarrow yz$, as well as a symmetry with respect to the reflection in the plane (z, $x = -y$) ($Q \longrightarrow -Q$) with the change $\sigma \longrightarrow -\sigma$.

The required BCS-type spiral state is determined by the occupation of one-particle eigenstates $\chi^\dagger_{\lambda\nu k}$ corresponding to the energy levels $E_\lambda(k)$,

$$\chi^\dagger_{\lambda\nu k} = b^\dagger_{ik} S_{i\lambda}(k),$$
$$h_{ij}(k) S_{j\lambda}(k) = S_{i\lambda}(k) E_\lambda(k). \quad (19)$$

Here, the omitted index ν is implied. The matrices $S_{i\lambda}(k)$ of the eigenvectors and the Fermi populations $f(E_{\lambda\nu k})$ of levels determine the normal and anomalous OPs (7) and (8). This completes the self-consistency procedure.

3. RESULTS

Since a complete solution with SC order is easily obtained for large pairing constants, we first consider models with large $k^{s(t)}$ and then calculate the phase curves $T_c(k^s)$ for more realistic models with small k^s and k^t. The results are obtained for two types of models in (10), with attraction in the singlet channel alone (case I) and in both singlet and triplet channels (case II). In the first case, the α and β bands do not display any SC order. The reason is that the singlet d-wave order, just as the s-wave one, is suppressed by an on-site repulsion in bands with inequivalent hopping integrals in the x and y directions: $t_x^\alpha \gg t_y^\alpha$ or $t_y^\beta \gg t_x^\beta$ (see the parameters of the three-band model [25]). In contrast to the α and β bands, a mixed-type SC order arises in the γ band of a system with a spiral spin configuration. The d-wave singlet order is accompanied by the formation of triplet pairs even for $\kappa_\gamma^t > 0$. Figure 1 shows the temperature dependence of the singlet and triplet OPs (17) in the γ band for $\kappa^s = -\kappa^t = -0.6$ eV. The values of the triplet OPs obtained satisfy the relation $\theta_{+1, \gamma} = \theta_{-1, \gamma} \gg \theta_{0, \gamma}$. Taking into account the definition of triplet OPs in (17) and (18) and their momentum representation, one can conclude that coupled triplet pairs of particles in the γ band arise mainly in the form ($\uparrow\uparrow$) or ($\downarrow\downarrow$) with the total quasimomenta $-Q$ or Q, respectively. This fact distinguishes between triplet SC orders in the spiral state and in an isotropic Fermi liquid, where only Cooper-type pairs ($k\uparrow$, $-k\uparrow$) or ($k\downarrow$, $-k\downarrow$) with zero total momentum are possible. Moreover, unlike the isotropic model, triplet pairs can arise in the state with the spin structure even for a positive triplet constant $\kappa^t > 0$, which corresponds to repulsion in the triplet channel, due to the coupling between singlet and triplet OPs.

The Cooper pairs with nonzero total momenta Q were first predicted in the Fulde–Ferrel–Larkin–Ovchinnikov (FFLO) states [26]. The latter have spatial variations of the OPs and can actually exist only if the scale of $2\pi/Q$ is much smaller than the coherence length

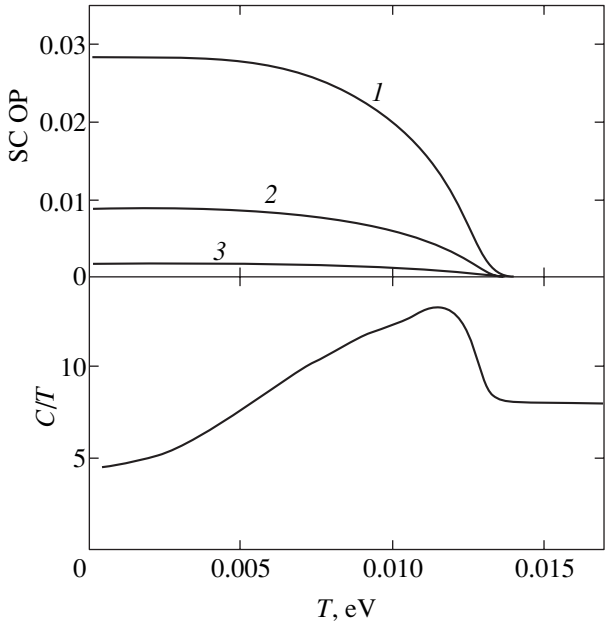

Fig. 1. Total specific heat divided by T, $C(T)/T$, and superconducting order parameters in the γ band as functions of temperature for a model with large interaction constants $\kappa^s = -\kappa^t = -0.6$ eV. Curves *1–3* refer to w_d, $-\theta$, and $-\theta_0$, respectively, that are defined by Eqs. (17).

ξ. In our case of coexisting spiral spin and mixed SC orders, only the anomalous triplet components

$$\langle c^\dagger_{\nu n\sigma} c^\dagger_{\nu m\sigma}\rangle \propto \exp\left\{\frac{i}{2}\mu Q(n+m)\right\}\theta_{\nu,2\sigma},$$

$$m = n \pm e_{x(y)}, \quad \mu = 2\sigma,$$

are characterized by the spatial phase modulation according to Eq. (8). At the same time, the leading singlet component w_ν in (7) is constant and is independent of the number of bond $\langle nm\rangle$. Therefore, there is no constraint on the relation between ξ and $1/Q$ in these solutions.

The emergence of coupled pairs with large total momenta of $2k_F$, equal to the nesting vector, is also substantiated in the new theory of high-temperature superconductivity (HTSC) [27]. In [27], such pairs are assumed to be singlet and are associated with the stripe structure. In our model, such moving pairs are triplet and are synchronized by the static spin structure. Note that a photoemission technique capable of distinguishing between the spin polarizations of photoelectrons could also distinguish between the polarization asymmetries of photospectra. The latter are associated with the spiral spin structure that breaks the time-reversal symmetry in both the normal and the SC state. In [20], it is demonstrated that electrons from different segments of the Fermi boundary—with $kQ < 0$ (or $kQ > 0$)—are characterized by different spin polarizations $k\uparrow$ (or $k\downarrow$). When the spin order has a local or dynamic character and manifests itself within finite domains or finite time intervals, the asymmetry phenomena are suppressed.

Thus, in states with the spiral structure due to the nesting of α and β bands, the attraction solely in the singlet channel gives rise to both singlet and triplet pairs. Figure 1 also represents the specific heat of the system. The finite limit of $C(T)/T$ as $T \longrightarrow 0$ is attributed to the contribution of the α and β bands that remain in the normal state. This fact does not agree with the observed behavior of $C(T)/T \propto T$ as $T \longrightarrow 0$.

Now, let us consider a model of the second type with attraction in both channels: $\kappa^s = \kappa^t < 0$ in (10). For large $|\kappa^s|$ and $|\kappa^t|$ and small T, an SC order arises in all three bands. For equal values of constants (9) on each bond with a large hopping integral, the SC order in the γ band is more clearly pronounced than that in the α and β bands. For $\kappa^s \le 0.65$ eV and $T \sim 10^{-3}$ eV, the SC order in the α and β bands vanishes. The ensemble of coupled pairs in the γ band mainly consists of *d*-wave singlet Cooper pairs $\{k\uparrow, -k\downarrow\}^s$ and moving triplet pairs $\{k\uparrow, -(k+Q)\uparrow\}$ and $\{k\downarrow, -(k-Q)\downarrow\}$ with the total momenta $-Q$ or Q, respectively.

In the α and β bands, only a triplet order is possible for $k^t < 0$. The corresponding transition temperatures are significantly lower than T_c in the γ band: $T_c^{\alpha\beta}(k^t = k^s) \ll T_c^\gamma$. The triplet *p*-wave SC order in the α and β bands is mainly attributed to the formation of triplet pairs $\{k\uparrow, -k\downarrow\}^t$ with zero total momenta. They correspond to the OP $\theta_0^\alpha(e_x) = -\theta_0^\beta(e_y) \neq 0$. Figure 2 shows the temperature dependence of the SC OP in the α, β, and γ bands for large constants $\kappa^s = \kappa^t = -0.8$ eV. Note that the relation $|\theta_0(l)| > |\theta_{\pm1}(l)|$ for the triplet components for $l = e_{x(y)}$ in the α and β bands differs from the relation $|\theta_0(l)| \ll |\theta_{\pm1}(l)|$ for the OP in the γ band. The differences in T_c and the symmetry of the SC order in the α, β, and γ bands are associated with the quasi-one-dimensional or quasi-two-dimensional character of the bands and with different densities of states on the Fermi level.

Thus, for models with intralayer interaction of neighboring sites, only the γ band is characterized by large T_c. Models with different scales of T_c in the γ band and in the α and β bands are characterized by a two-step behavior of the specific heat (Fig. 2). This fact contradicts the observed dependence $C(T)/T$ which is indicative of the simultaneous SC transition in all three bands. Nevertheless, the solutions obtained are instructive because they show the possibility of new mixed types of SC order that are compatible with the spiral spin order in a correlated system.

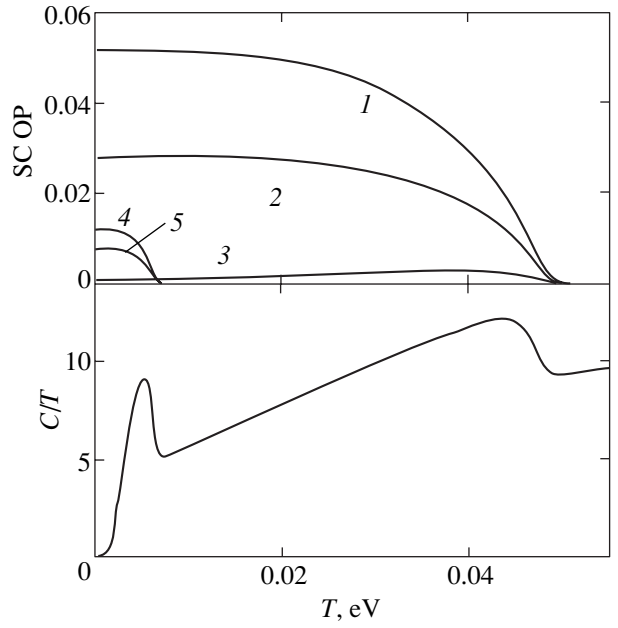

Fig. 2. Same as in Fig. 1, but for a model with $\kappa^s = -\kappa^t = -0.8$ eV. Curves *1–3* refer to the same SC OPs for the γ band as those in Fig. 1; curves *4* and *5* correspond to $\theta_0^\alpha(e_x) = -\theta_0^\beta(e_y)$ and $\theta_{\pm1}^\alpha(e_x) = -\theta_{\pm1}^\beta(e_y)$.

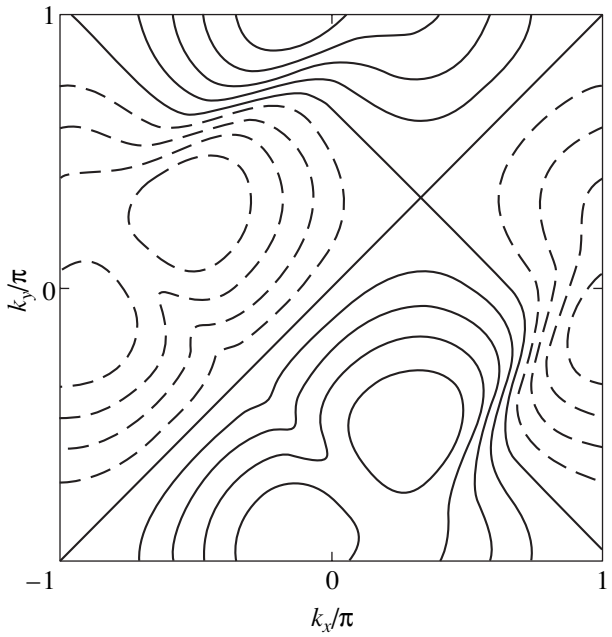

Fig. 3. Contour map of the gap function (23) for the same model as in Fig. 1 in the entire domain of the momentum space $|k_{x(y)}| < \pi$. Solid (dashed) lines correspond to positive (negative) values of the gap function $G(k_x, k_y)$ defined by Eq. (22).

Pairing potentials in the active γ band with the SC OPs (17) can be represented as

$$H_{\mathrm{Lin}}^{\mathrm{SC}} = \sum_{k \in G} \{[A(k) + B_0(k)]c_{k\uparrow}^\dagger c_{-k\downarrow}^\dagger + B_1(k)[c_{k-Q/2,\uparrow}^\dagger c_{-k-Q/2,\uparrow}^\dagger + c_{k+Q/2,\downarrow}^\dagger c_{-k+Q/2,\downarrow}^\dagger] + \mathrm{H.c.}\}. \quad (20)$$

Here, k runs over the entire region G of the phase space (in contrast to representation (14), where k runs over half of the entire region G), and the omitted band index $\nu = \gamma$ is implied. The functions $A(k)$ and $B_\mu(k)$ are defined by Eqs. (16) and are given by

$$A(k) = \kappa^s w_d(\cos k_x - \cos k_y), \quad B_\mu(k) = \kappa^t \theta_\mu(\sin k_x - \sin k_y). \quad (21)$$

These functions have the following symmetry: $A(k_x, k_y) = -A(k_y, k_x)$ and $B(k_x, k_y) = -B(k_y, k_x)$; hence, the diagonal $k_x = k_y$ along the vector Q is a node line for the SC gap in the solution with a mixed *d*-wave singlet and *p*-wave triplet SC order. In the case of an isotropic normal state without a spiral spin structure ($d_\nu = 0$, $Q = 0$), the pairing potential (21) would correspond to the superposition of contributions corresponding to different representations of a tetragonal point group classified in [5]. In the notation of [5], this superposition can schematically be represented as $\{\theta_1(A_{1u} - B_{1u} - A_{2u} + B_{2u}) + \theta_0(E_{ux} - E_{uy})\}$. In contrast to the paramagnetic state, in the spiral state, the coupled pairs $(\uparrow\uparrow)$, $(\downarrow\downarrow)$ are moving pairs with the total momenta $\mp Q$. The spin currents $j_{\uparrow\uparrow} = -j_{\downarrow\downarrow}$ associated with the motion of pairs have the same sign as the spin currents $j_\uparrow = -j_\downarrow$ in the normal state with the spiral spin structure. Recall that the spins are projected here onto an axis perpendicular to the spin rotation plane in the spiral structure.

The SC band, as a function of k, which corresponds to the pairing potential (21) for the γ band, is determined by the real matrix element

$$G(k) = \langle \eta_{-k} | H^{\mathrm{SC}} | \eta_k \rangle \quad (22)$$

between electron and hole quasiparticles $\eta^\dagger$, η of the upper Hubbard band of the normal spiral state.

Figure 3 represents a level map of the gap function $G(k)$ for the γ band for $\kappa^s = -k^t < 0$. This function is antisymmetric with respect to the change $k_x \longleftrightarrow k_y$ but does not possess the inversion symmetry. However, a hypothetical photoemission experiment for the γ band would give two different gaps $|G(k)|$ and $|G(-k)|$ for every k for different polarizations ($\uparrow$ and $\downarrow$) of photoelectrons. Note that, for a quasimomentum k that varies along the known Fermi boundary of the γ band, the function $G(k)$ is close to the *d*-wave function proportional to $\cos k_x - \cos k_y$. This fact corresponds to the fourfold anisotropy of thermal conductivity in a longitudinal (in the *ab* plane) magnetic field [9, 10].

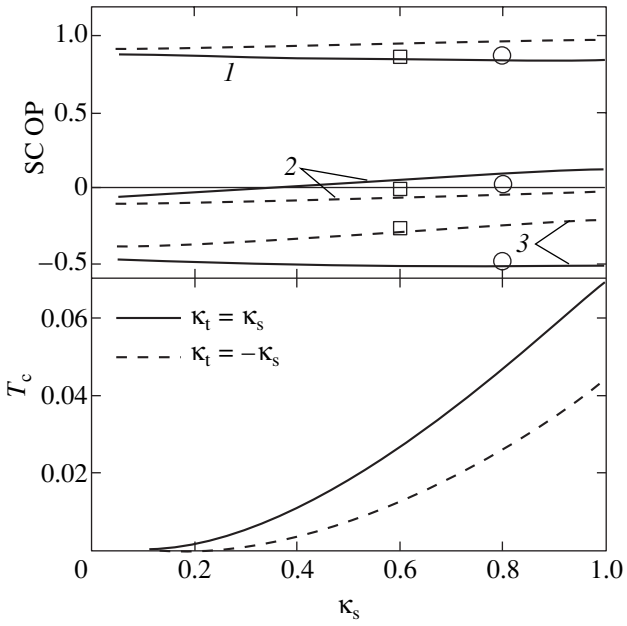

Fig. 4. Phase curves $T_c(\kappa^s)$ and relative normalized values of the superconducting OPs (25) and (17) in the γ band as functions of the interaction constants in the singlet channel. Solid (dashed) curves refer to models with $\kappa^t = +\kappa^s$ and $\kappa^t = -\kappa^s$, respectively. Curves *1*, *2*, and *3* correspond to $\tilde{z}_i$, $i = 1, 2, 3$, obtained from the solution of homogeneous equations (25) ($T \longrightarrow T_c$). Symbols (circles and squares) correspond to the same quantities at $T = 0.6T_c$ obtained from the full mean-field solution for models represented in Figs. 1 and 2, respectively.

Up to now, the results referred to models with unrealistically large interaction constants and temperatures T_c. For more realistic models that correspond to small T_c and constants (10) of both types, we calculated the phase curves $T_c(\kappa^s)$. The function $T_c(\kappa^s)$ for the SC-transition temperature in the γ band is determined by the equation obtained by a linear expansion of Eqs. (7) and (8) in terms of the arising SC OPs w_γ and $\theta_{\lambda\mu}$. This equation for $T_c(\kappa^s)$ has the form

$$\det\|\delta_{ij} - R_{ij}\kappa_j\| = 0. \qquad (23)$$

Here, i and j number the SC OPs $\{z_i\}$ defined by Eq. (17), and the matrix R_i is given by

$$R_{ij} = \frac{1}{N}\sum_k \sum_{\lambda,\lambda'} M^i_{\lambda\lambda'} M^j_{\lambda\lambda'} \frac{f(-E_\lambda) - f(E_{\lambda'})}{E_\lambda + E_{\lambda'}}, \qquad (24)$$

where $E_\lambda = E_\lambda(k)$ and $f(E_\lambda)$ are the normal-state energies and the Fermi populations of one-electron levels, respectively. The matrices $M^i(k)$, $i = 1, 2, 3$, corresponding to the SC OPs (17) are given in the Appendix, while the constants κ_j in (23) are given by $\kappa_j = \{\kappa^s, \kappa^t, \kappa^t\}_j$. The indices $\lambda, \lambda' = 1, 2$ number the normal-state levels of the upper and lower Hubbard subbands of the γ band. At the SC-transition point $T = T_c$, where Eq. (23) is satisfied, the solution of the corresponding homogeneous equations

$$(\delta_{ij} - R_{ij}\kappa_j)\tilde{z}_j = 0, \quad \tilde{z}_j = z^\gamma_j / \sqrt{z_1^2 + z_2^2 + z_3^2} \qquad (25)$$

gives relative normalized values $\tilde{z}_j$ of the SC OPs. Figure 4 shows the phase curves $T_c(\kappa^s)$ and the relative values of the OPs $\tilde{z}_j$ for $T \longrightarrow T_c$ as functions of κ^s for two signs of the triplet constant κ^t in (10). The symbols refer to the values of $\tilde{z}_j$ for $T \sim 0.6T_c$ obtained from full mean-field calculations for the models with large constants $|\kappa^s|$ discussed above. These values agree with those obtained from Eqs. (25). The models with realistic $T_c \sim 10^{-4}$ eV display the same symmetry properties as the models with large κ^s and T_c. The transition temperatures $T_c = 1.5$ K observed in Sr_2RuO_4 correspond to the constants $\kappa^s = -0.145$ eV or $\kappa^s = -0.12$ eV, respectively, for two types (10) of models. In the first case, when $k^t = -k^s > 0$, the SC transition occurs only in the γ band. In the second case, when $k^t = k^s < 0$, transition temperatures in the α and β bands are estimated to be $T_c \sim 10^{-3}$ K. Actually, this means a normal metallic state of the α and β bands for models of both types (10).

4. CONCLUSIONS

Thus, models with intralayer pairing interactions of neighboring sites admit the SC order only in the γ band. This fact does not agree with the situation in superconducting Sr_2RuO_4. Nevertheless, the models considered are instructive in that they demonstrate the possibility of new mixed types of SC order when a correlated system possesses a spin structure. We have shown that the SC order in the γ band may coexist with a spiral spin order due to the nesting of the α and β bands in Sr_2RuO_4. The mixed *d*-wave singlet and *p*-wave triplet SC orders emerge from the pairing interactions of adjacent sites on the basis of the normal state with a spiral structure with the nesting vector $Q = 2\pi(1/3, 1/3)$. For two types of constants of pairing interactions—with attraction in both (singlet and triplet) channels or only in the singlet channel—the main coupled pairs in the system are the singlet *d*-wave pairs $(k, -k)^s_{\uparrow\downarrow}$ and the moving triplet pairs $(k - Q/2, -k - Q/2)^t_{\uparrow\uparrow}$ and $(k + Q/2, -k + Q/2)^t_{\downarrow\downarrow}$ with large total quasimomenta $\mp Q$ and the spin projections $\mu = \pm 1$ onto an axis perpendicular to the spin rotation plane of the spiral structure. The predominant *d*-wave SC order in the γ band is consistent with the observed fourfold anisotropy of thermal conductivity in Sr_2RuO_4 in a longitudinal (in the plane of RuO_4) magnetic field [9, 10]. The problems

of SC order in the α and β bands and of the Knight shift behavior remain unsolved within the models considered. The extension of the calculations to other periodic spin structures requires the consideration of other, in particular, interlayer interactions. The calculation of the behavior of the spin susceptibility under the SC transition should clear up the following question: Can the triplet pairs accompanying the *d*-wave SC order guarantee the invariance of the Knight shift under the SC transition?

ACKNOWLEDGMENTS

I am grateful to A.A. Ovchinnikov† and V.Ya. Krivnov for useful remarks and help, as well as to R. Werner for kindly submitting the preprints of [15] before their publication.

This work was supported by the Russian Foundation for Basic Research, project nos. 00-03-32981 and 00-15-97334.

APPENDIX

The matrices M^i in (24) are given by

$$M^i_{\lambda\lambda'}(k) = \left[\begin{pmatrix} c & s \\ s & -c \end{pmatrix}\overline{M}^i\begin{pmatrix} s & c \\ c & -s \end{pmatrix}\right]_{\lambda\lambda'}, \qquad (26)$$

$$\overline{M}^1 = \begin{pmatrix} 0 & c_{\mathrm{d}}(k_1) \\ -c_{\mathrm{d}}(k_2) & 0 \end{pmatrix},$$

$$\overline{M}^2 = \begin{pmatrix} 0 & s_p(k_1) \\ -s_{\mathrm{d}}(k_2) & 0 \end{pmatrix},$$

$$\overline{M}^3 = s_p(\bar{k})\begin{pmatrix} 1 & 0 \\ 0 & 1 \end{pmatrix}.$$

Here, $s = \sin\varphi$, $c = \cos\varphi$, and $\varphi = \varphi(k)$ for band ν are determined by the equation $\tan(2\varphi) = -[\partial\overline{H}/\partial d_\nu][\epsilon(k_1) - \epsilon(k_2)]^{-1}$. Other functions are given by $c_d(k) = (\cos k_x - \cos k_y)/2$, $s_p(k) = (\sin k_x - \sin k_y)/2$; $k_1 = k$, $k_2 = k + Q$, and $\bar{k} = k + Q/2$.

REFERENCES

1. Y. Maeno, T. M. Rice, and M. Sigrist, Phys. Today **54** (1), 42 (2001).
2. T. M. Rice and M. Sigrist, J. Phys.: Condens. Matter **7**, L643 (1995).
3. K. Ishida, H. Mukuda, Y. Kitaoka, *et al.*, Nature **396**, 658 (1998).
4. M. E. Zhitomirsky and T. M. Rice, Phys. Rev. Lett. **87**, 057001 (2001).
5. M. Sigrist, D. Agterberg, A. Furusaki, *et al.*, cond-mat/9902214.
6. K. M. Luke, Y. Fudamoto, K. M. Kojima, *et al.*, Nature **394**, 558 (1998).
7. S. Nishizaki, Y. Maeno, and Z. Mao, J. Low Temp. Phys. **117**, 1581 (1999); J. Phys. Soc. Jpn. **69**, 572 (2000).
8. K. Ishida, H. Makuda, Y. Kitaoka, *et al.*, Phys. Rev. Lett. **84**, 5387 (2000).
9. M. A. Tanatar, M. Suzuki, S. Nagai, *et al.*, Phys. Rev. Lett. **86**, 2649 (2001); M. A. Tanatar, S. Nagai, Z. Q. Mao, *et al.*, Phys. Rev. B **63**, 064505 (2001).
10. K. Izawa, H. Takahashi, M. Yamaguchi, *et al.*, Phys. Rev. Lett. **86**, 2653 (2001).
11. I. Bonalde, B. D. Yanoff, M. B. Salamon, *et al.*, Phys. Rev. Lett. **85**, 4775 (2000).
12. C. Lupien, W. A. MacFarlane, C. Proust, *et al.*, Phys. Rev. Lett. **86**, 5986 (2001); cond-mat/0101319.
13. H. Won and K. Maki, Europhys. Lett. **52**, 427 (2000).
14. I. Eremin, D. Manske, C. Joas, and K. M. Bennemann, cond-mat/0102074.
15. R. Werner, Phys. Rev. B **67**, 014505 (2003); Phys. Rev. B **67**, 014506 (2003); R. Werner and V. J. Emery, Phys. Rev. B **67**, 014504 (2003).
16. M. Eschrig, J. Ferrer, and M. Fogelström, cond-mat/0101208; Phys. Rev. B **63**, 220509 (2001).
17. D. F. Agterberg, T. M. Rice, and M. Sigrist, Phys. Rev. Lett. **78**, 3374 (1997).
18. J. F. Annett, G. Litak, B. L. Györffy, and K. I. Wysokinski, Phys. Rev. B **66**, 134514 (2002).
19. G. Litak, J. F. Annett, B. L. Györffy, and K. I. Wysokinski, cond-mat/0203601.
20. A. A. Ovchinnikov and M. Ya. Ovchinnikova, cond-mat/0201536; A. A. Ovchinnikov and M. Ya. Ovchinnikova, Zh. Éksp. Teor. Fiz. **122**, 101 (2002) [JETP **95**, 87 (2002)].
21. Y. Sidis, M. Braden, P. Bourges, *et al.*, Phys. Rev. Lett. **83**, 3320 (1999).
22. M. Braden, O. Friedt, Y. Sidis, *et al.*, cond-mat/0107579.
23. A. Damascelli, D. H. Lu, K. M. Shen, *et al.*, Phys. Rev. Lett. **85**, 5194 (2000).
24. I. I. Mazin and D. J. Singh, Phys. Rev. Lett. **79**, 733 (1997); Phys. Rev. Lett. **82**, 4324 (1999).
25. A. Liebsch and A. Lichtenstein, Phys. Rev. Lett. **84**, 1591 (2000).
26. P. Fulde and R. A. Ferrell, Phys. Rev. A **135**, 550 (1964); A. I. Larkin and Yu. N. Ovchinnikov, Zh. Éksp. Teor. Fiz. **47**, 1136 (1964) [Sov. Phys. JETP **20**, 762 (1964)].
27. V. I. Belyavsky and Yu. V. Kopaev, cond-mat/0203138; V. I. Belyavskiĭ and Yu. V. Kopaev, Zh. Éksp. Teor. Fiz. **121**, 175 (2002) [JETP **94**, 149 (2002)]; V. I. Belyavskiĭ, V. V. Kopaev, and Yu. V. Kopaev, Zh. Éksp. Teor. Fiz. **118**, 941 (2000) [JETP **91**, 817 (2000)].

† Deceased.

Translated by I. Nikitin

Journal of Experimental and Theoretical Physics, Vol. 96, No. 6, 2003, pp. 1140–1148.
Translated from Zhurnal Éksperimental'noĭ i Teoreticheskoĭ Fiziki, Vol. 123, No. 6, 2003, pp. 1297–1307.

SOLIDS
Electronic Properties

Structures of Order Parameters in Inhomogeneous Phase States of Strongly Correlated Systems

L. S. Isaev and A. P. Protogenov*
Nizhni Novgorod State University, Nizhni Novgorod, 603950 Russia
Institute of Applied Physics, Russian Academy of Sciences, Nizhni Novgorod, 603950 Russia
**e-mail: alprot@appl.sci-nnov.ru*

Abstract—The structures of order parameters which determine the bounds of the phase states within the framework of the CP^1 Ginzburg–Landau model are considered. Using the formulation of this model [1] in terms of the gauged order parameters (the unit vector field **n**, density ρ^2 and momentum **c** of particles), we found that some universal properties of phases and field configurations are determined by the Hopf invariant Q and its generalizations. At a sufficiently high level of doping, it is found that, outside the superconducting phase, the charge distributions in the form of loops may be more preferable than those in the form of stripes. It is shown that, in phase with its mutual linking number $L < Q$, the transition to an inhomogeneous superconducting state with nonzero total momentum of pairs takes place. A universal mechanism of breaking of the topological coherence of the superconducting state due to a decrease of the charge density is discussed. © *2003 MAIK "Nauka/Interperiodica".*

1. INTRODUCTION

Among the challenging problems of cooperative phenomena in planar systems near Mott transition, there are such that, at first glance, may not be associated with the appearance of high-temperature superconducting states in doped antiferromagnetic insulators. For example, we are interested in the origins of qualitatively similar cooperative behavior in various compounds and very rich content of their phase diagram, as well as in origin of the emergence of inhomogeneous states typical of such systems [2–6]. Low-dimensional structures in the distribution of spin [2, 3] and charge [4–6] degrees of freedom exist in the state which precedes a high-temperature superconducting phase. Keeping this property in mind [7], we should choose a model for describing the aforementioned phases that contains them as limiting cases. The mean-field Ginzburg–Landau theory with the appropriate choice of the order parameters may be used for understanding general problems of such kind. A key question in this universal approach is the method with the aid of which the order parameters encode simultaneously the content and the distribution of charge and spin degrees of freedom of excitations in various phase states.

The recent progress in solving analogous problems in the non-Abelian field theory [8] and its development in the physics of condensed matter [1] showed that the CP^1 Ginzburg–Landau model is preferable. The two-component order parameter of this model is used for solving the problems of two-gap superconductivity [9]. In the theory of electroweak interaction [10], this parameter has the sense of the Higgs doublet of the standard model. In this paper, we will assume that the order parameter is a spinor realizing a two-dimensional representation of the braid group which arises due to classification of the quantum states upon permutations of particles in (2 + 1)-dimensional systems. Considering factorization with respect to the center of this non-Abelian group, we obtain the gauged CP^1 Ginzburg–Landau model. Note that the order parameter of this model is two-dimensional [1, 11]. Only in this case can we introduce the unit vector field which describes the distribution of one-half spin degrees of freedom in the long-wavelength limit as well as use the Hopf invariant for classifying **n**-field configurations and consider correctly the phases with different distribution of charge degrees of freedom. For the above reasons, we use the generalized **n**-field model which, after the exact mapping of the CP^1 Ginzburg–Landau model [1], includes the Faddeev term [12]. Because of the non-Abelian gauge theory origin of this significant part of the model, we hope that the obtained answers are universal and will give a deeper insight into the problems under consideration.

The Hopf invariant describes the degree of linking or knotting of the filament manifolds where the field of the unit vector **n** is defined. The study of the behavior of the vortex filament tangle is a separate problem and attracts attention for several reasons. First, at small distances, the topological order associated with the linking exists against the background of the disorder caused by arbitrary motion of separate parts of the system of entangled vortex filaments. Thus, unlike point particles, the properties of the tangle are determined by the behavior of its fragments in the ultraviolet and infrared limits. Since the coordinates of the vortex core are

canonically conjugated, the indicated circumstances are manifested by noncommutativity of these variables depending on the degree of linking. Second, a soft medium such as the tangle of linked filaments is a hot problem in the physics condensed matter and beyond, in particular, in connection with the DNA problem. When the coupling constants are transformed into the sought functions, the appearance of a double helix as the solution of the equations of motion in the soft variant [13] of the **n**-field model is its general property.

In the present paper, we consider some properties of the field configuration in the CP^1 Ginzburg–Landau model defined in the following section. The main goal of the paper is to find the bounds of free energy in the superconducting state and in the inhomogeneous phase with broken antiferromagnetic order, as well as to describe the properties of the charge density distributions corresponding to this state. Considering the nonsuperconducting phase in the soft version of the model [13], we analyze the contribution to the free energy from the charge density distributions in the form of loops and stripes. In the third and fourth sections, we discuss, along with the results from brief publications [14–16], the properties of the inhomogeneous superconducting state with nonzero total momentum of pairs and compare this with the LOFF states [17, 18] and with the results from the recently proposed [19] BCS-like model with two types of particles. We also pay attention to the dependence of the bounds of phase states on the generalized (2 + 1)D Hopf invariant in the case of $S^2 \times S^1 \longrightarrow S^2$ and $S^1 \times S^1 \times S^1 \longrightarrow S^2$ mapping classes and on the external magnetic field. In the Conclusions, we discuss some open problems. The Appendix gives the proof of the inequality which determines the relation between the contributions to the free energy of **n**- and **c**-field configurations.

2. CP^1 GINZBURG–LANDAU MODEL

We will use the Ginzburg–Landau model

$$F = \int d^3x \left[\sum_\alpha \frac{1}{2m} \left| \left(\hbar \partial_k + i \frac{2e}{c} A_k \right) \Psi_\alpha \right|^2 + \sum_\alpha \left(- b_\alpha |\Psi_\alpha|^2 + \frac{c_\alpha}{2} |\Psi_\alpha|^4 \right) + \frac{\mathbf{B}^2}{8\pi} \right] \quad (1)$$

with a two-component order parameter,

$$\Psi_\alpha = \sqrt{2m}\rho\chi_\alpha, \quad \chi_\alpha = |\chi_\alpha| e^{i\varphi_\alpha}, \quad (2)$$

which satisfies the condition $|\chi_1|^2 + |\chi_2|^2 = 1$. This coupling of two components χ_α takes place in the complex projective space CP^1, for which the given model is defined. The model (1), (2) with different masses was used before [1, 6, 9] in the context of two-gap superconductivity, as well as in the standard model of the non-Abelian field theory [8, 10]. In the present paper, we consider the states in planar systems and suppose that Ψ has the sense of the order parameter realizing two-dimensional non-Abelian representations of the braid group used for classifying quantum states upon permutations of particles in systems with two spatial dimensions. Realizing Abelian projection [20], the vector A_k compensates the local choice of the phase of the function Ψ. The last terms in (1) describe the Ginzburg–Landau potential $V(\Psi_1, \Psi_2)$ and the self-energy of the gauge field.

It has been shown recently [1] that there is an exact mapping of the model (1), (2) into the following version of the **n**-field model:

$$F = \int d^3x \left[\frac{1}{4}\rho^2 (\partial_k \mathbf{n})^2 + (\partial_k \rho)^2 + \frac{1}{16}\rho^2 \mathbf{c}^2 + (F_{ik} - H_{ik})^2 + V(\rho, n_3) \right]. \quad (3)$$

The free energy in Eq. (3) is defined by a scalar—the density of particles ρ^2, the field of the unit vector $n^a = \bar{\chi}\sigma^a\chi$ (where $\bar{\chi} = (\chi_1^*, \chi_2^*)$, and σ^a is the Pauli matrix), and the field of the momentum $\mathbf{c} = \mathbf{J}/\rho^2 = 2(\mathbf{j} - 4\mathbf{A})$. The total current $\mathbf{J}$ contains the paramagnetic part $\mathbf{j} = i[(\chi_1 \nabla \chi_1^* - \text{c.c.}) + (\chi_2 \nabla \chi_2^* - \text{c.c.})]$ and the diamagnetic term $-4\mathbf{A}$. Equation (3) is written with the use of the following notation: $F_{ik} = \partial_i c_k - \partial_k c_i$, $H_{ik} = \mathbf{n} \cdot [\partial_i \mathbf{n} \times \partial_k \mathbf{n}]$, and dimensionless units of the length $L = (\xi_1 + \xi_2)/2$ (with the coherence length $\xi_a = \hbar/\sqrt{2mb_\alpha}$), the momentum $\hbar/L$ (as the unit of momentum $\mathbf{c}$), the particle density $c^2/(512\pi e^2 L^2)$ (per unit mass for the parametrization of Ψ_α in the form (2)), and the energy γ/L with $\gamma = (c\hbar/e)^2/512\pi$.

In formulation (3), the Ginzburg–Landau functional depends on gauged order parameters ρ^2, $\mathbf{c}$, and $\mathbf{n}$. They characterize spatial distributions of the charge and spin degrees of freedom with or without current. The functions χ_α determine the orientation of the unit vector $\mathbf{n}$ which describes (in the long-wavelength limit) the properties of the magnetic order. In addition, functions χ_α define the value of the paramagnetic part of the current. Comparing different forms of representation of the CP^1 Ginzburg–Landau model, we note that vortex field configurations Ψ_α in the model (1), (2) are equivalent to textures of the field $\mathbf{n}$ in terms of the model (3). We must also note that the ansatz (2) has the sense of factorization of the longitudinal ρ and transversal χ_α degrees of freedom. In the superconducting state, the composition of spin $\mathbf{j}$ and charge degrees of freedom is important, since the current contains diamagnetic $U(1)$ gauge component $-4\mathbf{A}$.

In the soft variant of the extended model of **n** field (3), the multipliers of the first term describe the distributions of spin stiffness and the square of the inverse length of the density screening. It is seen from this example that the competition of the order parameters ρ, **n**, and **c** may account for the coexistence of the phase states with different ordering of charge and spin degrees of freedom. We enumerate the limiting cases of the model (3) in inhomogeneous ($\mathbf{n} \neq \text{const}$) situations:

(1) a state with broken antiferromagnetic order: $\mathbf{c} = 0$, $\rho = \text{const}$;

(2) a state with quasi-one-dimensional density distributions: $\mathbf{c} = 0$, $\rho \neq \text{const}$;

(3) an inhomogeneous superconducting state: $\mathbf{c} \neq 0$, $\rho = \text{const}$;

(4) $\mathbf{c} \neq 0$, $\rho \neq \text{const}$.

In the case of $\mathbf{n} = \text{const}$ and $\mathbf{c} \neq 0$, $\rho \neq \text{const}$, functional (1) is equivalent to the one-component Ginzburg–Landau model.

3. THE BOUNDS OF THE FREE ENERGY

3.1. A Phase State with Broken Antiferromagnetic Order

Let us consider the first case in the above list. In this limit, the free energy is

$$F = \int d^3x [g_1(\partial_k \mathbf{n})^2 + g_2(\mathbf{n} \cdot [\partial_i \mathbf{n} \times \partial_k \mathbf{n}])^2]. \quad (4)$$

We supposed that, in the phase under consideration, the constant value $\rho = \rho_0$ can be found from the minimum of the potential V, and we introduced the notation g_i for the coupling constants. The properties of the model (4) were studied in detail in [21–27]. The analysis of the dimensionality shows that the first term in Eq. (4) is proportional to the characteristic size R_Q of the **n**-field configurations, and the second term is inversely proportional to this scale. Therefore, the energy (4) has a minimum which is achieved at $R_Q = \sqrt{g_2/g_1}$. This explains why the second term in Faddeev–Niemi model (4) allows us to avoid Derrik's restriction of the existence of three-dimensional static configurations with finite size. In the infrared limit, this term characterizes the mean degree of noncollinearity $\langle 0|\mathbf{S}_1 \cdot [\mathbf{S}_2 \times \mathbf{S}_3]|0\rangle$ in the orientation of three spins located at the sites of the quadratic plaquette.

It was shown [25–27] that the lower energy bound in the model (4)

$$F \geq 32\pi^2 |Q|^{3/4} \quad (5)$$

is determined by the Hopf invariant

$$Q = \frac{1}{16\pi^2} \int d^3x \varepsilon_{ikl} a_i \partial_k a_l. \quad (6)$$

In this equation, the vector a_i denotes the gauge potential which parametrizes the mean degree of the noncollinearity of the orientation of neighboring spins in the following way:

$$H_{ik} = \mathbf{n} \cdot [\partial_i \mathbf{n} \times \partial_k \mathbf{n}] \equiv \partial_i a_k - \partial_k a_i.$$

The dependence $F_{\min} \propto |Q|^{3/4}$ (5) with the boundary conditions $\mathbf{n} \longrightarrow (0, 0, 1)$ in the space infinity was verified in [22–24] in simulation of the **n**-field configurations. Such a boundary condition means that the space $\mathbb{R}^3$ of the **n**-field definition effectively compacts into a three-dimensional sphere S^3. Thus, the unit vector **n** accomplishes the mapping of the S^3 sphere into the space of the two-dimensional sphere S^2. Let the vector **n** be directed to some general point of a two-dimensional sphere. We are interested in answering the following question: what is the pullback of this point in the space S^3 or, in other words, what set of points from the domain of definition of the vector $\mathbf{n}(x, y, z)$ contributes to a given point of the target two-dimensional sphere? Since the space S^3 is compact and its dimensionality is greater by unity than that of the sphere S^2, the pullbacks of points on the sphere S^2 are closed and, in the general case, linked lines on the S^3 sphere.

The Hopf invariant Q (6) describes the degree of linking or knotting of these lines. It belongs to a set of integers $\mathbb{Z}$ to which the considered homotopy group $\pi_3(S^2) = \mathbb{Z}$ is equal. In particular, for two once-linked circles, $Q = 1$; for one of the simplest knots (a trefoil), $Q = 6$; etc. As a result, the **n**-field configurations are divided into classes corresponding to the values of the Hopf invariant. We should emphasize once again that linked or knotted configurations may be numbered by the Hopf index only in the case of the CP^1 Ginzburg–Landau model with its two-component order parameter, because at $M > 1$ the homotopy group $\pi_3(CP^M) = 0$ is trivial [11].

3.2. Quasi-One-Dimensional Density Distributions

Let us consider the states outside the superconducting phase from the second line of the list of limiting cases, to which the CP^1 Ginzburg–Landau model leads. In this soft version of the model, the functional (3) has the form

$$F = \int d^3x \times \left[\frac{1}{4}\rho^2(\partial_k \mathbf{n})^2 + (\partial_k \rho)^2 + H_{ik}^2 - b\rho^2 + \frac{d}{2}\rho^4\right]. \quad (7)$$

In Eq. (7), the positive constant b corresponds to the phase with broken antiferromagnetic order.

The state with the broken antiferromagnetic order considered above has a lower energy than the "soft" state we are interested in now. The latter may be metastable [28]. In this section, we will consider only such states and compare their contribution to the Ginzburg–Landau energy without studying the problems of their

relaxation, the critical sizes of nuclei of different phases, etc., which are of separate interest.

Under the condition that the electron spin and charge are transferred from one of four sites of some plaquettes to the dopant reservoir, the terms with H_{ik} in Eq. (1) characterize (in the infrared limit) the mean degree of noncollinearity $\langle 0|\mathbf{S}_1 \cdot [\mathbf{S}_2 \times \mathbf{S}_3]|0\rangle$ in the orientation of three spins, which remain in the sites of a quadratic lattice plaquettes. Therewith, the deficit of the charge density ρ_h^2 relates to the density ρ^2, describing the distribution of the exchange integral in (1), by the relation $\rho^2 + \rho_h^2 = \text{const}$. From the long-wavelength point of view, the distribution of the spin density ρ^2 in a limited region with an exponential law of decrease at the boundary (for example, for a distribution in a circle with radius r_0 with an exponential decrease over a length $R \ll r_0$) will be accompanied by a quasi-one-dimensional distribution of the charge density ρ_h^2 along the boundary of this region, i.e., along a ring with thickness R and radius r_0. From this, it is seen that studying spatial configurations of the density field ρ^2 in planar systems makes it possible to find the form of one-dimensional distributions of the electric charge density with the aid of the above-mentioned holographic projection.

It has been known for a long time that, in such a phase state, the distributions of the charge density $(\partial_k\rho)^2$ have the form of stripes.[1] Due to the gradient term $(\partial_k\rho)^2$ in (7), quasi-one-dimensional field ρ configurations are really preferable. It seems almost obvious that a density distribution in the form of rings give the smallest contribution to the energy. Let us find the contribution to the free energy (7) from quasi-one-dimensional density distributions ρ^2 in the form of rings and stripes and compare the computation results with the experimental data. We will choose the following trial functions for the field ρ configurations in the form of a ring and a stripe:

$$\rho = \rho_0 \exp[-(r - r_0)^2/2R^2] \tag{8}$$

and

$$\rho = \rho_0 \exp\left(-\frac{x^2}{2L_x^2}\right) \times \begin{cases} 1, & |y| \le L_y, \\ \exp\left[-\dfrac{(|y| - L_y)^2}{2L_x^2}\right], & |y| > L_y. \end{cases} \tag{9}$$

[1] We suppose that the characteristic size of the stripe is substantially greater than the lattice scale. In this case, the use of a phenomenological approach of the mean-field Ginzburg–Landau theory is justified.

Here $\rho_0 = \sqrt{b/d}$, r_0 is the ring radius, R is its width, $2L_y = 2\pi r_0$ is the stripe length, and $L_x = R$ is its width. Since configurations (8) and (9) do not depend on the third coordinate, we will assume that the size in this direction is limited by the length L_z and also that $R < r_0$.

The calculation of energy (7) with the aid of (8) and (9) yields the following results for the contribution to the free energy from the ring F_r (at $R \ll r_0$) and the stripe F_{xy}:

$$F_r = \pi\rho_0^2 L_z \frac{\bar{r}_0}{R}\left(1 + \frac{R^2}{\xi^2}\right), \tag{10}$$

$$F_{xy} = \pi\rho_0^2 L_z \frac{\bar{r}_0}{R}\left[1 + \frac{R^2}{\xi^2} + \frac{R}{\bar{r}_0} + \left(n_0 - \frac{3}{4}b\right)\frac{R^3}{\bar{r}_0}\right]. \tag{11}$$

Here,

$$\bar{r}_0 = \sqrt{\pi} r_0, \quad 1/\xi^2 = 2[n_0 - (1 - 1/\sqrt{8})b],$$

n_0 is a certain characteristic value of the "multiplier" $(\partial_k \mathbf{n})^2$ in (7), which is of the order $c_1 R^{-2}$, whereas $b = c_2 R^{-2}\delta T$, where $c_i \sim 1$ and $\delta T = (T_c - T)/T_c$. In these equations, we omitted the term H_{ik}^2 from Eq. (7) since we consider that it is approximately the same for both types of distributions.

The exact equation for F_r (in units $\pi\rho_0^2 L_z$) contains the term

$$\delta F_r = 2[I_3(x_0) - x_0 I_2(x_0)] + \frac{bR^2}{2}[I_1(x_0\sqrt{2}) - x_0\sqrt{2} I_0(x_0\sqrt{2})] + \frac{R^2}{\lambda^2}[I_1(x_0) - x_0 I_0(x_0)],$$

where

$$x_0 = \frac{R}{r_0}, \quad \frac{1}{\lambda^2} = 2(n_0 - b), \quad I_m(z) = \int_z^\infty x^m e^{-x^2} dx.$$

However, this value is already exponentially small at $R/r_0 \sim 1/4$ and $R \sim \lambda$ with $1/\lambda^2 = 2(n_0 - b)$: $\delta F_r \sim 10^{-7}$.

For the optimum width $R = \xi$ (at $R \ll r_0$), the difference in free energies $\Delta F = F_{xy} - F_r$ in units $\pi\rho_0^2 L_z$ has the form

$$\Delta F = 1 + c_1 - \frac{3}{4}c_2\delta T.$$

From this equation, one can see that, at $4(1 + c_1)/3c_2 < 1$ in the temperature range

$$[1 - 4(1 + c_1)/3c_2]T_c < T < T_c,$$

bordering on the critical temperature T_c of the transition

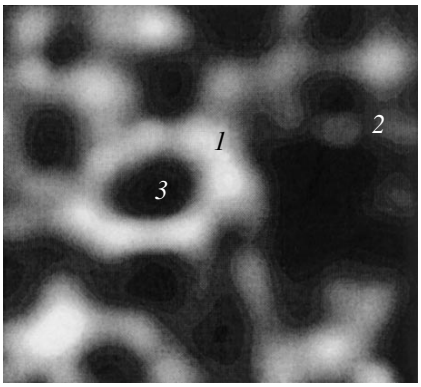

Schematic representation of closed (*1*) and open (*2*) quasi-one-dimensional structures of the charge density (see [29]) around antiferromagnetic dielectric nanoclusters (*3*).

to the state with the spin pseudogap, rings are preferable (see figure). In the temperature range

$$T < T_c[1 - 4(1 + c_1)/3c_2],$$

stripes are the main configurations. As is known, one may approach T_c keeping the temperature constant by increasing the level of doping. The recent paper [29] gave evidence of the existence of ring-shaped charge structures obtained just under such experimental conditions. In a certain sense, the tunneling microscope in this experiment [29] collects data from a two-dimensional slice of knots [21].

Let us make several remarks concerning the spin density ρ^2 distribution in the disk surrounded by a ring charge distribution. The above considerations referred to the case when the spin disorder arose only in the region directly adjacent to the disk edge, and, as a result, we had an antiferromagnetic phase inside. If the antiferromagnetic order is broken everywhere in the disk, it is necessary to consider the corresponding distribution of the density ρ^2 in the form of a disk in order to compare its contribution with F_r. When we consider the contribution of the density distributions ρ^2 to the free energy in the form of a disk, we get a double gain (in comparison with rings) due to the existence of one edge and have a loss due to the area. The calculation shows that at small R/r_0 the distributions in the form of rings appear to be more preferable.

Let us consider the dependence of the critical temperature T_c on the level of doping. To do this, we present the relation of F_r to F_{xy} in the following form:

$$\frac{F_r}{F_{xy}} = \frac{1}{1 + BR/\bar{r}_0}, \tag{12}$$

where

$$B = \frac{1}{2}\left[1 + \frac{1}{2}\frac{n_0 - 3b/4}{n_0 - (1 - 1/\sqrt{8})b}\right] = \frac{3}{4}\frac{n_0 - 0.68b}{n_0 - 0.65b}.$$

One can see that configurations in the form of stripes are more preferable in the range $0.65 < n_0/b < 0.68$, where $F_{xy} < F_r$. Normalizing the density ρ_0^2 to the particle number N by the condition $N = 2\pi r_0 \xi L_z m \rho_0^2$, we obtain a relation between the parameters n_0 and b, which we write in the form

$$x = b/\sqrt{n_0 - 0.65b},$$

where $x = Nd/(\sqrt{2}\, m\pi L_z r_0)$. Thus, for the bounds of the range considered above, where $n_0 \sim b \sim \delta T$, we have $T(x) = T_c(1 - Ax^2)$ with a certain constant A. Therefore, inside the region belonging to the phase state with broken antiferromagnetic order, there is a narrower region, located between the parabolas $T(x)$, where the charge structures have the form of stripes.

3.3. The Inhomogeneous Superconducting State

Let us consider a superconducting state with finite value of the total current **J** which exists against the background of a certain **n**-field distribution, assuming that $\rho = \rho_0 = \text{const}$. In this case, the free energy is

$$F = F_n + F_c - F_{\text{int}}$$
$$= \int d^3x\left[((\partial_k \mathbf{n})^2 + H_{ik}^2) + \left(\frac{1}{4}\mathbf{c}^2 + F_{ik}^2\right) - 2F_{ik}H_{ik}\right]. \tag{13}$$

The negative sign of the interaction energy F_{int} of **c** and **n** fields appears because of diamagnetism of the considered state. As a result, the coupling constant $g_2 = 1$ of the term H_{ik}^2 decreases due to renormalization in such a way that energy of the superconducting state $\mathbf{c} \neq 0$ is smaller than the minimum value in inequality (5). To find the exact lower bound of the free energy in the superconducting state $\mathbf{c} \neq 0$, we will use the auxiliary inequality

$$F_n^{5/6} F_c^{1/2} \geq (32\pi^2)^{4/3}|L|, \tag{14}$$

where the invariant

$$L = \frac{1}{16\pi^2}\int d^3x \varepsilon_{ikl} c_i \partial_k a_l \tag{15}$$

determines the degree of the mutual linking [30, 31] of the current lines and the lines of the magnetic field $\mathbf{H} = [\nabla \times \mathbf{a}]$. Like Q, it is the integral of motion [31, 32] in the considered barotropic state. The proof of inequality (14) [14] is given in the Appendix.

Linking indices, which characterize the correlations of spin and charge degrees of freedom, form the following matrix:

$$K_{\alpha\beta} = \frac{1}{16\pi^2}\int d^3x \varepsilon_{ikl} \alpha_i^\alpha \partial_k a_l^\beta = \begin{pmatrix} Q & L' \\ L & Q' \end{pmatrix}. \tag{16}$$

In this symmetric matrix ($L = L'$) with $a_i^1 \equiv a_i$ and $a_i^2 \equiv c_i$, the integral might also be determined by the asymptotic linking number [30]. Let us pay attention to a circumstance which will be important below. Being normalized to the charge density, unlike the unit vector **n**, the vector of momentum $\mathbf{c} = \mathbf{J}/\rho^2$ belongs to the noncompact manifold. Because of this, the Hopf numbers defined with the aid of this vector in (16) are not integers in general: $(L, Q') \notin \mathbb{Z}$. In the superconducting state, where Abelian $U(1)$ gauge symmetry is broken and the charge is not conserved, the numbers L and Q' play the role of continuous interpolation parameters which unite the compressed and uncompressed ($K_{\alpha\beta} \in \mathbb{Z}$) phases under consideration. From this point of view, the superconducting states with $K_{\alpha\beta} \in \mathbb{Z}$ and $K_{\alpha\beta} \notin \mathbb{Z}$ belong to one and the same class of universality [33].

To find the lower bound of the functional (13), along with Eq. (14), we will use the Schwarz–Cauchy–Bunyakovski inequality

$$F_{\text{int}} \le 2\|F_{ik}\|_2 \cdot \|H_{ik}\|_2 \le 2F_c^{1/2}F_n^{1/2}, \tag{17}$$

where $\|F_{ik}\|_2 \equiv [\int d^3x F_{ik}^2]^{1/2}$. Note that the equality on the right-hand side of Eq. (17) is achieved in the ultraviolet limit, when the size of linked vortex configurations is small enough. Substituting the boundary value F_{int} into (13), we obtain

$$F \ge F_{\min} = (F_n^{1/2} - F_c^{1/2})^2. \tag{18}$$

The Hopf configuration with $Q = 1$, for which the lower limit occurs in Eq. (5), represents two linked rings with radius R and

$$(F_n)_{\min} = 2\pi^2 R^3\left(\frac{8}{R^2} + \frac{8}{R^4}\right)\Bigg|_{R=1} = 32\pi^2.$$

We will assume that, in our case of $\mathbf{c} \neq 0$, there are configurations for which the equality in Eq. (14) is valid. Let us emphasize an important circumstance which will be discussed more thoroughly in the next section. For small values of ρ and, therefore, for large values of the field **c** (since all terms in (13) are of the same order), we encounter the instability of linked configurations with respect to small perturbations. This leads to the restriction of values F_c from above. Keeping in mind this remark and using in Eq. (18) for F_c the lower bound

$$F_c^{1/2} = (32\pi^2)^{4/3}F_n^{-5/6}|L|,$$

we obtain from Eq. (14) and relation $F_n = 32\pi^2|Q|^{3/4}$, for the states with $Q \neq 0$, that

$$F \ge 32\pi^2|Q|^{3/4}(1 - L/|Q|)^2. \tag{19}$$

One can see from Eq. (19) that, for all numbers $L < Q$, the energy of the ground state is smaller than that in model (4), for which inequality (5) is valid. The origin of the energy decrease may be understood by comparing the values of different terms in Eq. (13). Even under the conditions of a considerable paramagnetic contribution **j** to the current, the diamagnetic interaction in the superconducting state for all classes of states with $L < Q$ reduces in (13) its own energy F_c of the current and part of the energy F_n associated with dynamics of the **n** field. In the state under consideration, the total momentum of superconducting pairs **c** is not equal zero. In this respect, the inhomogeneous state with current is analogous [34] to the state proposed in [17, 18].

4. THE PROPERTIES OF PHASE STATES

The phase state with a broken antiferromagnetic order at $(\partial_k\rho)^2 \neq 0$ is a background on which the transition to the inhomogeneous superconducting phase with $F_{ik} \neq 0$ occurs. It is convenient to discuss the characteristics of this transition upon a change in the density ρ^2, beginning with the superconducting state. In this phase, the constant value of the charge density, related to the breakage of the gauge invariance $U(1)$, plays the role of the tuning parameter of the system.

Let the parameter ρ_0 change in some range. Since all terms in Eq. (3) are of the same order, the momentum **c** and, consequently, the index of the mutual linking L decrease when ρ_0 increases. In this case, for sufficiently small L, the smallest superconducting gap decreases with an increase in Q against the background of a large value of $32\pi^2|Q|^{3/4}$ of the spin pseudogap.

When ρ_0 decreases, the following effect takes place. Being proportional to $g_1^{-1/2} \propto \rho_0^{-1}$, the radius $\mathcal{R}$ of compactification $\mathbb{R}^3 \longrightarrow S^3$ grows until it exceeds some critical value $\mathcal{R}_{cr}$. At $\mathcal{R} > \mathcal{R}_{cr}$, the Hopf mapping is not stable [27] relative to small perturbations of linked vortex field configurations. As a result, the $U(2)$ symmetry which is associated with identical Hopf mapping appears to be spontaneously broken. This means that the topological configurations of field **n** and **c**, instead of being spread out over the whole space S^3, localize around a particular point (the base point of the stereographic projection $\mathbb{R}^3 \longrightarrow S^3$) and collapse to localized structures [27]. We can see that there is an optimal value of ρ_0 and, consequently, values of the characteristic momentum **c** and the relation $|L|/|Q|$ for which there arises the greatest gain upon the transition to the superconducting state.

Until now, the vector **A** has characterized the degrees of freedom, associated with the internal charge gauge symmetry $U(1)$. If the external electromagnetic field is applied, the vector **A** equals the sum of internal and external gauge potentials. In the external magnetic field, due to diamagnetism of the superconducting

state, the momentum **c** decreases. Similar to the case of increasing ρ_0, this leads to suppression of the superconducting gap. Playing the role of a smooth tuning parameter, the external magnetic field determines the boundary conditions of the problem. As a result, the answer to the question of completeness of the Meissner screening depends on the results of the competition of contributions from a paramagnetic (spin) **j** and diamagnetic (charge) $-4\mathbf{A}$ parts of the total current **J**.

Similar to energy distribution in the fractional quantum Hall effect with the filling factor $\nu = p/q$ and $p, q \in \mathbb{Z}$, the energy gain in Eq. (19) depends on the relation $|L|/|Q|$. The Hopf invariant $Q \in \mathbb{Z}$ numbers vacuums [35] and is equivalent to the degree of degeneracy q of the ground state. The index L plays the role of the filling degree p of incompressible charged fluid state in the fractional quantum Hall effect. From this point of view, the multiplier $(1 - |L|/|Q|)$ in Eq. (19) is equivalent to the filling factor $1 - \nu$ for holes. The distinction of our system from the states in the fractional quantum Hall effect is that the superconducting state is compressible and here (as was mentioned above) the effective number L of the charge degrees of freedom is not an integer in the general case. The configurations of fields **n** and $\mathbf{c} = \mathbf{a}$ with the integers $L = Q$, satisfying the relation of self-duality $F_n = F_c$, correspond to the minimum value of free energy (13). In this limit, $K_{\alpha\beta}$ is proportional to the matrix $\begin{pmatrix} 1 & 1 \\ 1 & 1 \end{pmatrix}$, which was used in [36] to describe the topological order in the theory of fractional quantum Hall effect with the filling factor $1 - \nu$ at $\nu = 1/2$.

The boundary conditions which determine the momentum **c** and the topological invariants L, Q depend not only on the values of the tuning parameter ρ_0 of the model and the external magnetic field. Their physical sense and value also depend on the dimensionality of the manifold for which the model is defined. In the (3 + 0)-dimensional case of the free energy (3), the Hopf invariant (6) is analogous to the Chern–Simons action

$$\frac{k}{4\pi}\int dt d^2x \varepsilon_{\mu\nu\lambda}\alpha_\mu \partial_\nu \alpha_\lambda.$$

This term in the action of (2 + 1)-dimensional systems describes the dependence of the contribution of nonlinear modes to the free energy on the statistical parameter k. The coefficient k in the Chern–Simons action has the geometrical sense of the braiding number of the excitation world lines. In particular, when semifermion excitations (semions) permutate and return to the initial positions on the plane, the world lines braid twice and $k = 2$. Therewith, the statistical correlations of nonlinear modes have the character of attraction, and for the values $k \sim 2$ their greatest contribution to the energy is of the order of several percent [37]. For the energy scale (0.1–1) eV, this gives several tens or hundreds of degrees. Taking into account the relation between the dimensionality of the systems at their dynamic and statistical descriptions, we note that the (2 + 1)-dimensional case $k = 2$ with the open ends of excitation world lines is equivalent (after identification of the ends) to the compact statistical (3 + 0)-dimensional example of the Hopf linking with $Q = 1$.

The (3 + 0)-dimensional and (2 + 1)-dimensional situations differ by the topology of the regions of the field definition **n** [38–40]. When the system is periodic in one of the space variables and also when calculating the partition function in planar systems, one of three coordinates—Matsubara variable—is a periodic variable. This means that instead of the sphere S^3, we deal with the topology of a three-dimensional torus $T^{2\times 1} = S^2 \times S^1$ or $T^3 = S^1 \times S^1 \times S^1$ and with the corresponding mapping classes. The content of Hopf invariant in this case appears to be richer [38–40]. For a three-dimensional torus T^3, the Hopf invariant is defined modulo $2q$, where q is the greatest common divisor of the numbers $\{q_1, q_2, q_3\} \in \mathbb{Z}$. Here, q_i is the degree of mapping $T^2 \longrightarrow S^2$, where T^2 is the section of T^3 with the fixed ith coordinate. Four integral numbers $\{q_i, Q\}$, where Q is defined by modulo value $2q$, give us the complete homotopic classification of mappings $T^3 \longrightarrow S^2$ with $\pi_1[\mathrm{Map}_q(S^2 \longrightarrow S^2)] = \mathbb{Z}_{2q}$ and a fixed degree q [38–40]. The geometrical meaning of this modified Hopf invariant (an integer from the range $\{0, 2q - 1\}$) is the same. It is a linking index of the preimages of two generic points in $T^3 \longrightarrow S^2$. The cases $T^{2\times 1}$ and T^3 are characterized physically by different boundary conditions. The boundary conditions change if an angular velocity of the rotation of the neutral superfluid phase in ^{3}He increases [38, 39] or an external magnetic field in our charged system grows. Restricting the Hopf invariant change, the transition $T^{2\times 1} \longrightarrow T^3$ promotes the appearance of the incompressible phase.

5. CONCLUSION

One can see from the above analysis that the gain of the free energy upon the transition to the superconducting state with $\mathbf{c} \neq 0$ arises when there is a coherent phase associated with the spin degrees of freedom. This phase is characterized by a pseudogap (5) and a topological order associated with linking. If the density ρ_0^2 is rather large, the momentum **c** is small and the transition to the superconducting state is not preferable. According to our classification, this second state is characterized by changing values of the order parameters ρ and **n**. The energy loss due to the term $(\partial_k \rho)^2$ may be reduced because of the development of one-dimensional structures. Whether these one-dimensional charge structures will be open, forming stripes, or closed almost one-dimensional structures in the form of rings depends on the parameters of the potential $V(\rho, n_3)$. In the phase

n_3 = const with neutral spin currents, the answer will depend on the value and the sign of the multiplier $b(n_3)$ in the potential

$$V(\rho, n_3) = -b\rho^2 + \frac{d}{2}\rho^4.$$

If $b > 0$, then far from T_c charge structures with open ends are preferable [13], and in the case $T \longrightarrow T_c$ we should prefer rings. The first experiments that verified the existence of charge structures in the form of rings in the underdoped phase of planar systems were described in [29].

On the "temperature–charge density" phase diagram, the superconducting phase occupies only part of the region belonging to the phase with the broken antiferromagnetic order. The bounds of its existence on the phase diagram, associated with the characteristic values of the density ρ_0^2, are determined for great ρ_0 by the inequality (14) [14], while for small ρ_0 these bounds depend on the critical size of the knot [27], beginning from which instability of the Hopf mapping arises.

Comparing the results of this paper based on consideration of the local fields with the conclusions following from the BCS-like model [19] with two species of fermions, we pay attention to the following qualitative coincidence. One can conclude from Eq. (3) that the parameter ρ_0 determines the value of the coupling constant. Therefore, the appearance of the solutions (different from the standard BCS model) for the superconducting gap in the paper [19] with a finite value of the coupling constant is analogous to the existence of the threshold for small values of ρ_0 in this paper.

In contrast to the model [19], the states considered in the present paper are significantly inhomogeneous. The analysis of the state $F_{ik} \neq 0$, $\rho \neq$ const is still an open problem. Here, we only mention that the superconducting current with the amplitude $\mathbf{c}_0$, flowing around the rings (8), gives the additional term $\mathbf{c}_0^2 R^2$ to the multiplier in Eq. (10). This explains, in particular, why the superconducting region on the "temperature–doping level" phase diagram is shifted to the line $\delta T(x) = 0$ of the transition to the state with the spin pseudogap. Indeed, in this case,

$$V_{\text{eff}}(\rho, n_3) = -b_{\text{eff}}\rho^2 + \frac{d}{2}\rho^4,$$

with

$$b_{\text{eff}} = b - (n_0 + \mathbf{c}_0^2) = \frac{\text{const}}{R^2}\delta T.$$

Therefore, the finite value of the momentum $\mathbf{c}$ of superconducting pairs decreases δT. In addition, the contribution to the free energy in the inhomogeneous state due to $(\partial_k \rho)^2 \neq 0$ decreases the gain in Eq. (19).

The superconductivity in cluster systems may evidently be studied on the basis of approaches beyond the mean field theory. For example, we may use the exact Richardson solution and Bethe ansatz equation [41], as well as the methods of the conformal field theory [42]. The exact solution of the ground state problem under the condition of a finite value of the total momentum of pairs in such an approach is one of the important problems. Since the conformal nature of the dimensionality 3/4 [30] in (5) and (14) influences the character of the scale which enters into energy dependent response functions (which is proportional to $T^{3/4}$ [43]), it should also be studied carefully.

ACKNOWLEDGMENTS

The authors are grateful to A.G. Abanov, S.A. Brazovsky, S. Davis, L.D. Faddeev, S.M. Girvin, V.E. Kravtsov, E.A. Kuznetsov, B. Lake, A.I. Larkin, A.G. Litvak, C. Renner, H. Takagi, V.A. Verbus, G.E. Volovik, Yu. Lu, and Y.-S. Wu for advice and useful discussions.

This paper was supported in part by the Russian Foundation for Basic Research, project no. 01-02-17225.

APPENDIX

The proof of Eq. (14) uses the following chain of inequalities:

$$\begin{aligned} |L| < \|\mathbf{c}\|_6 \cdot \|\mathbf{H}\|_{6/5} &\le 6^{1/6}\|[\nabla \times \mathbf{c}]\|_2 \cdot \|\mathbf{H}\|_{6/5} \\ &\le 6^{1/6}\|[\nabla \times \mathbf{c}]\|_2 \|\mathbf{H}\|_1^{2/3}\|\mathbf{H}\|_2^{1/3} \\ &\le (32\pi^2)^{-4/3} F_c^{1/2} F_n^{2/3} F_n^{1/6} = (32\pi^2)^{-4/3} F_c^{1/2} F_n^{5/6}. \end{aligned} \tag{20}$$

Here, $\|\mathbf{H}\|_p \equiv \left(\int d^3x |\mathbf{H}|^p\right)^{1/p}$. At the first and third steps, we used the Hölder inequality

$$\|\mathbf{f} \cdot \mathbf{g}\| \le \|\mathbf{f}\|_p \cdot \|\mathbf{g}\|_q$$

with $1/p + 1/q = 1$. Under the condition $\nabla \cdot \mathbf{c} = 0$, we employ at the second step the Ladyzhenskaya inequality [40, 44]:

$$\|\mathbf{c}\|_6 \le 6^{1/6}\|[\nabla \times \mathbf{c}]\|_2.$$

The fourth step in the set of inequalities arises after the comparison of the terms $\|[\nabla \times \mathbf{c}]\|$ and $\|\mathbf{H}\|$ with the terms F_n and F_c in Eq. (13). The last line also shows separate contributions from $\mathbf{n}$ and $\mathbf{c}$ parts of the free energy (13) to the finite result (14). Using a chain of Hölder and Ladyzhenskaya inequalities, analogously one may find that

$$F_n^{1/2} F_c^{5/6} \ge (16\pi^2)^{4/3}|L'|.$$

The coefficient in this inequality differs from (14) due to the coefficient 1/4 (because of the charge $2e$ of superconducting pairs) of the first term of the free energy F_c in (13).

REFERENCES

1. E. Babaev, L. D. Faddeev, and A. J. Niemi, Phys. Rev. B **65**, 100512 (2002).
2. B. Lake, G. Aeppli, K. N. Clausen, *et al.*, Science **291**, 1759 (2001).
3. B. Lake, H. M. Rönnow, N. B. Christensen, *et al.*, Nature **415**, 299 (2002).
4. J. E. Hoffman, E. W. Hudson, K. M. Lang, *et al.*, Science **295**, 466 (2002).
5. S. H. Pan, J. P. O'Neal, R. L. Badzey, *et al.*, Nature **413**, 282 (2001).
6. S. J. L. Billinge, E. S. Bozin, M. Gutmann, and H. Takagi, cond-mat/0005032.
7. S. Caprara, C. Castellani, C. Di Castro, *et al.*, cond-mat/9907265.
8. L. D. Faddeev and A. J. Niemi, Phys. Rev. Lett. **82**, 1624 (1999); Phys. Lett. B **525**, 195 (2002).
9. E. Babaev, Phys. Rev. Lett. **88**, 177002 (2002).
10. Y. M. Cho, Phys. Rev. Lett. **87**, 252001 (2001); hep-th/0110076.
11. A. G. Abanov and P. W. Wiegmann, hep-th/0105213.
12. L. D. Faddeev, Preprint No. IAS-75-QS70 (Princeton, 1975).
13. M. Lübke, S. M. Nasir, A. Niemi, and K. Torokoff, Phys. Lett. B **534**, 195 (2002).
14. A. P. Protogenov and V. A. Verbus, Pis'ma Zh. Éksp. Teor. Fiz. **76**, 60 (2002) [JETP Lett. **76**, 53 (2002)].
15. A. P. Protogenov, cond-mat/0205133.
16. L. S. Isaev and A. P. Protogenov, cond-mat/0210295.
17. A. I. Larkin and Yu. N. Ovchinnikov, Zh. Éksp. Teor. Fiz. **47**, 1136 (1964) [Sov. Phys. JETP **20**, 762 (1964)].
18. P. Fulde and R. A. Ferrell, Phys. Rev. A **135**, 550 (1964).
19. W. V. Liu and F. Wilczek, cond-mat/0208052.
20. P. van Baal, hep-th/0109148.
21. L. D. Faddeev and A. J. Niemi, Nature **387**, 58 (1997).
22. J. Gladikowski and M. Hellmund, Phys. Rev. D **56**, 5194 (1997).
23. R. A. Battye and P. M. Sutcliffe, Phys. Rev. Lett. **81**, 4798 (1998).
24. J. Hietarinta and P. Salo, Phys. Lett. B **451**, 60 (1999).
25. A. F. Vakulenko and L. V. Kapitanskiĭ, Dokl. Akad. Nauk SSSR **246**, 840 (1979) [Sov. Phys. Dokl. **24**, 433 (1979)].
26. A. Kundu and Yu. P. Rubakov, J. Phys. A **15**, 269 (1982).
27. R. S. Ward, Nonlinearity **12**, 1 (1999); hep-th/9811176.
28. H. Takagi, http://agenda.ictp.trieste.it/agenda/current/fullAgenda.php?email=0&ida=a01152.
29. V. I. Arnold and B. A. Khesin, *Topological Methods in Hydrodynamics* (Springer, New York, 1998), Appl. Math. Sci., Vol. 125, Chap. 3.
30. H. K. Moffatt, J. Fluid Mech. **106**, 117 (1969).
31. V. E. Zakharov and E. A. Kuznetsov, Usp. Fiz. Nauk **167**, 1137 (1997) [Phys. Usp. **40**, 1087 (1997)].
32. N. Read and D. Green, Phys. Rev. B **61**, 10267 (2000).
33. A. I. Larkin, private communication.
34. P. van Baal and A. Wipf, hep-th/0105141.
35. X.-G. Wen, cond-mat/9506066.
36. A. P. Protogenov, Usp. Fiz. Nauk **162**, 1 (1992).
37. L. A. Abramyan, V. A. Verbus, and A. P. Protogenov, Pis'ma Zh. Éksp. Teor. Fiz. **69**, 839 (1999) [JETP Lett. **69**, 887 (1999)]; A. P. Protogenov, Pis'ma Zh. Éksp. Teor. Fiz. **73**, 292 (2001) [JETP Lett. **73**, 255 (2001)].
38. V. M. H. Ruutu, U. Parts, J. H. Koivuniemi, *et al.*, Pis'ma Zh. Éksp. Teor. Fiz. **60**, 659 (1994) [JETP Lett. **60**, 671 (1994)].
39. Yu. G. Makhlin and T. Sh. Misirpashaev, Pis'ma Zh. Éksp. Teor. Fiz. **61**, 48 (1995) [JETP Lett. **61**, 49 (1995)].
40. A. G. Abanov, private communication.
41. J. von Delft and R. Poghossian, cond-mat/0106405.
42. G. Sierra, Nucl. Phys. B **572**, 517 (2000); hep-th/0111114.
43. P. Coleman, C. Pepin, Q. Si, and R. Ramazashvili, J. Phys.: Condens. Matter **13**, 723 (2001).
44. O. A. Ladyzhenskaya, *The Mathematical Theory of Viscous Incompressible Flow*, 2nd ed. (Gordon and Breach, New York, 1969; Nauka, Moscow, 1970).

Translated by L. Isaev

Journal of Experimental and Theoretical Physics, Vol. 96, No. 6, 2003, pp. 1149–1162.
Translated from Zhurnal Éksperimental'noĭ i Teoreticheskoĭ Fiziki, Vol. 123, No. 6, 2003, pp. 1308–1322.

SOLIDS
Electronic Properties

Stark Ladder Laser with a Coherent Electron Subsystem

V. F. Elesin[a,*] and Yu.V. Kopaev[b]

[a] *Moscow State Institute of Engineering Physics, Kashirskoe sh. 31, Moscow, 115409 Russia*
**e-mail: VEF@supercon.mephi.ru*
[b] *Lebedev Institute of Physics, Russian Academy of Sciences, Leninskiĭ pr. 53, Moscow, 119991 Russia*

Received February 6, 2003

Abstract—A theory of generation in a two-subband "Stark ladder" with a coherent electron subsystem is developed. In the proposed model, electrons reach the upper level of a quantum well due to resonant tunneling and pass to the lower level of the well (vertical transitions), emitting a photon $\hbar\omega$, then tunnel resonantly to the upper level of a neighboring well, performing a radiative transition, and so on until electrons leave the lower level of the last well. A static electric field applied to the superlattice shifts the levels so that the lower level of the nth well coincides with the upper level of the $(n + 1)$th well. Analytic expressions are derived for the wave functions and polarization currents of an N-well structure. The possibility of bulk oscillation of the N-well structure in the optimal mode with an efficiency close to unity, weak reflection, and a linear dependence of the power on the pumping current is demonstrated. The total generation power is proportional to the number of wells. For structures with an even number of wells, the energy of electrons from the emitter must simply coincide with the resonance energy for any laser fields; i.e., the energy tuning which is necessary in a single-well structure is not required. Universal relations are derived for parameters of the N-well structure, which ensure the simultaneous fulfillment of resonance conditions in all the wells. The possibility of coherent lasing in a one-subband Stark ladder with a lower gain is also indicated. © *2003 MAIK "Nauka/Interperiodica".*

1. INTRODUCTION

In 1972, Kazarinov and Suris [1] proposed a new type of a semiconductor laser in which radiative transitions occur between size-quantization levels (subbands). This idea was implemented in 1994 in nanostructures (so-called cascade lasers) [2, 3], in which the main elements are two quantum wells (QWs) with working levels in each well [2] ("diagonal transitions") or a single QW with two working levels [3, 4] ("vertical transitions").

The main advantage of cascade lasers is the possibility of wavelength tuning from the infrared to the submillimeter range. Cascade lasers are characterized by unipolarity, identical masses of subbands, etc. Another fundamental feature is the coherent nature of resonant tunneling ensuring pumping. This leads to the possibility of lasing without participation of dissipative processes. Indeed, an electron reaches the upper level as a result of coherent resonant tunneling; passes to the lower level, emitting a photon; and leaves the well, thus interrupting the process of interaction with the electromagnetic field (in conventional lasers, lasing is interrupted due to dissipative processes such as the emission of a phonon [5]). Such a single-quantum-well laser (referred to as a coherent laser) was proposed and analyzed theoretically in [6]. It was shown that a strong field can be generated in the absence of population inversion. The optimal operating conditions were determined, for which the efficiency is close to unity [6, 7], the reflection from the structure is equal to zero, and amplification line broadening due to the field is absent.

A natural question arises: Is effective lasing possible for a structure consisting of N tunnel-coupled QWs? This problem is closely related to the problem of Stark ladder lasing, for which a certain difficulty exists. According to Bastard *et al.* [8], Stark ladder lasing is a surface effect. The reason is that radiative transitions in the sample are compensated, and the gain is determined by the population inversion between the levels at the left and right boundaries.

However, this conclusion is valid if the electron subsystem is incoherent and the concept of radiative transition probability per unit time is applicable. The situation in a coherent system is fundamentally different. Under certain conditions, an electron supplied to a QW performs coherently radiative transitions irrespective of the difference in the occupancies of the levels [6]. Consequently, we can expect that lasing takes place in the entire volume of the N-well structure.

It should be noted that radiative transitions in the one-subband model occur between the Stark levels in neighboring QWs (diagonal transitions). It was shown in [4, 9] that diagonal transitions lead to a much lower gain as compared to transitions between two energy levels in the same QW (vertical transitions). For this reason, we consider here a superlattice with vertical radiative transitions (see figure). After the transition of an electron from the upper to the lower level of the nth

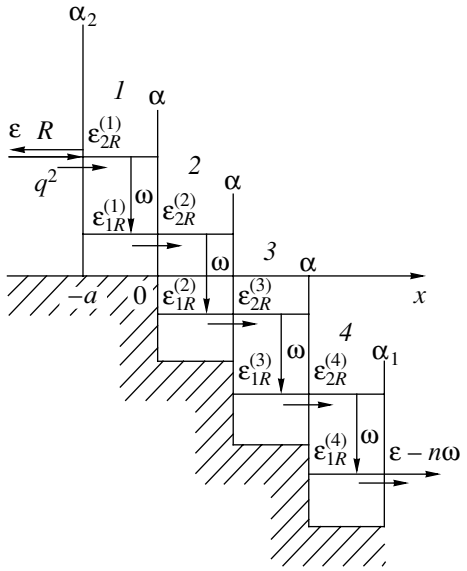

Schematic diagram of a four-well structure ($N = 4$).

QW, accompanied by the emission of a photon, the electron performs resonant tunneling to the upper level of the neighboring QW, and so on. This is the model of a coherent laser in which an electron passes through N QWs, emitting photons in each QW. It is well known that an electron in a cascade laser [2, 3] after each radiative transition gets into the relaxation region, where its state is prepared for the next radiative transition.

This study is aimed at the development of the theory of a coherent laser for N QWs with vertical transitions. It should be noted that some preliminary results were obtained in [10]. However, the formalism used in [10] for solving the system of $4N \times 4N$ algebraic equations is quite cumbersome, which did not permit one to carry out a comprehensive analysis and to clarify the optimal lasing conditions.

We succeeded in deriving exact analytic solutions to this system of equations for 2, 3, 4, and N wells. It is shown that optimal bulk lasing of a structure with N wells can be obtained with an efficiency close to unity, a small reflectance, and a linear dependence of the power on the pumping current. For structures with an even number of wells, the energy of supplied electrons must simply coincide with the resonant energy for any fields. In other words, the energy tuning, which is inevitable in a structure with a single well [6, 7], is not required. Universal relations are derived for the parameters of an N-well structure, ensuring the fulfillment of the resonance conditions in all the wells simultaneously.

The article has the following structure. In Section 2, the model is described and the steady-state solution to the time-dependent Schrödinger equation is given; the boundary conditions and expressions for currents are also derived. Section 3 is devoted to a single-well structure; the results obtained in this section are used in the subsequent analysis. The wave functions of an N-well structure, which are valid both for weak and strong fields, are determined in Section 4. A detailed analysis of a two-well structure is carried out in Sections 5 and 6, while a three-well structure is treated in Section 7. Structures with an even number of wells $N \geq 4$ are analyzed in Section 8. An analysis of resonance conditions is carried out in the Appendix.

2. DESCRIPTION OF THE MODEL: BASIC EQUATIONS

Let us consider the following model of a one-dimensional N-well structure (see figure), which is a generalization of the models described in [7, 10]. The figure shows schematically the structure in the form of a set of δ-functional barriers positioned at points $x = an$, $n = -1, 0, 1, \ldots, N-1$. The parameters of the QWs are chosen so that the energies ε_{2R} and ε_{1R} of the two lower levels of an isolated well differ by a value approximately equal to the electromagnetic field frequency ω ($\hbar = 1$): $\varepsilon_{2R} - \varepsilon_{1R} = \omega$. The application of a constant external electric field shifts the energy of the nth well relative to the $(n-1)$th well by quantity E_0 equal to ω. The energy $\varepsilon_{1R}^{(n-1)}$ of the lower level of the $(n-1)$th well coincides with the energy $\varepsilon_{2R}^{(n)}$ of the upper level of the nth well. The steady-state electron flux with a density proportional to q^2 and with energy ε approximately equal to $\varepsilon_{2R}^{(1)}$ is supplied to the system from the left ($x = -\infty$).

The electromagnetic field, which is regarded as classical,

$$E_x(z, t) = E\sin(kz)\cos(\omega t + \varphi),$$

is emitted during electron transitions from levels "2" to levels "1" of the QWs. We assume that the field is polarized at right angles to the plane of a well (i.e., along the x axis), while the wave vector lies in the plane (along the z axis). The optical resonator of length L separates the modes. We confine our analysis to single-mode lasing. The equations for the stationary amplitude E and phase φ (frequency ω) can be written in the form [5]

$$\frac{E}{2\tau_0} = -\frac{2\pi}{\kappa}J_c^{(N)}, \tag{1}$$

$$(\omega - \Omega)E = -\frac{2\pi}{\kappa}J_s(N), \tag{2}$$

$$J_{c,s}^{(N)} = \frac{1}{Na}\int_{-a}^{(N-1)a} dx J_{c,s}(x), \tag{3}$$

where J_c and J_s are the reduced polarization currents coinciding in phase with the field (J_c) and shifted by $\pi/2$ relative to the field (J_s). Currents J_c and J_s describe transition between energy levels. Here, τ_0 is the photon lifetime in the resonator, κ is the dielectric constant, Ω is the natural frequency of the resonator, and c is the velocity of light (we will henceforth assume that $c = 1$).

Currents $J_c(x)$ and $J_s(x)$ can be determined using the well-known expression

$$J(x, t) = -ie\left(\Psi^*\frac{\partial\Psi}{\partial x} - \text{c.c.}\right), \tag{4}$$

where the wave function $\Psi(x, t)$ of the system obeys the Schrödinger equation

$$i\frac{\partial\Psi}{\partial t} = -\frac{\partial^2\Psi}{\partial x^2} + U(x)\Psi + \hat{V}(x, t)\Psi. \tag{5}$$

Here,

$$U(x) = \alpha_2\delta(x + a) + \sum_{n=0}^{N}\alpha\delta(x - an) + \alpha_1\delta(x - a(N-1)) - E_0\varphi(x), \tag{6}$$

$$\varphi(x) = \sum_n \Theta(x - (n-1)a), \quad \Theta(x) = \begin{cases}1, & x > 0,\\ 0, & x < 0;\end{cases} \tag{7}$$

α_j are the barrier intensities, α_2, α_1, and α being the barrier heights of the left, extreme right, and internal wells, respectively; and $2m = \hbar = 1$. The last term in Eq. (5), i.e.,

$$\hat{V}(x, t) = 2eiA_x\frac{\partial\Psi}{\partial x},$$

describes the interaction between electrons and the electromagnetic field and A_x is the vector potential in the Coulomb gauge, which differs from zero in the nanostructure region. Expressing A_x in terms of the field amplitude, we can write the last term in the form

$$\hat{V}\Psi = V(e^{i\omega t} - e^{-i\omega t})\frac{\partial\Psi}{\partial x}, \quad V = -\frac{eE}{\omega}. \tag{8}$$

It should be noted that we have omitted in this expression the term quadratic in A_x. This approximation, which is usually employed in the theory of lasers, is also valid here if parameter V/p is small; i.e.,

$$\frac{V}{p} = \frac{eE}{p\omega} \ll 1,$$

where p is the electron momentum. Equation (5) should be supplemented with boundary conditions. The form of the boundary conditions will be specified below after obtaining a solution for $\Psi(x, t)$.

Following [6], we seek the steady-state solution to Eq. (5) in the form

$$\Psi(x, t) = \sum_n\sum_m \exp[-it(\varepsilon + m\omega - E_0(n+1))] \times \psi_{nm}(N, x), \quad m = 0, \pm1, \pm2, \ldots, \quad 1 \le n \le N. \tag{9}$$

Functions $\psi_{nm}(x, N)$ describe the states with quasienergies $\varepsilon + m\omega$ in the nth well and satisfy the following system of equations:

$$[\varepsilon + m\omega - E_0(n+1)]\psi_{nm} + \frac{d^2\psi_m}{dx^2} = V\left[\frac{d\psi_{n,m-1}}{dx} - \frac{d\psi_{n,m+1}}{dx}\right]. \tag{10}$$

It is well known that the main contribution to lasing comes from two resonance levels with the energy difference equal to frequency ω. In the present case, for the nth well, these levels are the upper level with energy $\varepsilon_{2R}^{(n)}$ and the lower level with energy $\varepsilon_{1R}^{(n)}$. The corresponding wave functions are $\psi_{n2}(x)$ and $\psi_{n1}(x)$, so that wave function (9) can be reduced to two terms in each well:

$$\Psi(x, t) = \psi_{n2}(x)\exp[-it(\varepsilon - E_0(n-1))] + \psi_{n1}(x)\exp[-it(\varepsilon - \omega - E_0(n-1))], \quad (n-2)a \le x \le (n-1)a, \quad 1 \le n \le N. \tag{11}$$

Functions ψ_{n2} and ψ_{n1} satisfy the system of equations

$$[\varepsilon - E_0(n-1)]\psi_{n2} + \frac{d^2\psi_{n2}}{\partial x^2} = V\frac{d\psi_{n1}}{dx}, \tag{12}$$

$$[\varepsilon - \omega - E_0(n-1)]\psi_{n1} + \frac{d^2\psi_{n1}}{dx^2} = -V\frac{d\psi_{n2}}{dx} \tag{13}$$

with the following boundary conditions (see [6]):

$$\psi_{12}(-a)\left(1 - \frac{\alpha_2}{ip_2}\right) + \frac{1}{ip_2}\frac{d\psi_{12}(-a)}{dx} = q,$$

$$\psi_{12}(0) = 0, \quad \psi_{11}(-a) = 0, \quad \psi_{22}(a) = 0,$$

$$\frac{d\psi_{22}(0)}{dx} - \frac{d\psi_{11}(0)}{dx} = \alpha\psi_{11}(0),$$

.....

$$\psi_{N1}((N-2)a) = 0, \quad \psi_{N2}((N-1)a) = 0, \quad (14)$$

$$\psi_{N1}((N-1)a)\left(1-\frac{\alpha_1}{ip_1}\right) - \frac{1}{ip_1}\frac{d\psi_{N1}((N-1)a)}{dx} = 0,$$

$$\frac{d\psi_{N2}((N-2)a)}{dx} - \frac{d\psi_{N-1,1}((N-2)a)}{dx} = \alpha\psi_{N-1,1}((N-2)a).$$

The boundary conditions describe the electron flux from $x = -\infty$, their reflection and departure to $x = \infty$, and the continuity conditions for the wave functions as well as the jump in their derivatives at the boundaries of the QWs.

For $N = 1$, Eqs. (12) and (13) and boundary conditions (14) are transformed into their counterparts for a single well [7]. It should be noted that the boundary conditions prohibit the departure of electrons from the energy levels of internal wells as well as from the lower level of the first well and the upper level of the last well. This situation optimizes lasing and is realized in practice.

Using the form of wave function (11), we can express current (4) in terms of functions $\psi_{nm}(x)$:

$$J_c(N, x) = \sum_{n=1}^{N} J_{nc}(x),$$
$$J_{nc}(x) = -ie\left[\left(\psi_{n2}^*\frac{d\psi_{n1}}{dx} + \psi_{n1}^*\frac{d\psi_{n2}}{dx}\right) - \text{c.c.}\right]. \quad (15)$$

3. SINGLE-WELL STRUCTURE

For $N = 1$, the general system of equations and boundary conditions described in Section 2 is transformed into the corresponding system for a single well:

$$\varepsilon\psi_2 + \psi_2'' = V\psi_1', \quad (\varepsilon-\omega)\psi_1 + \psi_1'' = -V\psi_2',$$
$$\psi_2 \equiv \psi_{12}, \quad \psi_1 \equiv \psi_{11}, \quad \psi' \equiv \frac{d\psi}{dx}, \quad (16)$$

$$\psi_2(-a)\left(1-\frac{\alpha_2}{ip_2}\right) + \frac{\psi_2'(-a)}{ip_2} = q, \quad \psi_2(0) = 0,$$
$$\psi_1(-a) = 0, \quad \psi_1(0)\left(1-\frac{\alpha_1}{ip_1}\right) - \frac{\psi_1'(0)}{ip_1} = 0. \quad (17)$$

Following [6], we will find the exact solution to system (16), (17) without using perturbation theory in the field. The strong-field parameter will be determined below.

We seek the solution to system (16) in the form

$$\psi_1 = A_1 e^{\gamma x}, \quad \psi_2 = A_2 e^{\gamma x}. \quad (18)$$

The eigenvalues γ satisfy the equation

$$\gamma^4 + 2\gamma^2\left(\varepsilon + \frac{V^2-\omega}{2}\right) + \varepsilon^2 - \omega\varepsilon = 0$$

and are given by

$$\gamma_{1,2} = \pm i\sqrt{\varepsilon + \frac{V^2-\omega}{2} - \sqrt{\left(\frac{V^2-\omega}{2}\right)^2 + \varepsilon V^2}},$$
$$\gamma_{3,4} = \pm i\sqrt{\varepsilon + \frac{V^2-\omega}{2} + \sqrt{\left(\frac{V^2-\omega}{2}\right)^2 + \varepsilon V^2}}. \quad (19)$$

The general solution to Eqs. (16) has the form

$$\psi_l(x) = \sum_{j=1}^{4} A_l^j \exp(\gamma_j x), \quad l = 1, 2. \quad (20)$$

Coefficients A_1^j and A_2^j are connected through the relations following from Eqs. (16),

$$A_1^j = \varepsilon_j A_2^j, \quad \varepsilon_j = -\frac{\gamma_j V}{\varepsilon - \omega + \gamma_j^2}. \quad (21)$$

Substituting ψ_l from Eq. (20) and A_1^j from Eq. (21) into boundary conditions (17), we arrive at the system of algebraic equations for the coefficients,

$$\sum_{j=1}^{N} A_2^j \exp(-\gamma_j a)(1-\beta_j) = q, \quad \sum_{j=1}^{4} A_2^j = 0,$$
$$\sum_{j=1}^{N} \varepsilon_j A_2^j \exp(-\gamma_j a) = 0,$$
$$\sum_{j=1}^{4} \varepsilon_j A_2^j (1-\tilde{\beta}_j) = 0, \quad (22)$$

where

$$\beta_j = \frac{\alpha_2 - \gamma_j}{ip_2}, \quad \tilde{\beta}_j = \frac{\alpha_1 + \gamma_j}{ip_1},$$
$$p_2^2 = \varepsilon, \quad p_1^2 = \varepsilon - \omega.$$

The solution to system (22) can be written in the form

$$A_2^{(j)} = \frac{2q}{\Delta_1(1)} \sum_{k \neq l \neq j} (-1)^{k+l+1} \varepsilon_k \varepsilon_l \tilde{\Delta}_{kl}. \quad (23)$$

Here, $\Delta_1(1)$ is the determinant of system (22),

$$\Delta_1(1) = \sum_{i\neq j\neq k\neq l} (-1)^{i+j}\tilde{\Delta}_{ij}\Delta_{kl}, \tag{24}$$

where

$$\begin{aligned}\tilde{\Delta}_{ij} &= \exp(\gamma_j a)(1-\tilde{\beta}_j) - \exp(\gamma_i a)(1-\tilde{\beta}_i),\\ \Delta_{ij} &= \exp(-\gamma_j a)(1-\beta_j) - \exp(-\gamma_i a)(1-\beta_i).\end{aligned} \tag{25}$$

The expressions for γ_j and ε_j can be simplified by taking into account the smallness of ratio V/p:

$$\gamma_{1,2} \approx \pm ip_2\left(1+\frac{V^2}{2\omega}\right), \quad \gamma_{3,4} \approx \pm ip_1\left(1-\frac{V^2}{2\omega}\right), \tag{26}$$

$$\begin{aligned}&\varepsilon_{1,2} \approx \mp\frac{i\omega}{Vp_1}, \quad \varepsilon_{3,4} \approx \pm\frac{iVp_2}{\omega}, \quad \varepsilon_1\varepsilon_2 = \frac{2}{\tilde{V}^2},\\ &\varepsilon_1\varepsilon_3 \approx \frac{p_2}{p_1}, \quad \tilde{V}^2 = \frac{2V^2p_1^2}{\omega^2} \ll 1.\end{aligned} \tag{27}$$

These results are also valid for an N-well structure and will be used in the subsequent analysis. We assume that one more inequality, which is universal for any N, is satisfied:

$$\frac{\alpha_j}{p_j} \gg 1. \tag{28}$$

This inequality corresponds to a small resonance level width Γ_j as compared to the resonance energy ε_{jR}. It is well known that resonant tunneling exhibits most clearly its remarkable properties precisely when inequalities (28) are satisfied.

It was shown in [6] that determinant (24) and coefficients A_m^j (23) can be represented in the form of expansions in $\tilde{V}^2$. Omitting terms on the order of $\tilde{V} \ll 1$ and $\tilde{V}^2\alpha/p \ll 1$, we arrive at the following expression for $\Delta_1(1)$:

$$\begin{aligned}\Delta_1(1) &= -\varepsilon_1\varepsilon_2\left(\tilde{\Delta}_{12}\Delta_{34} - \tilde{V}^2\frac{8\alpha_1\alpha_2}{p_1^2}\right)\\ &= \varepsilon_1\varepsilon_2\frac{\alpha_1\alpha_2}{(p_1p_2)^2}\tilde{\Delta}_1(1),\\ \tilde{\Delta}_1(1) &= \lambda^2 - (\xi+i\Gamma_1)(\xi+i\Gamma_2),\\ \lambda^2 &= \frac{16p_1p_2\tilde{V}^2}{a^2}, \quad \Gamma_j = \frac{2p_j^3}{a\alpha_j^2},\\ \varepsilon_{jR} &= p_{jR}^2, \quad \xi = \varepsilon - \varepsilon_{2R},\\ p_{1R} &= \frac{\pi\alpha_1}{1+\alpha_1 a}, \quad p_{2R} = \frac{2\pi\alpha_2}{1+\alpha_2 a}.\end{aligned} \tag{29}$$

It can easily be seen from these expressions that the electromagnetic field starts influencing the resonant tunneling significantly if

$$\lambda^2 > \Gamma_1\Gamma_2 \text{ or } \tilde{V}^2 > \frac{p_1^2p_2^2}{2\alpha_1^2\alpha_2^2}. \tag{30}$$

Since $\alpha/p \gg 1$, condition (30) holds simultaneously with the inequality $\tilde{V} \ll 1$. A field satisfying condition (30) will be referred to as a strong field.

Assuming that ratio $\tilde{V}^2\alpha/p$ is small, we derive coefficients $A_2^{(j)}$ from relations (23):

$$\begin{aligned}A_2^{(3)} &= -A_2^{(4)} = \frac{2q}{\Delta(1)}\varepsilon_1\varepsilon_2\tilde{\Delta}_{12},\\ A_2^{(1)} &= A_2^{(2)} = \frac{8qp_2i\alpha_1}{\Delta(1)p_1^2}.\end{aligned} \tag{31}$$

Using relations (31), (20), and (15), we obtain current (3) in the form

$$\begin{aligned}J_c(1) &= -4ie\varepsilon_1M_{12}K(1),\\ K(1) &= [A_2^{(1)}(1)A_2^{(3)}(1) + \text{c.c.}]\\ &= \frac{(4q)^2p_2\alpha_1\varepsilon_1\varepsilon_2 2\,\mathrm{Im}\tilde{\Delta}_{12}}{p_1^2|\Delta(1)|^2},\end{aligned} \tag{32}$$

$$\begin{aligned}M_{12} &= \frac{1}{a}\int_0^a dx[p_1\sin(p_2x)\cos(p_1x)\\ &\quad - p_2\sin(p_1x)\cos(p_2x)] = \frac{8}{3a}.\end{aligned}$$

Substituting relations (25) and (29), carrying out some transformations, and assuming that $\alpha_2 = 2\sqrt{2}\,\alpha_1$ and $\Gamma_1 = \Gamma_2 = \Gamma$ for the optimal mode [7], we obtain

$$\begin{aligned}J_c(1) &= E\frac{\Gamma^2Q\eta(1)}{|\tilde{\Delta}(1)|^2}, \quad \eta(1) = \frac{64e^2p_1p_2}{3\omega^2a^2},\\ |\tilde{\Delta}(1)|^2 &\equiv f(1,\xi) = (\lambda^2+\Gamma^2-\xi^2)^2 + 4\Gamma^2\xi^2.\end{aligned} \tag{33}$$

The equation for the laser field can be derived from Eq. (1):

$$1 = \frac{\tilde{Q}\Gamma^2}{|\tilde{\Delta}(1)|^2}, \quad \tilde{Q} = \frac{4\pi\tau_0Q\eta(1)}{\kappa}. \tag{34}$$

The basic quantity determining the dependence of current $J_c(1)$ and of the laser field corresponding to wavelength λ on ξ is the square of resonance determi-

nant $f(1, \xi)$. The minimum of $f(1, \xi)$ corresponds to the maximum of the current and of the laser field. The equation for the extreme values of ξ, i.e.,

$$\frac{df(1,\xi)}{d\xi} = 0 = \xi(\xi^2 + \Gamma^2 - \lambda^2),$$

has two solutions. The first solution, $\xi_1 = 0$, corresponds to the minimum of f for $\lambda < \Gamma$ and to its maximum for $\lambda > \Gamma$. The second solution,

$$\xi_2^2 = \lambda^2 - \Gamma^2, \quad \lambda > \Gamma, \tag{35}$$

gives a minimum of $f(1, \xi)$ for a strong field for $\lambda > \Gamma$.

Using relations (34), we obtain the laser power $P(1)$ which is a linear function of pumping current $\tilde{Q}$ for $\xi = \xi_2$,

$$P(1) = \lambda^2 = \frac{\tilde{Q}^2}{4}, \tag{36}$$

and a root function of $\tilde{Q}$ for $\xi = \xi_1 = 0$,

$$P(1) = \Gamma(\sqrt{\tilde{Q}} - \Gamma).$$

The physical meaning of solution ξ_2 becomes clear after calculating the reflectance

$$R(\xi) = \frac{(\xi^2 + \Gamma^2 - \lambda^2)^2}{|\tilde{\Delta}(1)|^2}, \quad R(\xi_2) = 0. \tag{37}$$

It follows hence that energy $\varepsilon_2 = \varepsilon_{2R} + \xi_2$ coincides with the resonant energy of the structure in an ac field.

4. GENERAL SOLUTION FOR AN *N*-WELL STRUCTURE

Let us consider a structure with N QWs. The wave function satisfies the system of equations (12), (13) with boundary conditions (14). In analogy with the case of a single well, we seek the solution in the form (see Section 3)

$$\begin{aligned} \psi_{n1} &= \sum_{j=1}^{4} A_{n1}^j \exp(\gamma_j x), \\ \psi_{n2} &= \sum_{j=1}^{4} A_{n2}^j \exp(\gamma_j x), \end{aligned} \tag{38}$$

where γ_j is defined by expression (19) or (26) (for $\tilde{V} \ll 1$), and coefficients A_{nm}^j are connected through the relation

$$A_{n1}^j = \varepsilon_j A_{n2}^j. \tag{39}$$

Substituting ψ_{nm}^j from Eqs. (38) into boundary conditions (14) and expressing A_{n1}^j in terms of A_{n2}^j, we arrive at the following system of inhomogeneous algebraic equations for A_{n2}^j:

$$\begin{gathered} \sum_{j=1}^{4} A_{12}^j \exp(-\gamma_j a)(1 - \beta_j) = q, \quad \sum_{j=1}^{4} A_{12}^j = 0, \\ \sum_{j=1}^{4} \varepsilon_j A_{12}^j \exp(-\gamma_j a) = 0, \\ \sum_{j=1}^{4} (\varepsilon_j A_{12}^j - A_{22}^j) = 0, \\ \sum_{j=1}^{4} A_{22}^j \exp(\gamma_j a) = 0, \\ \sum_{j=1}^{4} (A_{22}^j \gamma_j - A_{12}^j \gamma_j \varepsilon_j - \alpha A_{12}^j \varepsilon_j) = 0, \\ \cdots\cdots\cdots\cdots\cdots\cdots\cdots\cdots\cdots\cdots \\ \sum_{j=1}^{4} A_{N2}^j \varepsilon_j \exp[\gamma_j (N-1)a](1 - \tilde{\beta}_j) = 0. \end{gathered} \tag{40}$$

The solution to this system of equations for an N-well structure can be written in compact form. In particular, for the first well, we have

$$A_{12}^j(N) = (-1)^{1+j} \frac{2q}{\Delta(N)} [d_j D(N) - P_j \Pi(N)], \tag{41}$$

$$d_j = \sum_{k \neq l \neq j} (-1)^{k+l+j} \varepsilon_k \varepsilon_l \Gamma_{kl}, \tag{42}$$

$$P_j = \sum_{k \neq l \neq j} (-1)^{k+l+j} \varepsilon_k \varepsilon_l \Delta_{kl}^{\alpha}, \tag{43}$$

$$\Delta(N) = -\Delta(1) D(N) + \tilde{\Delta}(1) \Pi(N). \tag{44}$$

Determinants $D(N)$ and $\Pi(N)$ satisfy the recurrence relations

$$D(n) = -\Delta D(n-1) + \tilde{\Delta} \Pi(n-1), \tag{45}$$

$$\Pi(n) = -\tilde{\Delta}(D)(n-1) + \tilde{\Delta} \Pi(n-1), \quad n \geq 3. \tag{46}$$

The remaining "elementary" determinants have the form

$$\Delta(1) = \begin{vmatrix} m_1 e^{-\gamma_1 a} & m_2 e^{-\gamma_2 a} & m_3 e^{-\gamma_3 a} & m_4 e^{-\gamma_4 a} \\ 1 & 1 & 1 & 1 \\ \varepsilon_1 e^{-\gamma_1 a} & \varepsilon_2 e^{-\gamma_2 a} & \varepsilon_3 e^{-\gamma_3 a} & \varepsilon_4 e^{-\gamma_4 a} \\ \varepsilon_1 & \varepsilon_2 & \varepsilon_3 & \varepsilon_4 \end{vmatrix}, \tag{47}$$

$$\underset{\sim}{\Delta}(1) = \begin{vmatrix} m_1 e^{-\gamma_1 a} & m_2 e^{-\gamma_2 a} & m_3 e^{-\gamma_3 a} & m_4 e^{-\gamma_4 a} \\ 1 & 1 & 1 & 1 \\ \varepsilon_1 e^{-\gamma_1 a} & \varepsilon_2 e^{-\gamma_2 a} & \varepsilon_3 e^{-\gamma_3 a} & \varepsilon_4 e^{-\gamma_4 a} \\ \varepsilon_1 n_1 & \varepsilon_2 n_2 & \varepsilon_3 n_3 & \varepsilon_4 n_4 \end{vmatrix}, \quad (48)$$

$$\Delta(2) = \begin{vmatrix} \gamma_1 & \gamma_2 & \gamma_3 & \gamma_4 \\ e^{\gamma_1 a} & e^{\gamma_2 a} & e^{\gamma_3 a} & e^{\gamma_4 a} \\ \varepsilon_1 & \varepsilon_2 & \varepsilon_3 & \varepsilon_4 \\ \varepsilon_1 e^{\gamma_1 a} & \varepsilon_2 e^{\gamma_2 a} & \varepsilon_3 e^{\gamma_3 a} & \varepsilon_4 e^{\gamma_4 a} \end{vmatrix}, \quad (49)$$

$$\underset{\sim}{\Delta}(2) = \begin{vmatrix} \gamma_1 & \gamma_2 & \gamma_3 & \gamma_4 \\ e^{\gamma_1 a} & e^{\gamma_2 a} & e^{\gamma_3 a} & e^{\gamma_4 a} \\ \varepsilon_1 & \varepsilon_2 & \varepsilon_3 & \varepsilon_4 \\ \varepsilon_1 n_1 e^{\gamma_1 a} & \varepsilon_2 n_2 e^{\gamma_2 a} & \varepsilon_3 n_3 e^{\gamma_3 a} & \varepsilon_4 n_4 e^{\gamma_4 a} \end{vmatrix}, \quad (50)$$

$$\tilde{\underset{\sim}{\Delta}}(2) = \begin{vmatrix} 1 & 1 & 1 & 1 \\ e^{\gamma_1 a} & e^{\gamma_2 a} & e^{\gamma_3 a} & e^{\gamma_4 a} \\ \varepsilon_1 & \varepsilon_2 & \varepsilon_3 & \varepsilon_4 \\ \varepsilon_1 n_1 e^{\gamma_1 a} & \varepsilon_2 n_2 e^{\gamma_2 a} & \varepsilon_3 n_3 e^{\gamma_3 a} & \varepsilon_4 n_4 e^{\gamma_4 a} \end{vmatrix}, \quad (51)$$

$$\tilde{\Delta}(2) = \begin{vmatrix} 1 & 1 & 1 & 1 \\ e^{\gamma_1 a} & e^{\gamma_2 a} & e^{\gamma_3 a} & e^{\gamma_4 a} \\ \varepsilon_1 & \varepsilon_2 & \varepsilon_3 & \varepsilon_4 \\ \varepsilon_1 e^{\gamma_1 a} & \varepsilon_2 e^{\gamma_2 a} & \varepsilon_3 e^{\gamma_3 a} & \varepsilon_4 e^{\gamma_4 a} \end{vmatrix}, \quad (52)$$

$$D(2) \equiv D = \begin{vmatrix} \gamma_1 & \gamma_2 & \gamma_3 & \gamma_4 \\ e^{\gamma_1 a} & e^{\gamma_2 a} & e^{\gamma_3 a} & e^{\gamma_4 a} \\ \varepsilon_1 & \varepsilon_2 & \varepsilon_3 & \varepsilon_4 \\ \tilde{\varepsilon}_1 & \tilde{\varepsilon}_2 & \tilde{\varepsilon}_3 & \tilde{\varepsilon}_4 \end{vmatrix}, \quad (53)$$

$$\Pi(2) \equiv \Pi = \begin{vmatrix} 1 & 1 & 1 & 1 \\ e^{\gamma_1 a} & e^{\gamma_2 a} & e^{\gamma_3 a} & e^{\gamma_4 a} \\ \varepsilon_1 & \varepsilon_2 & \varepsilon_3 & \varepsilon_4 \\ \tilde{\varepsilon}_1 & \tilde{\varepsilon}_2 & \tilde{\varepsilon}_3 & \tilde{\varepsilon}_4 \end{vmatrix}. \quad (54)$$

Here, we have introduced the following notation for the determinants: $\Delta(1)$ is the determinant for the first well, $\underset{\sim}{\Delta}(1)$ is that with a different lower line, and $\Delta(2) = \tilde{\Delta}(3) = \ldots \Delta(n) = \Delta$ are determinants for the internal wells ($2 < n \le N$), where $\underset{\sim}{\Delta}$, $\tilde{\Delta}$, and $\tilde{\underset{\sim}{\Delta}}$ are the determinants with other lower, upper, and upper and lower lines, respectively. Determinants $D(2)$ and $\Pi(2)$ correspond to the last well of the structure. In order to simplify the notation, we wrote the expression for $A_{12}^j(N)$ for the first well only, assuming that the internal wells are identical. These coefficients are sufficient for calculating the reduced current in the first well. There is no need to find the currents in the remaining wells since these currents are identical in the model considered here and for steady-state solution (9). Nevertheless, the proof for a two-well structure will be carried out through direct calculations.

The expressions for the determinants and coefficients can be simplified if we take into account the smallness of parameters $\tilde{V}$, p/α, and $\tilde{V}^2\alpha/p$:

$$\begin{gathered} D(2) \equiv D = \varepsilon_1\varepsilon_2\tilde{\Delta}_{12}\delta_{34}, \\ \Pi(2) \equiv \Pi \approx \varepsilon_1\varepsilon_2\left(\tilde{\Delta}_{34}\tilde{\Gamma}_{12} - i\tilde{V}^2\frac{8\alpha_2}{p_1}\right), \\ \Delta(1) \approx \varepsilon_1\varepsilon_2\left(\Delta_{34}\Gamma_{12} - i\tilde{V}^2\frac{8\alpha_2}{p_1}\right), \\ \underset{\sim}{\Delta}(1) \approx \varepsilon_1\varepsilon_2\left(\Delta_{34}\Delta_{12}^{\alpha} - i\tilde{V}^2\frac{8\alpha\alpha_2}{p_1}\right), \\ \Delta \approx \varepsilon_1\varepsilon_2\tilde{\Gamma}_{12}\delta_{34}, \\ \tilde{\Delta} \approx \varepsilon_1\varepsilon_2\left(\tilde{\Gamma}_{12}\tilde{\Gamma}_{34} - \tilde{V}^2\frac{8p_2}{p_1}\right), \\ \underset{\sim}{\Delta} \approx \varepsilon_1\varepsilon_2\tilde{\Delta}_{12}^{\alpha}\delta_{34}, \\ \tilde{\underset{\sim}{\Delta}} \approx \varepsilon_1\varepsilon_2\left(\tilde{\Delta}_{12}^{\alpha}\tilde{\Gamma}_{34} - \tilde{V}^2\frac{8\alpha p_2}{p_1}\right), \end{gathered} \quad (55)$$

$$\begin{gathered} d_{1,2} = \mp\frac{4p_2}{p_1}, \quad P_{1,2} = \mp\frac{4\alpha p_2}{p_1}, \\ d_{3,4} = \varepsilon_1\varepsilon_2\left(\Gamma_{12} \pm \tilde{V}^2\frac{2p_2}{p_1}\right), \\ P_{3,4} = \varepsilon_1\varepsilon_2\left(\tilde{\Delta}_{12}^{\alpha} \pm \tilde{V}^2\frac{2\alpha p_2}{p_1}\right). \end{gathered} \quad (56)$$

Here, the following definitions have been introduced:

$$\begin{gathered} \Delta_{ij}^{\alpha} = n_i\exp(-\gamma_j a) - n_j\exp(-\gamma_i a), \\ \tilde{\Delta}_{ij}^{\alpha} = n_j\exp(\gamma_j a) - n_i\exp(\gamma_i a), \\ \delta_{ij} = \gamma_i\exp(\gamma_j a) - \gamma_j\exp(\gamma_i a), \\ \Gamma_{ij} = \exp(-\gamma_j a) - \exp(-\gamma_i a) = \tilde{\Gamma}_{ij}^*, \\ \tilde{\varepsilon}_j = \varepsilon_j\tilde{m}_j\exp(\gamma_j a), \end{gathered} \quad (57)$$

$$m_j = 1 - \beta_j, \quad \tilde{m}_j = 1 - \tilde{\beta}_j,$$
$$n_j = \alpha + \gamma_j.$$

Using relations (55) and (56), we can derive simplified expressions for the remaining determinants and coefficients A_{nm}^j for an N-well structure.

5. TWO-WELL STRUCTURE

Many basic features of a multiwell structure are manifested even for $N = 2$. In view of the relative simplicity of this structure, we will analyze it in detail. Wave functions (38) for $N = 2$ assume the form

$$\psi_{k2}(2) = \sum_{j=1}^{4} A_{k2}^j(2)\exp(\gamma_j x),$$
$$\psi_{k1}(2) = \sum_{j=1}^{4} A_{k2}^j(2)\varepsilon_j\exp(\gamma_j x), \quad k = 1, 2. \tag{58}$$

Here, $\psi_{k2}(2)$ ($\psi_{k1}(2)$) is the wave function of the kth well ($k = 1, 2$) of the upper (lower) level of the two-well structure. In accordance with relations (41)–(44), corresponding coefficients $A_{12}^j(2)$ and determinant $\Delta(2)$ are given by

$$A_{12}^j(2) = (-1)^{1+j}\frac{2q}{\Delta(2)}(d_j D - P_j \Pi), \tag{59}$$

$$\Delta(2) = -\Delta(1)D + \underset{\sim}{\Delta}(1)\Pi. \tag{60}$$

Using approximate expressions for D, Π, $\Delta(1)$, and $\underset{\sim}{\Delta}(1)$ (see relations (55) and (56)), we obtain

$$A_{12}^{(1)}(2) = A_{12}^{(2)}(2) = -\varepsilon_1\varepsilon_2\frac{2q}{\Delta(2)}\frac{8ip_2}{p_1}\tilde{\Delta}_{12}\Phi_2, \tag{61}$$

$$A_{12}^{(3)}(2) = -A_{12}^{(4)}(2)$$
$$= -(\varepsilon_1\varepsilon_2)^2\frac{2q}{\Delta(2)}\left(\Phi_0\tilde{\Delta}_{12} + \tilde{V}^2\frac{16p_2\alpha_1}{p_1^2}\Phi_1\right), \tag{62}$$

$$\Delta(2) = (\varepsilon_1\varepsilon_2)^2\left(\tilde{\Delta}_{12}\Delta_{34}\Phi_0 - \tilde{V}^2\frac{16p_2}{p_1}\Phi_4\right). \tag{63}$$

Here, we have introduced the notation

$$\Phi_0 = \Delta_{12}^{\alpha}\tilde{\Gamma}_{34} - \delta_{34}\Gamma_{12} = 4[\alpha\sin(p_1 a)\cos(p_2 a)$$
$$+ p_1\cos(p_1\alpha)\sin(p_2 a) + p_2\cos(p_2 a)\sin(p_1 a)], \tag{64}$$

$$\Phi_1 = \alpha\sin(p_1 a) + p_1\cos(p_1 a),$$
$$\Phi_2 = \alpha\sin(p_2 a) + p_2\cos(p_2 a),$$
$$\Phi_4 = \frac{\alpha_2}{p_2}\tilde{\Delta}_{12}\Phi_2 - \frac{\alpha_1}{p_1}\Delta_{34}\Phi_1. \tag{65}$$

Taking into account relations (61) and (62), we can write the wave functions for the first well in the form

$$\psi_{12}(2) = 2iA_{12}^{(3)}(2)\sin(p_2 x),$$
$$\psi_{11}(2) = 2i\varepsilon_1 A_{12}^{(1)}(2)\sin(p_1 x). \tag{66}$$

Substituting these expressions into Eq. (15), we obtain the reduced current in the first well:

$$J_{1c}(2) = \frac{1}{a}\int_{-a}^{0} J_{1c}(2, x)dx$$
$$= -4ie\varepsilon_1 M_{12}[A_{12}^{(1)*}(2)A_{12}^{(3)}(2) + \text{c.c.}]. \tag{67}$$

Using relations (61) and (62), we arrive at the following expression:

$$J_{1c}(2) = 4ie\varepsilon_1 M_{12}(\varepsilon_1\varepsilon_2)^3\frac{8Q\Phi_2}{|\Delta(2)|^2 p_1}$$
$$\times\left[\left(i|\tilde{\Delta}_{12}|\Phi_0 + \tilde{V}^2\frac{16\alpha_1 p_2\Phi_1 i\tilde{\Delta}_{12}^*}{p_1}\right) + \text{c.c.}\right]. \tag{68}$$

It can easily be seen that the first term in this expression vanishes, and a contribution comes only from the second term proportional to the square of the field $\tilde{V}^2$ and to the imaginary part of $\tilde{\Delta}_{12}$,

$$J_{1c}(2) = -\frac{e\varepsilon_1 M_{12}(\varepsilon_1\varepsilon_2)^2 16\alpha_1 Q\tilde{\Phi}(\tilde{\Delta}_{12}^* - \tilde{\Delta}_{12})}{p_1|\Delta(2)|^2},$$
$$\tilde{\Phi} = \frac{64p_2}{p_1}\Phi_1\Phi_2. \tag{69}$$

This fundamental result indicates that the attenuation responsible for radiative transitions between the energy levels in the first well is induced by the current of the second (right) well and is proportional to $\tilde{V}^2$. The result is also valid for any number of wells $N \geq 2$, but the attenuation will be proportional to $\tilde{V}^{2(N-1)}$. Since there are no dissipative processes in a coherent system, the attenuation in the extreme right well, which is "transported" by the current, is responsible for lasing. For this reason, a description of coherent systems requires that the boundary conditions be taken into account correctly.

Let us analyze current $J_{c1}(2)$ in the first well of a two-well structure. The key quantity is the resonance determinant $\Delta(2)$ defined by expression (63). The basic

difference between $\Delta(2)$ and $\Delta(1)$ (see relations (29)) lies in the emergence of a new resonant determinant Φ_0 (64).

The equality

$$\Phi_0 = 0 \tag{70}$$

leads to the equation for the spectrum of two tunnel-coupled QWs. Equation (70) has two solutions: an antisymmetric solution with an unshifted energy and a symmetric solution. The energy of the latter solution is shifted downwards and the levels split (see the Appendix). The upper level in the first well and the lower level in the second well are also displaced downwards on the energy scale due to finite heights α_2 and α_1 of extreme barriers. Their shift is determined by the equations

$$\mathrm{Re}\tilde{\Delta}_{12} = 0, \quad \mathrm{Re}\Delta_{34} = 0. \tag{71}$$

Obviously, the resonance conditions

$$\varepsilon_{2R}^{(1)} - \varepsilon_{1R}^{(1)} = \omega, \quad \varepsilon_{2R}^{(2)} - \varepsilon_{1R}^{(2)} = \omega \tag{72}$$

are satisfied only if the levels are shifted identically. In particular, this means that a sharp resonance is possible only for a symmetric solution to Eq. (70). It will be proved below (see the Appendix) that resonance conditions (72) and Eqs. (70) and (71) can be satisfied simultaneously if the following relations hold for any α:

$$\alpha_2 = \frac{4\alpha}{5}, \quad \alpha_1 = \frac{\alpha}{5}, \quad \alpha_1 + \alpha_2 = \alpha. \tag{73}$$

These relations are preserved for multiwell structures also; in this case, α_2 and α_1 are the depths of the first and last wells, respectively.

Assuming that relations (73) and (72) are satisfied and that the energy ε of supplied electrons is close to the resonance energy ε_{2R}, we can write the resonance determinant and Φ_k in the form

$$\tilde{\Delta}_{12} = -\frac{a\alpha_1}{p_1^2}(\xi + i\Gamma_1), \quad \Delta_{34} = -\frac{a\alpha_2}{p_2^2}(\xi + i\Gamma_2), \tag{74}$$

$$\Phi_0 \approx 5\xi, \quad \xi = \varepsilon - \varepsilon_{2R}, \tag{75}$$

$$\Phi_1 \approx 2p_2, \quad \Phi_2 = -\frac{p_1}{2},$$

$$\Phi_4 = \frac{5\alpha_1^2}{p_1^2}\left(\xi + \frac{3}{5}\Gamma_1\right), \tag{76}$$

$$\Gamma_j = \frac{2p_j^3}{a\alpha_j^2}, \quad \Gamma_2 \approx \frac{\Gamma_1}{2}.$$

In relations (75) and (76), the terms on the order of $\xi/\delta\varepsilon$ have been omitted and $\delta\varepsilon \approx p^2/\alpha a$ is the energy shift exceeding considerably the level width Γ. Thus, relations (74)–(76) are valid for values of ξ from the interval $0 < \xi < \delta\varepsilon$.

In this approximation, current (69) in the first well assumes the form

$$J_{1c}(2) = \tilde{V}^3\frac{\Gamma_1\Gamma_2 Q\eta(2)}{|\tilde{\Delta}(2,\xi)|^2}, \qquad \eta(2) = 4e\sqrt{2}M_{12}\frac{64p_2^3}{25}, \tag{77}$$

$$\Delta(2,\xi) = \frac{5(\varepsilon_1\varepsilon_2)^2\alpha_1\alpha_2}{p_1^2p_2^2}\tilde{\Delta}(2,\xi), \tag{78}$$

$$\tilde{\Delta}(2,\varepsilon) = \left[\xi\left(\xi^2 - \lambda^2 - \frac{\Gamma_1^2}{2}\right) + i\frac{3\Gamma_1}{2}\left(\xi^2 - \frac{2}{5}\lambda^2\right)\right].$$

It follows from relations (77) that the dependence of the current on the electron energy ξ (and, hence, on the laser field) is determined only by the square of the modulus of the reduced determinant $|\tilde{\Delta}(2,\xi)|^2$:

$$f(2,\xi) = |\tilde{\Delta}(2,\xi)|^2 = \xi^2\left(\xi^2 - \lambda^2 - \frac{\Gamma_1^2}{2}\right)^2 + \frac{9\Gamma_1^2}{4}\left(\xi^2 - \frac{2}{5}\lambda^2\right)^2. \tag{79}$$

The optimal values of the energy ξ of supplied electrons can be determined from the condition for the minimum of $f(2,\xi)$ (or for the maximum of $\lambda^2(\xi)$):

$$\frac{df(2,\xi)}{d\xi} = 2\xi\left[\left(\xi^2 - \lambda^2 - \frac{\Gamma_1^2}{2}\right)^2 + 2\xi^2\left(\xi^2 - \lambda^2 - \frac{\Gamma_1^2}{2}\right) + \frac{9}{2}\Gamma_1^2\left(\xi^2 - \frac{2}{5}\lambda^2\right)\right] = 0. \tag{80}$$

This equation has three solutions:

$$\xi_1 = 0, \quad \xi_{2,3}^2 = \frac{1}{3}\left[\left(2\lambda^2 - \frac{5\Gamma^2}{4}\right) \mp \sqrt{\lambda^4 - \frac{13\lambda^2\Gamma_1^2}{5} + \frac{13\Gamma_1^4}{16}}\right], \tag{81}$$

$$\xi_2^2 \approx \frac{\lambda^2}{3}, \quad \xi_3^2 \approx \lambda^2, \quad \lambda \gg \Gamma_1.$$

Solutions ξ_1 and ξ_3 correspond to a minimum of $f(2,\xi)$, while ξ_2 corresponds to a maximum of this function, so that

$$f(0) = \frac{9}{25}\Gamma_1^2\lambda^4, \quad f(\lambda^2) = \frac{81}{100}\Gamma_1^2\lambda^4, \qquad f\left(\frac{\lambda^2}{3}\right) \approx \frac{4}{27}\lambda^6. \tag{82}$$

In contrast to a single-well structure, the minimum of $f(2)$ for $\xi_1 = 0$ exists for any λ. It should be noted that this minimum is lower than that for $\xi_3 \approx \lambda$. In addition, it is more convenient since it does not require electron energy tuning. It is solution ξ_1 that is of greatest importance.

The corresponding values of current $J_{1c}(2)$ for $\xi_1 = 0$ and $\xi_3 \approx \lambda$ are

$$J_{1c}(2, \xi_1 = 0) = \frac{Qe2\sqrt{2}M_{12}}{9\tilde{V}} = \frac{9}{4}J_{1c}(2, \lambda). \quad (83)$$

A comparison of current $J_{1c}(2, 0)$ (83) in the first well with current $J_{1c}(1, \lambda)$ (33) in a single-well structure shows that these currents are virtually identical:

$$J_{1c}(2, 0) = \frac{8}{9}J_{1c}(1, \lambda). \quad (84)$$

It should be noted that solutions ξ_1 and ξ_3 lead to a linear dependence of the lasing power on the pumping current, while ξ_2 leads to a root dependence.

Let us now determine the wave functions and the current for the second well, which will enable us to prove the equality of currents in the first and second wells and to calculate the populations of the levels.

Coefficients $A_{21}^{(j)}$ and $A_{22}^{(j)}$ of wave functions $\psi_{22}(2)$ and $\psi_{21}(2)$ can be determined from Eqs. (40) for $N = 2$. We can write approximate expressions with the above accuracy:

$$A_{22}^{(1)} = A_{22}^{(2)} \approx \frac{i(2q)D_2}{\Delta(2)}\frac{4\alpha_1 p_2}{p_1},$$
$$A_{22}^{(3,4)} = -\frac{2qD_2}{\Delta(2)}\varepsilon_1\varepsilon_2\left\{\tilde{\Delta}_{12}\exp(\gamma_{4,3}a) \pm i\tilde{V}^2\frac{2\alpha_1 p_2}{p_1^2}\right\}, \quad (85)$$

where the matrix is given by

$$D_2 = \begin{vmatrix} 1 & 1 & 1 & 1 \\ \varepsilon_1 e^{\gamma_1 a} & \varepsilon_2 e^{\gamma_2 a} & \varepsilon_3 e^{\gamma_3 a} & \varepsilon_4 e^{\gamma_4 a} \\ \varepsilon_1 & \varepsilon_2 & \varepsilon_3 & \varepsilon_4 \\ \varepsilon_1 n_1 & \varepsilon_2 n_2 & \varepsilon_3 n_3 & \varepsilon_4 n_4 \end{vmatrix}. \quad (86)$$

Accordingly, the wave functions assume the form

$$\psi_{22}(2, x) = -i\frac{8qD_2\tilde{\Delta}_{12}}{\tilde{V}^2\Delta(2)}\sin[p_2(x-a)],$$
$$\psi_{21}(2, x) = -i\frac{8\alpha_1 p_2 2qD_2\sqrt{2}}{\tilde{V}p_1^2\Delta(2)}\sin(p_1 x). \quad (87)$$

Using these functions, we can find the reduced current in the second well:

$$J_{2c}(2) = \frac{1}{a}\int_0^a dx J_{2c}(2, x) = -ie\frac{(2q)^2}{|\Delta(2)|^2} \times \frac{4\sqrt{2}|D_2|^2 8\alpha_1 p_2}{\tilde{V}^3 p_1^2}M_{12}(\tilde{\Delta}_{12}^* - \tilde{\Delta}_{12}). \quad (88)$$

Substituting the approximate value

$$D_2 \approx -\frac{8\sqrt{2}p_2}{\tilde{V}} \quad (89)$$

into expression (88), we find that $J_{2c}(2)$ coincides with current $J_{1c}(2)$ (83) in the first well. Thus, reduced current (3) of a two-well structure is equal to the reduced current in the first well: $J_c(2) = J_{1c}(2)$. Since currents $J_{1c}(2, 0)$ and $J_c(1, \lambda)$ coincide in accordance with relation (84) (to within a factor of 8/9), the field generated by the two-well structure for $\xi = 0$ is given by formula (36) (with $\tilde{Q} \longrightarrow (8/9)\tilde{Q}$). The total power $P(2)$ is naturally doubled:

$$P(2) = 2\frac{2\tilde{Q}}{9}. \quad (90)$$

6. LEVEL POPULATIONS AND REFLECTANCE FOR A TWO-WELL STRUCTURE

It would be interesting to compare the level populations n_{ij},

$$n_{ij} = \frac{1}{a}\int_0^a dx\,|\psi_{ij}|^2. \quad (91)$$

Calculations made for $\xi_1 = 0$ lead to the following results:

$$n_{12} = \left(\frac{4\lambda}{\Gamma_1}\right)^2 n_{11}, \quad n_{22} = \left(\frac{\Gamma_1}{\lambda}\right)^2 n_{21},$$
$$n_{12} = 4n_{21}, \quad n_{22} = 4n_{11}. \quad (92)$$

It can be seen that the mutual population of the levels in same well changes upon an increase in the field of wavelength λ. At the same time, the ratio of populations of the upper level in the first well and the lower level in the second well is preserved. For $\lambda \gg \Gamma_1$, we have $n_{12} \gg n_{11}$, while $n_{22} \ll n_{21}$; i.e., the first well exhibits

population inversion, while the second well does not. It follows hence that the inverse population condition is not required for coherent lasing. This conclusion is confirmed for $\xi_3 = \lambda$ also. Indeed, in the case of tuning $\xi = \lambda \gg \Gamma$, the level populations in each well are identical:

$$n_{12} = n_{11}, \quad n_{22} = n_{21}, \quad 4n_{11} = n_{22}. \tag{93}$$

It should be noted that a two-well structure for $\xi = 0$ and $\xi = \lambda$ behaves as a single-well structure for $\xi = \lambda$ in the sense that the ratio of populations of "extreme levels" (the upper level of the first well and the lower level of the second well) is independent of the field.

It was proved earlier for $N = 1$ [7] (see Section 3) that the optimal values of energy ξ correspond to a resonance of the nanostructure in the field in which the reflection from the structure becomes minimal. Let us find the reflectance for a two-well structure. The reflectance is defined as

$$R = \left|\frac{\psi_{12}(2, -a)}{q} - 1\right|^2. \tag{94}$$

Using formula (66) for $\psi_{12}(2, x)$, we obtain the reflectance

$$R = \left|\frac{i\Gamma_1\Phi_3}{5\tilde{\Delta}(2)} - 1\right|^2,$$
$$\Phi_3 = -\frac{p_1^2}{\alpha_1}\left(\Phi_0\tilde{\Delta}_{12} + \tilde{V}^2\frac{64p_2}{p_1^2}\Phi_1\right) = 5\xi(\xi + i\Gamma_1) - 4\lambda^2. \tag{95}$$

The reflectance in the $\xi = 0$ and $\xi^2 = \lambda^2$ modes is given, respectively, by

$$R(2, 0) = \frac{1}{9}, \quad R(2, \lambda) = \frac{49}{81}. \tag{96}$$

It follows hence that the mode with $\xi = 0$ is much more effective (90%) than that with $\xi = \lambda$ (40%).

Let us prove that the law of conservation of the number of transmitted and reflected electrons holds. For this purpose, we find the number of electrons performing a transition between the energy levels in the first well:

$$\frac{1}{2\pi}\int_0^a dx \int_0^{2\pi/\omega} dt J_{1c}(2, x, t)E(t).$$

It is found that, for $\xi = 0$, it is equal to 8/9 of the flux supplied to the structure, which gives unity together with the reflected fraction (1/9). A similar conservation law holds for $\xi = \lambda$ also.

7. THREE-WELL STRUCTURE

It will be shown below that the properties of structures with even and odd numbers of wells differ considerably. By way of the simplest example of an odd N, we consider a three-well structure. The expressions for coefficients of the first well in the three-well structure can be obtained from the general formulas (41)–(44):

$$A_{12}^j(3) = (-1)^{1+j}\frac{2q}{\Delta(3)}[d_j D(3) - P_j\Pi(3)], \tag{97}$$

$$\Delta(3) = -\Delta(1)D(3) + \underset{\sim}{\Delta}(1)\Pi(3),$$
$$D(3) = -\Delta D + \underset{\sim}{\Delta}\Pi, \quad \Pi(3) = -\tilde{\Delta}D + \underset{\sim}{\tilde{\Delta}}\Pi. \tag{98}$$

Using the smallness of parameters $\tilde{V}$, p/α, and $\tilde{V}^2\alpha/p$ and approximate expressions for Δ, D, and Π, we obtain

$$D(3) \approx -(\varepsilon_1\varepsilon_2)^2\delta_{34}\left\{\tilde{\Delta}_{12}\Phi_0 + \tilde{V}^2\tilde{\Delta}_{12}^{\alpha}\frac{8i\alpha_1 p_2}{p_1^2}\right\},$$
$$\Pi(3) \approx -(\varepsilon_1\varepsilon_2)^2\left\{\tilde{\Delta}_{12}\tilde{\Gamma}_{34}\Phi_0 + \tilde{V}^2\frac{8ip_2}{p_1}\right. \tag{99}$$
$$\left.\times\left[-2\tilde{\Delta}_{12}\Phi_2 + \frac{\alpha_1}{p_1}\tilde{\Delta}_{12}^{\alpha}\tilde{\Gamma}_{34}\right] - \tilde{V}^4\frac{64i\alpha\alpha_1 p_2^2}{p_1^3}\right\}.$$

Using these expressions, we derive from Eq. (97)

$$A_{12}^{(3)}(3) = -A_{12}^{(4)}(3) = \frac{2q}{\Delta(3)}(\varepsilon_1\varepsilon_2)^3\left\{\tilde{\Delta}_{12}\Phi_0^2 + \tilde{V}^2\frac{8ip_2}{p_1}\right.$$
$$\left.\times\left[\tilde{\Delta}_{12}^{\alpha}\frac{\alpha_1\Phi_0}{p_1} - 2\Delta_{12}^{\alpha}\tilde{\Delta}_{12}\Phi_2\right] - \tilde{V}^4\frac{64i\alpha\alpha_1 p_2^2}{p_1^3}\right\}, \tag{100}$$

$$A_{12}^{(1)}(3) = A_{12}^{(2)}(3) = \frac{2q}{\Delta(3)}(\varepsilon_1\varepsilon_2)^2\frac{4p_2}{p_1}$$
$$\times\left\{2i\tilde{\Delta}_{12}\Phi_0\Phi_2 - \tilde{V}^2\frac{16ip_2}{p_1}\Phi_2\left[\frac{2\alpha_1\Phi_1}{p_1} - \alpha\tilde{\Delta}_{12}\right]\right. \tag{101}$$
$$\left. + \tilde{V}^4\frac{64i\alpha^2\alpha_1 p_2^2}{p_1^3}\right\},$$

$$\Delta(3) = (\varepsilon_1\varepsilon_2)^3\Big\{-\tilde{\Delta}_{12}\Delta_{34}\Phi_0^2 + \tilde{V}^2\frac{16p_2}{p_1}$$

$$\times[\Phi_0\Phi_4 - 2\tilde{\Delta}_{12}\Delta_{34}\Phi_1\Phi_2] + \tilde{V}^4\frac{4\alpha_1\alpha_2\tilde{\Phi}}{p_1^2}\Big\}$$

$$= (\varepsilon_1\varepsilon_2)^3\frac{25\alpha_1\alpha_2}{p_1^2p_2^2}\tilde{\Delta}(3), \qquad (102)$$

$$\tilde{\Delta}(3) = -\xi^2(\xi + i\Gamma_1)(\xi + i\Gamma_2)$$

$$+ \lambda^2\left(\frac{29}{25}\xi^2 + i\xi\tilde{\Gamma}\right) - \frac{4}{25}\lambda^4,$$

$$\tilde{\Gamma} = \frac{3}{5}\Gamma_1 + \frac{4}{25}(\Gamma_1 + \Gamma_2).$$

It should be noted that, in the case of a three-well structure, we must retain the fourth-order term $\tilde{V}^4$ in the expression for $\tilde{\Delta}(3)$.

Let us begin our analysis with the resonance determinant $f(3) = |\tilde{\Delta}(3)|^2$. It can easily be demonstrated that $f(3)$ has four extrema ξ_i (we give ξ_i for large values of $\xi, \lambda \gg \Gamma$):

$$\xi_1^2 = 0, \quad \xi_2^2 = \frac{4}{25}\lambda^2, \quad \xi_3^2 = \frac{29}{50}\lambda^2, \quad \xi_4^2 = \lambda^2, \qquad (103)$$

which correspond to maxima for ξ_1 and ξ_3 and to minima for ξ_2 and ξ_4.

Thus, solutions $\xi_1 = 0$ and $\xi_4 = \lambda$ in the three-well structure correspond to a maximum and a minimum of $f(3)$, respectively. Consequently, the three-well structure is a combination of one- and two-well structures. It behaves analogously to a structure with $N = 1$ for $\xi_1 = 0$ and $\xi = \lambda$ and to a structure with $N = 2$ for $\xi = \lambda$.

Let us determine the current in the first well of a three-well structure:

$$J_{1c}(3) = \frac{(2q)^2(\varepsilon_1\varepsilon_2)^5}{|\Delta(3)|^2 p_1}(2i|\tilde{\Delta}_{12}|^2\Phi_0^3\Phi_2 + \text{c.c.})$$

$$+ \tilde{V}^2\Phi_0^2\frac{32p_2\alpha_1\Phi_1\Phi_2}{p_1^2}i(\tilde{\Delta}_{12} - \tilde{\Delta}_{12}^*) \qquad (104)$$

$$+ \tilde{V}^4\Phi_2^2\Phi_1^2\alpha_1 i(\tilde{\Delta}_{12} - \tilde{\Delta}_{12}^*).$$

The last term in this expression corresponds to $\xi = 0$ since for $\xi \sim \lambda$ the omitted terms are proportional to $\tilde{V}^6$.

It can be seen from Eq. (104) that the first term is equal to zero, as in the case of a structure with $N = 2$. The last two terms are proportional to $\tilde{V}^4\,\mathrm{Im}\tilde{\Delta}_{12}$ (see formula (68)). Indeed, for $\xi = 0$ and $\Phi_0 = 0$, the second term is zero, while for $\xi \sim \lambda$ it gives $\tilde{V}^4$.

Solution $\xi_1 = 0$ corresponding to a maximum of $f(3)$ is not optimal for $N = 3$. Indeed, substituting $\xi_1 = 0$ into formula (104) for current, we obtain

$$J_{1c}(3) \propto \frac{1}{\tilde{V}^3}, \qquad (105)$$

i.e., the root dependence $\tilde{V}^2 \propto Q^{1/2}$ (see Section 3), as in the case of a single well.

The optimal solution is $\xi_4 = \lambda$, for which $J_{1c}(3) \propto 1/\tilde{V}$ and $\tilde{V}^2 \propto Q$; the situation is similar to that in a single-well structure. Since the solution with $\xi = \lambda$ was analyzed in detail for $N = 1$ [6, 7] (see Section 3), we will consider below only even structures. This is justified the more so that the optimal situation in this case is that with $\xi = 0$, which can be realized in experiments more easily.

8. EVEN STRUCTURES WITH $N \geq 4$

We will start with a four-well structure. In order to find determinant $\Delta(4)$ as well as $D(4)$ and $\Pi(4)$, i.e.,

$$\Delta(4) = -\Delta(1)D(4) + \underline{\Delta}(1)\Pi(4),$$

$$D(4) = -\Delta D(3) + \underline{\Delta}\Pi(3), \qquad (106)$$

$$\Pi(4) = -\tilde{\Delta}D(3) + \tilde{\underline{\Delta}}\Pi(3),$$

we will use formula (99). In the approximation adopted here, we have

$$\Delta(4) = -(\varepsilon_1\varepsilon_2)^2\Big\{\tilde{\Delta}_{12}\Delta_{34}\Phi_0^3$$

$$+ \tilde{V}^2\frac{16p_2}{p_1}[\Phi_0^2\Phi_4 - 4\Phi_0\tilde{\Delta}_{12}\Phi_1\Phi_2] + \tilde{V}^4\frac{64p_2^2}{p_1^2} \qquad (107)$$

$$\times 2\left[\Phi_0\left(\alpha\Phi_4 + 2\frac{\alpha_1\alpha_2}{p_1p_2}\Phi_1\Phi_2\right) + 4\Phi_1\Phi_2\Phi_4\right]\Big\}.$$

The structure of the determinant has a clear physical meaning. The first term is the product of the determinants for the outer wells and three determinants of collectivized energy levels of the inner wells. It is important that the second term with $\tilde{V}^2$ also contains determinant Φ_0. In addition, we must retain the terms with $\tilde{V}^4$ as in $\Delta(3)$.

It can be proved that solution $\xi_1 = 0$ corresponds to a minimum of $|\Delta(4)|^2$ and is optimal. This property is universal for structures with an even N (in particular, for $N = 2$).

For the optimal solution $\xi_1 = 0$, $\Phi_0 = 0$, determinant $\Delta(4)$ and coefficients $A_{12}^j(4)$ assume the form

$$\Delta(4) = -(\varepsilon_1\varepsilon_2)^4\tilde{V}^4\frac{8p_2}{p_1}\Phi_4\tilde{\Phi}, \tag{108}$$

$$\begin{aligned} A_{12}^{(3)}(4) &= -\frac{2q(\varepsilon_1\varepsilon_2)^2}{\Delta(4)}\frac{8p_2}{p_1^2}4\alpha_1\Phi_1\tilde{\Phi}, \\ A_{12}^{(1)}(4) &= -\frac{2q(\varepsilon_1\varepsilon_2)^2}{\Delta(4)}\frac{8ip_2}{p_1^2}\tilde{\Delta}_{12}\Phi_2\tilde{\Phi}. \end{aligned} \tag{109}$$

It should be noted that, in the expression for $A_{12}^3(4)$, we have omitted the term proportional to $i\tilde{\Delta}_{12}$, which is compensated in the current in analogy with structures with $N = 2$ or 3. Comparing relations (108) and (109) with the corresponding formulas (for $\Phi_0 = 0$) (61)–(63) for a two-well structure, we can derive the following relations:

$$\Delta(4) = \Delta(2)(\varepsilon_1\varepsilon_2)\tilde{\Phi}, \tag{110}$$

$$A_{12}^{(1)}(4) = A_{12}^{(1)}(2), \quad A_{12}^{(3)}(4) = A_{12}^{(3)}(2). \tag{111}$$

Thus, the coefficients for the first well of a four-well structure coincide with the coefficients for a two-well structure. Consequently, the reduced current of a structure with $N = 4$ is given by

$$J_c(4, 0) = J_{1c}(2, 0). \tag{112}$$

Property (111) is preserved for any even N, so that the reduced current for such a structure has the form

$$J_c(N, 0) = J_{1c}(2, 0). \tag{113}$$

Generalizing formula (90), we find that the total power of an N-well structure is

$$P(N) = N\frac{2\tilde{Q}}{9}, \tag{114}$$

i.e., is proportional to the number N of wells.

Obviously, the reflectance remains unchanged ($R = 1/9$) and independent of N since the reflection is determined by the wave function for the first well.

9. CONCLUSIONS

We have proved the possibility of coherent lasing of a structure consisting of any number of wells in the absence of dissipative processes. It is well known (see, for example, [5]) that the emission of a photon requires attenuation determined by the interaction with phonons in bulk systems. In the structure studied by us here, attenuation is associated with the departure of electrons from the lower level of the extreme right well. The steady-state intersubband current "transports" this attenuation to all wells and causes the emission of photons in each well. The electrons supplied due to resonant tunneling perform N transitions from the upper to the lower levels, preserving their phase, this process being independent of the level occupancy. Consequently, the gain and lasing in such a system are volume effects in contrast to the incoherent case [8]. The total lasing power is proportional to the number N of the wells.

Thus, we can assume that lasing at vertical transitions (see the Introduction) in a superlattice with a strong constant field (Stark ladder) is possible. Proceeding from the results obtained in [9], we can expect Stark ladder lasing with diagonal transitions also.

It has been found that effective lasing requires the fulfillment of the following conditions: observance of resonance in each well, the choice of optimal energy of supplied electrons, the sharpness of the electron energy distribution $\Delta\varepsilon$, and, finally, the fulfillment of the coherence conditions for the electron subsystem.

We have proved that the resonance conditions can be satisfied by choosing the barrier parameters (see the Appendix). For structures with an even N, the problem of choosing energy can be solved quite easily: the energy must be equal to the resonance energy ($\varepsilon = \varepsilon_{2R}$) for any fields.

As regards the width $\Delta\varepsilon$, the optimal situation is attained for $\Delta\varepsilon \le \Gamma$. If $\Delta\varepsilon > \Gamma$, the lasing parameters (efficiency, reflectance, and current) naturally decrease. However, the equality $\Delta\varepsilon \approx \Gamma$ can be attained in different ways, e.g., by using energy filters based on QWs.

Naturally, the requirement of coherence is the most stringent: the time τ_φ of coherence breakdown must be longer than the time T_N of passage through the structure. This time can be estimated as $T_N = N\Gamma^{-1}$ for $\lambda < \Gamma$ or $T_N = N\lambda^{-1}$ for $\lambda > \Gamma$. In all cases, the length of the structure is finite:

$$N_{\max} < \tau_{ph}\Gamma, \tau_{ph}\lambda. \tag{115}$$

Parameter $\tau_{ph}\Gamma$ for high-quality QWs can in principle be much greater than unity. For example, in [11], a coherent effect of superfluorescence on ten wells (i.e., $\Gamma\tau_\varphi > 10$) was observed.

Condition (115) becomes less stringent if we take into account the fact that the fields being generated can be strong; i.e., $\lambda \gg \Gamma$. The use of quantum wires and dots weakens condition (115) still further. The technological breakthrough in producing ensembles of extremely high quality quantum dots [12] renders them quite promising for designing lasers with a coherent subsystem on their basis.

ACKNOWLEDGMENTS

This study was carried out in the framework of the Federal Special Program (project no. A0133) and supported by the Ministry of Industry and Science of the Russian Federation (project no. 99-1140) and the

project "Construction of the Theory of Interaction of Strong Electromagnetic Fields with the Electron System of Resonance-Tunnel Diodes and Lasers."

APPENDIX

In order to satisfy the resonance condition in a multiwell structure, it is necessary that the energy difference between the resonance levels of the wells be the same and equal to the frequency ω of the electromagnetic field. If the wells were isolated, these conditions could be satisfied by choosing identical wells. However, in order to ensure the passage of current, the heights α_2, α_1, and α of the barriers must be finite. This leads to splitting of degenerate levels and to a level shift in the outer wells, which is described by Eqs. (70) and (71). We will first prove that these equations are satisfied simultaneously when the last equality in (73) holds. It follows from Eqs. (71) that

$$\begin{aligned} p_1\cos(p_1 a) &= -\alpha_1\sin(p_1\alpha), \\ p_2\cos(p_2 a) &= -\alpha_2\sin(p_2\alpha). \end{aligned} \tag{A.1}$$

Substituting these relations into Eq. (70), we obtain

$$\Phi_0 = 4\sin(p_1 a)\sin(p_2 a)(\alpha - \alpha_1 - \alpha_2) = 0. \tag{A.2}$$

This leads to the last equality in (73).

We can now find the resonance values of energy for Eq. (70):

$$\varepsilon_{1R}^{AS} = \pi^2/a^2, \quad \varepsilon_{1R}^{S} = \frac{\pi^2}{a^2}\left(1 - \frac{10}{\alpha a}\right). \tag{A.3}$$

Energies ε_{1R}^{AS} and ε_{1R}^{S} correspond to the antisymmetric and symmetric solutions, respectively. The energy of the upper level in the first well is given by (see Section 3)

$$\varepsilon_{2R}^{(1)} = \frac{4\pi^2}{a^2}\left(1 - \frac{2}{\alpha_2 a}\right). \tag{A.4}$$

The resonance condition (72)

$$\varepsilon_{2R} - \varepsilon_{1R} = \omega = \frac{3\pi^2}{a^2} \tag{A.5}$$

together with formulas (A.2)–(A.4) leads to the relations

$$\alpha_2 = \frac{4\alpha}{5}, \quad \alpha_1 = \frac{\alpha}{5}. \tag{A.6}$$

It can easily be proved that the resonance condition (72) for the second well is also observed if relation (A.6) holds; α can assume any value. It should be noted that, if we choose

$$\alpha_2 = \frac{4\alpha}{5} + \frac{9}{10}, \quad \alpha_1 = \frac{\alpha}{5} - \frac{9}{10}, \tag{A.7}$$

the resonance conditions are observed to within the terms quadratic in $1/\alpha$.

REFERENCES

1. A. F. Kazarinov and R. A. Suris, Fiz. Tekh. Poluprovodn. (Leningrad) **6**, 135 (1972) [Sov. Phys. Semicond. **6**, 109 (1972)].
2. J. Fainst, F. Capasso, D. L. Sivco, *et al.*, Science **264**, 553 (1994).
3. J. Fainst, F. Capasso, C. Sirtori, *et al.*, Appl. Phys. Lett. **66**, 538 (1995).
4. V. F. Elesin and Yu. V. Kopaev, Solid State Commun. **96**, 987 (1995); V. F. Elesin and Yu. V. Kopaev, Zh. Éksp. Teor. Fiz. **108**, 2186 (1995) [JETP **81**, 1192 (1995)].
5. V. M. Galitskiĭ and V. F. Elesin, *Resonance Interaction of Electromagnetic Fields with Semiconductors* (Énergoatomizdat, Moscow, 1986).
6. V. F. Elesin, Zh. Éksp. Teor. Fiz. **112**, 483 (1997) [JETP **85**, 264 (1997)].
7. V. F. Elesin, Zh. Éksp. Teor. Fiz. **122**, 131 (2002) [JETP **95**, 114 (2002)].
8. G. Bastard, Y. A. Brum, and R. Rerrera, Solid State Phys. **44**, 229 (1991).
9. V. F. Elesin, V. V. Kapaev, Yu. V. Kopaev, and A. V. Tsukanov, Pis'ma Zh. Éksp. Teor. Fiz. **66**, 709 (1997) [JETP Lett. **66**, 742 (1997)].
10. V. F. Elesin and A. V. Tsukanov, Fiz. Tekh. Poluprovodn. (St. Petersburg) **34**, 1404 (2000) [Semiconductors **34**, 1351 (2000)]; V. F. Elesin and A. V. Tsukanov, Phys. Low-Dimens. Semicond. Struct. **11**/**12**, 125 (2000).
11. S. Haas, T. Stroucken, M. Hübner, *et al.*, Phys. Rev. B **57**, 14860 (1998).
12. D. Bimberg, M. Grundmann, F. Heinrichsdorff, *et al.*, Thin Solid Films **367**, 235 (2000).

Translated by N. Wadhwa

Journal of Experimental and Theoretical Physics, Vol. 96, No. 6, 2003, pp. 985–992.
Translated from Zhurnal Éksperimental'noĭ i Teoreticheskoĭ Fiziki, Vol. 123, No. 6, 2003, pp. 1123–1130.

GRAVITATION, ASTROPHYSICS

On the Evolution and Gravitational Collapse of a Toroidal Vortex

K. Yu. Bliokh and V. M. Kontorovich*

Institute of Radio Astronomy, National Academy of Sciences of Ukraine, Krasnoznamennaya ul. 4, Kharkov, 61002 Ukraine

**e-mail: vkont@ira.kharkov.ua*

Received December 23, 2002

Abstract—The evolution and collapse of a gaseous toroidal vortex under the action of self-gravitation are considered using the Hamiltonian mechanics approach. It is shown that evolution occurs in three main stages separated by characteristic time scales. First, a compression along the small radius to a quasi-equilibrium state takes place, followed by a slower compression along the large radius to a more stable compact vortex object. In the latter stage, the possibility of effective scattering and ejection of particles along the vortex axis (jet formation) is detected. As a result, mass, energy, and momentum losses take place, and the vortex collapses.

1. INTRODUCTION

Vortices, which are traditionally described in the framework of incompressible fluid dynamics [1, 2], are special objects of application of Hamiltonian methods. In the epoch of solitons, the interest in vortices as allied localized formations has grown considerably. The current state of this problem is described in reviews and articles [3–7] and in the references cited therein.

Compressibility and self-gravitation of such objects may play a significant role in astrophysical applications [8–10]. In some cases (e.g., in the vicinity of compact objects at the centers of galaxies), the effect of the external gravitational field on these objects may be significant. Both of these possibilities will be taken into account in this study.

Another extremely important problem in contemporary astrophysics is associated with the origin of cosmic jets arising, according to prevailing concepts, in accretion disks of various origins and scales (from galactic [11] to stellar [12]). The interpretation of such jets is a nontrivial problem. In spite of considerable advances made in this direction in the framework of magnetohydrodynamics (MHD) [13], serious difficulties still remain since solutions were obtained in a special geometry and strong magnetic fields are required. It will be shown below that the formation of (unidirectional) jets is a natural consequence of the evolution of self-gravitating vortices and is an indispensable condition of their collapse. Jets are also generated in zero magnetic fields.

A possible relation between this problem and the existence of occluding toroids[1] in the vicinity of central compact objects in the active galactic nuclei is mentioned [14].

2. FIRST STAGE: EVOLUTION OF A THIN VORTEX

We assume that the shape of a vortex at the initial stage is a thin toroid (Fig. 1) whose radii satisfy the inequality

$$r \ll R. \tag{1}$$

(An analog of such a vortex in fluid dynamics is a Maxwellian vortex [1, 2].) We will henceforth assume that the vortex evolution at the initial stage occurs without a change in the toroidal shape. Thus, in addition to a rotational degree of freedom, the system possesses two translational degrees of freedom corresponding to changes in r and R (we disregard the translational motion of the vortex as a whole). It should be noted that, in view of condition (1), the motion in r and rotation constitute a local compression of a rotating cylinder, while the motion in R indicates the collapse of a thin ring.

We write the system Hamiltonian in the form

$$H = \frac{1}{2M}\left[p_r^2 + p_R^2 + \frac{p_\varphi^2}{r^2}\right] + U(r, R). \tag{2}$$

[1] We do not touch upon the classical problem of stability of toroids rotating as a single entity, which dates back to Poincaré and Dyson. The modern state of affairs in the framework of the general theory of relativity and references can be found in [15].

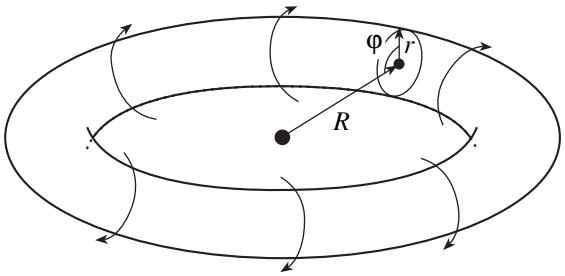

Fig. 1. Thin toroidal vortex of the Maxwellian type.

Here, M is the total mass of the vortex, p_s are the momenta corresponding to coordinates s, φ is the cyclic coordinate of rotation, and U is the gravitational potential energy of the system. Hamilton equations corresponding to Hamiltonian (2) have the form

$$\dot{r} = \frac{p_r}{M}, \quad \dot{R} = \frac{p_R}{M}, \quad \dot{\varphi} = \frac{p_\varphi}{Mr^2},$$
$$\dot{p}_r = \frac{p_\varphi^2}{Mr^3} - \frac{\partial U}{\partial r}, \quad \dot{p}_R = \frac{\partial U}{\partial R}, \quad \dot{p}_\varphi = 0. \tag{3}$$

This leads to the equations of motion for the translational degrees of freedom,

$$\ddot{r} = \frac{p_\varphi^2}{M^2 r^3} - \frac{1}{M}\frac{\partial U}{\partial r}, \tag{4a}$$

$$\ddot{R} = -\frac{1}{M}\frac{\partial U}{\partial R}, \tag{4b}$$

and to the integral of motion for the rotational degree of freedom:

$$p_\varphi = Mr^2\dot{\varphi} = \text{const}. \tag{5}$$

This integral of motion expresses the angular momentum conservation law (the quantity $2\pi p_\varphi/M$ in fluid dynamics corresponds to vorticity).

Let us now define function $U(r, R)$. We consider first Eq. (4a) describing the evolution of a rotating cylinder of radius r. The gravitational force acting on a test particle on the surface of the cylinder is given by

$$F_r = -G\frac{2\chi m}{r}, \tag{6}$$

where G is the gravitational constant, χ is the mass of the cylinder per unit length, and m is the mass of the test particle. Thus, the gravitational force appearing on the right-hand side of Eq. (4a) has the form

$$-\frac{1}{M}\frac{\partial U}{\partial r} = -G\frac{2\chi}{r}. \tag{7}$$

In the present case of a thin toroid, we have $\chi = M/2\pi R$, whence

$$U(r, R) = G\frac{M^2}{\pi R}\ln\frac{r}{R} + c_1(R). \tag{8}$$

In order to determine the dependence of potential energy U on large radius R, we consider the second equation of motion, Eq. (4b). It must describe the gravitational contraction of a thin ring of radius R. The force acting on a test particle located on an infinitely thin ring is given by

$$F_R = -G\frac{Mm}{2\pi R^2}\int_0^\pi \frac{d(\vartheta/2)}{\sin(\vartheta/2)} = \infty. \tag{9}$$

This formula can be derived by direct integration of the contributions from the interaction of the particle with all elements of the ring. In order to avoid divergence for $\vartheta \longrightarrow 0$, we must take into account the finite thickness of the ring. For this purpose, we truncate the diverging part of expression (9), replacing the integration domain $(0, \pi)$ by (ϑ_c, π), where $\vartheta_c = \alpha r/R$ ($\alpha \sim 1$ is a numerical factor). This gives

$$U(r, R) = G\frac{M^2}{2\pi R}\ln\frac{\tilde{\alpha}r}{R} + c_2(r), \tag{10}$$

where $\tilde{\alpha} = \alpha/e$. Setting

$$c_2 = 0$$

in Eq. (10) and

$$c_1(R) = \frac{GM^2}{\pi R}\ln\tilde{\alpha}$$

in Eq. (8), we note that formulas (8) and (10) can be reduced to the same form (the difference will be only in the coefficient 1/2). Such a difference is insignificant for our analysis, and we assume the true numerical coefficient in formula (8).

We can now write the Hamiltonian (2) of a thin toroidal vortex:

$$H = \frac{1}{2M}\left[p_r^2 + p_R^2 + \frac{p_\varphi^2}{r^2}\right] + G\frac{M^2}{\pi R}\ln\frac{\tilde{\alpha}r}{R}. \tag{11}$$

In this case, the equations of motion (4) assume the form

$$\ddot{r} = \frac{p_\varphi^2}{M^2 r^3} - G\frac{M}{\pi R r}, \tag{12a}$$

$$\ddot{R} = -G\frac{M}{\pi R^2}\ln\frac{\alpha r}{R}. \tag{12b}$$

In view of condition (1), we have

$$\frac{r}{R}\ln\frac{r}{R} \ll 1.$$

Then, the force of gravitational attraction along r (12a) is much stronger than the force of gravitational contraction along R (12b). This allows us to divide the evolution of the system over different scales: fast (in r) and slow (in R). It is natural to assume that fast evolution (for practically constant R) leads to the establishment of equilibrium in Eq. (12a). In this case, the force of gravitational attraction is compensated by the centrifugal rotational force:

$$\frac{p_\varphi^2}{M^2 r^3} - G\frac{M}{\pi R r} = 0, \tag{13}$$

whence

$$r_{eq} = \sqrt{\frac{\pi p_\varphi^2 R}{GM^3}}.$$

This expression determines the equilibrium small radius as a function of the large radius, $r_{eq} = r(R)$, while the inequality $r > r_{eq}$ corresponds to the criterion of gravitational instability with the Jeans scale r_{eq}. The latter becomes obvious if we assume that the toroid mass is $M \approx \rho\pi r^2 R$, where ρ is its density [8–10].

As a rough estimate of the time of vortex contraction along small radius r to the quasi-equilibrium state, we can use the expression

$$t_1 \sim \sqrt{\left|\frac{r_0 - r_{eq}(R_0)}{F_r(r_0, R_0)}\right|} = \sqrt{\left|\frac{M^2 R_0^4 - p_\varphi r_0^3\sqrt{\pi M R_0/G}}{p_\varphi^2 - GM^3 r_0^2/\pi R_0}\right|}, \tag{14}$$

where r_0, R_0, and F_r are the initial values of the small and large radii of the vortex and the force appearing on the right-hand side of Eq. (12a), respectively.

If inequality (1) holds at the initial instant, the toroidal vortex will experience, in accordance with the equation of motion (12b) and relation (13), a slow contraction along both radii until they become on the same order of magnitude:

$$r_{eq} \sim R = R_c = \frac{\pi p_\varphi^2}{GM^3} = \frac{r_{eq}^2}{R} \ll r_0. \tag{15}$$

At this stage, the initial assumptions (1) are violated, and the description used above becomes inapplicable. It is impossible in this case to divide the vortex evolution over two translational degrees of freedom r and R, and the vortex should be described as a single compact object with a complex internal structure.

Let us determine some of the most important parameters of the vortex, characterizing it at the second stage (15). Using the angular momentum conservation law (5) and (13), we obtain the following expression for the velocity of particles on the vortex surface:

$$v = \frac{p_\varphi}{Mr} \sim \sqrt{\frac{GM}{\pi R}} \sim \frac{GM^2}{\pi p_\varphi}\frac{r}{R}. \tag{16}$$

It can be seen that the rotational velocity of a vortex, which is in equilibrium in r, is determined only by its mass and the large radius and increases upon contraction along R.[2]

When the vortex reaches the end of the first stage, the velocity attains the value

$$v_{fin} \sim \frac{CM^2}{\pi p_\varphi} \tag{17}$$

and becomes much larger than the initial velocity v_0:

$$\frac{v_{fin}}{v_0} \sim \sqrt{\frac{R_0}{R_c}} \sim \frac{r_0}{R_c} \sim \frac{R_0}{r_0} \gg 1. \tag{18}$$

In analogy with relation (14), we can estimate the time of the vortex contraction along the large radius as

$$t_2 \sim \sqrt{\frac{R_0 - R_c}{F_R[r_{eq}(R_0), R_0]}} = \sqrt{\frac{\pi R_0^2(R_0 - \pi p_\varphi^2/GM^3)}{GM\ln(\alpha\sqrt{\pi p_\varphi^2/GM^3 R_0})}} \gg t_1, \tag{19}$$

where F_R is the force appearing on the right-hand side of Eq. (12b).

Let us also consider the distribution of the kinetic energy acquired by the vortex over the degrees of freedom. We assume that the substance in the vortex is initially almost free and its potential energy and kinetic energy (11) are small as compared to $GM^2/\pi R_c$. Then, at the critical stage (15) of the collapse, the potential and kinetic energies of the substance can be estimated as

$$U_{fin} \sim -\frac{GM^2}{\pi R_c}\ln\tilde{\alpha} \sim -\frac{GM^2}{\pi R_c} = -\frac{G^2M^3}{\pi^2 p_\varphi^2}, \qquad T_{fin}^{(rot)} \sim \frac{p_\varphi^2}{2MR_c^2} = \frac{G^2M^5}{2\pi^2 p_\varphi^2}. \tag{20}$$

(It should be noted that this result is in accordance with the virial theorem for $U \sim R^{-1}$; i.e., $E = -T < 0$.) Since the total energy is an integral of motion and its initial

[2] It should be noted that this is due to the fact that momentum p_φ is canceled out in relation (16). This is a consequence of the equilibrium condition (13), whose form is determined in turn by the form of potential (11).

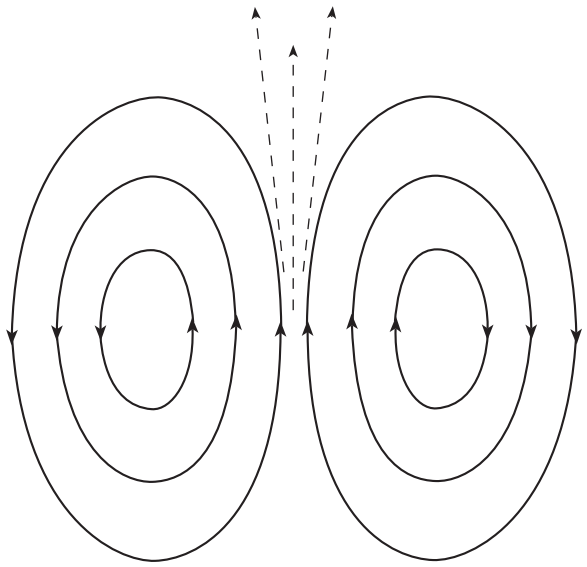

Fig. 2. Cross section of a compact spheroidal vortex of the Hill vortex type.

energy is close to zero, relations (11) and (20) imply that the kinetic energy of translational motion is of the same order of magnitude. Thus, we can conclude that the kinetic energy released during the contraction is distributed uniformly (in order of magnitude) between the rotational and translational degrees of freedom. This fact will be important for the subsequent analysis; in particular, this means that, if the rotational velocity of a particle of the substance is less than doubled at random, it is sufficient for the particle detachment and escape from the system.

3. SECOND STAGE: EVOLUTION OF A COMPACT VORTEX

Let us try to imagine the scenario of contraction of a gravitating vortex, when it is a compact object topologically equivalent to a toroid. We can expect that, under the action of gravitational forces, it will approach a certain spheroidal configuration resembling a Hill vortex [1, 2] (Fig. 2). If we consider such an object as an estimate, we can assume that it possesses a rotational and a translational degree of freedom. The latter is determined by a change in its radius R. The rotational radius of particles (which was the independent quantity r in the previous section) is now approximately equal to $R/2$. The Hamiltonian of such a vortex can be written in the form

$$H = \frac{p_R^2}{2M} + \frac{2p_\varphi^2}{MR^2} - \frac{GM^2}{R}. \tag{21}$$

Here, we have assumed that the form of the second term is the same as in relation (11) with $r = R/2$ and have taken the potential energy of a sphere for the potential energy of the vortex. Hamiltonian (21) corresponds to the equation of motion

$$\ddot{R} = \frac{4p_\varphi^2}{M^2R^3} - \frac{GM}{R^2}. \tag{22}$$

This equation has an equilibrium position, when

$$\frac{4p_\varphi^2}{M^2R^3} - \frac{GM}{R^2} = 0 \quad \text{or} \quad R_{c1} = \frac{4p_\varphi^2}{GM^3}, \tag{23}$$

where R_{c1} plays the role of the Jeans scale as before. Thus, this object is in equilibrium for a radius on the same order of magnitude as that at which the first stage of evolution terminates (cf. relation (15)). This means that, in the problem on the collapse of a thin toroidal vortex, there is no need to consider the evolution of a compact vortex separately. We can assume that equilibrium sets in immediately after the ring acquires parameters (15)–(18).

On the other hand, we can consider the problem of contraction of a vortex, which resembles a Hill vortex from the very outset (Fig. 2), but is initially far from equilibrium. Then, we ultimately arrive at an equilibrium compact vortex with a radius on the same order of magnitude as the radius in (23). The rotational velocity of particles in this case is of the order of velocity (16):

$$v_{\text{fin}} \sim \frac{GM^2}{2p_\varphi}, \tag{24}$$

where

$$\frac{v_{\text{fin}}}{v_{\text{o}}} \sim \frac{R_{\text{o}}}{R_{c1}} \gg 1.$$

Similarly, it can be easily proved that, upon the establishment of equilibrium (23), at least half the released potential energy is transformed into the kinetic energy of rotation (the remaining part being transformed into heat).

4. SCATTERING AND DETACHMENT OF PARTICLES

Thus, after various possible stages of evolution, a toroidal vortex is transformed into a compact object with characteristic parameters (15), (17), and (18) (or (23) and (24)) (see Fig. 2). The rotation velocity of the substance in it is much higher than in the initial vortex. It is worth noting that flows of matter passing through the vortex in the vicinity of its axis are closely spaced. This means that effective scattering of particles may take place in this region. Such a scattering will obviously increase the velocity of a certain fraction of particles. In accordance with the arguments given at the

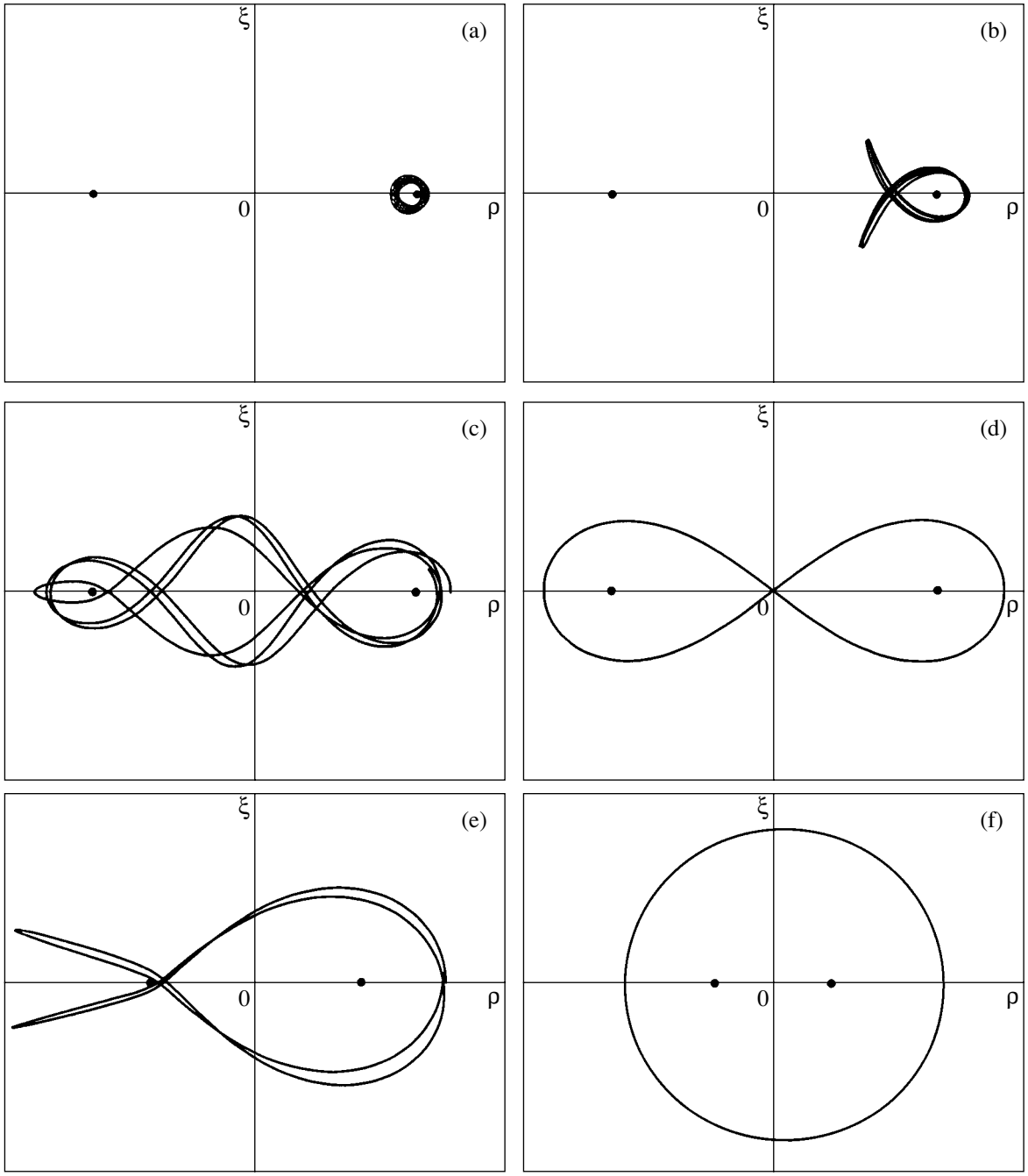

Fig. 3. Typical finite trajectories of a particle in the gravitational field of the ring. In the plane ($\rho = r/r_0$, $\xi = z/r_0$), the particle moves around two attracting centers formed as a result of the dissection of the ring. The initial conditions are $\rho = 1 + \rho_0$, $\xi = 0$, $\dot{\rho} = 0$, and $\dot{\xi} = \sqrt{2}$ (the value of $\dot{\xi}$ is chosen to coincide with the "orbital velocity" in Eq. (12a), which is valid in the vicinity of attracting centers). (a) $\rho_0 = 0.08$, rotation around a single center; (b) $\rho_0 = 0.17$, "dovetail"-type motion around a single center; (c) $\rho_0 = 0.22$, motion of the double "figure-of-eight" type around two centers; (d) $\rho_0 = 0.42$, motion of the "figure-of-eight" type around two centers; (e) $\rho_0 = 0.81$, motion of the "dovetail" type around two centers; (f) $\rho_0 = 2$, rotation around two centers.

end of the previous two sections, a less than double increase in the rotational velocity of particles is enough for gathering a kinetic energy sufficient for the detachment. Consequently, we can expect that a certain fraction of particles from the flows passing along the axis of a compact vortex acquire a sufficient energy as a result of scattering and are ejected from the vortex. Thus, a directional jet carrying away the matter from the center of the vortex can be formed. (Here, we disregard the change in the vortex configuration that

may take place as a result of the mass loss due to such ejection.)

Let us consider one more argument illustrating the above scenario. In the Appendix, we will consider the motion of a test particle in the gravitational field of a ring (thin toroid) with a fixed radius (Fig. 3). For low energies, the particle rotates in a small-radius orbit wound around the ring (Fig. 3a). This motion corresponds to a thin vortex (the possible first stage of the evolution). As the particle energy increases, various complex trajectories appear; however, the orientations of these trajectories do not correspond to vortex motion and we will not consider such trajectories here. Finally, starting from a certain energy value, the particle passes to almost closed trajectories of a figure-of-eight shape (Fig. 3d). The rotational radius of particles becomes on the order of the ring radius (15), which corresponds precisely to the final sage of vortex contraction. The kinetic energy of a particle in such trajectories is close to the energy required for the detachment of particles. The motion of particles in "figures-of-eight" will lead to their effective collisions and scattering in the vicinity of the vortex axis.[3]

We can state that the toroid contraction has qualitatively the same consequences for moving particles as an increase in their energy for a fixed size of the toroid. Obviously, a tendency ultimately leading to the detachment of a fraction of particles exists, the most favorable conditions for this effect being created in the vicinity of the vortex axis. In the long run, this leads to the emergence of an axial (unilateral) jet carrying away the energy, mass, and angular momentum of the vortex. As a result, the vortex contraction will continue (resulting in collapse), the contraction rate dR/dt being determined by the vortex mass loss rate (particle flux in the jet; see below). Thus, the vortex collapse and the emergence of a jet are correlated unambiguously.

5. VORTEX COLLAPSE

Let us consider the consequences of the ejection of particles from a vortex according to the scenario proposed in the previous section. The particle flow carries away the mass, energy, and angular momentum of the vortex. The latter quantities can be estimated as

$$E \sim -\frac{Mv^2}{2}, \quad p_\varphi \sim \frac{MRv}{2}, \tag{25}$$

where all the quantities correspond to an equilibrium compact vortex (see Section 3) and $E = -T$ (see above). Relations (25) lead to

$$R \sim \frac{p_\varphi}{\sqrt{-ME}}. \tag{26}$$

[3] The existence of flows of matter of the figure-of-eight type also follows from the hydrodynamic model of a Maxwell vortex (see, for example, [2]).

Differentiating this relation with respect to time, we obtain

$$\dot{R} \sim \frac{1}{\sqrt{-ME}}\dot{p}_\varphi - \frac{p_\varphi}{2(-ME)^{3/2}}(M\dot{E} + E\dot{M}). \tag{27}$$

We assume that the particle flux is comparatively small and this process occurs at a much lower rate than the rate of establishment of equilibrium of the compact vortex. In this case, we can estimate the change in the characteristics of the vortex carried away by the particle flow as

$$\begin{gathered}\dot{M} = -J, \quad \dot{E} \sim J\frac{v^2}{2} \sim -\frac{J}{M}E, \\ \dot{p}_\varphi \sim -J\frac{Rv}{2} \sim -\frac{J}{M}p_\varphi,\end{gathered} \tag{28}$$

where J is the mass flux in the ejected jet of matter. Substituting relations (28) into (27) and taking into account relation (26), we obtain

$$\dot{R} \sim -R\frac{J}{M} = R\frac{\dot{M}}{M}. \tag{29}$$

The solution to this equation has the form

$$R(t) = R(0)\left(\frac{M(t)}{M(0)}\right)^\beta. \tag{30}$$

Here, $\beta \sim 1$ is a certain positive constant (emerging due to the fact that we obtained above only order-of-magnitude estimates for the vortex parameters), and the initial instant of time corresponds to the arrival of the vortex at the compact equilibrium state and to the beginning of the effective scattering and detachment of particles. The time dependence of the vortex mass $M(t)$ is determined for the specific mechanism of particle scattering.

In the general case, the mass flux of matter, $J = -\dot{M}$, is a function of the main vortex parameters: mass, energy, and angular momentum. If we assume in the simplest case that the flux of matter is proportional to the vortex mass and weakly depends on other parameters ($J = kM$), Eqs. (28)–(30) will lead to the exponential laws

$$M(t) = M(0)e^{-kt}, \quad R(t) = R(0)e^{-\beta kt}. \tag{31}$$

Thus, Eqs. (29)–(31) show that the scattering of particles and ejection of matter indeed lead to the collapse of a compact vortex.

The characteristic time scale of the collapse is defined as

$$t_{\text{col}} \sim |M/\dot{M}|. \tag{32}$$

In accordance with the above assumptions, the collapse must be slow as compared to the characteristic time of the vortex contraction to the equilibrium state, which corresponds to $t_{\text{col}} \gg t_2$.

6. GENERALIZATIONS

We can easily generalize the above analysis to the case when a system contains a massive body at its center and when the vortex rotates about its axis. These factors lead to the emergence of additional terms in Eq. (12):

$$\ddot{R} = -G\frac{M}{\pi R^2}\ln\frac{\alpha r}{R} - G\frac{\tilde{M}}{R^2} + \frac{p_\vartheta^2}{M^2R^3}. \quad (33)$$

Here, $\tilde{M}$ is the mass of the central object and $p_\vartheta = MR^2\dot{\vartheta}$ = const is the angular momentum associated with the rotation of the toroid about its axis. The supplementary terms do not affect in any way the evolution of the system along the small radius. Their effect on the vortex evolution along R can be divided into the following limiting cases.

1. If $\max(G\tilde{M}/R_c^2,\ p_\vartheta^2/M^2R_c^3) \ll GM/\pi R_c^3$, the effect of these terms can be disregarded, and the entire dynamic analysis carried out in Sections 2 and 3, as well as the corresponding conclusions, remains in force. However, the presence of the central mass in the region of the most probable intersection of particle flows may affect their scattering and detachment.

2. If $\pi\tilde{M}/M \ll 1$ and $\pi p_\vartheta^2/GM^3R_c \gg 1$, the rotation of the toroid about its axis arrests contraction before it reaches its critical stage $r \sim R \sim R_c$. The equilibrium state corresponds to the large radius defined by the relation

$$\frac{GM^3R}{\pi p_\vartheta^2}\ln\left\{\alpha\sqrt{\frac{\pi p_\vartheta^2}{GM^3R}}\right\} = 1$$

and to the small radius defined by substituting the large radius into relation (18). In this case, the probability of effective scattering and detachment of particles at the middle of the vortex virtually vanishes and, hence, collapse does not take place.

3. If $\pi\tilde{M}/M \gg 1$ and $\pi p_\vartheta^2/GM^3R_c \ll 1$, the revolution of a vortex around its axis is insignificant, and the central mass enhances the contraction. The vortex contracts to a compact object and its subsequent behavior depends on the scenario of direct interaction of the vertex with the central mass. Naturally, the scattering of particles and the possible vortex collapse in this case also depend to a considerable extent on the interaction of the matter with the central mass.

4. If $\pi\tilde{M}/M \gg 1$ and $\pi p_\vartheta^2/GM^3R_c \gg 1$, the last two terms on the right-hand side of Eq. (33) compete. If the first term is greater than the second (the attraction of the central object prevails), the situation corresponds to case 3; for the opposite relation, we have case 2.

ACKNOWLEDGMENTS

This study was partly supported by INTAS (grant no. 00-00292).

APPENDIX

Motion of Particles in the Gravitational Field of the Ring

We assume that the gravitational field of a thin toroid is close to the field of an infinitely thin ring of the same mass. Let the ring radius be r_0 and r, φ, and z be the cylindrical coordinates, $z = 0$ corresponding to the plane of the ring. The gravitational potential of the ring is given by

$$U(r, z) = -\frac{GM}{2\pi}\int_0^{2\pi}\frac{d\varphi}{\sqrt{z^2 + r^2 + r_0^2 - 2rr_0\cos\varphi}}.$$

Introducing the dimensionless variables $\xi = z/r_0$ and $\rho = r/r_0$ and time $\tau = t\sqrt{GM/2\pi r_0^3}$, we obtain the equations of motion of a test particle in this potential:

$$\rho'' = -\int_0^{2\pi}\frac{(\rho - \cos\varphi)}{(\xi^2 + \rho^2 + 1 - 2\rho\cos\varphi)^{3/2}}d\varphi,$$

$$\zeta'' = -\int_0^{2\pi}\frac{\xi}{(\xi^2 + \rho^2 + 1 - 2\rho\cos\varphi)^{3/2}}d\varphi,$$

where the primes indicate differentiation with respect to τ, and we assume that $\dot{\varphi} = 0$ for a particle.

Figure 3 shows typical results of numerical calculations based on these equations for a finite motion. The trajectories lie in the (ρ, ξ) plane and are given in increasing order of the particle energy. It can easily be seen that, in trajectories of the "dovetail" type (see Figs. 3b and 3e), a particle moves practically along the same curve in opposite directions; consequently, such motion cannot be maintained in the framework of collective motion of particles since the latter motion would inevitably lead to collisions and strong scattering. In addition, the trajectories in Fig. 3c and 3f cannot exist for a collective vortex motion of particles since different segments of a trajectory correspond to opposite directions of vorticity. Thus, only the trajectories in Figs. 3a and 3d can exist in the framework of collective vortex motion of particles. The trajectory in Fig. 3a is the cross section of a thin toroidal vortex of the Maxwellian vortex type considered in Section 2, while the "figure-of-eight" in Fig. 3d can appear during motion of particles in a compact vortex of the type of a Hill vortex emerging at the late stage of contraction (see Section 3).

REFERENCES

1. H. Lamb, *Hydrodynamics*, 6th ed. (Cambridge Univ. Press, Cambridge, 1932; Gostekhizdat, Moscow, 1947).
2. M. A. Lavrent'ev and B. V. Shabat, *Problems of Hydrodynamics and Their Mathematical Models* (Nauka, Moscow, 1973).
3. P. G. Saffman, *Vortex Dynamics* (Cambridge Univ. Press, Cambridge, 1995; Nauchnyĭ Mir, Moscow, 2000).
4. V. I. Petviashvili and O. A. Pokhotelov, *Single Waves in the Plasma and Atmosphere* (Énergoatomizdat, Moscow, 1989).
5. Yu. A. Stepanyants and A. P. Fabrikant, *Wave Propagation in Shear Flows* (Nauka, Moscow, 1996).
6. E. A. Kuznetsov and V. P. Ruban, Zh. Éksp. Teor. Fiz. **118**, 893 (2000) [JETP **91**, 775 (2000)].
7. V. F. Kop'ev and S. A. Chernyshev, Usp. Fiz. Nauk **170**, 713 (2000) [Phys.–Usp. **43**, 663 (2000)].
8. D. Linden-Bell, NATO ASI Ser., Ser. B **156**, 155 (1986).
9. B. F. Schutz, NATO ASI Ser., Ser. B **156**, 123 (1986).
10. J. L. Tassoul, *Theory of Rotating Stars* (Princeton Univ. Press, Princeton, N.J., 1978; Mir, Moscow, 1982).
11. *Physics of Extragalactic Radio-Sources*, Ed. by R. D. Dagkesamanskiĭ (Mir, Moscow, 1987).
12. C. J. Lada, Annu. Rev. Astron. Astrophys. **23**, 267 (1985).
13. G. V. Ustyugova, R. V. E. Lavelace, M. M. Romanova, *et al.*, Astrophys. J. **541**, L21 (2000).
14. R. Antonucci, Annu. Rev. Astron. Astrophys. **31**, 473 (1993).
15. M. Ansorg, A. Kleinwachter, and R. Meinel, gr-qc/0211040.

Translated by N. Wadhwa

Journal of Experimental and Theoretical Physics, Vol. 96, No. 6, 2003, pp. 993–1005.
Translated from Zhurnal Éksperimental'noĭ i Teoreticheskoĭ Fiziki, Vol. 123, No. 6, 2003, pp. 1131–1144.

ATOMS, SPECTRA, RADIATION

Quantum Dynamics and Statistics of a Bose Condensate Generated by an Atomic Laser

A. V. Kozlovskii

Lebedev Institute of Physics, Russian Academy of Sciences, Moscow, 119991 Russia
e-mail: kozlovsk@sci.lebedev.ru

Received March 20, 2002

Abstract—A self-consistent quantum theory is developed for an atomic laser utilizing cooling of atoms in a trap by the method of stimulated evaporation. The model describes the pumping and extraction of the atomic field from a trap upon its interaction with independent atomic reservoirs. The stimulated collisions between atoms in the trap, which produce a Bose condensate in the lower state of the trap, are considered. The interaction of atoms with a phonon field causes spontaneous transitions between the discrete states of the trap. Calculations performed for the three- and four-level models of the trap showed the possibility of generation of a strongly squeezed sub-Poisson Bose condensate. *© 2003 MAIK "Nauka/Interperiodica".*

1. INTRODUCTION

The recent successful experiments on the production of a Bose condensate in traps showed the possibility of creation of coherent sources of material waves (atomic lasers) [1, 2]. As the resonator of an atomic laser, a parabolic magnetic trap is used, the discrete energy levels of the trap pumped by an external source of cooled atoms representing the resonator modes. The conditions for producing a Bose condensate are realized at least for the lower state of the trap (the condensate mode). The excitation of atoms from their inner states to the electronic states, in which atoms can be captured by a trap or extracted from it, is performed by a radio- or microwave electromagnetic field. The continuous and pulsed lasing regimes are achieved in atomic lasers by the same means, but at different values of the parameters of the electromagnetic field used for pumping and extraction of the atomic field from the trap. The lasing dynamics of the atomic laser is determined by the balance between the introduction of atoms to the trap and the extraction of the Bose condensate from the trap taking into account the cooling rate (population of the lower states of the trap), which is also stimulated by the external electromagnetic field. A fundamental property of the atomic laser is the coherence of the field produced. The coherence and quantum-statistical properties of the field are studied in the quantum optics of atomic fields [3–11]. The modern phenomenological semiclassical theories [12–18] and quantum-mechanical theories [3–11, 19–29], which consider models of the atomic laser with different schemes of pumping, cooling, and extraction of the field from the trap, predict the presence of the lasing threshold, saturation, and a high degree of coherence of the Bose condensate generated by the atomic laser [3, 9, 10, 23]. Note that the semiclassical theory of the atomic laser based on the mean field approximation [16–18] does not allow one to study the quantum statistics of the field because in this case the preliminarily specified phenomenological statistics of the atomic gas are used. Only a completely quantum-mechanical theory permits one to investigate quantum-statistical effects and to determine the coherent properties of the atomic-laser field. The quantum-mechanical theories of the atomic laser being currently developed use a model with a finite number of atomic-field modes in the trap. Such an approach allows one to study the effect of collisions between atoms inside the trap on the dynamics and statistics of a Bose condensate generated by the atomic laser. This model of the laser corresponds to the experimental conditions under which processes of stimulated cooling (evaporation) rapidly deplete the upper energy levels of the trap. In this paper, the self-consistent theory of Bose condensation is developed for an atomic gas in a trap, taking into account collisions between atoms under thermally nonequilibrium conditions. The theory is based on the solution of the control equation for the density matrix simultaneously with the system of generalized Hartree–Fock equations for the wave functions of the atomic field in the states of the trap.

The numerical calculations of the dynamics and statistics of an atomic field are performed in the approximation of the eigenfunctions of the trap for the three- and four-level models of a laser. The model describes pumping processes, the extraction of the field from the ground state of the trap, and spontaneous transitions, as well as the collision redistribution of atoms among the states of the trap. The lasing dynamics of an atomic laser is analyzed for different pump rates and different frequencies of collisions between atoms, and the rates of spontaneous transitions of atoms between the trap levels are calculated. It is shown that the Bose condensate generated by an atomic laser exists in a squeezed

quantum state with sub-Poisson fluctuations of the number of atoms. For large Bose condensates with the average number of atoms of the order of 10^6, the ratio of the dispersion of the number of atoms to their average number (the Fano factor for the atomic field) can achieve 0.5.

The model of an atomic laser is presented in Section 2. The effective many-particle Hamiltonian is considered for the open system of colliding Bose atoms in a trap, which describes their interaction with the atomic pump and loss reservoirs, as well as the phonon field inducing spontaneous transitions between the discrete energy levels of the trap. Section 3 is devoted to the analysis of the self-consistent dynamics of atomic fields. Approximations are considered which are used for calculations of the wave functions of the atomic field in the trap simultaneously with the solution to the equation for the reduced density matrix. In Section 4, the control equation is obtained, within the framework of the Born–Markoff approximation, for the density operator in the model of an atomic laser with a finite number of levels in the approximation of the eigenstates of the trap. The approximation is considered at which collisions of atoms in the trap do not affect the spatial distribution of the atomic field. The results of numerical calculations of the dynamics and statistics of the Bose gas are presented in Section 5. Conclusions are formulated in Section 6.

2. MODEL OF AN EVAPORATION-BASED ATOMIC LASER

We will describe the open system of atoms in a trap, which interact with reservoirs, by the method of secondary quantization of atomic fields using the creation and annihilation operators, which are defined as

$$\Psi_s(\mathbf{r}) = \sum_j a_j \phi_j(\mathbf{r}), \quad a_j = \int d^3\mathbf{r}\phi_j^*(\mathbf{r})\Psi_s(\mathbf{r}), \tag{1}$$

$$\Psi_\alpha(\mathbf{r}) = \sum_{\lambda=0}^{\infty} b_{\alpha\lambda}\psi_{\alpha\lambda}(\mathbf{r}),$$
$$b_{\alpha\lambda} = \int d^3r \psi_{\alpha\lambda}^*(\mathbf{r})\Psi_\alpha(\mathbf{r}), \quad \alpha = p, \text{out}, \tag{2}$$

where $\Psi_s(\mathbf{r})$ and $\Psi_s^\dagger(\mathbf{r})$ are the annihilation and creation operators for an atom at the point $\mathbf{r}$ in the trap, respectively, and $\Psi_\alpha(\mathbf{r})$ and $\Psi_\alpha^\dagger(\mathbf{r})$ are the annihilation and creation operators, respectively, for particles in pump reservoirs ($\alpha = p$) and in reservoirs performing the extraction of the atomic field from the trap (α = out). The *c*-numerical functions $\phi_j(\mathbf{r})$ and $\psi_{\alpha\lambda}(\mathbf{r})$ entering the right-hand sides of Eqs. (1) and (2) determine the spatial distributions of the fields.

The above operators satisfy the boson permutation relations

$$[\Psi_\alpha(\mathbf{r}), \Psi_{\alpha'}^\dagger(\mathbf{r}')] = \delta_{\alpha,\alpha'}(\mathbf{r}-\mathbf{r}'),$$
$$\alpha, \alpha' = s, p, \text{out}, \tag{3}$$
$$[\Psi_\alpha(\mathbf{r}), \Psi_{\alpha'}(\mathbf{r}')] = [\Psi_\alpha^\dagger(\mathbf{r}), \Psi_{\alpha'}^\dagger(\mathbf{r}')] = 0.$$

The quantum-mechanical average number of atoms captured by the trap is

$$\int d^3r \langle \Psi_s^\dagger(\mathbf{r})\Psi_s(\mathbf{r})\rangle = \sum_j \langle a_j^\dagger a_j\rangle = \bar{N}. \tag{4}$$

Along with the atomic reservoirs described above, we will consider the reservoir of a phonon field, which is a source of spontaneous transitions between the states of the trap (see also [27, 28]). In addition, we will consider an electromagnetic field involved in the processes of extraction of the field from the trap and trap pumping, as well as in the process of stimulated cooling of atoms in the trap [1, 2].

We consider the effective many-particle Hamiltonian of the problem, which contains the free-energy terms and the operators of interaction of the system with reservoirs, as well as operators describing the interaction between atoms in the trap, in the form

$$H = H_s + \sum_\beta H_{R\beta} + \sum_\beta V_{sR\beta} + V_{\text{coll}}. \tag{5}$$

The Hamiltonian (4) describing the atomic Bose condensate in the Hartree approximation can be written, using the field operators (1) and (2), as a sum of the following terms:

the energy of atoms in the trap,

$$H_s = \int d^3r \times\left[-\frac{\hbar^2}{2m}\nabla\Psi_s^\dagger(\mathbf{r})\nabla\Psi_s(\mathbf{r}) + \Psi_s^\dagger(\mathbf{r})V_{\text{tr}}(\mathbf{r})\Psi_s(\mathbf{r})\right]; \tag{6}$$

the energy operators of the atomic pump reservoir and the reservoir of extraction of atoms from the trap ($\beta = p$, out),

$$H_{R\beta} = \int d^3r \times\left[-\frac{\hbar^2}{2m}\nabla\Psi_\beta^\dagger(\mathbf{r})\nabla\Psi_\beta(\mathbf{r}) + \Psi_\beta^\dagger(\mathbf{r})V_\beta(\mathbf{r})\Psi_\beta(\mathbf{r})\right]; \tag{7}$$

the energy operator of the electromagnetic field applied to the trap (β = EM),

$$H_{R,\text{EM}} = \sum_j \hbar\omega_j b_{\text{EM},j}^\dagger b_{\text{EM},j}; \tag{8}$$

and the free energy of the phonon field (β = phon),

$$H_{R,\,\mathrm{phon}} = \sum_{\lambda=0}^{\infty} \hbar\omega_{\mathrm{phon},\,\lambda} b^{\dagger}_{\mathrm{phon},\,\lambda} b_{\mathrm{phon},\,\lambda}. \tag{9}$$

The terms describing the interaction of the system of atoms in the trap with the reservoirs have the form

$$V_{sR\mathrm{out}} = \hbar\int d^3r \Psi^{\dagger}_{\mathrm{out}}(\mathbf{r})\Lambda_{\mathrm{out}}(\mathbf{r}, t)\Psi_s(\mathbf{r}) + \mathrm{h.c.}, \tag{10}$$

$$V_{sRp} = \hbar\int d^3r \Psi^{\dagger}_{s}(\mathbf{r})\Lambda_{p}(\mathbf{r}, t)\Psi_p(\mathbf{r}) + \mathrm{h.c.}, \tag{11}$$

$$\begin{aligned} V_{sR\mathrm{phon}} &= \hbar\sum_{\lambda=0}^{\infty}\int d^3r \Psi^{\dagger}_{s}(\mathbf{r}) \\ &\times b_{\mathrm{phon},\,\lambda}\Lambda_{sp,\,\lambda}(\mathbf{r})\Psi_s(\mathbf{r}) + \mathrm{h.c.}, \end{aligned} \tag{12}$$

$$\begin{aligned} V_{\mathrm{coll}} &= \frac{1}{2}\int d^3r\int d^3r' \Psi^{\dagger}_{s}(\mathbf{r})\Psi^{\dagger}_{s}(\mathbf{r}') \\ &\times U(\mathbf{r}-\mathbf{r}')\Psi_s(\mathbf{r})\Psi_s(\mathbf{r}'). \end{aligned} \tag{13}$$

The functions Λ entering (10)–(12) are the coupling constants of the atomic field of the trap with the fields of reservoirs.

We will consider the electromagnetic field applied to the trap classically. In this case, the operator (8) represents a *c*-numerical constant.

Neutral atoms forming the Bose condensate are located in a parabolic trap with the potential

$$V_{\mathrm{tr}}(\mathbf{r}) = \frac{m}{2}\sum_{\alpha=x,y,z}\omega^2_{\alpha}r^2_{\alpha},$$

where m is the atom mass. The effective interaction between atoms in the trap is described by the pseudopotential

$$V(\mathbf{r}-\mathbf{r}') = u\delta(\mathbf{r}-\mathbf{r}'), \quad u = 4\pi a_0\hbar^2/m,$$

(where a_0 is the collision length for the scattering of *S* waves) and by the dipole–dipole two-particle interaction potential $V_{dd}(\mathbf{r}-\mathbf{r}')$, i.e.,

$$U(\mathbf{r}-\mathbf{r}') = V(\mathbf{r}-\mathbf{r}') + V_{dd}(\mathbf{r}-\mathbf{r}').$$

The terms in (11) and (10) containing the operators $\Psi_p(r)$ and $\Psi_{\mathrm{out}}(r)$ are related to the reservoirs from which the trap levels are pumped by external sources and the atoms are extracted from the trap. In particular, the atomic field can be extracted during the interaction of atoms with a resonance radio-frequency field, which induces electronic transitions between the Zeeman sublevels of the atoms [1, 2]. In this case, $\Lambda_{\mathrm{out}}(\mathbf{r}, t) = \Omega(\mathbf{r}, t)$, where $\Omega(\mathbf{r}, t) = \boldsymbol{\mu}\cdot\mathbf{B}(\mathbf{r}, t)/\hbar$ is the Rabi frequency of an atom in the magnetic field $\mathbf{B}(\mathbf{r}, t)$, $\boldsymbol{\mu}$ is the transition magnetic moment, and $\Psi_{\mathrm{out}}(\mathbf{r})$ is the creation operator for a free atom extracted from the trap. The pump operator (11) is defined similarly with the help of the annihilation operator $\Psi_p(\mathbf{r})$ for an atom in the incoherent pump reservoir, which is, in this particular case, in thermodynamic equilibrium. We will assume below that the interaction of atoms with the fields performing pumping, the extraction of the condensate, and stimulated evaporation are weak (low Rabi frequencies); i.e., we will consider the case of a cw atomic laser [1]. At the same time, we will take into account the time dependence of the coupling constants.

Using the field operators (1) and (2), we can write the Hamiltonian (5) in the form

$$\begin{aligned} H = &\sum_j \hbar\omega_j a^{\dagger}_j a_j + \sum_{\alpha=p,\,\mathrm{out},\,\mathrm{phon}}\sum_{\lambda=0}^{\infty}\hbar\omega_{\alpha\lambda}b^{\dagger}_{\alpha\lambda}b_{\alpha\lambda} \\ &+ \sum_{\lambda=0}^{\infty}\Bigg\{\sum_{i>j}\hbar(\Gamma_{\lambda,\,i,\,j}b^{\dagger}_{\mathrm{phon},\,\lambda}a_i a^{\dagger}_j + \mathrm{h.c.}) \\ &+ \sum_i \hbar[\kappa_{\lambda,\,i}(t)b_{P,\,\lambda}a^{\dagger}_i + \mathrm{h.c.}] \\ &+ \sum_j \hbar(\mu_{\lambda,\,j}(t)b^{\dagger}_{\mathrm{out},\,\lambda}a_j + \mathrm{h.c.})\Bigg\} \\ &+ \frac{1}{2}\sum_{ijkl}\hbar g_{i,\,j,\,k,\,l}a^{\dagger}_i a^{\dagger}_j a_k a_l, \end{aligned} \tag{14}$$

where the energy of the jth state of the trap is

$$\begin{aligned} \hbar\omega_j &= \int d^3r\phi^*_j(\mathbf{r})K(\mathbf{r})\phi_j(\mathbf{r}), \\ K(\mathbf{r}) &= -\frac{\hbar^2}{2m}\nabla^2 + V_{\mathrm{tr}}(\mathbf{r}), \end{aligned} \tag{15}$$

and $\hbar\omega_{\alpha\lambda}$ is the energy of the harmonic oscillator λ in the reservoir α.

The coupling constants characterizing the interaction with reservoirs are defined as

$$\mu_{\lambda,\,i}(t) = \int d^3r\Psi^*_{\mathrm{out},\,\lambda}(\mathbf{r})\Lambda_{\mathrm{out}}(\mathbf{r}, t)\phi_i(\mathbf{r}), \tag{16}$$

$$\kappa_{\lambda,\,j}(t) = \int d^3r\Psi_{p,\,\lambda}(\mathbf{r})\Lambda_{p}(\mathbf{r}, t)\phi^*_j(\mathbf{r}), \tag{17}$$

$$\Gamma_{\lambda,\,i,\,j} = \int d^3r\phi^*_j(\mathbf{r})\Lambda_{sp,\,\lambda}(\mathbf{r})\phi_i(\mathbf{r}). \tag{18}$$

The coupling constants for elastic and inelastic collisions between atoms in the trap are

$$\begin{aligned} g_{i,\,j,\,k,\,l} &= \frac{u}{2}\int d^3r\phi^*_i(\mathbf{r})\phi^*_j(\mathbf{r})\phi_k(\mathbf{r})\phi_l(\mathbf{r}) \\ &+ \frac{1}{2}\int d^3r'\int d^3r\phi^*_i(\mathbf{r})\phi^*_j(\mathbf{r}')V_{dd}(\mathbf{r}-\mathbf{r}')\phi_k(\mathbf{r})\phi_l(\mathbf{r}'). \end{aligned} \tag{19}$$

The first two terms in (14) are the energy of atoms in the trap and the intrinsic energy of oscillators in res-

ervoirs, respectively. The next three terms in (14), corresponding to $V_{sR\beta}$ in (4), are the sum of potentials of interaction of atoms in the trap with reservoirs, which cause the spontaneous decay from the discrete energy levels of the trap, the extraction of atoms from the trap, and pumping. The last term is the interaction potential V_{coll} for elastic and inelastic binary collisions between atoms captured by the trap.

In this paper, we consider the model of an atomic laser in which atoms are cooled during evaporation [1, 2]. Preliminarily cooled atoms enter a trap of reservoirs, which are in thermodynamic equilibrium. It is assumed that atoms in the trap can be in four energy states and are characterized by a set of creation (annihilation) operators $a_i^\dagger$ (a_i), where $i = 0, 1, 2, 3$. It is also assumed that the high-lying energy states of the trap are weakly populated due to stimulated evaporation performed with the help of a radio-frequency electromagnetic field applied to the trap [1, 2]. A Bose condensate is obtained in the lower energy state $|0\rangle$, from which the accumulated condensate enters, at the rate κ_{out}, a reservoir of the continuous spectrum of vacuum states (output laser radiation). Different methods for the extraction of the Bose condensate from a trap were considered in papers [17, 25]. Each of the states of the trap is pumped independently at the rate p_i from the corresponding incoherent reservoirs with the average occupation numbers $\bar{N}_i^{\text{pump}}$. Dissipation processes related to the exchange of atoms in the trap with the corresponding reservoirs with the average occupation numbers $\bar{N}_i^{\text{decay}}$ occur at the rates γ_i. The pumping of an atomic laser from thermal reservoirs was considered in papers [10, 19–21].

For binary collisions between atoms in the trap in a particular case of four levels considered below, the last term in (14) represents the interaction energy of colliding atoms in the dipole approximation and consists of the elastic and inelastic contributions

$$V_{\text{coll}} = V_{\text{elast}} + V_{\text{inelast}}, \tag{20}$$

where

$$V_{\text{elast}} = V_{jj} + V_{ij}$$
$$= \sum_{j=0}^{3} \hbar g_{jjjj} a_j^{\dagger 2} a_j^2 + \sum_{i,j=0,\, i<j} \hbar g_{ijij} a_i^\dagger a_j^\dagger a_i a_j,$$

$$V_{\text{inelast}} = \hbar g_{0211} a_0^\dagger a_2^\dagger a_1^2 + \hbar g_{1102} a_1^{\dagger 2} a_0 a_2 + \hbar g_{0312} a_1 a_2 a_3^\dagger a_0^\dagger + \hbar g_{1203} a_0 a_3 a_1^\dagger a_2^\dagger + \hbar g_{1322} a_1^\dagger a_3^\dagger a_2^2 + \hbar g_{2213} a_2^{\dagger 2} a_1 a_3, \tag{21}$$

$$g_{ijkl} = g_{ijkl}^*.$$

3. SPATIAL DISTRIBUTION OF ATOMS IN TRAP MODES

We will use the variational principle to derive equations determining the spatial dependences $\{\phi_j(\mathbf{r})\}$ of field operators (1). We will require the stationarity of the functional

$$E[\phi_j(\mathbf{r}), \phi_j^*(\mathbf{r})] = \int d^3 r \langle H(\mathbf{r}) \rangle$$

at each instant upon variation of $\{\phi_j(\mathrm{r})\}$. By imposing the orthonormality condition

$$\int d^3 r \phi_i^*(\mathbf{r}) \phi_j(\mathbf{r}) = \delta_{ij},$$

for a discrete spectrum on the basis of functions $\{\phi_j(\mathrm{r})\}$, we will use the Lagrange method of multipliers. In this case, the variational equation will take the form

$$\delta E - \sum_j \varepsilon_j \delta \int d^3 r \phi_j^*(\mathbf{r}) \phi_j(\mathbf{r}) = 0, \tag{22}$$

which gives the equations for the level energy eigenvalues $\{\boldsymbol{\varepsilon}_j\}$ and functions $\{\phi_j(\mathbf{r})\}$, whose form can be found from the relation

$$\frac{\delta}{\delta \varphi_j^*} \int d^3 r \langle \bar{H}(\mathbf{r}) \rangle = 0, \tag{23}$$

following from (22), where

$$\langle \bar{H}(\mathbf{r}) \rangle = \langle H[\phi_j(\mathbf{r}) \phi_j^*(\mathbf{r})] \rangle - \sum_j \varepsilon_j \phi_j(\mathbf{r}) \phi_j^*(\mathbf{r}) \langle n_j \rangle. \tag{24}$$

Let us define now the mean value of the total Hamiltonian (4) as

$$\langle H[\phi_j(\mathbf{r}, t), \phi_j^*(\mathbf{r}, t)] \rangle = \mathrm{Sp}(\sigma_{\text{total}}(t) H[\phi_j(\mathbf{r}), \phi_j^*(\mathbf{r})]),$$

where σ_{total} is the total density operator of the system and reservoirs interacting with the system. Upon averaging with a time-dependent density operator, one-particle eigenfunctions $\{\phi_j(\mathbf{r}, t)\}$ and eigenvalues $\{\boldsymbol{\varepsilon}_j(t)\}$ acquire a parametric dependence on time. By using the assumption of a weak interaction between the system and reservoirs (the Born approximation), we consider the total density operator in the form of a sum

$$\sigma_{\text{total}}(t) = \rho(t) f_0 + \Delta\rho^{(1)}(t), \tag{25}$$

where $\rho(t) = \mathrm{Sp}_R(\sigma_{\text{total}}(t))$ is the reduced density operator of the system representing the trace of the total density operator over the variables of reservoirs. The quantity f_0 in (25) is the product of the density operators of independent reservoirs in thermodynamic equilibrium. In the interaction representation, the last term in (25) in the first approximation over the potential of interaction

$V_{sR} = \sum_\beta V_{sR\beta}$ of the system with reservoirs has the form

$$\Delta\rho^{(1)}(t) = \frac{1}{i\hbar}\int_0^t [V_{sR}(t'), \rho(t') f_0]dt', \quad (26)$$

where […, …] is a commutator. By performing functional differentiation in the variational equation (23) and using (14)–(19), we obtain the system of coupled eigenvalue differential equations of the type (for any j)

$$L_{\text{coh}}[\phi_j(\mathbf{r}, t)] + L_{\text{irr}}[\phi_j(\mathbf{r}, t)] = 0. \quad (27)$$

The coherent part of Eq. (27) appears after the calculation of the quantum-mechanical mean for the terms containing the system operators with the help of the first term in (25). The terms determining the change of the wave functions of atoms in the trap caused by the interaction with reservoirs (irreversible processes) are contained in the second term in Eq. (27). For coherent terms, we obtain

$$L_{\text{coh}}[\phi_j(\mathbf{r}, t)] = K_j(\mathbf{r}, t)\phi_j(\mathbf{r}, t)\langle n_j(t)\rangle + \sum_{i,k,l}\phi_k(\mathbf{r}, t) \times \int d^3 r'\phi_i^*(\mathbf{r}', t)U(\mathbf{r}-\mathbf{r}')\phi_l(\mathbf{r}', t)\langle a_j^\dagger(t)a_i^\dagger(t)a_k(t)a_l(t)\rangle, \quad (28)$$

where

$$K_j(\mathbf{r}, t) = -\frac{\hbar^2}{2m}\nabla^2 + V_{\text{tr}}(\mathbf{r}) - \varepsilon_j(t).$$

The irreversible terms in (27), which appear after the calculation of the mean using the total density operator (25), prove to be, within the framework of our model, proportional to the mean values of the reservoir operators. Since we assume in our calculations that the reservoirs are incoherent or are in thermodynamic equilibrium, it is easy to see that

$$\begin{aligned}\langle b_{\beta,\lambda}\rangle &= \langle b_{\beta,\lambda}^\dagger\rangle = 0,\\ \langle b_{\beta,\lambda}b_{\beta',\lambda'}\rangle &= \langle b_{\beta,\lambda}^\dagger b_{\beta',\lambda'}^\dagger\rangle = 0,\\ \langle b_{\beta,\lambda}b_{\beta',\lambda'}^\dagger\rangle &= \delta_{\lambda,\lambda'}\delta_{\beta,\beta'}(\bar{N}_\lambda^{(\alpha)} + 1),\\ \langle b_{\beta,\lambda}^\dagger b_{\beta',\lambda'}\rangle &= \delta_{\lambda,\lambda'}\delta_{\beta,\beta'}\bar{N}_\lambda^{(\alpha)}.\end{aligned} \quad (29)$$

By virtue of these relations, the irreversible terms in (27) proportional to $b_{\beta,\lambda}$, $\langle b_{\beta,\lambda}^\dagger\rangle$, $\langle b_{\beta,\lambda}b_{\beta',\lambda'}\rangle$, $\langle b_{\beta,\lambda}^\dagger b_{\beta',\lambda'}^\dagger\rangle$ are zero. Therefore, in the Born–Markoff approximation for the interaction of the system with reservoirs, we have

$$L_{\text{irr}}[\phi_j(\mathbf{r}, t)] = 0. \quad (30)$$

This means that the irreversible processes under consideration lead to the appearance of additional terms in equations for the wave functions and introduce changes in the time of average values $\langle n_j(t)\rangle$ and $\langle a_j^\dagger(t)a_i^\dagger(t)a_k(t)a_l(t)\rangle$ entering into these equations.

The distribution of the Bose condensate density can be calculated using different approximate equations, which follow directly from the general equation (28). By considering a system of atoms in a trap as a canonical ensemble in thermodynamic equilibrium and assuming that the number of atoms in the trap is fixed [27–35], we obtain for the density operator, which is stationary in this case,

$$\rho_{\text{can}} = \frac{\exp[-\beta(H_0 - \mu N)]}{\text{Sp}[\exp(-\beta H_0)]}, \quad (31)$$

where

$$H_0 = \sum_j \varepsilon_j a_j^\dagger a_j \equiv \sum_j \varepsilon_j N_j, \quad \beta \equiv \frac{1}{k_B T},$$

and μ is the chemical potential.

The quantum-mechanical mean for the operators O of the system is defined in this case as

$$\langle O\rangle_T = \text{Sp}(\rho_{\text{can}}O)/\text{Sp}(\rho_{\text{can}}). \quad (32)$$

By using (31) and (32), we obtain from (28) the system of equations for $\{\varepsilon_j, \phi_j\}$

$$\begin{aligned}&K_j(\mathbf{r})\phi_j(\mathbf{r})\langle n_j\rangle_T\\ &+ \phi_j(\mathbf{r})\int d^3 r'\phi_j^*(\mathbf{r}')U(\mathbf{r}-\mathbf{r}')\phi_j(\mathbf{r}')\langle n_j(n_j-1)\rangle_T\\ &+ \sum_{i\neq j}\phi_j(\mathbf{r})\int d^3 r'\phi_i^*(\mathbf{r}')U(\mathbf{r}-\mathbf{r}')\phi_i(\mathbf{r}')\langle n_i\rangle_T\langle n_j\rangle_T = 0.\end{aligned} \quad (33)$$

The value of the chemical potential μ can be determined for any fixed number of atoms in the trap because the condition

$$\bar{N} = \langle N\rangle = \sum_j\{\exp[\beta(\varepsilon_j - \mu)] - 1\}^{-1} \quad (34)$$

is fulfilled in the case of thermal equilibrium.

The calculation of the spatial distribution of the Bose condensate is greatly simplified if we assume that the temperature of the canonical ensemble $T = 0$ and only the lower state of the trap with the wave function ϕ_0 is populated, and $\varepsilon_0 = \mu$. Because the number of particles in the canonical ensemble is fixed, the creation (annihilation) operators a_0 ($a_0^\dagger$) should be replaced by c numbers equal to $\sqrt{N_0}$. Then, we obtain from (28)

$$\left[K_0(\mathbf{r}) + N_0\int d^3 r'\phi_0^*(\mathbf{r}')U(\mathbf{r}-\mathbf{r}')\phi_0(\mathbf{r}')\right]\phi_0(\mathbf{r}) = 0, \quad (35)$$

where

$$K_0(\mathbf{r}) = -\frac{\hbar^2}{2m}\nabla^2 + V_{\text{tr}}(\mathbf{r}) - \mu, \quad \varepsilon_0 = \mu.$$

Equation (35) is reduced to the usual Gross–Pitaevskii equation if we assume that the effective interaction between atoms of the type

$$U(\mathbf{r}-\mathbf{r}') = u\delta(\mathbf{r}-\mathbf{r}') + V_{dd}(\mathbf{r}-\mathbf{r}')$$

contains only the first term (pseudopotential).

As the crudest approximation for the density distribution, we can consider the equation

$$T(\mathbf{r})\phi_j(\mathbf{r}) = \varepsilon_j\phi(\mathbf{r}),$$

$$T(\mathbf{r}) = -\frac{\hbar^2}{2m}\nabla^2 + V_{\text{tr}}(\mathbf{r})$$

for the eigenfunctions and energy eigenvalues of the trap. It is assumed that collisions of atoms in the trap have no effect on the spatial distribution of the atomic field.

The approximation of the trap eigenstates was used in the quantum-mechanical models of an atomic laser [3–11], the coupling parameters (16), (17), and (19) being constant in time due to the assumption that the atomic-field distributions for all modes of the trap were independent of time.

4. CONTROL EQUATION FOR THE REDUCED DENSITY OPERATOR OF THE SYSTEM

By excluding variable reservoirs in a standard way using the Born–Markoff approximation, we obtained the "control" equation for the reduced density operator of the system. The presence of the reservoirs leads to the appearance of the irreversible processes of dissipation and extraction of the field from the trap, pumping, and spontaneous decay in the equation of motion. In the self-consistent model of the nonequilibrium Bose gas considered here, the coupling parameters $\mu_{\lambda,i}(t)$ and $\kappa_{\lambda,i}(t)$ entering the Hamiltonian (14), which are determined by integrating the wave functions of the field over spatial variables [expressions (16)–(19)], depend on time in the general case. Because the self-consistent scheme assumes the calculation of the wave function $\phi_j(\mathbf{r}, t)$ by solving Eqs. (27) and (28) at each instant of time, the coupling parameters also depend on time. The simplest approximation of the trap eigenstates used at present in the models of an atomic laser [3–11, 19–29] leads in general to the violation of the self-consistency in the calculation of the dynamics of the nonequilibrium Bose gas. In this paper, we consider the time dependence of the coupling parameters describing pumping processes and losses in the trap caused by the time dependence of the wave functions of the trap modes.

Because all the operators (20), (21) entering the Hamiltonian are bilinear in the creation and annihilation operators, the contribution to the coherent (unitary) component of the evolution of diagonal matrix elements is zero. All elastic collision processes have a dispersion nature and affect the time dependence of nondiagonal matrix elements and, hence, determine the degree of coherence of the first-order field.

The equation of motion for the reduced density operator of the system $\rho(t) = \mathrm{Sp}_R(\sigma_{\text{total}})$ is a sum of terms responsible for the irreversible processes of pumping and extraction of atoms from the trap and of losses and spontaneous transitions in atoms. In the interaction representation, we have

$$\dot{\rho}(t) = \frac{i}{\hbar}[\rho, V_{\text{coll}}] - \frac{1}{\hbar^2}\sum_{\beta}\int_0^t \mathrm{Sp}_R\{[V_{SR\beta}(t), [V_{SR\beta}(t'), \rho(t')f_0]]\}dt'. \quad (36)$$

In this representation, the time dependences of the creation (annihilation) operators related to the system and reservoirs are determined by the equations

$$O_j(t) = O_j\exp(-i\omega_{Oj}t), \quad O_j^\dagger(t) = O_j^\dagger\exp(i\omega_{Oj}t),$$

where ω_{Oj} is the eigenfrequency of the jth oscillator of the field. By substituting expression (25) for the total density operator into (36), we will keep in the obtained equation the terms up to second order inclusive in the interaction potential. Then, we will use the expressions for the interaction potentials of the type (14) in the equation obtained. Assuming that the coupling constants in (14) are independent of coordinates and using the Born and Markoff approximations [36], we obtain the control equation

$$\dot{\rho} = -\frac{i}{\hbar}[V_{\text{coll}}, \rho] - \frac{1}{2}\sum_j\{\gamma_j[\bar{N}_j^{\text{decay}}D[a_j^\dagger] + (\bar{N}_j^{\text{decay}}+1)D[a_j]] + p_j[\bar{N}_j^{\text{pump}}D[a_j^\dagger] + (\bar{N}_j^{\text{pump}}+1)D[a_j]]\}\rho \quad (37)$$

$$+ \frac{1}{2}\sum_{j>0}\{\gamma_{\text{sp},j}[\bar{N}_{j-1j}^{\text{phon}}D[a_{j-1}^\dagger a_j] + (\bar{N}_{j,j-1}^{\text{phon}}+1)D[a_{j-1}a_j^\dagger]]\}\rho$$

for the reduced density operator, where $D[O]\rho \equiv 2O\rho O^\dagger - O^\dagger O\rho - \rho O^\dagger O$ for the corresponding operator O. The terms in the control equation that are proportional to the frequency shift caused by the interaction of the system with reservoirs are omitted in (37), and they are assumed to be small below. Equation (37) was derived using the stationarity of random processes

$$\langle O_1(\tau)O_2(0)\rangle = \langle O_1(0)O_2(-\tau)\rangle,$$

where $O_1(t)$ and $O_2(t)$ are the operators of random processes related to reservoirs.

The loss and pump rates entering (37) have the form

$$\frac{\gamma_i}{2} = \sum_{j=0}^{\infty} \mathrm{Re}\left\{\int_0^{\infty} d\tau \exp(i\omega_i\tau)\mu^*_{\mathrm{out},j,i}(0)\mu_{\mathrm{out},j,i}(\tau) \times (\langle b_{\mathrm{out},j}(\tau)b^\dagger_{\mathrm{out},j}(0)\rangle - \langle b^\dagger_{\mathrm{out},j}(0)b_{\mathrm{out},j}(\tau)\rangle)\right\}, \quad i > 0, \tag{38}$$

$$\frac{p_i}{2} = \sum_{j=0}^{\infty} \mathrm{Re}\left\{\int_0^{\infty} d\tau \exp(i\omega_i\tau)\kappa^*_{p,j,i}(0)\kappa_{p,j,i}(\tau) \times [\langle b_{p,j}(\tau)b^\dagger_{p,j}(0)\rangle - \langle b^\dagger_{p,j}(0)b_{p,j}(\tau)\rangle]\right\}, \tag{39}$$

and the average occupation numbers of the pump and loss reservoirs are

$$\bar{N}_i^{\mathrm{decay}} = \frac{2}{\gamma_i}\sum_{j=0}^{\infty} \mathrm{Re}\left\{\int_0^{\infty} d\tau \exp(i\omega_i\tau)\mu^*_{p,j,i}(0) \times \mu_{p,j,i}(\tau)\langle b^\dagger_{\mathrm{out},j}(0)b_{\mathrm{out},j}(\tau)\rangle\right\}, \tag{40}$$

$$\bar{N}_i^{\mathrm{pump}} = \frac{2}{p_i}\sum_{j=0}^{\infty} \mathrm{Re}\left\{\int_0^{\infty} d\tau \exp(i\omega_i\tau)\kappa^*_{p,j,i}(0) \times \kappa_{p,j,i}(\tau)\langle b^\dagger_{p,j}(0)b_{p,j}(\tau)\rangle\right\}. \tag{41}$$

Note that the quantities p_i, $\bar{N}_i^{\mathrm{pump}}$, and γ_i, $\bar{N}_i^{\mathrm{decay}}$ can be both positive and negative, depending on the reservoir properties and the interaction dynamics.

As mentioned above, we will consider a simplified model of an atomic laser that takes into account the four lower states of a trap. We assume that pumping is performed only into the first $|1\rangle$ excited state of the trap, i.e., $p_j = 0$ if $j \neq 1$. The Bose condensate is extracted from the lower $|0\rangle$ state to vacuum. In this case, Eq. (37) can be written in the form

$$\dot{\rho} = -\frac{i}{\hbar}[V_{\mathrm{coll}}, \rho] + \frac{1}{2}\sum_j \{\gamma_j[\bar{N}_i^{\mathrm{decay}}D[a_j^\dagger] + (\bar{N}_i^{\mathrm{decay}} + 1)D[a_j]]\}\rho + \frac{1}{2}\kappa_{\mathrm{out}}D[a_0]\rho + \frac{1}{2}[p_1^{\mathrm{eff}}\bar{N}_1^{\mathrm{eff}}D[a_j^\dagger] + \gamma_1^{\mathrm{eff}}\bar{N}_1^{\mathrm{eff}}D[a_1]]\rho + \frac{1}{2}\sum_{j>0}\{\gamma_{\mathrm{sp},j}[\bar{N}^{\mathrm{phon}}_{j,j-1}D[a^\dagger_{j-1}a_j] + (\bar{N}^{\mathrm{phon}}_{j,j-1} + 1)D[a_{j-1}a_j^\dagger]]\}\rho, \tag{42}$$

where

$$p_1^{\mathrm{eff}}\bar{N}_1^{\mathrm{eff}} = \gamma_1\bar{N}_1^{\mathrm{decay}} + p_1\bar{N}_1^{\mathrm{pump}},$$

$$\gamma_1^{\mathrm{eff}}(\bar{N}_1^{\mathrm{eff}} + 1) = \gamma_1(\bar{N}_1^{\mathrm{decay}} + 1) + p_1(\bar{N}_1^{\mathrm{pump}} + 1)$$

are the effective pump and loss rates for the $|1\rangle$ state. The superscript "eff" will be omitted below.

In the model under study, the stimulated cooling of atoms in the trap is performed by the evaporation method, where the atoms are removed from the states $|2\rangle$ and $|3\rangle$ by a radio-frequency field that changes their electronic states. Assuming that the rates of extraction of atoms in the upper states from the trap are high, i.e.,

$$\gamma_2, \gamma_3 \gg p_1, \kappa_{\mathrm{out}}, \Omega_j, \gamma_{sp,i}, \quad i = 1, 2, 3, \quad j = 1, 2, \tag{43}$$

for the density operator, we perform the adiabatic exclusion of modes $|2\rangle$ and $|3\rangle$.

Using the Hamiltonian (14), we write the stochastic Heisenberg–Langevin equations for the operators a_2 and a_3 in the interaction representation (see, for example, [35] in the form

$$\dot{a}_2 = \frac{i}{\hbar}[a_2, V_{\mathrm{coll}}] - \frac{\gamma_2}{2}a_2 + \sqrt{\gamma_2}B_2(t), \tag{44}$$

$$\dot{a}_3 = \frac{i}{\hbar}[a_3, V_{\mathrm{coll}}] - \frac{\gamma_3}{2}a_3 + \sqrt{\gamma_3}B_3(t), \tag{45}$$

where the operators B_2 and B_3 of random sources satisfy the conditions

$$\langle B_i(t)\rangle_R = 0, \quad \langle B_i^\dagger(t)B_i(t')\rangle_R = 0,$$

$$\langle B_i(t)B_i^\dagger(t')\rangle_R = \delta(t - t'), \quad i = 2, 3.$$

By using in (44) and (45) the terms V_{coll} from (20) and (21) and neglecting the dispersion terms of the type $i\Delta_2 a_2$, $i\Delta_3 a_3$, which are caused by inelastic collisions, i.e., assuming that $\Delta_2, \Delta_3 \ll \gamma_2, \gamma_3$, we can easily obtain

$$\dot{a}_2 = -\frac{\gamma_2}{2}a_2 - ig_{0211}a_0^\dagger a_1^2 + \sqrt{\gamma_2}B_2(t), \tag{46}$$

$$\dot{a}_3 = -\frac{\gamma_3}{2}a_3 - ig_{0312}a_2a_0^\dagger a_1 + \sqrt{\gamma_3}B_3(t). \tag{47}$$

According to the assumption of adiabaticity, we have $da_2/dt = 0$ and $da_3/dt = 0$. By solving algebraic

equations, we find

$$a_2^{\mathrm{ad}} = -i\frac{2g_{0211}}{\gamma_2}a_0^\dagger a_1^2 + \frac{2}{\sqrt{\gamma_2}}B_2(t), \tag{48}$$

$$\begin{aligned} a_3^{\mathrm{ad}} &= -i\frac{4g_{0312}g_{0211}}{\gamma_3\gamma_2}a_0^\dagger a_1^3 \\ &+ \frac{2}{\sqrt{\gamma_3}}B_3(t) - i\frac{2g_{0211}}{\gamma_3\sqrt{\gamma_2}}B_2(t). \end{aligned} \tag{49}$$

By substituting adiabatic values (48) and (49) into the terms $\gamma_2 D[a_2]\rho/2$ and $\gamma_3 D[a_3]\rho/2$ in Eq. (42) and averaging over the reservoirs, we obtain the terms

$$\frac{\Omega_1}{2}D[a_0^\dagger a_1^2]\rho, \quad \frac{\Omega_2}{2}D[a_0^{\dagger 2}a_1^3]\rho$$

of the control equation, where

$$\Omega_1 = \frac{4|g_{0211}|^2}{\gamma_2}, \quad \Omega_2 = \frac{16|g_{0211}|^2|g_{0312}|^2}{\gamma_2^2\gamma_3}. \tag{50}$$

As a result, the "control" equation for irreversible processes can be written in the form

$$\begin{aligned} \dot\rho|_{\mathrm{irr}} = \Bigg\{ &\frac{\kappa_{\mathrm{out}} + \gamma_0(\bar N_0 + 1)}{2}D[a_0] + \frac{p_0}{2}\bar N_0 D[a_0^\dagger] \\ &+ \frac{\gamma_1}{2}(\bar N_1 + 1)D[a_1] + \frac{p_1}{2}\bar N_1 D[a_1^\dagger] \\ &+ \frac{\gamma_{\mathrm{sp}}}{2}\{(\bar N_{01} + 1)D[a_0^\dagger a_1] + \bar N_{01}D[a_1^\dagger a_0]\} \\ &+ \frac{\Omega_1}{2}D[a_0^\dagger a_1^2] + \frac{\Omega_2}{2}D[a_0^{\dagger 2}a_1^3]\Bigg\}\rho. \end{aligned} \tag{51}$$

Here, γ_{sp} is the rate of spontaneous transitions between the modes $|1\rangle$ and $|0\rangle$ of the trap and $N_{01} = N(\omega_{\mathrm{phon},\lambda}) = \langle b_{\mathrm{phon},\lambda}^\dagger b_{\mathrm{phon},\lambda}\rangle$, $\hbar\omega_{\mathrm{phon},\lambda} = \hbar(\omega_1 - \omega_0) = \hbar\omega_{01}$ is the average number of phonons in the thermal reservoir of spontaneous decay at the frequency of the $|1\rangle \longrightarrow |0\rangle$ transition in the trap. The spontaneous decay is analyzed under the assumption that the density of states of oscillators in the phonon reservoir weakly depends on the frequency [27, 28]. The parameters $\bar N_0$ and $\bar N_1$ in (51) are the average numbers of atoms in reservoirs related to the $|0\rangle$ and $|1\rangle$ states, respectively. They are calculated in the general case from expressions (40) and (41).

The rates Ω_1 and Ω_2 defined in (50) represent the effective rates of inelastic collisions involved in the creation of the Bose condensate in the ground state of the trap and corresponding, therefore, to stimulated transition in a usual laser.

Note also that condition (43), which means that the loss rates for nonlasing modes of the field are much higher than the pump rate, the rate of the coherent output of the lasing mode, and the effective rates of inelastic collisions, provides the low population of modes $|2\rangle$ and $|3\rangle$.

The diagonal matrix elements of the reduced density matrix $\rho_{n_0n_1}(t) \equiv \langle n_0n_1|\rho(t)|n_0n_1\rangle$ have the form

$$\begin{aligned} \dot\rho_{n_0n_1} = &[\kappa_{\mathrm{out}} + \gamma_0(\bar N_0 + 1)] \\ &\times [(n_0 + 1)\rho_{n_0+1,\,n_1} - n_0\rho_{n_0n_1}] \\ &+ p_0\bar N_0[n_0\rho_{n_0-1,\,n_1} - (n_0 + 1)\rho_{n_0n_1}] \\ &+ \gamma_1(\bar N_1 + 1)[(n_1 + 1)\rho_{n_0,\,n_1+1} - n_1\rho_{n_0n_1}] \\ &+ p_1\bar N_1[n_1\rho_{n_0,\,n_1-1} - (n_1 + 1)\rho_{n_0n_1}] \\ &+ \gamma_{\mathrm{sp}}\{(\bar N_{01} + 1)[n_0(n_1 + 1)\rho_{n_0-1,\,n_1+1} - n_1(n_0 + 1)\rho_{n_0n_1}] \\ &+ \bar N_{01}[n_1(n_0 - 1)\rho_{n_0+1,\,n_1-1} - n_0(n_1 + 1)\rho_{n_0n_1}]\} \\ &+ \Omega_1[n_0(n_1 + 1)(n_1 + 2)\rho_{n_0-1,\,n_1+2} \\ &- (n_0 + 1)n_1(n_1 - 1)\rho_{n_0n_1}] \\ &+ \Omega_2[(n_0 - 1)n_0(n_1 + 1)(n_1 + 2)(n_1 + 3)\rho_{n_0-2,\,n_1+3} \\ &- (n_0 + 2)(n_0 + 1)n_1(n_1 - 1)(n_1 - 2)\rho_{n_0n_1}]. \end{aligned} \tag{52}$$

The quantum-mechanical means of the operators of the number of atoms in the lower energy state of the trap (lasing mode) and of dispersion (fluctuation) of the number of atoms are calculated using the diagonal elements of the density matrix:

$$\langle n_{BC}(t)\rangle = \mathrm{Sp}(a_0^\dagger a_0\rho(t)) = \sum_{n_0,\,n_1} n_0\rho_{n_0n_1}(t), \tag{53}$$

$$\begin{aligned} \langle(\Delta n_i(t))^2\rangle \equiv \mathrm{Var}n_i &= \mathrm{Sp}(a_i^\dagger a_i a_i^\dagger a_i\rho(t)) = \langle n_i\rangle^2 \\ &= \sum_{n_0,\,n_1}(n_i - \langle n_i\rangle)^2\rho_{n_0n_1}(t), \quad i = 0, 1. \end{aligned} \tag{54}$$

The Fano factors for the Bose condensate in the ground state and in the first excited state of the trap are defined as

$$F_i = \langle(\Delta n_i)^2\rangle/\langle n_i\rangle, \quad i = 0, 1. \tag{55}$$

We will neglect below the pump rates for all modes except the $|1\rangle$ mode. The transitions of atoms from the lasing $|0\rangle$ mode to the thermostat will also be neglected. We also assume that the Bose condensate is extracted from the lower state of the trap to vacuum at the rate $\kappa_{\mathrm{out}} \gg \gamma_0(\bar N_0 + 1)$.

5. QUANTUM DYNAMICS AND STATISTICS OF AN ATOMIC LASER

The self-consistent theory of an atomic laser developed above assumes that Eqs. (27) and (28) for the wave functions $\{\phi_j(\mathbf{r}, t)\}$ of the field representing a system of coupled eigenvalue equations are solved by the iteration method simultaneously with the solution of the control equation (51) for the reduced density operator for an open system. Such a coupled system of equations can be solved only numerically. Its solution seems impossible at present because it is too cumbersome. In this paper, we calculated numerically the density matrix of the system in the approximation of the eigenstates of the trap, when the dissipation and pump rates are independent of time, i.e., in the approximation used in [3–9, 11, 19–24, 27, 28].

We solved numerically the system of coupled differential equations (52) for matrix elements $\rho_{n_0 n_1}(t)$ using the initial conditions $\rho_{n_0 n_1}(0) = \delta_{n_0, 0}\delta_{n_1, 0}$, i.e., when atoms were initially absent in the trap.

The generation dynamics of the atomic field for the three-level model of an atomic laser considered here depends qualitatively on the relations between the rate p_1 of pumping of the $|1\rangle$ state of the atomic trap, the extraction rate κ_{out} for the Bose condensate in the ground $|0\rangle$ state, the rate Ω_1 of stimulated transitions from the $|1\rangle$ state to the $|0\rangle$ and $|2\rangle$ states, and the rate γ_{sp} of spontaneous transitions from the $|1\rangle$ state to the $|0\rangle$ state due to the interaction with the reservoir. Under the assumption that the rate γ_{sp} is much lower than all other rates mentioned above, the lasing regimes of an atomic laser can be divided into two characteristic types. If $p_1 > \Omega_1$ and $p_1, \Omega_1 \sim \kappa_{out}$, then two stages of lasing dynamics are typical (see Figs. 1a and 1b). At first, the $|1\rangle$ state is populated, and the number of particles of a slowly accumulated Bose condensate in the $|0\rangle$ state is small, the fluctuations in the number of particles drastically increasing up to values that are typical for a random thermal field: $\langle(\Delta n_{BC})^2\rangle \approx (\langle n_0\rangle + 1)\langle n_0\rangle$. At the next stage, the number $\langle n_1\rangle$ of atoms decreases, whereas $\langle n_0\rangle$ increases and fluctuations $\langle(\Delta n_0)^2\rangle$ decrease, approaching the Poisson value equal to $\langle n_0\rangle_{ss}$ in the stationary state. For $p_1 < \Omega_1$ and $p_1, \Omega_1 \gg \kappa_{out}$, the stationary Bose condensate in the $|0\rangle$ state can be in a weakly squeezed sub-Poisson state $F_0 < 1$ (Fig. 1c).

When $p_1 \ll \Omega_1$ and $p_1, p_1, \Omega_1 \gg \kappa_{out}$, another regime of generation of the Bose condensate is realized (Fig. 2). There is no stage of population of the $|1\rangle$ state; a drastic increase in the fluctuations of the Bose condensate in the $|0\rangle$ state is also absent. The fluctuations of the Bose condensate can achieve the sub-Poisson values of the squeezed state (Fig. 2a). The population n_1 of the $|1\rangle$ state proves to be low at any time until the establishment of the stationary state, and the fluctuations $\langle(\Delta n_1)^2\rangle$ of the number of particles become essen-

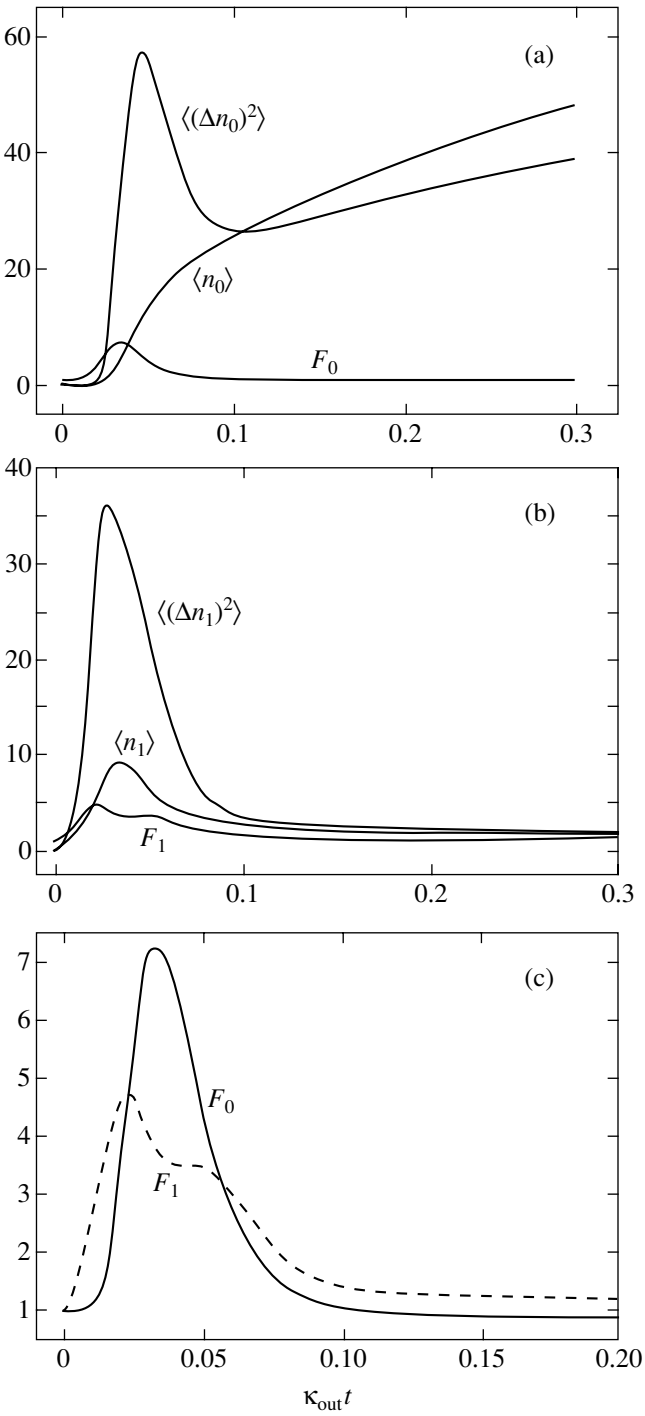

Fig. 1. (a) Dependences of the average number n_0 of atoms of the Bose condensate, the dispersion (fluctuations) $\langle(\Delta n_0)^2\rangle$ of the number of atoms, and the Fano factor $F_0 = \langle(\Delta n_0)^2\rangle/\langle n_0\rangle$ on the reduced time $\kappa_{out}t$ for the pump rate $p_1 = 100\kappa_{out}$, the rate of collision transitions $\Omega_1 = \kappa_{out}$, the average number of particles in the reservoir $\bar{N}_1 = 1$, and $\gamma_{sp} \ll \Omega_1$. (b) Dynamics of $\langle n_0\rangle$, $\langle(\Delta n_1)^2\rangle$, and $F_1 = \langle(\Delta n_1)^2\rangle/\langle n_1\rangle$ for the first excited state of the trap for the same parameters as in Fig. 1a. (c) Comparison of the dynamics of the Fano factors F_0 and F_1 for the same parameters as in Fig. 1a.

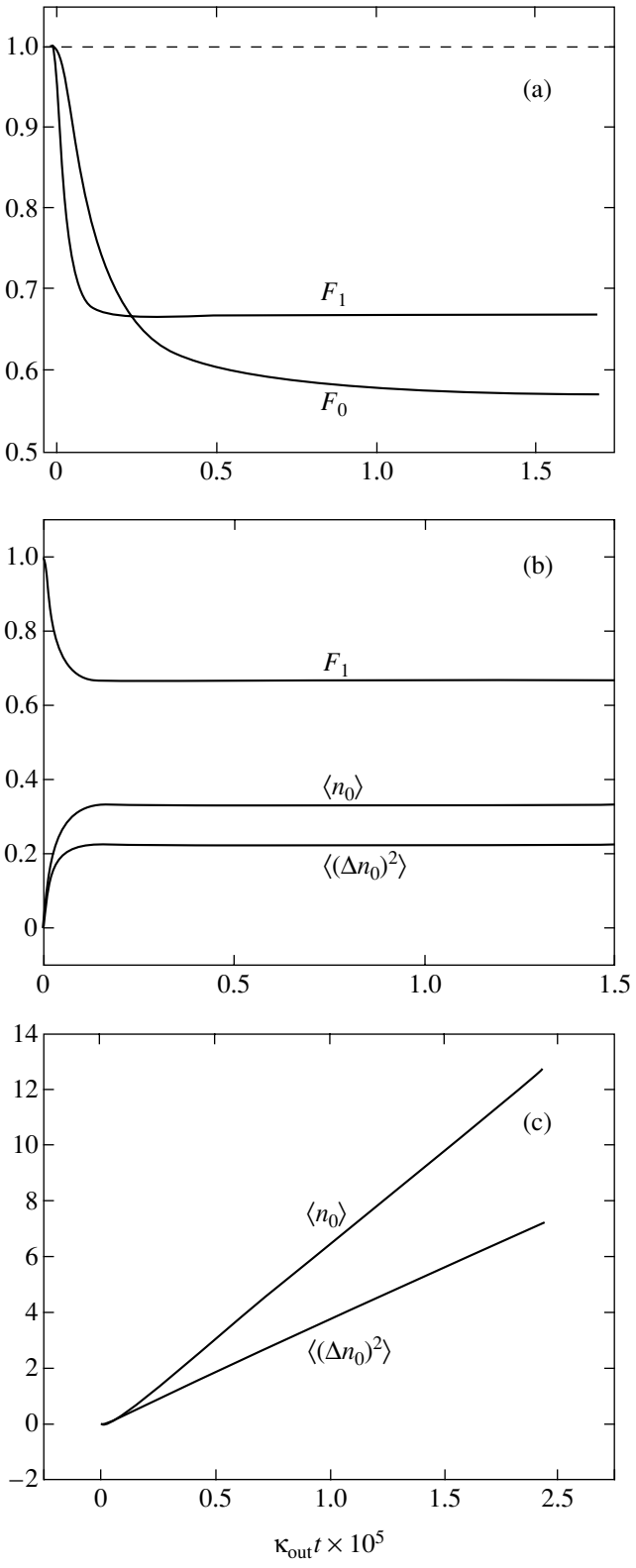

Fig. 2. (a) Dynamics of the Fano factors F_0 and F_1 for $p_1 = 10^6\kappa_{out}$, $\Omega_1 = 10^9\kappa_{out}$, $\bar{N}_1 = 1$, and $\gamma_{sp} \ll \kappa_{out}$. (b) Dynamics of $\langle n_1 \rangle$, $\langle (\Delta n_0)^2 \rangle$, and F_1 for the same parameters as in Fig. 2a: $\Omega_1 \gg p_1 \gg \kappa_{out} \gg \gamma_{sp}$. (c) Dynamics of n_0 and $\langle (\Delta n_0)^2 \rangle$ for the same parameters as in Fig. 2a.

tially sub-Poisson: $F_1 < 1$. In this regime, $p_1, \Omega_1 \gg \kappa_{out}$, and irrespective of the values of transition rates, the population $\langle n_1 \rangle_{ss}$ is equal to 0.333 for the dispersion of the number of particles $\langle (\Delta n_1)^2 \rangle_{ss} = 0.667 \langle n_1 \rangle_{ss}$ (Fig. 2b).

Systematic calculations showed that the condition for the creation of a Bose condensate in a squeezed sub-Poisson state is the relation $\Omega_1 \gg p_1 \gg \kappa_{out} \gg \gamma_1$, irrespective of the value of $\bar{N}_1$. The degree of squeezing increases with increasing number of bosons in the condensate, $\langle n_0 \rangle_{ss} \gg 1$, when $\Omega_1, p_2 \gg \kappa_{out}$. For the values of the laser parameters satisfying the inequalities $\Omega_1 \gg p_1 \gg \kappa_{out} \gg \gamma_1$, at which $\langle n_0 \rangle_{ss} \sim 10^6$, the maximum suppression of fluctuations achieves almost half the level of the shot noise. In this case, the Fano factor can achieve the value $F_{0,ss} \approx 0.54$ (Fig. 2a).

The calculations showed that, for $p_1 > \bar{N}_1 \gg \Omega_1$, $p_1\bar{N}_1 > \kappa_{out} \gg \gamma_1$, the stationary average number of atoms in the Bose condensate can be estimated from the expression

$$\langle n_0 \rangle_{ss} \approx \frac{p_1}{2\kappa_{out}}\left(\bar{N}_1 - \frac{1}{2} + \sqrt{\frac{1}{4} + \frac{\kappa_{out}}{\Omega_1}}\right). \qquad (56)$$

In [23], the control equation for the density operator in the model of an atomic laser, similar to that considered here, was transformed to the Fokker–Planck equation for the quasi-probability P function in the phase space of the amplitude and phase of the atomic field. The stochastic differential equations for the number of particles and phases of the fields in the trap modes, which were obtained from the Fokker–Planck equation, were solved in [23] under stationary conditions for average values. In the limit $\langle n_0 \rangle \gg 1$, the semiclassical average number of atoms in the lower state of the trap was found in [23, 26] in a form similar to (56). However, the sign of the square root, which was arbitrary within the framework of calculations performed in these papers, was chosen to be negative. Our exact quantum-mechanical calculations confirm the validity of expression (56), where the sign of the root is positive.

At the same time, for $p_1 \sim \bar{N}_1, \Omega_1$, the average number of atoms in the Bose condensate is described by the expression $\langle n_0 \rangle_{ss} = \eta p_1 \bar{N}_1 / \kappa_{out}$, where $\eta \approx 2$. This expression agrees qualitatively with calculations performed in [3] for a similar laser scheme, according to which $\langle n_0 \rangle_{ss} = 2p_1\bar{N}_1/3\kappa_{out}$ for the case $\Omega_1 > p_1$, $\bar{N}_1 \gg \kappa_{out}$ considered in [3]. The lasing threshold for the laser we considered is determined by the relation $p_1\bar{N}_1 > \kappa_{out}$.

It was assumed in calculations discussed above that the rate of spontaneous transitions between trap modes is much lower than the rates of other processes. The calculations performed under conditions when the rate of spontaneous transitions is comparable with the rate of extraction of the coherent condensate from the trap

($\gamma_{sp} = 0.5\kappa_{out}$ for $\bar{N}_{01} = 1$) are presented in Fig. 3. A comparison of the parameters characterizing the condensate under such conditions with the case of the absence of spontaneous decay ($\gamma_{sp} \ll \kappa_{out}$) shows that spontaneous transitions have no effect on the stationary mean value $\langle n_0 \rangle_{ss}$ but substantially enhance fluctuations $\langle (\Delta n_0)^2 \rangle_{ss}$ of the Bose condensate and change the lasing dynamics of an atomic laser.

The calculations of the lasing dynamics presented above were performed within the framework of the three-level model assuming that $\Omega_2 \ll \kappa_{out}$. To estimate the effect of high-lying energy levels of the trap on the dynamics and statistics of the generated condensate, we performed calculations for the case $\Omega_1 \sim \Omega_2$, i.e., for the four-level model of an atomic laser. Figure 4 shows the time dependences of the Fano factor for the four-level scheme at $\Omega_1 = \Omega_2$ and for the three-level scheme at $\Omega_2 = 0$. The comparison shows that, even when the upper levels are substantially populated, the fluctuations of the Bose condensate in the ground state of the trap increase only slightly (by several percent) at high rates of collision transitions.

Our calculations showed that a Bose condensate with minimal sub-Poisson fluctuations of the number of particles can be produced by the stimulated cooling of atoms, when the populations of the upper levels of the trap are always much lower than the population of the $|0\rangle$ ground state of the trap and of the $|1\rangle$ state through which pumping is performed.

The fluctuations of the number of particles in a Bose condensate were studied in [27–35] in thermal equilibrium for a fixed number of particles in a trap within the framework of a standard description of an ideal gas with the help of a canonical or a microcanonical ensemble. The numerical and analytic calculations of fluctuations in a canonical ensemble of noninteracting particles were performed in [31]. It was shown that the fluctuations of the Bose condensate consisting of 10^2–10^6 atoms in the trap approached almost linearly to zero at $T/T_c \longrightarrow 0$, where T_c is the critical temperature of the Bose condensation. The results obtained in [30, 32, 34, 35] for a microcanonical ensemble (the isolated state of atoms in the trap) agree qualitatively with data [31], fluctuations in a microcanonical ensemble always being greater than those in a canonical ensemble. It was found in [35] that, for small values of T/T_c, the magnitude of fluctuations was independent of the total number N of particles. Similar results were obtained in paper [32] for both canonical and microcanonical ensembles.

A canonical ensemble of particles with spontaneous transitions between the trap states was studied in [27–29]. Quantum-mechanical calculations performed in these papers also showed the achievement of the Fock state of an ideal Bose condensate at $T/T_c \longrightarrow 0$.

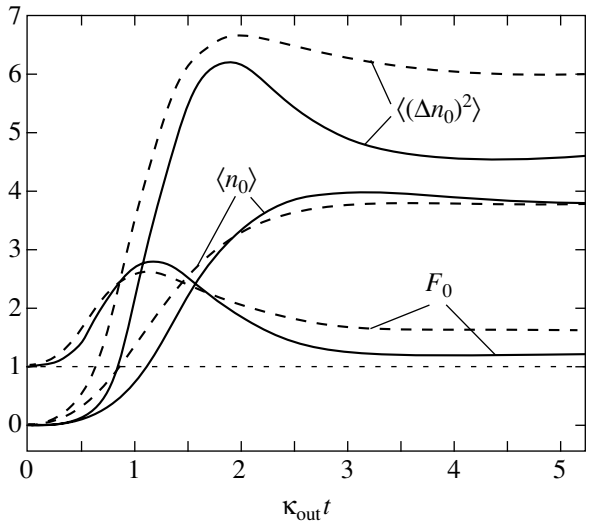

Fig. 3. Effect of spontaneous transitions on the dynamics of an atomic laser. The solid curves show the dynamics of the characteristics of the Bose condensate for the parameters of spontaneous transitions $\gamma_{sp} = 0.001\kappa_{out}$ and $\bar{N}_{01} = 0.001$. The dashed curves show the same quantities for $\gamma_{sp} = 0.5\kappa_{out}$ and $\bar{N}_{01} = 1$. The other parameters are $p_1 = 2\kappa_{out}$, $\Omega_1 = 0.1\kappa_{out}$, and $\bar{N}_1 = 1$.

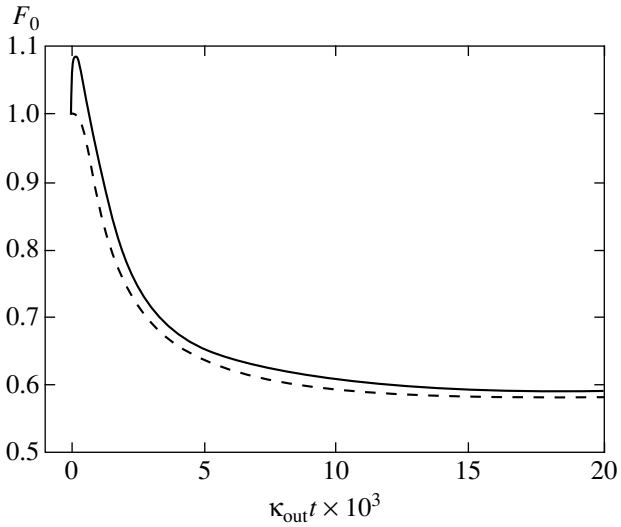

Fig. 4. Comparison of the dynamics of the Fano factor for the three- and four-level schemes of an atomic laser for $p_1 = 800\kappa_{out}$, $\Omega_1 = \Omega_2 = 1.6 \times 10^4 \kappa_{out}$, $\bar{N}_1 = 1$, γ_{sp}/κ_{out}, $\bar{N}_{01} \ll 1$ (four-level scheme: the solid curve) and $\Omega_2 = 0$ (three-level scheme: the dashed curve); other parameters are the same.

The authors of [35] have drawn other conclusions. The Hartree–Fock–Bogolubov–Popov theory used in this paper, which takes into account collisions between atoms in a trap at a fixed number of atoms and constant temperature, shows that the quantum statistics of the

atomic field tends to the Poisson statistics, which is typical for the coherent state of a Bose condensate when $T/T_c \longrightarrow 0$. The calculations [33] were performed under conditions of thermodynamic equilibrium ($T \neq 0$) for a large canonical ensemble of atoms taking into account collisions between atoms in a trap. A comparison of the results obtained in this paper with the data for the canonical and microcanonical ensembles of an ideal gas suggests that the Fock state with the sub-Poisson fluctuations of the number of particles can be obtained in thermal equilibrium only for an ideal gas when the number of particles is fixed. If the number of particles depends on other parameters of the system (a large canonical ensemble), an ideal Bose gas exhibits thermal (random) fluctuations at any temperature. However, collisions between atoms at low temperatures ($T < T_c$) reduce fluctuations to the Poisson level, which is typical for the coherent state of the field.

It has been shown in this paper that, under nonequilibrium thermodynamic conditions, a Bose condensate can be produced in a partially squeezed state. The model of an atomic laser considered in the paper provides a twofold reduction of fluctuations of the atomic field compared the Poisson level.

6. CONCLUSIONS

The model of interaction of a system of Bose particles in a trap with reservoirs considered in this paper predicts the possibility of realization of super-Poisson and sub-Poisson statistics of a Bose condensate produced in the trap. In the scheme of stimulated evaporation cooling, when only a small number of the lower energy states of the trap are noticeably populated during the establishment of a stationary regime, the sub-Poisson squeezing of the Bose condensate in the ground state of the trap is not stronger than twofold.

Our calculations have shown that the effect of the upper states of the trap on the statistics of the Bose condensate is negligible. At the same time, spontaneous transitions between the states of the trap lead to a considerable increase in the fluctuations in the number of particles.

Our calculations have shown that an evaporation-cooled cw atomic laser can produce both the Bose microcondensate with the average number of particles $\langle n_0 \rangle \sim 10$ and the Bose macrocondensate with $\langle n_0 \rangle \sim 10^6$ in a squeezed sub-Poisson state. However, the fluctuations in the number of particles in the microcondensate only slightly differ from the Poisson level, whereas, in the macrocondensate, a large, almost twofold, reduction of fluctuations is observed (the Fano factor $F_{BC} \longrightarrow 0.5$). The conditions for the generation of a squeezed Bose condensate are the low rates of extraction of the coherent atomic field from the trap and of spontaneous transitions between the trap modes compared to the rates of incoherent pumping and stimulated transitions in collisions between atoms in the trap. The results obtained in the paper suggest the existence of atomic lasers capable of generating relatively small Bose condensates in the states that are close to the Fock state. Such lasers can be considered as sources of individual groups of ultracold atoms with a prescribed exact number of atoms, which are required for a number of experiments of current interest in the optics of atoms and photons.

ACKNOWLEDGMENTS

I thank A.N. Oraevskiĭ for useful discussions.

REFERENCES

1. M.-O. Mewes, M. R. Andrews, D. M. Kurn, *et al.*, Phys. Rev. Lett. **78**, 582 (1997).
2. I. Bloch, T. W. Hansch, and T. Eslinger, Phys. Rev. Lett. **82**, 3008 (1999).
3. M. Holland, K. Burnett, C. Gardiner, *et al.*, Phys. Rev. A **54**, R1757 (1996).
4. H. M. Wiseman and M. J. Collett, Phys. Lett. A **202**, 246 (1995).
5. Ch. J. Borde, Phys. Lett. A **204**, 217 (1995).
6. U. Janicke and H. Wilkens, Europhys. Lett. **35**, 561 (1996).
7. M. Guzman, M. Moore, and P. Meystre, Phys. Rev. A **53**, 977 (1996).
8. H. M. Wiseman, A. Martin, and D. F. Walls, Quantum Semiclassic. Opt. **8**, 737 (1996).
9. H. M. Wiseman, Phys. Rev. A **56**, 2068 (1997).
10. M. J. Steel, M. K. Olsen, L. I. Plimak, *et al.*, Phys. Rev. A **58**, 4824 (1998).
11. R. Quadt, H. M. Wiseman, and D. F. Walls, Phys. Lett. A **219**, 19 (1996).
12. R. J. C. Spreew, T. Pfau, and M. Wilkens, Europhys. Lett. **32**, 469 (1995).
13. G. M. Moy, J. J. Hope, and C. M. Savage, Phys. Rev. A **55**, 3631 (1997).
14. A. N. Oraevskiĭ, Zh. Éksp. Teor. Fiz. **103**, 981 (1993) [JETP **76**, 480 (1993)].
15. A. Imamoglu, R. J. Ram, S. Pau, and Y. Yamamoto, Phys. Rev. A **53**, 4250 (1996).
16. A. N. Oraevskiĭ, Kvantovaya Élektron. (Moscow) **24**, 1127 (1997).
17. M. Naraschewski, A. Schenzle, and H. Wallis, Phys. Rev. A **56**, 603 (1997).
18. B. Kneer, T. Wang, K. Vogel, *et al.*, Phys. Rev. A **58**, 4841 (1998).
19. M. J. Steel and D. F. Walls, Phys. Rev. A **56**, 3832 (1997).
20. J. I. Cirac and M. Lewenstein, Phys. Rev. A **53**, 2466 (1996).
21. C. M. Savage, J. R. Roustekovski, and D. F. Walls, Phys. Rev. A **57**, 3805 (1998).
22. M. J. Moore and P. Meystre, Phys. Rev. A **56**, 2989 (1997).
23. O. Zobay and P. Meystre, Phys. Rev. A **57**, 4710 (1998).

24. E. V. Goldstein, O. Zobay, and P. Meystre, Phys. Rev. A **58**, 2373 (1998).
25. G. M. Moy, J. J. Hope, and C. M. Savage, Phys. Rev. A **59**, 667 (1999).
26. H. P. Breuer, D. Fallen, B. Kappler, and F. Petruccione, Phys. Rev. A **60**, 3188 (1999).
27. M. O. Scully, Phys. Rev. Lett. **82**, 3927 (1999).
28. V. V. Kocharovsky, M. O. Scully, S.-Y. Zhu, and M. S. Zubairy, Phys. Rev. A **61**, 023609 (2000).
29. J. J. Hope, G. M. Moy, M. J. Collett, and C. M. Savage, Phys. Rev. A **61**, 023603 (2000).
30. D. Jaksch, C. W. Gardiner, and P. Zoller, Phys. Rev. A **56**, 575 (1997).
31. H. D. Politzer, Phys. Rev. A **54**, 5048 (1996).
32. M. Gajda and K. Rzazewski, Phys. Rev. Lett. **78**, 2686 (1997).
33. R. J. Dodd, C. W. Clark, M. Edwards, and K. Burnett, Opt. Express **1**, 284 (1997).
34. N. L. Balazs and T. Bergeman, Phys. Rev. A **58**, 2359 (1998).
35. S. Grossman and M. Holthaus, Phys. Rev. Lett. **79**, 3557 (1997).
36. M. Lax, *Fluctuation and Coherence Phenomena in Classical and Quantum Physics* (Gordon and Breach, New York, 1968; Mir, Moscow, 1974).

Translated by M. Sapozhnikov